

COMPUTATIONAL INTERNAL DOSIMETRY METHODS AS APPLIED TO
THE UNIVERSITY OF FLORIDA SERIES OF HYBRID PHANTOMS

By

MICHAEL B. WAYSON

A DISSERTATION PRESENTED TO THE GRADUATE SCHOOL
OF THE UNIVERSITY OF FLORIDA IN PARTIAL FULFILLMENT
OF THE REQUIREMENTS FOR THE DEGREE OF
DOCTOR OF PHILOSOPHY

UNIVERSITY OF FLORIDA

2012

© 2012 Michael B. Wayson

To Leslie

ACKNOWLEDGMENTS

I would like to thank my doctoral dissertation chair, Dr. Wesley Bolch, for his extensive help, guidance, and mentoring throughout my time here at the University of Florida. My project would not be what it is if it wasn't for his input and guidance. He was always available when I needed a question answered or an idea critically assessed, and I was always able to talk out issues with him to make breakthroughs throughout my doctoral research. I will forever be grateful for the support he gave me during my time here.

I would like to thank the members of my committee (not in order of importance) – Dr. David Hintenlang, Dr. David Gilland, Dr. Stephen Hagen, Dr. George Sgouros, and Dr. Choonsik Lee. They were all instrumental in provided input and critically assessing my methods and approaches. I appreciate all they have done to maximize the effectiveness of my project. I would like to thank Dr. Choonsik Lee for his instruction in the use of MCNPX v2.6. Ever since 2006, he has helped me understand the intricacies and avoid the pitfalls of MCNPX v2.6.

I would like to thank all of my colleagues who have given me help along the way. The collaborative nature of our department truly facilitates progress. In no particular order I would like to thank Laura Padilla, Dr. Deanna Pafundi, Matthew Maynard, Dr. Perry Johnson, Dr. Justin Hanlon, Amir Bahadori, Daniel Long, Andres Abadia, Badal Juneja, and Lindsay Sinclair. There are others who have helped me, and if I left your name off this list, know that I am still appreciative.

Finally, I would like to thank my family for all of the support they have given me throughout the years, my loving wife who has always supported me in my academic endeavors, and my Lord and Savior Jesus Christ who has blessed me with many opportunities to pursue my goals.

TABLE OF CONTENTS

	<u>Page</u>
ACKNOWLEDGMENTS	4
LIST OF TABLES	10
LIST OF FIGURES	15
LIST OF ABBREVIATIONS.....	21
ABSTRACT.....	26
CHAPTER	
1 INTRODUCTION	28
Specific Aims.....	29
Hypothesis	29
Background.....	30
Overview of Nuclear Medicine Imaging Procedures and Dosimetry Concepts.....	32
History of Computational Dosimetry Phantoms.....	35
Stylized Phantoms	36
Voxel Phantoms.....	38
Hybrid Phantoms	39
Development of the UF Hybrid Computational Phantoms.....	40
Phantom Specificity.....	44
Relevant Radiological Physics	46
Photon Energy Deposition.....	47
Electron Energy Deposition	49
Photon-Electron Cascades	51
Absorbed Fraction of Energy	52
Effective Dose	53
Relevant Studies and Current Limitations.....	55
Phantom Blood Vessel Systems	56
MCAT to XCAT: the evolution of 4-D computerized phantoms for imaging research (Segars et al. 2009).....	56
The virtual family – development of surface-based anatomical models of two adults and two children for dosimetric simulations (Christ et al. 2010).....	57
Skeletal Photon Fluence-to-Dose Response Functions	58
Evolution and status of bone and marrow dose models (Stabin et al. 2002)	58
Specific absorbed fractions of energy at various ages from internal photon sources. I. methods” (Cristy et al. 1987)	60
Photon Specific Absorbed Fractions	62
Specific absorbed fractions of energy at various ages from internal photon sources. I. methods (Cristy et al. 1987)	62
ICRP 110: adult reference computational phantoms (ICRP 2009).....	65

Electron Specific Absorbed Fractions	67
Specific absorbed fractions of energy at various ages from internal photon sources. I. methods (Cristy et al. 1987)	67
ICRP 110: adult reference computational phantoms (ICRP 2009)	68
Dosimetric Sensitivity Analysis for Internal Sources	68
Patient-specific scaling of reference S-values for cross-organ radionuclide S-values: what is appropriate? (Petoussi-Henss et al. 2007).....	68
Changes in radiation dose with variations in human anatomy: larger and smaller normal-stature adults (Marine et al. 2010).....	70
Changes in radiation dose with variations in human anatomy: moderately and severely obese adults (Clark et al. 2010)	71
Internal Dosimetry Software	73
OLINDA/EXM: the second-generation personal computer software for internal dose assessment in nuclear medicine (Stabin et al. 2005).....	73
2 MATERIALS AND METHODS	95
Blood Vessel System for the UF Hybrid Phantom Family.....	95
Non-Uniform Rational B-Splines Model	95
Vascular Dosimetry for Blood Sources	98
Skeletal Photon Fluence-to-Dose Response Functions	102
Sub-Segmented Skeleton Development	102
Skeletal Photon Fluence-to-Dose Response Function Development	104
15-year-old and newborn phantoms	104
1-year-old, 5-year-old, and 10-year-old phantoms.....	107
Photon Specific Absorbed Fractions	113
Overview	113
Radiation Transport Code.....	114
Phantom Physical Characteristics.....	115
Blood-Inclusive Elemental Compositions	116
Phantom Preparation	125
Voxel Resolution	126
Initial Energies and Particle Histories	130
Tally Types	131
Miscellaneous Transport Details	133
Energy cutoff.....	133
Electron energy indexing algorithm	134
Source Tissues	137
Uniform source sampling	139
Non-uniform source sampling.....	140
Target Tissues.....	142
Photon Specific Absorbed Fraction Calculation	143
Variance Reduction Techniques	145
Overview	145
Reciprocity	146
Log-linear back-extrapolation	147
Three-point smoothing	149

Electron Specific Absorbed Fractions	149
Similarities to Photon Transport Methods.....	149
General Transport Methodology	150
Collisional Energy Loss Contribution to Dose.....	152
Tally types	152
Miscellaneous transport details	153
Collisional specific absorbed fraction calculation	153
Radiative Energy Loss Contribution to Dose.....	155
Methodology	155
Particle tracking.....	155
Particle histories	156
Radiative energy loss specific absorbed fraction calculation.....	158
Total Electron Specific Absorbed Fraction	159
Extra-skeletal sources.....	159
Intra-skeletal sources.....	160
Variance Reduction Techniques.....	161
Computing Resources and Runtimes.....	162
Radionuclide S Values.....	163
Biokinetics	166
Dosimetric Sensitivity Studies.....	168
Variation in Source and Target Size and Separation.....	170
Sphere studies.....	170
Validation studies.....	173
Variation in Anthropometric Characteristics.....	181
Sitting height	183
Weight	185
Constant weight with morphometry variation.....	186
Validation studies.....	189
Internal Dosimetry Software.....	193
3 RESULTS	239
UF Hybrid Phantom Blood Vessel System	239
Adult Male.....	239
Neck and clavicles.....	239
Arms	239
Thoracic and abdominal region.....	240
Legs	241
Whole-body.....	241
Remainder of Phantom Family.....	242
Vascular Dosimetry	243
Skeletal Photon Fluence-to-Dose Response Functions	244
Single-Image Radiation Transport Simulations	244
Response Functions	245
Photon Specific Absorbed Fractions	250
Electron Specific Absorbed Fractions	254
Dosimetric Sensitivity Studies.....	259

	Variation in Source and Target Size and Separation	259
	Photon self-dose	259
	Electron self-dose	261
	Photon cross-dose.....	262
	Electron cross-dose	265
	Variation in Anthropometric Characteristics.....	266
	Sitting height	266
	Weight	267
	Constant weight with morphometry variation.....	269
	Internal Dosimetry Software.....	270
4	DISCUSSION.....	320
	UF Hybrid Phantom Blood Vessel System	320
	Vascular Dosimetry	322
	Skeletal Photon Fluence-to-Dose Response Functions	325
	Photon Specific Absorbed Fractions	326
	Electron Specific Absorbed Fractions	329
	Dosimetric Sensitivity Studies.....	332
	Variation in Source and Target Size and Separation.....	332
	Photons	332
	Electrons.....	339
	Variation in Anthropometric Characteristics.....	343
	Sitting height dose scaling application.....	343
	Sitting height dose scaling validation.....	345
	Weight dose scaling application.....	347
	Weight dose scaling validation	349
	Combined dose scaling application.....	350
	Combined dose scaling validation.....	351
	Final morphometric dose scaling factors.....	353
	Internal Dosimetry Software.....	357
	Case Studies.....	359
	Radiopharmaceuticals.....	359
	Tc-99m labeled red blood cells	359
	Ga-67-citrate.....	360
	Biokinetics	360
	Dosimetry	360
	Results	361
	Clinical Application.....	364
5	CONCLUSIONS	409
	Blood Vessel Model	409
	Specific Absorbed Fractions and Skeletal Dosimetry	410
	Internal Dose Scaling.....	414
	Deliverables	415
	Future Work.....	416

APPENDIX

A	LARGE TABLES	419
B	SAMPLE FILES	466
	Lattice File	467
	Uniform Source File	469
	Non-Uniform Source File	471
	Input File.....	473
	LIST OF REFERENCES	480
	BIOGRAPHICAL SKETCH	488

LIST OF TABLES

<u>Table</u>	<u>Page</u>
1-1 Image set sources and voxel resolutions for the construction of the UF hybrid phantom family	76
2-1 Blood vessel wall thicknesses for the newborn to 1-year-old and adult reference individuals for the arterial, venous, and pulmonary systems.....	196
2-2 Width, height, and depth measurements and isotropic voxel resolutions for all bone sites in the UFH01MF, UFH05MF, and UFH10MF phantoms.....	197
2-3 Total matrix sizes and voxel numbers by width, depth, and height for all bone sites in the UFH01MF, UFH05MF, and UFH10MF phantoms	198
2-4 Percent regional blood distribution in the ICRP-reference adult male and female	199
2-5 Total blood volumes in the ICRP-reference human series	200
2-6 Derived vascular growth scaling factors for the brain, kidneys, trabecular bone, and cortical bone for the ICRP-reference human series	200
2-7 Derived regional blood distributions for the ICRP-reference pediatric human series and ICRP-reference adult regional blood distributions	201
2-8 Derived regional blood volumes for the ICRP-reference pediatric human series and ICRP-reference adult regional blood volumes.....	202
2-9 Derived regional blood distribution in volume percent for the UF series of hybrid computational phantoms	203
2-10 Derived regional blood masses for the UF series of hybrid computational phantoms	204
2-11 Voxel resolutions applied to the UF hybrid phantom family and resulting matrix sizes.....	205
2-12 Voxel resolution study showing doses calculated for a fine and course resolution phantom.....	205
2-13 Variance of energy deposition with changes in lower-bound electron energy cutoff values	206
2-14 Comparison of dosimetry results obtained using the MCNP-style bin-centered and ITS-style nearest-bin electron energy-indexing algorithms.....	207
2-15 Source tissues explicitly simulated in the UF hybrid computational phantom series.....	208
2-16 Source tissues mathematically assembled in the UF hybrid computational phantom	211

2-17	Target tissues explicitly simulated in the UF hybrid computational phantom series	212
2-18	Target tissues mathematically assembled in the UF hybrid computational phantom series	214
2-19	Biokinetic parameters for $^{99m}\text{Tc} - \text{DMSA}$ for the newborn patient	215
2-20	Morphometric measurements for the phantoms created to assess dosimetric sensitivity as a function of sitting height	216
2-21	Voxel resolutions and total matrix sizes for the phantoms created to assess dosimetric sensitivity as a function of sitting height	217
2-22	Morphometric measurements for the phantoms created to assess dosimetric sensitivity as a function of weight	218
2-23	Voxel resolutions and total matrix sizes for the phantoms created to assess dosimetric sensitivity as a function of weight.....	219
2-24	Morphometric measurements for the phantoms created to assess dosimetric sensitivity for patients of similar weight but different body morphometry	220
2-25	Voxel resolutions and total matrix sizes for the phantoms created to assess dosimetric sensitivity for patients of similar weight but different body morphometry ...	220
3-1	Volumes of the blood vessels in the UF phantom family.....	273
3-2	Superior (sup) and inferior (inf) diameters of the blood vessels in the UF phantom family	274
3-3	Photon SAFs (excerpt) for the UFH00MF pituitary gland source.....	275
3-4	Radiation absorbed dose per unit AA and comparison for two patients at the same weight but different body morphometry for $^{99m}\text{Tc} - \text{DMSA}$	276
3-5	Radiation absorbed dose and effective dose per unit AA and comparison for two patients at the same weight but different body morphometry.....	277
3-6	SAF and S value subroutine verification study for the liver source in the UFH00MF phantoms	278
4-1	Anterio-posterior (AP), lateral (LAT), and axial dimensions and prism volumes for blood vessel wall scaling methodology	367
4-2	SAFs to the blood vessel walls for a uniformly distributed blood source for the UF phantom family	367
4-3	Percent difference between the UFH00MF phantom and the ORNL adult stylized phantom skeletal fluence-to-dose response functions for selected bone sites	368

4-4	Energy-averaged percent differences between the UF hybrid phantom and ORNL stylized phantom monoenergetic photon SAFs	369
4-5	Absolute energy-averaged percent differences between the UF hybrid phantom and ORNL stylized phantom monoenergetic photon SAFs	369
4-6	Excerpt of the 3-D mass ratio scaling power matrix used to scaled photon self-dose.....	370
4-7	Photon self-dose scaling validation study for the photon spectrum of ^{99m}Tc	371
4-8	Photon self-dose scaling validation study for 4 MeV photons	372
4-9	Photon self-dose scaling validation study for 10 MeV photons	372
4-10	Patient-specific photon self-dose scaling validation study using all UF mass ratio scaling powers for ^{131}I photons.....	373
4-11	Excerpt of the photon cross-dose sphere SAFs showing a subset of the source masses, target masses, photon energies, and center-to-center separations	374
4-12	Photon cross-dose validation study using an arbitrary reference and non-reference set of spheres and liver- and pancreas-adjusted reference UFHADM phantom	375
4-13	Photon cross-dose scaling validation study showing predictive quality of UF scaling method as applied to patient-specific phantoms for ^{131}I photons	376
4-14	Excerpt of the 3-D mass ratio scaling power matrix used to scaled electron self-dose showing results for 4 MeV electrons	377
4-15	Electron self-dose scaling validation study for the electron spectrum of ^{99m}Tc	378
4-16	Electron self-dose scaling validation study for 4 MeV electrons	379
4-17	Electron self-dose scaling validation study for 10 keV electrons	379
4-18	Patient-specific electron self-dose scaling validation study using all UF mass ratio scaling powers for ^{90}Y beta particles.....	380
4-19	Electron cross-dose validation study using the liver- and brain-adjusted reference UFHADM phantom	381
4-20	Electron cross-dose validation study using the liver- and brain-adjusted reference UFHADM phantom	382
4-21	Percentage point gain in accuracy over reference values using dose scaling factors based on sitting height for the UFH00M-based phantom for ^{131}I photons.....	383
4-22	Percentage point gain in accuracy over reference values using dose scaling factors based on sitting height for the UFH00M-based phantom for ^{90}Y beta particles.....	384

4-23	Average percentage point gain in accuracy using dose scaling factors based on sitting height for all non-reference phantoms for ^{131}I photons	385
4-24	Average percentage point gain in accuracy using dose scaling factors based on sitting height for all non-reference phantoms for ^{90}Y beta particles	385
4-25	Percentage point gain in accuracy using dose scaling factors based on waist circumference for ^{131}I photons.....	386
4-26	Percentage point gain in accuracy using dose scaling factors based on waist circumference for ^{90}Y beta particles.....	387
4-27	Average percentage point gain in accuracy using dose scaling factors based on waist circumference for all non-reference phantoms for ^{131}I photons	388
4-28	Average percentage point gain in accuracy using dose scaling factors based on waist circumference for all non-reference phantoms for ^{90}Y beta particles	388
4-29	Percentage point gain in accuracy using dose scaling factors based on sitting height and waist circumference for the UFH00M-based phantom for ^{131}I photons.....	389
4-30	Percentage point gain in accuracy using dose scaling factors based on sitting height and waist circumference for the UFH00M-based phantom for ^{90}Y beta particles.....	390
4-31	Average percentage point gain in accuracy using dose scaling factors based on sitting height and waist circumference for all non-reference phantoms for ^{131}I photons	391
4-32	Average percentage point gain in accuracy using dose scaling factors based on sitting height and waist circumference for all non-reference phantoms for ^{90}Y beta particles ...	392
4-33	Photon internal dosimetry scaling factors (excerpt) for the shortest UFH00M-based phantom of the sitting height dosimetric sensitivity study	393
4-34	Photon internal dosimetry scaling factors (excerpt) for the tallest UFH00M-based phantom of the sitting height dosimetric sensitivity study	394
4-35	Percentage point gains in accuracy for interpolated sitting height- and waist circumference-based target-average dose scaling factors.....	395
4-36	Biokinetic data for $^{99\text{m}}\text{Tc} - \text{DMSA}$	396
A-1	All tissue names, tag identification numbers, and densities for all phantoms in the UF hybrid phantom family.....	420
A-2	Tissue masses in grams for all phantoms in the UF hybrid phantom family after voxelization.....	427

A-3	Blood inclusive elemental compositions in mass percent for all tissues in the UFH00MF phantoms	434
A-4	Blood inclusive elemental compositions in mass percent for all tissues in the UFH01MF phantoms	437
A-5	Blood inclusive elemental compositions in mass percent for all tissues in the UFH05MF phantoms	440
A-6	Blood inclusive elemental compositions in mass percent for all tissues in the UFH10MF phantoms	443
A-7	Blood inclusive elemental compositions in mass percent for all tissues in the UFH15M phantom	446
A-8	Blood inclusive elemental compositions in mass percent for all tissues in the UFH15F phantom	449
A-9	Blood inclusive elemental compositions in mass percent for all tissues in the UFHADM phantom	452
A-10	Blood inclusive elemental compositions in mass percent for all tissues in the UFHADDF phantom.....	455
A-11	Non-uniform source sampling probabilities for the UFH00MF phantoms	458
A-12	Non-uniform source sampling probabilities for the UFH01MF phantoms	459
A-13	Non-uniform source sampling probabilities for the UFH05MF phantoms	460
A-14	Non-uniform source sampling probabilities for the UFH10MF phantoms	461
A-15	Non-uniform source sampling probabilities for the UFH15M phantom	462
A-16	Non-uniform source sampling probabilities for the UFH15F phantom.....	463
A-17	Non-uniform source sampling probabilities for the UFHADM phantom	464
A-18	Non-uniform source sampling probabilities for the UFHADDF phantom.....	465

LIST OF FIGURES

<u>Figure</u>	<u>Page</u>
1-1 Artistic example of radiopharmaceutical biodistribution	77
1-2 Front and side views of the UF newborn physical phantom.....	78
1-3 The first stylized model of the trunk of an adult human.....	79
1-4 The MIRDP Pamphlet No. 5 revised stylized computational dosimetry phantom	80
1-5 The complete current ORNL stylized computational dosimetry phantoms series	80
1-6 The VIP-Man voxel phantom	81
1-7 Visual representation of the process by which patient images are used to create a hybrid NURBS phantom.....	82
1-8 The UF newborn hybrid female phantom as viewed in Rhinoceros™.....	83
1-9 The UF NURBS/PM-based hybrid phantom family.....	84
1-10 The continuum of phantom anatomic specificity.....	85
1-11 XCAT phantoms of the adult male, adult female, and newborn	86
1-12 Photon SAFs for the ICRP Publication 110 adult male voxel phantom	87
1-13 Electron SAFs for the ICRP Publication 110 adult male voxel phantom.....	88
1-14 Ratios of SAFs for a thyroid source of the original mass to SAFs for thyroid of the reference mass in each GSF voxel phantom to a kidney target	89
1-15 Ratios of SAFs for a liver source irradiating the red bone marrow to SAFs for the red bone marrow irradiating the liver for the family of GSF voxel phantoms	89
1-16 Ratios of SAFs for a self-irradiating thyroid source to SAFs for a self-irradiating thyroid source of reference mass for the family of GSF voxel phantoms	90
1-17 SAFs for selected source and target organs in the adult male phantom for varying weight percentiles	91
1-18. Cross-sections of the adult male and female voxelized NURBS phantoms at different levels of obesity	91
1-19 Input forms for OLINDA/EXM 1.0.....	92

2-1	Three-dimensional stylistic model showing different views for an excerpt of the irradiation geometries for the vascular dosimetry computational study.....	221
2-2	Sample heterogeneous skeletal sites of the UF newborn hybrid phantom showing the hand, right humerus, pelvis, and L-spine.....	222
2-3	Polygon mesh and voxel versions of the UFH01MF femur	223
2-4	Photon simulation flowchart used to generate monoenergetic photon SAFs	224
2-5	Illustration of artifact correction in <i>ImageJ</i> TM	225
2-6	UFH00F phantom voxelized at an isotropic resolution of 0.0663 <i>cm</i>	226
2-7	Number of particle histories simulated as a function of initial photon energy.....	226
2-8	Visual representation of uniform and non-uniform source sampling.....	227
2-9	Variance reduction technique flowchart used to improve the reliability of the monoenergetic photon and electron SAFs	228
2-10	Reverse Monte Carlo method demonstrating the reciprocity principle	229
2-11	Low energy photon back-extrapolation method.....	230
2-12	Three-point smoothing method.....	231
2-13	Electron simulation flowchart used to generate monoenergetic electron SAFs	232
2-14	Photon energy spectrum generated from simulating monoenergetic electrons in the liver of the UFH00M phantom	233
2-15	Graphical depiction of the systematic approach to studying dosimetric sensitivity with changes in source and target tissue size and separation.....	233
2-16	Patient-specific voxel phantom used for internal dosimetric mass-scaling analysis	234
2-17	Irradiation geometry for the photon cross-dose scaling validation study.....	234
2-18	Standing height as a function of total body mass for the NHANES III pediatric male population	235
2-19	Sample set of NURBS/PM phantoms created for the internal dosimetric standing height sensitivity study	236
2-20	Sample set of NURBS/PM phantoms created for the internal dosimetric weight sensitivity study	237
2-21	Phantoms created for the internal dosimetric body morphometry sensitivity study.....	238

3-1	Perspective views in Rhinoceros™ of the arteries and veins in the neck and clavicles, arms, thoracic and abdominal regions, and legs of the UFHADM phantom..	279
3-2	Blood vessel systems as implemented in the entire UF hybrid phantom family	280
3-3	Absorbed dose to the blood vessel wall from photons for vessels with 1 μm wall thickness as a function of vessel length and photon energy	281
3-4	Absorbed dose to the blood vessel wall from electrons for vessels with 1 μm wall thickness as a function of vessel length and electron energy.....	281
3-5	AFs as a function of initial electron energy for a uniform electron source in the spongiosa of the cranium in the UFH01MF phantom	282
3-6	Spongiosa/MC self-dose AFs as a function of initial electron energy for all bone sites in the UFH01MF phantom.....	282
3-7	AFs for spongiosa/MC irradiating cortical bone as a function of initial electron energy for all bone sites in the UFH01MF phantom	283
3-8	EFs for spongiosa/MC sources as a function of initial electron energy for all bone sites in the UFH01MF phantom.....	283
3-9	Skeletal fluence-to-dose response functions and skeletal fluence-to-kerma response functions for AM and TM50 targets in the mandible of the UFH00MF phantom	284
3-10	Skeletal fluence-to-dose response functions for all bone sites in the UFH00MF phantom for the AM target	285
3-11	Skeletal fluence-to-dose response functions for all bone sites in the UFH00MF phantom for the TM50 target.....	286
3-12	Skeletal fluence-to-dose response functions for the AM target in the cervical vertebra of all pediatric and adolescent phantoms	287
3-13	Skeletal fluence-to-dose response functions for the TM50 target in the cervical vertebra of all pediatric and adolescent phantoms	288
3-14	Excerpt of the photon SAF curves for a large (liver) and small (thyroid) source tissue in the UFH00MF phantoms	289
3-15	Photon mass attenuation coefficients as a function of initial photon energy.....	290
3-16	Photon SAFs showing $\Phi(liver \leftarrow liver)$ for all phantoms in the UF phantom family.....	291
3-17	Photon SAFs showing $\Phi(adrenals \leftarrow adrenals)$ for all phantoms in the UF phantom family	291

3-18	Photon SAFs showing $\Phi(\textit{muscle} \leftarrow \textit{lungs})$ for all phantoms in the UF phantom family	292
3-19	Photon SAFs showing $\Phi(\textit{brain} \leftarrow \textit{thyroid})$ for all phantoms in the UF phantom family	292
3-20	Photon SAFs showing $\Phi(\textit{adrenals} \leftarrow \textit{thyroid})$ for all phantoms in the UF phantom family	293
3-21	Electron SAFs for a uniform electron source in the liver of the UFH00M phantom using full transport techniques	293
3-22	A subset of the electron SAF curves for a large (liver) and small (thyroid) source tissue in the UFH00MF phantoms	294
3-23	Electron SAFs showing $\Phi(\textit{liver} \leftarrow \textit{liver})$ for all phantoms in the UF phantom family	295
3-24	Electron SAFs showing $\Phi(\textit{pituitary gland} \leftarrow \textit{pituitary gland})$ for all phantoms in the UF phantom family	295
3-25	Electron SAFs showing $\Phi(\textit{muscle} \leftarrow \textit{lungs})$ for all phantoms in the UF phantom family	296
3-26	Electron SAFs showing $\Phi(\textit{brain} \leftarrow \textit{thyroid})$ for all phantoms in the UF phantom family	296
3-27	Electron SAFs showing $\Phi(\textit{salivary glands} \leftarrow \textit{thyroid})$ for all phantoms in the UF phantom family	297
3-28	Sphere self-dose SAFs as a function of initial photon energy and sphere size for the photon self-dose scaling study	298
3-29	Mass scaling powers for photon self-dose showing the minimum, maximum, and average values at each photon energy	299
3-30	Mass scaling powers for photon self-dose as a function of both reference sphere mass and initial photon energy	299
3-31	Sphere self-dose SAFs as a function of initial electron energy and sphere size for the electron self-dose scaling study	300
3-32	Mass scaling powers for electron self-dose showing the minimum, maximum, and average values at each electron energy	301
3-33	Mass scaling powers for electron self-dose as a function of both reference sphere mass and initial electron energy	301

3-34	Photon specific absorbed fractions for different source spheres and 4 <i>MeV</i> photons as a function of sphere separation and target sphere mass.....	302
3-35	Photon specific absorbed fractions for the 2 <i>kg</i> source spheres and different photon energies as a function of sphere separation and target sphere mass	304
3-36	Photon specific absorbed fractions for the different source spheres and 4 <i>MeV</i> photons as a function of sphere separation and target sphere mass	305
3-37	Photon specific absorbed fractions for the 20 <i>g</i> source spheres and different photon energies as a function of sphere separation and target sphere mass	307
3-38	Electron specific absorbed fractions for the different source spheres and 4 <i>MeV</i> electrons as a function of sphere separation and target sphere mass	308
3-39	Electron specific absorbed fractions for the 20 <i>g</i> source spheres and different electron energies as a function of sphere separation and target sphere mass	310
3-40	Electron cross-dose SAFs for differing target sphere sizes for the 3.368 <i>cm</i> center-to-center separation and 20 <i>g</i> source sphere	311
3-41	Variations in SAF with changes in sitting height for uniform photon sources in the liver of the UFH00M-based phantoms	312
3-42	Variations in SAF with changes in sitting height for uniform electron sources in the liver of the UFH00M-based phantoms	313
3-43	Variations in whole-body SAF with changes in sitting height for uniform 4 <i>MeV</i> photon and electron sources in the liver of the study phantoms	314
3-44	Variations in SAF with changes in weight for uniform photon sources in the liver of the UFH00M-based phantoms	315
3-45	Variations in SAF with changes in weight for uniform electron sources in the liver of the UFH00M-based phantoms	316
3-46	Variations in whole-body SAF with changes in weightfor uniform 4 <i>MeV</i> photon and electron sources in the liver of the study phantoms.....	317
3-47	Radionuclide S values calculated using a summary of the radionuclide spectra compared to those calculated using the entire radionuclide spectra.....	318
3-48	Radionuclide S values calculated using direct spectrum sampling as compared to those calculated using an assembling of monoenergetic SAFs	318
3-49	Ratios of S values calculated using the internal dosimetry software S value subroutine to those calculated from direct spectrum sampling.....	319

4-1	Monoenergetic photon SAFs for a uniform blood source in the UFH00M phantom.....	401
4-2	Monoenergetic electron SAFs for a uniform blood source in the UFH00M phantom	401
4-3	Monoenergetic photon SAFs for a uniformly distributed blood source in all pediatric and adolescent phantoms in the UF hybrid phantom family	402
4-4	Average absorbed doses to the blood vessel wall of interest for the blood vessel wall dosimetry study	403
4-5	Top and perspective views of the final irradiation geometry designed to provide estimates of radiation absorbed dose to the walls of blood vessels in the human body ..	404
4-6	Monoenergetic photon SAFs to the blood vessel walls for a uniformly distributed blood source	404
4-7	Monoenergetic electron SAFs to the blood vessel walls for a uniformly distributed blood source	405
4-8	UF newborn hybrid phantom and ORNL adult male stylized phantom fluence-to-dose response functions for the cervical vertebra for the AM target.....	405
4-9	Comparison of specific absorbed fractions for photons sources in the liver and thyroid between UF, ORNL, and GSF phantoms	406
4-10	Two-simulation validation study for the UFH00M phantom	407
4-11	Internal anatomy comparison between the ORNL stylized 10-year-old and UFH10F phantoms	408

LIST OF ABBREVIATIONS

1-D	one-dimensional
2-D	two-dimensional
3-D	three-dimensional
4-D	four-dimensional
AA	administered activity
ACD	annihilation coincidence detection
AF	absorbed fraction
ALRADS	Advanced Laboratory for Radiation Dosimetry Studies
AM	active marrow
ANS	American Nuclear Society
AP	anterio-posterior
BMI	body mass index
BPR	blood perfusion rate
BS	bone surface
BVF	bone volume fraction
CAP	chest-abdomen-pelvis
CB	cortical bone
CBIST	chord-based infinites spongiosa transport
CBV	cortical bone volume
CDC	Centers for Disease Control and Prevention
CEL	collisional energy loss
CF	cellularity factor
CHO	channelized Hotelling observer
CMA	cortical marrow

CPE	charged particle equilibrium
CSDA	continuous slowing down approximation
CT	computed tomography
CV	coefficient of variation
DCF	dose conversion factor
DF	dose factor
DMSA	dimercaptosuccinic acid
DNA	deoxyribonucleic acid
DOCAL	dose calculations
DOD	Department of Defense
DRF	dose response function
EC	electron capture
EF	escape fraction
EGS4	Electron-Gamma-Shower version 4
EGSnrc	Electron-Gamma-Shower National Research Council
EXM	Exponential Modeling
FDA	Food and Drug Administration
FDG	fluorodeoxyglucose
FTM	full transport method
GSF	German Research Center for Environmental Health
GUI	graphical user interface
HCP	heavy charged particle
IC	internal conversion
ICRP	International Commission on Radiological Protection
ICRU	International Commission on Radiation Units and Measurements

IDL	Interactive Data Language
IM	inactive marrow
ITS	integrated TIGER series
KERMA	kinetic energy released per unit mass
LAT	lateral
LAR	lifetime attributable risk
LET	linear energy transfer
LUT	look-up table
<i>MATLAB</i> TM	Matrix Laboratory
MC	medullary cavity
mCBF	mean global cerebral blood flow
MCNPX	Monte Carlo N-Particle Extended
MIRD	Medical Internal Radiation Dose committee
MIRDOSE	MIRD dosimetry method-based internal dosimetry software
MR	magnetic resonance
MRI	magnetic resonance imaging
NCAT	NURBS cardiac torso phantom
NCI	National Cancer Institute
NHANES	National Health and Nutrition Examination Surveys
NIBIB	National Institute of Biomedical Imaging and Bioengineering
NIH	National Institutes of Health
NLM	National Library of Medicine
NURBS	non-uniform rational b-splines
OLINDA	Organ Level Internal Dose Assessment
OLINDA/EXM	Organ Level Internal Dose Assessment/Exponential Modeling

ORISE	Oak Ridge Institute for Science and Education
ORNL	Oak Ridge National Laboratory
PET	positron emission tomography
PIRT	paired-image radiation transport
PM	polygon mesh
PTRAC	particle tracking
RADAR	Radiation Dose Assessment Resource
RBC	red blood cells
RBE	relative biological effectiveness
rCBF	regional cerebral blood flow
REL	radiative energy loss
RIDIC	Radiation Internal Dose Information Center
ROC	receiver-operating-characteristic
ROI	region of interest
SAF	specific absorbed fraction
SIRT	single-image radiation transport
SNM	Society of Nuclear Medicine
Sp	spongiosa
SPECT	single photon emission computed tomography
TB	trabecular bone
TBS	trabecular bone surface
TBV	trabecular bone volume
TLD	thermoluminescent dosimeter
TM	total marrow
TM ₅₀	total shallow marrow

TMA	trabecular marrow
TSM	two-simulation method
UF	University of Florida
UFH00MF	UF newborn hybrid male and female computational phantoms (UFH00M indicates “male version”, and UFH00F indicates “female version”)
UFH01MF	UF 1-year-old hybrid male and female computational phantoms (UFH01M indicates “male version”, and UFH01F indicates “female version”)
UFH05MF	UF 5-year-old hybrid male and female computational phantoms (UFH05M indicates “male version”, and UFH05F indicates “female version”)
UFH10MF	UF 10-year-old hybrid male and female computational phantoms (UFH10M indicates “male version”, and UFH10F indicates “female version”)
UFH15M	UF 15-year-old hybrid male computational phantom
UFH15F	UF 15-year-old hybrid female computational phantom
UFHADM	UF adult hybrid male computational phantom
UFHADF	UF adult hybrid female computational phantom
VB	Visual Basic
XCAT	Extended Cardiac Torso Phantom

Abstract of Dissertation Presented to the Graduate School
of the University of Florida in Partial Fulfillment of the
Requirements for the Degree of Doctor of Philosophy

COMPUTATIONAL INTERNAL DOSIMETRY METHODS AS APPLIED TO
THE UNIVERSITY OF FLORIDA SERIES OF HYBRID PHANTOMS

By

Michael B. Wayson

August 2012

Chair: Wesley Bolch
Major: Biomedical Engineering

Two primary areas of consideration for dosimetry of nuclear medicine imaging and therapy procedures are (1) the organ absorbed dose calculations, taking into account size, shape, and proximity of all internal organs as well as the energy and type of radiation emitted, and (2) biokinetic models, taking into account how the radiopharmaceutical distributes throughout the body as a function of time. This study focuses on methods used to estimate radiation absorbed dose to organs of the human body from internal radiation emitting nuclides. Estimating absorbed dose to human tissues from radiations emitted from inside the body is known as internal dosimetry and is an integral part of performing risk assessment for the induction of secondary cancers, nuclear medicine image optimization, and limitation of dose to non-targeted organs in radiopharmaceutical therapy.

This study developed a new system of blood vessels, and the subsequent iteration of phantoms represents the latest University of Florida (UF) hybrid computational phantom (computerized representation of the human body) family. Skeletal photon fluence-to-dose response functions were computed for the pediatric and adolescent series of UF phantoms to allow for the determination of absorbed dose to the skeletal tissues at risk for radiogenic leukemia and osteosarcoma. A complete set of photon and electron specific absorbed fractions

(SAFs) were computed for the entire family of UF phantoms. SAFs are used with radiopharmaceutical biokinetic data to determine individual organ doses. Variations in radiation absorbed dose with changes in source and target organ masses, and source and target organ separation, and body habitus were investigated. These dosimetric sensitivity studies led to useful dose scaling methods for individual patients when patient-specific imaging-based methods of internal dosimetry are not available. Results of the SAF calculations and scaling methodologies can be incorporated into software, thus facilitating their ease of use.

Improvements in the accuracy of internal dose estimates allows for optimization of nuclear medicine imaging procedures and assessment of dose to normal tissues at risk during molecular radiotherapy procedures. In all cases, effectively balancing radiation dose with adequacy of clinical outcomes can be better achieved with more accurate patient dose estimates.

CHAPTER 1 INTRODUCTION

“Our goal is to ensure that all children receive safe, quality care when they undergo medical imaging examinations” (American College of Radiology 2009). This statement was made by Marilyn Goske, MD, chair of the Alliance for Radiation Safety in Pediatric Imaging in a press release honoring the Alliance for their Image Gently campaign initiative. The Alliance was founded by a society consortium including the Society for Pediatric Radiology, the American Society of Radiologic Technologists, the American College of Radiology, and the American Association of Physicists in Medicine. The Image Gently campaign was created to educate radiologic technologists, medical physicists, radiologists, pediatricians, and parents about the radiation dose to children during computed tomography (CT) exams (American College of Radiology 2009). Recently, the Alliance has created a new campaign that emphasizes radiation dose awareness during fluoroscopic procedures called Step Lightly (The Alliance for Radiation Safety in Pediatric Imaging 2009). It has been shown that children are at a higher risk of expressing radiation induced effects later in life than adults from medical procedures involving radiation (Harrison *et al.* 2007). This is explained by the fact that children are inherently more sensitive to radiation because their bodies are still developing along with the fact that children have a much longer time to express radiation induced effects. Although intuitive, these observations further emphasize that radiation dose to children must be minimized for any given medical diagnostic procedure. While the Image Gently and Step Lightly campaigns highlight the practice of minimizing radiation dose in CT and fluoroscopic imaging, they underscore the fact that radiation dose must be minimized for *any* medical procedure that involves ionizing radiation, including the imaging method of focus in this study: nuclear medicine. Very recently, a new official campaign called “Go with the Guidelines” was created to address this very issue

by publishing consensus guidelines for calculating patient-specific administered activities (AAs) for pediatric patients (SNM 2011). The scientific studies described in the current document work to improve the way nuclear medicine dosimetry is performed to help attain the ultimate goal of reducing radiation exposure to patients undergoing nuclear medicine procedures. The following numbered specific aims were performed to achieve this goal.

Specific Aims

1. Final improvements were made to the UF hybrid computational phantoms with the addition of large arteries and large veins, as well as the development of a model of organ distribution of blood by both age and gender.
2. Skeletal photon fluence-to-dose response functions were generated for the newborn (UFH00MF), one-year-old (UFH01MF), five-year-old (UFH05MF), ten-year-old (UFH10MF), fifteen-year-old male (UFH15M), and fifteen-year-old female (UFH15F) computational phantoms.
3. Photon specific absorbed fractions (SAFs) were computed for a variety of source-target-energy combinations for the UFH00MF, UFH01MF, UFH05MF, UFH10MF, UFH15MF, and UFHADMF computational phantoms.
4. Electron SAFs were computed for a variety of source-target-energy combinations for the UFH00MF, UFH01MF, UFH05MF, UFH10MF, UFH15MF, and UFHADMF computational phantoms.
5. Dosimetric sensitivity studies were performed to identify possible SAF scaling methodologies with respect to (1) variations in combinations of source and target size and separation and (2) variations in anthropometric characteristics.
6. *MATLAB*TM (The MathWorks, Inc., Natick, MA)-based subroutines were developed to implement the results of Aims 3 – 6 into a future internal dosimetry software package.

Hypothesis

The work that has taken place over the past several years within the Advanced Laboratory for Radiation Dosimetry Studies (ALRADS) has been focused on advanced techniques for modeling human anatomy and using these models to simulate the transport of ionizing radiation from medical imaging and therapy procedures. These advancements include updates to both the internal and external anatomy of human computational models used for dosimetry studies.

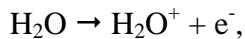
Because of these many improvements, the computational models and methods used in this study are arguably some of the most advanced in the field. As a result, the dosimetry performed in the current study is predicted to improve upon existing data, from the skeletal dosimetry models derived from actual human skeletal samples to the internal dose measures calculated for a complete set of source-target-energy combinations. The dosimetric sensitivity studies can be performed with powerful computing resources that allow for hundreds of simulations in parallel and so promise to reveal statistically reliable scaling techniques. Previous studies have shown that some scaling endpoints are difficult to achieve (e.g., photon and electron cross-dose), but predictable self-dose and human morphometric measurement-based scaling techniques are thought to be achievable based on the systematic nature of the studies and *a posteriori* knowledge of general dosimetric trends.

Background

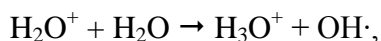
Occupational dosimetry in the clinical environment is typically assessed by way of physical dosimeters. Usually, thermoluminescent dosimeters (TLDs) and more recently optically stimulated luminescent dosimeters (OSLDs) are used to record an integral dose for medical workers whose duties include working with ionizing radiation sources. The dosimeters are then analyzed and the integral radiation dose is recorded for that worker. While this works well for determining occupational exposures, the patient undergoing a medical procedure involving ionizing radiation is rarely given physical dosimetry (e.g., select research investigations). This is due in large part to the difficult logistics and cost of patient physical dosimetry. Resultantly, alternative methods of determining patient organ and effective dose have been investigated extensively over the years. Accurately calculating both organ absorbed dose and patient effective dose are an important steps in managing the risks associated with medical imaging of the patient.

Quantifying radiation dose is essential for the purpose of radiation risk management. Retrospective studies performed on the Japanese atomic bomb survivors show that an increase in radiation dose leads to roughly proportional increases in excess cancer incidence for the study population (Hall *et al.* 2006). The result of that radiation risk study made it clear that excessive exposure to radiation is detrimental. While comprehensive studies of cancer risks associated with low doses of ionizing radiation are not feasible due to statistical reasons, the mechanisms for increased cancer risk from *any* exposure to radiation can be rationalized.

As a basic example, the mechanism for increased cancer risk from the absorption of electromagnetic radiation (a photon) is given below. The incident photon interacts with molecules within a cell in human tissue. Through either photoelectric absorption or Compton scattering interactions, electrons are liberated by these photon interactions. A free radical is thus formed, defined as an atom or molecule that possesses an unpaired orbital electron (Hall *et al.* 2006). For example, an interaction with a water molecule can produce the reaction



where the water molecule is ionized and an electron is liberated. The water ion radical then interacts with a second water molecule, producing the reaction



where $\text{OH}\cdot$ is a highly reactive species called the hydroxyl radical (Hall *et al.* 2006). The hydroxyl radical then may interact with deoxyribonucleic acid (DNA) to create a DNA radical which in turn may lead to a DNA single strand break. If the strand breaks are not repaired, DNA mutation can occur and lead to the induction of cancer. This is one example of how incident radiation, in this case, photons, may initiate cancer at the molecular level. It would follow that any incident ionizing radiation particle may initiate a similar cascade of damaging events.

The pertinent application to medical imaging is that one must always attempt to minimize the radiation dose to the patient. Obviously, medical imaging aims to procure a view of patient anatomy and/or physiology that can assist in an accurate diagnosis. Consequently, image quality is a priority when administering an imaging exam. There is a constant balance between radiation dose and image quality that medical professionals must always keep in mind when ordering and performing these patient exams. However, this is not always possible due to insufficient quantitative relationships between radiation dose and image quality. It is important for the dose estimates for these procedures involving radiation to be optimal in accuracy (i.e., the greatest accuracy should be achieved with reasonable runtimes), but uncertainties in risk estimates themselves probably always outweigh those of the dose estimates. In addition, uncertainties in biokinetic modeling usually outweigh those of the internal S value estimates.

Overview of Nuclear Medicine Imaging Procedures and Dosimetry Concepts

Nuclear medicine (or molecular) imaging is a powerful tool available to physicians for the diagnosis of many diseases. What sets nuclear medicine apart from other imaging modalities is that other modalities such as x-ray projection imaging, fluoroscopy, computed tomography (CT), and magnetic resonance imaging (MRI) are mostly useful for anatomic imaging, detailing the physical anatomy within a patient, while nuclear medicine is based fundamentally on imaging of patient metabolic processes, characterizing cell metabolism within the body (Cherry *et al.* 2003). Imaging modalities such as x-ray projection, fluoroscopy, and CT use a technique known as “transmission imaging”, so called because x rays are created *outside* of the body, transmitted through the body, and detected on the other side of the body by radiation detectors (Cherry *et al.* 2003). Nuclear medicine imaging uses a technique known as “emission imaging”, so called because photons are created (emitted) *inside* the body, travel through the body, and are detected outside of the body by radiation detectors (Cherry *et al.* 2003).

Two main modes of decay are utilized to create the nuclear medicine images: gamma emission and positron decay. Gamma emission is the mode used for single photon emission computed tomography (SPECT) and planar imaging (Cherry *et al.* 2003). SPECT uses position-sensitive gamma cameras to detect gamma rays at various angles around the body. A three-dimensional image is formed when the information collected from a subset of angles is assembled through reconstruction algorithms (Cherry *et al.* 2003). Planar images are formed when a single projection image is taken at one angle (Cherry *et al.* 2003). Positron decay is utilized for positron emission tomography (PET) imaging. Positrons annihilate¹ in human tissue and two photons are emitted in opposite directions and detected by radiation detectors. Using annihilation coincidence detection (ACD), PET system radiation detectors are able to localize where the annihilation event took place (Cherry *et al.* 2003).

A fundamental difference between nuclear medicine imaging/therapy procedures and structural imaging procedures such as x-ray projection imaging or CT scans is the location of the radiation source. For nuclear medicine imaging, a radiopharmaceutical is injected into the bloodstream of the patient and subsequently travels throughout the body to various organs/tissues of interest (Treves 1995). A typical radiopharmaceutical used for PET imaging is ¹⁸F –flurodeoxyglucose (¹⁸F – *FDG*), and the radionuclide, ¹⁸F, is produced using a cyclotron and the process ¹⁸O(*p, n*)¹⁸F (Cherry *et al.* 2003). The ¹⁸F is finally substituted into a glucose molecule for the purpose of assessing glucose metabolism (Cherry *et al.* 2003). Glucose is used by cells in the body in a process called glycolysis where the end product is adenosine triphosphate (ATP). ATP is subsequently used as energy for the cell (Cherry *et al.* 2003).

¹⁸F – *FDG* is an analog of glucose, and as such goes through phosphorylation step of glycolysis

¹ Positrons interact with electrons in tissue, and their rest mass energies are converted into two photons directly at approximately 180° from each other (Attix 2004).

(Joensuu *et al.* 1987). However, once phosphorylated, $^{18}\text{F} - \text{FDG}$ cannot proceed along the normal glycolysis pathway and it is not released from the cell (Joensuu *et al.* 1987). As a result, accumulation of $^{18}\text{F} - \text{FDG}$ in areas of the body is proportional to true levels of glucose metabolism (Joensuu *et al.* 1987). Energy requirements for diseased cells vary from healthy cells, so the accumulation of $^{18}\text{F} - \text{FDG}$ in a particular tissue of the body can be used to diagnose diseases or disorders (Cherry *et al.* 2003).

For radiation dosimetry purposes, the tissues in the body to which the radiopharmaceutical localizes are of great interest. When a radiopharmaceutical is injected into the bloodstream, it distributes throughout the body to various tissues, and these tissues in turn become sources of radiation emission and are called “source tissues”. This process is stylistically represented in Figure 1-1². Radiation is emitted from within the source tissues and deposits its energy in various tissues throughout the body, tissues known as “target tissues”, including the source tissue itself. Internal dosimetry refers to the process of estimating the amount of energy deposited in any target tissue per unit mass of that target tissue from radiation emitted from any source tissue. Once the energy deposited in all target tissues of interest from all source tissues of interest is determined, individual organ doses are estimated by combining absorbed doses from all source tissues according to the relative amount of radiopharmaceutical that localizes in the source tissues of interest. Finally, the individual organ doses may be mass-weighted to estimate whole-body dose. This description of estimating absorbed dose to individual organs and the whole body is presented in the way that internal dosimetry is approached in the current study but may not be the most utilized approach in the field. Those in the field think of dose to a certain tissue

² For reference modeling purposes, radiation emissions may be modeled as uniformly distributed throughout the tissues in which the radiopharmaceutical localizes. Non-uniform source distributions within a particular tissue can only be modeled if nuclear medicine images are available to determine voxel-by-voxel radiopharmaceutical uptake.

as a sum of dose contributions from a variety of source tissues, and the whole-body dose is calculated based on a whole-body S value. The mass weighting is not explicit to them.

History of Computational Dosimetry Phantoms

As previously discussed, it would not be feasible to use physical dosimeters to estimate organ doses for patients undergoing nuclear medical imaging procedures. Therefore, a quicker, more feasible method was developed in which computational dosimetry phantoms are used to determine organ doses in a virtual environment. Computational dosimetry phantoms are virtual/computerized representations of humans which are then input into radiation transport codes to calculate radiation dose from any number of radiation sources, both internal and external. This is in contrast to another type of phantom used for dosimetry – the physical dosimetry phantom. Physical dosimetry phantoms are actual constructs made to model human anatomy, based on the segmentation of tissue regions from CT or magnetic resonance (MR) image sets, that are imbedded with physical dosimeters to determine radiation absorbed doses to various points within the phantom (for nuclear medicine applications, cavities would be constructed that would be subsequently filled with radioactivity). An example of a physical phantom can be seen in Figure 1-2 (Jones *et al.* 2006). However, it is usually not optimal to utilize physical dosimetry phantoms for on-the-fly dosimetry because the construction process is time-consuming and difficult, and physical phantoms cannot be easily modified once built. Additionally, for nuclear medicine applications, biokinetics cannot be sufficiently modeled due to the immense complexity of constructing an activity transfer system (if even possible) and because any dose measuring devices inserted into the activity region must not displace any of the activity.

Computational dosimetry phantoms may be used to assess the radiation absorbed dose from a variety of radiation sources. Radiation sources from radiography, CT, or fluoroscopy are

known as external sources since the radiation is emitted from the machine and travels through the body while radiation sources from nuclear medicine imaging modalities such as PET and SPECT are known as internal sources since the radiation is emitted from within the body and travels out of the body. The emphasis of this study was the analysis of internal sources for the purpose of performing dosimetry for nuclear medicine imaging procedures.

Stylized Phantoms

Computational dosimetry phantoms composed of simple mathematical shapes are referred to as stylized phantoms. These phantoms are obviously not anatomically realistic in nature since internal and external structures of the human body can rarely, if ever, be accurately represented by simple shapes. However, the scalability of stylized phantoms makes it easy to change the body habitus or organ sizes of the phantoms.

An early attempt at creating a virtual representation of humans was described in the Society of Nuclear Medicine's (SNM) Medical Internal Radiation Dose (MIRD) committee Pamphlet No. 3 in 1968 (Brownell *et al.* 1968). The MIRD committee tabulated a set of photon absorbed fractions (AFs) for an adult phantom with internal and external structures represented by a combination of simple mathematical shapes such as spheres, ellipsoids, and elliptical and right circular cylinders (Brownell *et al.* 1968). Body tissues in this phantom were homogeneous in nature and elemental compositions included the elements hydrogen, carbon, nitrogen, oxygen, chlorine, and sodium (Brownell *et al.* 1968).

Another early model was developed by Oak Ridge National Laboratory (ORNL) in the early 1960s and was a whole-body model created for the purpose of external beam dosimetry (NCRP 1971). This model attempted to represent only the trunk of an adult and was a simple right circular cylinder 30 cm in diameter and 60 cm in height (NCRP 1971). While this model seems inordinately simple by modern standards, it was an effective way to obtain rough

estimates of whole-body radiation absorbed doses from a variety of medical procedures. This early generation phantom can be seen in Figure 1-3 (NCRP 1971).

In the mid-1960s, ORNL developed a new stylized adult phantom called the Fisher-Snyder Phantom (Snyder *et al.* 1969). This model consisted of three distinct regions: the head and neck, the trunk including arms, and the legs (Snyder *et al.* 1969). The head, neck, trunk, and arms were described by an elliptical cylinder, and the legs were represented by truncated elliptical cones (Snyder *et al.* 1969). Some structures left out of this model include hands, feet, ears, nose, lungs, and skeleton (Snyder *et al.* 1969). All tissues were assumed to be homogeneous (Snyder *et al.* 1969).

The MIRD committee published in 1969 an advancement of the Fisher-Snyder adult phantom in their 5th pamphlet (Snyder *et al.* 1969). The Fisher-Snyder phantom was a heterogeneous model of the adult and was officially called the MIRD Phantom (Snyder *et al.* 1969). In this phantom, 22 internal organs were modeled by way of three dimensional surface equations (Snyder *et al.* 1969). Three body tissues were modeled: skeletal tissue, lung tissue, and soft tissue (Snyder *et al.* 1969). Photon AFs were calculated for 12 energies, and particle histories between 25,000 and 50,000 were run for each simulation (Snyder *et al.* 1969). The MIRD Phantom was later revised in 1978 with improvements in the organ models and statistical reliability of the AFs. The number of photon histories was increased to 60,000 for each source organ (Snyder *et al.* 1978). The revised MIRD Pamphlet No. 5 adult phantom can be seen in Figure 1-4 (Snyder *et al.* 1978).

Development of pediatric models also took place in the 1970s at ORNL. Early attempts at pediatric models involved non-uniform down-scaling of the adult MIRD Phantom (Cristy *et al.* 1987). A newborn phantom along with 1-year-old, 5-year-old, 10-year-old, and 15-year-old

phantoms were created in this fashion (Cristy *et al.* 1987). Currently, the international standard for computational dosimetry phantoms is the phantom model series created in 1980 by Mark Cristy and Keith Eckerman (Cristy 1980, Cristy *et al.* 1987). These phantoms were a revision to the ORNL pediatric series of models and can be seen in Figure 1-5 (Cristy *et al.* 1987). The key improvements of these models were new models of the heart, breasts, and thyroid and a new model for skeletal dosimetry using skeletal fluence-to-dose response functions (Cristy *et al.* 1987). A complete set of SAFs were calculated for each of these phantoms.

Voxel Phantoms

In contrast to stylized phantoms where the internal and external structures of the human body are represented by mathematical equations and shapes, voxel phantoms are almost exactly representative of actual patient anatomy. Voxel phantoms are three-dimensional (3-D) matrices of rectangular prisms (voxels) where each voxel is assigned a unique identification number that indicates the type of tissue associated with the voxel of interest. This is accomplished by using image sets of actual patients and segmenting a variety of tissue volumes. Segmentation is performed by manually (and sometimes automatically) tracing the periphery of an organ of interest across all image slices containing the organ of interest. Once this is done for all pertinent image slices, the image segmentation software combines the image slice thickness and traced peripheries of the organ to create a three-dimensional volume. Once all tissues of interest are segmented, these volumes are then voxelized (converted into a three-dimensional matrix of rectangular prisms) for use in radiation transport codes. Frequently, but not always, the rectangular prisms are defined to have equal length sides, thereby forming a set of cubes known as isotropic voxels. If these cubes are created at a fine enough resolution, the original shape can be faithfully represented. It can be thought of as taking a photograph whereby a pixilated representation of a continuous object is created, and the higher the resolution of the image, the

more faithfully the person is represented. Voxelization is like taking a 3-D picture of a set of continuous objects, and the pixels, formerly in two-dimensions (2-D), are now voxels in 3-D.

Voxel phantoms are very anatomically realistic, but they are unable to be extended to a variety of patient morphometries due to their patient-specific nature. A phantom created from the image set of a specific patient can only be appropriately used for dosimetry on that patient or on patients with very similar body shapes and internal organ structure. It is very difficult to adjust the size and position of tissues within a voxel phantom to model changes in patient size since voxel phantoms are rigid in nature. Because the process of segmentation is time-consuming, individual voxel phantoms cannot be created for every patient who undergoes an imaging procedure. In addition, some structures in the body such as the large and small intestines are difficult to accurately segment on a CT or MR image set.

One previous voxel phantom was the VIP-Man, created using transverse color photographic images from the Visible Human Project of the National Library of Medicine (NLM); the subject was a recently executed 38-year-old male from Texas (Xu *et al.* 2000). The resulting voxel model can be seen in Figure 1-6 (Xu *et al.* 2000). Another example of previous voxel phantoms is the GSF voxel phantom family (Petoussi-Henss *et al.* 2002). This set of phantoms includes females of 8 weeks, 7 years, 26 years, and 40 years, males of 38 years, a second 38-year-old, 48 years, and an unknown age phantom, two physical phantoms representing a torso and head and the thorax, and one female standardized gastrointestinal tract (Petoussi-Henss *et al.* 2002). This family of voxel phantoms can be seen in Petoussi-Henss *et al.* (2002).

Hybrid Phantoms

Both voxel phantoms and stylized phantoms have positive and negative attributes. Stylized phantoms have unrealistic anatomy but are easily deformable while voxel phantoms have realistic anatomy but are difficult to modify. The drawbacks of these respective options for

computational radiation dosimetry necessitated a bridge between the stylized and voxel phantoms which would allow for anatomic realism as well as deformability. This study addresses that void and describes the recent addition of a new type of computational phantom: the hybrid phantom. The hybrid phantom combines elements of both stylized and voxel phantoms to create a phantom with anatomic realism and deformability.

Development of the UF Hybrid Computational Phantoms

The computational dosimetry phantoms discussed previously represent the 1st and 2nd generation phantoms. The simple stylized phantoms based on mathematical functions are 1st generation phantoms. The medical image-based voxel phantoms are 2nd generation phantoms. A 3rd generation phantom has recently emerged and has progressed extensively at UF. This 3rd generation phantom combines the concepts of the 1st and 2nd generation phantoms to yield a new type of phantom that is anatomically realistic and easily deformable.

NURBS modeling – A non-uniform rational b-spline (NURBS) surface is a mathematical modeling technique commonly used in computer animation whereby 3-D continuous surfaces are defined by a series of control points. NURBS surfaces can model virtually any free-form shape, and thus they are very useful in modeling complicated volumes such as human organs and body regions.

The mathematics of NURBS surfaces can be explained by addressing the mathematics behind NURBS curves. Instead of using explicit equations (such as a sine or cosine function, for example) to define curves in 3-D modeling software, parametric equations are used to allow curves to move back over themselves (Schneider 1996). As an example, the equation $Q(t) = [X(t), Y(t)]$ could be defined by $X(t) = \cos(t)$ and $Y(t) = \sin(t)$, giving the equation of a circle (Schneider 1996). A simple equation could not achieve shapes looping back on

themselves because two different values of Y would not be allowed for X . As previously mentioned, a NURBS surface, and hence a NURBS curve, is defined by a series of control points that define the shape of the surface or curve. Imagine a moving point that defines a NURBS curve. The position of this point at any time could be defined by Equation 1-1 (Schneider 1996).

$$Q(t) = \sum_{i=0}^{n-1} B_i N_{i,k}(t) \quad (1-1)$$

where $Q(t)$ is the position of the point for any time t , B_i is the position of control point i , $N_{i,k}(t)$ is the influence of each control point on the point defining the curve at time t (otherwise known as a “basis” function), and n is the number of control points.

The basis function (the “b” in NURBS) controls the strength with which the control point coordinates influence the position of the curve. At any point in time, the sum of all basis functions is equal to unity (Schneider 1996). An example given in Schneider (1996) is a series of bell curves at subsequent arbitrary time points 0 – 4 with widths at $N_{i,k}(t) = 0$ of 3. These are equally sized overlapping bell curves. The width of the basis functions can be modified to affect the overall area the function has influence on the curve position (i.e., the positions along the curve that the basis function of the control point has influence over), and the height of the basis functions can be modified to affect the magnitude of this influence (Schneider 1996). This ability to change basis function shapes is the reason the curves are called “non-uniform”. These curves are also referred to as “rational” because a weight can be assigned to each control point to change the amount the curve is pulled toward the control point (Schneider 1996).

NURBS surfaces are both flexible and easily modifiable, and thus NURBS technology was selected as the primary method to create a new generation of phantoms that are both anatomically realistic as well as easily deformable. Since this 3rd generation phantom combines

elements of stylized and voxel phantoms (as will be discussed later), the 3rd generation phantom has been termed a “hybrid” computational dosimetry phantom.

UF phantom family construction – To illustrate the process of creating the UF family of hybrid computational phantoms, construction of the newborn phantom will be described. The UF newborn hybrid phantom is an advancement of the previous UF newborn voxel phantom (Lee *et al.* 2007) that was constructed from a CT scan of a 6-day-old female (Nipper *et al.* 2002). This scan was saved as a $512 \times 512 \times 485$ data array with a slice thickness of 1 *mm*. At this slice thickness and data array size, the UF newborn voxel model was the highest resolution model at the time (Nipper *et al.* 2002). Delineation of organs was then performed using an in-house Interactive Data Language (IDL) (ITT Visualization Solutions, Boulder, CO) code, and 66 different anatomic regions were defined (Nipper *et al.* 2002). The UF newborn voxel model can be seen in Nipper *et al.* (2002).

The computer software *3D-DOCTOR*TM (Able Software Corp., Lexington, MA) was used to convert the UF newborn voxel phantom into polygon mesh (PM) geometry. The voxel phantom was imported into *3D-DOCTOR*TM, and individual organs were segmented using interactive segmentation tools (Lee *et al.* 2007). Once all organs of interest were segmented, the PM model was imported to *Rhinoceros*TM (McNeel North America, Seattle, WA), a NURBS modeling software, to transform the PM geometry into NURBS geometry. Seven distinct anatomic groups were defined and imported separately into *Rhinoceros*TM – the exterior body contour, the respiratory system, the alimentary system, the circulatory system, the urogenital system, other soft tissue organs, and the skeleton (Lee *et al.* 2007). The organs of interest were then converted to NURBS surfaces. NURBS surfaces are easier to manipulate than PM volumes because NURBS surfaces are defined by a series of control points which can be individually

manipulated in 3-D. Volumes bounded by NURBS surfaces can easily be scaled in one dimension (1-D), 2-D, or 3-D. Because of this, the majority of internal organs were modeled with NURBS surfaces rather than PM volumes.

Conversion from polygon mesh geometry originating from segmented images to NURBS geometry was relatively straightforward for most tissues, but several small organs and organs that were difficult to segment from the original CT data necessitated a different approach. Small organs such as the eyes, lenses, ovaries, urinary bladder, breasts, pituitary gland, and tonsils were modeled using stylistic NURBS-based models (Lee *et al.* 2007). The original shapes and positions of these organs were referenced from the CT data and faithfully followed in the construction of stylistic representative shapes. The contents of walled organs such as the heart, gall bladder, and urinary bladder were modeled by replicating the organ wall and scaling inward (Lee *et al.* 2007). The esophagus, small intestine, colon, and rectum were unable to be segmented from the original CT data, so a 3-D trace of the lumen centroid was approximated from the segmented UF newborn voxel phantom (Lee *et al.* 2007). This was not feasible for the small intestine due to CT slice discontinuity, so a stylistic model was created and approved by a pediatric radiologist (Lee *et al.* 2007). A visual representation of the process by which patient images are used to create a hybrid phantom is in Figure 1-7.

At this point, a non-reference newborn hybrid computational dosimetry phantom was completed, but the model only represented the patient from which the original CT data was obtained. This patient was not necessarily representative of reference³ values defined by the International Commission on Radiological Protection (ICRP) for the newborn. Therefore, ICRP

³ The term “reference” here is used by the International Commission on Radiological Protection (ICRP) to define an average individual. Dosimetry for this reference individual can be used to estimate radiation dose to a population of people but not typically for a single person undergoing a nuclear medicine procedure. Further consideration must be given when using reference individuals to represent an actual individual.

Publication 89 was utilized to adjust the UF newborn hybrid phantom to reflect the reference values for most organ masses detailed in the publication (Lee *et al.* 2007). Once the finalized ICRP-reference UF newborn hybrid phantom was created, it was voxelized for use in a radiation transport code as will be discussed later. The completed NURBS/PM-based UF hybrid newborn female phantom can be seen in Figure 1-8. The methodology used to construct the remainder of the UF hybrid phantom family was mostly consistent with that used to construct the UFH00MF phantoms. Subject ages and voxel resolutions used to construct the UF family of hybrid phantoms are in Table 1-1 (Lee *et al.* 2010). The final UF NURBS/PM hybrid phantom family can be seen in Figure 1-9.

Phantom Specificity

Ideally, one would like to have a computational phantom that was constructed directly from images taken of the patient of interest to perform dosimetry. However, current standards of technology are not sophisticated enough to automatically generate phantoms specific to the patient of interest in the amount of detail desired in a timely manner. Current methods do allow for real-time patient-specific dosimetry, and are very good for high-dose radionuclide therapy applications (Kolbert *et al.* 1997, Prideaux *et al.* 2007, Hobbs *et al.* 2009). However, even the methods used in the referenced studies required user-defined region of interest (ROI) definitions and were limited by scan coverage. Because of radiation dose concerns, most CT scans do not cover the entire body, and without a whole-body scan, whole-body models cannot be constructed. The referenced studies did not require whole-body patient-specific models because only certain tissues were identified as dose limiting, and the focus was given to those tissues. Due to the inability to construct whole-body phantoms closely representative of the patient of interest on-the-fly, other levels of patient specificity had to be explored for the purpose of whole-body internal dosimetry. “Patient specificity” refers to how closely the phantom represents the

external and internal anatomy of the patient. Three major levels of patient-specificity can be defined as follows (in order of specificity):

Patient-specific – These phantoms are almost exactly specific to the patient for which the dosimetry is being performed. Patient-specific phantoms are constructed from actual CT or MR image sets taken of the patient by manual (and sometimes automated) segmentation of organ volumes. To a certain extent, even these phantoms segmented directly from the patient cannot currently be considered truly patient-specific since the detailed microstructure within the skeleton cannot be segmented from ex-vivo CT or MR images. In addition, CT and MR images are not perfect and not all organs of interest can be effectively segmented. Furthermore, segmentation is a subjective human-driven process for the most part, so human error comes into effect. Despite these limitations, organ dose estimates for most organs in these phantoms will always be more accurate than in other phantom types.

Patient-dependent – These phantoms are initially created as a library of phantoms covering a range of physical characteristics. Based upon a series of reference phantoms, statistical analysis of morphometric measurements of thousands of individuals is performed, and a grid of measurements is determined that covers the majority of patient morphometries that would be seen in the clinic. For example, a grid could be created for adult males where phantoms are created for the 10th, 25th, 50th, 75th, and 90th percentiles by height, and at each height phantoms are created for the 10th, 25th, 50th, 75th, and 90th percentiles by weight⁴. Then, when an adult male patient walks through the door for a procedure, the phantom in the grid that most closely matches the measurements taken for the patient would be selected for dosimetry.

⁴ This is just an example. Recent developments in patient-dependent phantom library construction have made it clear that a grid of equal height and weight increments is more effective than percentiles because percentiles change over time.

The dosimetry for the selected patient-dependent phantom would have already been performed ahead of time, so dose estimates could be obtained immediately. Patient-dependent phantoms more closely approximate the true anatomy of an arbitrary patient than reference phantoms, but uncertainty still lies in the internal anatomy since the internal organs were segmented from images for a different patient.

Reference – These phantoms are defined by the ICRP and represent the average person by height and weight. They were originally developed to be applied to prospective radiation protection where radiation environments are investigated to see if the average worker or member of the general population would incur radiation doses above recommended limits or action levels. The reference individual would represent an “average” of the population that was irradiated. While this application is strictly for prospective radiation protection, reference phantoms were not intended to be applied to individual dosimetry for medical procedures or occupational radiation accidents. Since most patients are not average, dosimetry calculations performed on reference phantoms can only be taken as rough estimates for the actual absorbed doses for the patient of interest.

These three classes of phantom specificity cover the spectrum of phantom detail, but within each class there are further distinctions between phantom sub-types and their level of specificity as depicted in Figure 1-10.

Relevant Radiological Physics

The underlying physical occurrence important for radiation dosimetry is energy deposition in human tissue. An example was given earlier that described the process by which DNA strand breaks can occur from radiation energy deposition, so understanding energy deposition from radiation sources is crucial. Since a primary purpose of the current study was to determine

radiation dose measures from photons and electrons, some basic mechanisms by which photons and electrons deposit their energy will be discussed.

Photon Energy Deposition

Two types of ionizing radiation are currently defined – (1) indirectly ionizing radiation and (2) directly ionizing radiation (Attix 2004). Indirectly ionizing radiation first transfers its kinetic energy to another particle, and the particle to which the energy was transferred directly deposits its energy to the medium. Photons are considered indirectly ionizing since they give up their energy to electrons in tissue, and the electrons subsequently deposit their energy in the tissue. For the purpose of this study, the three most frequently encountered photon interactions will be discussed, and they are as follows:

Photoelectric effect – The kinetic energy of the incident photon is absorbed by an orbital electron that is then ejected from the atom (Attix 2004). The energy of the incoming photon must be greater than the binding energy of the electron, and the resulting kinetic energy of the electron is given by Equation 1-2 (Attix 2004).

$$T = h\nu - E_b \quad (1-2)$$

where T is the initial kinetic energy of the electron, $h\nu$ is the kinetic energy of the incoming photon, and E_b is the binding energy of the electron. The vacancy left by the electron may be filled by electrons in other orbitals, leading to x-ray emission or Auger electrons. The probability of this interaction occurring is given by Equation 1-3 (Attix 2004).

$${}_a\tau \propto \frac{Z^4}{(h\nu)^3} \quad (1-3)$$

where ${}_a\tau$ is the interaction cross-section per atom (effectively the interaction probability) for the photoelectric effect, Z is the atomic number of the atom, and $h\nu$ is the kinetic energy of the

incoming photon. The powers on the atomic number and photon energy vary as a function of photon energy, but Equation 1-3 gives a useful relationship for $E = 100 \text{ keV}$ and below, where the photoelectric effect is most important. From this relationship, it can be seen that the photoelectric effect is highly probably for high- Z elements at low photon energies. As applied to the phantoms, one would expect higher interaction rates in bone than in soft tissue since the effective atomic number for bone is higher.

Compton scattering – An incoming photon scatters off of a bound electron (kinematically, the electron can be treated as free and stationary), and some of the photon energy is transferred to the electron and some is retained by the photon (Attix 2004). The photon changes direction, and the electron is ejected from the atom, depositing its newly attained kinetic energy along its path. The initial kinetic energy of the electron is given by Equation 1-4 (Attix 2004).

$$T = hv - \frac{hv}{1 + (hv / m_o c^2)(1 - \cos \varphi)} \quad (1-4)$$

where T is the initial kinetic energy of the electron, hv is the kinetic energy of the incoming photon, $m_o c^2$ is the rest mass energy of the electron (511 keV), and φ is the scattering angle of the photon relative to the path of travel of the incoming photon. The probability of this interaction occurring is given by Equation 1-5 (Attix 2004).

$$\frac{\sigma}{\rho} \propto Z^0 \quad (1-5)$$

where σ/ρ is the Compton mass attenuation coefficient and Z is the atomic number of the atom. It can be seen that the Compton mass attenuation coefficient, another form of interaction probability, is mostly independent of the atomic number of the material. Compton interaction probability depends more on electron density of the material.

Pair production – A photon disappears in a nuclear Coulomb field, and its energy is converted into an electron-positron pair (Attix 2004). The nucleus is required for this type of photon interaction to occur in order to conserve momentum. Some of the energy of the photon is used to create the electron and positron rest mass equaling $2m_0c^2$ or 1.022 MeV . The remainder of the kinetic energy is transferred as kinetic energy to the electron and positron, not necessarily in equal quantity (Attix 2004). In the threshold situation where the photon has just enough energy to create the electron-positron pair, the electron and positron will have no momentum. Since the incoming photon had momentum, another body has to absorb that momentum. The average kinetic energy attained by the electron or positron in a pair production interaction is given by Equation 1-6 (Attix 2004).

$$\bar{T} = \frac{hv - 1.022 \text{ MeV}}{2} \quad (1-6)$$

where \bar{T} is the average initial kinetic energy of the electron or positron and hv is the kinetic energy of the incoming photon. The probability of this interaction occurring is given by Equation 1-7 (Attix 2004).

$${}_a\kappa \propto Z^2 \bar{P} \quad (1-7)$$

where ${}_a\kappa$ is the interaction cross-section per atom for pair production, Z is the atomic number of the atom, and \bar{P} is the P-value and is a function of the incoming photon energy and atomic number of the atom. The interaction cross-section increases roughly logarithmically with photon energy.

Electron Energy Deposition

While each photon interaction removes a large fraction of the initial energy of the photon, either by total absorption (photoelectric effect and pair production) or by hard scattering collisions with electrons, electrons lose their energy in a large number of very small interactions

(Attix 2004). Due to its Coulomb electric field, a free electron interacts with the valence electrons with every atom it passes (Attix 2004). Since electrons lose their energy in small increments over the entire path it travels, it can be considered to continuously slow down, a concept known as the “continuous slowing down approximation” (CSDA) (Attix 2004).

Electrons lose energy in the following two ways:

Radiative energy loss – This type of energy loss can be attributed to Coulomb-force inelastic interactions with the external nuclear field (Attix 2004). The electron passes near the nucleus and is deflected, transferring its energy to a photon, or bremsstrahlung radiation (Attix 2004). As electrons travel through a material, a continuous spectrum of photon radiation is emitted, resulting from the electron interactions with the nucleus (Attix 2004). This interaction is proportional to Z^2 , so radiative emission is more likely in bone than in soft tissue. Radiative energy does not account for energy deposition in the medium since the kinetic energy of the electron is converted into photons – only energy transfer has occurred in this case.

Collisional energy loss – Two types of collisional energy loss are prevalent in electron physics – (1) soft collisions and (2) hard collisions (Attix 2004). Soft electron collisions are the most common type of interaction, and they transfer energy to the medium of interest (Attix 2004). The Coulomb field of the electron affects the atom and either excites it to a higher level or ejects a valence-shell electron (Attix 2004). Hard collisions are a result of the electron interacting directly with a valence-shell electron and ejecting it from the atom (Attix 2004). The electron liberated from the atom is known as a delta (δ)-ray, and it continues on its own path of ionization and excitation (Attix 2004).

Photon-Electron Cascades

A combination of all of the previously discussed photon and electron interactions are possible within a radiation transport simulation. Radiation “showers” take place when cascades of different interaction events occur. For example, a monoenergetic photon source could be started within a radiation transport code, and the following sequence could be one possible interaction path for a single photon.

The photon could scatter and eject an inner shell electron from an atom. The photon loses some energy and changes direction. The liberated electron transfers energy to the medium and simultaneously creates bremsstrahlung photons that then proceed to experience their own interactions. The vacancy left by the ejected electron is filled by an outer shell electron, and an x ray is emitted⁵, and the x ray proceeds to experience its own interactions. The scattered primary photon experiences the photoelectric effect and is absorbed by an atom. The energy is transferred to an inner shell electron which is subsequently ejected from the atom. The liberated electron transfers energy to the medium and simultaneously creates bremsstrahlung photons that then proceed to experience their own interactions. The vacancy left by the ejected electron is filled by an outer shell electron, and an x ray is emitted, and the x ray proceeds to experience its own interactions.

Again, this is only one example of the interaction path a photon could take and is not an exclusive list. This series of processes continues until all energy has been expended into the medium. When computing radiation dose to tissues in the human body with computational phantoms and radiation transport codes, these types of interactions showers are occurring, and the amount of energy deposited to the tissues of interest is modeled.

⁵ The vacancy could also lead to energy transfer to another electron that is subsequently ejected from the atom.

Absorbed Fraction of Energy

Having considered how radiation deposits energy in tissues of the body, the dose measure important to this study and to nuclear medicine dosimetry in general will be discussed. In nuclear medicine dosimetry, the final dose measure of interest is the radionuclide S value, a measure that gives absorbed dose to a target tissue from a source tissue per nuclear transformation in the source tissue for a particular radionuclide in units of milligray per megabecquerel second ($mGy/MBq - s$). Along with the radionuclide S value, biokinetic models are needed but development of detailed biokinetic models are beyond the scope of this study. Within the S value, only one measure must be determined by means of radiation transport – the AF and SAF of energy, given in Equations 1-8 and 1-9.

$$\phi(r_T \leftarrow r_s, E_i) = AF(r_T \leftarrow r_s, E_i) = \frac{E_{deposited}(r_T \leftarrow r_s, E_i)}{E_{emitted}(r_s, E_i)} \quad (1-8)$$

$$\Phi(r_T \leftarrow r_s, E_i) = SAF(r_T \leftarrow r_s, E_i) = \frac{\phi(r_T \leftarrow r_s, E_i)}{m_T} \quad (1-9)$$

where $\phi(r_T \leftarrow r_s, E_i)$ and $AF(r_T \leftarrow r_s, E_i)$ are both the absorbed fraction of energy to target volume r_T from source volume r_s for radiation of energy E_i , $E_{deposited}(r_T \leftarrow r_s, E_i)$ is the amount of energy deposited in target volume r_T from source volume r_s for radiation of energy E_i , $E_{emitted}(r_s, E_i)$ is the total amount of energy emitted from source volume r_s for radiation of energy E_i , $\Phi(r_T \leftarrow r_s, E_i)$ and $SAF(r_T \leftarrow r_s, E_i)$ are both the specific absorbed fraction of energy to target volume r_T from source volume r_s for radiation of energy E_i , and m_T is the mass of target volume r_T .

The process by which a radiopharmaceutical distributes throughout the body was previously discussed. When a radiopharmaceutical distributes to a particular organ or tissue, that tissue becomes a source of radiation and is indicated in Equation 1-8 by r_s . All tissues in the

body, including r_S , become target tissues, indicated in Equation 1-8 by r_T , potential points in the body where radiation energy may be deposited. The point of simulating radiation with a radiation transport code is to determine the fraction of energy emitted from the source tissue that is deposited in each target tissue, the AF. The AF includes both information about the geometry of the problem as well as the initial energy of the radiation of interest. All other factors that compose the S value can be determined from outside sources without simulation, so the AF, and ultimately the SAF, is the dosimetric measure of interest for this study. The SAF is usually preferred over the AF because the mass of the target tissue is already considered, eliminating the need to obtain that information separately.

Effective Dose

At the most basic level, the quantity most relevant to radiation dosimetry is the absorbed dose. Absorbed dose refers to the amount of energy imparted to a material per unit mass of the material with units of joules per kilogram (J/kg) or grays (Gy) (Attix 2004). This is a good metric to compare dose information about a certain nuclear medicine imaging study, but the absorbed dose does not take into account differences in radiation or tissue types. Photons, electrons, protons, neutrons, etc. have different properties and are thus predicted (and observed) to have different effects on body tissues for the same amount of energy deposition (Attix 2004).

The radiation weighting factor was introduced to account for the impact each radiation type has on materials and is based on the linear energy transfer (LET) characteristics of the radiation type. High-LET particles (e.g., protons, neutrons, heavy charged particles (HCPs), recoil atoms, etc.) deliver more energy per unit penetration distance into a material than low-LET radiations (e.g., photons and electrons) (Attix 2004). Since biological damage toward an arbitrary biological endpoint depends partially on the spatial distribution of the ionizing events, high-LET particles are more biologically damaging than low-LET particles (Hall *et al.* 2006).

Relative biological effectiveness (RBE) is a direct measure by which the relative contribution of a particular radiation type has toward a particular biological endpoint, either stochastic or deterministic⁶ (Hall *et al.* 2006). For an example where photons are the reference radiation (the reference radiation could be any radiation type), RBE is measured by selecting a biological endpoint and determining the amount of absorbed dose needed from a type of radiation to produce the same endpoint as photons (Hall *et al.* 2006). The RBE is then calculated by dividing the dose needed by photons by the dose needed by the arbitrary radiation type. RBE increases with decreasing absorbed dose because ionization tracks become more spatially dense, so the radiation weighting factors were assigned the maximum RBE (RBE_m) (ICRP 2007). When multiplied by the radiation weighting factor, an absorbed dose to any tissue in the body is then referred to as the equivalent dose to that tissue and is given in units of sieverts (*Sv*).

The tissue weighting factor was introduced to account for differences in the way different body tissues react to energy deposition from radiation, otherwise known as their radiosensitivity (Attix 2004). Tissue weighting factors are based on radiation stochastic risk data and takes into account lifetime cancer incidence, dose and dose-rate effectiveness, lethality, quality of life for non-fatal cancers, and years of life lost (ICRP 2007). The unit of measure used for effective dose is also the sievert, an issue that can cause confusion. It is important to judge based on the context whether the unit sievert refers to individual organ equivalent doses or whole-body effective dose. Typically, authors should include the organ name if referring to the equivalent dose. Individual organ equivalent doses are calculated using Equation 1-10, and the whole-body effective dose is calculated using Equation 1-11 (ICRP, 2007):

⁶ Tissue weighting factors as defined by ICRP Publication 103 are based on stochastic biological endpoints (ICRP 2007).

$$H_{r_T} = \sum_R w_R D_{r_T,R} \quad (1-10)$$

$$E = \sum_{r_T} w_{r_T} H_{r_T} \quad (1-11)$$

where w_R is the radiation weighting factor for radiation type R , w_{r_T} is the tissue weighting factor for target organ r_T , $D_{r_T,R}$ is the absorbed dose to target organ r_T from radiation type R in units of mGy/MBq , H_{r_T} is the organ-specific equivalent dose in units of mSv/MBq , and E is the whole-body effective dose in units of mSv/MBq . The units of dose in these equations may also be in mGy and mSv , but nuclear medicine dose are generally generated normalized to the administered activity (AA) so that the final dose estimates may be simply scaled by the AA.

Relevant Studies and Current Limitations

Each of the specific aims in this study addresses an area of work that could be improved in some way. Prior to exploring the methods used to improve these areas of study, previous investigations by other researchers will be discussed to illuminate other approaches and identify areas of improvement. Some of the studies discussed in the upcoming sections have valid approaches that work for the particular application of the research group from which the study originated. In these cases, the approach used by the research group was not ideal for the UF phantom family, so other approaches were developed to improve the UF phantom family, not necessarily to improve the area of study as a whole. In other cases, room for improvement of general methodology was identified, and results from the current study could potentially be used by the nuclear medicine community as a whole. Each specific aim was addressed individually and by summarizing relevant studies. References were omitted from each summary section because, unless otherwise indicated, the quoted article serves as the reference.

Phantom Blood Vessel Systems

MCAT to XCAT: the evolution of 4-D computerized phantoms for imaging research (Segars et al. 2009)

The four-dimensional (4-D) NURBS CArdiac Torso (NCAT) phantom was first developed by Dr. Paul Segars as part of his dissertation at the University of North Carolina, Chapel Hill (Segars 2001). This phantom was created primarily to model cardiac and respiratory motion in the NURBS environment as applied to different medical imaging techniques. The internal anatomy was taken from the Visible Human project of the NLM (Segars 2001). The dataset was described by 512×512 axial matrix elements at a 1 mm slice resolution and a pixel width of 0.898 mm over the entire body. Initially, this phantom was only a torso phantom, lacking any arms or legs.

The eXtended CArdiac Torso (XCAT) phantom was an improvement on the NCAT phantom and extended the NCAT to include arms, legs, and a much more detailed internal anatomy. The XCAT phantom was based on the high-resolution Visible Male and Female of the NLM. This was done to extend the phantom to high-resolution applications such as CT or MRI. In this iteration of the original NCAT phantom, a circulatory system was included from direct segmentation. It was then desired that the XCAT phantom be extended to other ages and was done by obtaining several CT datasets covering a range of ages from newborn to adult. The datasets were first manually segmented to include the easily observable anatomy. Then, the organs which were not able to be directly segmented from the datasets were scaled down from the adult XCAT phantom to match the existing framework of the pediatric XCAT phantoms. All organs were scaled to match ICRP Publication 89 volumes. However, the study did not quote blood vessel volumes or masses and did not explicitly state that the blood vessels were scaled to match ICRP Publication 89 reference volumes.

Figure 1-11 shows the current XCAT blood vessel model for the adult male and female and newborn phantom. While there are limitations with some of the other aspects of the XCAT phantom series, the circulatory system is well modeled. This model is described by approximately one artery and one vein (with some branching) in the legs and arms and two arteries and two veins in the neck. However, there is fairly detailed vasculature in the heart and lungs.

The present proposal does not aim to create a more detailed circulatory system, only to provide a circulatory system for the UF series of hybrid phantoms. The level of detail used in the lungs of the XCAT phantom is not critical since blood can be apportioned uniformly throughout the lung volume.

The virtual family – development of surface-based anatomical models of two adults and two children for dosimetric simulations (Christ et al. 2010)

The blood vessel models in this study were derived from a volunteer study. Two adults and two children were subjected to whole-body MR scans. The subjects were scanned on a 1.5 T Siemens Magnetom Avanto Total Imaging Matrix whole-body scanner. A contrast agent was used to facilitate imaging of the blood vessels. After the contrast agent was administered, a first-pass scan was performed to capture only the arteries. Then, after the agent reached equilibrium, a second-pass scan was performed to capture all the blood vessels. From these two scans, the arteries and veins could be distinguished and subsequently segmented, creating a realistic whole-body blood vessel system. Vessels less than 2 mm in diameter were excluded due to difficulty in segmenting.

These models were of a 34-year-old male, 26-year-old female, 11-year-old female, and 6-year-old male. The models were not scaled to ICRP Publication 89 reference values and represent a set of patient-specific phantoms. Smoothing was done to the PM models using the

software Amira 4.0 by reducing the number of surface triangles. This blood vessel model closely resembles the model by Segars *et al.* (2009) with the exception that no pulmonary vessel system was modeled. The location and number of the arteries and veins is essentially the same as the XCAT phantom series. However, there is no mention of blood vessel masses or volumes and their comparison to ICRP Publication 89 reference volumes. Despite this, the blood vessel model provides an effective vehicle for the simulation of a distributed blood source.

Skeletal Photon Fluence-to-Dose Response Functions

Evolution and status of bone and marrow dose models (Stabin *et al.* 2002)

Radiation absorbed dose to hematopoietically active marrow (AM) and bone endosteum (more recently referred to as “total shallow marrow” (TM₅₀) (Hough *et al.* 2011)) has been of interest for quite some time due to concerns over marrow toxicity as a possible side effect of radiopharmaceutical therapy as well as the risk for genesis of leukemia or osteosarcoma from irradiation of the AM or TM₅₀, respectively. The trabecular microstructure of the skeleton is so small and intricate that it presently cannot be explicitly integrated into a computational phantom for use in radiation transport codes.

F. W. Spiers was one of the first to attempt to develop a method for determining skeletal dose based on actual microstructure of bone. Spiers created a model for the calculation of radiation absorbed dose to marrow from the volume of trabecular bone (TB)⁷. First, optical scanning was performed on TB samples from several cadavers, and chord-length distributions were produced for TB and marrow cavities from the acquired images. Chord-length distributions describe the frequency of lengths of straight lines which intersect two surfaces (Jokisch *et al.*

⁷ Each bone in the human body is surrounded by a hard mineral bone shell called cortical bone (CB). For most bone sites, this CB shell is filled with a material called spongiosa, which includes both trabecular bone (TB) and total marrow (TM). Trabecular bone is a complicated network of hard mineral bone spicules, the cavities of which are filled with TM. TM is made up of both active marrow (AM) and inactive marrow (IM). TB is generally not present in the shafts of the long bones. These long bone shafts are known as medullary cavities (MCs).

2001). Then, transport was performed stochastically by basing the electron paths on the resultant chord-length frequency distributions. The average energy deposition to marrow was then calculated from electron sources in the TB volume (TBV). Snyder *et al.* (1975) subsequently derived AFs for sources in TBV and marrow. The results of these derivations were incorporated into Monte Carlo radiation transport simulations to determine S values in the Fisher-Snyder computational phantom for use in MIRD Pamphlet No. 11. However, these simulations were known to show conservatively high doses for initial monoenergetic photon energies below 300 keV because it was assumed that marrow absorbs energy per gram as efficiently as mineral bone.

Using Spiers's chord-length distributions and electron transport methods, Eckerman later calculated electron AFs for 7 bone types for a range of energies. The AFs for these bone types were distributed to the 15 skeletal regions of the Cristy/Eckerman phantoms, weighted by the mass fraction of each bone type within each skeletal region.

Fairly recently, Bouchet *et al.* (2000) calculated AFs for 7 adult TB sites treating the trabecular marrow space and bone volume all as sources and targets. They did this using Spiers's chord-length distributions and the Electron-Gamma-Shower version 4 (EGS4) radiation transport code.

Three major differences exist between the Eckerman and Bouchet models. The first difference is that the Eckerman model assumes that the AF for red marrow (AM) irradiating red marrow is equal to the AF for the total marrow (TM) space irradiating the TM space multiplied by the cellularity, the fraction of TM occupied by red marrow. The Bouchet model assumes that the AF for red marrow irradiating red marrow is equal to the AF for the TM space irradiating the TM space with no correction. Because of this, the Bouchet model predicts doses approximately

twice as large as the Eckerman model. A second difference between the two models stems from the definition of the bone endosteum, or TM_{50} . The Eckerman model treats TM_{50} as a 2-D planar surface at the interface between the marrow space and trabecular bone while the Bouchet model simulates the endosteum as a bone surface (BS) source, a $10 \mu m$ deep layer of tissue within the marrow space adjacent to the TB. Accordingly, the Bouchet dose conversion factors (DCFs) (mathematically equivalent to S values) for bone surface sources are up to 2 times as great as the Eckerman model.

Specific absorbed fractions of energy at various ages from internal photon sources. I. methods” (Cristy et al. 1987)

With this report came the introduction of skeletal photon fluence-to-dose response functions for the determination of absorbed dose to AM and BS. The BS was used as a surrogate for osteoprogenitor cells (cells at risk for osteosarcoma) and at that point was defined as the volume of TM that was $10 m$ deep from the TB of the spongiosa and $10 \mu m$ deep from the cortical shell in the shafts of the long bones (ICRP 1979). The following equations were used to develop the skeletal photon fluence-to-dose response functions in Cristy *et al.* (1987).

$$\frac{D(AM)}{\Psi(E)} = \sum_r \frac{m(r)}{m(AM)} \sum_i \int_0^\infty \phi(AM \leftarrow r, T_i)(i/\rho)_r n_r(T_i) T_i dT_i \quad (1-12)$$

$$\frac{D(BS)}{\Psi(E)} = \sum_r \frac{m(r)}{m(BS)} \sum_i \int_0^\infty \phi(BS \leftarrow r, T_i)(i/\rho)_r n_r(T_i) T_i dT_i \quad (1-13)$$

where $\phi(AM \leftarrow r, T_i)$ “is the absorbed fraction in AM from r for electrons of energy T_i ”, $\phi(BS \leftarrow r, T_i)$ “is the absorbed fraction in BS from r for electrons of energy T_i ”, $(i/\rho)_r$ is the photon mass attenuation coefficient where “ $i = \tau, \sigma$, and κ denotes the mass attenuation coefficients in medium r for the photoelectric, Compton, and pair-production interactions,

respectively”, and $n_r(T_i)dT_i$ “denotes the number of electrons of energy between T_i and $T_i + dT_i$ liberated in region r per interaction i ”.

The AFs were developed based on Spiers’s chord-length distributions. Integration over the energy dependent AFs, photon mass interaction coefficients, secondary electron spectrum, and electron energy over the whole secondary electron spectrum gives the energy deposited in either the AM or BS per unit photon fluence per unit source mass. This integration was performed for the three dominant photon interaction processes (photoelectric absorption, Compton scattering, and pair production) and summed. To obtain the absorbed dose per unit photon fluence to the target region, the integrations were performed for each source region and weighted by the mass ratio of the source region to the target region. These are the formulations that are used in the current study, but full 3-D electron transport will be completed for the determination of skeletal AFs rather than chord-based calculations.

Skeletal photon fluence-to-dose response functions were computed for 7 bone sites, but Cristy and Eckerman recommended the use of skeletal photon fluence-to-dose response functions from only two bone sites to apply to the whole skeleton. The authors noted that the parietal bone skeletal photon fluence-to-dose response function seemed to differ noticeably from the other bone sites, and the lumbar vertebra appeared to faithfully represent the other bone sites. Also, the age dependence of the trabecular microstructure did not show appreciable influence on the skeletal photon fluence-to-dose response functions for the AM target. Based on these discoveries, the authors recommended that the parietal fluence-to-dose response functions be used to calculate the dose to AM and BS in the cranium and the lumbar vertebra fluence-to-dose response functions be used to calculate the dose to all other bone sites. They also recommended that the same fluence-to-dose response functions be used across all ages.

Photon Specific Absorbed Fractions

Specific absorbed fractions of energy at various ages from internal photon sources. I. methods (Cristy et al. 1987)

The SAFs calculated by Cristy and Eckerman at Oak Ridge National Laboratory (ORNL) in 1987 for the computational phantoms developed by the MIRD committee, or MIRD-type phantoms, represents the current standard for internal dosimetry. The ICRP has recently migrated to new voxel phantoms as the reference for the adults, but the work by Cristy and Eckerman is still the standard for the pediatric series of phantoms.

Stylized computational phantoms based on the adult phantom of Snyder *et al.* (1975) were used for the calculation of SAFs. Pediatric phantoms were constructed with the same general body shape but slightly different proportions as described by Cristy (1980). However, the 15-year-old phantom was modified to represent the adult female. Though having the same body dimensions, breast tissue, ovaries, and a uterus were added. Three materials were used to describe the structures of the phantoms: soft tissue, lung, and bone. Correspondingly, three tissue densities and compositions were used, and these material descriptors were only unique for the newborn phantom. The 1-year-old, 5-year-old, 10-year-old, 15-year-old, and adult phantoms all had the same tissue densities and compositions. The Cristy-Eckerman phantoms can be seen in Cristy *et al.* (1987). It is obvious that these phantoms are not anatomically realistic, and this is one immediate drawback to using these phantoms for internal dosimetry.

The radiation transport techniques used in the development of these SAFs were similar to those used by Snyder *et al.* (1975) with the primary deviation being the treatment of skeletal tissues. For non-skeletal target organs, it was assumed that all liberated electron energy was locally deposited, an assumption known as the kerma approximation which refers to the phrase “kinetic energy released per unit mass”. The kerma approximation is generally only valid for

situations in which charged particle equilibrium (CPE) is established. In this situation, electrons leaving the volume of interest are compensated by electrons entering the volume of interest. This assumption was considered valid for any organs which were not on an interface with different tissue compositions. The report did not explicitly state the number of histories used in the models but only discussed acceptable statistical errors. Snyder *et al.* (1975) simulated up to 60,000 particle histories, but it is unclear to what degree the number of particles was increased for the ORNL calculations. Since “soft tissue” was the only material used for non-lung and non-skeletal organs, the kerma approximation was justified to a degree. However, for internal dosimetry, CPE is not definitely established for every target organ. In the case of self-dose, the dose to the source could be over-estimated using the kerma approximation since secondary electron escape is not considered. The total energy deposited in each target organ was recorded and divided by the mass of the target organ and the initial energy of the photon to obtain the SAF. Skeletal photon fluence-to-dose response functions were used to calculate the SAFs to AM and BS.

The reliability of an SAF was assessed based on the coefficient of variation (CV), which is the ratio of the standard deviation to the mean, multiplied by 100%. It was known previous to these calculations that Monte Carlo techniques alone would not be sufficient to provide reliable SAFs. The point-source kernel method was used in cases where the CV was greater than 50%. The point-kernel equation can be seen in Equation 1-13.

$$\Phi(r) = \frac{\mu_{en}}{\rho} \cdot \frac{1}{4\pi r^2} \cdot e^{-\mu r} \cdot B(\mu r) \quad (1-14)$$

where $\Phi(r)$ is the point isotropic SAF at r , μ_{en} is the linear energy-absorption coefficient at the source energy, μ is the linear attenuation coefficient at the source energy, ρ is the density of the medium, and $B(\mu r)$ is the buildup factor, “a factor representing the contribution of the scattered

radiation to the energy absorption”. This equation was integrated over the volume of the source and target organ. Numerically, this was performed by randomly sampling a point in the source organ and a point in the target organ to obtain r , the point-pair distance, in the equation. The process was repeated many times to produce statistically reliable results (all point-kernel CVs were less than 1.2%). The drawback of the use of this equation is that it assumes a homogenous water phantom embedded in an infinite water medium. Obviously, with the incorporation of bone and lung tissue in the phantoms, the point-kernel method will be an approximation. The authors compensate for this with the introduction of correction factors for certain source-target combinations.

Since the computing power at the time was far inferior to what is available today, a variety of variance reduction techniques were used to produce more reliable results. The “inverse Monte Carlo estimate” referred to below indicates that the reciprocity theorem was invoked. That is, the Monte Carlo simulation was performed for the target irradiating the source. The reciprocity theorem states that the SAF for the source irradiating the target is equal to the SAF for the target irradiating the source. The following were techniques used by Cristy and Eckerman to smooth the SAF curves.

If the CV for the direct and inverse Monte Carlo estimate and point-kernel estimate were greater than 50%, the SAF was rejected. For all SAF estimates, an average was taken of the direct and reverse Monte Carlo estimates with each SAF weighted by the inverse of its variance. If the reverse Monte Carlo estimate was not available, the direct Monte Carlo estimate was taken as the weighted average. If the CV for the weighted average was greater than 30% an average was taken of the weighted average and the corrected point-kernel estimate with each SAF weighted by the inverse of its variance. Once the first three conditions were assessed and

appropriate actions taken, a cubic spline technique was used to smooth the data on a log-log plot of the final weighted average versus initial photon energy. If the spline did not fit well at low energies, more weight was given to the first two values. If the CV at 4 MeV was greater than 10%, and the results appeared poor, the weighted average of the uncorrected and corrected point-kernel estimate was taken at 4 MeV. The spline technique was then reapplied. After all smoothing techniques were applied, if the SAF curve still appeared unreliable, the smoothing was done subjectively by hand. If no acceptable Monte Carlo estimates were available, the corrected point-kernel estimate was taken as the recommended value. If neither organ was simulated as a source organ, no recommendation was made.

There are many limitations to the approaches in the Cristy-Eckerman series of SAFs. While this work is dated, until the ICRP officially adopts a new full series of pediatric phantoms, the Cristy-Eckerman work is still the standard dataset for a broad range of radiation dose coefficients. The phantoms used were stylized/mathematical phantoms, and while easily deformable, these phantoms lack the anatomic realism of voxel or hybrid phantoms. Also, only 3 material types were used, a simplistic tissue characterization compared to the information and computing abilities today. The data smoothing techniques were convoluted and unduly complicated, but this was necessitated by the poor statistical uncertainties resulting from only being able to simulate approximately 6×10^4 particle histories. In the present study, 10^7 to 10^8 particle histories were simulated. Resultantly, much improved precision is achieved, and complicated variance reduction techniques will be unnecessary.

ICRP 110: adult reference computational phantoms (ICRP 2009)

This publication of the ICRP lays out the groundwork for SAF calculations in the future. Work has been done by other groups to calculate some photon SAFs for certain source-target

combinations in the ICRP Publication 110 voxel phantoms. However, full scale, complete internal dosimetric characterization is presently underway at the time of this writing. It is important to note that complete tables of SAFs are currently unavailable.

The ICRP recently adopted new reference adult male and female voxel phantoms. These phantoms were developed from whole-body CT data sets. The adult male was segmented from images of a 38-year-old at a height of 176 *cm* and a weight of 70 *kg*, the same as the ICRP Publication 89 reference adult male. The adult female was segmented from a 43-year-old at a height of 167 *cm* and a weight of 59 *kg*; the reference adult female detailed in ICRP Publication 89 has a height of 163 *cm* and a weight of 60 *kg*. All segmented organs were scaled to match ICRP Publication 89 reference values. A noted limitation was that the surface shapes of the organs were unique to the individual that they were segmented from.

The voxel resolutions used were $2.137 \times 2.137 \times 8.0 \text{ mm}^3$ and $1.775 \times 1.775 \times 4.84 \text{ mm}^3$ for the male and female, respectively. Some complications were noted by the ICRP and included skin thicknesses that were not equal to the reference value and the inability to accurately model the gall bladder. Utilizing the resolutions quoted, the skin masses were 13% and 18% greater than the reference values for the male and female, respectively. The gall bladder was difficult to model due to the voxel resolutions. The wall mass was greater than the reference value, but the total gall bladder mass (including the contents) was matched to the ICRP Publication 89 reference value.

Since the trabecular microstructure in the skeleton was too small to segment from the CT images, three regions of bone were explicitly modeled: CB, spongiosa, and medullary cavities (MCs). Masses of skeletal constituents were apportioned based on ICRP Publication 70 and ICRP Publication 89. For source simulations, cortical bone will be simulated uniformly since the

volume is explicitly defined. The marrow and TB sources will be created by assigning bone site-specific sampling probabilities based on the relative distribution of marrow. SAFs to AM and TM_{50} will be calculated using either correction factors as described by Zankl *et al.* (2002) and Schlattl *et al.* (2007) or the skeletal photon fluence-to-dose response functions developed by Cristy and Eckerman (1987). The publication does not go into detail about skeletal dosimetry methods to be used.

The ICRP Task Group on DOse CALculations (DOCAL) produced a set of photon SAFs for the liver, lungs, and thyroid as source regions and the colon, lungs, stomach wall, and breasts as target tissues using two radiation transport codes: Electron Gamma Shower of the National Research Council Canada (EGSnrc) and Monte Carlo N-Particle eXtended (MCNPX) (Los Alamos National Laboratory, Los Alamos, NM). The results from two irradiation geometries are displayed in Figure 1-12. The two radiation transport codes used showed good agreement for most of the combinations of sources and targets.

Electron Specific Absorbed Fractions

Specific absorbed fractions of energy at various ages from internal photon sources. I. methods (Cristy *et al.* 1987)

Electron absorbed fractions were assumed to be equal to unity in the case of self-irradiation of non-walled organs and equal to zero for cross-fire (Snyder *et al.* 1975). Consequently, to calculate any given SAF for non-walled organs, one would simply take the inverse of the target mass. To calculate the SAF for a walled organ being irradiated by its contents, one would take the inverse of twice the target mass (this would assume an absorbed fraction of 0.5) (Snyder *et al.* 1975). These were clearly approximations, but no simulations were performed to verify their validity.

ICRP 110: adult reference computational phantoms (ICRP 2009)

The DOCAL task group performed full electron transport in both EGSnrc and MCNPX to calculate a small set of electron SAFs for the ICRP Publication 110 adult male and female voxel phantoms. The source and target regions simulated in the development of the photon SAFs were used for the electron SAFs. Results from two irradiation scenarios can be seen in Figure 1-13. It is clear from these curves that the assumption of complete electron energy absorption for self-irradiation and insignificant electron energy absorption for cross-fire was a poor one. At high energies, electron escape was found to be appreciable and electron cross-fire, significant. Some minor disagreements between EGSnrc and MCNPX and poor statistical uncertainties were seen at electron energies less than 100 keV.

Dosimetric Sensitivity Analysis for Internal Sources

Patient-specific scaling of reference S-values for cross-organ radionuclide S-values: what is appropriate? (Petoussi-Hens et al. 2007)

MIRD Pamphlet No. 11 was one of the first to give any guidelines on SAF scaling methodology, and the Petoussi-Hens *et al.* (2007) study aimed to verify the MIRD Pamphlet No. 11 recommendations. The authors attempted to uncover any further information on patient-specific SAF scaling. This investigation was performed solely with computational phantoms, and for the most part, validation was the focus. The German Research Center for Environmental Health (GSF) voxel phantoms (Petoussi-Hens *et al.* 2002) and ORNL MIRD-type stylized phantoms (Cristy *et al.* 1987) were used for comparison.

First, photon cross-fire dose variation with changes in source organ mass was examined by comparing the photon SAFs for a particular source organ from the GSF voxel phantoms as originally segmented to the SAFs for the same source organ when scaled to the ICRP Publication 89 reference mass. $\Phi(kidneys \leftarrow thyroid)$, $\Phi(stomach \leftarrow liver)$, and

$\Phi(\text{red bone marrow} \leftarrow \text{liver})$ were shown (note: target \leftarrow source). Ratios of the SAFs for source organs of the original mass to the SAFs for the source organs of the ICRP Publication 89 matched mass were close to 1.00, so the authors claim that no corrections are necessary for changes in source organ mass, even for distributed target organs such as red bone marrow. However, Figure 1-14 showed that there can be some variability up to around 5%.

Next, the reciprocity principle was investigated for a distributed organ, the red bone marrow. The reciprocity theorem states that the SAF from a particular source/target combination is equal to the SAF if the source and target are reversed. However, this had not yet been proven for distributed organs, so this study simulated the liver and red bone marrow as sources and targets, and the results can be seen in Figure 1-15. No mass correction was recommended for initial photon energies 100 keV or greater since deviations were only seen from about 5% to 8%.

Finally, the authors sought to verify the photon self-dose mass scaling recommendation of MIRD Pamphlet No. 11 that the SAFs for photon energies greater than 100 keV should scale as the inverse 2/3 power of the organ mass. That is, to scale an SAF for the self-irradiation scenario, one must multiply the original SAF by the factor $(m_{reference}/m_{non-reference})^{2/3}$. To verify that the scaling was performed correctly, the SAF should decrease for a larger source organ. Results were shown for photon self-irradiation of the thyroid in the GSF family of voxel phantoms and can be seen in Figure 1-16. The SAFs for the thyroid irradiating the thyroid at the original segmented mass were divided by the SAFs for the thyroid irradiating the thyroid at the reference mass. The results were found to be in good agreement with the MIRD Pamphlet No. 11 recommendation. Red bone marrow self-irradiation was also examined, but no conclusions could be drawn.

While some previously recommended methods of SAF scaling for a variety of scenarios were explored, the results seemed to be in fairly good agreement but with some variation. No mass scaling was recommended for distant organs, but variations were seen up to 5%. Also, the MIRD Pamphlet No. 11 SAF scaling methodology for photon self-irradiation was claimed to be valid, but graphical, and no numerical, verification was offered. There seemed to be deviations from the inverse 2/3 power recommendation which were not taken into account. It is possible to develop energy-dependent scaling methodologies which could scale the SAFs in an even more accurate manner, as was investigated in this study.

Changes in radiation dose with variations in human anatomy: larger and smaller normal-stature adults (Marine et al. 2010)

This study sought to examine the general trends of changes in dose with variations in stature. The 50th percentile NURBS phantoms were constructed according to ICRP Publication 89 reference data. Anthropometric data from Dekaban (1978), Grandmaison *et al.* (2001), the U.S. Department of Defense (DOD), and the Centers for Disease Control (CDC) were used to construct 25th and 75th percentile by height adults. Organ masses for which autopsy data was unavailable were approximated by a 5% increase or decrease. The 10th and 90th percentiles by height adults were constructed using data from the DOD-HDBK-743A (anthropometry of U.S. military personnel) and total body masses were calculated from assumed body mass indices (BMIs). Scaling factors were used to adjust organ masses until the constructed total body mass matched the calculated total body mass. The radiation transport code Geant 4 was used to calculate SAFs for a variety of source-target combinations. The results were compared to both the 50th percentile Cristy-Eckerman phantom and 50th percentile NURBS ICRP-reference phantom SAFs.

The SAFs were found to decrease with increases in percentile size because the effect of increases in organ mass dominates the effect of increases in organ separation. The percent differences between the SAFs of the 50th percentile and non-50th percentile phantoms were averaged over all photon energies and absolute differences were reported. For self-irradiation, SAFs vary from 0.5%/kg to 1.0%/kg variation in organ mass. Organs outside of the main trunk area showed SAF differences which were within the uncertainty of the SAFs themselves. Organs inside the main trunk area showed SAFs with difference between 0.3%/kg and 1.1%/kg target organ mass. Absolute percent differences were seen between about 8% (*heart* ← *kidneys*, adult female) and 33% (*liver* ← *pancreas*, adult male), comparing the 10th percentile to the 90th percentile by height phantoms. Results from selected source organs in the adult male can be seen in Figure 1-17.

While this study presented a systematic method for examining variations in SAFs based on the patient's stature, the conclusion drawn by the authors was that the results were "interesting" and could help understand how the dose varies from patient to patient. In addition, the analysis was only performed for adults, and the differences in SAFs were averaged over all photon energies. The current study aimed to generate empirical equations or look-up-table (LUT)-type scaling factors which would allow for the scaling of SAFs at all photon energies, based on the patient's stature for a range of ages or 50th percentile heights.

Changes in radiation dose with variations in human anatomy: moderately and severely obese adults (Clark et al. 2010)

This study sought to examine the general trends of changes in dose for individuals of varying levels of obesity. The 50th percentile NURBS phantoms were constructed according to ICRP Publication 89 reference data. First, two adult male and two adult female phantoms were created at larger BMIs than the reference phantom by adjusting the outer-body contours and

scaling to match typical body circumferences. Visceral fat deposits were modeled for the kidneys and the intestines. The small and large intestines were scaled in an elliptical fashion to model mesenteric fat deposits, and the kidneys were moved in the anterior direction to model pararenal and perirenal fat deposits. Cross-sections of the phantoms simulated are displayed in Figure 1-18. The radiation transport code Geant 4 was used to calculate SAFs for a variety of source-target combinations. The results were compared to the 50th percentile NURBS ICRP-reference phantom SAFs.

The SAFs were found to decrease with increases in percentile size, because the effect of increases in organ mass dominates the effect of increases in organ separation. The percent differences between the SAFs of the 50th percentile non-50th percentile phantoms were averaged over all photon energies, but only a few examples were discussed. For the most part, the SAFs showed about a maximum of a few percent difference overall, but target organs in the abdominal area were up to 1.6 times lower in the moderately obese phantom and up to 2 times lower in the severely obese phantom than in the 50th percentile phantom. The large intestines irradiating the liver showed the greatest differences while the lungs and large intestines showed little differences in the moderately obese case up to a difference of a factor of 1.3 for the severely obese case due to mesenteric adipose deposits.

While this study presented a systematic method for examining variations in SAFs based on the patient's BMI, the conclusion drawn by the authors was that there is not much SAF variation with patient obesity with the exception of a few organ pairs. However, the analysis was only performed for adults, the differences in SAFs were averaged over all photon energies, and BMIs less than the reference BMI were not examined. The current study aimed to generate empirical equations or LUT-type scaling factors which would allow for the scaling of SAFs for all photon

energies, based on the patient's weight percentile for a range of ages and weight percentiles both below and above the 50th percentile.

Internal Dosimetry Software

OLINDA/EXM: the second-generation personal computer software for internal dose assessment in nuclear medicine (Stabin et al. 2005)

One of the first widely distributed internal dose calculation software packages was the Radiation Internal Dose Information Center (RIDIC) at the Oak Ridge Institute for Science and Education's (ORISE) MIRD dosimetry method-based internal dosimetry personal computer software (MIRDOSE). However, the code was written in Visual Basic (VB) and did not translate very well to Windows 2000. In addition, the U.S. Food and Drug Administration (FDA) discovered that the code was being used as a "medical device" in the FDA's definition. A rewrite was needed since MIRDOSE was in unstructured VB, and it was subsequently translated to Java. The converted software was named Organ Level Internal Dose Assessment (OLINDA). Also, exponential fitting to biokinetic data was made available, so a naming extension of EXponential Modeling (EXM) was added. The final product was called OLINDA/EXM 1.0, and the FDA subsequently approved it for worldwide marketing. OLINDA/EXM 2.0 has recently been released, but not much is currently known about the phantoms or methods used in the software.

The input screens for OLINDA/EXM can be seen in Figure 1-19. Figure 1-19 (A) shows the main input form. This form can be used to either produce dose factors (DFs) or final doses calculated from the DFs and kinetic data. DFs are mathematically equivalent to S values, but OLINDA/EXM includes the radiation weighting factors in the calculation of DFs. While this is insignificant for radionuclides whose radiation emission consist only of photons and electrons, the inclusion of radiation weighting factors becomes important when considering alpha emission.

Figure 1-19 (B) shows the nuclide input form. The user simply selects the element of interest, then the isotope. The decay data comes from the RAdiation Dose Assessment Resource (RADAR), a group who maintains a web site useful for internal and external radiation dose assessment (Stabin *et al.* 2003). Figure 1-19 (C) shows the model input form. The user selects from a list of computational phantoms or individual region models. The Fisher-Snyder (MIRD-type) stylized phantom is used for the adult male and female phantoms, and the Cristy-Eckerman stylized pediatric phantoms are used for the pediatric series. Figure 1-19 (D) shows the biokinetics input form. The user enters the total number of nuclear transformations per unit AA, which is mathematically equivalent to the old unit of residence time, in the desired source regions. The term “residence time” is not used in OLINDA/EXM because the author deemed it too confusing, and the new accepted term is “total number of nuclear transformations”. Figure 1-23 (E) shows the final output window. Absorbed doses per unit AA to individual organs are listed by radiation type, and the total radiation absorbed dose is listed by organ. Effective dose equivalents per unit AA as defined by ICRP Publication 30 and equivalent doses per unit AA as defined by ICRP Publication 60 are listed by organ (Stabin 2005). Finally, the whole-body effective dose equivalent and effective dose per unit activity are given. The OLINDA/EXM 1.0 software program is intuitive to use and delivers results in an easy to understand format.

Some improvements have been introduced with the creation of OLINDA/EXM 2.0. Decay data for over 1200 radionuclides from ICRP Publication 107 has been included. New realistic NURBS-based phantoms have been introduced (Stabin *et al.* 2006). The NURBS phantoms in version 2.0 were scaled from the existing models to match reference values given in ICRP Publication 89. However, there is little documentation on the phantoms used in this version of the code, and it is unclear exactly how the phantom series was created or what they look like.

Also, tissue weighting factors from ICRP Publication 103 were included in this version (Stabin *et al.* 2010). The old weighting factors and phantoms were retained for comparison purposes.

Table 1-1. Image set sources and voxel resolutions for the construction of the UF hybrid phantom family. Adapted from Lee *et al.* (2010).

Phantom	Head	Body region		
		Torso	C-vertebrae	Arms and Legs
UFH00MF			6 day F 0.586 x 0.586 x 1 mm ³	
UFH01MF	2 year F 0.379 x 0.379 x 4.5 mm ³	1 year F 0.406 x 0.406 x 3 mm ³		
UFH05MF		4 year F 0.451 x 0.451 x 5 mm ³		
UFH10MF	12 year M 0.469 x 0.469 x 6 mm ³	11 year M 0.469 x 0.469 x 6 mm ³		
UFH15M	18 year M ^a 1 mm	14 year M 0.625 x 0.625 x 6 mm ³	15 year M 0.21 x 0.21 x 0.75 mm ³	18 year M ^c 1 mm
UFH15F	15 year F 0.449 x 0.449 x 4.5 mm ³	14 year F 0.742 x 0.742 x 6 mm ³	(all ages except newborn)	(all ages except newborn)
UFHADM	18 year M 1 mm	36 year M 1.97 x 1.97 x 3 mm ³		
UFHADF	15 year F ^b 0.449 x 0.449 x 4.5 mm ³	25 year F 0.66 x 0.66 x 5 mm ³		

^aHead model of UFHADM was downscaled to create the UFH15M model.

^bHead model of UFH15F was upscaled to create the UFHADF head model.

^cHigh resolution (1 mm slice thickness) CT images of arms and legs were obtained from an 18 year male cadaver.

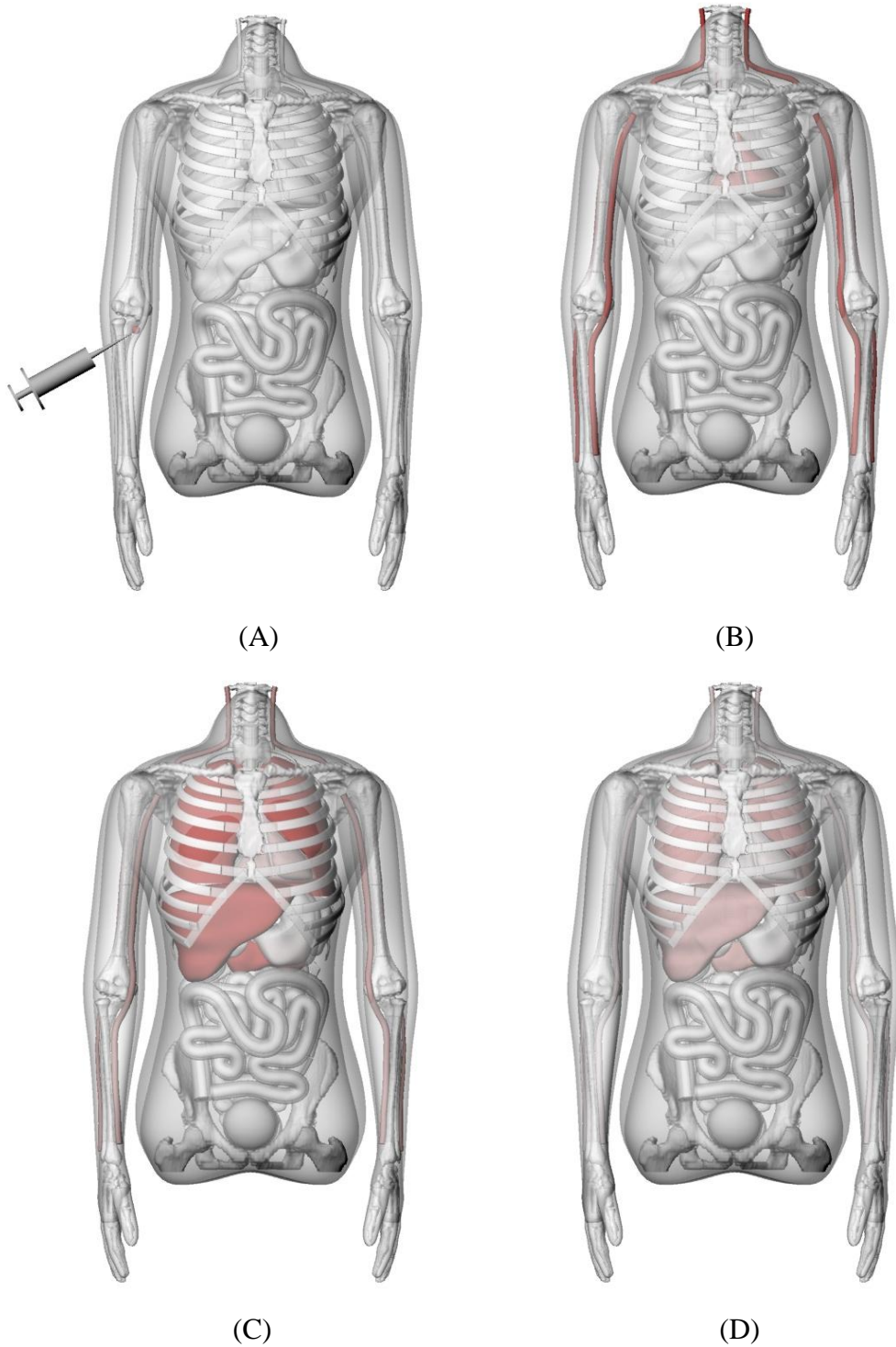


Figure 1-1. Artistic example of radiopharmaceutical biodistribution including (A) injection of radiopharmaceutical, (B) distribution through the bloodstream, (C) uptake in various organs in the body, and (D) excretion of radiopharmaceutical from the organs receiving uptake.



(A)



(B)

Figure 1-2. (A) Front and (B) side views of the UF newborn physical phantom (Jones *et al* 2006). Reproduced with permission (© 2006 American Association of Physicists in Medicine).

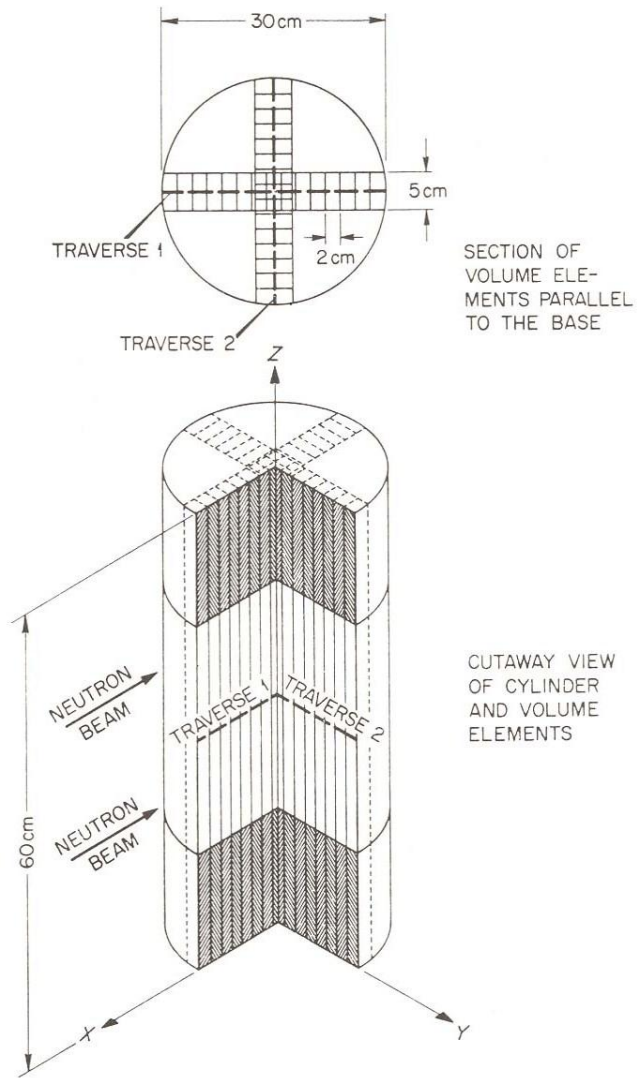


Figure 1-3. The first stylized model of the trunk of an adult human. A right circular cylinder 30 cm in diameter and 60 cm in height (NCRP 1971). Reproduced with permission (© 1971 National Commission on Radiological Protection).

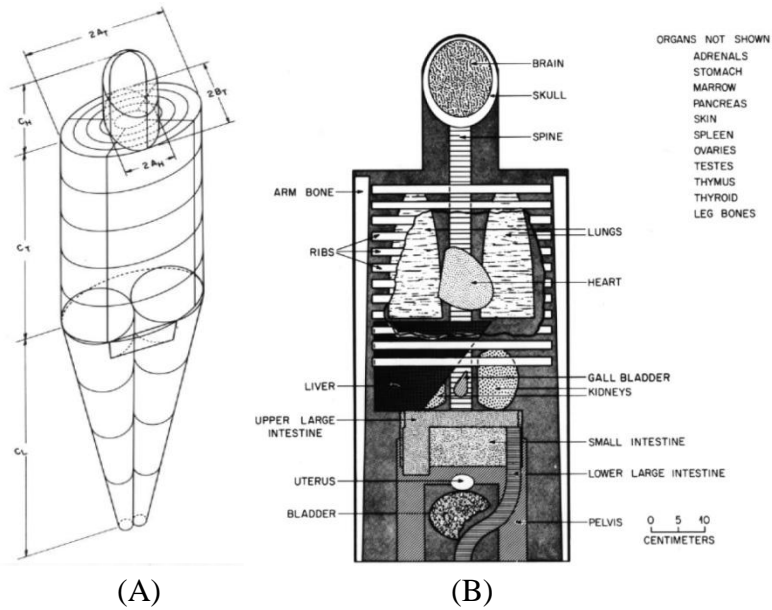


Figure 1-4. The MIRD Pamphlet No. 5 revised stylized computational dosimetry phantom (Snyder *et al.* 1978). (A) Outer body contour and (B) anterior view of principle organs in head and trunk. Reproduced with permission (© 1978 Society of Nuclear Medicine).

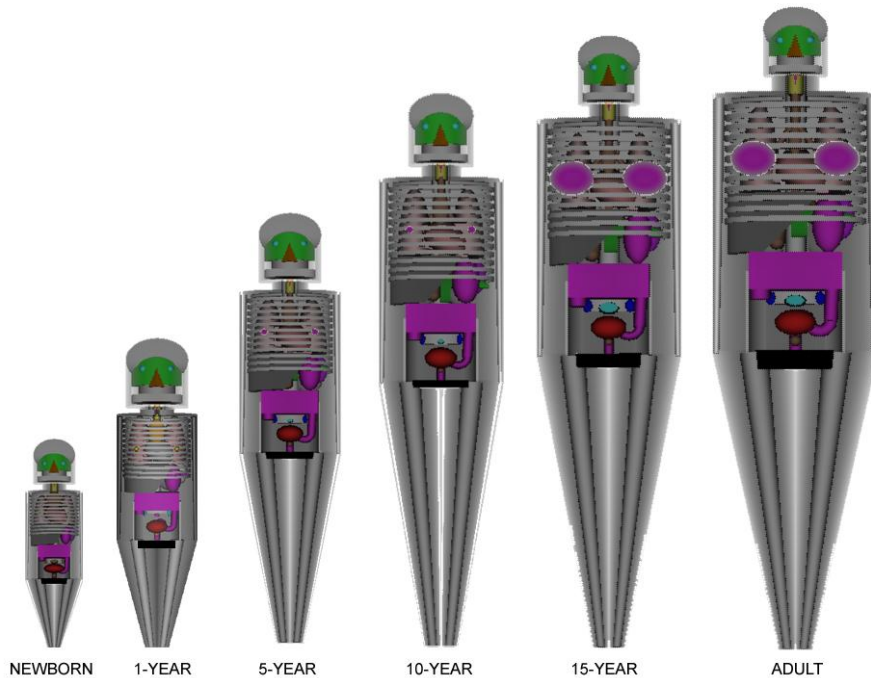


Figure 1-5. The complete current ORNL stylized computational dosimetry phantoms series. Adapted from Cristy *et al.* (1987).

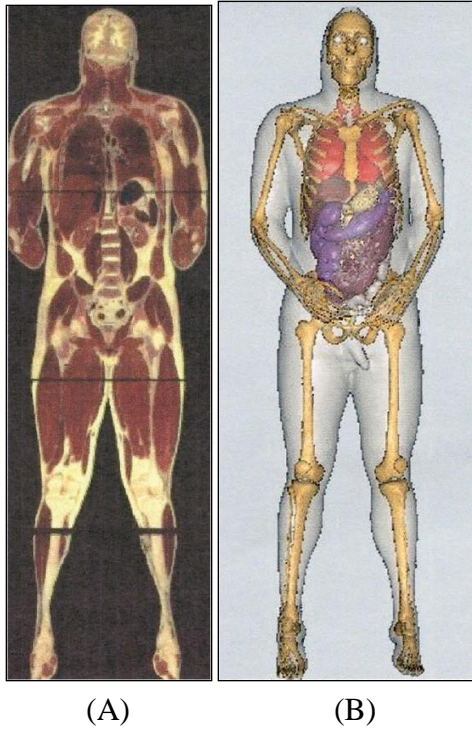
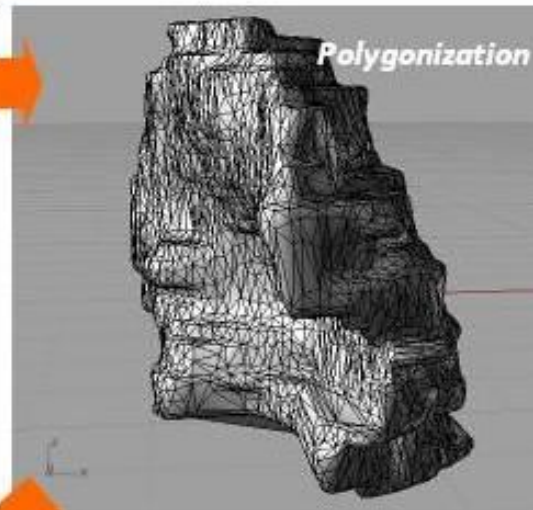
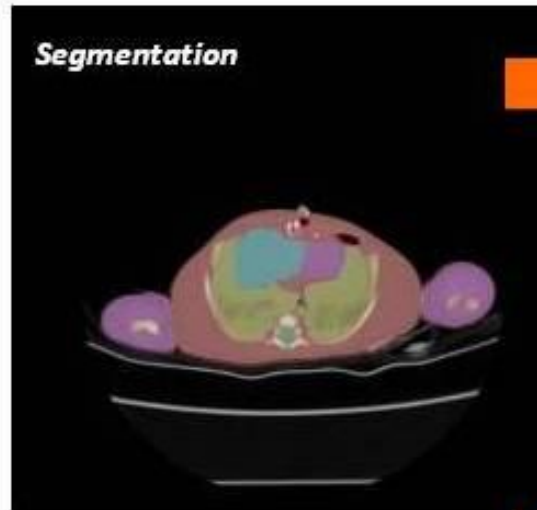


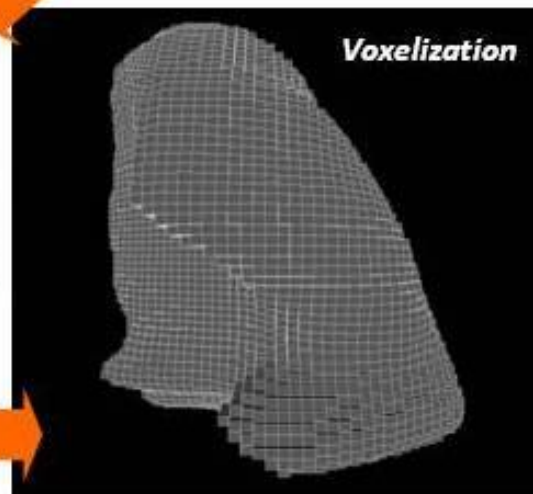
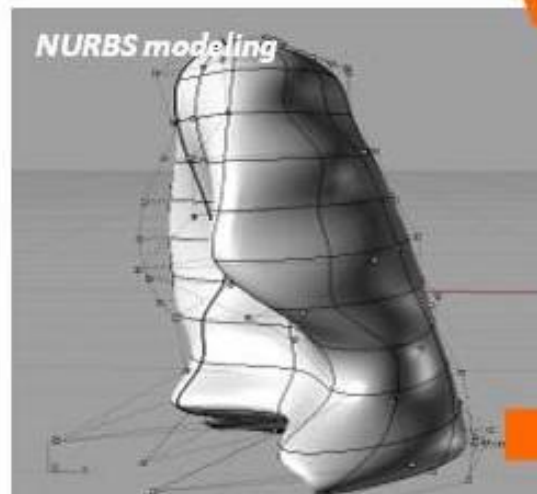
Figure 1-6. The VIP-Man voxel phantom (Xu *et al.* 2000). (A) Original image used for segmentation and (B) final VIP-Man voxel model. Reproduced with permission (© 2000 Health Physics Society).

Segment patient
CT images using
3D-DOCTOR



Convert into
polygon mesh
using **3D-DOCTOR**

Make NURBS
model from
polygon mesh
using **Rhinoceros**



Convert NURBS
model into voxel
model using
MATLAB code
Voxelizer

Figure 1-7. Visual representation of the process by which patient images are used to create a hybrid NURBS phantom.

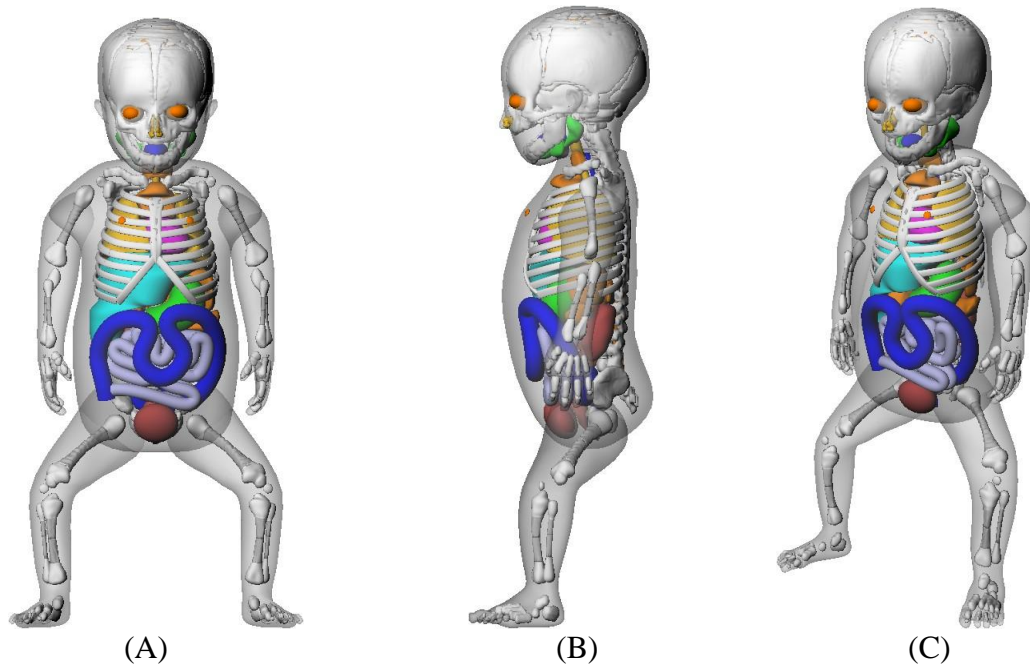


Figure 1-8. The UF newborn hybrid female phantom as viewed in *Rhinoceros*TM showing the (A) coronal, (B) sagittal, and (C) perspective views.

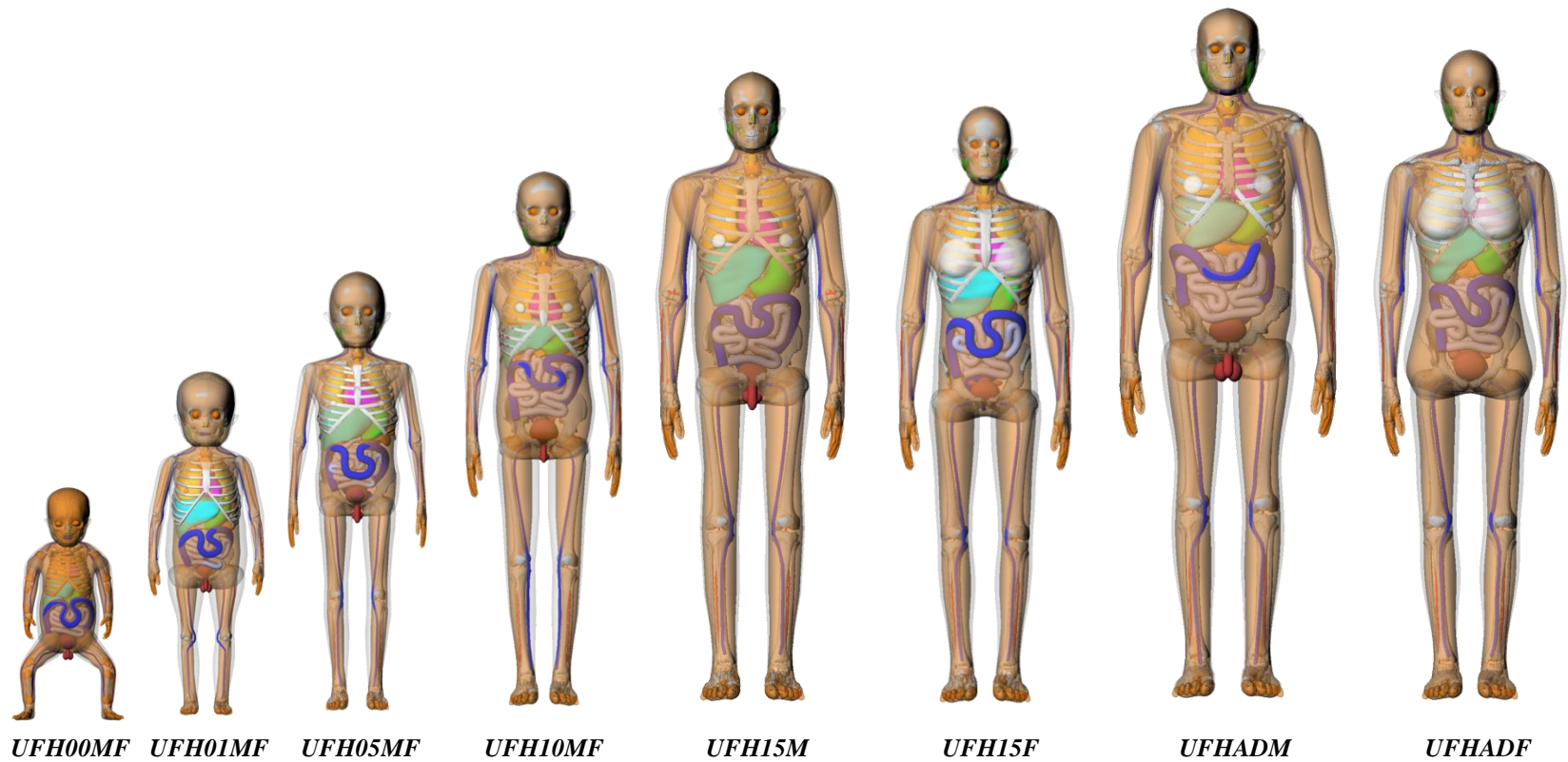


Figure 1-9. The UF NURBS/PM-based hybrid phantom family.

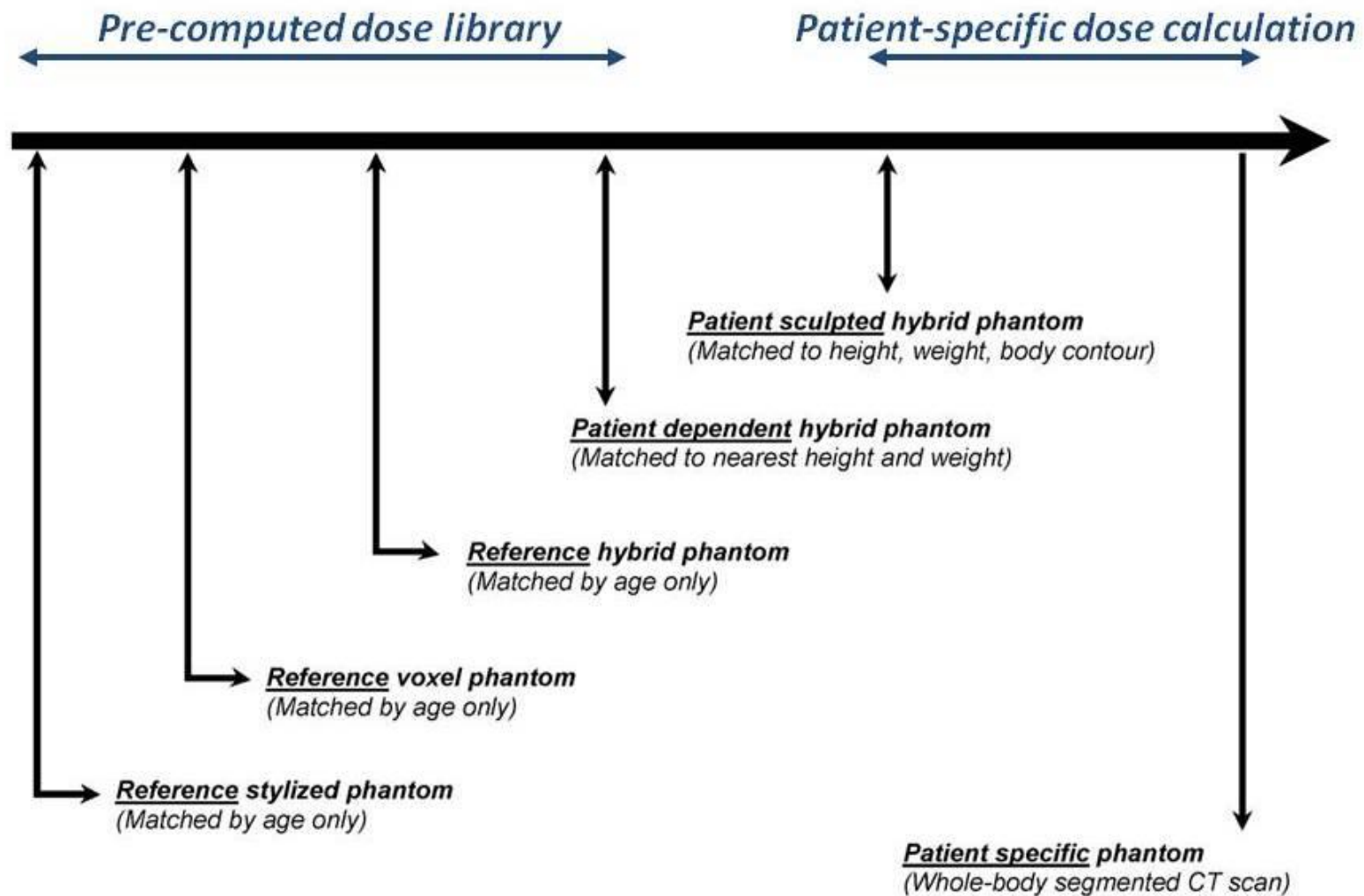
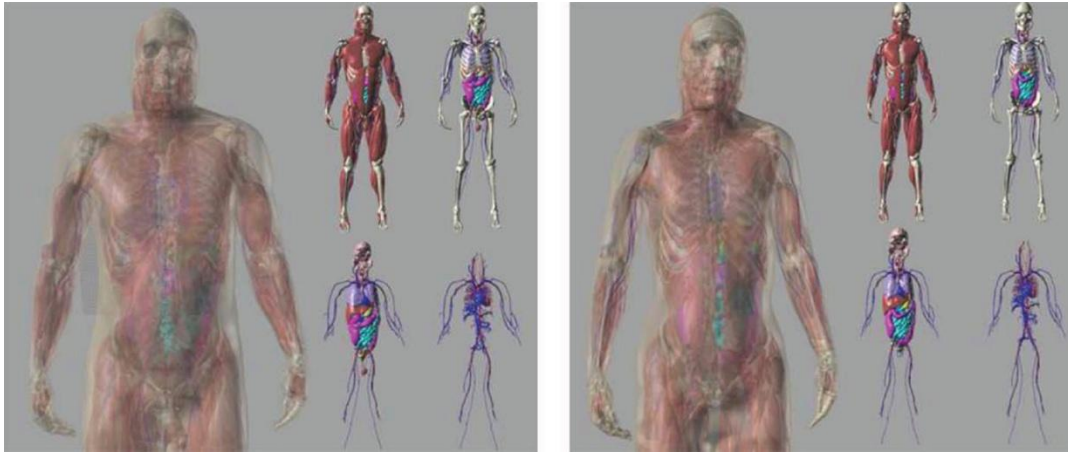
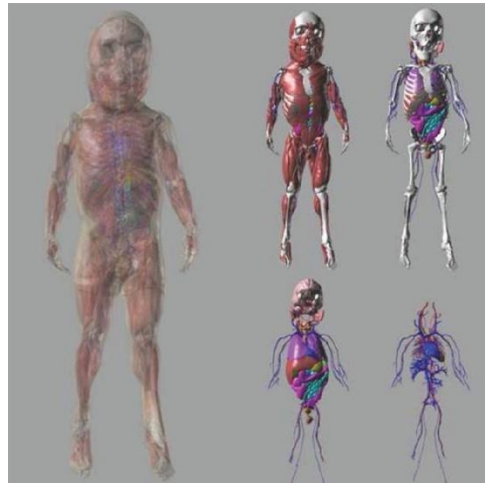


Figure 1-10. The continuum of phantom anatomic specificity showing the progression from population averaged reference phantoms to phantoms almost exactly representative of the patient of interest.



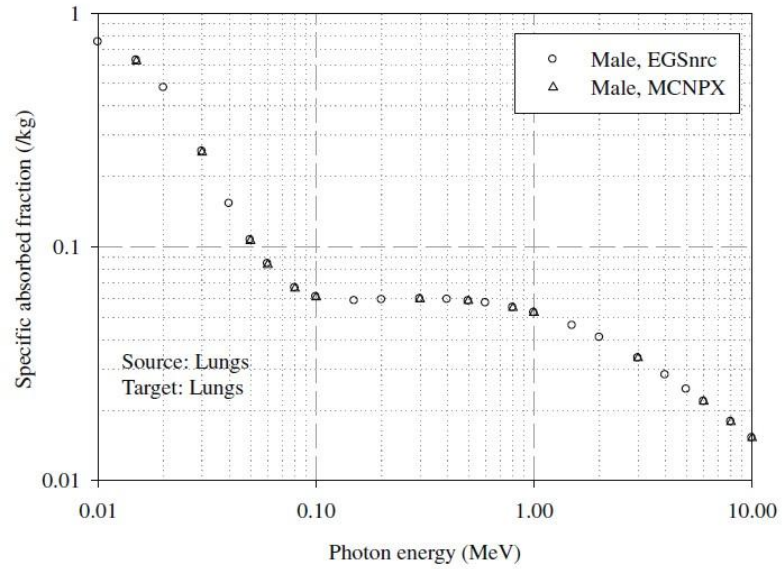
(A)

(B)

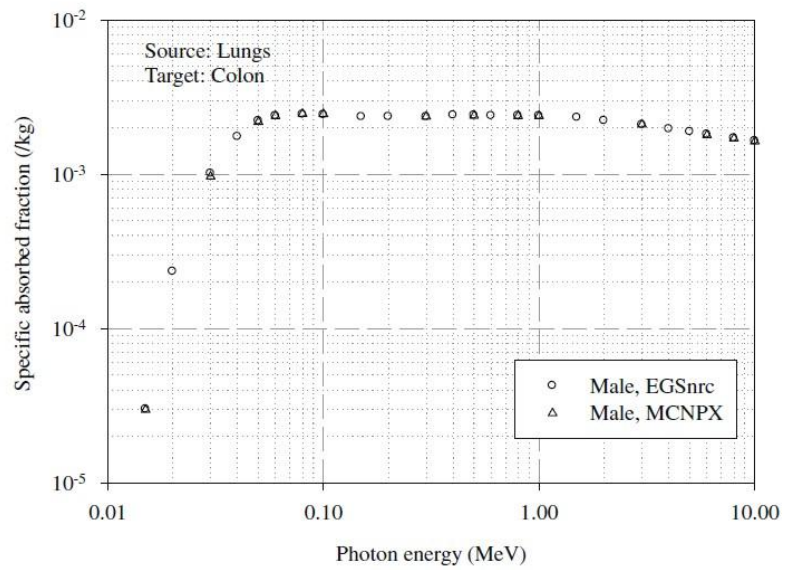


(C)

Figure 1-11. XCAT phantoms of the (A) adult male, (B) adult female, and (C) newborn (Segars *et al* 2009). Reproduced with permission (© 2009 IEEE).

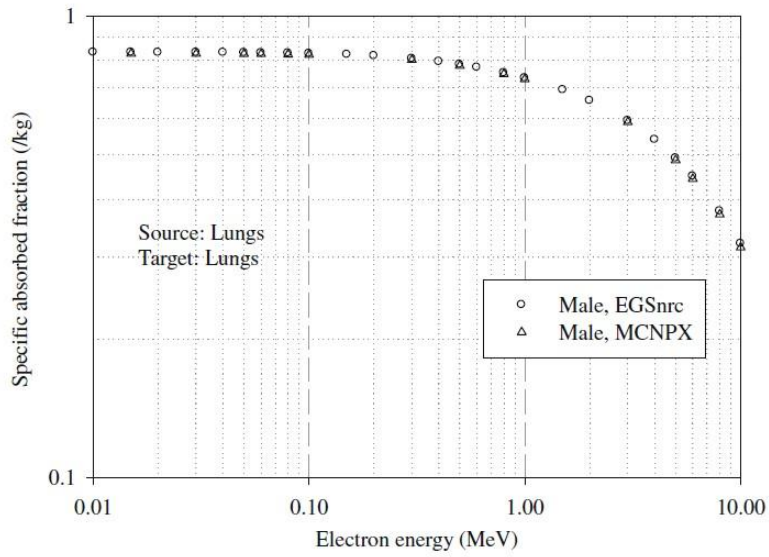


(A)

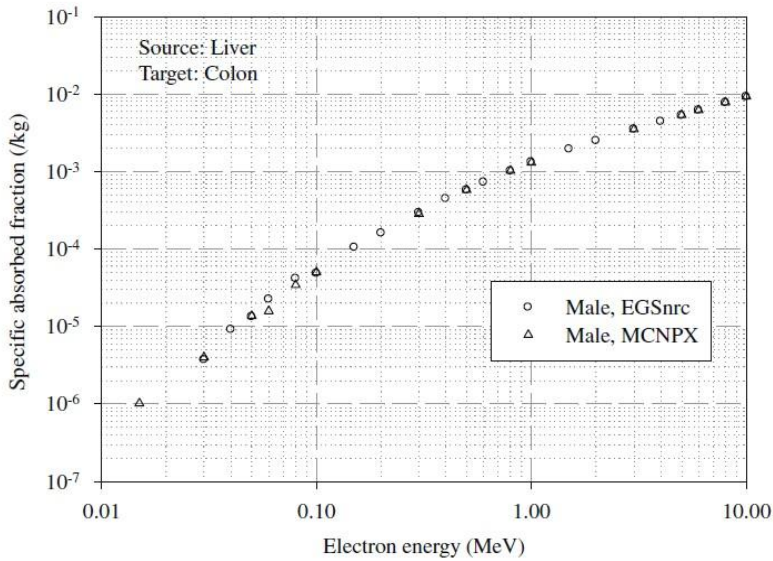


(B)

Figure 1-12. Photon SAFs for the ICRP Publication 110 adult male voxel phantom for (A) the lungs irradiating the lungs and (B) the lungs irradiating the colon using the EGSnrc and MCNPX radiation transport codes (ICRP 2009). Reproduced with permission (© 2009 ICRP).



(A)



(B)

Figure 1-13. Electron SAFs for the ICRP Publication 110 adult male voxel phantom for (A) the lungs irradiating the lungs and (B) the liver irradiating the colon using the EGSnrc and MCNPX radiation transport codes (ICRP 2009). Reproduced with permission (© 2009 ICRP).

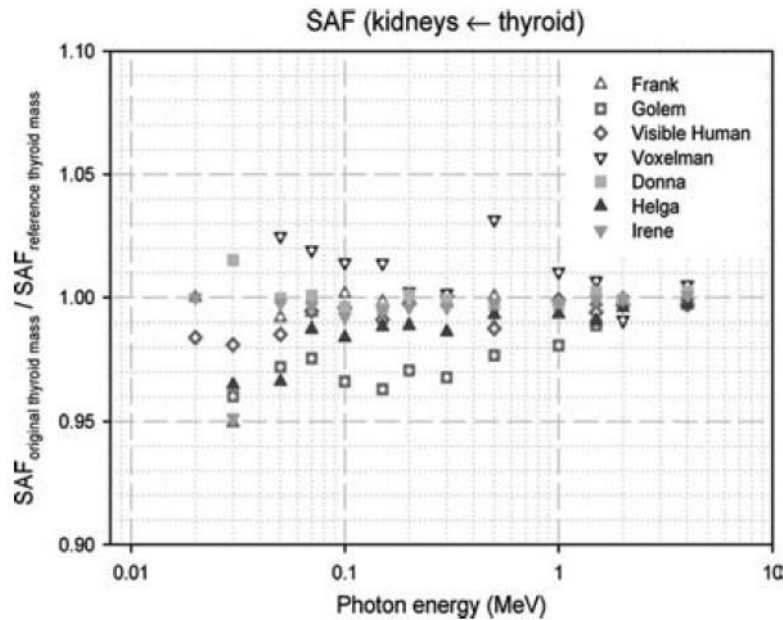


Figure 1-14. Ratios of SAFs for a thyroid source of the original mass to SAFs for thyroid of the reference mass in each GSF voxel phantom to a kidney target (Petoussi-Henss *et al* 2007). Reproduced with permission (© 2007 Petoussi-Henss).

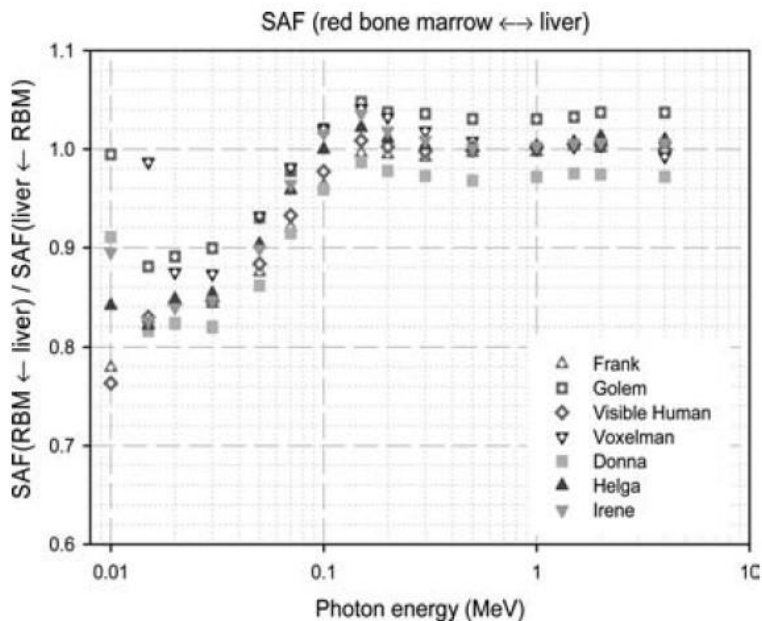


Figure 1-15. Ratios of SAFs for a liver source of the original mass irradiating the red bone marrow to SAFs for the red bone marrow irradiating the liver for the family of GSF voxel phantoms (Petoussi-Henss *et al* 2007). Reproduced with permission (© 2007 Petoussi-Henss).

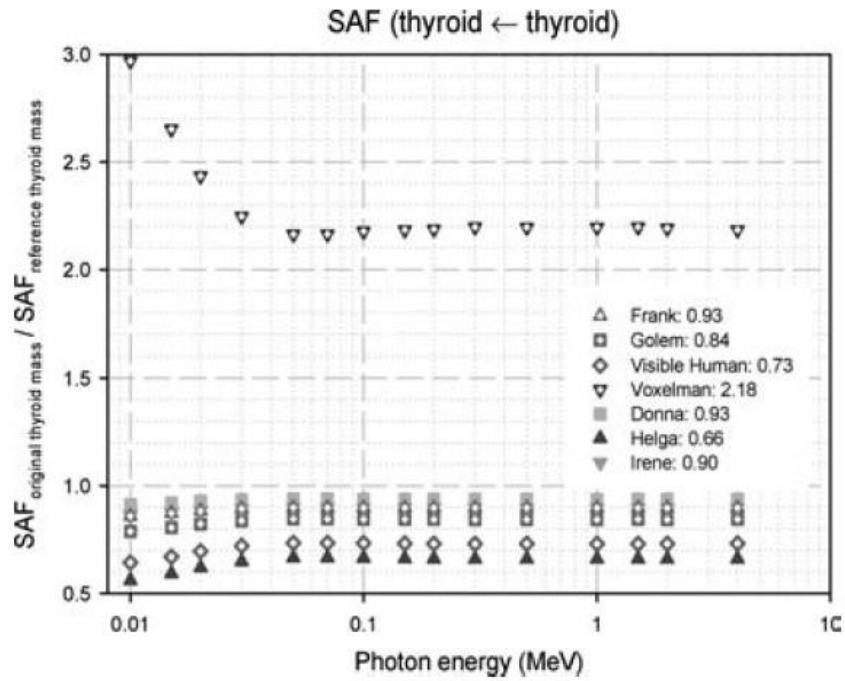


Figure 1-16. Ratios of SAFs for a self-irradiating thyroid source of the original mass to SAFs for a self-irradiating thyroid source of reference mass for the family of GSF voxel phantoms (Petoussi-Henss *et al* 2007). Reproduced with permission (© 2007 Petoussi-Henss).

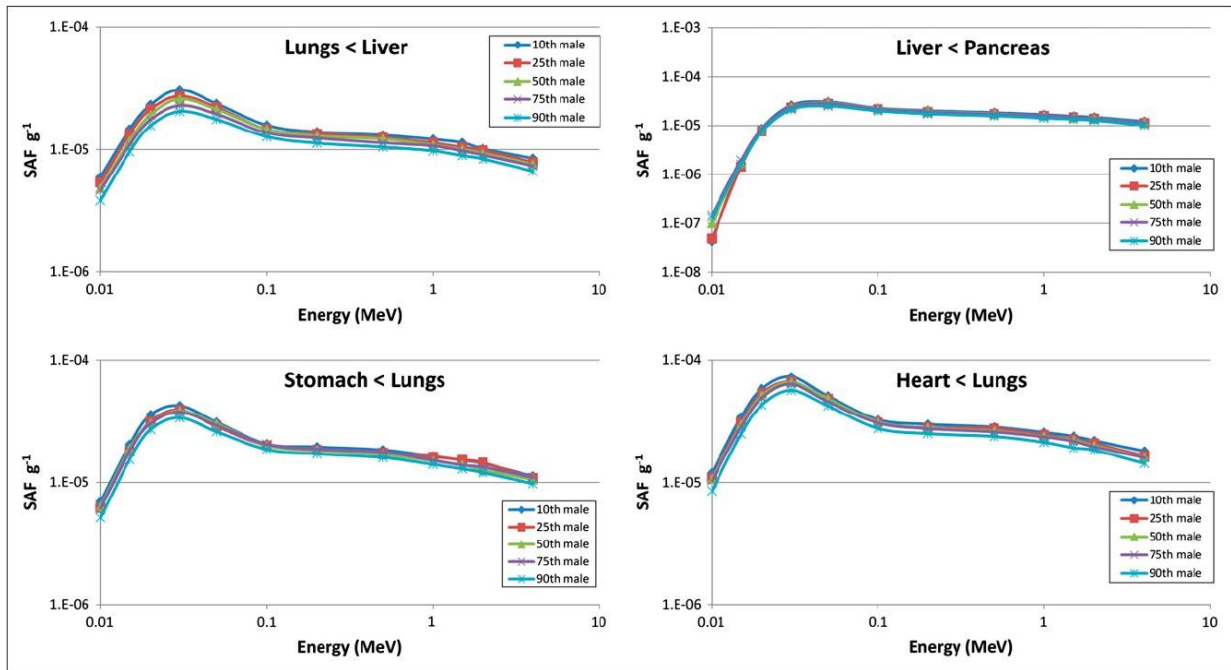


Figure 1-17. SAFs for selected source and target organs in the adult male phantom for varying weight percentiles (Marine *et al* 2010). Reproduced with permission (© 2010 Society of Nuclear Medicine).

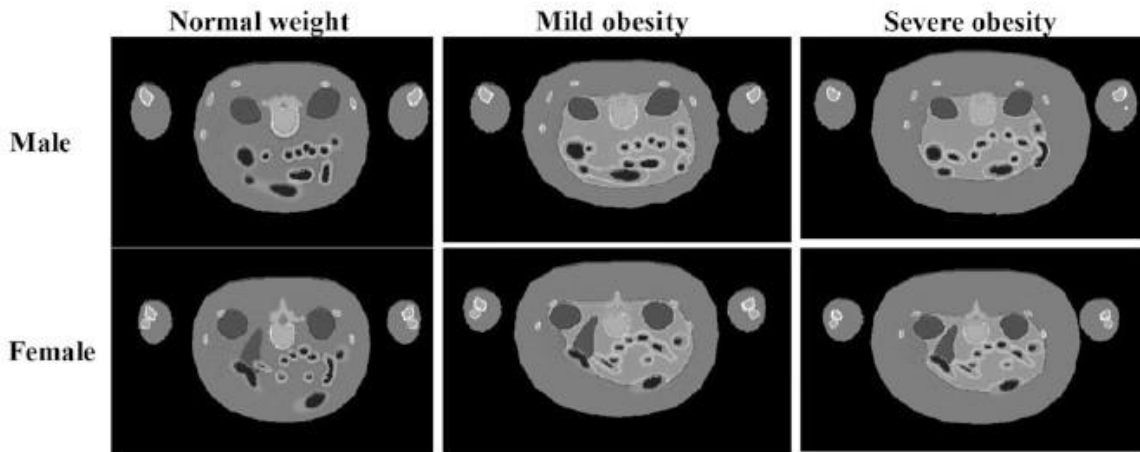
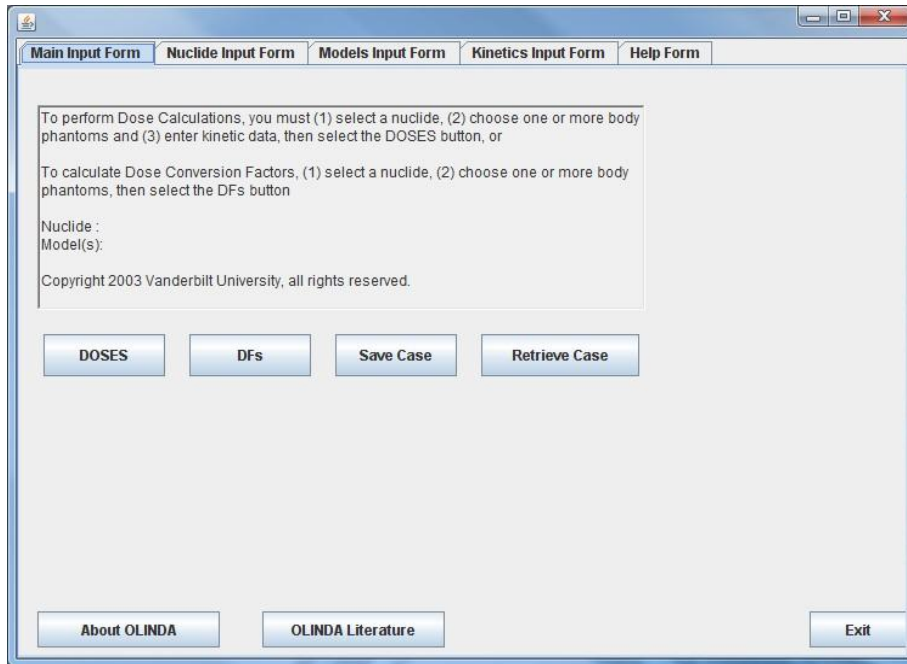
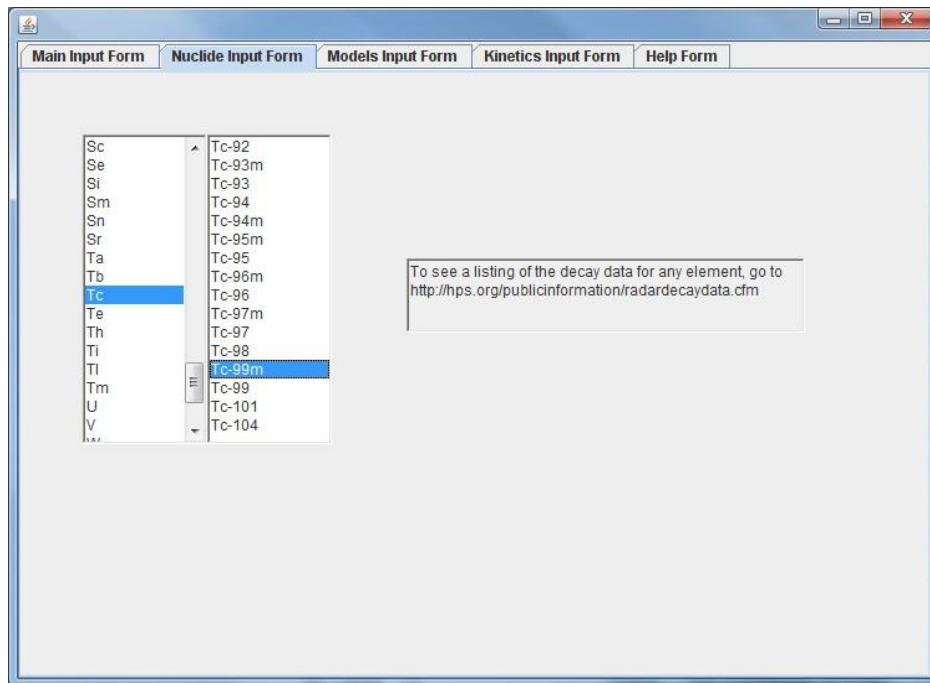


Figure 1-18. Cross-sections of the adult male and female voxelized NURBS phantoms at different levels of obesity (not to scale) (Clark *et al* 2010). Reproduced with permission (© 2010 Society of Nuclear Medicine).



(A)



(B)

Figure 1-19. The (A) main input form, (B) radionuclide input form, (C) phantom models input form (following pages), (D) biokinetics input form (following pages), and (E) output window (following pages) for OLINDA/EXM 1.0 (Stabin 2005).

The screenshot shows the 'Models Input Form' window with the following content:

- Demographic options (checkboxes):
 - Adult Male
 - Adult Female
 - 15-year-old
 - 10-year-old
 - 5-year-old
 - 1-year-old
 - Newborn
 - 3 month pregnant woman
 - 6 month pregnant woman
 - 9 month pregnant woman
- Model selection buttons:
 - Prostate Gland
 - Peritoneal Cavity
 - Spheres
 - Head Model
 - Kidney Model

(C)

The screenshot shows the 'Kinetics Input Form' window with the following content:

The previously used quantity of residence time was confusing to many users. This was only a measure of the number of disintegrations occurring in a source organ. This code works with the number of disintegrations per unit activity administered (uCi-hr/uCi or Bq-hr/Bq), either entered directly, or as calculated from formulas. This is mathematically equivalent to residence times, but is perhaps easier to understand. You may also enter data from a kinetic model, involving values of activity and half-lives, and fit them to a function.

Enter the number of disintegrations for the source organs, or use some of the special options below.

Note: for the Tot Body/Rem. Body field - enter value for Rem. Body if any other organ has been chosen.

Adrenals	0.0000	Ovaries	0.0000
Brain	0.0000	Pancreas	0.0000
Breasts	0.0000	Red Mar.	0.0000
GB Cont	0.0000	CortBone	0.0000
LLI Cont	0.0000	TrabBone	0.0000
SI Cont	0.0000	Spleen	0.0000
StomCont	0.0000	Thymus	0.0000
ULI Cont	0.0000	Thyroid	0.0000
HeartCon	0.0000	UB Cont	0.0000
Hrt Wall	0.0000	Uterus	0.0000
Kidneys	0.0000		
Liver	0.0000		
Lungs	0.0000		
Muscle	0.0000	Tot Body/Rem Body	0.0000

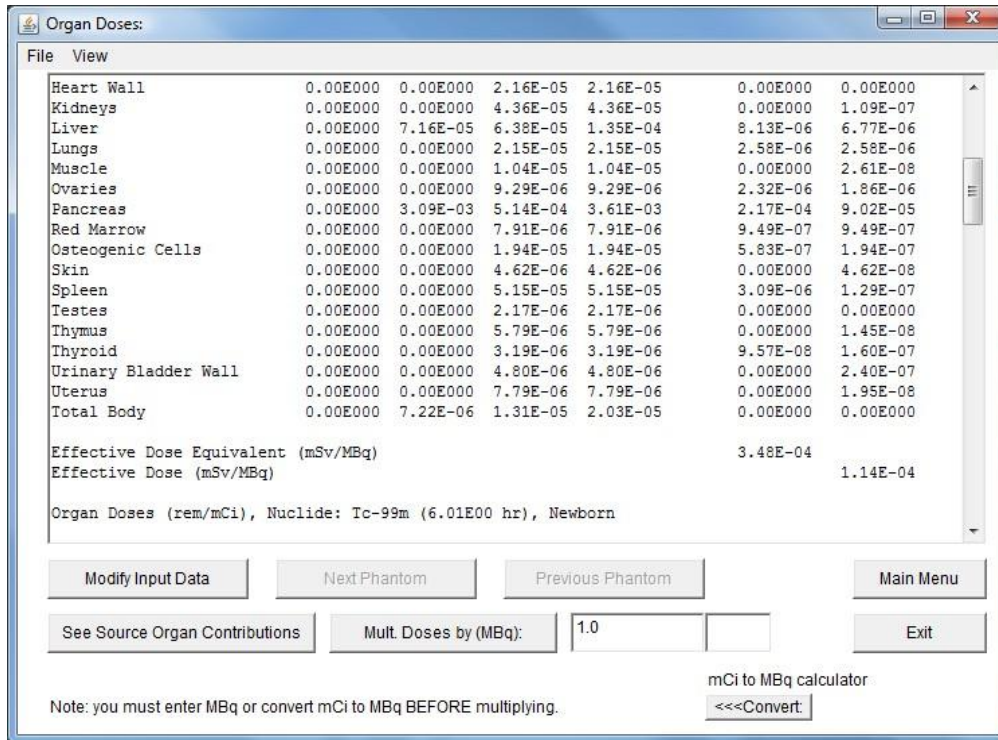
Buttons and options on the right side:

- Get setup (stp) file
- Bone Activity on Bone Surfaces
- Bone Activity in Bone Volume
- Voiding Bladder Model
- ICRP GI Model
- Fractions and Half-times
- Fit data to Model
- Show me some examples

Clear All Data button at the bottom left.

(D)

Figure 1-19. Continued.



(E)

Figure 1-19. Continued.

CHAPTER 2 MATERIALS AND METHODS

Blood Vessel System for the UF Hybrid Phantom Family

Non-Uniform Rational B-Splines Model

The previous iteration of the UF hybrid phantom family was described by 64 unique structures including a separation of CB and spongiosa/MC. The final desired improvements to the phantoms included the addition of separate delineation of skeletal muscle, subcutaneous fat, lymphatic nodes, and major blood vessels. A blood vessel model was needed for the simulation of distributed blood sources as well as completeness of the computational model itself.

Currently, a distributed blood source would be apportioned 9% to the heart chambers, 10.5% to the lungs, and 80.5% to the remaining tissues (the “remaining tissues” compartment is broken down further in Tables 2.13 and 2.14 of ICRP Publication 89 for the adult male, for which newborn values can be approximated) (ICRP 2002). It was desired that a higher level of detail be achieved with the addition of a system of blood vessels. Upon examining the list of documented reference vessels, it was determined that the pulmonary vessels could be appropriately modeled by uniformly apportioning 10.5% of the total blood volume to the lungs. Consequently, the available vessels to consider were the systemic vessels: aorta and large arteries, small arteries, capillaries, small veins, and large veins. Capillaries typically have diameters less than $10\ \mu\text{m}$ in the adult male (ICRP 2002), so those structures were ruled out. Small arteries have diameters less than $2\ \text{mm}$, and small veins have diameters less than $5\ \text{mm}$. Due to these small dimensions and the lack of space between organs in the phantoms, it was determined that small arteries and veins would not be modeled explicitly. Large arteries have diameters between $2\ \text{mm}$ and $6\ \text{mm}$ and large veins have diameters between $5\ \text{mm}$ and $10\ \text{mm}$ in the adult male (ICRP 2002). These dimensions could be modeled effectively in the NURBS

environment for the adult male, so it was determined that the explicit blood vessel system would consist of large arteries and veins only.

Values for the distribution of blood volume by organ and vessel system are only given for the adult male and female in ICRP Publication 89. While it is noted that there may be age-dependent variations in blood volume distribution, no reference values have been adopted. Based on the adult distribution information in ICRP Publication 89, the ratio of large vein volume to large artery volume is 3:1. In this study, this same volume ratio was matched consistently across all phantom ages. Reference blood vessel diameter information is only available for the adult male, so the adult male blood vessel system was constructed with the available reference information. The blood vessel systems of the newborn and adult female were then constructed artistically due to lack of imaging data. The one-year-old, five-year-old, ten-year-old, and fifteen-year-old male systems were subsequently created by interpolating vessel diameters between those in the newborn and adult male systems. The fifteen-year-old female system was constructed by interpolation of blood vessel diameter between the newborn and adult female systems. The vessels were then adjusted to match the 3:1 vein to artery volume ratio.

Since the major blood vessels were not directly segmented from CT or MR scans, they were artistically created. It was not necessary to match the total blood volume since the purpose of designing the blood vessel system was to provide a vehicle for the apportionment of blood volume rather than create an anatomically exact representation of the human systemic blood vessel system. Furthermore, the modeling space available for placing blood vessels is very limited in the torso of these phantoms, and thus compromises had to be made. It is a possibility that the aortic arch and other vessels in the torso may not appear visually accurate due to lack to space. Again, the purpose of these vessel models is to provide a dosimetric source region in the

phantoms for radiopharmaceutical decays occurring in circulation, and not necessarily to provide for realistic imaging of these tissue structures.

The major arteries roughly represented in the blood vessel model include the common carotid arteries and subclavian artery in the neck and clavicles regions, the brachial, radial, and ulnar arteries in the arms, the aortic arch and thoracic and abdominal aortas in the thoracic and abdominal regions, and the femoral, popliteal, anterior tibial, and posterior tibial arteries in the legs. Each vessel mentioned was not necessarily explicitly modeled, but the positions of these vessels were occupied by the constructed surrogate vessels.

The major veins roughly represented in the blood vessel model include the external and internal jugular vein and subclavian vein in the neck and clavicles regions, the axillary, cephalic, brachial, basilica, radial, and ulnar veins in the arms, the superior and inferior vena cava in the thoracic and abdominal regions, and the femoral vein in the legs. Each vessel mentioned was not necessarily explicitly modeled, but the positions of these vessels were occupied by the constructed surrogate vessels.

It was decided that the blood vessels would be modeled by pipe structures within *Rhinoceros*TM NURBS modeling software. The foundation of a pipe structure in the 3-D software package is a curve which is created by user-defined control points. For this purpose, the free-form method of curve creation was used, wherein the curve itself was not connected directly from control point to control point but by spline fitting from the addition of each subsequent control point. Consequently, the blood vessel systems were created stylistically, based on the placement of series of control points. The control points were adjusted independently in 3-D to produce the desired shapes.

Vascular Dosimetry for Blood Sources

Blood vessel systems in computational phantoms serve a purpose in that they both assist in the simulation of a distributed blood source and move the computational phantoms towards a higher level of anatomic realism. The construction methodology detailed in the previous section pertains exclusively to the blood vessel lumen, the volume in the blood vessel through which blood flows. Neglected in this blood vessel construction was consideration for blood vessel walls. Blood vessel wall toxicity is an issue that should be considered in some radionuclide therapy applications, including myeloablative therapy, a high dose procedure where AA is determined by dose limitations to normal organs other than bone marrow, and possibly some other standard dose radioimmunotherapy procedures (Hobbs *et al.* 2010). Hobbs *et al.* (2010) found that arterial wall absorbed doses for standard radioimmunotherapy ranged from approximately 0.6 Gy to 3.7 Gy and from approximately 9.4 Gy to 11.4 Gy for myeloablative therapy (one patient had a dose of 32.6 Gy) (Hobbs *et al.* 2010). Early studies had placed the dose limit for arterial toxicity in the neighborhood of 35 Gy (Brosius *et al.* 1981), but more recent studies have shown that long-term complications can present at doses as low as about 23 Gy (Hull *et al.* 2003). Certain nuclear medicine therapy procedures approach these limits, but blood vessel toxicity does not seem to be as much of a concern for nuclear medicine imaging, although one should always be cognizant of it.

It was clear from the outset that blood vessel walls could not be effectively modeled in the voxel environment due to the small dimensions. NURBS versions of blood vessel walls could have been constructed, but they would all but disappear from the voxel model since the limiting voxel resolutions are generally larger than blood vessel wall thicknesses. Table 2-1 shows typical blood vessel wall thicknesses for the newborn to 1-year-old and adult arterial, venous,

and pulmonary systems (ICRP 1975). Minimum, maximum, and average values for this set of blood vessel wall thicknesses are $1 \mu\text{m}$, 1.63 mm , and 0.905 mm , respectively (ICRP 1975). The minimum voxel resolution used in the UF hybrid computational phantom family in this study is 0.663 mm for the UFH00MF phantoms (see the “Voxel Resolution” section of the “Photon Specific Absorbed Fractions” section of Chapter 2). While the walls of some vessel types could have been modeled, many of the wall thicknesses are smaller than the voxel resolutions used in the phantoms. In addition, only a select set of blood vessels were able to be modeled at all, so assigning a wall thickness to those vessels would be difficult.

Instead of explicitly modeling blood vessel walls within the NURBS phantoms, a computational dosimetry study was designed to develop an estimation model for determining radiation absorbed dose to blood vessel walls. Simple coaxial cylinders were selected as the geometry to represent both blood vessels and blood vessel walls. For a blood source, the blood vessel lumen would act as the source of radiation, so the inner cylinder in this model was assigned a uniform distribution of radiation emissions. Blood vessels with varying luminal areas, wall thickness, and lengths were designed based on luminal diameters determined from the blood vessel systems developed for the UF hybrid phantom family (discussed in the previous section), minimum, maximum, and average wall thicknesses calculated from ICRP Publication 23 (Table 2-1) (ICRP 1975), and typical lengths of vessels measured from the UFHADM phantom. Varying these parameters allowed investigation into the dependence of blood vessel wall dose on overall size of the blood vessel. Then, depending on the results, certain dosimetric trends could be eliminated from consideration. Two radiation types, photons and electrons, and three energies, 10 keV , 500 keV , and 4 MeV , were simulated to assess dose dependence on particle type and particle energy.

For each blood vessel modeled, a second, identical blood vessel was created with its center located at a distance equal to the radius of the original blood vessel plus the wall thickness of the blood vessel. In a similar simulation the newly created blood vessel was moved from its current position 5 *cm* further from the original blood vessel. Relative contributions from blood located in vessels near the blood vessel of interest to blood vessel wall absorbed dose were determined in this way. If relative contributions were low, adjacent vessels could be ignored, and a one-vessel model could be adopted. In contrast, if relative contributions from adjacent vessels were significant, a model could be developed to give a best estimate of absorbed dose to the blood vessel walls. Absorbed dose to the first blood vessel wall from its contents will be referred to as “self”-dose in this context even though the source and target are not the same tissue. Absorbed dose to the second blood vessel from the source blood vessel will be referred to as cross-dose in this context. Single blood vessels imbedded in an infinite soft tissue medium were also simulated for verification purposes, ensuring differences between blood vessel wall, blood, and soft tissue elemental compositions would not perturb dose estimates.

MCNPX v2.6 was used for radiation transport, and the energy deposited in both the blood vessel wall surrounding the source and the adjacent blood vessel wall was recorded. Particle histories were set to 10^7 , 5×10^6 , and 10^6 for radiation energies of 10 *keV*, 500 *keV*, and 4 *MeV*, respectively. Secondary electrons were followed, and the Integrated Tiger Series (ITS)-style electron energy bin indexing algorithm was used¹. Elemental compositions for blood, heart wall, and adult soft tissue from ICRP Publication 89 were used for the blood vessel contents,

¹ The ITS-style secondary electron indexing algorithm is explained in the subsection “Electron energy indexing algorithm” of the subsection “Miscellaneous Transport Details” of the subsection “Photon Specific Absorbed Fractions” of Chapter 2.

blood vessel walls, and soft tissue, respectively (ICRP 2002). The geometry for this study can be seen in Figure 2-1.

In this simulation environment, a true blood source would fill both blood vessel contents and cross-irradiate both blood vessel walls. However, relative contributions to dose (self-dose versus cross-dose) could not be deciphered if both blood vessel contents were treated as the radiation source. Both blood vessels in each simulation scenario were geometrically identical, so the absorbed dose from one blood vessel contents to its own wall and the wall of the other blood vessel wall was considered to be unchanged when the blood vessel contents source was located in the other blood vessel. The true absorbed dose to both walls was mathematically derived using Equation 2-1.

$$D(\text{wall}_1 \leftarrow \text{cont}) = D(\text{wall}_2 \leftarrow \text{cont}) = \frac{V_1^{\text{cont}} D(\text{wall}_1 \leftarrow \text{cont}_1) + V_2^{\text{cont}} D(\text{wall}_2 \leftarrow \text{cont}_1)}{V_1^{\text{cont}} + V_2^{\text{cont}}} \quad (2-1)$$

where $D(\text{wall}_1 \leftarrow \text{cont})$ is the absorbed dose to the wall of the first blood vessel from the contents of both blood vessels, $D(\text{wall}_2 \leftarrow \text{cont})$ is the absorbed dose to the wall of the second blood vessel from the contents of both blood vessels, $D(\text{wall}_1 \leftarrow \text{cont}_1)$ is the absorbed dose to the wall of the first blood vessel from its own contents, $D(\text{wall}_2 \leftarrow \text{cont}_1)$ is the absorbed dose to the wall of the second blood vessel from the contents of the first blood vessel, V_1^{cont} is the volume of the contents of the first blood vessel, and V_2^{cont} is the volume of the contents of the second blood vessel. Equation 2-1 reduces to a simple linear average of $D(\text{wall}_1 \leftarrow \text{cont}_1)$ and $D(\text{wall}_2 \leftarrow \text{cont}_1)$ since V_1^{cont} and V_2^{cont} are equal for each irradiation scenario.

Skeletal Photon Fluence-to-Dose Response Functions

Sub-Segmented Skeleton Development

In the first iterations of the UF hybrid computational phantoms, the skeletons in the phantoms were homogeneous, a uniform mixture of all relevant sub-regions of the skeleton – AM, IM, TB, and CB. The homogeneous skeletal model was created by segmenting the skeleton in actual patient images and importing the segmented volumes into *Rhinoceros*TM. Once imported into *Rhinoceros*TM, the skeletal sites were left in the default polygon mesh (PM) format (the PM format defines a volume by a series of polygons connected at their vertices). Since many bone sites could not be effectively modeled with NURBS surfaces, they were left in the PM format. However, the ribs were sometimes distorted due to the slice thickness of the original CT imaging, and so they were built stylistically by creating pipe shapes based on central tracks taken from the original PM rib cage model (Pafundi *et al.* 2009). While the homogeneous model provided adequate information to compute reasonable dose estimates to the skeleton, a considerable amount of anatomic detail was lost. Further anatomic detail was needed for the human skeleton, so a sub-segmented skeletal model was developed.

The process of creating a multiple region skeletal model began with the segmentation of all bone sites from a set of whole-body cadaver CT data (Pafundi *et al.* 2009). This was done automatically by adjusting the lower bound of the thresholding window in *3D-DOCTOR*TM to exclude cartilage (Pafundi *et al.* 2009). Application of this thresholding window allowed for automatic segmentation of the whole skeleton from every CT slice, creating a whole-body homogeneous skeletal model in one action step. This initial segmentation provided the outer contour of the skeleton. Next, the cartilage was manually segmented and two distinct cartilage regions were identified: bone-associated cartilage and non-bone-associated cartilage (Pafundi *et al.* 2009). The spongiosa region and associated sub-regions were then delineated by the analysis

of microCT images of selected bone sites (Pafundi *et al.* 2009). The sternum, occipital bone, 2nd right rib, 2nd left rib, L₂-L₅ vertebrae, T₉-T₁₂ vertebrae, C₃-C₇ vertebrae, T₁-T₅ vertebrae, T₁₀-T₁₂ vertebrae, L₁-L₅ vertebrae, 4th right rib, 4th left rib, and a portion of the right iliac crest obtained from two specimens were imaged using microCT at an isotropic resolution of 30 μm (Pafundi *et al.* 2009). The TM and TB within each bone site were automatically segmented by applying a filter based on visual inspection of the image gradient magnitude (Rajon *et al.* 2006). This technique separated the TM and TB and created a new binary image file with all gray-scale values attributed to TM converted to black pixels and all gray-scale values attributed to TB converted to white pixels. These files were then used to calculate the fraction of spongiosa occupied by trabeculae and the fraction occupied by TM. This was performed for every bone site, and skeletal tissue masses were then obtained using methods detailed in Pafundi *et al.* (2009) and Hough *et al.* (2011).

A detailed model of the human skeleton including the marrow cavities of the spongiosa cannot be effectively represented in voxel models because voxel resolutions required to preserve the detail of the skeletal microstructure would create voxel models too large to efficiently simulate with radiation transport codes. For example, if all the phantoms in the UF phantom family were voxelized at an isotropic resolution of 30 μm , the average binary file size would be well over 1 *TB*. Consequently, while the previously discussed advancements in skeletal tissue modeling for the purpose of computational radiation dosimetry produced extensive data characterizing the distribution of skeletal tissues, the results were not directly applicable to the corresponding whole-body NURBS phantom. However, the results *did* lay the groundwork for the development of skeletal dosimetry methods that would be incorporated in steps separate from the primary dosimetry simulations. While the AM and TB sub-regions of the spongiosa could

not be explicitly modeled in *Rhinoceros*TM, the spongiosa itself was able to be modeled. Resultantly, the final heterogeneous skeletal model was visualized in *Rhinoceros*TM as a three region model with the regions being the cartilage, cortical bone, and trabecular spongiosa. Examples of heterogeneous bone sites in *Rhinoceros*TM can be seen in Figure 2-2. The orange wireframe regions are cartilage. The black wireframe regions indicate cortical bone, spongiosa, and medullary cavities. Examining the long bone in Figure 2-2 (B), outer and inner black wireframe regions can be seen, the outer region representing cortical bone and the inner region representing the medullary cavities in the shaft and spongiosa in the proximal and distal ends. A similar situation is seen in non-long bones where the inner black wireframe region is spongiosa.

Skeletal Photon Fluence-to-Dose Response Function Development

15-year-old and newborn phantoms

Since the intricacies of the spongiosa could not be explicitly modeled in the NURBS/PM environment, another technique was used to incorporate the lost spongiosa detail into the phantom – the skeletal photon fluence-to-dose response function. A dose response function (DRF) allows for the pre-calculation of the absorbed dose of a particular region per arbitrary unit of measure, in this case photon fluence in regions of the skeleton. In other words, separate simulations were performed which were able to model much smaller volumes. The results of these simulations were then used in conjunction with the NURBS-based computational phantom so that the skeletal microstructure did not have to be explicitly modeled in *Rhinoceros*TM.

First, the radiosensitive cells in skeletal tissue had to be identified. Much research has been done to determine this, and the radiosensitive cells were found to be hematopoietic stem cells, osteoprogenitor cells, and chondrocytes (Pafundi *et al.* 2010). The surrogate tissues for these radiosensitive cells were determined to be active marrow (AM) for hematopoietic stem cells, endosteum or total shallow marrow (TM₅₀) for osteoprogenitor cells, and unossified

cartilage for chondrocytes (Pafundi *et al.* 2010). The endosteal region of the spongiosa was defined as all bone marrow that is within $50\ \mu\text{m}$ of either the trabecular bone surfaces or the inner cortical bone surfaces of the long bone shafts (Bolch *et al.* 2007). For the newborn, only AM is present within the skeleton, and so total shallow marrow TM_{50} and active shallow marrow AM_{50} are equivalent.

Photons that interact with human tissue liberate electrons, and those electrons then directly ionize the medium. The energy deposited in this process, divided by the total mass of the medium irradiated results in the calculated radiation absorbed dose. Consequently, while it is of great interest where the emitted photons are transported, the electrons liberated by those photons must also be taken into account. Because of the small dimensions of the skeletal microstructure, secondary electron transport is a concern within whole-body phantom radiation transport. This is due to the fact that electrons liberated by high energy photons have ranges which are relatively large compared to the spacing of the trabeculae in the spongiosa. To properly characterize the behavior of secondary electrons liberated in the skeleton, the AFs for different skeletal source-target combinations were calculated.

The paired-image radiation transport (PIRT) model was used in conjunction with the EGSnrc radiation transport code to calculate the skeletal AFs (Pafundi *et al.* 2010). The combined model allows for tracking of electrons within the microstructure of the spongiosa simultaneously with the macrostructure of the hybrid phantom heterogeneous skeletal sites (Shah *et al.* 2005). The microstructure was described with voxels of $60\ \mu\text{m}$ isotropic resolution, and the macrostructure was described with voxels ranging from isotropic resolutions of $50\ \mu\text{m}$ to $200\ \mu\text{m}$ (Pafundi *et al.* 2010). Skeletal AFs were calculated for photons incident on the spongiosa with energies ranging from $1\ \text{keV}$ to $10\ \text{MeV}$ (Pafundi *et al.* 2010). Tissue regions of

AM, TBV, and CB volume (CBV) were all simulated as source tissues, and AM and TM₅₀ were simulated as target tissues.

An in-house *MATLAB*TM code was used to calculate the skeletal photon fluence-to-dose response functions, based on the AFs of the two target tissues, AM and TM₅₀, the elemental compositions of mineral bone (trabecular and cortical), AM, and cartilage, and the masses of both source and target regions. The code uses the formulation in Equation 2-2 (Cristy *et al.* 1987, Johnson *et al.* 2011):

$$\frac{D(r_T)}{\Phi(E)} = \sum_{r_S} \frac{m_S}{m_T} \int_0^{\infty} \phi(r_T \leftarrow r_S, T_i) (i/\rho)_{r_S} n_{r_S}(T_i) T_i dT_i \quad (2-2)$$

where m_S and m_T are the masses of the source and target tissues, respectively, $\phi(r_T \leftarrow r_S, T_i)$ is the AF in target tissue r_T from source tissue r_S for electrons of energy T_i , $(i/\rho)_{r_S}$ are the mass attenuation coefficients for source tissue r_S where i represents the photoelectric (τ), Compton (σ), and pair production (κ) processes, $n_{r_S}(T_i) T_i dT_i$ is the number of electrons with energies between T_i and $T_i + dT_i$ liberated in source tissue r_S for interaction type i , and $D(r_T)/\Phi(E)$ is the skeletal photon fluence-to-dose response function relating the absorbed dose to target tissue r_T to the incident fluence of photons with energy E on the spongiosa.

Calculations were also performed setting the AF to unity for self-irradiation and to zero for cross-fire for every bone site, thereby modeling the kerma approximation. The kerma approximation assumes that all of the energy of the liberated secondary electrons is locally deposited; none of the energy escapes into any adjacent regions. Thus, for a source region emitting electrons liberated by the incident photons, all of the electrons will be absorbed by that source region, resulting in an AF of approximately unity for the self-dose irradiation scenario. Alternately, no electrons emitted from the source region will penetrate into adjacent regions, so

the AF for the irradiation geometry of the source and target regions not being the same is approximately zero. The reason for this will be explained in greater detail later, but to summarize, the skeletal fluence-to-dose response functions were assumed to conform to the kerma approximation for energies greater than 200 keV.

1-year-old, 5-year-old, and 10-year-old phantoms

Methodology – Skeletal photon fluence-to-dose response functions as developed for the UFH00MF and UFH15MF phantoms were derived based on electron AFs that were calculated using the PIRT algorithm (Pafundi *et al.* 2010). Cadaver bone samples were used to generate the detailed geometries within spongiosa and the medullary cavities for these phantoms. However, even though the macroscopic images of all bone sites with CB, homogeneous spongiosa, and homogeneous MCs were used to generate the skeletal models for the UFH01MF, UFH05MF, and UFH10MF phantoms, cadavers were not available to create detailed microstructure models for these phantoms. Therefore, a different approach was used to calculate skeletal electron AFs for sources in spongiosa and MCs, and these results were used in the skeletal fluence-to-dose response function equation (Equation 2-2).

A combination of chord-based infinite spongiosa transport (CBIST) and single-image radiation transport (SIRT) was used to generate the set of electron AFs for the UFH01MF, UFH05MF, and UFH10MF phantoms. CBIST refers to the simulation of electrons traversing spongiosa by way of measured chord-length distributions. Most current skeletal fluence-to-dose response functions are based on the chord-length distributions measured by Spiers and his colleagues at the University of Leeds in the 1970s (Spiers 1969, Whitwell 1973, Beddoe 1976). In those studies, linear path lengths were measured through alternating regions of trabecular bone and bone marrow (Stabin *et al.* 2002). By generating frequency distributions of varying chord

lengths, the complicated microarchitecture was represented without having to generate explicit computer models (computer models were not an option at the time).

Bouchet *et al.* (2000) used these chord-length distributions in combination with the EGS radiation transport code to calculate electron AFs in 7 different bone sites. Electron AFs were determined by randomly sampling chord-lengths of trabecular bone and marrow cavities alternately. Once a chord-length was chosen, electron range-energy relationships were used to determine the residual kinetic energy of the electron. From this, the energy deposited in each region of spongiosa could be determined. Electrons were transported until all of their energy was expended which effectively created an infinite region of spongiosa – hence the name chord-based *infinite* spongiosa transport. Since only 7 bone sites were analyzed, the AFs calculated in the Bouchet *et al.* (2000) study were assigned to all other bone sites based on their similarity to the microstructure of each respective bone site.

However, this infinite transport did not take into account electron escape into cortical bone or any other surrounding tissues. So, in the current study, the macroscopic images of each bone site were used to calculate electron escape fractions (EFs) using the SIRT transport methodology. SIRT uses the macroscopic bone models that include the CB, homogeneous spongiosa, and homogeneous MCs in each bone site. These models were converted into voxel models, and electrons were transported. Energy deposition in spongiosa and MC regions was tracked, and the electron AF was calculated. The complement of the electron AF gives the fraction of electron energy that escapes spongiosa and MC regions. By multiplying the electron AFs obtained from the CBIST simulations by the spongiosa/MC AFs calculated in the SIRT simulations, complete electron AFs were obtained for use in the skeletal photon fluence-to-dose response function formulation (Pafundi 2009). Equation 2-3 was used to calculate the CBIST electron AFs for the

TBV, AM, and IM sources, and Equation 2-4 (derived from Pafundi (2009)) was used to calculate the CBIST electron AFs for the CBV source (Pafundi 2009).

$$\phi_x(r_T \leftarrow r_S, E_i) = \phi_{CBIST}(r_T \leftarrow r_S, E_i) \cdot \phi_{SIRT}(Sp / MC_x \leftarrow r_S, E_i) \quad (2-3)$$

$$\phi_x(r_T \leftarrow CBV, E_i) = \phi_{SIRT}(Sp / MC_x \leftarrow CBV, E_i) \left[\frac{A}{BVF + 1} \right] \quad (2-4)$$

$$\text{where } A = \phi_{CBIST}(r_T \leftarrow AM, E_i) \cdot CF + \phi_{CBIST}(r_T \leftarrow IM, E_i) \cdot (1 - CF) \\ + \phi_{CBIST}(r_T \leftarrow TBV, E_i) \cdot BVF$$

where $\phi_x(r_T \leftarrow r_S, E_i)$ is the electron AF for source tissue r_S irradiating target tissue r_T (either AM or TM₅₀) for electrons of energy E_i for bone site x , $\phi_{CBIST}(r_T \leftarrow r_S, E_i)$ is the electron AF obtained during the CBIST simulations for the same source-target-energy combination, $\phi_{SIRT}(Sp/MC_x \leftarrow r_S, E_i)$ is the electron AF obtained during the SIRT simulations for the same source tissue and electron energy irradiating the spongiosa or medullary cavity sites of bone site x , $\phi_x(r_T \leftarrow CBV, E_i)$ is the electron AF for the CBV irradiating target tissue r_T at electron energy E_i for bone site x , $\phi_{SIRT}(Sp/MC_x \leftarrow CBV, E_i)$ is the electron AF obtained during the SIRT simulations for the CBV irradiating the spongiosa or medullary cavity sites of the same bone site for the same electron energy, $\phi_{CBIST}(r_T \leftarrow AM, E_i)$, $\phi_{CBIST}(r_T \leftarrow IM, E_i)$, and $\phi_{CBIST}(r_T \leftarrow TBV, E_i)$ are all the electron AFs obtained during the CBIST simulations for the various source tissues in the spongiosa and medullary cavities of each bone site irradiating the target tissues for the same electron energy, CF is the cellularity factor indicating the fraction of TM occupied by AM, and BVF is the bone volume fraction indicating the fraction of spongiosa occupied by TBV (Pafundi 2009).

Single-image radiation transport simulations – The purpose of the SIRT simulations was to obtain electron AFs/EFs for all macroscopic bone models in the UFH01MF, UFH05MF, and UFH10MF phantoms. Escape of electrons created in spongiosa and MCs into surrounding

CB and subsequently into tissues beyond was modeled. Recalling concepts described in the development of the skeletal fluence-to-dose response functions, photons interact with tissues in the spongiosa and medullary cavities and create secondary electrons. These electrons then deposit their energy through ionization and excitation. Since explicit bone trabeculae models cannot be efficiently simulated in the NURBS/PM format, mathematical methods were developed to virtually represent the physical model. Weighting electron AFs in spongiosa/MC by corresponding AFs obtained from CBIST modeling is a good approximation for electron energy deposition physics in spongiosa and MCs.

First, all 20 bone sites in the three phantoms of interest were isolated in the NURBS/PM model and voxelized for insertion into the radiation transport code MCNPX v2. Based on previous experience, the computing resources were able to efficiently simulate voxel models with a total matrix size of approximately 5.42×10^7 . Therefore, this total matrix size was targeted when selecting the voxel resolutions for each bone site. Since the three-dimensional matrix dimensions in the x -, y -, and z -directions depend on the total extent of the width, depth, and height of the object of interest, *Rhinoceros*TM, the 3-D modeling software used to create the UF hybrid phantoms, was utilized to take measurements of these same dimensions for all 20 bone sites in the three phantoms of interest. Each individual bone site (including spongiosa, MCs, and CB) was isolated and, using the multiple-view option in *Rhinoceros*TM, a linear measurement was taken from the leftmost point to the rightmost point in the front-view window, which represented the width of the bone site. A linear measurement was taken from the leftmost point to the rightmost point in the side-view window, which represented the depth of the bone site. Finally, a linear measurement was taken from the bottommost point to the topmost

point in the front-view window, which represented the height of the bone site. Then, an isotropic voxel resolution was calculated for each bone site using Equation 2-5.

$$r_{isotropic} = \left(\frac{X \cdot Y \cdot Z}{N} \right)^{\frac{1}{3}} \quad (2-5)$$

where X is the measured width of the bone site in cm , Y is the measured depth of the bone site in cm , Z is the measured height of the bone site in cm , N is the total targeted matrix size in number of voxel elements, and $r_{isotropic}$ is the isotropic voxel resolution for the bone site of interest.

The final width, depth, and height measurements along with the final voxel resolutions and total matrix sizes are in Tables 2-2 and 2-3. An example of a bone site, the femur of the UFH01MF phantoms, in NURBS/PM format and post-voxelization is in Figure 2-3. Due to human measurement of dimensions and some oddities in the software package *Rhinoceros*TM, not all bone sites achieved a total matrix size close to the targeted matrix size. However, all bone sites were individually inspected after voxelization using the image processing software package *ImageJ*TM (National Institutes of Health, Bethesda, MD), and all regions of interest in all bone sites for the three phantoms were faithfully represented. In addition, any artifacts introduced during the voxelization process were corrected using *ImageJ*TM. All voxels in the voxelized bone models not associated with spongiosa/MC or CB was designated “soft tissue” and assigned a material composition and density consistent with the reference “adult and children” values published in ICRP Publication 89 (ICRP 2002). A sphere of exclusion (interface at which radiation is no longer transported) was placed around the entire voxel model for each bone site and was also designated “soft tissue” with the same material composition and density as the soft tissue located within the voxel model itself.

Once all bone sites were voxelized and any resulting artifacts were corrected, input files and all associated files were assembled for electron transport. Lattice files were generated for the 20 voxelized bone models for each phantom – files that indicate to the radiation transport code tissue tag identification numbers associated with all voxels in the simulation. Skeletal photon fluence-to-dose response functions are applied to energy-dependent photon fluence incident upon regions of spongiosa and MCs in the skeleton, so the source of electrons in these cases would be those same regions. It followed that, for each bone site, all sub-regions of spongiosa and medullary cavities were simulated as source regions for the SIRT simulations. CBV was also simulated as a source region to generate electron AFs for CBV sources. Source files were created for each sub-region – files that indicate to the radiation transport code the location of all voxels associated with the source region of interest. A total of 34 source regions were simulated per phantom. The number of source regions was greater than the number of bone sites because some bones (the long bones) were divided up into several sub-regions. Long bones in the phantoms consisted of a separate proximal end, shaft, and distal end with the humerus and femur having shafts separated into upper and lower regions.

Twenty-eight monoenergetic electron energies, mirroring those of Pafundi *et al.* (2010), were simulated per source region, giving a total of 952 simulations per phantom and an overall total of 2856 simulations. Following all photons and electrons produced during the simulations, energy deposition was tracked in spongiosa/MCs, CB, and soft tissue located in the voxel model. Any energy deposited beyond these tissues was calculated as the total energy emitted less the energy deposited in the three tissues just mentioned. Electron EFs were calculated using Equation 2-6.

$$EF_x(r_S, E_i) = 1 - AF_x(r_T \leftarrow r_S, E_i) = 1 - \frac{E_x^{dep}(r_T \leftarrow r_S, E_i)}{E_i} \quad (2-6)$$

where $EF_x(r_S, E_i)$ is the escape fraction for bone site x at initial electron energy E_i for source region r_S , $AF_x(r_T \leftarrow r_S, E_i)$ is the electron absorbed fraction for bone site x for source region r_S , target region r_T , and electron energy E_i , and $E_x^{dep}(r_T \leftarrow r_S, E_i)$ is the energy deposited in target region r_T from source region r_S at electron energy E_i .

Ten million particle histories were simulated at each initial electron energy, ensuring that all statistical uncertainties would be well below 1%. Since the lowest electron energy was 1 keV and the default cutoff energy in MCNPX is 1 keV, the lower bound energy cutoff for both photons and electrons was lowered to 500 eV. The ITS-style electron energy bin indexing algorithm was used (described later).

Photon Specific Absorbed Fractions

Overview

The purpose of the photon SAF calculations was to generate a complete set of monoenergetic SAFs that would later be incorporated into an internal dosimetry software package. These SAF values were considered to be a complete set because all source-target combinations of importance were modeled. The software package would take information about radiation emission spectra from radionuclides of interest and use the monoenergetic photon SAFs to calculate radionuclide-specific S values. With biokinetics of the radiopharmaceutical known, final absorbed dose estimates would be obtained.

To generate monoenergetic photon SAFs, the UF hybrid computational phantom family was used with a radiation transport code to model the transmission of photons throughout the body from internal sources. The physical characteristics all tissues in the phantoms (densities, volumes, elemental compositions) were incorporated into the models to ensure maximum

accuracy from the available information. Photons were transported throughout each phantom for a variety of source tissues. The energy deposited in a number of target tissues was recorded. From the energy deposited, the AFs, and subsequently the SAF, were calculated. This process was repeated for many monoenergetic photon energies. Afterwards, several variance reduction techniques were used to ensure quality of the data. A flowchart schematic of the photon dosimetry scheme is in Figure 2-4. All aspects of the flowchart will be described in greater detail in the following sections but the flowchart can be referred to as a visual aid.

Radiation Transport Code

The radiation transport code MCNPX v2.6 was used for the calculation of the SAFs in this work. MCNPX is a three-dimensional computational environment that models the movement of radiation through geometries specified by the user (LANL 2005). These geometries can be created by combinations of simple surfaces (planes or cylindrical shells) or macrobodies (cubes, spheres, ellipsoids, etc.) (LANL 2005). However, to utilize the complicated geometries of NURBS-based computational dosimetry phantoms, the phantoms had to be reformed into voxel arrays because MCNPX cannot currently handle NURBS surfaces or PM geometries. Usually, the user must define a set of surfaces and construct cells of interest by combining the defined surfaces. While some of this is retained in the simulation of voxel phantoms, the phantoms themselves were largely defined by a technique known as “universes”. A separate file that is called by the main MCNPX input file defines the organ/tissue tag identification number associated with each voxel in the model. Then, a universe is defined by grouping all voxels with the same identification number. From this, MCNPX can know where any particular tissue is in the phantom.

MCNPX stochastically models the transport of radiation through any geometry by way of random number generation. Since statistical processes are utilized in MCNPX, larger numbers

of particle histories simulated produce lower uncertainty results. Incoherent and coherent scattering, fluorescent emission after photoelectric absorption, and absorption in electron-positron pair production are all accounted for during photon transport (LANL 2005). Angular deflection through multiple scattering events, collisional energy loss, and production of secondary particles are all accounted for during electron transport (LANL 2005).

Unfortunately, phantoms at this time must be voxelized prior to use within most radiation transport codes. The voxelization process decreases some of the detail attained using NURBS/PM surfaces. Progress has been made in the radiation transport code GEANT4 that allows for direct input of PM surfaces, but researchers comment that simulation runtimes increase drastically, up to 10 times the normal runtime for a voxel model (Jeong *et al.* 2011). Considering that some voxel-based runtimes reach 24 hours, this was abandoned as an option. However, the MCNP development team is currently working on this problem, and direct simulation of NURBS/PM surfaces may be feasible in the near future.

Phantom Physical Characteristics

MCNPX requires input of several physical parameters to assist in completely defining the phantom model. Tissue density, elemental composition, and volumes were required for MCNPX to both calculate tissue masses and perform accurate radiation transport. Since radiation interaction processes depend heavily on the atomic number of tissues, thorough analysis of the elemental composition of each material/tissue was necessary and will be addressed later.

Methods used for the construction of the UF hybrid phantom family were detailed earlier, but it is necessary to give some pertinent physical information about the phantoms here. Detailed characteristics and morphometric measurements of the entire phantom family can be found in Lee *et al.* (2010), but some information was reproduced since some information changed slightly during voxelization. All tissues modeled in all phantoms along with the

associated tissue tag identification numbers and tissue densities are given in Table A-1 in Appendix A, and tissue masses for all phantoms are given in Table A-2 in Appendix A.

Elemental compositions will be addressed in the next section.

Blood-Inclusive Elemental Compositions

The elemental compositions of the various materials used in the phantoms were initially taken from ICRP Publication 89 (ICRP 2002). However, these elemental compositions were only relevant to the organ parenchyma and did not include the elemental composition of the organ blood content (ICRP 2009). Therefore, the Equation 2-7 was used to apportion the elemental composition of blood to the overall elemental composition of the organ (ICRP 2009).

An example of adjustment of the relative abundance of hydrogen in the liver is shown.

$$(\% H)_{liver}^{blood-inclusive} = \frac{(\% H)_{liver}^{parenchyma} (m_{liver}^{blood-inclusive} - m_{blood-in-liver}) + (\% H)_{blood} (m_{blood-in-liver})}{m_{liver}^{blood-inclusive}} \quad (2-7)$$

where $(\%H)_{liver}^{blood-inclusive}$ is the final adjusted weight percent of hydrogen in the liver, $(\%H)_{liver}^{parenchyma}$ is the reference weight percent of the liver parenchyma, $m_{liver}^{blood-inclusive}$ is the reference mass of the liver, inclusive of blood, $m_{blood-in-liver}$ is the mass of blood located in the liver, and $(\%H)_{blood}$ is the reference weight percent of hydrogen in blood. This methodology was used for all elements documented for all blood-containing organs as listed in ICRP Publication 89 (ICRP 2002).

Before Equation 2-7 could be applied to account for the material composition of blood in all blood-containing organs, regional blood masses had to be calculated. Unfortunately, ICRP Publication 89 only defines regional blood distribution for the adult male and female, and this distribution can be seen in Table 2-4 (ICRP 2002).

Since only adult male and female regional blood distributions were officially defined and no large-scale detailed measurements had been performed, in lieu of embarking on a multiple-year data collection project, a mathematical method was developed to attempt to predict the regional blood distributions in the newborn, 1-year-old, 5-year-old, 10-year-old, and 15-year-old male and female.

First, it generally assumed that the volume of blood per unit volume organ did not vary by age. If this was indeed the case, one could simply perform volume scaling to predict the regional distribution of blood at different ages. Following this theory, the volume of blood within a particular organ in the adult male or female (depending on the gender of interest) was scaled by the ratio of volumes of organ of interest (Equation 2-8).

$$V_{blood}^{organ}(i, s) = V_{blood}^{organ}(adult, s) \times \frac{V_{organ}(i, s)}{V_{organ}(adult, s)} \quad (2-8)$$

where V_{blood}^{organ} is the volume of blood located in the organ of interest, i is the age of interest, s is the gender of interest, and V_{organ} is the volume of the organ itself. The volume of blood in any organ in the adult male or female was obtained using Equation 2-9.

$$V_{blood}^{organ}(adult, s) = f_{blood}^{organ}(adult, s) \times V_{blood}^{total}(adult, s) \quad (2-9)$$

where f_{blood}^{organ} is the fraction of whole-body blood located in the organ of interest (taken from Table 2-4), s is the gender of interest, and V_{blood}^{total} is the reference volume of whole-body blood (taken from ICRP Publication 89). Whole-body blood volumes can be seen in Table 2-5 (ICRP 2002).

Once the volume of blood in each organ had been calculated, the regional distribution was determined by applying Equation 2-10.

$$f_{blood}^{organ}(i, s) = \frac{V_{blood}^{organ}(i, s)}{\sum_{organ} V_{blood}^{organ}(i, s)} \quad (2-10)$$

where f_{blood}^{organ} is the fraction of whole-body blood located in the organ of interest, i is the age of interest, s is the gender of interest, and V_{blood}^{organ} is the volume of blood located in the organ of interest, obtained from Equation 2-8. It is important to note that the sum of all organ-specific calculated blood volumes was not necessarily equal to the reference whole-body blood volume. This is because assumptions were made in the development of this model which, while reasonable in theory, may not be exactly accurate for everyone. Additionally, the reference values themselves were averaged over a population of people (ICRP 2002). However, fractional blood distribution values obtained from this procedure were applied to the reference total blood volumes to obtain final organ-dependent regional blood volumes. In essence, the volume scaling was performed to develop a regional blood distribution, which could then be used to appropriately apportion blood volumes to the tissues listed in Table 2-4.

After further investigation, it was determined that some organs did not behave as predicted by the previously mentioned theory – that the volume of blood in any organ per unit volume of that organ ($ml\ blood/ml\ organ$) was independent of age. ICRP Publication 89 indicates that, in children, the kidneys may receive more cardiac output than adults, the brain have a higher blood perfusion rate (BPR) ($ml/min/100\ g\ tissue$) than adults, and the skeletal tissues may have BPRs and blood content up to 2 to 3 times more than adults (based on animal studies) (ICRP 2002).

These three organs were investigated further to determine if scaling factors could be developed to effectively correct for the regional changes in blood volume per unit organ volume. When direct information on blood volume per unit organ volume was not available, it was

assumed that relative BPRs were direct indicators of regional changes in vascular growth. From the outset, it was decided that a ratio of either BPR or blood volume per unit organ volume would be used as a scaling factor. In other words, the volume scaling methodology would be retained, but a scaling factor would be introduced to further adjust the calculated regional blood volumes for the kidneys, brain, and skeletal tissues.

Rubin *et al.* (1949) provided renal plasma flow normalized to the adult body surface area ($cm^3/min/1.73 m^2$) for 5 ages between 0 and 3 years. The renal plasma flow rate reached the adult value at 3 years of age (Rubin *et al.* 1949). At the reference ages of the newborn (100-days-old) and the 1-year-old, Figures 2A and 2B from Rubin *et al.* (1949) were used to assign an average renal plasma flow rate. The age-specific values were then divided by the adult value to obtain the scaling factor. However, since dramatic growth was not seen between the ICRP-reference newborn and the 1-year-old and the values themselves were variable, the renal plasma flow rate for the 1-year-old was assigned to the newborn.

Data from Chiron *et al.* (1992) were used to calculate blood volume scaling factors for the brain. This study provided mean global cerebral blood flow (mCBF) in $ml/min/100 g tissue$ for 22 ages between 0 and 22 years. Forty-two children between the ages of 2 days and 19 years (Chiron *et al.* 1992) were imaged using ^{133}Xe SPECT. The adult value was taken as the average obtained over 32 patients between the ages of 19 and 29 years (Chiron *et al.* 1992). The authors used an algorithm described in Celsis *et al.* (1981) to calculate the regional cerebral blood flow (rCBF) for 25 regions of interest (ROIs) covering the cortical ribbon, thalamus, and both hemispheres as a whole (Chiron *et al.* 1992). mCBF was calculated as the average of all hemisphere ROIs on the upper 4 image slices and whole brain on the bottom image slice (Chiron *et al.* 1992). The adult mCBF was taken to be $51 ml/min/100 g tissue$ (22-year-old value).

Scaling factors for all reference ages were calculated as the ratio of the mCBF at the age of interest to the adult mCBF.

Simonet *et al.* (1988) reported direct measurements of vascular volume per unit volume organ (*ml/ml organ*) for mineral bone in dogs for a pup, adolescent, and adult dog. The value reported for the pup was assigned to the reference newborn and 1-year-old human, and the value reported for the adolescent was assigned to the reference 15-year-old human. Vascular volumes per unit volume organ for the reference 5-year-old and 10-year-old humans were linearly interpolated between the 1-year-old and 15-year-old measures. The scaling factor was calculated as the ratio of the age-dependent vascular volumes to the adult vascular volume. From other literature searches, it could not be proven that bone marrow vascular volume per unit volume organ changes as a function of age. Therefore, scaling factors were applied to CB and TB but not to bone marrow or “other skeleton” (see Table 2-4). As a result, total skeletal blood volume was taken to be the sum of the derived blood volumes of the skeletal constituents. A table of age-dependent scaling factors for the kidneys, brain, and skeleton can be seen in Table 2-6.

Since regional changes in vascular growth were accounted for using scaling factors, Equation 2-8 was amended to include these changes, resulting in Equation 2-11.

$$V_{blood}^{organ}(i, s) = R_{growth}(i, s) \times V_{blood}^{organ}(adult, s) \times \frac{V_{organ}(i, s)}{V_{organ}(adult, s)} \quad (2-11)$$

where R_{growth} is the scaling factor used to correct for regional changes in vascular growth (for organs other than kidneys, brain, and mineral bone, this factor was set to unity). Equation 2-12 is the aggregate equation used to calculate regional blood distribution fractions for the whole reference human series. Reference regional blood volumes were finally obtained by multiplying the regional blood fractions by the reference whole-body blood volume.

$$f_{blood}^{organ}(i, s) = \frac{R_{growth}(i, s) \times V_{blood}^{organ}(adult, s) \times \frac{V_{organ}(i, s)}{V_{organ}(adult, s)}}{\sum_{organ} R_{growth}(i, s) \times V_{blood}^{organ}(adult, s) \times \frac{V_{organ}(i, s)}{V_{organ}(adult, s)}} \quad (2-12)$$

ICRP Publication 89 gives reference organ masses in its Table 8.2 but, for various organs, no reference volumes or tissue densities are given (e.g., density of lung) (ICRP 2002). Resultantly, when available, ICRP-reference organ masses and densities were used to calculate reference organ volumes. When reference masses or densities were unavailable, either surrogate tissues were assigned or the tissue properties detailed in Lee *et al.* (2010) were used. Lung density was taken from Lee *et al.* (2010) and includes relative contributions from parenchyma, blood, and air. These densities were calculated based on the ICRP Publication 89 reference mass and segmented lung volume of the various phantoms. No reference mass for bronchi was found, so the trachea alone was used for “bronchial tissue”. This was considered to be reasonable since the bronchial tree probably grows at roughly the same rate as the trachea. Whole skeleton average density was taken from Lee *et al.* (2010), and “other skeleton” mass and volume was calculated as the whole skeleton mass and volume less the AM, TB, and CB masses and volumes. The “other skeleton” density was then calculated as the “other skeleton” mass divided by the “other skeleton” volume. The “all other tissues” compartment was calculated as the ICRP Publication 89 reference whole-body mass less the mass of the listed tissues and organ contents. A density of 1.03 g/cm^3 was assumed for the “all other tissues” compartment. No reference pediatric values of mass or volume were found for aorta and large arteries or large veins, so the adult regional blood portion values of 6% (aorta and large arteries) and 18% (large veins) were used to calculate the reference masses for all other ages. Combining elements of the ICRP-reference models and the UF phantom models to develop the regional blood distribution model

did not pose a problem because the important measure was the age-dependent organ volumes relative to the adult organ volumes. Consequently, the actual volumes themselves were somewhat irrelevant. Regional blood distributions and blood volumes for the entire ICRP-reference family can be seen in Tables 2-7 and 2-8, respectively.

These regional distributions were initially developed for the intent of ICRP adoption as reference values. However, the regional distributions of Tables 2-7 and 2-8 do not directly translate to the UF hybrid phantom family. Specifically, while the UF phantoms are ICRP-reference, they do not necessarily have explicit compartments for all of the listed organs. For example, "other skeleton" is not an explicit compartment in the UF phantoms. These developed regional blood volumes were apportioned according to the available structures in the UF hybrid phantom family.

First, the regional blood volumes were multiplied by the ICRP-reference blood density of 1.06 g/cm^3 to obtain regional blood masses for implementation in Equation 2-7 (ICRP 2002). The blood volumes in all organs explicitly defined in the UF hybrid phantom family were retained, which included the fat, brain, small intestine, large intestine, coronary tissue, kidneys, liver, pulmonary, bronchial tissue, skeletal muscle, pancreas, cortical bone, skin, spleen, thyroid, lymph nodes, gonads, and adrenals. The large intestine, kidneys, and bronchial tissue blood volumes were not apportioned to their constituent organs (i.e., large intestine into left colon, right colon, and rectosigmoid walls) because their constituents share the same material composition. The "stomach and esophagus" combined blood volume was parceled out to the stomach and esophagus separately by volume weighting since they do not share the same material composition (Equations 2-13 and 2-14).

$$m_{blood}^{stomach}(i, s) = m_{blood}^{stomach + esophagus}(i, s) \frac{V_{organ}^{stomach}(i, s)}{V_{organ}^{stomach}(i, s) + V_{organ}^{esophagus}(i, s)} \quad (2-13)$$

$$m_{blood}^{esophagus}(i, s) = m_{blood}^{stomach + esophagus}(i, s) - m_{blood}^{stomach}(i, s) \quad (2-14)$$

where $m_{blood}^{stomach}$ is the mass of blood in the stomach wall, i is the age of interest, s is the gender of interest, $m_{blood}^{stomach+esophagus}$ is the combined mass of blood in the stomach wall and esophagus, $V_{organ}^{stomach}$ is the volume of the stomach wall, $V_{organ}^{esophagus}$ is the volume of the esophagus, and $m_{blood}^{esophagus}$ is the mass of blood in the esophagus.

Blood volumes in the right and left heart chambers were added together and assigned to the “heart contents” compartment of the UF phantoms. The “all other tissues” compartment was defined to be all tissues not specifically documented in the regional blood distribution less air in the body as well as walled organ contents. These tissues were found to be the breasts, ears, external nose, gall bladder wall, larynx, nasal layers, oral cavity layer, pharynx, pituitary gland, salivary glands, spinal cord, thymus, tongue, tonsils, penis, prostate, scrotum, and uterus. Volume weighting was applied to apportion the mass of blood in “all other tissues” to the individual constituents. The aorta, large arteries, and large veins were not considered since they consist entirely of blood.

AM, TB, and "other skeleton" were more complicated to appropriately distribute since these compartments were not explicitly modeled in NURBS/PM format (Lee *et al.* 2010). AM, IM, and TB are homogeneously combined in the UF phantom models, and material compositions are calculated as site-specific homogeneous mixtures of these materials. These homogenous volumes are known as either spongiosa or MCs. As a result, blood volumes for the 34 delineated spongiosa/MC sites were necessarily a fractional combination of AM, TB, and some portion of the “other skeleton” compartment. Since AM, TB, and CB were explicitly defined in the

regional blood distribution, "other skeleton" consists of bone-associated cartilage and IM. The volume of blood attributed to each skeletal spongiosa/MC site was calculated as the fraction of total AM, TB, and IM located in each site multiplied by the total AM, TB, and IM volume as described in Equation 2-15. The volume of blood located in the bone-associated cartilage was calculated using Equation 2-16.

$$\begin{aligned}
 V_{blood}^{sp-mc}(i, s, j) &= V_{blood}^{AM}(i, s) \times \frac{V_{AM}(i, s, j)}{\sum_j V_{AM}(i, s, j)} + V_{blood}^{IM}(i, s) \times \frac{V_{IM}(i, s, j)}{\sum_j V_{IM}(i, s, j)} \\
 &+ V_{blood}^{TB}(i, s) \times \frac{V_{TB}(i, s, j)}{\sum_j V_{TB}(i, s, j)} \\
 V_{blood}^{IM}(i, s) &= V_{blood}^{other}(i, s) \times \frac{\sum_j V_{IM}(i, s, j)}{\sum_j V_{IM}(i, s, j) + V_{cartilage}(i, s)}
 \end{aligned}
 \tag{2-15}$$

where V_{blood}^{sp-mc} is the volume of blood located in either spongiosa or a medullary cavity, i is the age of interest, s is the gender of interest, j is the bone site of interest, V_{blood}^{AM} is the total volume of blood located in whole-body AM, V_{AM} is the volume of AM, V_{blood}^{IM} is the total volume of blood located in whole-body IM, V_{IM} is the volume of IM, V_{blood}^{TB} is the volume of blood located in whole-body TB, V_{TB} is volume of TB, V_{blood}^{other} is the volume of blood located in the "other skeleton" compartment, and $V_{cartilage}$ is the total volume of whole-body cartilage.

$$V_{blood}^{cartilage}(i, s) = V_{blood}^{other}(i, s) - \sum_j V_{blood}^{IM}(i, s, j)
 \tag{2-16}$$

where $V_{blood}^{cartilage}$ is the volume of blood located in whole-body bone-associated cartilage.

Once the mass of blood in each tissue of interest was determined, Equation 2-7 was used to adjust the material composition of those tissues to include the blood content. After calculating the blood-inclusive compositions, the UF hybrid phantom family consisted of 88 unique

materials. Regional blood distributions and blood masses as applied to the UF hybrid phantom family are in Tables 2-9 and 2-10 (with gender differences averaged for the UFH00MF, UFH01MF, UFH05MF, and UFH10MF phantoms), and the final blood-inclusive material compositions (with gender differences averaged for the UFH00MF, UFH01MF, UFH05MF, and UFH10MF phantoms) for the UF hybrid phantom family can be found in Tables A-3 through A-10 in Appendix A.

Phantom Preparation

The UF hybrid phantoms are NURBS/PM-based in their original, but since MCNPX cannot currently utilize continuous 3-D surfaces, the phantom was reconstituted into a voxel model, a 3-D array of rectangular prisms. Once a phantom was finalized in its NURBS/PM form in *Rhinoceros*TM, it was exported as a raw triangles (*.raw) file. This raw triangles file approximates the continuous and PM surfaces with millions of triangles. The hundreds of contours in the phantom was represented by defining the coordinates of the vertices of all the triangles in the model. An in-house *MATLAB*TM code was used to convert the raw triangles model into a voxel model at the voxel resolution defined for the specific phantom (selection of voxel resolutions will be addressed later). An illustration of the process by which an object was taken from the original segmented image data, imported into *Rhinoceros*TM in PM format, converted into NURBS format, and voxelized was previously illustrated in Figure 1-9.

The skin of the phantom was not modeled explicitly in the NURBS/PM format because there was a chance that the skin could be lost during the voxelization procedure due to the thinness of the structure. Consequently, a *MATLAB*TM code was written to insert skin in the voxel phantom, which was accomplished by replacing the outermost layer of non-air voxels with skin voxels, all while avoiding the eye balls. After the skin was placed on the phantom, the phantom was examined using *ImageJ*TM, an image processing software package, and any

artifacts introduced during voxelization were manually corrected. An example of a voxelization artifact and the correction of the artifact can be seen in Figure 2-5. Streaking artifacts occur in the rare case where two surfaces touch each other in *Rhinoceros*TM and the MATLABTM code cannot resolve the conflict. An example of a voxelized UF hybrid phantom (UFH00F) is shown in Figure 2-6.

Using the binary file output from *ImageJ*TM, a *MATLAB*TM code was written to create the lattice (*.lat) file. The lattice file for each phantom communicates to MCNPX the number of voxel elements in the x -, y -, and z -directions and defines, in raster fashion, a tissue identification number to each voxel. For example, the header of the lattice file contains a definition of the number of voxels in the x -, y -, and z -directions, and the body of the file contains a single array of tissue tag identification numbers. MCNPX will read through the tag numbers until the number of tag numbers read is equal to the number of voxels in the x -direction. Then MCNPX will move to the next row of y -voxels and continue reading the tag numbers. Once the number of voxels in the y - and x -directions are filled, MCNPX moves to the next layer of z -voxels. In this way, the 3-D phantom is virtually represented. Once these steps were completed, the phantom is ready to be integrated into the MCNPX input file structure. A sample lattice file and detailed description can be found in Appendix B.

Voxel Resolution

Ideally, isotropic voxel resolutions for the entire phantom family would be set equal to the skin thickness at each age. Selecting resolutions at these thicknesses would ensure that the skin and almost all other structures would be effectively represented during particle transport. This follows since the skin in every phantom is the thinnest structure (except for some CB sites in some phantoms). However, voxelizing all phantoms at isotropic skin thickness resolution creates

unreasonably large matrix sizes for all but the newborn phantom as the thickness of the skin does not grow as quickly as the overall phantom dimensions. Resultantly, isotropic skin thickness resolution had to be abandoned and replaced by a different methodology for defining the final voxel resolutions.

It was found that simulation times for the UFH00MF phantoms voxelized at an isotropic resolution equal to the skin thickness were reasonable, and so a total matrix size of 54.18×10^6 for the UFH00MF phantoms was selected as the target total matrix size. Initially, the in-plane voxel resolutions (width and depth) were set equal to the skin thickness, and the z –axis resolution was derived so that the total matrix size of the phantom of interest was equal to the total matrix size of the UFH00MF phantoms using Equations 2-17 through 2-19.

$$N_{UFH00MF} = \left(\frac{X}{r_x} \right) \left(\frac{Y}{r_y} \right) \left(\frac{Z}{r_z} \right) \quad (2-17)$$

$$r_x = r_y \quad (2-18)$$

$$r_z = \left(\frac{1}{N_{UFH00MF}} \right) \left(\frac{1}{r_x^2} \right) (X \cdot Y \cdot Z) \quad (2-19)$$

where $N_{UFH00MF}$ is the total number of voxel elements in the UFH00MF phantom, X is the total width of the phantom, Y is the total depth of the phantom, Z is the total height of the phantom, r_x is the voxel resolution in the x –direction (width), r_y is the voxel resolution in the y –direction (depth), and r_z is the voxel resolution in the z –direction (height). X , Y , and Z were obtained by measuring the total extent from the nearest point to the most distant point as viewed from the front and side of the phantoms (e.g., the height was measured by viewing the phantoms from the front and measuring from the bottom of the feet to the top of the head).

This calculation was performed for the entire phantom family. In so doing, it was discovered that by setting the in-plane resolution equal to the skin thickness and deriving the z –axis resolution based on the total matrix size of the UFH00MF phantom, the number of voxels in the z –direction was unsatisfactory. That is, there were too few voxels in the z –direction. While determining total matrix sizes for voxel phantoms is a somewhat subjective procedure, one typically would like to keep any “stair-step” artifacts optimized across all dimensions. Since the inherent approximation in voxelization is the representation of continuous surfaces by a 3-D matrix of voxels, voxels with resolutions close to isotropic are optimal. In light of this, the in-plane voxel resolutions were slightly increased, and the z –resolution was again derived to match the total matrix size of the UFH00MF phantom. Resulting voxel dimensions and matrix sizes are in Table 2-11. It is important to note that for a single voxel matrix, all voxels must be the same shape and size, otherwise gaps and overlaps may occur.

Optimization of voxel resolutions led to some concerns, primarily that by somewhat subjectively changing the voxel dimensions, dose estimates may change correspondingly. If dose to the target tissue of interest was highly dependent on the voxel dimension, selection of the appropriate voxel dimensions would necessarily need to be a more rigorous process. To examine this possible phenomenon, the UFH15F phantom was voxelized at resolutions of $0.1 \times 0.1 \times 0.15 \text{ cm}^3$ and $0.12 \times 0.12 \times 0.2828 \text{ cm}^3$, resulting in total matrix sizes of $492 \times 285 \times 1078$ and $410 \times 238 \times 574$, respectively. The fine resolution voxel produced a total matrix size that was about 2.7 times greater than the coarse resolution voxel. Annihilation photons from ^{18}F were simulated as uniformly distributed throughout the liver, and energy deposition events (following secondary electrons) were recorded in various target tissues. Comparison of the results can be seen in Table 2-12. It was found that of the target tissues examined, there was a

range of differences from -0.68% (gall bladder wall) to 3.34% (ovaries) with an average deviation of 0.22% (indicating how well a course resolution approximates a fine resolution with regards to total dose over all organs) and an absolute average deviation of 0.81% (indicating how well a course resolution approximates a fine resolution with regards to individual organ doses).

In addition to comparing differences in absorbed doses, it was of interest to examine how much the mass of all tissues change with changes in voxel resolution. The masses of all tissues in both versions of the voxelized phantom were compared, and the largest deviation in mass was seen for the skin at -19.60% . This made sense since the skin was defined as a single layer of voxels on the outside surface of the phantom. Any changes in voxel resolution will affect the skin mass the most. Interestingly, while the difference in skin mass was the greatest, the difference in calculated absorbed dose was only -0.68% . A conclusion could be drawn from this observation: the amount of energy deposited in tissues tends to change proportionally with changes in tissue mass resulting from changes in voxel resolution. As the skin voxels increased in size from the fine resolution to the coarse resolution, more energy was deposited in the voxels. Acting in opposition to the increase in energy deposition, the mass of the skin also increased. Since absorbed dose is equal to energy absorbed in the tissue divided by its mass, these two occurrences offset. From this analysis, it was determined that voxel resolution, while having some influence on recorded doses as applied to internal dosimetry, does not affect the outcome of the simulations in such a way that rigorous testing is needed to determine the voxel resolutions of all the phantoms in the UF hybrid phantom family.

Initial Energies and Particle Histories

A range of starting monoenergetic photon energies was selected for simulation. The list of 333 “commonly” used radionuclides given in ICRP Publication 107 was examined to determine a maximum photon energy cutoff (ICRP 2008). The maximum photon energy (between x rays and gamma rays) was found to be 5 *MeV*, and 99.9% of all 25,256 photon emissions were below 4 *MeV*. Therefore, a maximum energy of 4 *MeV* was selected, and the remaining energies for simulation were modeled after the simulations of the ORNL stylized phantoms (Cristy *et al.* 1987). The electron energy grid was set equal to the photon energy grid to promote symmetry.

While the results from the current work will be applicable to nuclear medicine imaging and therapy procedures as well as radiation protection purposes, nuclear medicine imaging was the focus. Photon energies up to 4 *MeV* in nuclear medicine imaging are rarely seen, but certain radionuclides used in nuclear medicine imaging do have emission energies approaching that limit. Several commonly used nuclear medicine imaging radionuclides were referenced for examples, and these radionuclides were ^{11}C , ^{13}N , ^{15}O , ^{18}F , ^{67}Ga , $^{81\text{m}}\text{Kr}$, ^{82}Rb , $^{99\text{m}}\text{Tc}$, ^{111}In , ^{123}I , ^{131}I , ^{133}Xe , ^{178}Tl , $^{191\text{m}}\text{Ir}$, $^{195\text{m}}\text{Au}$, and ^{201}Tl (Treves 1995). Average photon emission energies were calculated for each radionuclide and the average of these average energies was 180 *keV* (4 *keV* – 511 *keV*) (ICRP 2008). These are the typical average energies of emission for nuclear medicine imaging procedures – in the range of hundreds of *keV*. The mid-energy range allows for adequate escape from the body but optimal detection quality (Cherry *et al.* 2003). However, the average maximum energy of emission for these same radionuclides was found to be 757 *keV* (129 *keV* – 3.95 *MeV*) (ICRP 2008). Consequently, while primary emission energies for nuclear medicine image studies may be in the range of hundreds of *keV*, energies up to 4 *MeV* are observed and should be taken into account.

Next, the number of particle histories was determined. As the initial energy of the photons increases, the simulation runtimes increase. From previous trial simulations in the UFH00MF phantoms, 10^7 particles are generally sufficient to give satisfactory statistical uncertainties (other specific dosimetry studies were performed with other phantoms, and 10^7 particles gave satisfactory results). However, lower initial photon energies lead to higher statistical uncertainties. Consequently, a range of particle histories, dependent upon the initial energies of the photons was developed with a maximum of 10^8 particle histories at a photon energy of 10 keV and a minimum of 10^7 particle histories at a photon energy of 4 MeV . An anchor value of 2×10^7 was set for the photon energy 150 keV to control runtimes for energies of 150 keV and greater. Numbers of particle histories for starting energies between 10 keV and 4 MeV were log-linearly interpolated, and the resulting photon energies and associated numbers of particle histories are given in Figure 2-7.

Tally Types

A “tally” in MCNPX refers to the measure that is being tracked. Tally types available for use in MCNPX are current integrated over a surface (units of particles or MeV), flux averaged over a surface (units of $\text{particles}/\text{cm}^2$ or MeV/cm^2), flux averaged over a cell (units of $\text{particles}/\text{cm}^2$ or MeV/cm^2), flux at a point or ring detector (units of $\text{particles}/\text{cm}^2$ or MeV/cm^2), energy deposition averaged over a cell (units of MeV/g or jerks/g), collision heating (units of MeV/g), fission energy deposition averaged over a cell (units of MeV/g or jerks/g), energy distribution of pulses created in a detector by radiation (units of pulses or MeV), and deposition (units of charge) (LANL 2005). After selecting the tally type, the user must indicate a tally type for all cells of interest (in this case, cells are equivalent to tissue tag identification numbers), and multiple tally types are allowed.

Two primary tally types were used for the calculation of photon SAFs for the UF hybrid phantom family. The first tally type was “energy distribution of pulses created in a detector by radiation” in units of *MeV* (*F8 tally in MCNPX syntax (LANL 2005)), and this tally was selected to track the total energy deposition in non-skeletal target tissues of interest. When coupled with the MCNPX photon-electron mode, this tally accounts for contributions from all secondary particles. The photon-electron mode indicates to MCNPX that both photons and electrons should be followed throughout the entire geometry until they either reach a particle killing boundary or fall below the energy threshold of the problem (LANL 2005). Since no dose enhancement takes place for general (non-skeletal) organs, only the total energy deposition needed to be recorded to eventually calculate the absorbed dose (or SAF) to the organ. Secondary electrons incident upon spongiosa were accounted for through application of the skeletal photon fluence-to-dose response functions as these functions include electrons born in surrounding soft tissue and cortical bone.

The second tally type was “flux (fluence) averaged over a cell” in units of *particles/cm²* (F4 tally in MCNPX syntax (LANL 2005)). The volume-averaged fluence tally was selected for application to the skeletal photon fluence-to-dose response functions. Energy-dependent photon fluences throughout regions of spongiosa and MCs were needed to eventually calculate the SAF to AM and TM₅₀ within each bone site (Johnson *et al.* 2011). The SAFs for each bone site would then be weighted by the mass fraction of the skeletal tissue of interest to obtain whole-skeleton SAFs to AM and TM₅₀. Resultantly, the volume-averaged fluence tallies were divided into energy bins reflective of the energies at which the skeletal photon fluence-to-dose response functions were assembled. The MCNPX output files would then contain the number of photons per square centimeter per starting source particle incident on spongiosa or medullary cavities

between the upper and lower energy bounds of each energy bin. After extraction from the output files, the energy-dependent photon fluences were multiplied by their corresponding energy-dependent photon fluence-to-dose response function, and the results were summed to obtain the dose to radiosensitive skeletal tissues in each bone site.

A *MATLAB*TM code was written to extract all output data from the photon dosimetry simulations, and the code performed all data extraction and post-processing. During each post-processing phase, the resulting SAFs were recorded into separate Microsoft® Excel (Microsoft Corporation, Redmond, WA) files to isolate any errors in processing, if present. The code handled all tally information discussed here and all variance reduction techniques subsequently discussed.

Miscellaneous Transport Details

Energy cutoff

The default cutoff for all particle types in MCNPX is 1 *keV*, the energy at which the particle is no longer followed and assumed to be locally deposited (LANL 2005). This means that any particle falling below this energy threshold during the course of radiation transport is terminated. The lower-bound energy threshold feature can be used in some cases to decrease overall simulation times. For example, if high energy (in the case of this study, 4 *MeV*) photons were simulated with a lowered electron energy cutoff of 100 *eV*, the simulation time would increase quite drastically in order to follow secondary electrons down to that energy. In turn, the true physics of the model would be more accurately represented. However, while the physics would be more accurately modeled, the actual recorded energy deposition may not change at all due to the short range of 100 *eV* electrons. A different scenario occurs when the lower-bound energy threshold is increased from 1 *keV* to 100 *keV*. In this case, simulation time would decrease since secondary electrons would be terminated once they achieve an energy of

100 keV, but the true physics would be inadequately modeled since electrons at 100 keV could escape the region of interest.

Given that simulation time could be saved if dosimetry results did not vary drastically with changes in the lower-bound energy threshold, this issue was further pursued. A uniform photon source of energy 4 MeV was simulated for the UFH00M phantom with lower-bound electron energy thresholds of 1 keV, 10 keV, 50 keV, and 100 keV, and the energy deposition was recorded in various target tissues of interest. The results were examined for many target tissues, and several of them are displayed in Table 2-13. It was found that for some tissues, the recorded energy deposition did not vary drastically across the different electron cutoff energies. However, for others, the variation was seen to be significant. In the interest of adequately modeling the true physics, the lower-bound electron cutoff energy of 1 keV was selected. Ranges in soft tissue for electrons of energy 1 keV are on the order of micrometers, so electron escape from target tissues of interest was not of great concern.

Electron energy indexing algorithm

The default electron energy indexing algorithm used in MCNPX is the MCNP-style bin-centered algorithm (LANL 2005). Another option available for use is the ITS-style nearest-bin algorithm. According to the 2005 American Nuclear Society (ANS) Topical Meeting in Mathematics and Computations in Avignon, France, the ITS-style nearest-bin algorithm can be evidenced as the consistently more accurate of the two, and the reasons will be described here (Hughes 2005).

Electron physics within MCNPX are handled using energy bins. Under the MCNP-style bin-centered algorithm, an electron with energy E would be assigned to the energy group n , and the energy group structure would be $E_n > E \geq E_{n+1}$ (Hughes 2005). Within this energy group,

a range S_n (which will be called an energy-group range here) is calculated so that if an electron with initial energy E_n travels a distance S_n , it will attain an energy of E_{n+1} , giving a mean energy loss of $\Delta E = E_n - E_{n+1}$ (Hughes 2005). This assumes that the electron *actually* has an energy of E_n , an obvious approximation. Once S_n is selected, the number of angular sub-steps taken within S_n is defined as M (dependent on the elemental composition of the material), and the sub-step range is calculated as $R_n = S_n/M$ (Hughes 2005). The sub-step range is the distance traveled after each angular deflection. The energy-group straggled energy loss Δ is sampled from the Landau straggling distribution based on E_n , S_n and ΔE (Hughes 2005). The term “straggled energy loss” refers to the statistical spread of electron energies observed after a certain path length of tissue has been traversed. The sub-step straggled energy loss is calculated as $\Delta_{sub-step} = \Delta/M$ (Hughes 2005). MCNPX attempts to transport the electron through M sub-steps, and if all sub-steps are successfully completed, the electron is reassigned to a new energy group (Hughes 2005). If the electron crosses a cell boundary or attains an energy below E_{n+1} , it is assigned to a new energy group (Hughes 2005).

While the MCNP-style bin-centered algorithm assigns electrons of energy E to a bin n so that $E_n > E \geq E_{n+1}$, the ITS-style nearest-bin algorithm assigns electrons of energy E to a bin n so that $(E_{n-1} + E_n)/2 > E \geq (E_n + E_{n+1})/2$ (Hughes 2005). Using the ITS-style method, the electron will be assigned to the energy group whose upper limit is closest to the energy of the electron. For example, if $E = 2.4 \text{ MeV}$, $E_{n-1} = 3 \text{ MeV}$, $E_n = 2 \text{ MeV}$, and $E_{n+1} = 1 \text{ MeV}$, the electron would be assigned to E_{n-1} using the MCNP-style method since the energy of the electron is between 3 MeV and 2 MeV . However, this same electron would be assigned to E_n using the ITS-style method since its energy falls between 2.5 MeV and 1.5 MeV .

The MCNP-style algorithm is referred to as “bin-centered” because the parameters used for calculating predicted energy loss are pre-computed at the center of each bin (Hughes 2005). The bin-centered algorithm presents problems because the electron will likely not achieve the predicted range due to the fact that the electron will typically have an energy less than the upper limit of the energy bin and hence a lower range (Hughes 2005). This leads to linear interpolation of energy loss in a process which is non-linear (Hughes 2005). In addition, the final energy loss sub-step within the energy group usually carries over into the next energy bin, resulting in systematic error (Hughes 2005). These problems are not encountered in the ITS-style algorithm because the electron is assigned to the energy bin whose upper limit is closest to the energy of the electron, and the electron is not assigned to a new energy bin if it attains an energy below the current energy bin (Hughes 2005). These factors minimize the negative effects introduced by linear interpolation of non-linear processes.

To investigate the effect these electron energy-indexing algorithms have on computational internal dosimetry, test cases were simulated using both algorithms and the results were compared. Uniform photon sources of energies 150 *keV* and 4 *MeV* were simulated in the adipose tissue of the UFH00M phantom, and the energy deposited in a variety of target tissues of interest was recorded using both the MCNP-style and ITS-style algorithms. Results can be seen in Table 2-14.

Differences in energy deposition estimates were seen between -0.46% and 1.97% for the 150 *keV* simulations and between -11% and 19% for the 4 *MeV* simulations. Disagreement between the MCNP-style and ITS-style algorithms increased over all target tissues from the 150 *keV* simulations to the 4 *MeV* simulations with pronounced effect for smaller target tissues. Resultantly, it was decided that the recommendation of the MCNP development team would be

taken and the ITS-style nearest bin electron energy-indexing algorithm was selected for the photon and electron SAF simulations.

Source Tissues

The UF series of pediatric hybrid computational phantoms has recently been in consideration for adoption by the ICRP as the new reference series of pediatric computational phantoms. While the UF adult phantoms will not be adopted by the ICRP, the UF adult phantoms were included in the current study for in-house use. In anticipation of the UF pediatric series being adopted by the ICRP, it was prudent to model both the photon and electron simulations and any relevant details after the latest ICRP document, ICRP Publication 110. In this publication, the ICRP introduced a reference adult male and female voxel phantom and laid out detailed plans about the future calculation of monoenergetic photon and electron SAFs (ICRP 2009).

In an effort to model the UF work after the ICRP intentions, all source tissues listed in ICRP Publication 110 were simulated as source tissues in the UF phantoms. Since the ICRP and UF phantoms were developed separately, several structures were not consistent between the two models, so approximations were made in these cases. For example, the ICRP has explicitly modeled intrapulmonary bronchi (ICRP 2009) while the UF phantoms have a homogenous lung model. In this case, the ICRP models a bronchiole source explicitly while the lungs were assigned as the surrogate tissue for the UF phantoms. In addition, several extra source tissues were simulated in the UF phantoms that were not included in the ICRP phantoms.

Some source tissues were not explicitly simulated since their components were simulated individually, as in the case of the colon. The right colon wall, left colon wall, and rectosigmoid wall were all simulated as source tissues, so simulating a combined colon source would only duplicate efforts. Because of this, volume weighting was used to calculate the SAF to target

tissues from composite sources, and Equation 2-20 was used to calculate the volume weighted SAFs.

$$SAF_{composite}(r_T \leftarrow r_S, E_i) = \frac{\sum_x SAF_x(r_T \leftarrow r_x, E_i) \cdot V_x}{\sum_x V_x} \quad (2-20)$$

where $SAF_{composite}(r_T \leftarrow r_S, E_i)$ is total SAF for source tissue r_S irradiating target tissue r_T at an initial photon energy of E_i with all contributions from individual components of r_S included, $SAF_x(r_T \leftarrow r_x, E_i)$ is the SAF for source component r_x irradiating target tissue r_T at an initial photon energy of E_i , and V_x is the volume of source component r_x . A *MATLAB*TM code was written to perform all composite source tissue calculations. A final list of all explicitly simulated source tissues and all mathematically assembled source tissues in the UF hybrid computational phantom series are in Tables 2-15 and 2-16, respectively.

For use in MCNPX, source tissues were represented in the form of source files. Source files define the x -, y -, and z -coordinates of voxels located in the source tissue along with the sampling distribution type and sampling probabilities. MCNPX accesses the source file to randomly select a voxel within the source tissue of interest. Once a voxel is selected, a point within the voxel is randomly selected to start a particle history. Source files were either uniform or non-uniform in nature, but the sampling algorithm assigned to the voxel level remained unchanged regardless of the type of source. Essentially, any non-uniformity in the source was handled by adjusting the probability of selecting a certain set of voxels, but once the voxel was selected, all source points within the voxel were equally likely to be selected. Uniform source sampling at the voxel level was accomplished by defining three dimension bins – one in the x -direction, one in the y -direction, and one in the z -direction. Each bin was assigned a sampling probability of unity across its entire extent. In this way, all points along its length had

an equal probability of being selected as a starting source point. With equal probabilities of source point selection for all points along the x -, y -, and z -directions, all points within the voxel volume were equally likely to be selected as a starting source point.

Uniform source sampling

For most source tissues, specifically those whose entire physical structure was explicitly represented within the hybrid phantoms, uniform source sampling was used to sample points of radiation emission. Two sampling steps were required to select a starting emission point for the photons – (1) selecting a voxel and (2) selecting a point within the voxel (selecting a point within the chosen voxel was described in the previous section).

A distribution of source voxels was defined for MCNPX to sample. Many uniform sources only consisted of one tissue element (e.g., the spleen with tissue tag identification number 45) while some uniform sources were composed of several elements (e.g., the salivary glands with tissue tag identification numbers 39, 60, and 61). For both cases, only one source distribution was defined even though different numbers of tissues were involved simply because it was the most efficient way to compose the source file. Separate distributions could have been defined for each sub-component, but the distributions would be fundamentally equal. All voxels in the phantom that had tissue tag identification numbers equal to those in the source tissue(s) of interest were recorded into a source file along with the coordinates (in numbers of voxels) of each voxel. The discrete source variable flag “L” was used to indicate that each voxel should be considered separately as one “point”. Next, a probability of selection of unity was assigned to all voxels in the source file. This ensured that all voxels would be equally likely to be selected for source sampling. A sample uniform source file and detailed description can be found in Appendix B.

To visually represent uniform source sampling, a simulation was performed, and the x -, y -, and z -coordinates of the starting source particle were recorded. A small subset of these points was chosen, and a red sphere was created at each point. Visual modeling was done in *Rhinoceros*TM, and a subset of points was chosen so that the distribution could be more easily visualized. The lungs of the UFH00M phantom were chosen as the source tissue, and the resulting source points can be seen in Figure 2-8 (A). It should be noted that the concentration of source points appears to be uniform, indicating that uniform source sampling was correctly executed.

Non-uniform source sampling

Uniform source tissues were defined to be uniform because all structures of interest were present in the voxel model. In the case of several skeletal source tissues, the tissues of interest were unable to be explicitly represented in the voxel models. As mentioned in the “Skeletal Photon Fluence-to-Dose Response Functions” section of Chapter 2, bone trabeculae and marrow cavities were too small to be effectively modeled in voxel format. If the structures that could not be explicitly modeled in the voxel model were distributed proportional to the volume of their parent tissues (e.g., bone marrow throughout spongiosa and medullary cavities), non-uniform source sampling would not be necessary because the amount of source tissue per unit volume parent tissue would be equal across the entire sampling volume. However, skeletal source tissues such as TBV are unevenly distributed throughout the spongiosa and MCs (Pafundi *et al.* 2009) and thus were sampled non-uniformly with respect to phantom regions volumes (e.g., spongiosa for an active marrow source).

Similar to the method used to accomplish uniform source sampling, the x -, y -, and z -coordinates of all voxels in the parent tissues of interest were defined. For example, if total

marrow was simulated as the source, the parent tissues were identified as all spongiosa and medullary cavities since bone marrow is found in all of these sites. Thus, spongiosa of the cranium with tissue tag identification number 201 was found in the voxel phantom, and the coordinates of all those voxels were recorded and assigned a sampling probability of unity. Next, in a separate distribution but in the same file, spongiosa of the mandible with tissue tag identification number 202 was found in the voxel phantom, and the same information was recorded. For the total marrow example, this process was completed for tissue tag numbers 201 through 234.

If the example source file for TM were left in this condition, a uniform source distribution throughout whole-body spongiosa and MCs would have been defined. Since a non-uniform source distribution was desired, a final step was added. The purpose of creating separate uniform distributions for each spongiosa and medullary cavity site was to separate the sites for which sampling probabilities would be defined. Each separate site-specific voxel distribution was given a distribution number, and a sampling probability was assigned to that distribution number. The sampling probability f_x , where f_x is the fraction (either volume or surface fraction) of tissue located in spongiosa or MC site x , was set equal to the volume (whole-body AM, TM in spongiosa, TM in medullary cavities, TBV, and CBV) or surface (TBS) fraction of the tissue. In this way, a non-uniform source was created. A sample non-uniform source file and detailed description can be found in Appendix B. All sampling probabilities for the UF hybrid phantom family are in Tables A-11 through A-18 in Appendix A. The fractional source distributions for the UFH00MF, UFH01MF, UFH05MF, UFH10MF, and UFH15MF phantoms were taken from the doctoral dissertation of Deanna Pafundi (Pafundi 2009). Fractional source distributions for the UFHADM phantom were taken from Hough *et al.* (2011). Fractional source distributions for

the UFHADF phantom were recently developed in the master's thesis by Lindsay Sinclair at UF (Sinclair *et al.* 2009).

To visually represent non-uniform source sampling, a simulation was performed, and the x -, y -, and z -coordinates of the starting source particle were recorded. A small subset of these points was chosen, and a red sphere was created at each point. Visual modeling was done in *Rhinoceros*TM, and a subset of points was chosen so that the distribution could be more easily visualized. The lungs of the UFH00M phantom were again chosen as the source tissue, but this time the sampling probability of the right lung was set to 0.9 and the sampling probability of the left lung was set to 0.1. The resulting source points can be seen in Figure 2-8 (B). It should be noted that the concentration of source points no longer appears to be uniform with the right lung being sampled more heavily than the left lung, indicating that non-uniform source sampling was correctly executed.

Target Tissues

Like the source tissues simulated in this study, the list of target tissues was also modeled after those given in ICRP Publication 110. Again, since the ICRP and UF phantoms were developed separately, several target tissues were not consistent between the two models, so approximations were made in these cases as they were with the source tissue definitions. For example, the ICRP has explicitly modeled both adipose and glandular tissue in the breasts (ICRP 2009) while the UF phantoms have a homogenous breast model. In this case, the ICRP models left and right adipose and glandular breast tissue sources explicitly while the left and right homogeneous breast tissue were assigned as the surrogate tissues for the UF phantoms. In addition, several extra target tissues were simulated in the UF phantoms that were not included in the ICRP phantoms.

Some target tissues comprised of several sub-components were not explicitly simulated since their sub-components were simulated individually, as in the case of the kidneys. The left and right kidney cortex, medulla, and pelvis were all considered as separate target tissues, so tallying energy deposition in all regions simultaneously would simply replicate efforts. Consequently, mass weighting was used to calculate the SAF to the composite target tissue, and Equation 2-21 was used to calculate the mass weighted SAFs.

$$SAF_{composite}(r_T \leftarrow r_S, E_i) = \frac{\sum_x SAF_x(r_x \leftarrow r_S, E_i) \cdot m_x}{\sum_x m_x} \quad (2-21)$$

where $SAF_{composite}(r_T \leftarrow r_S, E_i)$ is total SAF for source tissue r_S irradiating target tissue r_T at an initial photon energy of E_i with all contributions from individual components of r_T included, $SAF_x(r_x \leftarrow r_S, E_i)$ is the SAF for source r_S irradiating target tissue component r_x at an initial photon energy of E_i , and m_x is the volume of target component r_x . A *MATLAB*TM code was written to perform all composite target tissue calculations. A final list of all explicitly simulated target tissues and all mathematically assembled target tissues in the UF hybrid computational phantom series are in Tables 2-17 and 2-18, respectively.

Photon Specific Absorbed Fraction Calculation

The primary goal of the photon simulations was to use the UF hybrid phantoms to calculate a set of SAFs at various photon energies. The SAF is an important measure which reflects the geometry of the irradiation scenario as well as the radiation energy. It is ultimately used to calculate either individual organ absorbed doses, individual organ equivalent doses, or whole-body effective dose. Dosimetry of internal emitters is derived from the emission of radiation from any source tissue r_S and the absorption of that radiation in target tissue r_T . For any target tissue, the time independent formulation of radiation absorbed dose from a set of

arbitrary source tissues emitting radiation is described by Equations 2-22 and 2-23 (Bolch *et al.* 2009):

$$D(r_T) = \sum_{r_s} \left[\int_0^{\infty} A(r_s, t) dt \right] S(r_T \leftarrow r_s) = \sum_{r_s} \tilde{A}(r_s) S(r_T \leftarrow r_s) \quad (2-22)$$

$$S(r_T \leftarrow r_s) = \sum_i \frac{E_i Y_i \phi(r_T \leftarrow r_s, E_i)}{m_T} = \sum_i \Delta_i \Phi(r_T \leftarrow r_s, E_i) \quad (2-23)$$

where $\tilde{A}(r_s)$ is the time-integrated activity or the total number of nuclear transformations occurring in source tissue r_s , $S(r_T \leftarrow r_s)$ is the radionuclide S value, defined as the mean absorbed dose rate to target tissue r_T per unit activity in source tissue r_s , E_i is the energy of the i^{th} radiation, Y_i is the yield of the i^{th} radiation, $\phi(r_T \leftarrow r_s, E_i)$ is the AF, defined as the fraction of radiation energy emitted in source tissue r_s that is absorbed in target tissue r_T at radiation energy E_i , m_T is the mass of the target tissue r_T , Δ_i is the delta value for the i^{th} radiation, defined as the product of the energy and the yield of the i^{th} radiation, and $\Phi(r_T \leftarrow r_s, E_i)$ is the SAF, defined as the ratio of the AF to the target tissue mass.

As discussed previously, the tally type used for non-skeletal target tissues recorded energy deposition over a cell (target tissue) in units of *MeV* per photon. To obtain the SAF for any target tissue, the tally results were divided by the initial photon energy and the mass of the target tissue. This equation was validated conceptually because the tally described the amount of energy deposited in the target tissue by a single photon emitted in the source tissue. The deposited energy divided by the emitted energy determined the fraction of that emitted energy that was deposited in the target tissue which is, by definition, the AF. The SAF is defined as the AF divided by the mass of the target tissue. When multiplied by the appropriate conversion factors, the SAF was expressed in units of kg^{-1} .

A different method was used to convert the volume-averaged fluence tallies in the spongiosa and medullary cavity regions to SAFs for the AM and TM₅₀ target tissues because the skeletal photon fluence-to-dose response functions were used instead of direct dose or energy tallying. Equation 2-24 was used to calculate the SAFs for both AM and TM₅₀ target regions for the whole skeleton.

$$\Phi(r_T \leftarrow r_S, E_o) = \frac{k}{E_o} \sum_x w(r_T)_x \sum_i \left[\frac{D(r_T)}{\Phi(E_i)} \right] \Phi(x \leftarrow r_S, E_i) \quad (2-24)$$

where k is a unit conversion constant, E_o is the initial photon energy, $w(r_T)_x$ is the mass fraction of target tissue r_T in bone site x , $[D(r_T)/\Phi(E_i)]$ is the skeletal photon fluence-to-dose response function for target tissue r_T (AM or TM₅₀) at photon energy E_i , $\Phi(x \leftarrow r_S, E_i)$ is the photon fluence emitted from source tissue r_S incident on the spongiosa or medullary cavity of bone site x for photons of energy E_i , and $\Phi(r_T \leftarrow r_S, E_o)$ is the SAF for target tissue r_T from any source tissue r_S . Unfortunately, the symbol used to indicate the SAF and photon fluence are the same, so the reader will have to discern which measure is referred to based on the context.

SAFs were calculated for every source-target-energy combination for the entire UF hybrid phantom family. This was considered to be a complete set of photon SAFs and thus a complete internal photon dosimetry characterization of the UF hybrid phantom family. These SAFs can be used to perform dosimetry calculations for *any* nuclear medicine procedure, provided the radiopharmaceutical biokinetics are known.

Variance Reduction Techniques

Overview

While the majority of SAFs obtained from the radiation transport simulations had relative uncertainties around 1% and were thus considered to be statistically reliable, a small subset of

source-target-energy combinations had relative errors that were less than satisfactory. In the interest of providing the most reliable data possible, steps were taken to make educated adjustments of the data to improve the reliability of some of the less reliable data. These steps included application of – (1) the reciprocity principle, (2) log-linear back-extrapolation, and (3) three point data smoothing. A flowchart schematic of the variance reduction scheme is in Figure 2-9. All aspects of the flowchart will be described in greater detail in the following sections but the flowchart can be referred to as a visual aid to this discussion.

Reciprocity

Most source-target-energy combinations for the photon simulations gave SAFs with satisfactory statistical uncertainties. The MCNP manual gives the recommendation that values with uncertainties above 50% should be disregarded, values with uncertainties between 20% and 50% can be believed to within a factor of a few, values with uncertainties between 10% and 20% are questionable, and values with uncertainties less than 10% are generally reliable (X-5 Monte Carlo Team 2003). However, some source-target-energy combinations had unsatisfactory uncertainties, and methods to correct this undesirable behavior were explored.

The reciprocity theorem states that the SAF from a source organ irradiating a target organ is equivalent to the SAF when the source-target designations are reversed as given in Equation 2-25 (Loevinger 1969).

$$\Phi(r_T \leftarrow r_S, E_i) \approx \Phi(r_S \leftarrow r_T, E_i) \quad (2-25)$$

where $\Phi(r_T \leftarrow r_S, E_i)$ is the SAF for source tissue r_S irradiating target tissue r_T for radiation energy E_i and $\Phi(r_S \leftarrow r_T, E_i)$ is the SAF for target tissue r_T irradiating source tissue r_S for radiation energy E_i . The theorem is rigorously valid for an infinite uniform homogenous media but it has also been shown to be approximately true for heterogeneous media (Petoussi-Henss *et*

al. 2007). When applied in heterogeneous media, this methodology is referred to as the reciprocity “principle” (Cristy *et al.* 1987). However, the principle is not valid when one of the organs is a skeletal tissue for initial energies between 10 *keV* and 200 *keV* (owing to photon dose enhancements), and it is not valid when one of the organs is the left or right lung for initial energies between 10 *keV* and 100 *keV* (due to differences in density and elemental composition) (Petoussi-Hens *et al.* 2007).

Reverse (adjoint) Monte Carlo was performed for most source-target combinations by reversing the source and target designations and retaining the SAF with the lowest statistical uncertainty. The reciprocity principle was not applied for skeletal target tissues at initial energies less than or equal to 200 *keV* or for the lungs at initial energies less than or equal to 100 *keV*. The uncertainties were seen to improve for the larger organ targets as more energy absorption events were recorded. An example of an application of the reciprocity principle is given in Figure 2-10.

Log-linear back-extrapolation

For some SAFs at low initial photon energies, no energy deposition was recorded. However, due to the penetrating nature of electromagnetic radiation, it was determined to be an unphysical artifact of the Monte Carlo radiation transport methodology. If sufficient source points were sampled, some, albeit insignificant, energy deposition would take place. Additionally, it was indicated from other more statistically reliable curves that photon SAFs where the source and target are not the same tissue tend to decrease in a log-linear fashion with respect to decreases in initial photon energy. Therefore, it was not unreasonable to log-linearly back-extrapolate from adjacent SAFs to estimate low energy photon SAFs, and a *MATLAB*TM code was written to perform this operation on the data via Equation 2-26:

$$SAF_{i,j} = 10^{\left(\log(SAF_{i,j+1}) - \frac{\log\left(\frac{SAF_{i,j+2}}{SAF_{i,j+1}}\right)}{\log\left(\frac{E_{j+2}}{E_{j+1}}\right)} \log\left(\frac{E_{j+1}}{E_j}\right) \right)} \quad (2-26)$$

where $SAF_{i,j}$ is the SAF for target tissue i and energy index j and E_j is the initial energy of the photon at energy index j . An example of low energy photon back-extrapolation is shown in Figure 2-11.

A potential argument against this method is that the SAFs were created using equations rather than data generated by explicit radiation transport simulation. There are three reasons why the low energy photon back-extrapolation method is reasonable within this study – (1) an SAF of zero is unphysical since at a certain radiation level, energy deposition will occur, no matter how low the photon energy (based on the exponential attenuation equation), (2) a log-linear trend was indicated by other reliable SAF curves at low initial photon energies, (3) a best-guess estimate is better than no estimate for the purpose of conservativeness. In addition, the impact of any errors introduced by the back-extrapolation method was minimized by the fact that if no energy deposition was recorded, no particles reached the target tissue. That meant that if there had been enough particles simulated to give an adequate number of photon interactions in the target tissue, the dose would have been very low in the first place. Interestingly, the photon SAF simulations displayed a good characteristic in that target tissues of the highest importance (those receiving the greatest dose) displayed the most favorable statistical uncertainties while those of lower importance (those receiving the least dose) displayed the most unfavorable statistical uncertainties. Essentially, when the dose estimate mattered, the dose estimate was good; when the dose estimate mattered less, the dose estimate was not as good. A follow-up argument to this point would question why the back-extrapolation was necessary at all if the results did not

impact final radionuclide S values. No matter what the circumstance, it is always the goal to give the best dose estimates possible, regardless of the perceived importance.

Three-point smoothing

For some source-target combinations, invoking the reciprocity principle was not sufficient to improve the statistical uncertainties of the SAFs. These cases were seen when both the source and target tissues were small in size. Distant organs displayed reasonable statistical uncertainties if they were moderate to large in size. When poor statistical uncertainties were seen across all energies of a particular target organ, they almost always (if not always) manifested themselves as an un-smooth curve that seemed to behave erratically around a perceived central tendency. Since curves of similar general shape were observed for other source-target combinations, it was concluded that the true shape of the erratic curve could be approximated by applying a three-point smoothing algorithm to the range of energies where the curve was seen to be the most erratic. In cases where the initial energy of the photon was equal to 10 *keV* or 4 *MeV* (the lower and upper energy limits), two point smoothing was applied. An example of the three-point smoothing technique is in Figure 2-12.

Electron Specific Absorbed Fractions

Similarities to Photon Transport Methods

Many of the details used to generate the input files and all associated files for the photon simulations were identical to those used to generate the files for the electron source simulations. The phantom physical characteristics were all the same since the electron dosimetry was performed for the same phantoms. Lattice files, source files, voxel resolutions, total matrix sizes, tissue densities, material compositions, tissue masses, source tissues, target tissues, and radiation emission energies were identical in both the photon and electron dosimetry simulations.

General Transport Methodology

A significant difference observed between photon and electron computational dosimetry was that the uncertainties associated with any tally for electron dosimetry in cross-dose scenarios were typically higher than those for photon dosimetry². In fact, many estimates of electron cross-dose (especially for low initial electron energies) for several test simulations had uncertainties of 100% or no energy deposition at all. This characteristic was mostly seen when the source tissue and target tissue were separated by a distance greater than the CSDA range of the electrons. When this was the case, energy deposition to target tissues was a result of electrons created by photons that were themselves created by the initial electrons. Uncertainties were high because the number of photons created during the course of a single source electron losing energy was lower than the number of particle histories. In addition, since the photons were mostly bremsstrahlung photons, the photon spectrum was more heavily weighted toward energies lower than the initial energies of the monoenergetic electrons. The combination of low yield and low energy photons expectedly produced high uncertainties in the electron SAFs. When target tissues received energy deposition from collisional energy losses of the primary electrons (electrons started in the simulation), the statistical uncertainties were much lower.

To combat the undesirable characteristic of high uncertainties, a novel method was created to produce lower uncertainty electron SAFs. This method consists of two simulations separately modeling the two mechanisms of electron energy loss – (1) a collisional energy loss (CEL) simulation and (2) radiative energy loss (REL) simulation. When an arbitrary electron (primary electron) was started in any particular source tissue, it deposited energy in the target tissues through excitation and ionization from the primary electron and its secondary electrons

² This is observed when electron dosimetry is performed in the traditional way by simply starting monoenergetic electrons and following all photons and electrons created during the course of simulation.

(collisional energy loss) and through excitation and ionization from electrons created by photons generated during the course of the primary electron traversal through tissue (radiative energy loss). The photons were mostly created in the source tissue itself due to comparatively short electron ranges. If sufficient electrons were simulated, the photons created during particle transport could be approximated as uniformly distributed throughout the source tissue and isotropic in their angular emissions. In light of this, the connection was made that this very scenario had already been modeled with reliable results in the previous photon simulations. Since the photon simulations had relatively low uncertainties, and variance reduction techniques had already been applied, it was a natural extension to somehow replace the radiative energy loss component of the electron simulations with the already completed photon simulations.

To accomplish this separation of the electron energy loss components, a feature within MCNPX was utilized to record the initial energies of all photons created during the electron simulations³. Next, the pre-computed, low-uncertainty, monoenergetic photon SAFs could be used to calculate a photon spectrum-weighted SAF that would represent the radiative energy loss contribution to absorbed dose in the target tissue of interest. The collisional energy loss simulation accounted for the removal of energy from bremsstrahlung photon creation but did not follow those photons, thus saving simulation time. Collisional energy loss from primary electrons was thus simulated entirely separately from the radiative energy loss component. Since the photon SAF simulations followed all secondary electrons and any subsequent photon-electron showers, the physics of a full electron dosimetry simulation (following all photons and electrons created during simulation) was accurately modeled with the added effect of virtually simulating many more particle histories through application of the previously constructed

³ Bremsstrahlung photons are primarily created in these simulations, but characteristic x rays are also observed.

monoenergetic photon SAF dataset. A flowchart schematic of the electron dosimetry scheme is given in Figure 2-13. All aspects of the flowchart will be described in greater detail in the following sections, but the flowchart is given here as a visual aid to the discussion.

It was of slight concern that the lack of an explicit blood vessel wall model could perturb the bremsstrahlung spectrum of a source within the blood vessels. In addition, possible shielding effects could be introduced when considering electron emitters in the blood vessels. However, in the end, distributed blood sources were of primary interest, not blood vessel-only sources. Any slight perturbations in the results from a lack of blood vessel wall model were considered to be compensated by the averaging of the results from all blood-containing organs.

Collisional Energy Loss Contribution to Dose

Tally types

Energy deposition over a cell was used for all target tissues for the CEL electron simulations. Regions of spongiosa and MCs in the skeleton were tallied separately, giving a total of 34 tallies for these regions. Fluence tallies were not needed for application of the skeletal photon fluence-to-dose response functions because the dose resulting from photons created during electron transport to AM and TM_{50} from extra-skeletal sources were handled in the REL simulations. Skeletal photon fluence-to-dose response functions were needed for photon simulations to account for the dose-enhancement effect of electrons created in TB of the skeleton (Pafundi *et al.* 2010). However, when considering ionization and excitation from primary electrons in AM and TM_{50} , there is no dose-enhancement effect, indicating that energy is not preferentially deposited in one tissue over another per unit mass. As a result, absorbed dose to homogeneous spongiosa and the marrow within medullary cavities can be used as a surrogate for the absorbed dose to AM and TM_{50} in those same tissue regions. Total dose to AM and TM_{50} was calculated as a weighted average over the whole skeleton.

Miscellaneous transport details

The initial monoenergetic electron energies and number of particle histories simulated at each energy for the CEL simulations was the same as was used for the photon simulations and can be seen in Figure 2-7. The default electron energy cutoff of 1 keV was used, and the ITS-style nearest-bin algorithm was selected for electron energy indexing.

Collisional specific absorbed fraction calculation

Energy deposition over a cell was tallied for all non-skeletal target tissues in the CEL simulations. Equation 2-27 was used to calculate the SAFs for all non-skeletal target tissues.

$$\Phi_{CEL}^{non-skel}(r_T \leftarrow r_S, E_o) = \frac{E}{E_o m_T} \quad (2-27)$$

where $\Phi_{CEL}^{non-skel}(r_T \leftarrow r_S, E_o)$ is the SAF due to collisional energy loss of the primary electrons for source tissue r_S irradiating target tissue r_T at initial electron energy E_o for non-skeletal target tissues, E is the energy deposited in target tissue r_T , and m_T is the mass of the target tissue.

For extra-skeletal sources, energy deposition over a cell was tallied for all regions of spongiosa and MCs. For reasons previously detailed, the SAFs to AM and TM₅₀ were approximated by the SAF to whole-body spongiosa or medullary marrow. A weighted average of energy deposited in all spongiosa and MCs was used to calculate the SAFs to AM and TM₅₀ and is detailed in Equation 2-28:

$$\Phi_{CEL}^{skel}(r_T \leftarrow r_S, E_o) = \frac{1}{E_o} \sum_i \left(\frac{E_i}{m_{T,i}} \right) w(r_T)_i \quad (2-28)$$

where $\Phi_{CEL}^{skel}(r_T \leftarrow r_S, E_o)$ is the SAF due to collisional energy loss of the primary electrons for source tissue r_S irradiating target tissue r_T at initial electron energy E_o for skeletal target tissues and extra-skeletal sources, E_i is the energy deposited in spongiosa or MC region i , $m_{T,i}$ is the

mass of spongiosa or MC region i , and $w(r_T)_i$ is the mass fraction of target tissue r_T in spongiosa or MC region i .

Since the skeletal target tissues for extra-skeletal sources each had an associated uncertainty, an uncertainty was calculated for the whole-skeleton estimates for variance reduction purposes. Whole-skeleton uncertainties for AM and TM₅₀ for extra-skeletal sources were calculated using Equation 2-33 and was derived using Equations 2-29 through 2-32.

$$\Phi_{CEL}^{skel}(r_T \leftarrow r_S, E_o) = \sum_i w(r_T)_i \cdot \Phi_i(i \leftarrow r_S, E_o) \quad (2-29)$$

$$\sigma_\Phi^2 = \sum_i \left[\frac{\partial(\Phi_{CEL}^{skel}(r_T \leftarrow r_S, E_o))}{\partial(\Phi_i(i \leftarrow r_S, E_o)_i)} \right]^2 \sigma_{\Phi_i}^2 \quad (2-30)$$

$$\sigma_{\Phi_i} = \Phi_i(i \leftarrow r_S, E_o) \cdot \sigma_{MCNP_i} \quad (2-31)$$

$$\sigma_\Phi^2 = \sum_i w(r_T)_i^2 \cdot \Phi_i(i \leftarrow r_S, E_o)^2 \cdot \sigma_{MCNP_i}^2 \quad (2-32)$$

$$\sigma_\Phi = \left[\sum_i w(r_T)_i^2 \cdot \Phi_i(i \leftarrow r_S, E_o)^2 \cdot \sigma_{MCNP_i}^2 \right]^{\frac{1}{2}} \quad (2-33)$$

where $\Phi_{CEL}^{skel}(r_T \leftarrow r_S, E_o)$ is the SAF due to collisional energy loss of the primary electrons for source tissue r_S irradiating target tissue r_T at initial electron energy E_o for skeletal target tissues and extra-skeletal sources, $\Phi_i(i \leftarrow r_S, E_o)$ is the SAF due to collisional energy loss of the primary electrons for source tissue r_S irradiating spongiosa or MC region i at initial electron energy E_o , $w(r_T)_i$ is the mass fraction of target tissue r_T in spongiosa or MC region i , σ_Φ is the absolute uncertainty for the whole-skeleton SAF, σ_{Φ_i} is the absolute uncertainty associated with the SAF for spongiosa or MC region i , and σ_{MCNP_i} is the relative uncertainty associated with the SAF for spongiosa or MC region i as given in the output of the MCNPX simulations. The

relative uncertainty for the whole skeleton was obtained by dividing the absolute uncertainty for the whole skeleton by $\Phi_{CEL}^{skel}(r_T \leftarrow r_S, E_o)$.

Radiative Energy Loss Contribution to Dose

Methodology

The basis for the REL simulation was laid out in the “General Transport Methodology” sub-section of the “Electron Specific Absorbed Fractions” portion of Chapter 2, but the important points will be restated here. For each source tissue and initial electron energy, instead of tracking energy deposition over a cell, the initial energies of all photons created during the simulation were recorded. As previously noted, photons generated during transport include both bremsstrahlung and characteristic x rays, but large fraction of photon intensity can be attributed to bremsstrahlung radiation. By simulating a number of particle histories, a photon spectrum was created. This photon spectrum was then weighted by the previously generated set of monoenergetic photon SAFs for the source tissue of interest to obtain the SAF to all target tissues of interest due exclusively to contributions from radiative energy loss by the primary electrons.

Particle tracking

The particle tracking (PTRAC) file feature within MCNPX was utilized to record the initial energies of all photons (bremsstrahlung and characteristic x rays, in particular) created during the transport of the primary electrons in the source tissue. Relevant input parameters available for use and values used in the simulations were as follows (LANL 2005).

FILE – This input parameter determines the type of output file generated, and the value was set to “ASCII” since text files were needed for post-processing with *MATLAB*TM.

MAX – This input parameter specifies the maximum number of events to write to the output file, and the value was set to 10^8 to ensure that all events would be recorded to the output file. This number was arbitrary but equal to the greatest number of particles simulated.

WRITE – This input parameter details what measures are to be written to the output file, and the value was set to “all” since particle energy was the measure of interest and is only reported when all parameters are written.

EVENT – This input parameter determines what physical occurrence should be recorded in the output file, and the value was set to “bank” because MCNPX handles photon production by banking them for later transport.

TYPE – This input parameter filters events based on the selected particle type, and the value was set to “photons” since photons were the particles of interest.

Particle histories

Unlike the photon and CEL electron simulations, minimizing uncertainties associated with energy deposition tallies was not considered. A different endpoint was defined for the REL electron simulations: a reliable photon energy spectrum. Two factors were considered when determining the number of particle histories to be used for the REL simulations. The first consideration was file size. During the course of several test simulations, it was found that simulating 10^6 particle histories produced PTRAC files that were too large to be efficiently processed. Additionally, SAF values for the REL simulations showed little variation between particle histories of 10^4 and 10^6 . The second consideration was the desire to model the photon spectra as accurately as possible. Photon spectra accuracy increases with increasing number of particle histories, but at a certain point, further technical accuracy did not significantly change the SAF estimates.

After considering the tradeoff between simulation time, file size, and photon spectrum accuracy, the number of particle histories was set to 2×10^5 . Photon energy spectra were generated for a uniform electron source in the liver of the UFH00M phantom, and the results are in Figure 2-14. The photon spectra match the predicted bremsstrahlung spectra fairly well and seem to indicate that the number of particle histories chosen was reasonable. At the chosen number of particle histories, the *MATLAB*TM code written to process the REL simulation output took approximately 8 hours to process all output for each phantom. If many more particle histories had been simulated, the time required to process the output would be unreasonable and would push the memory limits of *MATLAB*TM.

It is important to remember that a REL photon spectrum was generated for each monoenergetic electron energy for every source organ. If the resulting spectra were not heavily dependent on the source organ, perhaps a single spectrum could be used and applied for each source organ. To investigate this possibility, photon spectra were generated for all 21 electron energies for the adipose tissue, left and right adrenals (separately), brain, left breast, and “rest of body” compartment for the UFH00M phantom. Spectra as depicted in Figure 2-14 were compared to the spectrum obtained by averaging the results of all the modeled source organs. Differences up to about 20% were observed for the statistically reliable energy bins across the different source organs. In addition, the left and right adrenals showed about 5% – 15% deviation from each other, even given the equivalent elemental compositions. This is due to the inherent approximation that all photon created outside of the source organ are treated as a photon emission in the source organ. Because of these differences in photon spectra, each source tissue was individually simulated instead of using an average photon spectrum.

Radiative energy loss specific absorbed fraction calculation

Once all REL simulations were complete for all source tissue in all phantoms, the resulting photon energy spectra were converted into REL SAFs using Equation 2-37 derived from Equations 2-34 through 2-36. Equation 2-35 gives the equation that would be used if a continuous photon and electron energy spectrum were available. However, since only a certain number of photon energies were recorded, the continuous equation was discretized. The important concept in these equations is that the absorbed fraction of energy in any target tissue of interest due to radiative energy losses by the primary electrons is equal to the energy deposited in the target tissue from electrons created by photon interactions divided by the total electron energy emitted from the source tissue.

$$\Phi_{REL}(r_T \leftarrow r_S, E_o^{electron}) = \frac{\phi_{REL}(r_T \leftarrow r_S, E_o^{electron})}{m_T} \quad (2-34)$$

$$\phi_{REL}(r_T \leftarrow r_S, E_o^{electron}) = \frac{E_{deposit}^{photon}(r_T)}{E_{emit}^{electron}(r_S)} = \frac{\int_0^{E_{max}^{photon}} \phi_{photon}(r_T \leftarrow r_S, E^{photon}) \cdot E^{photon} dE^{photon}}{\int_0^{E_{max}^{electron}} E^{electron} dE^{electron}} \quad (2-35)$$

$$\phi_{REL}(r_T \leftarrow r_S, E_o^{electron}) = \frac{\sum_i \phi_{photon}(r_T \leftarrow r_S, E_i^{photon}) \cdot E_i^{photon}}{E_o^{electron} \cdot N^{electron}} \quad (2-36)$$

$$\Phi_{REL}(r_T \leftarrow r_S, E_o^{electron}) = \frac{\sum_i \Phi_{photon}(r_T \leftarrow r_S, E_i^{photon}) \cdot E_i^{photon}}{E_o^{electron} \cdot N^{electron}} \quad (2-37)$$

where $\Phi_{REL}(r_T \leftarrow r_S, E_o^{electron})$ is the SAF to target tissue r_T from source tissue r_S at initial electron energy $E_o^{electron}$ due to radiative energy losses of the primary electrons, $\phi_{REL}(r_T \leftarrow r_S, E_o^{electron})$ is the AF to target tissue r_T from source tissue r_S at initial electron energy $E_o^{electron}$ due to radiative energy losses of the primary electrons, m_T is the mass of target tissue r_T ,

$E_{deposit}^{photon}(r_T)$ is the energy deposited in target tissue r_T that can be attributed to the photons created during simulation (photons are indirectly ionizing), $E_{emit}^{electron}(r_S)$ is the total primary electron energy emitted from source tissue r_S , E_{max}^{photon} is the maximum photon energy in an arbitrary continuous photon energy spectrum, $\phi_{photon}(r_T \leftarrow r_S, E^{photon})$ is the photon AF to target tissue r_T from source tissue r_S at photon energy E^{photon} , $E_{max}^{electron}$ is the maximum electron energy in an arbitrary electron energy spectrum, $E^{electron}$ is the energy of an electron in an arbitrary electron energy spectrum, $\phi_{photon}(r_T \leftarrow r_S, E_i^{photon})$ is the photon AF to target tissue r_T from source tissue r_S at energy E_i^{photon} of the i^{th} photon, $N^{electron}$ is the total number of primary electrons simulated, and $\Phi_{photon}(r_T \leftarrow r_S, E_i^{photon})$ is the photon SAF to target tissue r_T from source tissue r_S at energy E_i^{photon} of the i^{th} photon.

While the REL simulations were effectively performed in all source tissues in all phantoms, the REL simulations were not physically performed in several instances. The UFH00MF, UFH01MF, UFH05MF, and UFH10MF phantoms share the same internal structure between genders with the only difference being the gender-specific organs (Lee *et al.* 2010). Since the structures and tissue elemental compositions were the same between genders, REL simulations were only performed for the gender-specific organs in the UFH00F, UFH01F, UFH05F, and UFH10F phantoms. The photon spectra generated for the common organs in the male phantoms were used for the common organs in the female phantoms.

Total Electron Specific Absorbed Fraction

Extra-skeletal sources

The CEL simulations were performed to model dose contributions due to collisional energy loss, and the REL simulations were performed to model dose contributions due to radiative energy loss. Since these simulations modeled two separate processes that did not

included any overlap in dose contributions, the final total electron specific absorbed fraction for extra-skeletal source tissues was determined from Equation 2-38.

$$\Phi(r_T \leftarrow r_S, E_o) = \Phi_{CEL}(r_T \leftarrow r_S, E_o) + \Phi_{REL}(r_T \leftarrow r_S, E_o) \quad (2-38)$$

where $\Phi(r_T \leftarrow r_S, E_o)$ is the total electron SAF for source tissue r_S irradiating target tissue r_T at initial electron energy E_o , $\Phi_{CEL}(r_T \leftarrow r_S, E_o)$ is the SAF obtained from the CEL simulation for source tissue r_S irradiating target tissue r_T at initial electron energy E_o , and $\Phi_{REL}(r_T \leftarrow r_S, E_o)$ is the SAF obtained from the REL simulation for source tissue r_S irradiating target tissue r_T at initial electron energy E_o . This equation was applied when the source tissue was not located within the skeleton and the target tissue was either a non-skeletal tissue or a skeletal tissue.

Intra-skeletal sources

When the source tissue was located within the skeleton and the target tissue was a non-skeletal target tissue, Equation 2-38 was applied to calculate the total electron SAF. However, a special case arose when calculating the total electron SAF for intra-skeletal target tissues from intra-skeletal source tissues as in the case of TBV irradiating AM. In these cases, the trabecular microstructure must be taken into account since electrons were being transported with starting points in the complicated geometries of spongiosa (all regions with bone trabeculae and marrow cavities) and the medullary cavities of the long bones.

To account for the complicated microstructure, previous work was used in addition to methods described in this study. Intra-skeletal electron SAFs had already been computed by Pafundi *et al.* (2010) for the UFH00MF and UFH15MF (Pafundi 2009) phantoms and by Hough *et al.* (2011) for the UFHADM phantom. The following SAFs were taken from those studies: $\Phi(AM \text{ and } TM_{50} \leftarrow AM)$, $\Phi(AM \text{ and } TM_{50} \leftarrow TBS)$, $\Phi(AM \text{ and } TM_{50} \leftarrow TBV)$, and $\Phi(AM \text{ and } TM_{50} \leftarrow CBV)$. The following SAFs were mathematically derived:

$\Phi(AM \text{ and } TM_{50} \leftarrow TMA)$ and $\Phi(AM \text{ and } TM_{50} \leftarrow CMA)$. CMA refers to total bone marrow associated with the shafts of the long bones, and TMA refers to total bone marrow associated with all other skeletal sites. As this is the case, the CMA and TMA SAFs will be computed by taking a volume weighted average of the SAFs across all relevant skeletal sites. Intra-skeletal electron SAFs assembled from the CBIST-SIRT calculations were used in this study for the UFH01MF, UFH05MF, UFH10MF, and work by Sinclair *et al.* (2009) was utilized in this study for the UFHADDF.

Variance Reduction Techniques

Variance reduction had already been performed for the SAFs from the REL simulations since they were derived from the photon SAFs. Therefore, no further variance reduction techniques were applied to the REL simulation SAFs. However, the CEL simulation SAFs had not been post-processed, so variance reduction techniques were considered for this subset of the electron SAFs.

Log-linear back-extrapolation was not an option because the physics behind the argument that photon dose will not be zero at low energies does not apply as rigorously to electron physics. Electrons have a definite range, so if no energy deposition was recorded, the SAF was taken to be zero. Occasionally, energy deposition with high uncertainty was seen at a particular energy, or one or more SAFs at greater energies were zero. In these cases, the positive, high-uncertainty SAF was set to zero.

Finally, the reciprocity principle described in the “Variance Reduction Techniques” section of the “Photon Specific Absorbed Fractions” section of Chapter 2 was used for the CEL simulation SAFs. Cristy and Eckerman detailed the use of the reciprocity principle and explained that the principle applies to all radiation types (Cristy *et al.* 1987), and thus the application of the principle for dose due to electron collisional energy loss was considered valid.

Computing Resources and Runtimes

The ALRADS research group in the Department of Biomedical Engineering at UF has four computing clusters available for use. Most of the *MATLAB*TM simulations were performed on a 6-node cluster built with Dell, Inc. (Round Rock, TX) computers. Each node in the Dell cluster has 8 processors per node with a CPU speed of 2 *GHz* per processor. Each processor has 2 *GB* of memory, and the whole cluster has 750 *GB* of hard disk space.

All of the MCNPX simulations were performed on the other three clusters. The first cluster was built with PSSC Labs (Lake Forest, CA) computers and has 4 nodes with 8 processors per node and 9 nodes with 4 processors per node. Each processor has a CPU speed of 2 *GHz* and 2 *GB* of memory. The whole cluster has 500 *GB* of hard disk space. The second cluster was built with Dell (Round Rock, TX) computers and has 4 nodes with 16 processors per node and 1 node with 24 processors per node. Each processor has a CPU speed of 2.66 *GHz* and 4 *GB* of memory. The whole cluster has 500 *GB* of hard disk space. The third cluster was built independently by another research group and has 17 nodes with 4 processors per node. Each processor has a CPU speed of 2.00 *GHz* and 4 *GB* of memory. The whole cluster has 1900 *GB* of hard disk space.

The vast computing resources available were needed to simulate the large of input files needed for the current study. Average runtimes for the photon, CEL, and REL simulations were approximately 9 *h*, 10 *h*, and 8 *min*, respectively. An approximate total runtime for all simulations was calculated as 36 *cpu – yrs*. However, running on an average of 50 processors (due to cluster down-time and shared usage) gave an approximate real-time runtime of 0.72 *yrs* or about 8.5 *mos*. A myriad other simulations were performed across the span of this entire

study that required the vast computing resources as well, and it is estimated that well over 50,000 simulations were performed.

Radionuclide S Values

Monoenergetic photon and electron SAFs may be useful in and of themselves for academic purposes, but radionuclide S values are needed to perform relevant clinical dosimetry studies. SAFs provide necessary information about the internal geometry of the patient phantom and radiation energy, but they do not directly estimate the radiation absorbed dose to radiosensitive organs. Radionuclide S values give the radiation absorbed dose to a target organ of interest from a source organ of interest for a particular radionuclide of interest per nuclear disintegration in the source tissue, the formulation of which is given in Equation 2-39. When combined with the total number of disintegrations in the source tissue, repeated and summed over all source tissues, the final absorbed dose estimate to the target tissue of interest is determined (Equation 2-36).

$$S(r_T \leftarrow r_S) = \sum_i \Phi(r_T \leftarrow r_S, E_i) \cdot E_i \cdot Y_i \quad (2-39)$$

where $S(r_T \leftarrow r_S)$ is the S value to target tissue r_T from source tissue r_S in units of $mGy/MBq \cdot s$, $\Phi(r_T \leftarrow r_S, E_i)$ is the SAF to target tissue r_T from source tissue r_S for radiation of energy E_i , and Y_i is the yield of the i^{th} radiation. This equation is summed over all radiation emission types.

A *MATLAB*TM code was written to calculate radionuclide S values for all source-target combinations detailed in the monoenergetic photon and electron models based on provided radionuclide emission energies and yields. Monoenergetic photons (gamma rays and x rays), monoenergetic electrons (Auger and internal conversion (IC) electrons), and beta particles were considered for contributions to the S value. ICRP Publication 107 was used for radionuclide spectra information (energies and yields) (ICRP 2008). The methodology for implementing

Equation 2-39 for monoenergetic photon and electrons emissions was relatively straightforward since each photon and electron emission had an associated absolute yield. Absolute yield refers to the number of particles emitted per nuclear disintegration at the energy of interest (Attix 2004). The code cycles through each radiation energy and yield, and at each energy the SAF for all source-target combinations is calculated by log-linear interpolation between the two nearest energy points for which the SAFs were evaluated. For both monoenergetic photons and electrons, if the energy is less than 10 keV and the pre-computed monoenergetic SAF at 10 keV is greater than zero, the energy-specific SAF is log-linearly back-extrapolated.

Beta particle yields were given in units of number of beta particles per nuclear transformation per MeV, so the methodology for monoenergetic photons and electrons could only be applied once the beta spectra were converted into absolute yields. This was done by reconstituting the beta spectra into absolute yield spectra by breaking up the spectra into energy bins and calculating the absolute yield at each energy bin. For the continuous spectra, absolute yield at each energy would be calculated using Equation 2-40.

$$Y(E_i) = \int_{E_i - \Delta E / 2}^{E_i + \Delta E / 2} y(E_i) dE \quad (2-40)$$

where $Y(E_i)$ is the absolute beta yield at energy E_i and $y(E_i)$ is the beta yield density. However, Equation 2-40 was reduced to Equation 2-41 for practical implementation.

$$Y(E_i) = y(E_i) \cdot \Delta E \quad (2-41)$$

where $Y(E_i)$ is the absolute beta yield at energy E_i , $y(E_i)$ is the beta yield density, and ΔE is an arbitrary energy bin width for which $y(E_i)$ was evaluated.

When approximating a continuous function with discrete bins, care must be taken in selecting the bin width. A sensitivity study was performed to determine the point at which the calculated S value deviates from the “accurate” estimate by more than approximately 1%. SAFs

from the UFH00MF phantoms were used to calculate the S value beta contributions for ^{90}Y . The beta spectrum was taken from ICRP Publication 107 (ICRP 2008). An energy bin width of 25 eV was chosen as the finest energy bin width that would be selected and was considered the energy bin width that would give the most accurate S value estimate for reasonable computation times. S values were calculated using additional energy bin widths of 100 eV, 500 eV, 1 keV, and 10 keV for comparison. $^{99\text{m}}\text{Tc}$ and ^{90}Y radionuclide beta-component of the S values were computed at these energy bin widths and compared to the beta-component of the S values computed when using a bin width of 25 eV.

Differences in results were seen for ^{90}Y at the 10 keV bin width of up to about 0.1% (as compared to results from the reference bin width of 25 eV), and differences in results were seen for $^{99\text{m}}\text{Tc}$ at the 10 keV bin width of up to about 5%. Statistically insignificant (0.00%) differences were seen for ^{90}Y at an energy bin width of 500 eV. It was quickly determined that the difference between the ^{90}Y and $^{99\text{m}}\text{Tc}$ results was due to the difference in overall number of bins. At the 500 eV energy bin width, with a maximum beta particle energy of 2.28 MeV, the ^{90}Y beta spectrum had 4561 bins while for the same energy bin width, $^{99\text{m}}\text{Tc}$ had 873 bins due to the maximum beta particle energy of 436 keV. $^{99\text{m}}\text{Tc}$ was reevaluated using an energy bin width of 95.63 eV, an energy bin width that would yield 4561 total bins. The difference between the 25 eV bin width results and the 95.63 eV bin width results for $^{99\text{m}}\text{Tc}$ were statistically insignificant (0.00%). Since computation time was reasonable for 4561 energy bins, a round number of 5000 energy bins was selected for all radionuclides. This number of energy bins should ensure that the accuracy of the beta component of the S values will not depend on the numerical methods in the code.

Biokinetics

Radionuclide S values give the dosimetric information regarding the radionuclide and phantom of interest. Biokinetic information, information regarding how the radiopharmaceutical distributes throughout the body, is needed to determine the source tissues in which the radiopharmaceutical localizes and to calculate the number of radioactive decays in those source tissues using both physical and biological half-lives.

As an example, the radiopharmaceutical ^{99m}Tc – dimercaptosuccinic acid (DMSA) was selected for demonstration of biokinetic analysis. The total number of radioactive decays must be calculated for each organ that retains the radiopharmaceutical as described by $\tilde{A}(r_S)$ in Equation 2-22. This was defined as the AA multiplied by the total number of nuclear transformations per unit AA for each source tissue. An alternative approach, one that was used in the current study, is to simply multiply the radionuclide S value for the source tissue of interest by the total number of nuclear transformations in that source tissue to obtain an absorbed dose per unit AA. Then, the dose for a variety of AAs may be calculated. The total number of nuclear transformations in each source tissue takes into account both the physical and biological half-lives. The source tissues for ^{99m}Tc – DSA were determined to be the left and right kidneys (the kidney cortex was assumed to receive all of the kidney activity), liver, spleen, urinary bladder contents, heart contents, lungs, and rest of body (Arnold *et al.* 1975, Evans *et al.* 1996, Smith *et al.* 1996). For illustration purposes, the biodistribution parameters for the newborn patient can be seen in Table 2-19 (Arnold *et al.* 1975, Smith *et al.* 1996). Blood kinetics were analyzed separately to obtain the total number of nuclear transformations in the lung and heart contents.

From the information in Table 2-19 as well as additional information not reported here, the total number of nuclear transformations were calculated based on Equations 2-22 and 2-42 (Faw *et al.* 1999):

$$A(t) = A_m (1 - e^{-\lambda_+ t}) e^{-(\lambda_- + \lambda_p) t} \quad (2-42)$$

where A_m is the fractional maximum uptake, A_o is the fractional initial uptake, λ_+ is the uptake rate in units of h^{-1} , λ_- is the clearance rate in units of h^{-1} , λ_{eff-} is the effective clearance rate in h^{-1} , and $A(t)$ is the time dependent fractional injected activity. Equation 2-42 was integrated over all time to obtain the tissue-specific radiopharmaceutical number of nuclear transformations, as detailed in Equation 2-22. In-depth biokinetic analysis was beyond the scope of this study, so the biokinetic calculations were simply patterned after a previous completion of the $^{99m}Tc - DMSA$ biokinetic analysis (Evans *et al.* 1996). For any subsequent studies requiring dose calculations using biokinetics of a radiopharmaceutical, the methodology outlined in this section was used.

It is important to note that uncertainties associated with the biokinetic models generally greatly outweigh those associated with the internal dose parameters obtained through radiation transport. Uncertainties in the radiation transport simulations arise from three main contributions – (1) uncertainties in the modeling algorithm, (2) uncertainties in the internal anatomic structure of the phantoms, and (3) uncertainties in the tissue compositions and densities of the phantoms. Uncertainties in the modeling algorithm are probably the least of all uncertainty contributions between the biokinetic models and internal dose parameter calculations due to relatively well-understood physical phenomena and modeling methods. Uncertainties in the internal structure and tissue compositions and densities are reduced through definitions with regard to actual patient data. The internal anatomy in the UF phantoms was based on actual patient images, and

tissue elemental compositions and densities were based on population averages of actual measurements (ICRP 2002).

Uncertainties in biokinetic model could potentially arise from 4 main contributions – (1) uncertainties in the structure of the biokinetic models, (2) uncertainties in applications of human data, (3) uncertainties in inter-element extrapolations of biokinetics, and (4) uncertainties in inter-species extrapolations of biokinetic data (Leggett 2001). For most relevant radionuclides, human data is available and is the preferred method for developing biokinetic models (Leggett 2001). However, even when biokinetic data is available, a quote on page 201 of Leggett (2001) indicates that uncertainty is introduced due to “small study groups, coupled with potentially large inter-subject variability in the biokinetics of an element; short observation periods, coupled with potentially large intra-subject variability; use of unhealthy subjects whose diseases may alter the biokinetics of the element; paucity of observations for women and children; collection of small, potentially non-representative samples of tissue; inaccuracies in measurement techniques; uncertainty in the pattern of level of intake of the element; atypical study conditions; and inconsistency in reported values”. It is evident from this quote that there are many ways uncertainty is introduced in the development of biokinetic models. It is important to keep this in perspective because it is always attempted to minimize the uncertainties in the internal dose factors developed in the current study, but in reality the final internal dose factor uncertainties will probably always be less than those of the biokinetic modeling.

Dosimetric Sensitivity Studies

The analyses up to this point have been directed at developing internal dosimetry models applicable to phantoms that are ICRP-reference. That is, the phantoms are a reference set of phantoms that apply to the average individual by height and weight (ICRP 2002). These phantoms may be applied as an estimate for patient dosimetry, but there is a high probability that

the patient for whom the dosimetry is being performed is not 50th percentile in either height and/or weight. In these cases, dose estimates based on the ICRP-reference phantoms is more desirable than crude estimates using outdated or simplified models, but they may not truly represent the individual undergoing the nuclear medicine exam. To further personalize dose estimates provided by this work, dosimetric sensitivity studies were performed to attempt to characterize changes in radiation absorbed dose with changes in a variety of measurable parameters. The goal was to develop equations that could be implemented within the internal dosimetry software or to generate sets of LUT-style scaling factors. These equations or scaling factors would require the input of known organ masses, known organ separations, and patient sitting height and weight. Other parameters were introduced as they were found relevant. Based on these inputs, the reference dose measure could be scaled to better predict the actual dose to organs in the patient of interest. If dosimetric trends were found, a vast number of “virtual phantoms”, phantoms that were never actually simulated in MCNPX would be created.

The final implementation of this section of the dissertation will be based on user selection of either explicit definition of either organ volumes or morphometric characteristics.

Presumably, one would not typically be able to readily extract organ volumes for every single scan in a clinic, so morphometry-based internal dosimetry scaling will probably be used more frequently. If organ volumes are available, the user will select the organ-specific dose scaling option, and the results from the “Variation in Source and Target Size and Separation” section would be applied based on the entered organ volumes. If organ volumes are *not* available, the user will select the morphometry-specific dose scaling option, and the results from the “Variation in Anthropometric Characteristics” section would be applied based on input parameters such as sitting height and waist circumference.

Variation in Source and Target Size and Separation

Sphere studies

Self-dose – A computational study in MCNPX was designed to examine the relationship between radiation absorbed dose and source/target region size and separation. For the self-dose study, twenty-one spheres were constructed with masses ranging from 1 *g* to 10 *kg*. The spheres were assigned a density of 1.0 *g/cm*³ and a tissue composition of average adult male soft tissue, as defined in Report 46 of the International Commission on Radiation Units and Measurements (ICRU) (ICRU 1992). The surrounding medium consisted of ICRU Report 46 average adult male soft tissue and represented an “infinite” surrounding media. Photons were simulated first to both investigate the validity of the MIRD Pamphlet No. 11 recommendation to use a mass ratio scaling factor of $-2/3$ for photon self-dose scaling and attempt to predict dose scaling algorithms for photon cross-dose (Snyder *et al.* 1975). Uniform photon sources were simulated within each source sphere, and the energy deposited in the source sphere was recorded.

Based on MIRD Pamphlet No. 11, it was clear that changes in photon self-dose with changes in tissue size could be predicted to assume some power of the ratio of masses of the reference tissue size and non-reference tissue size (Snyder *et al.* 1975). However, MIRD Pamphlet No. 11 simplified the power to a single number that could be applied for a select range of energies (Snyder *et al.* 1975), although the scaling power is actually applied across all energies in OLINDA/EXM 1.0. This study used the general formula provided by MIRD Pamphlet No. 11 to develop energy- and mass-dependent scaling powers, and the formula is given in Equation 2-43 (Snyder *et al.* 1975). Additionally, the scaling power is given in Equation 2-44.

$$\Phi(r_T \leftarrow r_S, E_o, m_{non-ref}) = \Phi(r_T \leftarrow r_S, E_o, m_{ref}) \cdot \left(\frac{m_{non-ref}}{m_{ref}} \right)^{R(E_o, m_{ref}, m_{non-ref})} \quad (2-43)$$

$$R(E_o, m_{ref}, m_{non-ref}) = \frac{\log \left[\frac{\Phi(r_T \leftarrow r_S, E_o, m_{non-ref})}{\Phi(r_T \leftarrow r_S, E_o, m_{ref})} \right]}{\log \left[\left(\frac{m_{non-ref}}{m_{ref}} \right) \right]} \quad (2-44)$$

where $\Phi(r_T \leftarrow r_S, E_o, m_{non-ref})$ is the SAF from source tissue r_S to target tissue r_T where r_S and r_T are the same tissue at initial photon energy E_o for non-reference tissue mass $m_{non-ref}$,

$\Phi(r_T \leftarrow r_S, E_o, m_{ref})$ is the SAF from source tissue r_S to target tissue r_T where r_S and r_T are the same tissue at initial photon energy E_o for the reference tissue mass m_{ref} , and

$R(E_o, m_{ref}, m_{non-ref})$ is the scaling power as a function of initial photon energy E_o , reference tissue mass m_{ref} and non-reference tissue mass $m_{non-ref}$.

The primary difference between this study and the MIRD Pamphlet No. 11 recommendation was that the MIRD recommendation treated the scaling power, R , as a constant while this study treated it as a function of three variables (Snyder *et al.* 1975). In this study, it was predicted that the scaling power was not only dependent upon the energy of the photons emitted, but it was also dependent upon the size of the tissue in question (e.g., scaling photon self-dose for the pituitary gland could be different than scaling photon self-dose for the brain due to differences in original organ size). SAFs for all combinations of tissue masses and photon energies were computed by dividing the energy deposited in the source/target tissue and the initial photon energy, and the resulting value of $R(E_o, m_{ref}, m_{non-ref})$ was computed using Equation 2-44.

MIRD Pamphlet No. 11 also recommended that the electron self-dose SAFs scaled as the inverse of the ratio of reference to non-reference masses (Snyder *et al.* 1975). The same analysis was completed for monoenergetic electrons at the energies equal to those simulated for photons to further examine this recommendation. All photons and electrons created during transport were tracked, and energy deposition in the target tissues of interest was recorded. The same methodology for determining scaling factors used for the photon simulations was additionally applied to the electron simulations.

Cross-dose – For the cross-dose study, seventeen spheres were constructed with masses of 1 g to 2 kg since 2 kg was the upper limit for discrete (non-distributed) organ masses in the adult male phantom (Lee *et al.* 2010). The spheres were assigned a density of 1.0 g/cm³ and a tissue composition of average adult male soft tissue, as defined by ICRU Report 46 (ICRU 1992). The surrounding medium consisted of ICRU Report 46 average adult male soft tissue and represented an “infinite” surrounding media.

Each sphere mass was simulated as a source tissue, with every sphere included as a target tissue. The set of target spheres was incrementally placed away from the source sphere with an initial center-to-center separation of 16 cm, approximately equal to the diameter of the largest sphere, and a final center-to-center separation of 100 cm, greater than the largest discrete organ-to-organ separation seen in the UF hybrid phantom family (~75 cm from the urinary bladder wall to the brain) with a total of five equal increments. Photon energies and particle histories used for the photon SAF simulations were used for these simulations as well. Energy deposition accounting for all photons and electrons created during the simulation was recorded in all target spheres. The default photon and electron cutoff energy of 1 keV was used, and the ITS-style nearest-bin algorithm was selected for electron energy indexing. A visual representation of the

simulation geometry is in Figure 2-15. Previous studies have determined radiation absorbed cross-dose from a source tissue to a target tissue to be relatively insensitive of changes in source and target tissue masses (Petoussi-Henss *et al.* 2007). However, these studies did not investigate this issue in a rigorous fashion, and this study aimed to further test this matter. In addition, the current study investigated changes in absorbed dose with variations in separation.

The SAFs for all source-target-energy combinations were calculated as the energy deposited in the target tissue of interest divided by the mass of the target tissue and the initial energy of the photons. No scaling equations were predicted beforehand, so results were examined upon completion for any trends or need for further analysis.

The cross-dose study was not immediately repeated for electrons because it was hypothesized that results for electrons would be insufficient for two reasons – (1) poor statistical uncertainties at the defined center-to-center separations and (2) no primary electron dose contributions at any of the center-to-center separations. Because of this, photon cross-dose was first analyzed, and electron cross-dose was addressed after the photon results were processed. The electron cross-dose computational experiment is described in the “Electron cross-dose” section of the “Variation in Source and Target Size and Separation” section of the “Dosimetric Sensitivity Studies” section of Chapter 3.

Validation studies

The MCNPX sphere studies were designed to attempt to predict dosimetric sensitivity trends by somewhat eliminating the dependence on the shape of the tissue of interest. It was hypothesized that by simulating objects of the same shape but different sizes, the dose to non-reference size organs could be predicted since the general shape of the organ would be similar to that in the reference case. Obviously, individual variability will introduce error in the predictions since organ shapes in the actual patient will most likely vary to some degree from the shape of

the reference organs. Despite this, the sphere approach was determined to be the most reasonable to obtain a “best estimate”. However, before any scaling methods could be applied to the monoenergetic SAFs, the results of the dosimetric sensitivity studies required validation, so actual hybrid phantoms were used to test the self-dose scaling powers and any cross-dose trends that were discovered.

To assist the investigation into the efficacy of any discovered photon or electron dose scaling techniques, patient-specific phantoms constructed by Johnson *et al.* (2011) were utilized. Patient-specific phantoms were generated by segmenting CT image sets of each patient to create three-dimensional organ and body volumes. The phantom resulting from the segmentation was a very good physical model of the patient of interest, but due to human error from subjective visual examination of the images, patient-specific models should not be considered perfect.

CT image sets of 14 adult male patients and 13 adult female patients covering broad ranges of height and weight were segmented to create patient-specific phantoms (Johnson *et al.* 2011). These CT image sets were chest-abdomen-pelvis (CAP) scans, so tissues in the head and legs were not present (Johnson *et al.* 2011). Several organs were difficult to visualize in the scans, so only the pericardium, liver, spleen, stomach wall, stomach contents, pancreas, kidneys, urinary bladder wall, urinary bladder contents, skeleton, subcutaneous fat, and outer body contour were segmented (Johnson *et al.* 2011). All phantoms were voxelized at an isotropic resolution of 2 mm (Johnson *et al.* 2011).

BEXXAR® (^{131}I –Tositumomab) and Zevalin® (^{90}Y –ibritumomab tiuxetan) were selected as the radiolabeled antibodies for analysis. ICRP Publication 107 was consulted for radionuclide spectra for ^{131}I and ^{90}Y (ICRP 2008). Photons were simulated for ^{131}I , and beta particles were simulated for ^{90}Y . The package inserts for BEXXAR® and Zevalin® were

consulted (as well as a case study for BEXXAR®) to determine possible source tissues for simulation (GlaxoSmithKline 2005, Spectrum Pharmaceuticals, Inc. 2011, Hong *et al.* 2010).

The liver and spleen were selected as the source tissues, and all tissues segmented in the patient-specific phantoms were treated as target tissues. Liver and spleen self-dose were of interest for the self-dose validation studies, and liver to pancreas cross-dose was of interest for the cross-dose validation studies.

Radionuclide spectra were directly sampled and uniformly distributed throughout each source tissue. All photons and electrons created during transport were followed until reaching the lower-bound energy cutoff where the remaining energy was assumed to be locally deposited. Energy deposition in all target tissues was recorded, and the radionuclide S value was calculated using Equation 2-45.

$$S(r_T \leftarrow r_S) = k \cdot E_{dep}(r_T \leftarrow r_S) \frac{\sum Y_i}{m_T} \quad (2-45)$$

where $S(r_T \leftarrow r_S)$ is the radionuclide S value from source tissue r_S to target tissue r_T , k is a unit conversion coefficient, $E_{dep}(r_T \leftarrow r_S)$ is the energy deposited in target tissue r_T from source tissue r_S , Y_i is the yield of the i^{th} radiation, and m_T is the mass of target tissue r_T . Tissue densities and material compositions were taken from ICRP Publication 89 (ICRP 2002). Ten million particle histories were simulated to ensure adequate uncertainties. A particle energy cutoff of 1 keV was used as well as the ITS-style nearest-bin electron energy indexing algorithm. The applications of these patient-specific simulations will be discussed in the next section.

Photon self-dose – To demonstrate the effectiveness of the scaling powers obtained in the self-dose study, the masses of the liver and thyroid of the UFH00M phantom were both increased and decreased by isotropically scaling both tissues in *Rhinoceros*TM. The liver was scaled from

the reference voxelized mass of 128.69 *g* to both 54.44 *g* and 252.12 *g*, 58% smaller and 96% larger than the reference mass, respectively. The thyroid was scaled from the reference voxelized mass of 1.28 *g* to both 0.55 *g* and 2.51 *g* – 57% smaller and 96% larger, respectively. Each organ was voxelized separately at the resolution used for the SAF calculations, 0.0663 *cm*. Instead of ^{131}I or ^{90}Y , $^{99\text{m}}\text{Tc}$ was selected as the radionuclide of interest for these validation studies. The photon spectrum of $^{99\text{m}}\text{Tc}$ was simulated separately in each source tissue as uniformly distributed throughout the organ. ICRP Publication 107 was consulted for the photon energy spectrum (ICRP 2008). Energy deposition was recorded in both organs, and the photon component of the radionuclide S value was calculated using Equation 2-23. Then, the SAFs from both source tissues calculated in the reference UFH00M phantom were used in conjunction with the scaling powers developed in the photon self-dose scaling study to calculate the non-reference photon component of the $^{99\text{m}}\text{Tc}$ S value. In addition, the MIRD Pamphlet No. 11 recommendation of a mass ratio scaling power of $-2/3$ was also used with the reference SAFs to calculate a “MIRD recommended” scaled photon component of the $^{99\text{m}}\text{Tc}$ S value, and the results was compared with those found using the scaling powers calculated in the current study. To ascertain any energy-dependent phenomena, the same liver and thyroid self-dose irradiation scenario was repeated using monoenergetic 10 *keV* and 4 *MeV* photons. Energy deposition accounting for all photons and electrons created during the simulation was recorded in all target tissues. The default photon and electron cutoff energy of 1 *keV* was used, and the ITS-style nearest-bin algorithm was selected for electron energy indexing. Ten million particle histories were simulated to ensure reasonable statistical uncertainties.

While the previous validation study looked at applying the sphere studies to isotropic scaling of the UF hybrid phantom organs, a second validation study was performed to test the

results on an actual patient. A patient-specific phantom of the torso for an adult female constructed in Johnson *et al.* (2011) (discussed earlier) was used to calculate the self-dose photon component of the ^{99m}Tc radionuclide S value for the liver and spleen. To discover any energy-dependent phenomena, the same irradiation geometry was simulated using monoenergetic 10 keV and 4 MeV photons. The patient chosen for the study had a voxelized liver mass of 2176.34 g and a voxelized spleen mass of 256.75 g, as compared to the UFHADF liver and spleen masses of 1392.31 g and 129.25 g, respectively. The patient-specific phantom representing this patient can be seen in Figure 2-16. The ^{99m}Tc photon spectrum was taken from ICRP Publication 107 (ICRP 2008). Energy deposition was recorded in the target tissues of interest, and the S value was calculated using Equation 2-39. Like the previous isotropic scaling validation study, reference photon SAFs for the UFHADF phantom were scaled using both the mass ratio scaling powers developed in the current study and the MIRD Pamphlet No. 11 recommendation, and the results were compared. The default photon and electron cutoff energy of 1 keV was used, and the ITS-style nearest-bin algorithm was selected for electron energy indexing. Ten million particle histories were simulated to ensure reasonable statistical uncertainties.

To further investigate the accuracy of the photon self-dose scaling methodology, results from the patient-specific internal dose simulations were analyzed. Uniform ^{131}I photon sources were simulated in the liver and spleen of all the patient-specific phantoms. Both UF and MIRD photon self-dose scaling methodologies were applied to the UFHADM and UFHADF liver and spleen self-dose S values based on the reference masses of the liver and spleen and non-reference masses from each patient-specific phantom. The UF and MIRD results were compared and analyzed to determine the more appropriate scaling approach.

Electron self-dose – Electron self-dose was validated using the same processes described for the photon self-dose validation study – comparing self-dose scaling as applied to the UFH00M hybrid phantom and as applied to a patient-specific adult female phantom. However, the ^{99m}Tc monoenergetic electron spectrum was used instead of the ^{99m}Tc photon spectrum, according to data in ICRP Publication 107 (ICRP 2008). Additionally, the dosimetry results from the series of patient-specific adult male and adult female phantoms were utilized to compare electron self-dose scaling approaches. Uniform ^{90}Y beta sources were simulated in the liver and spleen of all the patient-specific phantoms. Mirroring the approach in the photon self-dose study, the reference UFH00M, UFHADM, and UFHADDF SAFs were scaled using the MIRD Pamphlet No. 11 recommendation and the mass ratio scaling powers calculated in the present study and combined to yield the electron component of the radionuclide S values, and the results were compared.

Photon cross-dose – From the outset, it was unclear what scaling methodology (if any) would materialize upon examination of the cross-dose simulation results. Despite this, two validation studies were created to check any scaling techniques that may have developed. A sphere study was first conducted to validate the results. Mimicking the geometry stated in the cross-dose sphere study⁴, a “reference” set of spheres was designed so that the source sphere was 150 g and the target sphere was 450 g with a separation of 16 cm. A second “non-reference” sphere set was constructed so that the source sphere was 205 g, the target sphere was 550 g, and the separation was 30 cm. A visual representation of the differing irradiation geometries may be seen in Figure 2-17. Monoenergetic photons at 3.5 MeV were simulated, and energy deposition was recorded in the target tissues. Energy deposition was then divided by the initial energy of

⁴ Unit density spheres in an infinite soft tissue medium with the elemental composition set to that of the adult in ICRP Publication 89 (ICRP 2002).

the photons and the mass of the target to obtain the SAF. This study was repeated using the photon spectrum of ^{99m}Tc , obtained from ICRP Publication 107 (ICRP 2008). Since the reference and non-reference SAFs were known, any scaling factors developed in the photon cross-dose study could be applied to the reference SAF and the result compared to the actual non-reference SAF. Scaling factors were also applied to all reference SAFs needed to compute the ^{99m}Tc radionuclide S value. The default photon and electron cutoff energy of 1 keV was used, and the ITS-style nearest-bin algorithm was selected for electron energy indexing. Ten million particle histories were simulated to ensure reasonable statistical uncertainties.

A second, phantom-based validation study was performed in which the liver and pancreas of the UFHADM phantom were scaled to smaller volumes and translated slightly. The reference masses of the liver and pancreas for the UFHADM phantom were 1791.61 g and 149.20 g, respectively, and the non-reference masses of the liver and pancreas for the UFHADM phantom were 690.79 g and 61.91 g, respectively. Reference and non-reference center-to-center separations were determined using the volume centroid feature in *Rhinoceros*TM. Centroids of the liver and pancreas were recorded, and the separation was calculated using basic vector mathematics. The reference and non-reference separations were 13.68 cm and 15.79 cm, respectively. A uniform 3.5 MeV photon source was simulated in the pancreas, and the liver was treated as the target tissue. This was then repeated for the ^{99m}Tc photon spectrum, as defined in ICRP Publication 107 (ICRP 2008). All photons and electrons were tracked during simulation, and energy deposition was recorded in the liver. The reference UFHADM SAF for the pancreas-liver irradiation combination was then scaled using any scaling methodologies discovered during the cross-dose sphere study and compared to the actual non-reference SAF for the 3.5 MeV photons. Reference SAFs were scaled in the same way for the ^{99m}Tc photon spectrum and

combined to yield the photon component of the radionuclide S value. The default photon and electron cutoff energy of 1 keV was used, and the ITS-style nearest-bin algorithm was selected for electron energy indexing. Ten million particle histories were simulated to ensure reasonable statistical uncertainties.

To further investigate the accuracy of the photon cross-dose scaling methodology, results from the patient-specific internal dosimetry simulations were used. Uniform ^{131}I photon sources were simulated in the liver of all patient-specific phantoms, and the cross-dose S values to the pancreas were calculated. The volume centroid feature in *Rhinoceros*TM was utilized to measure the center-to-center non-reference distances for each patient-specific phantom. Liver and pancreas masses for all patient-specific phantoms were calculated and used for dose scaling.

Electron cross-dose – Electron cross-dose was difficult to assess before the SAF scaling analysis was performed because cross-dose for electrons behaves quite differently than for photons. Since primary electron dose contributions depend heavily on the surface shape and surface-to-surface distance of the source and target tissues, the primary electron dose contribution would probably not be able to be scaled since defining these parameters in the clinic is very difficult. It was predicted that the radiative contribution to dose could be effectively scaled to non-reference conditions but not the primary electron contribution to dose.

Bearing this in mind, a validation study was designed to address the radiative dose component alone. A phantom-based validation study was performed in which the liver and brain of the UFHADM phantom were scaled to smaller volumes and translated slightly. The reference masses of the liver and brain for the UFHADM phantom were 1791.61 g and 1441.65 g, respectively, and the non-reference masses of the liver and brain for the UFHADM phantom were 690.79 g and 755.53 g, respectively. A uniform 3.5 MeV electron source was simulated

in the liver, and the brain was treated as the target tissue. The ^{82}Rb beta spectrum⁵ was also simulated in the liver according to data in ICRP Publication 107 (ICRP 2008). The reference UFHADM SAF for the brain-liver irradiation combination was then scaled using any scaling methodologies discovered during the cross-dose sphere study and compared to the actual non-reference SAF for the 3.5 MeV electrons. Reference SAFs were scaled in the same way for the ^{82}Rb beta spectrum and combined to yield the beta component of the radionuclide S value. The non-reference beta component of the ^{82}Rb radionuclide S value was subsequently compared to the predicted S value.

Reflecting the validation approach to photon cross-dose scaling, results from the patient-specific internal dosimetry simulations were utilized to assess the efficacy of the electron cross-dose scaling method. Uniform ^{90}Y beta sources were simulated in the liver of all patient-specific phantoms, and the SAF to the pancreas was calculated. The volume centroid feature in *Rhinoceros*TM was utilized to measure the center-to-center non-reference distances for each patient-specific phantom. Liver and pancreas masses for all patient-specific phantoms were calculated and used for dose scaling.

Variation in Anthropometric Characteristics

Reference phantoms are ideally suited to act as computation dosimetry models for an average population but are inadequately suited to serve the role of patient-specific models because reference phantoms are average in height and weight (ICRP 2002). Chances are that patients undergoing nuclear medicine procedures are not average in height and weight.

Therefore, steps were taken to address this issue.

⁵ The ^{82}Rb beta spectrum was used in lieu of $^{99\text{m}}\text{Tc}$ monoenergetic electron spectrum because the ^{82}Rb beta spectrum had a higher average beta particle energy than the average $^{99\text{m}}\text{Tc}$ monoenergetic electron energy and was thus expected to give more statistically reliable results.

The UF ALRADS research group developed a library of phantoms that covered a large percentage of patient morphometries seen on a day-to-day basis (Johnson *et al.* 2009). Primary target parameters were defined as standing height, sitting height, and total body mass, and secondary target parameters were defined as waist, buttocks, arm, and thigh circumferences (Johnson *et al.* 2009). A set of phantoms were created with each of these parameters derived from the National Health and Nutrition Examination Surveys (NHANES) conducted by the National Center for Health Statistics of the CDC (Johnson *et al.* 2009). The NHANES III database covering 33,994 individuals between 2 months and 90 years of age from years 1988 to 1994 was consulted when deriving the previously mentioned morphometric parameters (Johnson *et al.* 2009). Statistical analysis was performed to create 25 adult male and 25 adult female phantoms at standing height percentiles of 10th, 25th, 50th, 75th, and 90th with weight percentiles of 10th, 25th, 50th, 75th, and 90th at each standing height (Johnson *et al.* 2009). Average values of sitting height were calculated at each standing height, average values of waist, buttocks, arm, and thigh circumferences were calculated at each standing height/weight combination (Johnson *et al.* 2009). The same analysis was performed for pediatric ages but standing height bins were created rather than standing height percentiles for a total of 100 pediatric phantoms (Johnson *et al.* 2009).

Morphometric parameterization for standing height as a function of total body mass for the pediatric male population can be seen in Figure 2-18 (Johnson *et al.* 2009). This figure demonstrates the grid of phantoms that was created to represent a population of patients. The library of phantoms was created by modifying one of the ICRP-reference phantoms (known in this case as an anchor phantoms) by scaling the upper body in 3-D to match sitting height and then the legs to match standing height (Johnson *et al.* 2009). Next, the secondary parameters

were matched by both uniformly and non-uniformly scaling arm, thigh, waist, and buttocks circumferences (Johnson *et al.* 2009). If a patient came for a nuclear medicine procedure, the phantom that mostly closely matched the morphometric characteristics of the patient would be selected to perform dosimetry. The computational phantom library published by Johnson *et al.* (2009) is currently undergoing an update in the UF ALRADS research group with up-to-date data, but the concept of a phantom library remains the same.

Despite the advantage of having a library of computational phantoms, performing Monte Carlo radiation transport simulations for every patient's procedure is currently impractical due to simulation times needed for reasonable results. The monoenergetic photon and electron SAFs previously developed were incorporated into a *MATLAB*TM computer code so that on-the-fly dose estimates could be provided for the average individual. Instead of performing the same immensely time-consuming task of generating monoenergetic photon and electron SAFs for all of the phantoms in the library, several studies were done to attempt to develop patient-specific scaling relationships based on in-clinic measureable morphometric characteristics such as sitting height, body circumferences, and weight. These scaling relationships would be applied to the ICRP-reference set of phantoms for which the detailed simulations were already completed.

Sitting height

While organ sizes have been shown to correlate fairly well with standing height (Grandmaison *et al.* 2001), sitting height was isolated as a possible metric by which reference dose estimates could be scaled because it is intuitive that the size of important internal organs would correlate more closely with changes in the trunk of the body rather than the length of the legs. This is because standing height is heavily influenced by leg length. Because the chest cavity expands or contracts with increases or decreases in sitting height relative to the reference sitting height of the anchor phantoms from which the library of phantoms was derived, it was

expected that radiation absorbed doses to tissues of interest would be affected by the change in position and size of organs within the chest cavity. Therefore, a computational study was designed to attempt to derive a correlation between changes in dose from internal emitters and changes in sitting height.

Two phantoms of shorter stature and two phantoms of taller stature were created using the UFH00M, UFH10M, and UFHADM as the anchor phantoms for a total of 12 scaled phantoms. All tissues except those located in the legs of the phantoms were scaled in 3-D, consistent with the methodology described in Johnson *et al.* (2009), to achieve these different statures. NURBS/PM models of the UFH00M phantoms created for the sitting height study are in Figure 2-19. The phantoms were all voxelized at the resolutions used for the monoenergetic photon and electron simulations. Phantom morphometric measurements are in Table 2-20, and voxel resolutions and total matrix sizes are in Table 2-21.

Uniform monoenergetic photon and electron sources were simulated in the brain, liver, lungs, and spleen. A whole-body AM source was simulated based on the AM mass distributions of the UFH00M, UFH10M, and UFHADM phantoms (e.g., the tallest scaled UFHADM-based phantom was assigned an AM distribution of the UFHADM reference phantom). Tissues simulated as targets in the monoenergetic photon and electron SAF simulations were used in this sitting height study. Fifteen monoenergetic photon and electron energies were simulated based on the energies used in the monoenergetic SAF simulations. Each energy selected was assigned a particle history value consistent with those given in the monoenergetic SAF simulations. The tally structure was identical to that used in the monoenergetic SAF simulations except that full transport was run for the electron simulations rather than the separate CEL/REL simulations. A

particle energy cutoff of 1 keV was used as well as the ITS-style nearest-bin electron energy indexing algorithm.

Weight

Previous studies had shown that radiation absorbed doses do not heavily depend on increases in subcutaneous fat (Clark *et al.* 2010), but dose dependencies for underweight individuals were not examined. It would be expected that internal doses would not change much, if at all, for increases in subcutaneous fat because the internal structure of the patient remains fairly constant⁶. Only the absorbed dose to subcutaneous fat and possibly the skin would be expected to change noticeably. However, when underweight individuals were modeled in the UF patient-dependent computational phantom library, some were scaled in 2-D to match the waist and buttocks circumferences (Johnson *et al.* 2009). According to a French autopsy study correlating changes in organ size with changes in anthropometric characteristics, the 2-D scaling technique created reasonably accurate organ sizes (Johnson *et al.* 2009). However, individual variability is unavoidable, and a range of organ sizes was noted. As a result of two-dimensional scaling for underweight individuals, organ volumes decrease, and the separation between the organs decreases. Dose variation for underweight individuals was therefore expected, and a dosimetric sensitivity study was created similar to that created for variations in sitting height.

Two underweight phantoms and one overweight phantom were created using the UFH00M, UFH10M, and UFHADM as the anchor phantoms for a total of 9 scaled phantoms. The underweight phantoms were created by decreasing the arm, thigh, waist, and buttocks circumferences through 2-D scaling in the transverse plane. The overweight phantom was

⁶ Clark *et al.* (2010) showed that some dose variations could occur depending on intra-abdominal fat deposits. However, the current study does not consider any fat deposits aside from the subcutaneous fat layer.

created by increasing the arm, thigh, waist, and buttocks circumferences in addition to adding subcutaneous fat elsewhere in the body. NURBS/PM models of the UFH00M phantoms created for the weight study are in Figure 2-20. The phantoms were all voxelized at the resolutions used for the monoenergetic photon and electron simulations. Phantom morphometric measurements are in Table 2-22, and voxel resolutions and total matrix sizes are in Table 2-23.

Uniform monoenergetic photon and electron sources were simulated in the brain, liver, lungs, and spleen. A whole-body AM source was simulated based on the AM mass distributions of the UFH00M, UFH10M, and UFHADM phantoms (e.g., the thinnest scaled UFHADM-based phantom was assigned an AM distribution of the UFHADM reference phantom). Tissues simulated as targets in the monoenergetic photon and electron SAF simulations were used in this weight study. Fifteen monoenergetic photon and electron energies were simulated based on the energies used in the monoenergetic SAF simulations. Each energy selected was assigned a particle history value consistent with those given in the monoenergetic SAF simulations. The tally structure was identical to that used in the monoenergetic SAF simulations except that full transport was run for the electron simulations rather than the separate CEL/REL simulations. A particle energy cutoff of 1 *keV* was used as well as the ITS-style nearest-bin electron energy indexing algorithm.

Constant weight with morphometry variation

When pediatric patients undergo nuclear medicine imaging procedures, one of several AA scaling equations may be used to adjust the amount of radiopharmaceutical given to the patient from the amount given to an adult. A short list of these equations is as follows: Clark's Rule (Equation 2-46), Young's Rule (Equation 2-47), Webster's Rule (Equation 2-48), and Fried's Rule (Equation 2-49) (Radiopharmacy, Inc. 2004). These rules are applied based on the patient's weight and age.

$$AA_{pediatric} = AA_{adult} \left(\frac{W_{pediatric}}{150 \text{ lbs}} \right) \quad (2-46)$$

$$AA_{pediatric} = AA_{adult} \left(\frac{a_y^{pediatric}}{a_y^{pediatric} + 12} \right) \quad (2-47)$$

$$AA_{pediatric} = AA_{adult} \left(\frac{a_y^{pediatric} + 1}{a_y^{pediatric} + 7} \right) \quad (2-48)$$

$$AA_{pediatric} = AA_{adult} \left(\frac{a_m^{pediatric}}{150} \right) \quad (2-49)$$

where $AA_{pediatric}$ is the scaled administered activity for the pediatric patient, AA_{adult} is the administered activity that would be given to an adult patient for the exam of interest, $W_{pediatric}$ is the weight of the pediatric patient in pounds, $a_y^{pediatric}$ is the age of the pediatric patient in years, and $a_m^{pediatric}$ is the age of the pediatric patient in months. More recently, pediatric radiopharmaceutical dose guidelines were released that are based on weight only (Gelfand *et al.* 2011).

These equations attempt to adjust the AA because pediatric patients have less attenuating material between the source of radiation emission and the detectors in the imaging system. As a result, less AA is needed to create an image with diagnostic value equal to that achieved when giving a higher AA to an adult patient. The decreased AA ensures good diagnostic quality while reducing the radiation exposure to the child. However, even though the described scaling equations are a first attempt at personalizing the AA to the patient, they do not account for body morphometry. Two pediatric patients at the same weight but different statures could be given a diagnostic nuclear medicine exam with the same AA. In this case, one patient could be short and heavy while the other is tall and thin. The tall patient has less attenuation than the short patient,

so better diagnostic quality would result for the tall patient. One of two situations would then present itself – (1) the tall patient could be given less AA if the diagnostic quality for the short patient was adequate or (2) the short patient could be given more AA if the diagnostic quality for the short patient was inadequate. In the first case, the radiation absorbed dose to the tall patient would be reduced while in the second case, the diagnostic quality of the image generated for the short patient would be improved. The AA scaling equations do not account for this scenario, so a dosimetric sensitivity study was designed to examine this further. This particular body morphometry study has been looked at recently, but a second study was performed to uncover any possible dosimetric trends.

Two phantoms were constructed at the same weight but different heights. The latest UF patient-dependent phantom library was consulted when selecting the weight at which the phantoms would be constructed, and the common weight was set to 50 *kg*. The short, heavy phantom was constructed based on the UFH10F phantom, and the tall, thin phantom was constructed based on the UFH15F phantom. NURBS/PM models of the phantoms created for the body morphometry study are in Figure 2-21. Both phantoms were voxelized at the resolutions used for the monoenergetic photon and electron simulations. Phantom morphometric measurements are in Table 2-24, and voxel resolutions and total matrix sizes are in Table 2-25.

Instead of simulating monoenergetic photons and electrons, the photon and monoenergetic electron (Auger and IC electrons) spectra for ^{99m}Tc were directly sampled and simulated uniformly in the heart chambers, kidney cortex, liver, lungs, muscle, spleen, and urinary bladder contents, consistent with the source tissues of interest for $^{99m}\text{Tc} - \text{DMSA}$, the same radiopharmaceutical modeled in the study by Sgouros *et al.* (2011). Radionuclide spectra were obtained from ICRP Publication 107 (ICRP 2008), and only photons (both x rays and gamma

rays) and Auger and IC electrons were simulated since the delta value, a measure in units of $Gy - kg/nt$ indicating the contribution of a particular radiation type to dose, for the ^{99m}Tc beta particles was on the order of 10^{-19} while the delta values for photons and monoenergetic electrons were on the order of 10^{-14} and 10^{-15} , respectively (ICRP 2008). Tissues that were simulated as targets in the monoenergetic photon and electron SAF simulations were used in this body morphometry study. Ten million particle histories were simulated, and the tally structure was identical to that used in the monoenergetic SAF simulations except that full transport was run for the electron simulations rather than the separate CEL/REL simulations. A particle energy cutoff of 1 keV was used as well as the ITS-style nearest-bin electron energy indexing algorithm.

Validation studies

Dose scaling based on anthropometric characteristics was the goal of the phantom-based dosimetric sensitivity study, so ultimately the results would be applied to the UF reference hybrid phantom monoenergetic SAFs. To verify the efficacy of this method, a series of validation studies were performed, and the general process was as follows:

1. Create a unique non-reference phantom based on one of the reference phantoms that was scaled in the dosimetric sensitivity study.
2. Separately simulate a photon and electron spectrum in one source tissue within the reference phantom using MCNPX v2.6 and determine the radionuclide S values to all target tissues of interest.
3. Calculate the radionuclide S values to all target tissues of interest for the reference phantom upon which the unique non-reference phantom is based, applying scaling factors estimated in the phantom-based dosimetric sensitivity study.
4. Compare the actual non-reference S values to the scaled reference S values for both photons and electrons.

Scaling the reference SAFs should yield more accurate estimates of radionuclide S values for a non-reference phantom than radionuclide S values for the reference phantom. If this is the case, the dosimetric sensitivity studies will improve dose estimates for individual dosimetry.

However, while the dose estimates are said to have “improved”, the estimates are actually improved for an imaginary patient-dependent phantom, not a patient-specific phantom, since the scaling methodology was developed based on the original reference hybrid phantoms.

Sitting height – Conditions of the sitting height dose variation study were such that dose variations were valid for uniform 3-D scaling of the torso of the UF hybrid phantoms with no additional weight adjustments. As this is the case, three non-reference phantoms were scaled from the reference UFH00M, UFH10M, and UFHADM phantoms (one scaled phantom per anchor phantom), and uniform photon and electron sources were separately simulated within the liver of each phantom. The ^{131}I photon spectrum and ^{90}Y beta spectrum were selected, and the radiation energies and yields were obtained from ICRP Publication 107 (ICRP 2008). Any dose scaling techniques derived from the anthropometric variation sitting height dose sensitivity study were applied to the reference SAFs at each radiation energy and combined to yield the photon component of the ^{131}I radionuclide S value and the beta component of the ^{90}Y radionuclide S value. Scaling techniques for the UFH00M phantom were applied to provide estimates for the UFH00M-based non-reference phantom, scaling techniques for the UFH10M phantom were applied to provide estimates for the UFH10M-based non-reference phantom, and scaling techniques for the UFHADM phantom were applied to provide estimates for the UFHADM-based non-reference phantom. These scaled results were compared to the actual radionuclide S values obtained for the three non-reference phantoms through simulation in MCNPX v2.6 to determine the efficacy of dose scaling based on sitting height. In both the photon and electron simulations, all particles created during transport were tracked. Ten million particle histories were simulated, and the tally structure was identical to that used in the monoenergetic SAF simulations except that full transport was run for the electron simulations rather than the separate

CEL/REL simulations. A particle energy cutoff of 1 *keV* was used as well as the ITS-style nearest-bin electron energy indexing algorithm. The physical characteristics of the sitting height-based validation phantoms were as follows:

- UFH00M-based non-reference phantom with a sitting height of 31.24 *cm* and a weight of 2.74 *kg*.
- UFH10M-based non-reference phantom with a sitting height of 68.15 *cm* and a weight of 25.23 *kg*.
- UFHADM-based non-reference phantom with a sitting height of 95.97 *cm* and a weight of 79.56 *kg*.

Weight – The patient-dependent phantoms based on the UFHADM reference phantom described at the beginning of this section were simulated with uniform photon (^{131}I spectrum) and electron (^{131}I monoenergetic electron and beta spectra and ^{90}Y beta spectrum) sources in the liver of each phantom. The 50th percentile by height phantoms were used for the weight dose variation validation study because several phantoms were available at a constant sitting height but varying weights. Scaling factors developed in the weight dose variation study were applied to reference UFHADM monoenergetic SAFs to calculate the photon component of the radionuclide S value for ^{131}I and the beta component of the radionuclide S value for ^{90}Y for the non-reference 50th percentile by height phantoms. These results were compared to the actual radionuclide S values found using MCNPX v2.6 for each of the non-reference 50th percentile by height phantoms. All explicitly simulated patient-dependent phantoms at the 50th height percentile were selected for comparison.

Two additional phantoms were created for comparison purposes – one based on the UFH00M phantom and one based on the UFH10M phantom. One scaled phantom was created for each reference phantom, holding the height constant and varying the weight. The weight for the UFH00M phantom was decreased, and the weight for the UFH10M phantom was increased

to capture trends in both circumstances. Photons and electrons were simulated in the liver of these phantoms via the ^{131}I photon spectrum and ^{90}Y beta spectrum using MCNPX v2.6. Scaling methods discovered in the weight dose variation study were applied to reference UFH00M and UFH10M monoenergetic SAFs to calculate the photon and electron components of the radionuclide S values for ^{131}I and ^{90}Y , respectively, for the non-reference 50th percentile by height phantoms. These results were compared to the actual radionuclide S values found using MCNPX v2.6. The physical characteristics of the weight-based validation phantoms were as follows (excluding the previously defined UFHADM-based phantoms):

- UFH00M-based non-reference phantom with a sitting height of 33.97 *cm*, a weight of 3.08 *kg*, and a waist circumference of 34.97 *cm*.
- UFH10M-based non-reference phantom with a sitting height of 75.64 *cm*, a weight of 38.34 *kg*, and a waist circumference of 83.57 *cm*.

Arbitrary morphometry – The approach used for validating dose dependencies on variations in patient weight was used to validate the combination of the sitting height and weight scaling factors. Previously constructed patient-dependent phantoms described earlier were used to simulate ^{131}I and ^{90}Y sources in the liver of each phantom. The key difference for analyzing a combinatorial approach to dose scaling is that phantoms at non-50th percentile height were used. Radionuclide S values for ^{131}I and ^{90}Y were calculated for phantoms of various weights at non-50th percentile heights by applying scaling factors derived from the sitting height and weight dose variation studies to the UFHADM reference monoenergetic SAFs. These results were compared to the actual radionuclide S values found using MCNPX v2.6. All explicitly simulated non-50th percentile by height/non-50th percentile by weight patient-dependent phantoms were selected for comparison.

Two additional phantoms were created for comparison purposes – one based on the UFH00M phantom and one based on the UFH10M phantom. One scaled phantom was created for each reference phantom, varying both the height and weight. Height was increased, and weight was decreased for the UFH00M phantom. Height was decreased, and weight was increased for the UFH10M phantom. Photons and electrons were simulated in the liver of these phantoms via the ^{131}I photon spectrum and ^{90}Y beta spectrum using MCNPX v2.6. Scaling methods discovered in the height and weight dose variation studies were combined and applied to reference UFH00M and UFH10M monoenergetic SAFs to calculate the photon and electron components of the radionuclide S values for ^{131}I and ^{90}Y , respectively, for the non-reference phantoms. These results were compared to the actual radionuclide S values found using MCNPX v2.6. The physical characteristics of the combined height and weight validation phantoms were as follows (excluding the previously defined UFHADM-based phantoms):

- UFH00M-based non-reference phantom with a sitting height of 37.08 *cm*, a weight of 3.69 *kg*, and a waist circumference of 36.58 *cm*.
- UFH10M-based non-reference phantom with a sitting height of 68.39 *cm*, a weight of 29.14 *kg*, and a waist circumference of 75.28 *cm*.

Internal Dosimetry Software

Development of the internal dosimetry software is a collaborative effort between researchers at UF and the National Cancer Institute (NCI) of the National Institutes of Health (NIH). Initial software development was completed at UF in the *MATLAB*TM coding language and will be migrated to a more easily deployable format at NCI. Therefore, all graphical user interfaces (GUIs) will be developed at NCI while the core coding originated at UF.

Development of the internal dosimetry code is an ongoing process.

The dosimetry code was primarily written by Laura Padilla of the ALRADS research group at UF to include her work towards internal dosimetry for arbitrarily inserted tumors.

However, radionuclide spectrum generation and the S value algorithm were developed by both researchers and cross-verified. Radionuclide spectra were taken from ICRP Publication 107 (ICRP 2008). Methodology behind the S value algorithm was previously discussed in the “Radionuclide S Values” section of Chapter 2. Non-reference dose scaling will be addressed in the “Dosimetry Sensitivity Studies” sections of Chapters 3 and 4. Any apparent dose trends were applied in the dosimetry code with simple scaling mechanisms. For instance, if waist circumference was identified as a dose-dependent measure, the user would be given a “waist circumference” data entry field, and the code would scale the dose to all pertinent organs based on the identified scaling equation.

In this software, the user is able to select the radionuclide (and multiple radionuclides) and phantom (and multiple phantoms). The user is then able to enter the total number of nuclear transformations for all relevant source tissues, non-reference tissue masses and body measures, and total AA. Based on these inputs, the software extracts pre-calculated radionuclide S values (to save computation time, S values were pre-calculated for all phantoms in the UF series), performs any necessary dose scaling, and applies the total number of nuclear transformations to calculate absorbed doses to all target tissues per unit AA in addition to total absorbed doses based on the given AA. Effective dose is also provided using the tissue weighting factors (radiation weighting factors for both photons and electrons are unity) from ICRP Publication 103 (ICRP 2007).

In addition to these necessities, Laura Padilla developed a tumor insertion feature which allows the user to define an ellipsoidal tumor from definition of the x -, y -, and z -axes. Using a ray-trace algorithm, the code uses a point-kernel method to determine the dose from

source tissues to the tumor and vice-versa. This feature will be more fully described in Laura Padilla's Ph.D. dissertation.

Table 2-1. Blood vessel wall thicknesses for the newborn to 1-year-old and adult reference individuals for the arterial, venous, and pulmonary systems. Adapted from ICRP Publication 23 (ICRP 1975).

Age / system	Blood vessel	Gender	Wall Thickness (mm)
Newborn to one year of age	Aorta	M/F	0.830
	Pulmonary artery	M/F	0.790
	Carotis communis artery	M/F	0.550
	Superior vena cava	M/F	--
	Inferior vena cava	M/F	--
Adult arterial system	Aorta		
	Ascending	M	1.630
		F	1.480
	Descending	M	1.200
		F	1.110
	Abdominalis	M	1.140
		F	1.080
	Arteries		
	Common iliac	M	0.930
		F	0.890
	Common carotid	M	0.910
		F	0.810
	Small arteries	M/F	0.800
	Arterioles	M/F	0.020
	Capillaries	M/F	0.001
Adult venous system	Venae cavae		
	Superior	M/F	1.500
	Inferior	M/F	1.500
	Veins	M/F	0.500
	Venules	M/F	0.002
Adult pulmonary system	Arteries	M	1.270
		F	0.960
	Veins	M/F	--
	Capillaries	M/F	--
	Maximum	M/F	1.630
	Minimum	M/F	0.001
	Average	M/F	0.905

Table 2-2. Width, height, and depth measurements and isotropic voxel resolutions for all bone sites in the UFH01MF, UFH05MF, and UFH10MF phantoms.

Site	Bone size (cm)									Voxel resolution (cm)		
	UFH01MF			UFH05MF			UFH10MF			UFH01MF	UFH05MF	UFH10MF
	Width	Depth	Height	Width	Depth	Height	Width	Depth	Height			
Cranium	12.74	15.25	13.32	14.08	16.69	14.91	14.69	17.20	15.57	0.0363	0.0401	0.0417
Mandible	7.50	5.75	4.35	10.06	7.23	5.69	10.46	7.69	5.83	0.0151	0.0197	0.0205
Scapulae	15.01	3.33	6.19	24.40	4.77	8.93	28.66	6.88	12.53	0.0179	0.0268	0.0357
Clavicles	14.09	3.41	1.19	21.01	4.65	1.32	24.99	4.10	3.91	0.0102	0.0133	0.0195
Sternum	1.89	3.07	5.75	3.26	3.24	8.05	4.39	5.21	10.38	0.0085	0.0116	0.0164
Ribs	15.36	9.20	15.99	20.53	11.94	23.44	23.71	15.32	29.06	0.0347	0.0473	0.0580
Vertebrae-C	3.86	3.63	5.82	4.23	4.25	6.03	6.63	6.17	7.82	0.0115	0.0126	0.0181
Vertebrae-T	4.33	3.64	14.56	4.44	5.31	19.77	6.79	7.54	26.03	0.0162	0.0205	0.0291
Vertebrae-L	3.79	3.94	10.59	5.45	5.94	10.61	6.87	7.38	14.29	0.0143	0.0185	0.0237
Sacrum	4.56	3.75	5.61	6.66	5.56	7.35	7.03	6.47	10.06	0.0121	0.0171	0.0204
Os Coxae	11.92	5.32	9.19	19.63	6.88	12.41	22.75	10.12	18.36	0.0221	0.0314	0.0427
Femora	3.23	2.51	15.85	4.99	4.00	26.84	8.62	5.92	34.89	0.0133	0.0215	0.0320
Tibiae	2.76	2.16	13.53	4.05	3.10	22.34	6.71	4.80	29.00	0.0114	0.0173	0.0258
Fibulae	1.56	1.33	13.30	2.10	2.32	21.94	2.55	2.93	28.50	0.0080	0.0126	0.0158
Patellae	1.26	0.58	0.91	2.50	1.16	2.64	3.59	1.62	2.95	0.0023	0.0052	0.0068
Ankles and feet	3.42	8.34	3.23	4.86	13.00	5.27	6.79	18.36	7.35	0.0119	0.0183	0.0257
Humera	5.57	2.97	14.10	5.76	3.69	20.95	8.78	5.41	27.54	0.0163	0.0202	0.0289
Radii	1.34	2.22	10.58	1.73	2.83	15.47	2.63	4.60	20.44	0.0084	0.0112	0.0166
Ulnae	2.01	2.72	11.22	3.33	2.93	16.85	3.83	4.30	22.04	0.0104	0.0145	0.0189
Wrists and hands	2.91	5.63	7.24	2.50	5.77	11.17	4.15	8.60	14.61	0.0130	0.0144	0.0213

Table 2-3. Total matrix sizes and voxel numbers by width, depth, and height for all bone sites in the UFH01MF, UFH05MF, and UFH10MF phantoms.

Site	Number of voxels									Matrix size (x 10 ⁶)		
	UFH01MF			UFH05MF			UFH10MF			UFH01MF	UFH05MF	UFH10MF
	Width	Depth	Height	Width	Depth	Height	Width	Depth	Height			
Cranium	360	426	374	352	447	384	346	438	376	57.36	60.42	56.98
Mandible	501	391	297	517	378	298	508	383	290	58.18	58.24	56.42
Scapulae	822	304	337	900	169	320	804	194	354	84.21	48.67	55.22
Clavicles	1356	327	137	1562	371	110	1272	219	212	60.75	63.75	59.06
Sternum	209	380	673	282	270	678	261	310	635	53.45	51.62	51.38
Ribs	452	267	462	436	254	499	418	265	503	55.76	55.26	55.72
Vertebrae-C	331	332	511	398	406	468	359	451	444	56.15	75.62	71.89
Vertebrae-T	263	269	894	226	348	947	227	456	891	63.25	74.48	92.23
Vertebrae-L	321	327	579	282	327	572	296	516	601	60.78	52.75	91.79
Sacrum	358	309	466	395	502	422	336	315	478	51.55	83.68	50.59
Os Coxae	544	246	413	624	219	401	531	237	419	55.27	54.80	52.73
Femora	276	200	1178	255	239	1246	264	285	1099	65.03	75.94	82.69
Tibiae	270	194	1166	209	325	1264	142	220	851	61.08	85.86	26.59
Fibulae	193	238	1623	141	151	1711	213	188	1787	74.55	36.43	71.56
Patellae	575	225	441	457	293	453	495	216	453	57.05	60.66	48.43
Ankles and feet	287	700	269	268	708	286	267	711	280	54.04	54.27	53.15
Humera	340	187	860	285	194	1031	296	189	946	54.68	57.00	52.92
Radii	153	274	1236	163	264	1381	146	272	1219	51.82	59.43	48.41
Ulnae	216	274	1073	226	194	1146	202	226	1159	63.50	50.25	52.91
Wrists and hands	168	394	516	169	399	761	174	405	672	34.16	51.31	47.36

Table 2-4. Percent regional blood distribution in the ICRP-reference adult male and female.
Adapted from ICRP Publication 89 (ICRP 2002).

Organ / tissue	Blood content (% total blood volume)	
	Male	Female
Fat	5.00	8.50
Brain	1.20	1.20
Stomach and esophagus	1.00	1.00
Small intestine	3.80	3.80
Large intestine	2.20	2.20
Right heart	4.50	4.50
Left heart	4.50	4.50
Coronary tissue	1.00	1.00
Kidneys	2.00	2.00
Liver	10.00	10.00
Pulmonary	10.50	10.50
Bronchial tissue	2.00	2.00
Skeletal muscle	14.00	10.50
Pancreas	0.60	0.60
Skeleton	7.00	7.00
Red marrow	4.00	4.00
Trabecular bone	1.20	1.20
Cortical bone	0.80	0.80
Other skeleton	1.00	1.00
Skin	3.00	3.00
Spleen	1.40	1.40
Thyroid	0.06	0.06
Lymph nodes	0.20	0.20
Gonads	0.04	0.02
Adrenals	0.06	0.06
Urinary bladder	0.02	0.02
All other tissues	1.92	1.92
Aorta and large arteries	6.00	6.00
Large veins	18.00	18.00

Table 2-5. Total blood volumes in the ICRP-reference human series. Adapted from ICRP Publication 89 (ICRP 2002).

Age	Blood volume (L)	
	Male	Female
Newborn	0.27	0.27
1 year	0.50	0.50
5 years	1.40	1.40
10 years	2.40	2.40
15 years	4.50	3.30
Adult	5.30	3.90

Table 2-6. Derived vascular growth scaling factors for the brain, kidneys, trabecular bone, and cortical bone for the ICRP-reference human series.

Age	Brain	Kidneys	Skeleton	
			Trabecular bone	Cortical bone
Newborn	1.04	0.67	4.7	2.6
1-year-old	1.16	0.67	4.7	2.6
5-year-old	1.39	1.00	4.4	2.4
10-year-old	1.33	1.00	4.0	2.2
15-year-old	1.13	1.00	3.7	1.9
Adult	1.00	1.00	1.0	1.0

Table 2-7. Derived regional blood distributions for the ICRP-reference pediatric human series and ICRP-reference adult regional blood distributions (ICRP 2002).

Organ/Tissue	Blood distribution (%)											
	Newborn		1-year-old		5-year-old		10-year-old		15-year-old		Adult	
	Male	Female	Male	Female	Male	Female	Male	Female	Male	Female	Male	Female
Fat	5.73	5.78	9.32	9.47	5.94	6.04	5.35	5.43	3.90	7.68	5.00	8.50
Brain	6.42	5.57	6.97	6.09	5.31	4.18	3.25	2.47	1.59	1.47	1.20	1.20
Stomach and esophagus	0.92	0.78	1.00	0.85	1.10	0.94	1.13	0.96	0.95	0.93	1.00	1.00
Small intestine	3.41	2.88	3.77	3.20	4.48	3.80	4.53	3.83	3.65	3.57	3.80	3.80
Large intestine	1.97	1.57	2.26	1.82	2.48	2.00	2.61	2.10	2.14	1.99	2.20	2.20
Right heart	4.42	4.74	3.21	3.47	4.15	4.48	4.25	4.57	4.56	4.22	4.50	4.50
Left heart	4.42	4.74	3.21	3.47	4.15	4.48	4.25	4.57	4.56	4.22	4.50	4.50
Coronary tissue	1.19	1.22	1.16	1.20	0.91	0.94	0.90	0.92	0.85	0.96	1.00	1.00
Kidneys	2.13	1.87	2.31	2.04	2.49	2.20	2.45	2.16	1.96	1.91	2.00	2.00
Liver	14.31	14.33	14.04	14.14	11.13	11.21	9.74	9.79	8.76	10.16	10.00	10.00
Pulmonary	5.52	5.59	8.22	8.37	7.73	7.89	9.15	9.31	9.76	9.85	10.50	10.50
Bronchial tissue	1.06	1.04	1.58	1.56	1.51	1.50	1.73	1.72	1.85	1.88	2.00	2.00
Skeletal muscle	7.58	7.33	7.03	6.84	9.50	9.25	11.22	10.90	14.06	11.16	14.00	10.50
Pancreas	0.50	0.45	0.65	0.59	0.52	0.47	0.54	0.49	0.57	0.54	0.60	0.60
Skeleton	9.38	9.83	11.84	12.50	11.06	11.66	11.52	12.10	10.86	12.04	7.00	7.00
Red marrow	3.32	3.36	3.89	3.96	4.05	4.12	4.51	4.58	4.44	4.82	4.00	4.00
Trabecular bone	4.02	4.30	5.34	5.75	4.67	5.03	4.56	4.90	4.15	4.70	1.20	1.20
Cortical bone	1.43	1.53	1.93	2.08	1.72	1.85	1.67	1.80	1.42	1.61	0.80	0.80
Other skeleton	0.61	0.64	0.68	0.71	0.63	0.66	0.79	0.82	0.85	0.92	1.00	1.00
Skin	3.09	3.46	2.41	2.71	1.80	2.03	1.56	1.75	2.19	2.40	3.00	3.00
Spleen	1.76	1.58	2.05	1.86	1.62	1.47	1.56	1.41	1.46	1.52	1.40	1.40
Thyroid	0.08	0.07	0.04	0.04	0.04	0.03	0.05	0.05	0.04	0.05	0.06	0.06
Lymph nodes	0.19	0.17	0.21	0.20	0.18	0.17	0.18	0.17	0.18	0.19	0.20	0.20
Gonads	0.02	0.01	0.01	0.01	0.01	0.01	0.00	0.01	0.02	0.01	0.04	0.02
Adrenals	0.50	0.42	0.13	0.11	0.07	0.06	0.06	0.05	0.05	0.05	0.06	0.06
Urinary bladder	0.03	0.03	0.03	0.03	0.02	0.02	0.02	0.02	0.02	0.02	0.02	0.02
All other tissues	1.52	1.29	1.38	1.17	1.47	1.40	1.60	1.48	1.38	1.17	1.92	1.92
Aorta and large arteries	5.97	6.31	4.29	4.57	5.58	5.94	5.59	5.93	6.16	5.51	6.00	6.00
Large veins	17.90	18.93	12.88	13.71	16.73	17.82	16.76	17.80	18.48	16.52	18.00	18.00

Table 2-8. Derived regional blood volumes for the ICRP-reference pediatric human series and ICRP-reference adult regional blood volumes (ICRP 2002).

Organ/Tissue	Blood volume (cm ³)											
	Newborn		1-year-old		5-year-old		10-year-old		15-year-old		Adult	
	Male	Female	Male	Female	Male	Female	Male	Female	Male	Female	Male	Female
Fat	15.67	15.82	46.60	47.35	84.06	85.46	126.28	128.07	176.43	253.51	264.15	328.77
Brain	17.55	15.24	34.84	30.43	75.08	59.11	76.59	58.19	72.11	48.42	63.40	46.42
Stomach and esophagus	2.52	2.13	4.99	4.24	15.56	13.24	26.75	22.70	42.97	30.68	52.83	38.68
Small intestine	9.33	7.87	18.85	15.99	63.37	53.79	106.73	90.38	165.45	117.87	200.75	146.98
Large intestine	5.38	4.30	11.28	9.08	35.15	28.31	61.61	49.50	97.08	65.61	116.23	85.09
Right heart	12.09	12.97	16.07	17.34	58.69	63.39	100.13	107.89	206.49	139.29	237.74	174.06
Left heart	12.09	12.97	16.07	17.34	58.69	63.39	100.13	107.89	206.49	139.29	237.74	174.06
Coronary tissue	3.25	3.34	5.80	6.00	12.81	13.25	21.13	21.81	38.30	31.80	52.83	38.68
Kidneys	5.83	5.12	11.53	10.18	35.30	31.18	57.85	50.98	88.62	63.07	105.66	77.36
Liver	39.16	39.19	70.21	70.70	157.51	158.68	229.68	230.85	396.81	335.50	528.30	386.79
Pulmonary	15.11	15.31	41.08	41.87	109.44	111.60	215.87	219.61	441.98	325.39	554.72	406.13
Bronchial tissue	2.89	2.85	7.88	7.82	21.40	21.24	40.88	40.48	83.70	61.93	105.66	77.36
Skeletal muscle	20.74	20.07	35.13	34.19	134.47	130.95	264.51	256.99	636.57	368.53	739.62	406.13
Pancreas	1.37	1.23	3.25	2.94	7.39	6.69	12.69	11.46	25.66	17.89	31.70	23.21
Skeleton	25.67	26.90	59.21	62.52	156.56	165.05	271.75	285.33	491.55	397.56	369.81	270.75
Red marrow	9.09	9.20	19.45	19.81	57.27	58.34	106.27	108.00	200.95	159.06	211.32	154.72
Trabecular bone	10.99	11.77	26.71	28.77	66.08	71.20	107.53	115.58	187.82	155.15	63.40	46.42
Cortical bone	3.91	4.18	9.65	10.39	24.27	26.15	39.43	42.38	64.30	53.12	42.26	30.94
Other skeleton	1.68	1.75	3.39	3.56	8.93	9.37	18.51	19.37	38.48	30.22	52.83	38.68
Skin	8.46	9.45	12.07	13.56	25.53	28.70	36.78	41.25	98.95	79.36	158.49	116.04
Spleen	4.81	4.32	10.27	9.28	22.99	20.79	36.84	33.23	66.03	50.11	73.96	54.15
Thyroid	0.21	0.19	0.20	0.19	0.50	0.46	1.17	1.08	1.96	1.52	3.17	2.32
Lymph nodes	0.51	0.47	1.04	0.98	2.56	2.42	4.33	4.06	8.35	6.25	10.57	7.74
Gonads	0.05	0.02	0.07	0.04	0.10	0.14	0.11	0.25	1.00	0.39	2.11	0.77
Adrenals	1.37	1.14	0.65	0.54	1.05	0.87	1.47	1.22	2.33	1.49	3.17	2.32
Urinary bladder	0.09	0.08	0.14	0.13	0.32	0.31	0.49	0.48	0.87	0.63	1.06	0.77
All other tissues	4.16	3.52	6.90	5.86	20.84	19.87	37.77	34.98	62.60	38.61	101.43	74.26
Aorta and large arteries	16.32	17.27	21.47	22.85	78.93	84.05	131.74	139.95	279.00	181.80	316.98	232.08
Large veins	48.96	51.80	64.42	68.56	236.79	252.15	395.22	419.86	837.00	545.41	950.94	696.23

Table 2-9. Derived regional blood distribution in volume percent for the UF series of hybrid computational phantoms.

Tissue	Phantom							
	UFH00MF	UFH01MF	UFH05MF	UFH10MF	UFH15M	UFH15F	UFHADM	UFHADF
Adipose tissue (separable)	8.68	12.43	8.77	7.91	5.88	11.04	7.46	12.69
Adrenals	0.69	0.16	0.10	0.08	0.08	0.06	0.09	0.09
Brain	9.03	8.63	6.93	4.19	2.40	2.11	1.79	1.79
Cartilage	0.94	0.65	0.29	0.24	0.13	0.14	0.08	0.06
Cortical bone	2.23	2.65	2.61	2.55	2.14	2.31	1.19	1.19
Ears	0.16	0.10	0.14	0.08	0.09	0.07	0.23	0.16
Esophagus	0.28	0.24	0.25	0.27	0.29	0.27	0.31	0.30
External nose	0.05	0.06	0.09	0.12	0.06	0.04	0.14	0.25
Extrapulm. bronch. + trachea	0.02	0.02	0.02	0.03	0.03	0.03	0.03	0.03
Heart	1.82	1.56	1.35	1.34	1.28	1.38	1.49	1.49
Kidneys	3.02	2.87	3.44	3.38	2.95	2.75	2.98	2.99
Large intestine	2.66	2.69	3.28	3.45	3.24	2.86	3.28	3.28
Liver	21.60	18.64	16.35	14.33	13.23	14.61	14.92	14.93
Lung	9.95	13.03	13.59	16.06	17.49	16.84	18.62	18.63
Lymph nodes	0.27	0.27	0.26	0.26	0.28	0.27	0.30	0.30
Muscle	11.25	9.17	13.72	16.22	21.22	16.05	20.88	15.67
Nasal layers	0.09	0.06	0.18	0.14	0.12	0.10	0.22	0.19
Oral cavity layer	0.08	0.01	0.03	0.02	0.05	0.09	0.02	0.03
Ovaries	0.02	0.01	0.01	0.01	0.03	0.02	0.06	0.03
Pancreas	0.72	0.82	0.73	0.75	0.86	0.78	0.89	0.90
Penis	0.09	0.10	0.17	0.12	0.29	0.00	0.26	0.00
Pharynx	0.03	0.02	0.04	0.03	0.03	0.03	0.02	0.03
Salivary glands	0.68	0.62	0.73	0.68	0.71	0.73	0.81	1.31
Scrotum	0.19	0.08	0.07	0.03	0.24	0.00	0.47	0.00
Skin	4.94	3.39	2.81	2.43	3.30	3.46	4.47	4.48
Small intestine	4.74	4.61	6.05	6.13	5.51	5.13	5.67	5.67
Spinal cord	0.73	0.64	0.67	1.05	0.49	0.62	0.69	0.89
Spleen	2.51	2.58	2.26	2.18	2.20	2.18	2.09	2.09
Spongiosa and medullary cavities	11.32	12.81	13.74	14.56	14.12	14.86	9.17	9.19
Stomach	1.00	0.98	1.24	1.27	1.15	1.07	1.18	1.19
Testes	0.02	0.01	0.01	0.01	0.03	0.02	0.06	0.03
Thyroid	0.11	0.05	0.05	0.07	0.07	0.07	0.09	0.09
Urinary bladder wall	0.05	0.04	0.03	0.03	0.03	0.03	0.03	0.03

Table 2-10. Derived regional blood masses for the UF series of hybrid computational phantoms.

Tissue	Phantom							
	UFH00MF	UFH01MF	UFH05MF	UFH10MF	UFH15M	UFH15F	UFHADM	UFHADF
Adipose tissue (separable)	16.17	67.45	93.68	140.52	182.12	292.83	280.90	351.39
Adrenals	1.29	0.86	1.06	1.49	2.41	1.72	3.37	2.48
Brain	16.88	46.97	74.46	74.79	74.44	55.93	67.42	49.61
Cartilage	1.76	3.51	3.07	4.19	3.87	3.72	2.87	1.71
Cortical bone	4.15	14.37	27.84	45.16	66.37	61.35	44.94	33.07
Ears	0.30	0.52	1.46	1.42	2.78	1.91	8.64	4.54
Esophagus	0.53	1.33	2.66	4.79	8.88	7.11	11.79	8.27
External nose	0.09	0.34	1.02	2.09	1.84	0.97	5.36	6.80
Extrapulm. bronch. + trachea	0.03	0.11	0.23	0.45	0.86	0.72	1.12	0.83
Heart	3.39	8.47	14.40	23.72	39.53	36.73	56.18	41.34
Kidneys	5.63	15.62	36.82	60.25	91.48	72.85	112.36	82.68
Large intestine	4.99	14.67	35.20	61.60	100.21	75.79	123.60	90.95
Liver	40.24	101.17	174.76	254.47	409.61	387.53	561.80	413.40
Lung	18.54	70.71	145.25	285.10	541.78	446.67	701.13	515.92
Lymph nodes	0.50	1.45	2.76	4.64	8.62	7.22	11.24	8.27
Muscle	20.97	49.80	146.78	288.31	657.11	425.68	786.52	434.07
Nasal layers	0.18	0.30	1.97	2.46	3.80	2.65	8.24	5.37
Oral cavity layer	0.16	0.08	0.27	0.30	1.63	2.31	0.73	0.92
Ovaries	0.04	0.08	0.13	0.20	1.03	0.45	2.25	0.83
Pancreas	1.34	4.45	7.80	13.36	26.48	20.67	33.71	24.80
Penis	0.17	0.54	1.84	2.21	8.98	0.00	9.92	0.00
Pharynx	0.06	0.12	0.43	0.55	0.93	0.81	0.82	0.80
Salivary glands	1.28	3.40	7.77	12.02	21.99	19.39	30.65	36.20
Scrotum	0.35	0.41	0.72	0.54	7.35	0.00	17.65	0.00
Skin	9.19	18.37	29.92	43.05	102.15	91.67	168.54	124.02
Small intestine	8.85	25.09	64.93	109.20	170.79	136.15	213.48	157.09
Spinal cord	1.36	3.47	7.12	18.65	15.32	16.56	25.86	24.75
Spleen	4.69	14.06	24.24	38.78	68.17	57.88	78.65	57.88
Spongiosa and medullary cavities	21.07	69.46	146.71	258.27	437.16	394.13	345.45	254.59
Stomach	1.86	5.32	13.30	22.61	35.47	28.32	44.39	33.07
Testes	0.04	0.08	0.13	0.20	1.03	0.45	2.25	0.83
Thyroid	0.20	0.28	0.53	1.24	2.02	1.75	3.37	2.48
Urinary bladder wall	0.09	0.19	0.35	0.54	0.90	0.72	1.12	0.83

Table 2-11. Voxel resolutions applied to the UF hybrid phantom family and resulting matrix sizes.

Phantom	Voxel Resolution (cm)			Number of Voxels			Total Matrix Size (x 10 ⁶)
	X-direction	Y-direction	Z-direction	X-direction	Y-direction	Z-direction	
UFH00MF	0.0663	0.0663	0.0663	350	215	720	54.18
UFH01MF	0.0663	0.0663	0.1400	396	253	550	55.10
UFH05MF	0.0850	0.0850	0.1928	416	235	576	56.31
UFH10MF	0.0990	0.0990	0.2425	428	226	580	56.10
UFH15M	0.1250	0.1250	0.2832	414	226	590	55.20
UFH15F	0.1200	0.1200	0.2828	410	238	574	56.01
UFHADM	0.1579	0.1579	0.2207	362	195	796	56.19
UFHADDF	0.1260	0.1260	0.2700	390	241	610	57.33

Table 2-12. Voxel resolution study showing doses calculated for a fine and course resolution phantom. Uniform photon source in the liver of the UFH15F phantom.

Target Tissue	S value (mGy/MBq-s)		Difference
	Fine Resolution	Coarse Resolution	
Brain	4.78E-08	4.76E-08	0.39%
Breast	2.16E-06	2.17E-06	-0.44%
Esophagus	2.30E-06	2.30E-06	0.22%
Gall bladder wall	1.26E-05	1.27E-05	-0.68%
Kidneys	2.25E-06	2.26E-06	-0.22%
Liver	1.80E-05	1.81E-05	-0.30%
Lungs	1.91E-06	1.92E-06	-0.50%
Oral cavity layer	1.63E-07	1.60E-07	1.81%
Ovaries	2.64E-07	2.55E-07	3.34%
Pancreas	3.16E-06	3.17E-06	-0.48%
Skin	4.03E-07	4.06E-07	-0.68%
Stomach wall	3.75E-06	3.77E-06	-0.54%
Thyroid	3.40E-07	3.40E-07	-0.08%
Urinary bladder wall	1.88E-07	1.84E-07	1.96%
Uterus	2.27E-07	2.28E-07	-0.47%

Table 2-13. Variance of energy deposition with changes in lower-bound electron energy cutoff values. Uniform 4 MeV photon source in the UFH00M liver.

Target	Energy Deposition (MeV)				Difference (%)		
	Electron Cutoff Energy				Electron Cutoff Energy		
	1 keV	10 keV	50 keV	100 keV	10 keV	50 keV	100 keV
Adipose tissue	7.175E-02	7.183E-02	7.177E-02	7.174E-02	-0.11%	-0.03%	0.01%
Adrenal glands	2.409E-03	2.406E-03	2.389E-03	2.387E-03	0.13%	0.83%	0.91%
Brain	5.429E-03	5.432E-03	5.423E-03	5.432E-03	-0.06%	0.11%	-0.06%
Breasts	1.250E-05	1.115E-05	1.300E-05	1.316E-05	10.81%	-3.99%	-5.27%
Lungs, bronchi, and trachea	1.602E-02	1.597E-02	1.607E-02	1.603E-02	0.28%	-0.34%	-0.09%
Esophagus	5.503E-04	5.425E-04	5.447E-04	5.457E-04	1.42%	1.00%	0.84%
Lens	3.567E-06	3.320E-06	2.961E-06	3.184E-06	6.92%	16.99%	10.74%

Table 2-14. Comparison of dosimetry results obtained using the MCNP-style bin-centered and ITS-style nearest-bin electron energy-indexing algorithms. Uniform photon source in the adipose tissue of the UFH00M phantom.

Target	MCNP-style		ITS-style		Difference (%)	
	Initial Energy (MeV)		Initial Energy (MeV)		Initial Energy (MeV)	
	0.15	4.00	0.15	4.00	0.15	4.00
Adipose tissue	5.85E-03	8.51E-02	5.85E-03	8.57E-02	-0.01%	-0.63%
Adrenals	2.77E-05	5.67E-04	2.78E-05	5.79E-04	0.00%	-2.12%
Brain	5.24E-04	1.21E-02	5.24E-04	1.21E-02	0.00%	-0.07%
Breasts	5.33E-07	8.77E-06	5.36E-07	9.74E-06	-0.46%	-9.99%
Cartilage	4.87E-04	9.55E-03	4.87E-04	9.54E-03	0.03%	0.12%
Esophagus	7.73E-06	1.48E-04	7.72E-06	1.47E-04	0.06%	1.06%
ET1	2.18E-07	4.12E-06	2.17E-07	3.74E-06	0.59%	10.21%
Extrathoracic lymph nodes	2.18E-07	3.11E-06	2.13E-07	3.01E-06	1.97%	3.34%
Heart Wall	1.06E-04	2.03E-03	1.05E-04	2.02E-03	0.04%	0.64%
Kidneys - Cortex	9.94E-05	1.94E-03	9.94E-05	1.95E-03	0.02%	-0.34%
Kidneys - Medulla	3.49E-05	6.70E-04	3.49E-05	6.82E-04	-0.01%	-1.70%
Left colon wall	5.75E-05	1.06E-03	5.75E-05	1.06E-03	0.02%	0.08%
Lens	2.71E-07	5.51E-06	2.72E-07	6.21E-06	-0.21%	-11.27%
Liver	7.31E-04	1.43E-02	7.31E-04	1.43E-02	0.00%	0.06%
Lungs	2.73E-04	5.54E-03	2.73E-04	5.51E-03	-0.01%	0.60%
Muscle	7.55E-03	1.46E-01	7.55E-03	1.46E-01	0.00%	-0.16%
Pituitary gland	1.49E-07	3.76E-06	1.48E-07	3.16E-06	0.85%	19.15%
Prostate	4.20E-06	8.02E-05	4.20E-06	8.41E-05	0.00%	-4.64%
Right colon wall	5.75E-05	1.05E-03	5.76E-05	1.06E-03	-0.15%	-0.36%
Salivary glands	1.87E-05	3.87E-04	1.87E-05	3.98E-04	0.04%	-2.74%
Skin	6.03E-04	8.50E-03	6.03E-04	8.55E-03	-0.01%	-0.60%
Stomach wall	3.97E-05	7.72E-04	3.97E-05	7.70E-04	0.01%	0.36%
Testes	3.21E-06	6.67E-05	3.22E-06	6.73E-05	-0.25%	-0.88%
Thoracic lymph nodes	1.36E-06	3.15E-05	1.36E-06	2.92E-05	0.02%	8.02%
Thymus	6.07E-05	1.24E-03	6.07E-05	1.23E-03	0.01%	0.34%
Thyroid	4.86E-06	1.01E-04	4.86E-06	1.02E-04	-0.02%	-0.89%
Trachea	1.86E-06	3.56E-05	1.86E-06	3.79E-05	0.00%	-6.11%
Urinary bladder wall	2.35E-05	4.61E-04	2.36E-05	4.56E-04	-0.03%	0.92%

Table 2-15. Source tissues explicitly simulated in the UF hybrid computational phantom series (ICRP 2009).

UF ID number (s)	Simulated Source Region	Acronym
30	Oral cavity	O-cavity
30	Oral mucosa	O-mucosa
185	Teeth surface activity	Teeth-S
185	Teeth volume activity	Teeth-V
51	Tongue	Tongue
52	Tonsils	Tonsils
10	Oesophagus fast	Oesophagus-f
10	Oesophagus slow	Oesophagus-s
10	Oesophagus wall	Oesophagus
47	Stomach contents	St-cont
46	Stomach wall	St-wall
42	Small intestine contents	SI-cont
41	Small intestine wall	SI-wall
8	Right colon contents	RC-cont
7	Right colon wall	RC-wall
59	Left colon contents	LC-cont
58	Left colon wall	LC-wall
38	Rectosigmoid colon contents	RSig-cont
37	Rectosigmoid colon wall	RSig-wall
28	Surface of anterior nasal passages	ET1-sur
23, 29, 34	Surface of posterior nasal passages + pharynx (excluding OCL)	ET2-sur
23, 29, 34	Sequestered ET2 region (excluding OCL)	ET2-seq
71	Lymph nodes in ET region	LN-ET
6, 53	Bronchi fast	Bronchi-f
6, 53	Bronchi slow	Bronchi-s
6, 53	Bronchi bound	Bronchi-b
6, 53	Bronchi sequestered	Bronchi-q
26, 27	Bronchioles fast	Brchiole-f
26, 27	Bronchioles slow	Brchiole-s
26, 27	Bronchioles bound	Brchiole-b
26, 27	Bronchioles sequestered	Brchiole-q
26, 27	Alveolar-interstitium	AI

Table 2-15. Continued.

UF ID number (s)	Simulated Source Region	Acronym
73, 74	Lymph nodes in thoracic region	LN-Th
27	Right lung lobe	RLung
26	Left lung lobe	LLung
3	Right adrenal gland	RAdrenal
2	Left adrenal gland	LAdrenal
65	Blood vessels of head	HBlood
66	Blood vessels of trunk	TBlood
67	Blood vessels of arms	ABlood
68	Blood vessels of legs	LBlood
16	Blood in heart	Ht-cont
a	Cortical bone mineral surface	C-bone-S
a	Cortical bone mineral volume	C-bone-V
b	Trabecular bone mineral surface	T-bone-S
c	Trabecular bone mineral volume	T-bone-V
d	Cortical bone marrow	C-marrow
e	Trabecular bone marrow	T-marrow
f	Active bone marrow	A-marrow
4	Brain	Brain
62	RBreast-a + RBreast-g	RBreast
5	LBreast-a + LBreast-g	LBreast
24	Lenses of eye	Eye-lens
13	Gall bladder wall	GB-wall
14	Gall bladder contents	GB-cont
15	Heart wall	Ht-wall
18	Right kidney cortex	RKidney-C
20	Right kidney medulla	RKidney-M
22	Right kidney pelvis	RKidney-P
17	Left kidney cortex	LKidney-C
19	Left kidney medulla	LKidney-M
21	Left kidney pelvis	LKidney-P
25	Liver	Liver
72, 75-86	Lymph nodes, except LN-ET + LN-TH	Lymph

Table 2-15. Continued.

UF ID number (s)	Simulated Source Region	Acronym
64	Muscle	Muscle
63	Right ovary	ROvary
31	Left ovary	LOvary
32	Pancreas	Pancreas
35	Pituitary gland	P-gland
36	Prostate	Prostate
39, 60, 61	Salivary glands	S-glands
43	Skin	Skin
44	Spinal cord	Sp-cord
45	Spleen	Spleen
48	Testes	Testes
49	Thymus	Thymus
50	Thyroid	Thyroid
54	Urinary bladder wall	UB-wall
55	Urinary bladder contents	UB-cont
56	Uterus/cervix	Uterus
1	Adipose/residual tissue	Adipose
g	Rest of body (for blood source simulation)	ROB

^a Cortical bone volume distribution applied to tissue tag ID numbers 151 - 184.

^b Trabecular bone surface distribution applied to tissue tag ID numbers 201 - 234.

^c Trabecular bone volume distribution applied to tissue tag ID numbers 201 - 234.

^d Total marrow volume distribution in medullary cavities of bone applied to tissue tag ID numbers 213, 214, 217, 220, 225, 226, 229, and 232.

^e Total marrow volume distribution in spongiosa of bone applied to tissue tag ID numbers 201 - 212, 215, 216, 218, 219, 221 - 224, 227, 228, 230, 231, 233 and 234.

^f Active marrow volume distribution applied to tissue tag ID numbers 201 - 234.

^g Ears, external nose, nasal layers, oral cavity layer, pharynx, salivary glands, spinal cord, penis, scrotum, tongue, gall bladder wall, pituitary gland, larynx, thymus, tonsils, breasts, prostate, and uterus.

Table 2-16. Source tissues mathematically assembled in the UF hybrid computational phantom series (ICRP 2009).

UF ID number (s)	Calculated Source Region	Acronym
23, 29, 30, 34	Surface of posterior nasal passages + pharynx (including OCL region)	ET2-sur
23, 29, 30, 34	Sequestered ET2 region (including OCL region)	ET2-seq
26, 27	RLung + LLung	Lungs
2, 3	RAdrenal + LAdrenal	Adrenals
18, 20, 22	Right kidney C+M+P	RKidney
17, 19, 21	Left kidney C+M+P	LKidney
17-22	RKidney + LKidney	Kidneys
31, 65	ROvary + LOvary	Ovaries
5, 62	RBreast + LBreast	Breast
7, 37, 58	Colon	Colon
a	Total body tissues (total body minus contents of walled organs)	T-body
b	Soft tissue (T-body - mineral bone)	S-tissue
c	HBlood + TBlood + ABlood + LBlood + Ht-cont + Lung left, blood + Lung, right, blood + blood in organs	Blood

^a All tissues except ROB, RC-cont, GB-cont, RSig-cont, SI-cont, St-cont, UB-cont, LC-cont, HBlood, TBlood, ABlood, LBlood, T-bone-S, and A-marrow.

^b All tissues except ROB, RC-cont, GB-cont, RSig-cont, SI-cont, St-cont, UB-cont, LC-cont, HBlood, TBlood, ABlood, LBlood, T-bone-S, A-marrow, T-bone-V, and C-bone-V.

^c Blood distribution applied to T-marrow, C-marrow, T-bone-V, ROB, HBlood, TBlood, ABlood, LBlood, Muscle, Adrenals, Oesophagus, St-wall, SI-wall, Colon, Liver, Pancreas, Ht-cont, Brain, Ht-wall, Adipose, Skin, Trachea, Bronchi, Lungs, Spleen, Thyroid, Kidneys, UB-wall, Testes, Ovaries, Cartilage, C-bone-V, LN-ET, LN-Th, and Lymph.

Table 2-17. Target tissues explicitly simulated in the UF hybrid computational phantom series (ICRP 2009).

UF ID number (s)	Target Region	Acronym
a	Active (red) marrow	R-marrow
46	Stomach wall	St-wall
47	Stomach contents	St-cont
48	Testes	Testes
54	Urinary bladder wall	UB-wall
55	Urinary bladder contents	UB-cont
10	Oesophagus wall	Oesophagus
25	Liver	Liver
50	Thyroid	Thyroid
b	50 um endosteal region	Endost-BS
4	Brain	Brain
39, 60, 61	Salivary glands	S-glands
43	Skin	Skin
13	Gall bladder wall	GB-wall
14	Gall bladder contents	GB-cont
15	Heart wall	Ht-wall
72, 75-86	Lymph nodes, except LN-ET + LN-TH	Lymph
64	Muscle	Muscle
30	Oral mucosa	O-mucosa
32	Pancreas	Pancreas
36	Prostate	Prostate
41	Small intestine wall	SI-wall
42	Small intestine contents	SI-cont
45	Spleen	Spleen
49	Thymus	Thymus
56	Uterus/cervix	Uterus
51	Tongue	Tongue
52	Tonsils	Tonsils
7	Right colon wall (ascending + right transverse)	RC-wall
8	Right colon contents (ascending + right transverse)	RC-cont
58	Left colon wall (left transverse + descending)	LC-wall
59	Left colon contents (left transverse + descending)	LC-cont

Table 2-17. Continued.

UF ID number (s)	Target Region	Acronym
37	Sigmoid colon wall + rectum wall	RSig-wall
38	Sigmoid colon contents + rectum contents	RSig-cont
28	Basal cells of anterior nasal passages	ET1-bas
23, 29, 34	Basal cells of posterior nasal passages + pharynx (exluding OCL)	ET2-bas
71	Lymph nodes of ET region	LN-ET
6	Basal cells of bronchi	Bronchi-bas
6	Secretory cells of bronchi	Bronchi-sec
26, 27	Secretory cells of bronchioles	Brchiol-sec
26, 27	Alveolar-interstitium	AI
73, 74	Lymph nodes in thoracic region	LN-Th
27	Right lung lobe	RLung
26	Left lung lobe	LLung
3	Right adrenal gland	RAdrenal
2	Left adrenal gland	LAdrenal
70	RBreast-a + RBreast-g	RBreast
5	LBreast-a + LBreast-g	LBreast
24	Lenses of eye	Eye-lens
18	Right kidney cortex	RKidney-C
20	Right kidney medulla	RKidney-M
22	Right kidney pelvis	RKidney-P
17	Left kidney cortex	LKidney-C
19	Left kidney medulla	LKidney-M
21	Left kidney pelvis	LKidney-P
31	Right ovary	ROvary
65	Left ovary	LOvary
35	Pituitary gland	P-gland
44	Spinal cord	Sp-cord
1	Adipose/residual tissue	Adipose
c	Whole body	WBody
d	Rest of body (for blood source simulation)	ROB

Table 2-17. Continued.

UF ID number (s)	Target Region	Acronym
65	Blood vessels of head	HBlood
66	Blood vessels of trunk	TBlood
67	Blood vessels of arms	ABlood
68	Blood vessels of legs	LBlood

^a Active marrow skeletal photon fluence-to-dose response function applied to tissue tag numbers 201 - 234.

^b Total shallow marrow skeletal photon fluence-to-dose response function applied to tissue tag numbers 201 - 234.

^c All tissues except ROB, RC-cont, GB-cont, RSig-cont, SI-cont, St-cont, UB-cont, LC-cont, HBlood, TBlood, ABlood, LBlood, T-bone-S, R-marrow, and Endost-BS.

^d Ears, external nose, nasal layers, oral cavity layer, pharynx, salivary glands, spinal cord, penis, scrotum, tongue, gall bladder wall, pituitary gland, larynx, thymus, tonsils, breasts, prostate, and uterus.

Table 2-18. Target tissues mathematically assembled in the UF hybrid computational phantom series (ICRP 2009).

UF ID number (s)	Calculated Target Region	Acronym
7, 37, 58	Colon	Colon
17-22	RKidney + LKidney	Kidneys
26, 27	RLung + LLung	Lungs
2, 3	RAdrenal + LAdrenal	Adrenals
23, 28, 29, 30, 34	ET region (including OCL)	ET
23, 29, 30, 34	Basal cells of posterior nasal passages + pharynx (including OCL)	ET2-bas
5, 70	Breast-a + Breast-g	Breast
31, 65	ROvary + LOvary	Ovaries
23, 28, 29, 34	ET region (excluding OCL)	ET
18, 20, 22	Right kidney C+M+P	RKidney
17, 19, 21	Left kidney C+M+P	LKidney

Table 2-19. Biokinetic parameters for $^{99m}\text{Tc} - \text{DMSA}$ for the newborn patient (Evans *et al.* 1996). A_m is fractional maximum uptake, A_o is fractional initial uptake, λ_+ is the uptake rate, λ_- is the clearance rate, and λ_{eff-} is the effective clearance rate.

Source Tissue	A_m	A_o	$\lambda_+ (\text{h}^{-1})$	$\lambda_- (\text{h}^{-1})$	$\lambda_{eff-} (\text{h}^{-1})$	Fraction Excreted	
						6 h	24 h
Left kidney cortex	0.21	--	0.72	0.009	--	--	--
Right kidney cortex	0.21	--	0.64	0.008	--	--	--
Liver	--	0.057	--	--	0.14	--	--
Spleen	--	0.016	--	--	0.16	--	--
Urinary bladder contents	--	--	--	--	--	0.066	0.13
Whole body	--	--	--	--	--	--	--

Table 2-20. Morphometric measurements for the phantoms created to assess dosimetric sensitivity as a function of sitting height.

Phantom	Mass (kg)	Standing Height (cm)	Sitting Height (cm)	Arm Circumference (cm)	Thigh Circumference (cm)	Waist Circumference (cm)	Buttocks Circumference (cm)
UFH00M							
Shortest	1.28	38.95	25.41	9.39	16.46	27.78	27.04
Short	2.38	43.35	29.72	11.61	16.44	32.41	31.63
Reference	3.45	47.37	33.92	13.72	16.96	37.04	36.04
Tall	4.54	51.70	38.16	15.67	16.72	41.67	40.53
Tallest	6.07	55.92	42.29	17.38	16.82	46.29	44.91
UFH10M							
Shortest	17.73	121.25	56.93	14.96	31.27	53.25	54.05
Short	23.77	130.42	66.09	17.46	30.96	62.41	62.59
Reference	32.42	139.86	75.50	19.89	31.23	71.04	71.84
Tall	42.30	149.24	85.39	22.29	31.23	79.89	80.74
Tallest	55.42	158.24	95.20	24.88	31.41	88.69	89.75
UFHADM							
Shortest	40.35	151.69	70.57	19.86	41.69	73.37	72.88
Short	53.47	162.84	81.71	22.90	42.21	85.57	83.37
Reference	73.08	174.90	92.91	26.17	41.70	97.79	93.97
Tall	93.99	185.88	104.89	29.68	42.20	110.07	107.02
Tallest	122.82	198.23	117.79	32.83	41.65	122.36	114.19

Table 2-21. Voxel resolutions and total matrix sizes for the phantoms created to assess dosimetric sensitivity as a function of sitting height.

Phantom	Voxel Resolution (cm)			Number of Voxels			Matrix Size (x 10 ⁶)
	Width	Depth	Height	Width	Depth	Height	
UFH00M							
Shortest	0.0663	0.0663	0.0663	350	189	593	39.23
Short	0.0663	0.0663	0.0663	350	202	656	46.38
Reference	0.0663	0.0663	0.0663	350	215	720	54.18
Tall	0.0663	0.0663	0.0663	350	228	784	62.56
Tallest	0.0663	0.0663	0.0663	353	242	847	72.36
UFH10M							
Shortest	0.0990	0.0990	0.0990	322	201	503	32.56
Short	0.0990	0.0990	0.0990	374	211	542	42.77
Reference	0.0990	0.0990	0.0990	428	226	580	56.10
Tall	0.0990	0.0990	0.0990	480	248	619	73.69
Tallest	0.0990	0.0990	0.0990	533	275	658	96.45
UFHADM							
Shortest	0.1579	0.1579	0.2207	272	181	690	33.97
Short	0.1579	0.1579	0.2207	317	184	743	43.34
Reference	0.1579	0.1579	0.2207	362	195	796	56.19
Tall	0.1579	0.1579	0.2207	406	206	849	71.01
Tallest	0.1579	0.1579	0.2207	451	220	902	89.50

Table 2-22. Morphometric measurements for the phantoms created to assess dosimetric sensitivity as a function of weight.

Phantom	Mass (kg)	Standing Height (cm)	Sitting Height (cm)	Arm Circumference (cm)	Thigh Circumference (cm)	Waist Circumference (cm)	Buttocks Circumference (cm)
UFH00M							
Lightest	1.62	47.50	33.84	10.23	11.91	25.24	24.29
Light	2.21	47.50	33.93	11.83	13.64	29.45	28.16
Reference	3.45	47.37	33.92	13.72	16.96	37.04	36.04
Heavy	5.21	47.76	36.04	15.09	22.81	48.73	47.91
UFH10M							
Lightest	16.37	139.66	75.30	11.81	19.84	52.59	52.52
Light	22.29	140.43	75.56	13.84	23.14	60.66	60.90
Reference	32.42	139.86	75.50	19.89	31.23	71.04	71.84
Heavy	53.58	139.92	76.32	30.78	42.50	92.69	94.86
UFHADM							
Lightest	36.08	175.11	94.04	18.42	27.93	69.64	67.03
Light	49.14	175.69	93.68	21.01	32.32	81.21	77.80
Reference	73.08	174.90	92.91	26.17	41.70	97.79	93.97
Heavy	124.85	175.10	94.36	41.84	62.85	126.97	126.79

Table 2-23. Voxel resolutions and total matrix sizes for the phantoms created to assess dosimetric sensitivity as a function of weight.

Phantom	Voxel Resolution (cm)			Number of Voxels			Matrix Size (x 10 ⁶)
	Width	Depth	Height	Width	Depth	Height	
UFH00M							
Lightest	0.0663	0.0663	0.0663	264	160	720	30.41
Light	0.0663	0.0663	0.0663	306	185	720	40.76
Reference	0.0663	0.0663	0.0663	350	215	720	54.18
Heavy	0.0663	0.0663	0.0663	350	242	720	60.98
UFH10M							
Lightest	0.0990	0.0990	0.0990	316	171	580	31.34
Light	0.0990	0.0990	0.0990	368	198	580	42.26
Reference	0.0990	0.0990	0.0990	428	226	580	56.10
Heavy	0.0990	0.0990	0.0990	452	289	580	75.76
UFHADM							
Lightest	0.1579	0.1579	0.2207	268	145	796	30.93
Light	0.1579	0.1579	0.2207	312	169	795	41.92
Reference	0.1579	0.1579	0.2207	362	195	796	56.19
Heavy	0.1579	0.1579	0.2207	386	245	796	75.28

Table 2-24. Morphometric measurements for the phantoms created to assess dosimetric sensitivity for patients of similar weight but different body morphometry.

Phantom	Mass (kg)	Standing Height (cm)	Sitting Height (cm)	Arm Circumference (cm)	Thigh Circumference (cm)	Waist Circumference (cm)	Buttocks Circumference (cm)
UFH10F							
Reference	32.41	139.86	75.50	19.89	31.23	71.04	71.84
Short/heavy	49.60	135.01	69.74	28.48	50.18	85.33	87.88
UFH15F							
Reference	52.99	161.33	84.07	28.07	43.47	76.87	80.21
Tall/thin	49.67	174.95	89.25	23.03	42.72	69.20	82.36

Table 2-25. Voxel resolutions and total matrix sizes for the phantoms created to assess dosimetric sensitivity for patients of similar weight but different body morphometry.

Phantom	Voxel Resolution (cm)			Number of Voxels			Matrix Size
	Width	Depth	Height	Width	Depth	Height	(x 10 ⁶)
UFH10F							
Reference	0.0990	0.0990	0.0990	428	226	580	56.10
Short/heavy	0.0990	0.0990	0.0990	286	209	933	55.77
UFH15F							
Reference	0.1200	0.1200	0.2828	410	238	574	56.01
Tall/thin	0.1200	0.1200	0.2828	296	189	1103	61.71

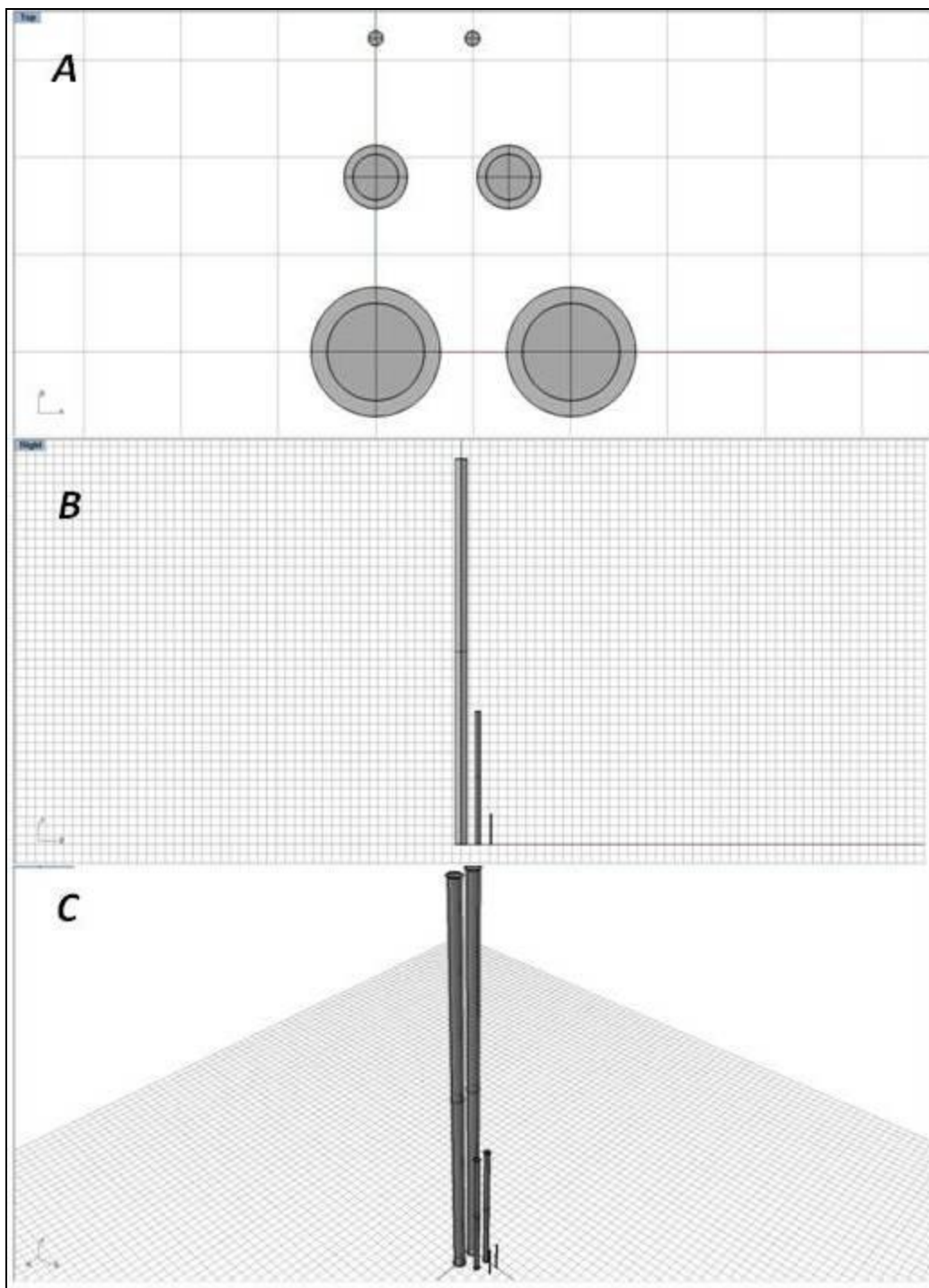


Figure 2-1. Three-dimensional stylistic model showing the (A) top, (B) side, and (C) perspective views for an excerpt of the irradiation geometries for the vascular dosimetry computational study.

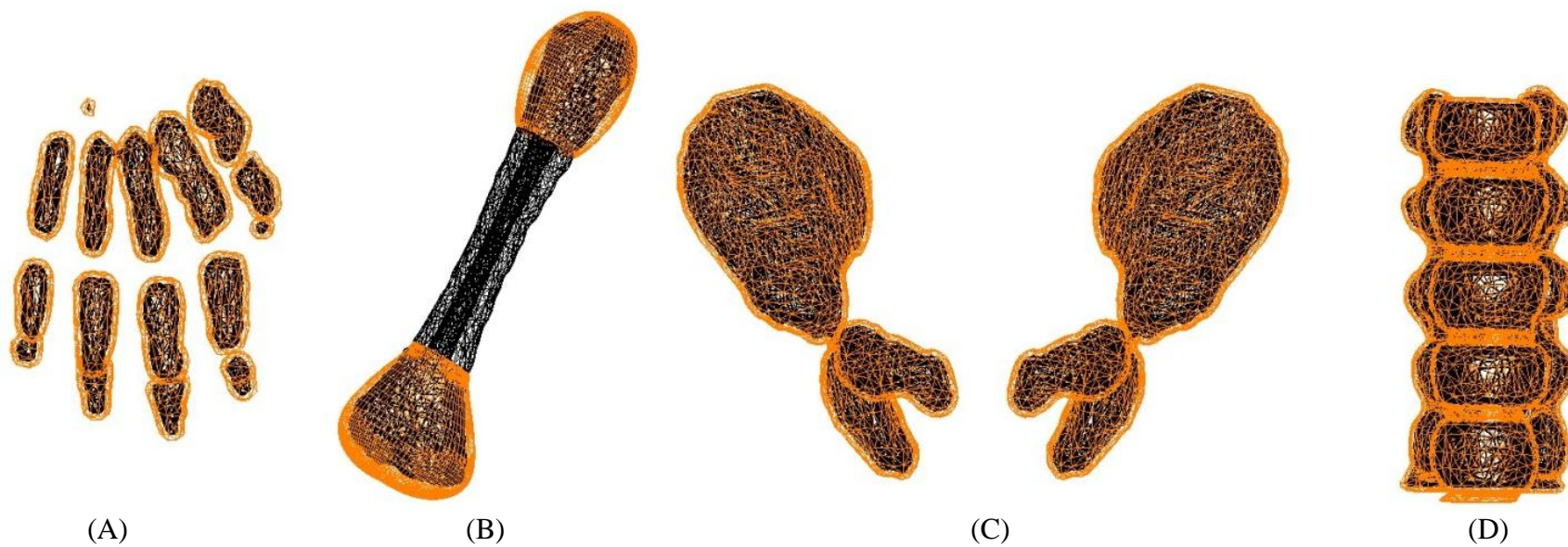


Figure 2-2. Sample heterogeneous skeletal sites of the UF newborn hybrid phantom showing the (A) hand, (B) right humerus, (C) pelvis, and (D) L-spine.

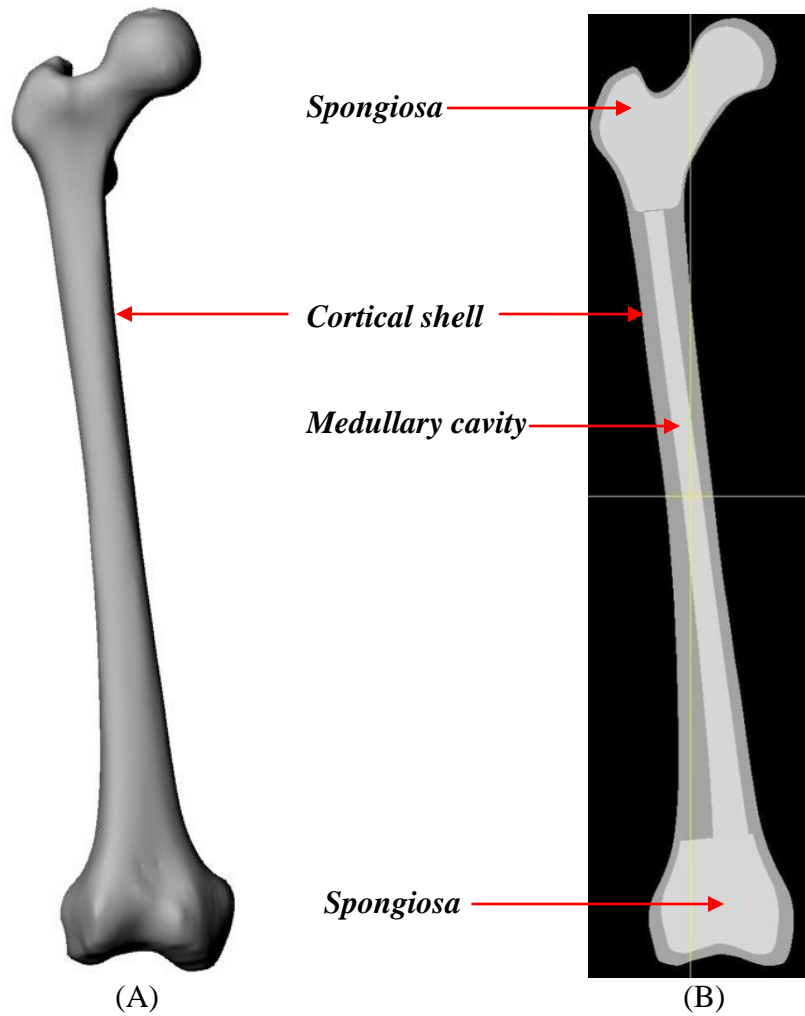


Figure 2-3. (A) Polygon mesh and (B) voxel versions of the UFH01MF femur for use in the SIRT simulations. In the voxel version, dark gray regions are cortical bone and light gray regions are both spongiosa and medullary cavities.

Photon Simulations

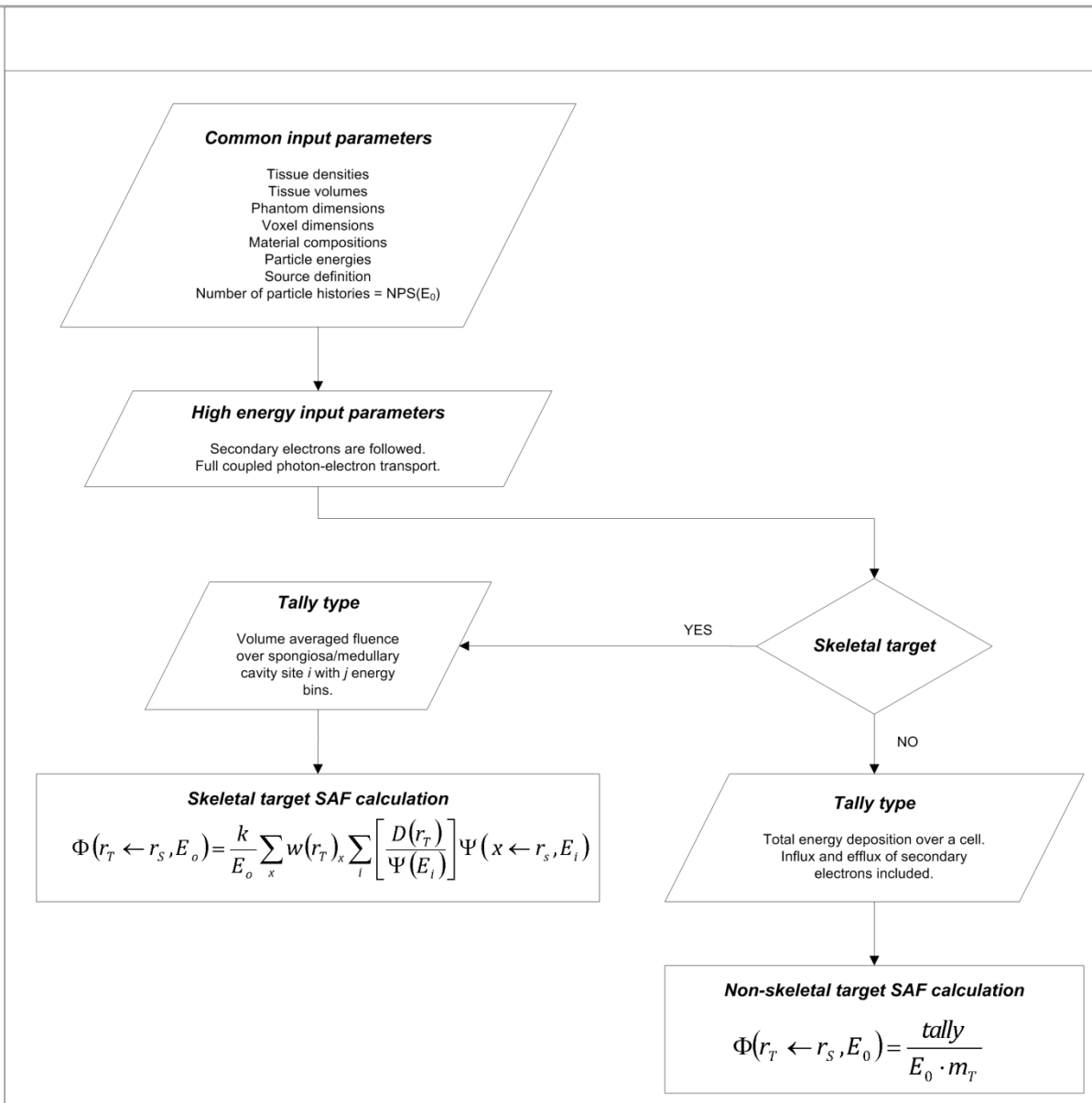
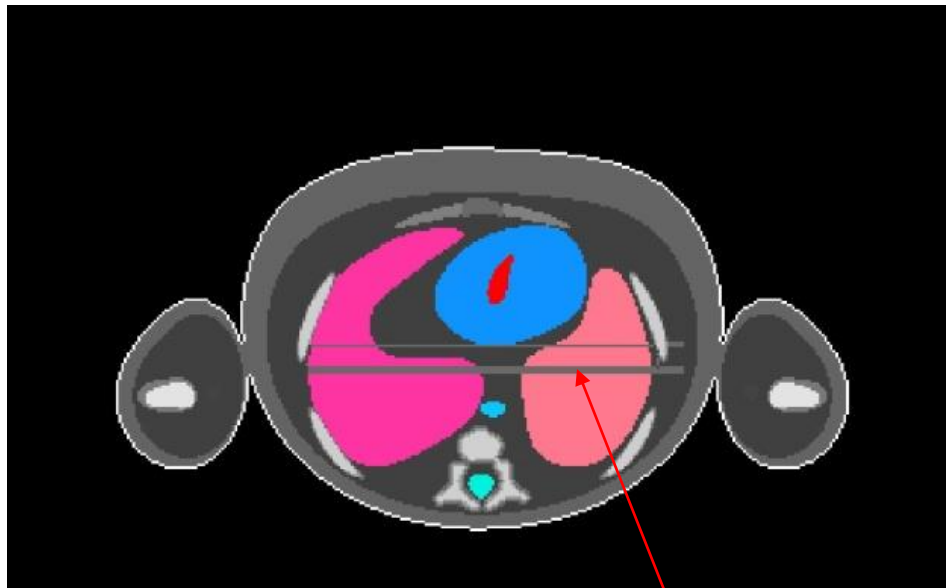
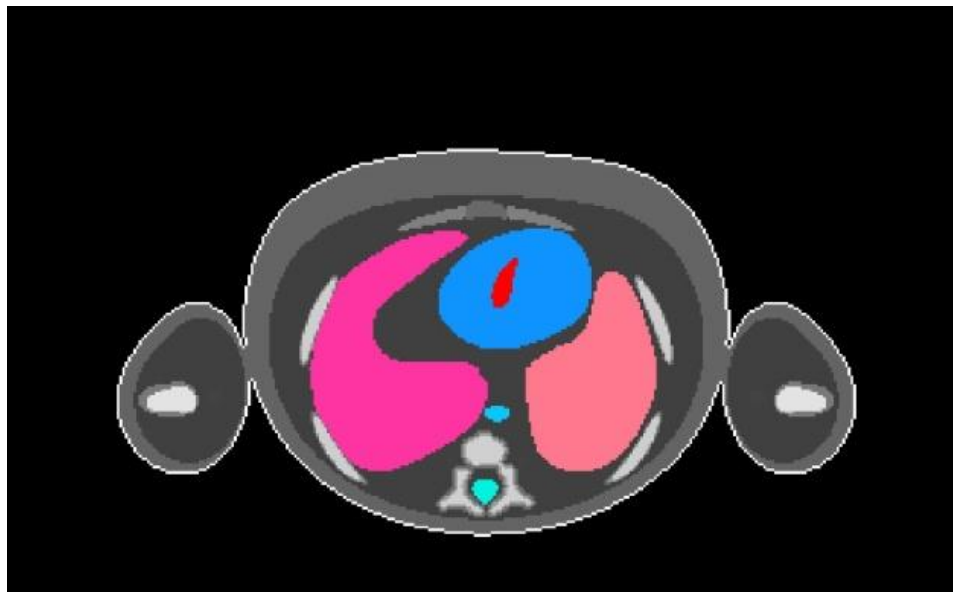


Figure 2-4. Photon simulation flowchart used to generate monoenergetic photon SAFs.



(A)

Streaking artifacts



(B)

Figure 2-5. Illustration of artifact correction in *ImageJ*TM. (A) Streaking artifacts in the UFH00M phantom and (B) artifacts corrected.

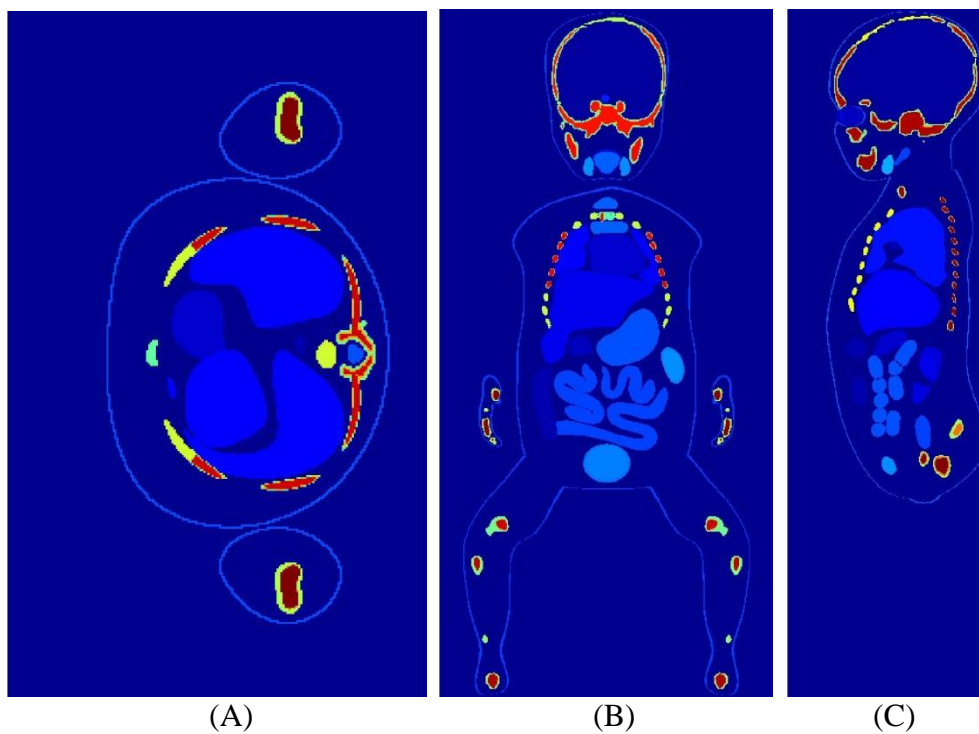


Figure 2-6. UFH00F phantom voxelized at an isotropic resolution of 0.0663 cm showing the (A) axial, (B) coronal, and (C) sagittal views.

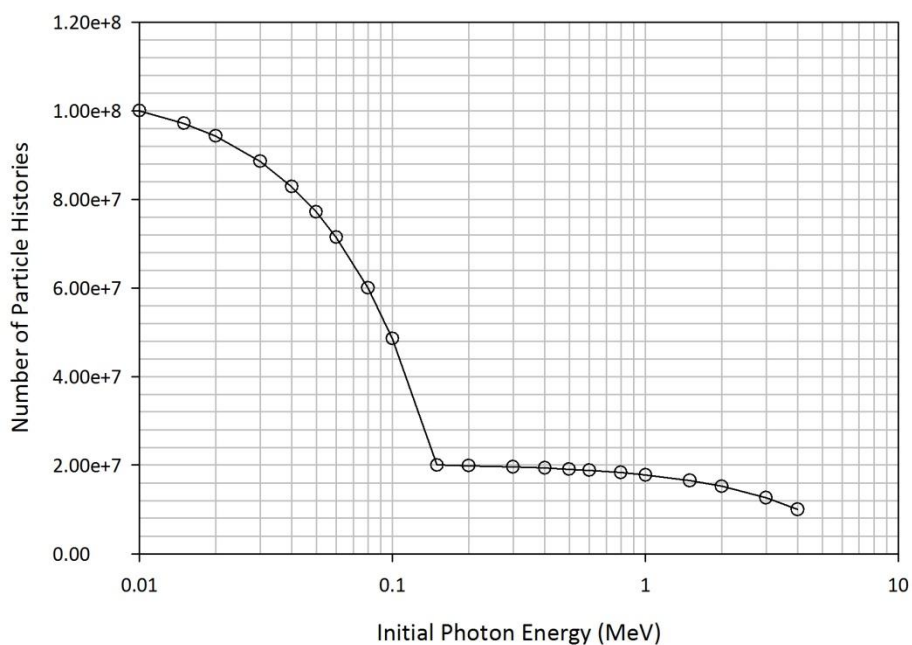


Figure 2-7. Number of particle histories simulated as a function of initial photon energy.

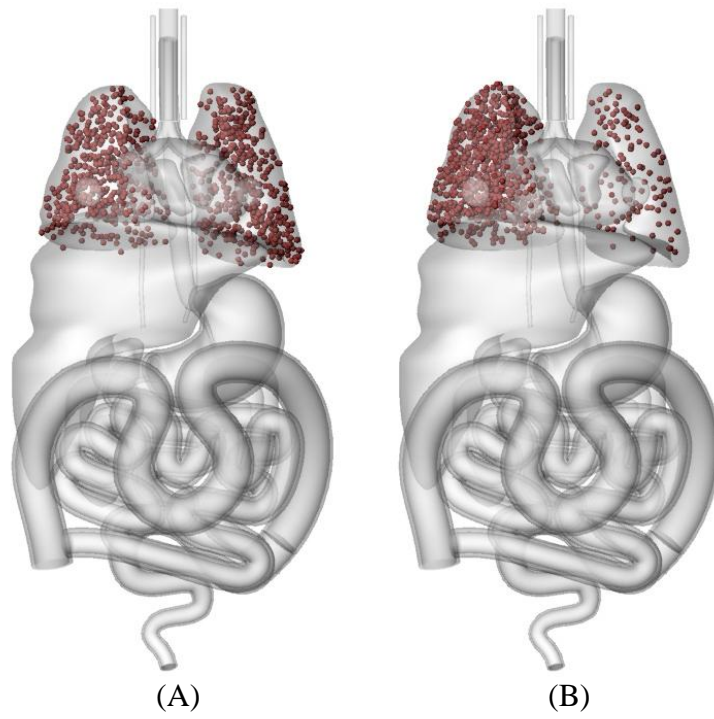


Figure 2-8. Visual representation of (A) uniform and (B) non-uniform source sampling. Points of emission were recorded and represented as red spheres in the UFH00M phantom. Arbitrary radiation source in the lungs of the UFH00M phantom.

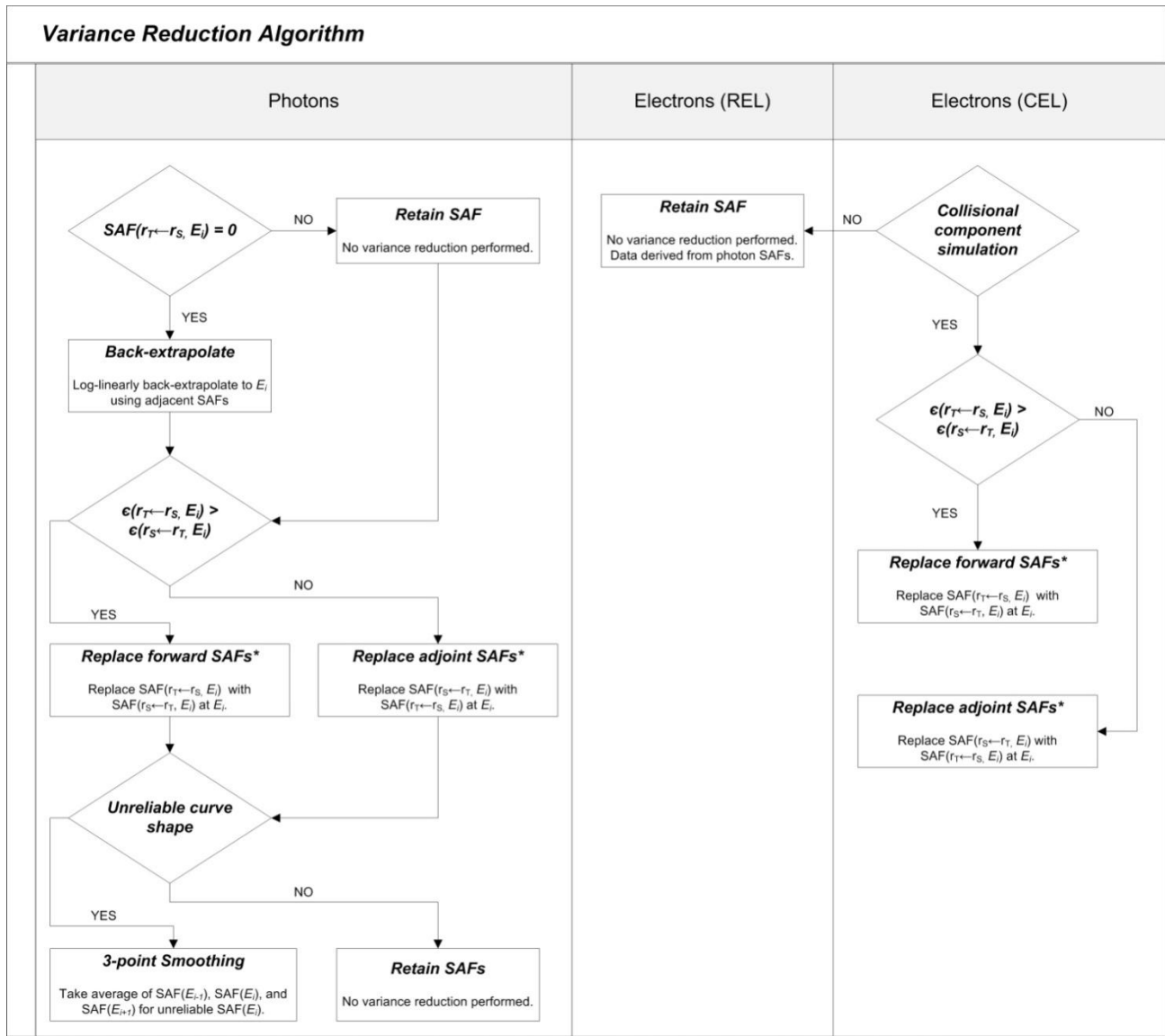


Figure 2-9. Variance reduction technique flowchart used to improve the reliability of the monoenergetic photon and electron SAFs.

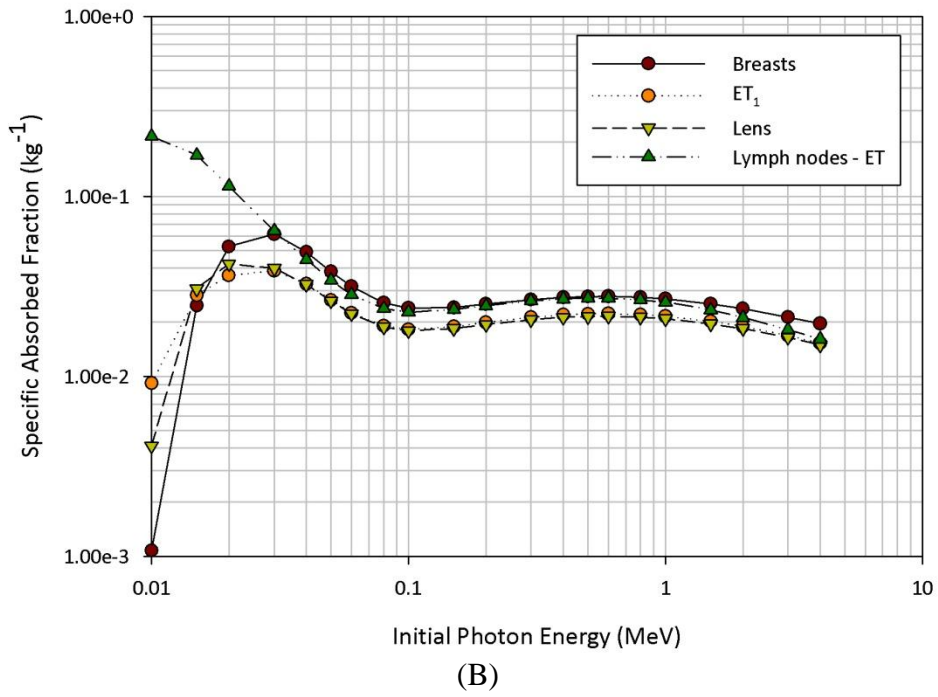
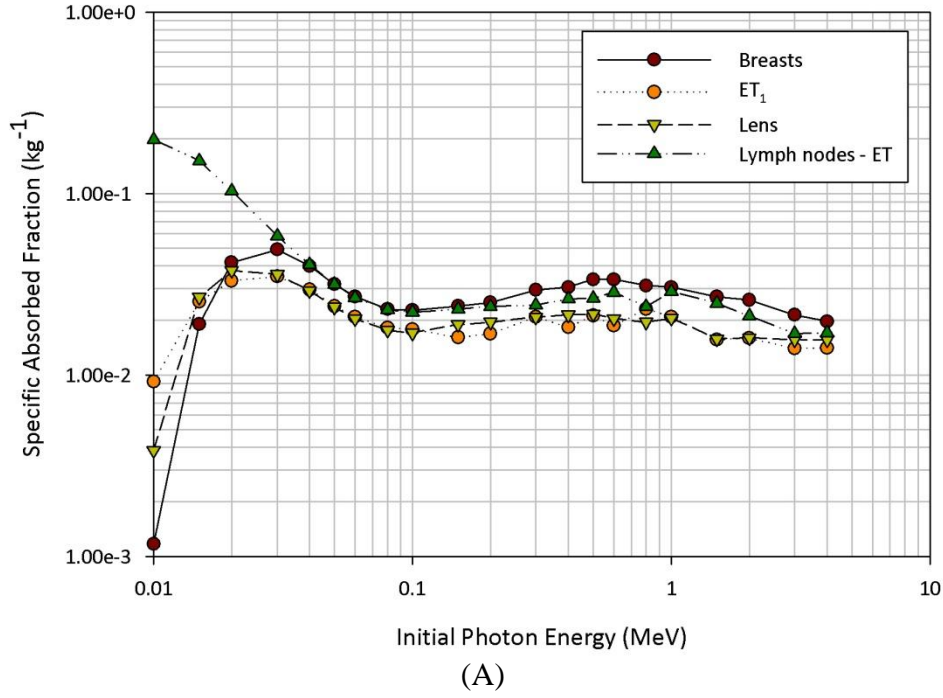


Figure 2-10. Reverse Monte Carlo method demonstrating the reciprocity principle showing both (A) raw SAF data and (B) reciprocal data. Uniform photon source in the muscle of the UFH00M phantom.

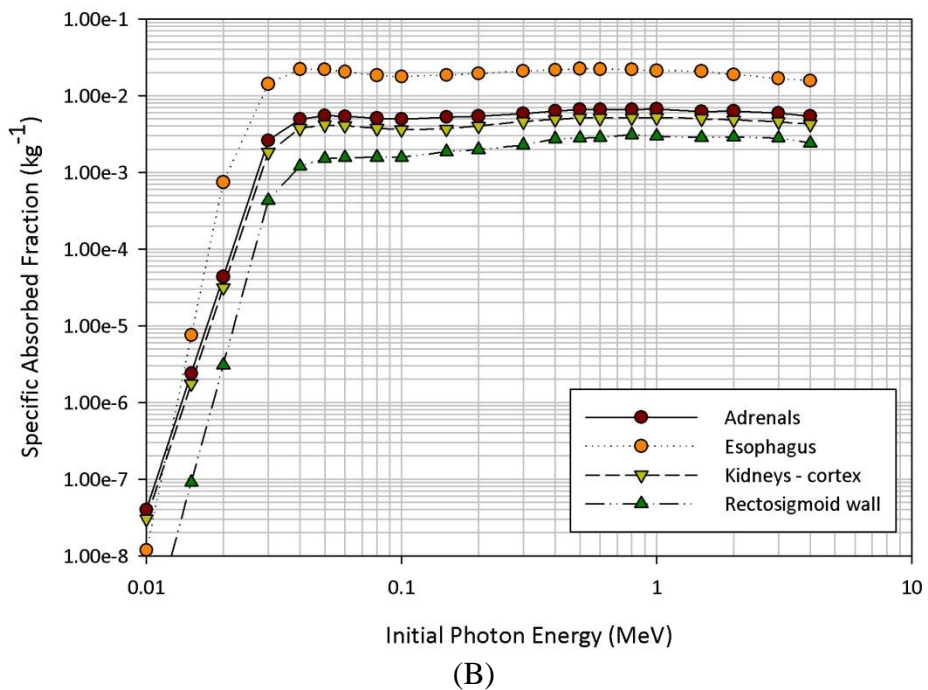
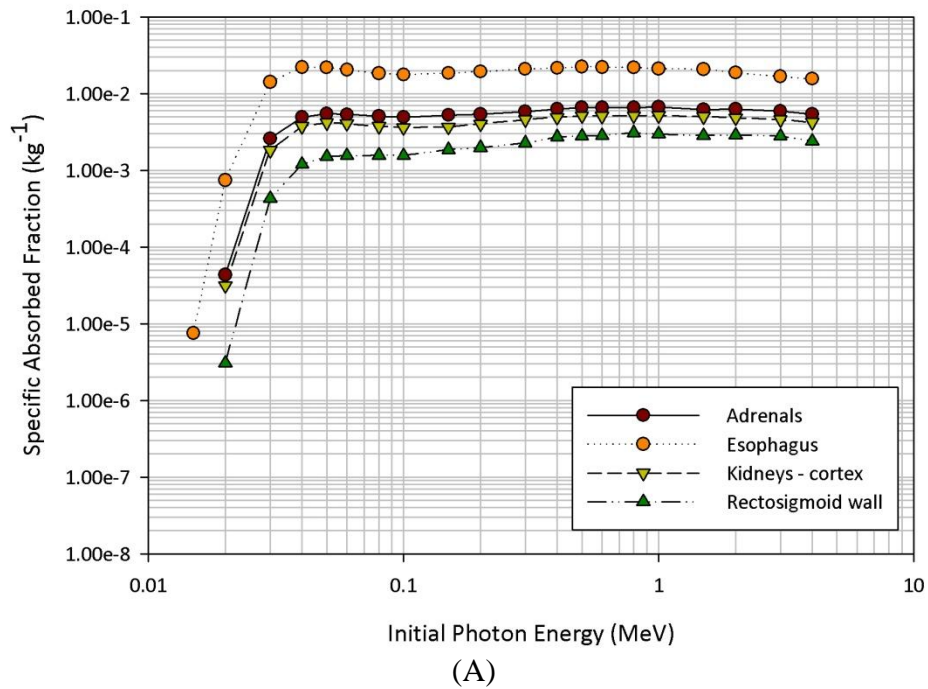


Figure 2-11. Low energy photon back-extrapolation method showing both (A) raw SAF data and (B) extrapolated data. Uniform photon source in the anterior nasal layer (ET_1) of the UFH00M phantom.

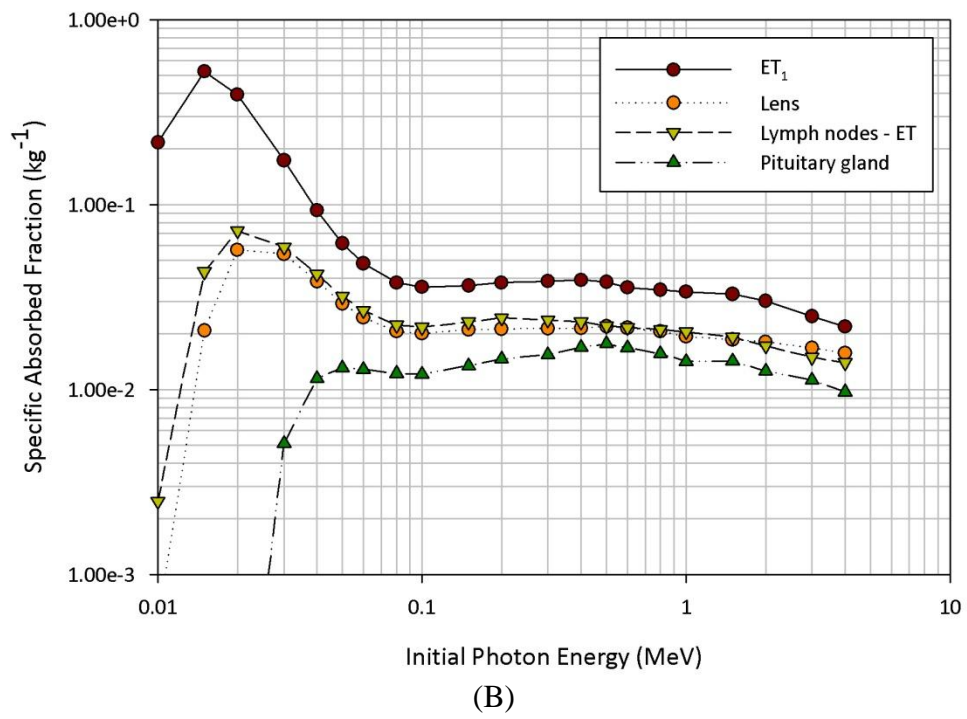
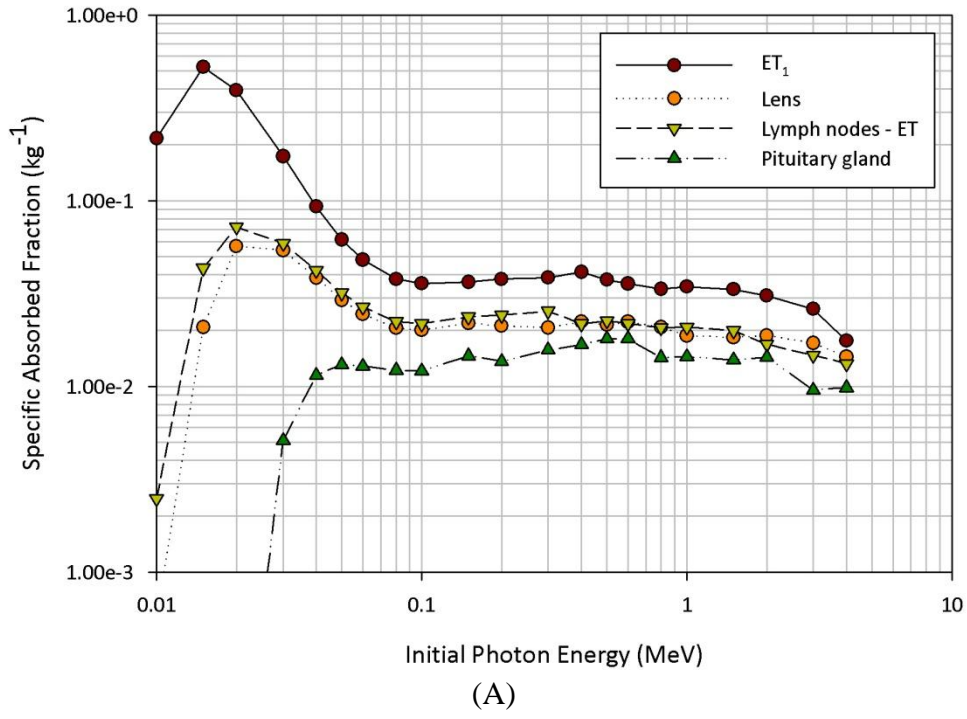


Figure 2-12. Three-point smoothing method showing both (A) raw SAF data and (B) smoothed data. Uniform photon source in the breasts of the UFH00M phantom.

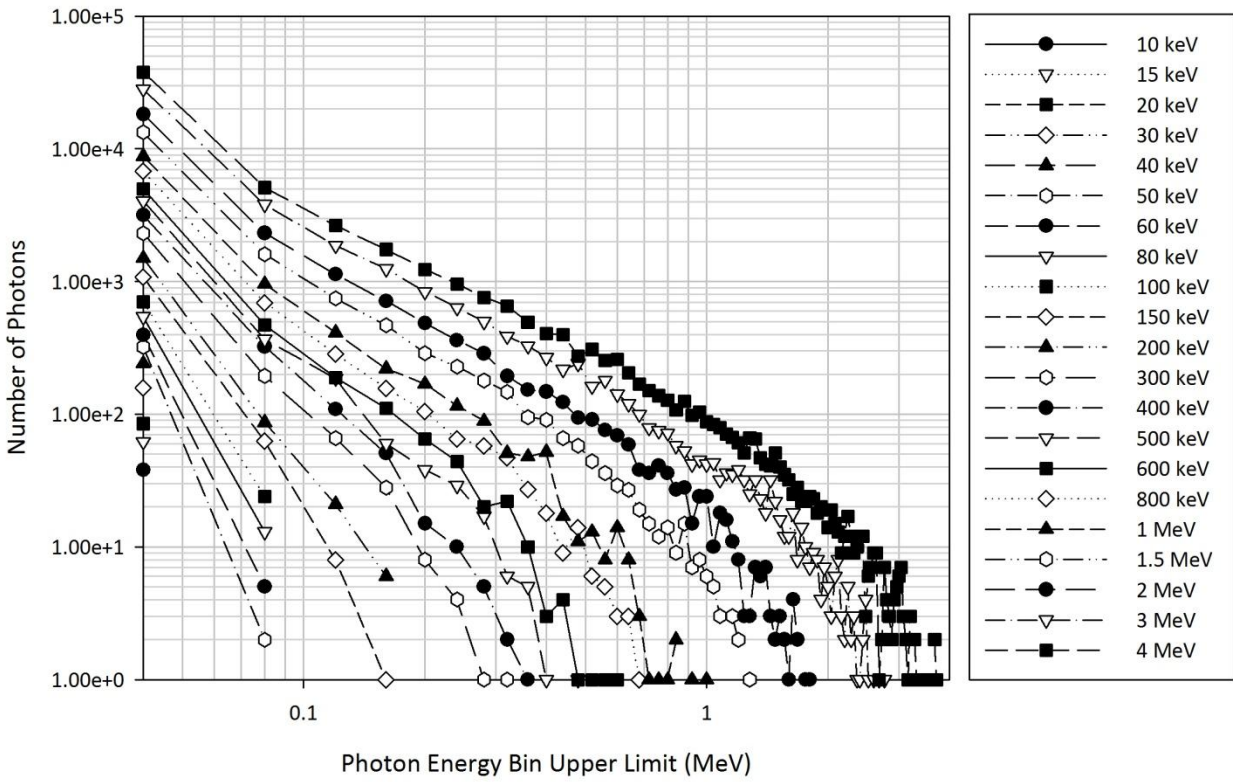


Figure 2-14. Photon energy spectrum generated from simulating monoenergetic electrons in the liver of the UFH00M phantom. Energy bins were created at 40 keV intervals from 40 keV to 4 MeV. Photon energies on the horizontal axis represent the upper limit of the energy bin, so the number of photons at a photon energy of 40 keV represents the number of photons generated at energies between 0 keV and 40 keV. The energies in the legend are the initial monoenergetic electron energies.

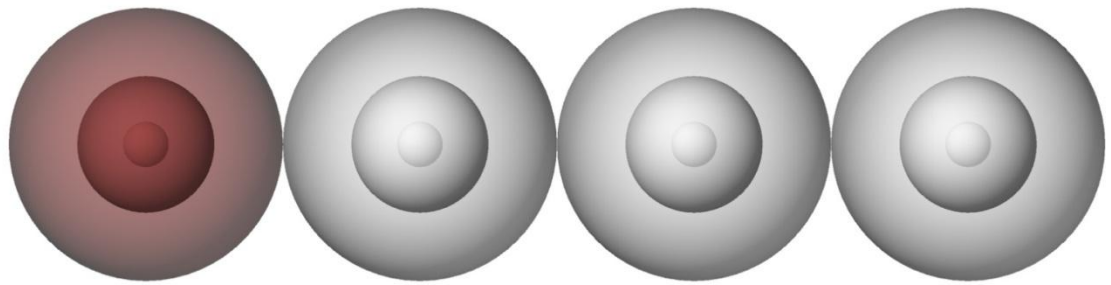


Figure 2-15. Graphical depiction of the systematic approach to studying dosimetric sensitivity with changes in source and target tissue size and separation. Uniform spherical sources are indicated by the red set of spheres, and targets are indicated by gray spheres. Sources were also simulated as targets.

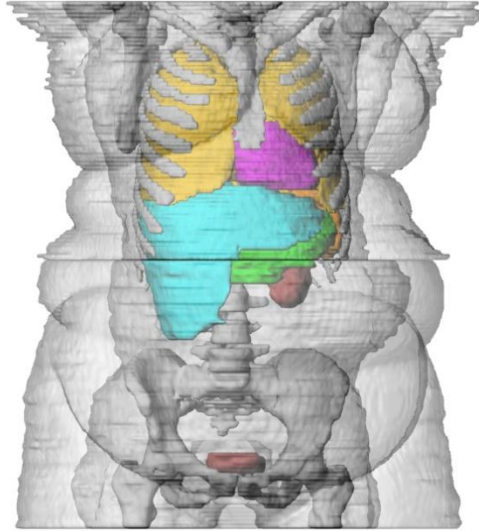


Figure 2-16. Patient-specific voxel phantom used for internal dosimetric mass-scaling analysis – adult female at 175 *cm* and 136 *kg* (Johnson *et al.* 2011).

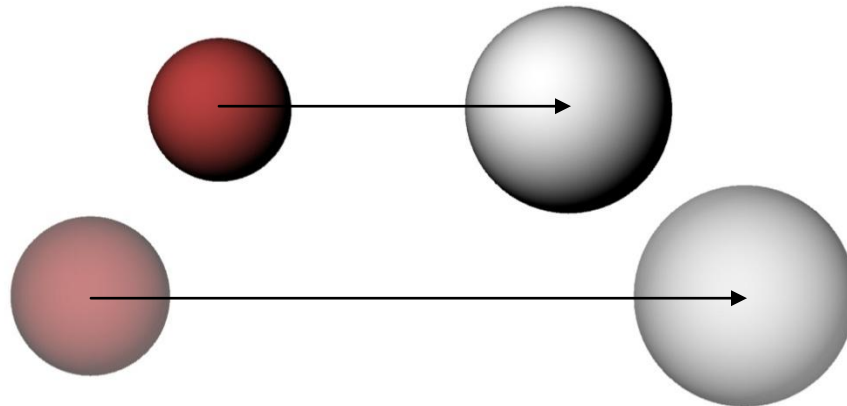


Figure 2-17. Irradiation geometry for the photon cross-dose scaling validation study. The red spheres are the source tissues, and the gray spheres are the target tissues. The solid spheres represent the reference geometry, and the transparent spheres represent the non-reference geometry.

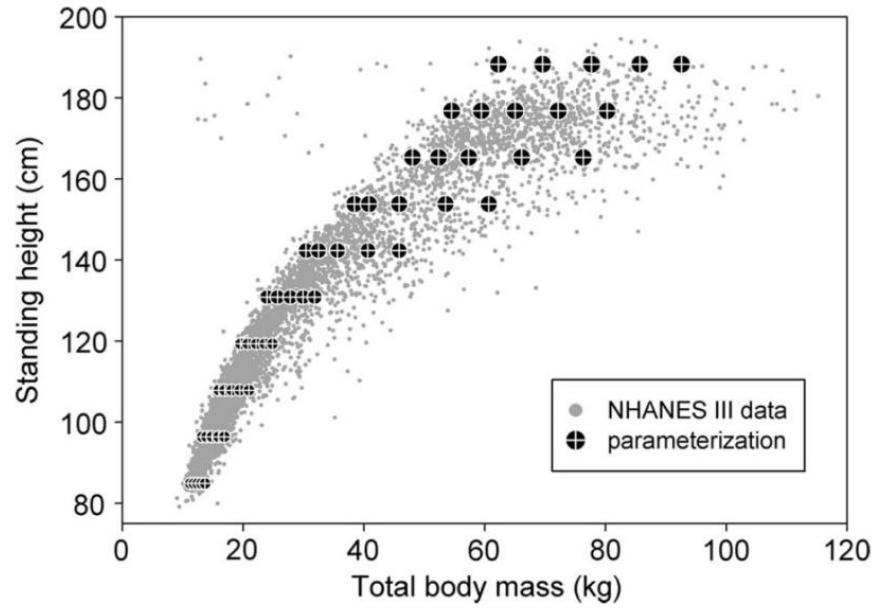


Figure 2-18. Standing height as a function of total body mass for the NHANES III pediatric male population. Grey dots represent actual patients, and black dots with crosshairs represent the library of phantoms (Johnson *et al.* 2009). Reproduced with permission (© 2009 IEEE).

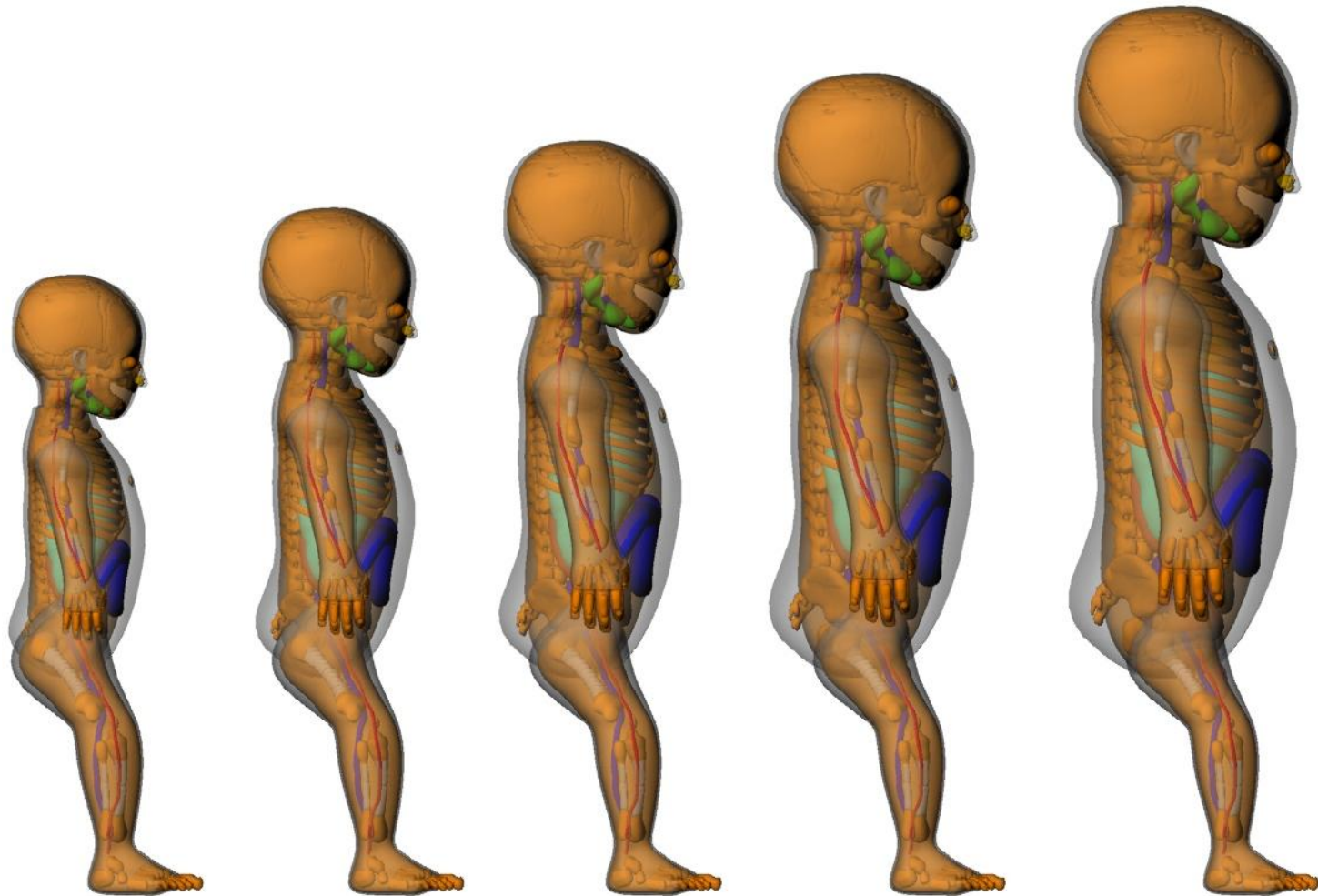


Figure 2-19. Sample set of NURBS/PM phantoms created for the internal dosimetric standing height sensitivity study. UFH00M phantoms shown at standing heights of 38.95 cm, 43.35 cm, 47.37 cm (ICRP-reference), 51.70 cm, and 55.92 cm.

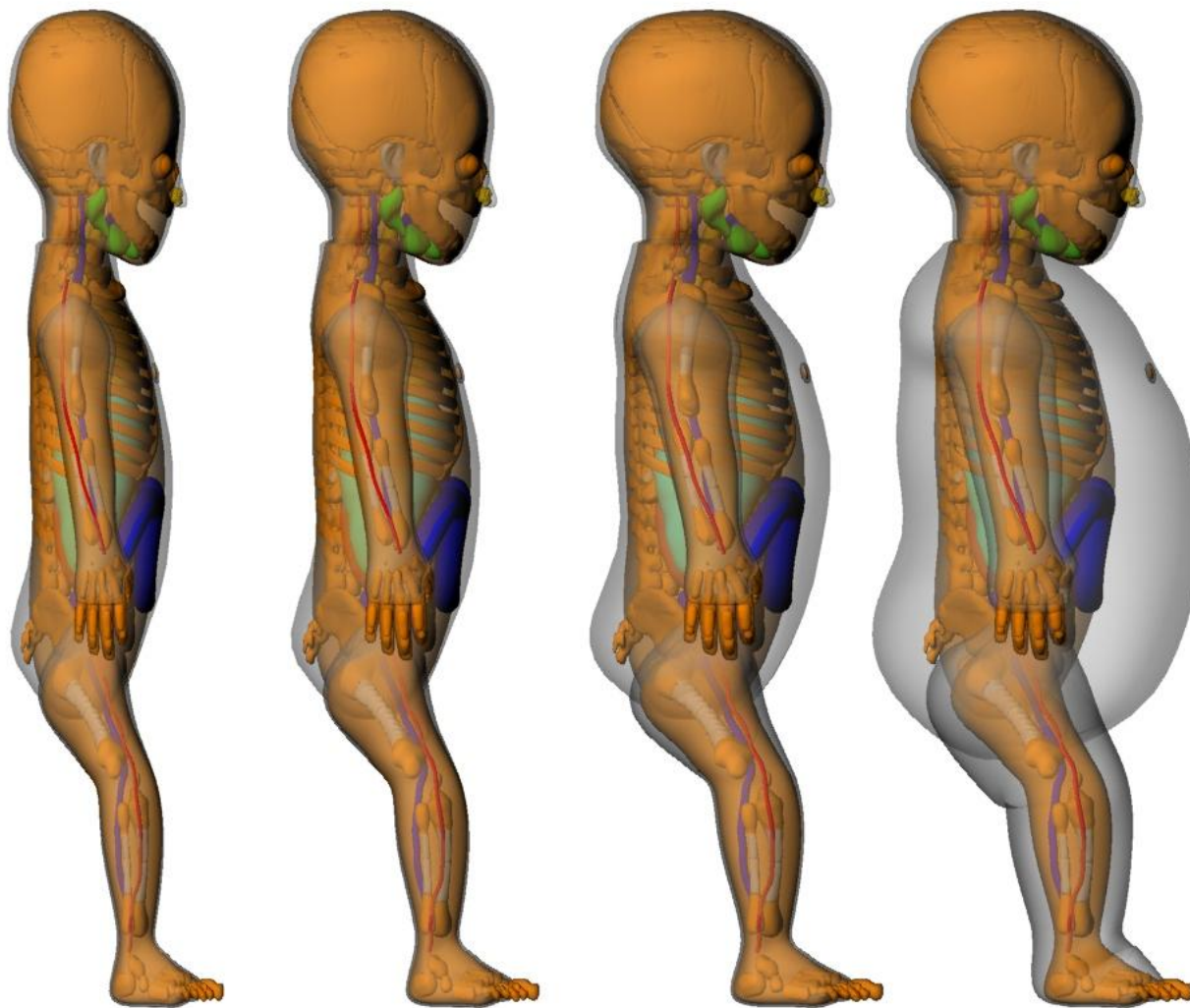


Figure 2-20. Sample set of NURBS/PM phantoms created for the internal dosimetric weight sensitivity study. UFH00M phantoms shown at weights of 1.62 *kg*, 2.21 *kg*, 3.45 *kg* (ICRP-reference), and 5.21 *kg*.

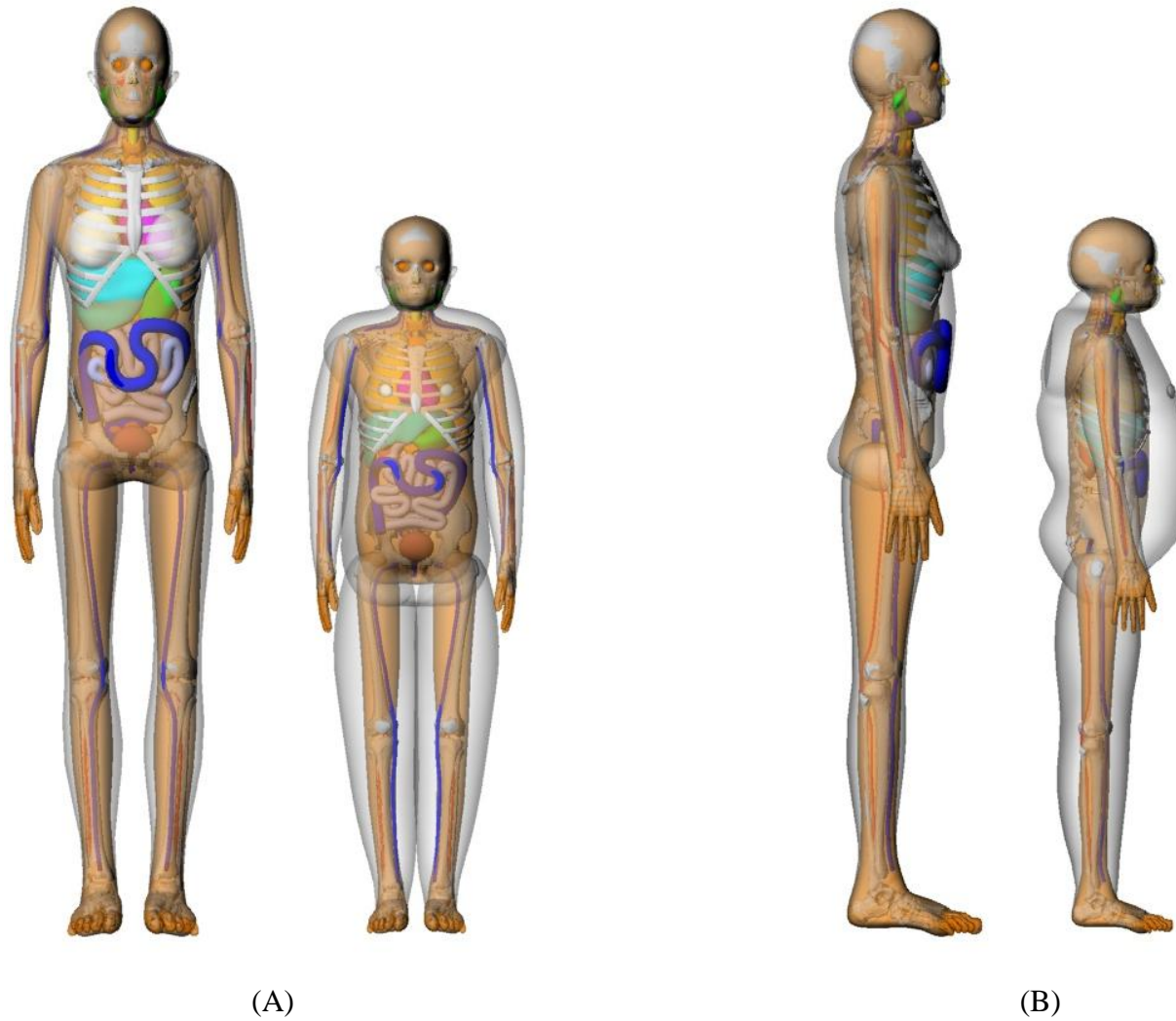


Figure 2-21. Phantoms created for the internal dosimetric body morphometry sensitivity study. Two phantoms at 50 *kg* but at heights of 174.95 *cm* and 135.01 *cm*.

CHAPTER 3 RESULTS

UF Hybrid Phantom Blood Vessel System

Adult Male

Neck and clavicles

The arteries modeled in the neck and clavicles represent the common carotid arteries and subclavian artery. The veins modeled in the neck and clavicles represent the external and internal jugular vein and subclavian vein. One artery and one vein were placed on either side of the neck with the veins being located anteriorly and the arteries posteriorly. The decision to place the veins in front of the arteries was arbitrary but not critically important to the simulation of a blood source.

Both veins and arteries were modeled as tube structures with the initial tube diameter equal to the final tube diameter. The artery diameters were set to 0.40 cm , which is the average large artery diameter reported in ICRP Publication 89 (ICRP 2002). The initial vein diameters were set to 0.75 cm , the average large vein diameter reported by ICRP Publication 89 (ICRP 2002), and the terminal vein diameters were set to 0.85 cm at the distal end of the vessel. The arteries originate just below the base of the skull and terminate just above the thoracic spine. The veins originate just below the base of the skull, curve over the first rib, and terminate in the space adjacent to the junction of the clavicles and scapulae. The artery and vein volumes in the neck and clavicles for the adult male were 2.5 cm^3 and 20.0 cm^3 , respectively. The NURBS blood vessel model of the neck and clavicles can be seen in Figure 3-1 (A).

Arms

The arteries modeled in the arms represent the brachial, radial, and ulnar arteries. The veins modeled in the arms represent the axillary, cephalic, brachial, basilica, radial, and ulnar

veins. One artery was placed on the anterior of the arms and one vein was placed on the posterior. Only one vessel was used on either side due to space constraints and difficulty of modeling. Both the artery and the vein originate just below the distal humerus and terminate just above the carpal bones. The artery diameter was set to 0.58 *cm*, the average of the large artery and vein diameters reported in ICRP Publication 89 (ICRP 2002), and the vein diameter was set to 1.0 *cm*, the maximum vein diameter reported in ICRP Publication 89 (ICRP 2002). These diameters were chosen to stay within the bounds of the vessel diameters reported in ICRP Publication 89 but were defined according to the space available. The artery and vein volumes in the arms for the adult male were 29.9 *cm*³ and 91.5 *cm*³, respectively. The NURBS blood vessel model of the arms can be seen in Figure 3-1 (B).

Thoracic and abdominal region

The arteries modeled in the thoracic and abdominal regions represent the aortic arch and thoracic and abdominal aortas. The veins modeled in the thoracic and abdominal regions represent the superior and inferior vena cava. Due to space constraints, only two vessels were placed in the thoracic region and only two were placed in the abdominal region. Because of this, the actual form of the aortic arch could not be modeled. The artery and vein in the thoracic region were placed just anterior to the thoracic spine, originating inferior to the larynx and terminating just superior to the bronchi. Both vessel diameters were set to 0.58 *cm*, the average of the large artery and vein diameters reported in ICRP Publication 89 (ICRP 2002). The artery and vein in the abdominal region were placed just anterior to the thoracic spine, originating just inferior to the bronchi and terminating just superior to the small intestine. The initial (superior end) vessel diameters for the abdominal vessels were set to 0.58 *cm*, the average of the large artery and vein diameters reported in ICRP Publication 89 (ICRP 2002), and the terminal

(inferior end) vessel diameters were set to 0.40 *cm* due to space constraints. The artery and vein volumes in the thoracic and abdominal regions for the adult male were both 5.7 *cm*³. The NURBS blood vessel model of the thoracic and abdominal regions can be seen in Figure 3-1 (C).

Legs

The arteries modeled in the legs represent the femoral, popliteal, anterior tibial, and posterior tibial arteries. The veins modeled in the legs represent the left and right femoral veins. One artery was placed on the anterior of the arms and one vein was placed on the posterior. Only one vessel was used on either side due to space constraints and difficulty of modeling. Both vessels originate just below the distal femur and terminate just above the talus bone. The vein diameter was set to 1.0 *cm*, the maximum vein diameter reported in ICRP Publication 89 (ICRP 2002). The artery diameter was set to 0.58 *cm*, the average of the large artery and vein diameters reported in ICRP Publication 89 (ICRP 2002). The artery and vein volumes in the legs for the adult male were 45.2 *cm*³ and 133.0 *cm*³, respectively. The NURBS blood vessel model of the legs can be seen in Figure 3-1 (D).

Whole-body

The total large artery and vein volume was not matched because of space constraints. As previously discussed, this was not considered critical because the remainder of the volume would be apportioned uniformly to the rest of the body for the simulation of a whole-body blood source. The total reference blood volume in the adult male is 5.3 *L*, and large arteries and veins account for 24% of the total blood volume (ICRP 2002). Therefore, the targeted large artery and vein volume was 1.27 *L*. The actual total artery and vein blood volume modeled in the adult male phantom was 0.33 *L*, 74% less than the targeted value.

Remainder of Phantom Family

The anatomy of the blood vessel systems for the rest of the UF hybrid phantom family was held constant from the UFHADM phantom model. The same large arteries and veins were represented in each region of the body, and the same method of creating blood vessels in *Rhinoceros*TM was used in each phantom.

The blood vessel system for the UFHADDF phantom was created by slightly scaling down the vessel diameters from the adult male. The total reference blood volume in the adult female is 3.9 L, and large arteries and veins account for 24% of the total blood volume (ICRP 2002). Consequently, the targeted large artery and vein volume was 0.94 L. The actual total artery and vein blood volume modeled in the adult female phantom was 0.28 L, 70% less than the targeted value.

The blood vessel system for the UFH00MF phantom was then created by scaling down the vessel diameters from the adult male to proportionally fit the newborn phantom. It was assumed that the regional percent volume distribution of blood in the large arteries and veins, relative to total blood volume, was independent of age. The total reference blood volume in the newborn is 0.27 L, and large arteries and veins account for 24% of the total blood volume (ICRP 2002). As a result, the targeted large artery and vein volume was 0.065 L. The actual total artery and vein blood volume modeled in the newborn phantom was 0.011 L, 83% less than the targeted value.

The blood vessels in the UFH01MF, UFH05MF, UFH10MF, and UFH15M male phantoms were created by linearly interpolating between the vessel diameters in the UFH00MF and UFHADM phantoms. Next, the diameters of the veins in the legs were adjusted to preserve the desired total vein to artery volume ratio of 3:1. The final NURBS models of the UF hybrid phantom family blood vessel systems can be seen in Figure 3-2. The blood vessel volumes and

comparisons to reference values as a function of age can be seen in Table 3-1, and the blood vessel diameters as a function of age can be seen in Table 3-2.

Vascular Dosimetry

Since blood vessel walls could not be explicitly modeled in the UF phantom family and the existing blood vessel system is not comprehensive, calculating absorbed dose to the blood vessel walls presented a challenge. A systematic methodology was used to ascertain a reasonable approach for providing absorbed dose estimates to blood vessel walls by varying the size of the blood vessel lumen, wall thickness, vessel length, and vessel separation and simulating photons and electrons of varying energies. An abbreviated set of simulations was executed to investigate any possible perturbation of the dosimetry results due to variations in elemental composition in the surrounding tissue. For example, how does the absorbed dose to the blood vessel wall from photon and electron sources in its own lumen change if soft tissue surrounds the vessel rather than more blood vessels? The answer to this question would determine if backscatter contributions from surrounding tissue change significantly depending on the tissue adjacent to the blood vessel. A 0.72% average absolute variation was observed for this study, indicating that the results of the extensive simulation set could be taken at face value and not subjected to further criticism based on elemental composition variations surround the vessel.

Figures 3-3 and 3-4 show some initial dosimetric trends from the comprehensive simulation study. These figures show absorbed dose to the blood vessel wall from its contents but does not include any cross-dose from the adjacent blood vessel. As expected, absorbed dose to the blood vessel walls is highly dependent on source particle energy. According to Figures 3-3 and 3-4, absorbed dose estimates are also influenced by the physical size of the vessel (lumen diameter and vessel length). Absorbed dose to the vessel wall decreases with increases in lumen diameter and vessel length. More attenuating material is present when lumen diameter increases,

so the dose to the vessel walls would be expected to decrease due to more interactions in the blood. Additionally, increases in lumen diameter also presents more attenuating material along the axis of the blood vessel in addition to an increase in the overall mass of the vessel wall, leading to a decrease in the vessel wall dose.

In keeping with the average dose approach used in the monoenergetic photon and electron SAF studies, an approach to estimate the average whole-body SAF for the blood vessel walls was investigated. It was beyond the scope of this study to estimate local absorbed dose to vessel walls for non-uniform irradiation scenarios. Therefore, for a distributed blood source, it was assumed that the radiation source was actually uniformly distributed throughout all blood vessels in the body. A dose-averaging methodology for estimating vessel wall dose is presented in Chapter 4.

Skeletal Photon Fluence-to-Dose Response Functions

Single-Image Radiation Transport Simulations

As detailed earlier, electrons were simulated as uniform sources in voxel models of the spongiosa and MCs in whole bone sites of the UFH01MF, UFH05MF, and UFH10MF skeletons to calculate AFs and their complement, EFs. Results for the uniform electron source in the spongiosa of the cranium of the UFH01MF phantom are shown in Figure 3-5. According to the figure, $\phi(\text{spongiosa} \leftarrow \text{spongiosa}, E_i)$ remained close to 1.00 until approximately 100 keV due to the short range of low- to mid-energy electrons and the large volume of the source tissue. At energies greater than 100 keV, the AF for spongiosa self-dose decreased as the electrons attained sufficient energy to escape the spongiosa. $\phi(\text{cortical bone} \leftarrow \text{spongiosa}, E_i)$ was approximately zero until an energy of 100 keV. The AF then increased to a peak at around 1 MeV and decreased at energies greater than 1.5 MeV. Initially, the electrons did not attain enough kinetic energy to deposit energy in the surrounding cortical bone. Then, as the initial

energy increased, electrons began to deposit an increasing amount of energy in the cortical bone until the electrons had sufficient energy to penetrate through the cortical bone and deposit energy in tissues outside of the whole cranium. Finally, $\phi(\text{other} \leftarrow \text{spongiosa}, E_i)$ remained close to zero until an energy of about 400 keV and increased with increasing energy as the high energy electrons began to penetrate through the cortical bone and deposit energy in tissues outside of the whole cranium.

Spongiosa/MC self-dose AFs for all bone sites in the UFH01MF phantom are depicted in Figure 3-6, and AFs for the spongiosa/MC irradiating cortical bone for all bone sites in the UFH01MF phantom are in Figure 3-7. Spongiosa/MC EFs for all bone sites in the UFH01MF phantom can be seen in Figure 3-8. Due to the large number of bone sites, a legend was omitted so that the general shape of the various curves could be observed. All bone sites exhibit the same general behavior for spongiosa/MC self-dose and spongiosa/MC irradiating cortical bone but to varying degrees. MCs tended to have the greatest EFs due to very little or no trabecular bone present in addition to their overall dimensions. Electrons have greater ranges in bone marrow than homogeneous spongiosa due to the high atomic number of mineral bone, and so they escape into cortical bone and beyond at lower energies than other bone sites. The shape of $\phi(\text{spongiosa/MC} \leftarrow \text{spongiosa/MC}, E_i)$, $\phi(\text{cortical bone} \leftarrow \text{spongiosa/MC}, E_i)$, and $EF(\text{spongiosa/MC}, E_i)$ are all driven by the geometry and elemental composition of the bone sites themselves.

Response Functions

Described in Chapter 2, skeletal fluence-to-dose response functions were developed to allow the assessment of absorbed dose to radiosensitive skeletal tissues given tallied values of photon fluence incident upon the spongiosa or medullary cavity regions of the phantom's

skeleton. The mandible was chosen as a representative bone site to display the skeletal photon fluence-to-dose response function results. Values of both fluence-to-dose and fluence-to-kerma response functions for photon interactions in the mandible can be seen in Figure 3-9. The results were shown with units of absorbed dose or kerma per unit photon fluence ($Gy - m^2/photons$). As shown in Equation 2-24, a unit conversion factor is needed to convert the original skeletal photon fluence-to-dose response function units to the final desired SAF units in units of kg^{-1} .

Examining first the skeletal photon fluence-to-dose response function calculated for the AM target, it should be noted that the source was total spongiosa which was comprised of both TM (in the case of the UFH00MF phantom, TM and AM are equal) and TB, and thus the dose response was assessed for a fluence of photons incident on the spongiosa. In turn, the source term was defined as electrons liberated in both TM and TB. The skeletal photon fluence-to-dose response function for the AM target originates at a value just below $10^{-15} Gy - m^2/photons$ for a photon energy of $10 keV$. This was due to the fact that the resultant secondary electrons, initiated at a comparable low energy, had very short ranges and primarily deposited most of their energy at the site in which they were born. Consequently, secondary electrons born to photon interactions in bone trabeculae were unlikely to exit and irradiate the adjacent marrow cavities. As the incident photon energy increased to about $90 keV$, the skeletal photon fluence-to-dose response function declined due to the sharp decline in the photon mass interaction coefficient. As the incident photon energy increased past $90 keV$, the skeletal photon fluence-to-dose response function increased because the secondary electrons had enough energy to penetrate completely through the trabeculae and into adjacent regions of AM. At energies greater than $1 MeV$, the skeletal photon fluence-to-dose response function began to decline because those response function calculations were based on AF data which assumed that all initiated electrons

attained enough energy to mostly escape from the spongiosa into the cortical bone (Pafundi *et al.* 2010). However, as will be discussed later, the escape of electrons into cortical bone is actually compensated by electrons born in cortical bone and entering spongiosa.

The shape of the skeletal photon fluence-to-dose response function for the TM_{50} target can be explained in the same way as the skeletal photon fluence-to-dose response function for the AM target. However, it was evident that at intermediate incident photon energies, the response function for the TM_{50} target was slightly greater than the response function for the AM target. This is because as incident photon energy increased, the first layer of tissue that the secondary electrons escaping from TB regions encounters is the TM_{50} layer. While some AM is also included in the TM_{50} layer, the TM_{50} is much smaller, so energy deposition drives the absorbed dose for TM_{50} more drastically as electrons begin to escape the TB regions.

While this discussion addresses the general shape of the skeletal photon fluence-to-dose response functions in light of physical processes taking place, the shape and dose enhancement characteristics were heavily dependent upon the photon interaction cross-sections (probabilities of photons undergoing interactions in the various materials of interest). For example, dose enhancement takes place because photons are more likely to interact with high atomic number materials such as mineral bone at lower energies than low atomic number materials such as bone marrow (Attix 2004). Electrons created in marrow begin to escape into adjacent regions of trabeculae while electrons created in trabeculae begin to escape into adjacent marrow cavities. However, since photons preferentially interact in trabeculae, more electrons are escaping into marrow cavities at lower (10 keV to 90 keV) energy ranges than into trabeculae.

As previously noted, the skeletal photon fluence-to-dose response functions were calculated based on AF data which assumed secondary electron escape from the spongiosa into

surrounding cortical bone (Pafundi *et al.* 2010). However, this model did not take into account secondary electrons born in the surrounding cortical bone entering the spongiosa. At high incident photon energies (200 *keV* and greater), electrons born in cortical bone entering spongiosa compensate for electrons born in spongiosa entering cortical bone, creating CPE conditions. Physically, this process can be represented by assuming the secondary electrons created in the spongiosa as depositing all of their initial energy at the site of interaction, a model known as the kerma approximation. Therefore, the final skeletal photon fluence-to-dose response functions were constructed as a forced convergence between the skeletal photon fluence-to-dose response functions based on the original AF data and response functions based on the kerma approximation. At the point where the skeletal photon fluence-to-dose response functions began to deviate from the skeletal photon fluence-to-kerma response functions, the dose response functions were replaced by the kerma response functions. This divergence point was generally around 200 *keV*. It can be seen that there was a slight difference between the kerma response for spongiosa and the kerma response for the AM target. The kerma response for spongiosa was chosen to develop the final the skeletal photon fluence-to-dose response functions because no skeletal microstructure is present in the UF computational phantoms. The spongiosa/MC regions were the only regions that were able to be tallied for photon fluence. Complete skeletal photon fluence-to-dose response functions for the AM and TM₅₀ targets in the UFH00MF phantom can be seen in Figures 3-10 and 3-11, respectively. Due to the large number of bone sites, a legend was omitted so that the general shape of the various curves could be observed.

Age-related variations in the response functions for the AM and TM₅₀ targets are shown in Figures 3-12 and 3-13, respectively, and the cervical vertebra was chosen as the bone site for

demonstration. For the AM target in Figure 3-12, the response functions are mostly equal at high and low incident photon energies where dose enhancement is not a driving factor. At low energies, most of the liberated electrons are absorbed in the vicinity of where they are created while at high energies CPE conditions eliminate dose enhancement effects. In the mid-range energies, from about 30 *keV* to about 100 *keV*, dose enhancement becomes important, and a noticeable separation of response function values materializes. A systematic age-dependence is observed for the AM target in this case where the younger phantoms experience higher doses per unit photon fluence incident upon the spongiosa of the cervical vertebra. Higher dose to AM at younger ages probably occurs because of the smaller thicknesses of bone trabeculae. Electrons escape the trabeculae quicker at younger ages than for older ages when the bone trabeculae are thicker. Relative to the UFH00MF response functions, absolute percent differences for the rest of the pediatric and adolescent response functions across all energies were on average 5% with minimum and maximum differences of 1% and 18%, respectively.

As was the case for the AM target, Figure 3-13 shows that all response functions are approximately equal at higher energies for the TM_{50} , from about 300 *keV* to 10 *MeV*, due to CPE conditions. Age-related differences are evident from 10 *keV* to about 200 *keV*. The differences do not appear to be systematic, but this is plausible because the irradiation geometry is different than that for the AM target. AM is distributed throughout the marrow cavities in different concentrations depending on cellularity (fraction of marrow space occupied by AM) while TM_{50} is always the 50 μm deep tissue layer directly adjacent to trabecular bone, containing both AM and IM. Since this tissue is a thin layer adjacent to the enhanced source of electrons (trabecular bone), it is more greatly affected by dose enhancement at lower energies than the AM target. Relative to the UFH00MF response functions, absolute percent differences

for the rest of the pediatric and adolescent response functions across all energies were on average 4% with minimum and maximum differences of 0.1% and 24%, respectively.

Photon Specific Absorbed Fractions

Photon SAFs were computed for the entire UF hybrid phantom family (12 phantoms) using simulation and variance reduction techniques described in the “Photon Specific Absorbed Fractions” section of Chapter 2. One large organ and one small organ, the liver and thyroid, in the UFH00MF phantoms were chosen as two representative source tissues to display the photon SAF results. A small subset of the photon SAF curves for these source tissues can be seen in Figure 3-14. Since the liver is a large organ, the reverse Monte Carlo method of variance reduction was very effective and is evident in the smoothness of the SAF curves. Average statistical uncertainties for initial photon energies greater than or equal to 20 keV for the liver and thyroid sources were 0.23% and 1.77% respectively. The final SAF values for both the liver and thyroid sources were considered to be very reliable since most statistical uncertainties were well below 10%. In fact, over the energy range of $E \geq 20 \text{ keV}$, the greatest average statistical uncertainty was 3.69% for the pituitary gland target. The SAFs will be made available in table format with the variance reduction techniques specified for each target organ – an *E* is used to indicate log-linear back-extrapolation, an *R* was used to indicate reverse Monte Carlo, and an *S* was used to indicate 3-point smoothing. These tables will be made available as electronic appendices in upcoming publications. An abbreviated excerpt of the SAFs for the UFH00MF pituitary gland source is in Table 3-3. While these extensive tables will be available for direct usage, they will be incorporated into the internal dosimetry software for ease of use. Most applications will not directly access the SAFs, but they are integral to the establishment of a final set of radionuclide *S* values for the dosimetry software.

The different shapes of the photon SAF curves can be explained by a combination of organ shapes, separation, and photon interaction coefficients (Figure 3-15) (NIST 2011, ICRP 2002). Most photon SAFs curves had the same approximate shape as seen in Figure 3-14. An initial increase is seen as the photon fluence incident on the target tissues increases. At this energy range between approximately 10 *keV* to just less than 100 *keV*, the total photon mass attenuation coefficient is about an order of magnitude greater than at higher energies. Photon interaction effects begin to take over at energies just less than 100 *keV* and are visualized by a sharp decrease in the SAF until photon energies increase to just greater than 100 *keV*. At this point, the SAF remains somewhat constant, rising and falling slightly between 100 *keV* and 4 *MeV*, due to the interplay between the penetrability of high energy photons, the energy of those photons, and the slightly decreasing total photon interaction coefficient. As photon energy increases, interaction probabilities in the target tissues of interest decrease slightly, but the energy imparted when undergoing an interaction is generally greater, so these two processes work against each other. The only photon SAF curves that begin at a maximum and subsequently assume the general curve shape for any source tissue are the curves for the source tissue as a target (self-dose) and for cases when the whole body is the target tissue. This is because both target tissues include the source tissue as part of the target, and the source tissue experiences photon interactions at high fluences for the 10 *keV* photons. As the photons increase in energy, they increasingly escape from the source tissue, seen as an immediate decline in the SAF. While most curves have the same general shape, most are slightly different in curve grade and location of the peak. This characteristic may be due to both the 3-D shape of the target tissue and the distance from the source. Some anomalies also arise from the log-linear back-extrapolation variance reduction technique. For example, a curve may bend much sharper than

usual or may flatten out at lower energies. These artifacts were seen to occur at low SAF magnitudes.

Age-dependent SAF curves were generated to demonstrate the range of values and similarity of curve shapes for certain source-target combinations. Five irradiation scenarios were chosen to include most possible types of irradiation geometries: large and small organ self-dose, a large organ irradiating a large organ, a small organ irradiating a large organ¹, and a small organ irradiating a small organ. SAFs chosen to display age-related trends were $\Phi(\text{liver} \leftarrow \text{liver})$, $\Phi(\text{adrenals} \leftarrow \text{adrenals})$, $\Phi(\text{muscle} \leftarrow \text{lungs})$, $\Phi(\text{brain} \leftarrow \text{thyroid})$, and $\Phi(\text{adrenals} \leftarrow \text{thyroid})$, and these results are shown in Figures 3-16 through 3-20.

$\Phi(\text{liver} \leftarrow \text{liver})$ – Figure 3-16. This irradiation geometry examines the age- and energy-dependent trends for large organ self-dose. It was expected that as the phantom age increased, the liver self-dose SAF at each initial photon energy would decrease due to reasons discussed in the photon self-dose mass scaling sections of this document. As organ size increases, photon self-dose decreases due mainly to increasing organ mass, and this is observed in Figure 3-16. $m_{\text{liver}}(\text{UFH00MF}) < m_{\text{liver}}(\text{UFH01MF}) < m_{\text{liver}}(\text{UFH05MF}) < m_{\text{liver}}(\text{UFH10MF}) < m_{\text{liver}}(\text{UFH15M}) < m_{\text{liver}}(\text{UFH15F}) < m_{\text{liver}}(\text{UFHADDF}) < m_{\text{liver}}(\text{UFHADM})$, and thus $\Phi_{\text{liver}}(\text{UFH00MF}) > \Phi_{\text{liver}}(\text{UFH01MF}) > \Phi_{\text{liver}}(\text{UFH05MF}) > \Phi_{\text{liver}}(\text{UFH10MF}) > \Phi_{\text{liver}}(\text{UFH15M}) > \Phi_{\text{liver}}(\text{UFH15F}) > \Phi_{\text{liver}}(\text{UFHADDF}) > \Phi_{\text{liver}}(\text{UFHADM})$. In addition, the general shape of all the curves as a function of energy followed the description previously discussed. The SAFs originate at a peak at 10 keV, decrease through the mid-range energies, and form a gentle rise over the higher energies.

¹ A large organ irradiating a small organ was omitted from this demonstration because the reciprocity principle renders that irradiation scenario approximately equal to a small organ irradiating a large organ.

$\Phi(\textit{adrenals} \leftarrow \textit{adrenals})$ – **Figure 3-17.** This irradiation geometry examines the age- and energy-dependent trends for small organ self-dose. The same dose trend as $\Phi(\textit{liver} \leftarrow \textit{liver})$ was observed for $\Phi(\textit{adrenals} \leftarrow \textit{adrenals})$, and this was expected. The adrenal self-dose SAFs were in reverse order from the order of their masses. Energy-dependent trends for photon self-dose were also observed for this irradiation scenario.

$\Phi(\textit{muscle} \leftarrow \textit{lungs})$ – **Figure 3-18.** This irradiation geometry examines the age- and energy-dependent trends for a large organ irradiating a large organ. Muscle is distributed throughout the phantoms, so statistical uncertainties were very low, as evidenced by the smoothness of the SAF curves. Age-dependent trends follow what one would expect, in general. As phantom size increases (with increases in subject age), separation between the lungs and muscle increase, causing a decrease in SAF. In addition, the lungs and muscle are both increasing in size, causing more self-attenuation in the lungs. Increases in muscle mass increase the denominator in the SAF equation, and in combination with the increases in attenuation, cause the muscle SAF to decrease. Energy-dependent trends for photon cross-dose as discussed previously are also observed in this cross-dose example.

$\Phi(\textit{brain} \leftarrow \textit{thyroid})$ – **Figure 3-19.** This irradiation geometry examines the age- and energy-dependent trends for a small organ irradiating a large organ. Although a small organ is included in this cross-dose irradiation scenario, the target organ is large, ensuring low statistical uncertainties. Age-dependent trends follow those observed for $\Phi(\textit{muscle} \leftarrow \textit{lungs})$. Energy-dependent trends are a little different for this irradiation geometry. When the target organ is very distant from the source organ, curve shapes such as those for the UFHADM phantom in this example are observed. No peak around 40 keV to 50 keV is seen because most photons have experience multiple interactions before reaching the target tissue. A peak is present for the

UFH00MF phantom in this example and remains to an increasingly lesser degree for the UFH01MF and UFH05MF phantoms as the separation between the brain and the thyroid for these phantoms is much less than seen in the older phantoms. The separation between brain and thyroid for the UFH00MF phantom is less than that for the UFH01MF which is in turn less than that for the UFH05MF phantom.

$\Phi(\text{adrenals} \leftarrow \text{thyroid})$ – **Figure 3-20.** This irradiation geometry examines the age- and energy-dependent trends for a small organ irradiating a small organ. Since both organs in this example are small, statistical uncertainties could pose problems in establishing a reference set of SAF values. However, all three variance reduction techniques were applied in this situation, and the results, while not perfect, still give reasonable SAF curves. The same trends explained in the $\Phi(\text{brain} \leftarrow \text{thyroid})$ example apply here. Comparison of the SAF curves for the UFH00MF and UFH01MF phantoms may give one pause since the UFH00MF curve would be expected to be greater than the UFH01MF curve, but the reference masses of the adrenals in the UFH00MF phantom are actually larger than those in the UFH01MF phantom.

Electron Specific Absorbed Fractions

Electron SAFs were computed for the entire UF hybrid phantom family (12 phantoms) using simulation and variance reduction techniques described in the “Electron Specific Absorbed Fractions” section of Chapter 2. For comparison purposes, all SAFs generated in the validation study described later (uniform electron source in the UFH00M liver) were shown in Figure 3-21². Due to the large number of target tissues, a legend was omitted so that the general shape of the various SAF curves could be observed. Clearly, many target tissues suffer from poor statistical uncertainties, visualized as erratic and sometimes non-existent curve shapes.

² See the “Electron Specific Absorbed Fractions” section of the Chapter 4 for details on the validation simulation. Also, see Figure 4-10 for graphical results of the validation study.

To display the final electron SAF results, one large organ and one small organ, the liver and thyroid, in the UFH00MF phantoms were chosen as representative source tissues. A small subset of the electron SAF curves for these source tissues can be seen in Figure 3-22. Since the liver is a large organ, the reverse Monte Carlo method of variance reduction was very effective and is evident in the smoothness of the SAF curves. Additionally, the spectrum weighting method of calculating radiative energy loss contributions to dose is manifested in the smooth curves for those target tissues who do not receive primary electron dose. Average statistical uncertainties for initial electron energies greater than or equal to 20 keV for the liver and thyroid sources were 3.17% and 4.45%, respectively. The final SAF values for both the liver and thyroid sources were considered to be very reliable since most statistical uncertainties were below 10%. Over the energy range of $E \geq 20 \text{ keV}$, the greatest average statistical uncertainty was 11.26% for the testes source. Some statistical uncertainties associated with the electron SAFs exceeded 10%. However, while electron transport methods have been improved in this study, statistical uncertainties for computational electron dosimetry remain an area for improvement. The electron SAF tables are formatted in the same manner as the photon SAF tables (see Table 3-3 for reference). Again, while these extensive tables will be available for direct usage, they will be incorporated into the internal dosimetry software for ease of use. Most applications will not directly access the SAFs, but they will be integral to the establishment of the final set of radionuclide S values for direct use in the internal dosimetry software. A representative table of electron SAFs was not displayed because the electron SAF tables are exactly like the photon SAF tables in format.

The different shapes of the electron SAF curves can be explained by a combination of source/target organ separation and electron interaction mechanisms. Four distinct groups of

electron SAF curves may be defined with the following arbitrary terms – (1) self-dose, (2) full-collisional, (3) partial-collisional, and (4) full-radiative.

Self-dose curves are identified as relatively flat curves with slight downturns at the highest energies. For any given source tissue, the self-dose curves belong to the source tissue itself and the whole body as a target. Since electron ranges are so small, no appreciable electron energy escapes either the source tissue itself or the body as a whole. Only at the highest energies do bremsstrahlung losses begin to account for increasingly reduced energy deposition in these target tissues. The target tissues exhibiting self-dose SAF curve behavior in Figure 3-22 (A) are the liver and whole-body.

A second curve type has been designated the term “full-collisional”, indicating that from the lowest electron energies, the target tissue receives energy deposition from collisional energy losses. These curves can be identified as relatively log-linearly³ increasing over the energy range 10 keV to 4 MeV due to CSDA. Electrons experience many small interactions along their path rather than several catastrophic interactions as in the case of photons (Attix 2004). As the initial electron energy increases, a proportional amount of energy is deposited into the target material with no appreciable increase in target tissue escape. One tissue exhibiting full-collisional SAF curve behavior in Figure 3-22 (A) are the adrenal targets. Full-collisional electron SAF curves are generally characteristic of tissues directly adjacent to the source tissue.

Another electron SAF curve type can be thought of as “partial-collisional”. In other words, primary electrons are not incident upon the target until a certain energy threshold is reached. Until that point, dose contributions to the target are solely from radiative losses by the primary electrons. Partial-collisional curves can be recognized by two distinct curve regions,

³ Appearing linear on a log-log scale.

where the first region assumes a shape similar to many photon SAF curves for distant target tissues, and the second region demonstrated a sharp increase once primary electrons have CSDA ranges allowing them to reach the target tissue. One would expect the low energy region curve shapes to resemble photon SAF curve shapes since the low energy regions of electron SAFs for partial-collisional curves reflect only photon contributions. The thoracic lymph node target tissue is an example of a partial-collisional electron SAF curve in Figure 3-22 (A).

The final electron SAF curve type was named “full-radiative” to indicate that dose contributions to the target tissue of interest could be entirely attributed to radiative losses of the primary electrons. Absorbed dose to these target tissues are a result of bremsstrahlung and characteristic x ray energy deposition, and so the expected curve shape would be along the lines of what is seen for photon SAFs, and this is indeed observed. Note that the full-radiative curves are a spectrum weighting of many different monoenergetic photon SAFs, not a single photon SAF. Full-radiative curve behavior is seen for the brain target in Figure 3-22 (A).

Age-dependent SAF curves were generated to demonstrate the range of values and similarity of curve shapes for certain source-target combinations. Five irradiation scenarios were chosen to include most possible types of irradiation geometries: large and small organ self-dose, a large organ irradiating a large organ, a small organ irradiating a large organ⁴, and a small organ irradiating a small organ. SAFs chosen to display age related trends were $\Phi(\text{liver} \leftarrow \text{liver})$, $\Phi(\text{pituitary gland} \leftarrow \text{pituitary gland})$, $\Phi(\text{muscle} \leftarrow \text{lungs})$, $\Phi(\text{brain} \leftarrow \text{thyroid})$, and $\Phi(\text{salivary glands} \leftarrow \text{thyroid})$, and the results are shown in Figures 3-23 through 3-27.

$\Phi(\text{liver} \leftarrow \text{liver})$ – Figure 3-23. This irradiation geometry examines the age- and energy-dependent trends for large organ self-dose. It was expected that as the phantom age

⁴ A large organ irradiating a small organ was omitted from this demonstration because the reciprocity principle renders that irradiation scenario approximately equal to a small organ irradiating a large organ.

increased, the liver self-dose SAF at each initial electron energy would decrease due to reasons discussed in the electron self-dose mass scaling sections. As organ size increases, electron self-dose decreases, and this is observed in Figure 3-23. In addition, the general shape of all the curves as a function of energy followed the description previously discussed. The SAFs originate at a peak at 10 keV and slowly decrease as electron escape increases, accelerating at higher energies. The downturns of the electron self-dose SAFs are more pronounced for the younger phantoms because electron escape increases with decreases in organ size.

$\Phi(\text{pituitary gland} \leftarrow \text{pituitary gland})$ – Figure 3-24. This irradiation geometry examines the age- and energy-dependent trends for small organ self-dose. The same dose trend as $\Phi(\text{liver} \leftarrow \text{liver})$ was observed for $\Phi(\text{adrenals} \leftarrow \text{adrenals})$, and this was expected. Electron escape at higher energies is even more pronounced in this example because of the small size of the organ. The distinct electron escape region demonstrates that the MIRD Pamphlet No. 11 recommendation of self-dose absorbed fractions of unity for electrons cannot be considered valid at higher energies, in this case at energies greater than 300 keV.

$\Phi(\text{muscle} \leftarrow \text{lungs})$ – Figure 3-25. This irradiation geometry examines the age- and energy-dependent trends for a large organ cross-irradiating a large organ. Muscle is distributed throughout the phantoms, so statistical uncertainties were very good, as evidenced by the smoothness of the SAF curves. Age-dependent trends follow those seen for the $\Phi(\text{muscle} \leftarrow \text{lungs})$ photon example. Energy-dependent trends for electron cross-dose for this irradiation scenario are indicative of the full-collisional electron SAF curve type. The SAFs continue to increase as the electrons attain more and more energy, escaping into adjacent regions.

$\Phi(\text{brain} \leftarrow \text{thyroid})$ – Figure 3-26. This irradiation geometry examines the age- and energy-dependent trends for a small organ cross-irradiating a large organ. Although a small

organ is included in this cross-dose irradiation scenario, the target organ is large, ensuring low statistical uncertainties. These SAF curves are indicative of full-radiative electron SAF curves and were calculated as spectrum weighted photon SAFs. As a result, age-dependent and energy-dependent trends would be expected to follow those seen for large separation photon cross-dose SAF curves, and this is indeed the case. These SAFs decrease with increasing age/organ size and separation and increase gradually with electron energy.

$\Phi(\text{salivary glands} \leftarrow \text{thyroid})$ – Figure 3-27. This irradiation geometry examines the age- and energy-dependent trends for a small organ cross-irradiating a small organ. Since both organs in this example are small, statistical uncertainties could pose a problem. However, reciprocity and spectrum weighting were performed for this source-target combination, and the results give reasonable SAF curves. Both partial-collisional and full-radiative electron SAF curve types are observed in this example. Partial-collisional curves are seen for phantoms at a younger age due to decreased organ separation. Organ separations in these cases are approximately less than or equal to the electron range at the energy of interest, so primary electron interactions are taking place in the target tissue.

Dosimetric Sensitivity Studies

Variation in Source and Target Size and Separation

Photon self-dose

The largest absorbed doses are observed when the source and target are the same tissue, so non-reference dose scaling techniques for self-irradiation is important. Since any dose scaling will be accomplished with computer codes, simplistic empirical equations were not a priority. The data was processed to reveal the most accurate technique for scaling reference doses to non-reference doses. Statistical uncertainties were less than 0.1% for all sphere sizes due to the large number of interactions in the source tissue. Results for photon self-dose SAFs at all sphere

masses and photon energies are shown in Figure 3-28. Variable scaling parameters were expected due to the variations in curve shapes as a function of energy and sphere mass (e.g., it can be seen that the shape of the curve for the 1 kg sphere is markedly different that for the 1 g sphere).

The analysis was first performed for photon self-dose. At each photon energy, the SAF of the original sphere mass (termed the “reference” sphere mass) was divided by the SAFs of all other sphere masses (termed the “non-reference” sphere masses). For example, $\Phi(m = 1g)/\Phi(m = 2g)$, $\Phi(m = 1g)/\Phi(m = 3g)$, $\Phi(m = 1g)/\Phi(m = 4g)$, ..., $\Phi(m = 2g)/\Phi(m = 3g)$, $\Phi(m = 2g)/\Phi(m = 4g)$, ..., $\Phi(m = 8 kg)/\Phi(m = 10 kg)$. This approach was used because any dependence on the size of the original sphere would be illuminated, revealing any possibility that scaling the SAF of a small organ would require a different methodology than for a large organ. The variable R in Equation 3-1 was computed for every sphere mass combination.

$$\Phi_{non-ref} = \Phi_{ref} \left(\frac{m_{ref}}{m_{non-ref}} \right)^R \quad (3-1)$$

where $\Phi_{non-ref}$ is the SAF for the non-reference sphere, Φ_{ref} is the SAF for the reference sphere, m_{ref} is the mass of the reference sphere, and $m_{non-ref}$ is the mass of the non-reference sphere.

First, an overall average of the scaling power R was taken at each initial photon energy to examine possible energy dependence of the scaling powers, independent of the mass dependence. The results can be seen in Figure 3-29 along with the maximum, minimum, and MIRD Pamphlet No. 11 recommendation for the scaling power (Snyder *et al.* 1975). The mass scaling power was very much dependent on the initial photon energy with widely varying values

for energies less than 100 *keV* and greater than 1 *MeV*. After examining these scaling power curves, the recommendation to apply a scaling power of $-2/3$ seems only appropriate for a relatively narrow photon energy range, and not extendable to low and high energies (Snyder *et al.* 1975). Perhaps the recommendation was made for ease of use, but more rigorous approaches are possible with application of computer codes.

Wide variations of the mass scaling powers at high and low photon energies seemed to indicate that energy was only one of possibly several parameters upon which the mass scaling power depended. To investigate any possible mass dependence, the mass scaling powers were averaged over all non-reference sphere sizes at each energy and reference sphere size. The results can be seen in Figure 3-30. An 18% percent difference between the mass scaling powers of the 1 *g* and 10 *kg* spheres was observed at 30 *keV*, and a 37% difference was observed at 4 *MeV* between the same reference sphere sizes. Because of the apparent energy and mass dependence of the mass scaling powers, significant improvement over the MIRD 11 recommendation can be achieved by acknowledging and applying an energy and mass dependence on the photon self-dose scaling parameter.

Electron self-dose

Analysis methods used for the photon self-dose mass scaling study were repeated for electrons. Electron self-dose SAFs can be seen in Figure 3-31, and the results suggest from the outset that energy- and mass-independent scaling methodologies for electron self-dose may not be sufficient to accurately account for electron escape and photon production at higher electron energies (e.g., energy-dependence is evident for the 1 *g* sphere by the downward tilt of the SAF curve beginning at around 300 *keV*, and the curve shapes of the 1 *g* and 10 *kg* spheres are markedly different). Electron self-dose mass scaling powers are shown in Figure 3-32 along

with the MIRD Pamphlet No. 11 recommendation (Snyder *et al.* 1975). The MIRD recommendation of a scaling power of -1.00 relies on the assumption that the AF for electron self-dose is unity at all tissue masses and electron energies. However, results shown in Figure 3-32 indicate that energy dependence becomes important at electron energies around 300 *keV* as electron escape begins to become significant. In addition, Figure 3-33 suggests that electron self-dose scaling powers should vary as a function of mass as well. A 27% percent difference between the mass scaling powers of the 1 *g* and 10 *kg* spheres was observed at 4 *MeV*. Electron self-dose AFs do not appear to remain close to unity at high energies and small sphere sizes.

Photon cross-dose

Next, dosimetric trends were investigated for photon cross-dose, recalling the irradiation geometry of varying sizes of concentric spheres. Reverse Monte Carlo was performed for all sphere combinations, and the SAF of the source-target combination with the lowest statistical uncertainty was retained. Seventeen sphere masses were simulated at 21 initial photon energies and 7 center-to-center separations. A representative cross-section of the results is displayed in Figures 3-34 and 3-35. Figure 3-34 illustrates variations of SAFs as a function of both distance from the source and target sphere mass with sub-figures (A), (B), and (C) showing the change in these relationships with varying source sphere masses.

From Figure 3-34 (A), it is unclear at first glance whether the difference in SAFs at the largest separation is due to real differences in dose or to statistical uncertainties at that particular irradiation geometry (4 *MeV* photon energy and 1 *g* source mass). The average statistical uncertainty for that irradiation geometry is 32.85% (4.53% – 99.64%), which is considered to be unreliable. However, the statistical uncertainties at the first two (and possibly third) separations were considered reliable at average uncertainties of 4.96%, 8.42%, and 11.51%,

respectively. Predictably, as the source mass increased, the variations in the SAF were minimized, a result of the statistical uncertainty effects of reverse Monte Carlo techniques. As the source sphere increased in size, more interactions occurred in the target sphere for the reverse Monte Carlo designation (e.g., SAFs for the 2 kg sphere irradiating the 1 g sphere were actually the SAFs for the 1 g sphere irradiating the 2 kg sphere). At the largest source mass, it is clear that no appreciable trends exist for dose differences with variations in target mass size at large distances. In looking at variations in target sphere dose with changes in source sphere size, very little deviation is seen between the minimum and maximum SAFs across all photon energies at each target sphere size and separation (see Figure 3-35 for 50 keV and 500 keV photons). Across the first six source-target separation distances and all target spheres, an average of 12% difference was seen between the maximum and minimum SAFs at each source-target separation distance and target sphere size. Qualitatively, it is clear that no appreciable trend exists for variations in target dose as a function of source size. However, SAFs certainly decrease with increases in center-to-center separation, and an attempt to predict this trend will be made later. If the center-to-center distance could be determined from an imaging procedure, perhaps the reference dose could be scaled to account for this geometry variation.

For the first-pass investigation of dosimetry sensitivity for photon cross-dose, it appeared that previous recommendations that dose to target tissues distant from source tissues was constant with changes in source and/or target size could be implemented without further investigation (Petoussi-Henss *et al.* 2007). However, some results for the low statistical uncertainty 4 MeV – 2 kg irradiation geometry seemed to indicate that this recommendation breaks down at source-target separations less than 15.63 cm, separations considered to be medium-distance. Differences between the maximum and minimum SAFs for the 4 MeV –

2 kg irradiation geometry from the 5th (78.16 cm) separation to the 1st (15.63 cm) separation were 3%, 4%, 2%, 2%, and 11%, respectively. Since the statistical uncertainties associated with this irradiation geometry were all less than 4%, the marked increase from 2% to 11% difference between the maximum and minimum SAFs from the 2nd to the 1st separation was more than likely due to actual differences in SAFs rather than to statistical uncertainties.

To further explore the possibility of cross-dose scaling at medium- to close-distance separations, a similar cross-dose computational experiment was designed allowing for center-to-center separations less than 15.63 cm. The experiment shared all important characteristics to the original cross-dose experiment except that only separations of 3.37 cm, 6.74 cm, 10.10 cm, and 13.47 cm and sphere masses of 1 g, 2 g, 4 g, 6 g, 8 g, 10 g, and 20 g were used. The number of sphere masses was limited due to overlap when larger spheres were located at these center-to-center distances (e.g., the 2 kg sphere radius of 7.82 cm would cause the spheres to overlap when their center-to-center distance was 3.37 cm).

Figure 3-36 shows photon SAFs as a function of sphere separation, target mass, and source mass for 4 MeV photons in the close- to mid-range distance simulations. Additionally, Figure 3-37 shows photon SAFs as a function of separation, target mass, and photon energy for the 20 g source sphere. It can be perceived from these figures that for higher energies, even at these close separations, the SAF does not vary considerable as a function of source or target mass.

However, Figure 3-37 gives evidence that dose scaling may be necessary for low energies, even for larger source masses. At each photon energy, separation, and source size, the minimum and maximum SAFs were compared across all target sizes. On average, the maximum SAF was 2.88% greater than the minimum SAF for energies 50 keV or greater but 337% greater for energies less than 50 keV. These results supported findings by others in this topic that dose to

distant targets need not be scaled with changes in the size of either the source or target organ (Petoussi-Henss *et al.* 2007), but trends observed at low energies and close separations demanded the possibility of mass-based dose-scaling methods for photon cross-dose under these more limiting conditions.

Electron cross-dose

The close- to mid-separation simulation set was also performed for electrons. Distant separations were not simulated for electrons because it was assumed that statistical uncertainties would be too poor to generate meaningful results. Results similar in format to those displayed for the photon cross-dose analysis are shown in Figures 3-38 and 3-39. Figure 3-38 shows that differences in electron SAFs at more distant center-to-center separations mimic those seen in the photon cross-dose simulations. However, at the closest separation of 3.368 *cm*, differences by orders of magnitude appears between the minimum and maximum SAFs, presumably due varying levels of primary electron dose contributions. Figure 3-39 seems to corroborate this presumption as most SAFs follow the photon trend for the 50 *keV* and 500 *keV* electron energies with the one exception being the 20 *g* target tissue at 3.368 *cm* separation for 500 *keV* electrons. To further investigate the nature of electron SAF variations with changes in source and target tissues, SAFs as a function of initial electron energy and target tissue size are shown for the 20 *g* source tissue and 3.368 *cm* separation in Figure 3-40. As noted when discussing the monoenergetic electron SAFs, these curves all show partial-collisional characteristics. The surface of each target sphere is located at a different distance from the source sphere despite the constant center-to-center separation. Primary electrons interact with the largest target sphere first, so the dose to the largest target sphere is greater than each subsequently smaller target sphere. This trend can be observed in Figure 3-40 at electron energies 1 *MeV* and greater.

Primary electron cross-dose scaling may be impractical to address since surface shape and surface separation affect the dose estimate much more than they do for photons. Electron cross-dose contributions from radiative losses, on the other, can be handled in the same way as the photon cross-dose simulations, and results show that distance scaling may be an option. Development of actual scaling methodologies will be addressed in the Chapter 4 of this dissertation.

Variation in Anthropometric Characteristics

Sitting height

The sitting heights of three anchor phantoms, the UFH00M, UFH10M, and UFHADM phantoms, were systematically adjusted, consistent with methods outlined in Johnson *et al.* (2009), and simulated with both monoenergetic photons and electrons uniformly distributed throughout the AM, brain, lungs, liver, and spleen of those phantoms. Absorbed dose in the form of the SAF was calculated for all source-target-energy combinations, and the results were examined to uncover any potential dose scaling methods.

An excerpt of the results for the 500 *keV* and 4 *MeV* photon simulations in the liver of the UFH00M-based phantoms are in Figure 3-41, and an excerpt of the results for the 500 *keV* and 4 *MeV* electrons simulations in the liver of the UFH00M-based phantoms are given in Figure 3-42. These graphs show the extent to which the monoenergetic SAFs change as a function of sitting height of the UFH00M-based phantoms. An overall gradual decrease in SAF is observed across almost all target tissues for both photons and electrons. Increasing organ-to-organ separations and organ sizes with increases in sitting height both contribute to the overall decrease in SAFs. Target tissues with increasing SAFs as a function of sitting height were assumed to display poorer statistical uncertainties, and this was found to be the case. Some of the target

tissues in the 500 *keV* electron simulations had poor statistical uncertainties and were therefore not useful in developing dose scaling factors.

Figure 3-43 shows whole-body dose for uniform 4 MeV photon and electron sources in the liver of all phantoms in the sitting height dose variation study. The whole-body SAF appears to be log-linearly⁵ decreasing with increases in sitting height for both photons and electrons.

Another feature of interest is the dependence of the whole-body SAF on the anchor phantom. One would not be able to simply scale absorbed doses according to relative sitting height because the anthropometric structure of each phantom age is different. For any dose scaling to occur, the anchor phantom must be specified. Then, a sitting height measurement could be taken and compared to the sitting height of the anchor phantom. Actual scaling methodologies will be discussed in the next chapter.

Weight

The weights of the same three anchor phantoms used for the sitting height dose sensitivity study, the UFH00M, UFH10M, and UFHADM phantoms, were systematically adjusted, consistent with methods outlined in Johnson *et al.* (2009), and monoenergetic photons and electrons were simulated as uniformly distributed throughout the AM, brain, lungs, liver, and spleen of the weight adjusted phantoms. SAFs were calculated for all source-target-energy combinations, and the results were examined to ascertain any dose scaling methods.

An excerpt of the results for the 500 *keV* and 4 *MeV* photon simulations in the liver of the UFH00M-based weight-scaled phantoms are in Figure 3-44, and an excerpt of the results for the 500 *keV* and 4 *MeV* electrons simulations in the liver of the UFH00M-based weight-scaled phantoms are in Figure 3-45. These graphs show changes in monoenergetic SAFs as a function

⁵ Appearing linear on a log-linear scale.

of weight of the UFH00M-based phantoms. However, instead of comparing the SAFs against weight, waist circumference is given as the parameter by which dose variations are analyzed as waist circumference potentially gives more information about the stature of the phantom than overall weight. In addition, this parameter is also easily obtained in the clinic. An overall gradual decrease in SAF is observed across most target tissues for both photons and electrons for the underweight phantoms. However, no appreciable decrease in organ doses is observed for the severely overweight phantom, as predicted by a previous study (Clark *et al.* 2010). Decreasing organ-to-organ separations and organ sizes in the underweight phantoms explains the increase in dose with decreases in waist circumference. It is intuitive that the overweight patient does not experience any dramatic changes in absorbed dose because the internal structure is the same as that of the anchor phantom. Only adipose tissue is added to the outer contour of the phantom, causing only limited increases in photon backscatter⁶. Poor statistical uncertainties were considered the culprit for target tissues displaying increasing SAFs as a function of waist circumference, and this was found to be a reasonable explanation. Some of the target tissues in the 500 keV electron simulations had poor statistical uncertainties and were difficult to correct, proving these target tissues to have limited application in determining scaling protocols.

Figure 3-46 shows whole-body dose for uniform 4 MeV photon and electron sources in the liver of all phantoms in the weight dose variation study. The whole-body SAF appears to be almost (but not exactly) log-linearly decreasing with increases in waist circumference for both photons and electrons. Scaling methodologies could potentially be developed by interpolating between the given data points. Like the sitting height study, absorbed dose appears to depend on

⁶ Again, intra-abdominal fat deposits were not considered in the current study, but would be worthwhile to investigate in future work.

the anchor phantom, and this should be taken into account when developing scaling methodologies. Actual scaling mechanisms will be discussed next in the Chapter 4.

Constant weight with morphometry variation

A previous study had looked at the issue of constant weight with morphometry variation by performing computational internal dosimetry and had found that the effective dose per unit AA to a tall, thin 32 kg patient is approximately 44% greater than the effective dose per unit AA to a short, fat 32 kg patient for $^{99m}\text{Tc} - \text{DMSA}$ (Sgouros *et al.* 2011). In the current study, the analysis performed for the 32 kg patient was repeated for two female patients at 50 kg.

Absorbed dose results for a select number of target tissues are in Table 3-4, and whole-body effective dose estimates are in Table 3-5. It can be seen from Table 3-4 that absorbed doses to all selected target tissues for the short, fat patient were greater than for the tall, thin patient. The dose to each tissue for the short, fat patient was on average 92% greater than the dose to the tissues of the tall, thin patient with no tissues of the tall-thin patient having a higher dose. Table 3-5 shows that the effective dose to the short, fat patient was 88% greater than the effective dose to the tall, thin patient. It was expected based on the study of Sgouros *et al.* (2011) that the dose to the short patient would be greater than the dose to the tall patient, and this trend was indeed observed. The dose differences are due to the relative proximity of all organs in the body. Less separation between organs in the short, fat patient causes more energy deposition from source to target tissues. In addition, the organs in the short, fat patient were almost all smaller than those in the tall, thin patient with the one exception being adipose tissue, and smaller tissues have higher self-dose than larger tissues. In addition, the increase of the effective dose difference from 44% to 88% between the 32 kg patient study and the 50 kg patient study was probably due to the degree to which the body morphometries differed. On

average, the organs of the tall, thin patient were 56% larger than those of the short, fat patient for the Sgouros *et al.* (2011) study while the organs of the tall, thin patient were 211% greater than those of the short, fat patient for the 50 kg patients in the current study. This difference seemed to explain the increase in dose differences between the two studies.

Internal Dosimetry Software

The actual subroutines of the internal dosimetry code were written in *MATLAB*TM, and several demonstrations will be given in this section to prove the accuracy of the code. Before any demonstrations are given, two small topics of interest when performing computational dosimetry relating to the way radionuclides are modeled will be addressed.

First, when performing computational internal dosimetry, one must decide the level of spectral detail required to give adequate dosimetry results. Spectrum summaries are available that list only the most prevalent radiation emissions for each radionuclide, allowing for more simplistic simulations. For example, ^{99m}Tc has four primary photon emissions, three x rays and one gamma-ray at 18.21 keV, 18.33 keV, 20.59 keV, and 140.5 keV at yields of 0.0214, 0.0406, 0.00653, and 0.891, respectively (ICRP 2008). While these four emissions only make up about 15% of the total yield of 86 different photon emissions, they dominate the delta value (product of energy and yield) at 99.9% (ICRP 2008). The delta value is a much better metric than yield to evaluate relative contribution to dose. To assess the extent that detailed spectra should be used, a small study was performed wherein a point source was imbedded in human tissue spheres (tissue elemental compositions given for the adult in ICRP Publication 89 were used with a tissue density of 1.00 g/cm³) of various masses, and self-dose S values were calculated using the spectra summary and detailed spectra of photons, monoenergetic electrons,

and beta particles for ^{99m}Tc and ^{82}Rb as given by ICRP Publication 107 (ICRP 2002, ICRP 2008). MCNPX v2.6 was used for radiation transport, and 10^6 particle histories were simulated.

The results of this study are shown in Figure 3-47. All statistical uncertainties were less than 1%. It is clear that dose estimates can be considered adequate if the spectrum summary is used for on-the-fly simulations. However, since the internal dosimetry software uses S value LUTs for dosimetry calculations, the entire detailed spectra were used for all radionuclides.

A second issue for consideration is the validity of direct spectrum sampling as an adequate simulation technique instead of weighted monoenergetic SAF calculations. For many on-the-fly computational dosimetry studies for non-reference individuals, it is beneficial to directly input the radiation emission spectrum for the radionuclide of interest into the radiation transport code. In this way, the spectrum will be sampled based on the relative yields of the emission energies. Alternatively, one could mirror the data generation component of the current study and compute monoenergetic photon and electron SAFs for the individual and weight them by the relative yields at each emission energy, clearly an impractical task. A small computational experiment was performed using the same setup as the experiment designed to investigate using summarized radiation spectra versus detailed radiation spectra. However, only ^{99m}Tc was simulated, and the results are in Figure 3-48. All statistical uncertainties were less than 1%. The results prove that spectrum sampling is a viable option for on-the-fly computational internal dosimetry. Again, the internal dosimetry software uses monoenergetic SAFs for reference individuals.

The S value calculator subroutine of the internal dosimetry code was validated by comparing S values assembled from direct spectrum sampling of both ^{99m}Tc photons and ^{90}Y beta particles and S values calculated by interpolation and weighting of the monoenergetic photon and electron SAFs for the liver source in the UFH00MF phantoms. The photon spectrum

for ^{99m}Tc and the beta spectrum for ^{90}Y were taken from ICRP Publication 107 (ICRP 2008). MCNPX v2.6 was used as the radiation transport code for the direct spectrum simulation with 10^7 particles simulated. The results of this study are in Table 3-6 and Figure 3-49. Good agreement is seen across most target tissues, but greater disagreements occur when the target tissue is small. In addition, greater disagreements are seen for the beta spectrum than the photon spectrum. Both instances where disagreement is greater can be attributed almost entirely to less than satisfactory statistical uncertainties in the direct spectrum sampling simulation (e.g., the statistical uncertainty for the pituitary gland target and the ^{90}Y beta spectrum was about 42%, and the S value ratio was 40.69). Greater uncertainties are usually observed for small target tissues and beta particles, so these trends were expected. However, considering that the S values using both techniques for many of the distant and smaller sized target tissues were almost identical, the S value calculator was considered to be adequately validated. Similar results were seen for the monoenergetic electron spectra of ^{204}Bi and ^{122m}Xe (data not shown).

Table 3-1. Volumes of the blood vessels in the UF phantom family.

Blood Vessel	Volume (cm ³)							
	UFH00MF	UFH01MF	UFH05MF	UFH10MF	UFH15M	UFH15F	UFHADM	UFHADF
Large Arteries								
Neck	0.21	0.32	0.56	1.12	1.58	1.68	2.46	2.03
Thoracic	0.23	0.40	1.01	2.26	4.04	2.65	5.71	2.77
Arms	0.98	1.95	5.24	12.07	22.82	20.22	29.90	27.08
Legs	1.35	3.31	8.81	17.79	33.50	31.95	45.22	37.61
Large Veins								
Neck	1.06	2.05	4.53	8.39	17.25	16.27	20.02	16.87
Thoracic	0.23	0.40	1.01	2.25	4.04	2.65	5.71	2.74
Arms	3.31	6.91	17.39	36.99	67.67	60.17	91.49	78.92
Legs	3.75	8.61	23.92	52.09	96.69	90.39	133.00	109.81
Total Arteries	2.77	5.99	15.62	33.23	61.93	56.50	83.29	69.49
Total Veins	8.34	17.97	46.86	99.73	185.64	169.49	250.22	208.33
Ratio (Veins/Arteries)	3.00	3.00	3.00	3.00	3.00	3.00	3.00	3.00
Total Vessel Volume	11.11	23.96	62.48	132.96	247.58	226.00	333.50	277.81
Target Vessel Volume	64.80	120.00	336.00	576.00	1080.00	792.00	1272.00	936.00
Difference (Total/Target)	-83%	-80%	-81%	-77%	-77%	-71%	-74%	-70%

Table 3-2. Superior (sup) and inferior (inf) diameters of the blood vessels in the UF phantom family.

Blood Vessel	Vessel Diameter (cm)															
	UFH00MF		UFH01MF		UFH05MF		UFH10MF		UFH15M		UFH15F		UFHADM		UFHADDF	
	Sup	Inf	Sup	Inf	Sup	Inf	Sup	Inf	Sup	Inf	Sup	Inf	Sup	Inf	Sup	Inf
Arteries																
Neck	0.20	0.20	0.21	0.21	0.26	0.26	0.31	0.31	0.37	0.37	0.35	0.35	0.40	0.40	0.38	0.38
Thoracic - sup	0.20	0.20	0.22	0.22	0.31	0.31	0.41	0.41	0.52	0.52	0.37	0.37	0.58	0.58	0.40	0.40
Thoracic - inf	0.20	0.15	0.22	0.16	0.31	0.22	0.41	0.29	0.52	0.36	0.50	0.34	0.58	0.40	0.56	0.38
Arms	0.21	0.21	0.23	0.23	0.31	0.31	0.42	0.42	0.52	0.52	0.50	0.50	0.58	0.58	0.56	0.56
Legs	0.22	0.22	0.27	0.27	0.34	0.34	0.44	0.44	0.54	0.54	0.53	0.53	0.58	0.58	0.58	0.58
Veins																
Neck	0.30	0.40	0.33	0.43	0.43	0.53	0.55	0.65	0.68	0.78	0.66	0.76	0.75	0.85	0.73	0.83
Thoracic - sup	0.20	0.20	0.22	0.22	0.31	0.31	0.41	0.41	0.52	0.52	0.37	0.37	0.58	0.58	0.40	0.40
Thoracic - inf	0.20	0.15	0.22	0.16	0.31	0.22	0.41	0.29	0.52	0.36	0.50	0.34	0.58	0.40	0.56	0.38
Arms	0.40	0.40	0.43	0.43	0.57	0.57	0.73	0.73	0.90	0.90	0.88	0.88	1.00	1.00	0.98	0.98
Legs	0.40	0.40	0.43	0.43	0.57	0.57	0.73	0.73	0.90	0.90	0.88	0.88	1.00	1.00	0.98	0.98

Table 3-3. Photon SAFs (excerpt) for the UFH00MF pituitary gland source in units of kg^{-1} .

Organ / tissue	Variance			Energy (MeV)							
	Reduction	0.010	0.015	0.020	0.030	0.040	0.050	0.060	0.080	0.100	
Adipose	E		3.03E-07	4.91E-05	1.81E-03	9.99E-03	1.27E-02	1.23E-02	1.15E-02	1.07E-02	1.05E-02
Adrenals	E		3.31E-07	3.84E-06	2.18E-05	2.53E-04	1.44E-03	2.43E-03	2.87E-03	3.14E-03	3.23E-03
AI			2.55E-09	4.86E-07	2.02E-05	3.85E-03	1.15E-02	1.45E-02	1.49E-02	1.40E-02	1.35E-02
Brain			1.02E+00	1.64E+00	1.75E+00	1.24E+00	7.85E-01	5.41E-01	4.18E-01	3.19E-01	2.90E-01
Breast (F)	E	S	7.01E-09	9.63E-07	3.16E-05	4.35E-03	1.02E-02	1.20E-02	1.17E-02	1.15E-02	1.18E-02
Breast (M)	E	R S	9.15E-09	1.21E-06	3.86E-05	5.10E-03	1.15E-02	1.31E-02	1.28E-02	1.22E-02	1.21E-02
Bronchial	E		3.99E-09	6.54E-07	2.44E-05	3.99E-03	1.17E-02	1.48E-02	1.51E-02	1.43E-02	1.37E-02
Brchiol-sec			2.55E-09	4.86E-07	2.02E-05	3.85E-03	1.15E-02	1.45E-02	1.49E-02	1.40E-02	1.35E-02
Cartilage			1.36E-01	2.61E-01	2.71E-01	2.59E-01	2.01E-01	1.53E-01	1.22E-01	9.40E-02	8.44E-02
Colon			2.46E-10	1.20E-08	3.55E-07	9.97E-05	6.15E-04	1.08E-03	1.32E-03	1.47E-03	1.51E-03
Endost-BS			1.03E-02	8.11E-02	1.73E-01	2.64E-01	2.49E-01	2.17E-01	1.90E-01	1.56E-01	1.38E-01
ET			5.22E-05	4.97E-02	1.74E-01	2.90E-01	2.85E-01	2.42E-01	2.07E-01	1.71E-01	1.58E-01
ET1-bas	E		3.82E-04	8.67E-03	7.93E-02	1.81E-01	1.66E-01	1.39E-01	1.20E-01	1.03E-01	9.92E-02
ET2-bas			4.26E-05	5.09E-02	1.77E-01	2.93E-01	2.88E-01	2.45E-01	2.09E-01	1.72E-01	1.60E-01
Eye-lens	E		2.05E-04	1.05E-02	1.70E-01	3.90E-01	3.28E-01	2.57E-01	2.13E-01	1.75E-01	1.65E-01
GB-wall	E	S	2.38E-07	3.00E-06	1.81E-05	2.28E-04	1.37E-03	2.29E-03	2.69E-03	2.95E-03	2.99E-03
Ht-wall	E		4.53E-10	1.60E-07	1.03E-05	3.64E-03	1.14E-02	1.47E-02	1.50E-02	1.41E-02	1.35E-02
Kidney-C	E		6.76E-08	1.03E-06	7.15E-06	1.09E-04	7.57E-04	1.38E-03	1.71E-03	1.88E-03	1.92E-03
Kidney-M	E		3.68E-08	6.65E-07	5.19E-06	9.38E-05	7.32E-04	1.35E-03	1.67E-03	1.83E-03	1.88E-03
Kidneys			5.95E-08	9.37E-07	6.64E-06	1.05E-04	7.50E-04	1.38E-03	1.70E-03	1.86E-03	1.91E-03
LC-wall	E		4.45E-11	1.05E-08	5.08E-07	1.20E-04	7.40E-04	1.28E-03	1.54E-03	1.68E-03	1.73E-03
Liver	E		4.71E-12	4.96E-09	6.91E-07	7.26E-04	3.23E-03	4.77E-03	5.29E-03	5.30E-03	5.20E-03
LN-ET (F)	E		4.88E-04	1.16E-02	1.10E-01	2.57E-01	2.42E-01	2.01E-01	1.72E-01	1.47E-01	1.40E-01
LN-ET (M)	E		7.09E-03	7.63E-02	4.12E-01	5.82E-01	4.44E-01	3.38E-01	2.75E-01	2.23E-01	2.09E-01
LN-Th (F)	E	S	5.01E-06	3.49E-05	1.39E-04	9.67E-04	3.84E-03	5.52E-03	6.14E-03	6.25E-03	6.41E-03
LN-Th (M)	E	S	4.63E-10	1.29E-07	7.01E-06	1.95E-03	6.48E-03	8.75E-03	9.37E-03	9.25E-03	9.20E-03
Lymph (F)	E		6.47E-09	3.61E-06	3.21E-04	5.03E-03	9.40E-03	1.04E-02	1.01E-02	9.47E-03	9.26E-03
Lymph (M)	E		2.14E-09	2.23E-06	3.08E-04	6.06E-03	1.12E-02	1.22E-02	1.18E-02	1.08E-02	1.04E-02
LN-Total (F)			1.71E-06	4.18E-05	6.69E-04	5.72E-03	9.99E-03	1.08E-02	1.06E-02	9.82E-03	9.61E-03
LN-Total (M)			4.43E-05	4.79E-04	2.87E-03	9.53E-03	1.38E-02	1.41E-02	1.33E-02	1.21E-02	1.16E-02

Table 3-4. Radiation absorbed dose per unit AA and comparison for two patients at the same weight but different body morphometry. The radiopharmaceutical is $^{99m}\text{Tc} - \text{DMSA}$.

Target Tissue	Dose (mGy/MBq)		Difference Short-Fat/Tall-Thin
	Tall - Thin	Short - Fat	
WBody	1.66E-06	2.04E-06	22.72%
Adipose	6.01E-07	8.39E-07	39.58%
LAdrenal	6.61E-06	1.06E-05	60.24%
RAdrenal	6.37E-06	1.09E-05	71.43%
Brain	1.58E-07	3.27E-07	106.53%
LBreast	5.17E-07	5.77E-07	11.76%
Bronchi-bas	1.30E-06	2.43E-06	86.15%
RC-wall	1.16E-06	3.15E-06	170.67%
Oesophagus	1.56E-06	2.90E-06	85.24%
GB-wall	3.22E-06	5.56E-06	72.67%
Ht-wall	1.45E-06	3.09E-06	113.27%
Kidney-C	6.65E-05	1.10E-04	65.30%
Kidney-M	1.56E-05	2.52E-05	61.74%
ET2-bas	5.00E-07	1.12E-06	123.90%
Eye-lens	2.16E-07	2.88E-07	33.41%
Liver	3.59E-06	7.04E-06	96.42%
LLung	1.88E-06	3.81E-06	102.29%
RLung	1.80E-06	3.75E-06	108.43%
ET1-bas	1.59E-07	2.55E-07	60.05%
O-mucosa	4.91E-07	1.01E-06	105.08%
Pancreas	5.24E-06	7.88E-06	50.30%
P-gland	1.86E-07	5.69E-07	206.76%
RSig-wall	1.57E-06	3.00E-06	91.63%
SI-wall	2.29E-06	3.99E-06	74.57%
Skin	4.94E-07	5.30E-07	7.36%
Spleen	9.75E-06	1.95E-05	100.27%
St-wall	2.36E-06	4.95E-06	109.75%
Thymus	8.18E-07	1.94E-06	137.14%
Thyroid	5.92E-07	1.44E-06	143.24%
Trachea	9.80E-07	1.93E-06	96.85%
UB-wall	3.06E-06	5.11E-06	67.00%
LC-wall	1.07E-06	2.97E-06	176.11%
Muscle	1.77E-06	3.48E-06	96.21%
RBreast	5.10E-07	5.71E-07	12.10%
Cartilage	1.77E-06	4.06E-06	129.54%
C-bone-V	1.38E-06	2.35E-06	71.07%
LOvary	2.04E-06	3.74E-06	83.48%
ROvary	2.08E-06	3.81E-06	83.27%
Uterus	2.22E-06	4.09E-06	83.72%
AM	1.61E-06	2.93E-06	82.19%
TM50	1.46E-06	2.54E-06	74.24%

Table 3-5. Radiation absorbed dose and effective dose per unit AA and comparison for two patients at the same weight but different body morphometry for the radiopharmaceutical $^{99m}\text{Tc} - \text{DMSA}$.

Target Tissue	Tissue	Dose		Weighted Dose		Effective Dose		Difference Short-Fat/Tall-Thin
	Weighting Factor	Tall - Thin (mGy/MBq)	Short - Fat (mGy/MBq)	Tall - Thin (mSv/MBq)	Short - Fat (mSv/MBq)	Tall - Thin (mSv/MBq)	Short - Fat (mSv/MBq)	
Colon	0.12	1.20E-06	3.05E-06	1.44E-07	3.66E-07	2.18E-06	4.10E-06	1.88
Lungs	0.12	1.84E-06	3.78E-06	2.21E-07	4.53E-07			
Stomach W	0.12	2.36E-06	4.95E-06	2.83E-07	5.94E-07			
Ovaries	0.08	2.06E-06	3.78E-06	1.65E-07	3.02E-07			
Urinary Bladder W	0.04	3.06E-06	5.11E-06	1.22E-07	2.04E-07			
Esophagus	0.04	1.56E-06	2.90E-06	6.26E-08	1.16E-07			
Liver	0.04	3.59E-06	7.04E-06	1.43E-07	2.82E-07			
Thyroid	0.04	5.92E-07	1.44E-06	2.37E-08	5.76E-08			
Brain	0.01	1.58E-07	3.27E-07	1.58E-09	3.27E-09			
Salivary Glands (parotid)	0.01	4.47E-07	9.59E-07	4.47E-09	9.59E-09			
Breast	0.12	5.13E-07	5.74E-07	6.16E-08	6.89E-08			
Skin	0.01	4.94E-07	5.30E-07	4.94E-09	5.30E-09			
Remainder	0.12	6.09E-06	1.05E-05	7.31E-07	1.26E-06			
Red Bone Marrow	0.12	1.61E-06	2.93E-06	1.93E-07	3.52E-07			
Bone Surface	0.01	1.46E-06	2.54E-06	1.46E-08	2.54E-08			
Remainder								
Adrenals		6.49E-06	1.08E-05					
ET Region		4.94E-07	1.10E-06					
GB-wall		3.22E-06	5.56E-06					
Heart-wall		1.45E-06	3.09E-06					
Kidneys		5.11E-05	8.43E-05					
Lymph nodes		0.00E+00	0.00E+00					
Muscle		1.77E-06	3.48E-06					
Oral mucosa		4.91E-07	1.01E-06					
Pancreas		5.24E-06	7.88E-06					
Prostate		0.00E+00	0.00E+00					
SI-wall		2.29E-06	3.99E-06					
Spleen		9.75E-06	1.95E-05					
Thymus		8.18E-07	1.94E-06					
Uterus		2.22E-06	4.09E-06					

Table 3-6. SAF and S value subroutine verification study for the liver source in the UFH00MF phantoms. Ratio of the S values obtained from previously developed monenergetic SAFs to the S values obtained from direct simulation of the spectra.

Ratio - S(Calculator) / S(Direct)	Radionuclide and Emission Type	
	Tc-99m Photons	Y-90 Betas
Adipose	1.01	1.15
Adrenals	1.02	1.00
Brain	1.00	1.00
Breast (F)	0.96	1.75
Bronchial	1.01	1.01
Cartilage	1.01	1.02
ET1-sur	1.28	1.42
ET2-sur	0.98	0.95
Eye-lens	1.28	1.02
GB-wall	1.04	0.99
Ht-wall	1.01	1.01
Kidney-C	1.00	1.00
Kidney-M	1.01	1.30
LC-wall	1.03	1.04
Liver	1.01	1.00
LN-ET (F)	1.24	--
LN-Th (F)	1.04	0.68
Lungs	1.01	1.00
Lymph (F)	1.04	1.00
Muscle	1.01	1.00
Oesophagus	1.04	1.04
Ovaries	1.06	0.98
Pancreas	1.02	1.00
Pit-gland	1.02	40.69
RC-wall	1.02	0.99
RSig-wall	1.03	1.15
S-glands	1.06	1.31
SI-wall	1.02	1.01
Skin	1.02	1.04
Sp-cord	1.02	0.94
Spleen	1.00	1.01
St-wall	1.02	1.00
Thymus	1.04	0.99
Thyroid	1.00	1.40
Trachea	1.08	1.05
UB-wall (F)	1.00	1.13
Uterus	1.03	1.05

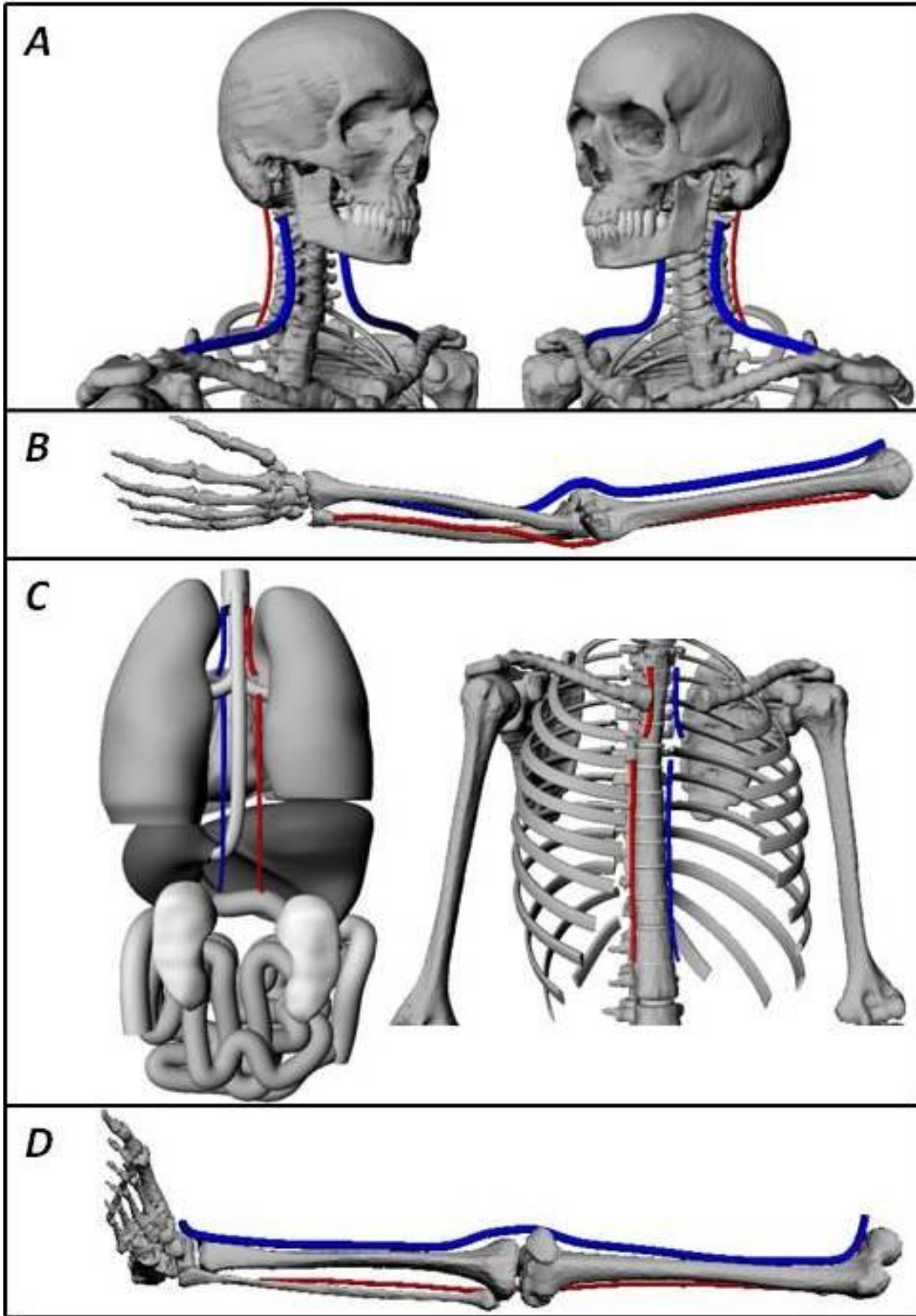


Figure 3-1. Perspective views in *Rhinoceros*[™] of the arteries and veins in the (A) neck and clavicles, (B) arms, (C) thoracic and abdominal regions, and (D) legs of the UFHADM phantom.

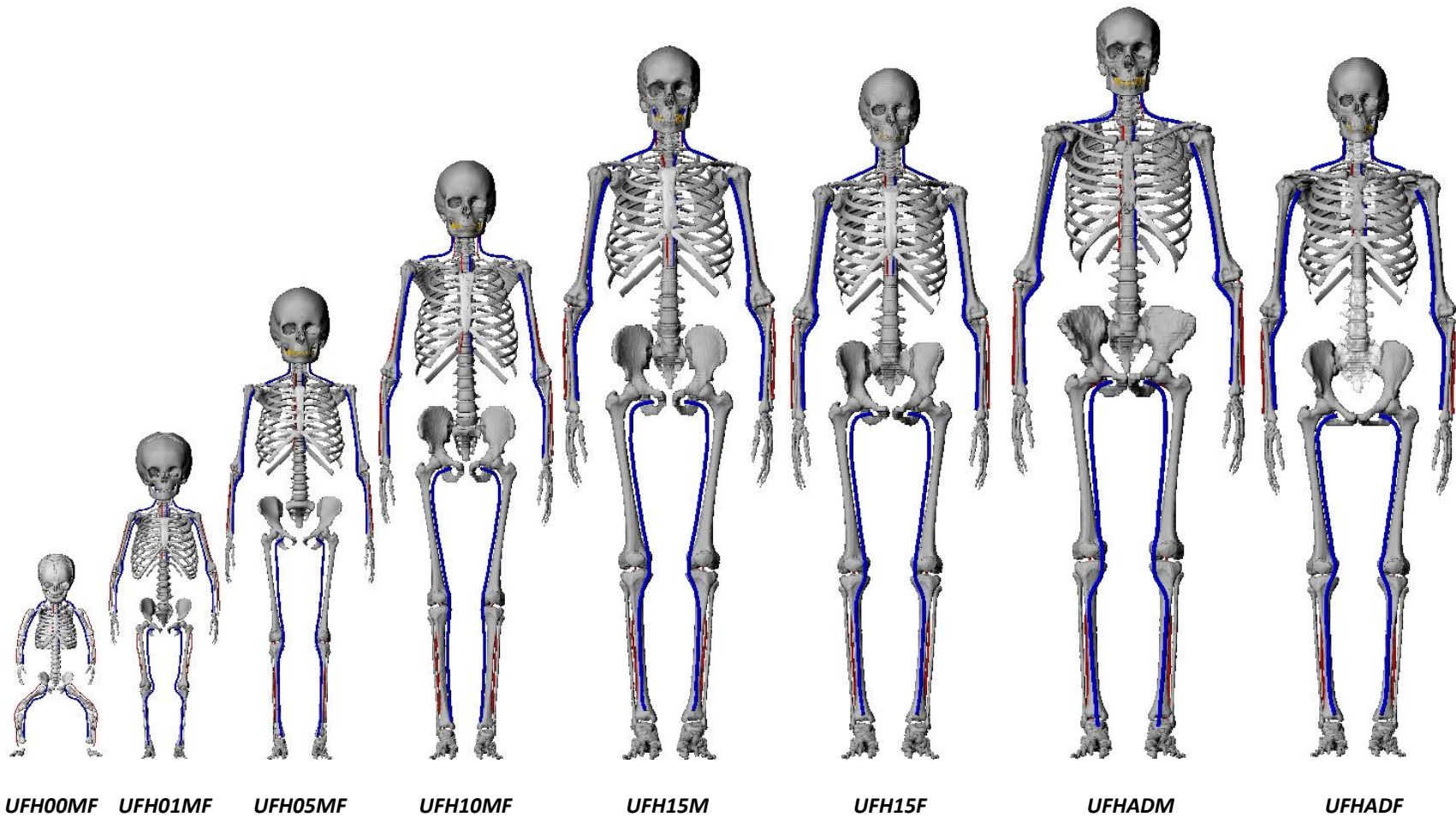
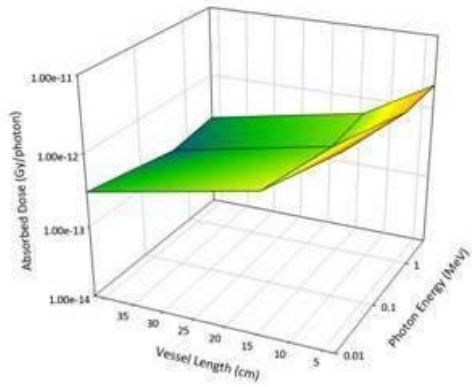
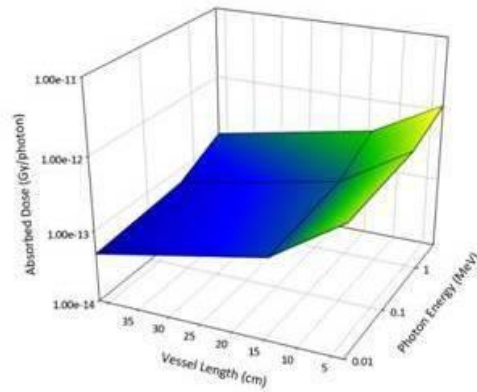


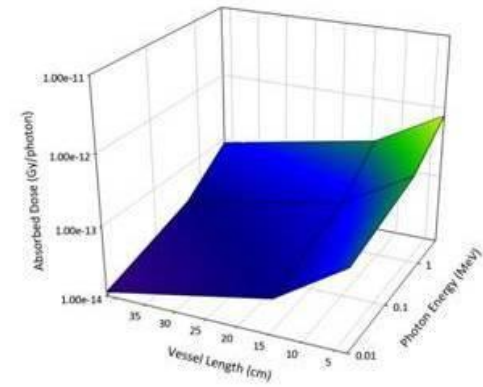
Figure 3-2. Blood vessel systems as implemented in the entire UF hybrid phantom family.



Lumen Diameter = 0.15 cm
Vessel Separation = 0.1503 cm

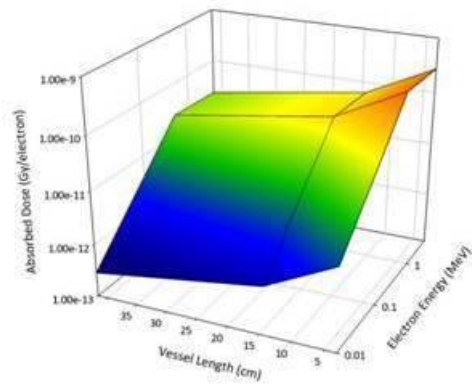


Lumen Diameter = 0.469 cm
Vessel Separation = 0.4692 cm

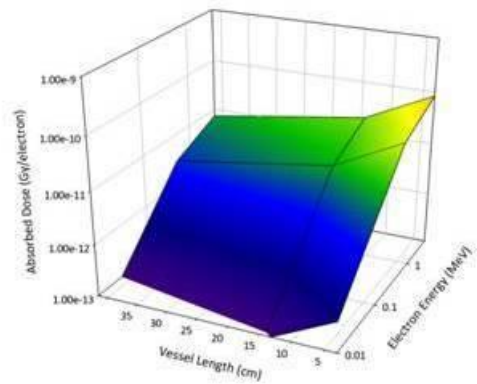


Lumen Diameter = 1.0 cm
Vessel Separation = 1.0002 cm

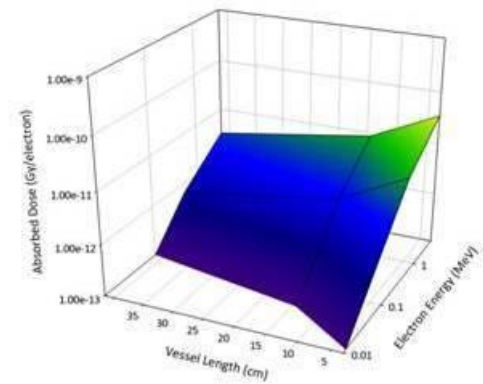
Figure 3-3. Absorbed dose to the blood vessel wall from photons for vessels with $1 \mu\text{m}$ wall thickness as a function of vessel length and photon energy.



Lumen Diameter = 0.15 cm
Vessel Separation = 0.1503 cm



Lumen Diameter = 0.469 cm
Vessel Separation = 0.4692 cm



Lumen Diameter = 1.0 cm
Vessel Separation = 1.0002 cm

Figure 3-4. Absorbed dose to the blood vessel wall from electrons for vessels with $1 \mu\text{m}$ wall thickness as a function of vessel length and electron energy.

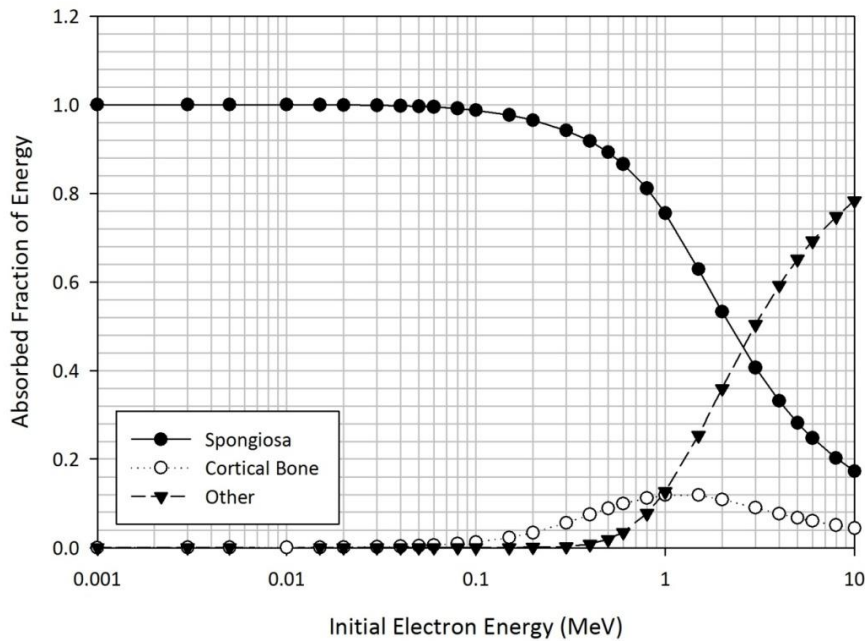


Figure 3-5. AFs as a function of initial electron energy for a uniform electron source in the spongiosa of the cranium in the UFH01MF phantom with spongiosa, cortical bone, and all other tissues as targets.

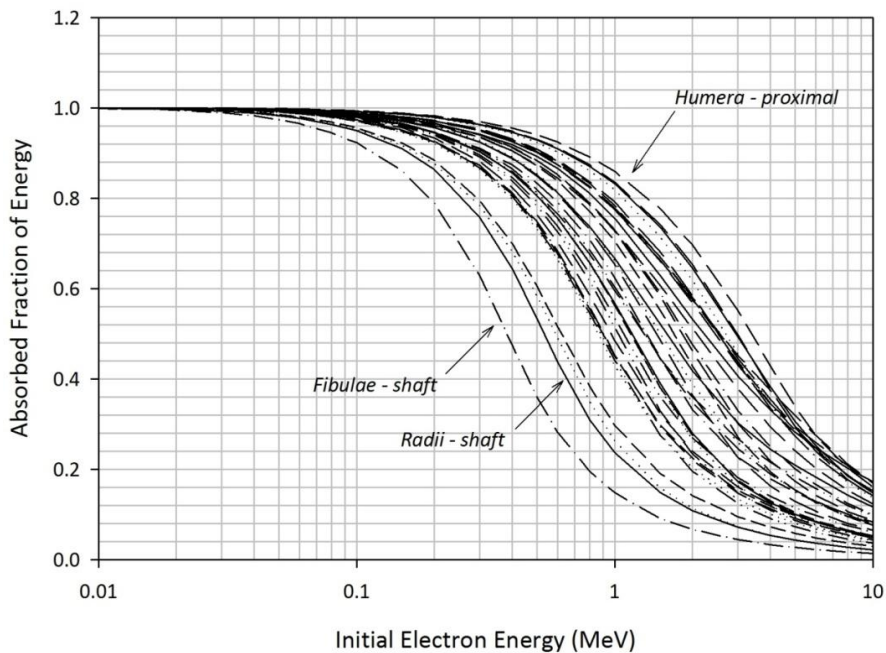


Figure 3-6. Spongiosa/MC self-dose AFs as a function of initial electron energy for all bone sites in the UFH01MF phantom. A legend was not given because the intent of the figure was to show general trends of the AFs.

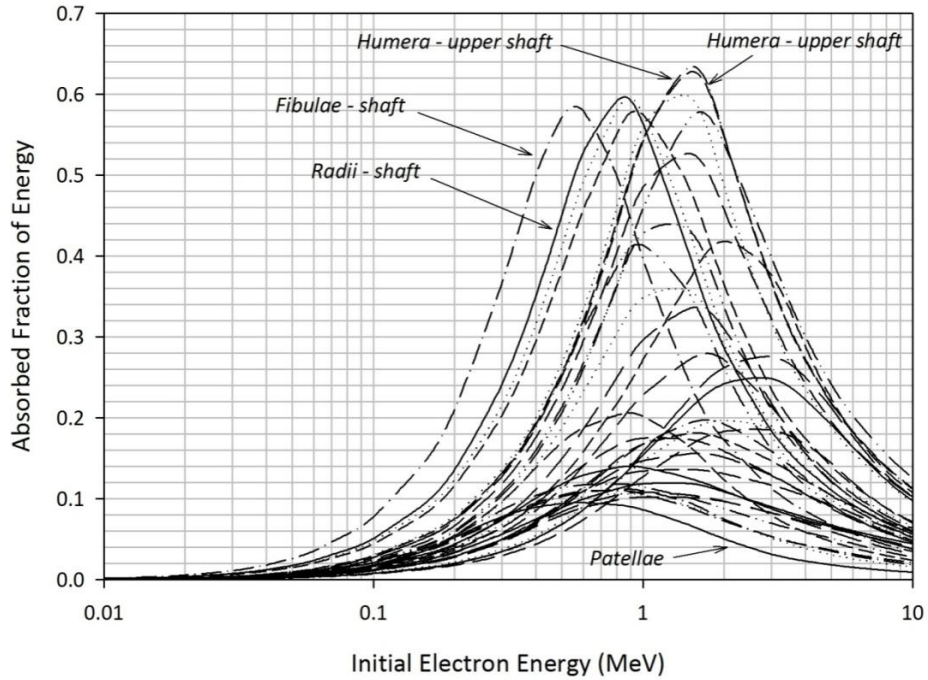


Figure 3-7. AFs for spongiosa/MC irradiating cortical bone as a function of initial electron energy for all bone sites in the UFH01MF phantom. A legend was not given because the intent of the figure was to show general trends of the AFs.

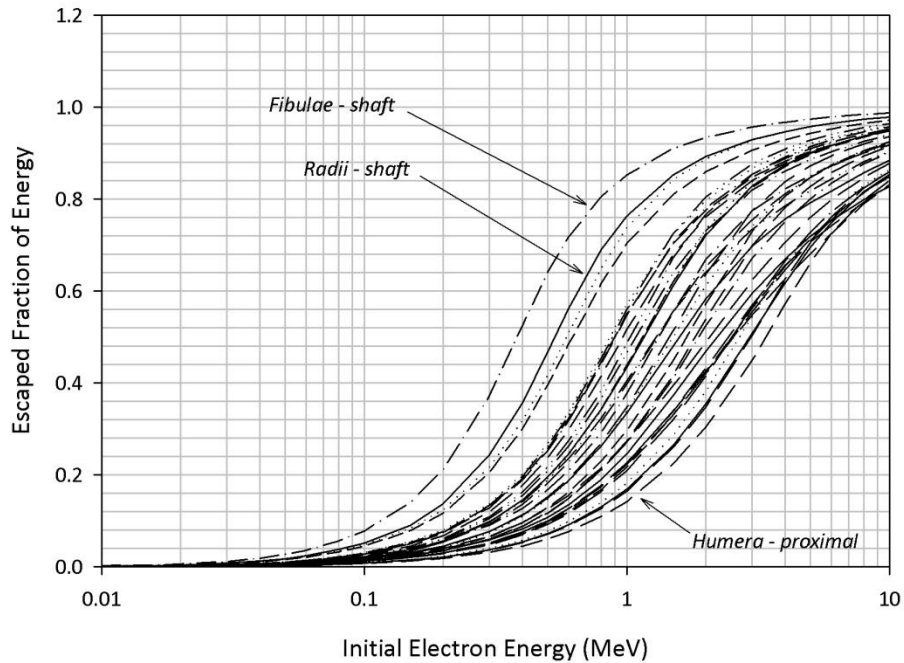


Figure 3-8. EFs for spongiosa/MC sources as a function of initial electron energy for all bone sites in the UFH01MF phantom. A legend was not given because the intent of the figure was to show general trends of the EFs.

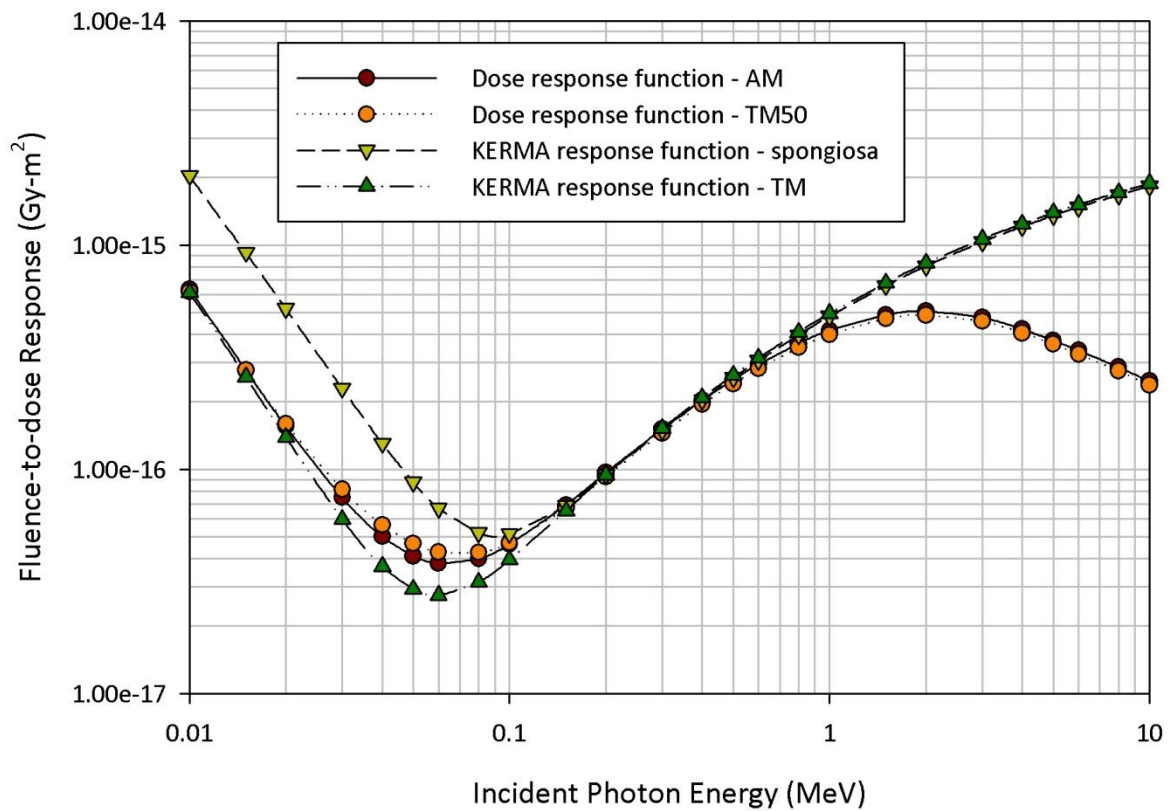


Figure 3-9. Skeletal fluence-to-dose response functions and skeletal fluence-to-kerma response functions for AM and TM_{50} targets in the mandible of the UFH00MF phantom.

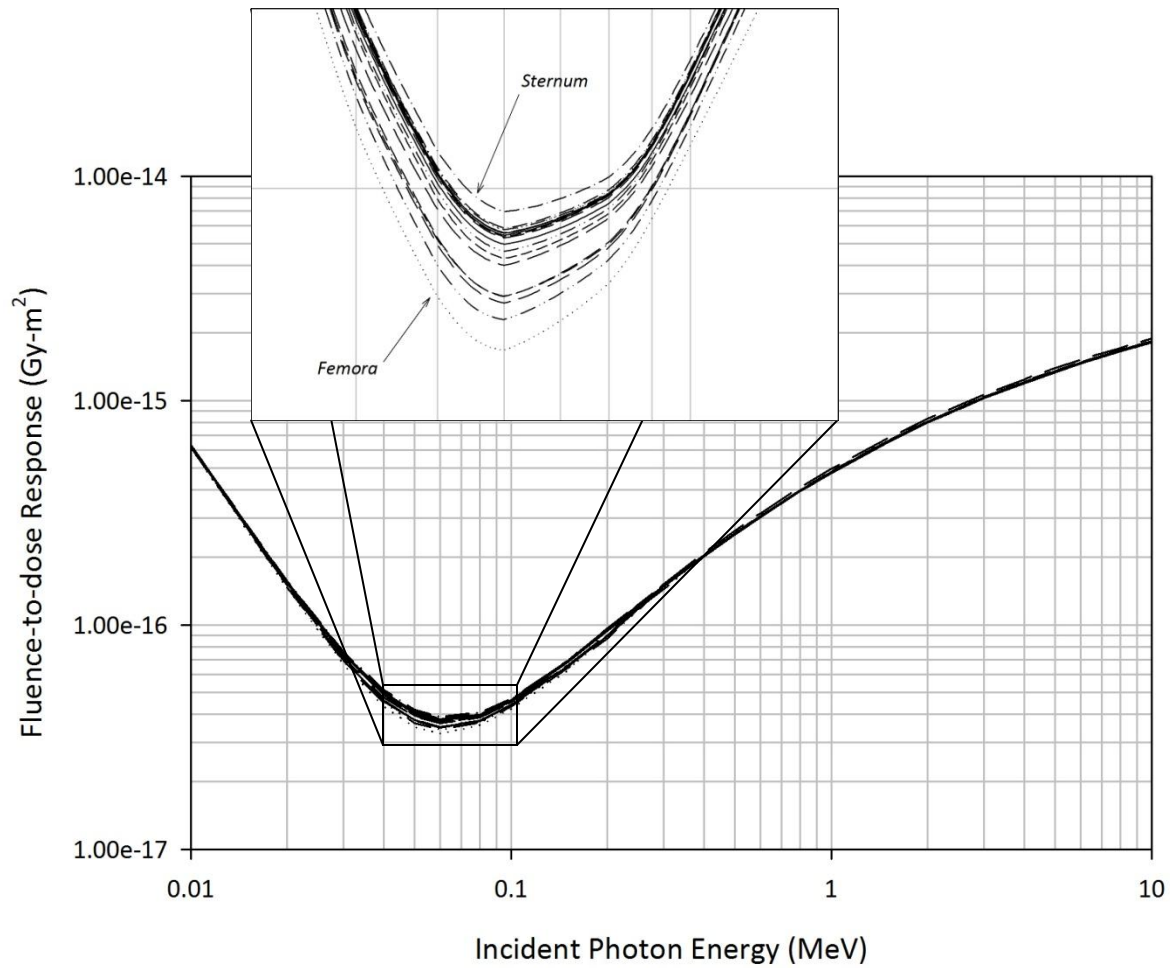


Figure 3-10. Skeletal fluence-to-dose response functions for all bone sites in the UFH00MF phantom for the AM target. A legend was not given because the intent of the figure was to show general trends of the response functions.

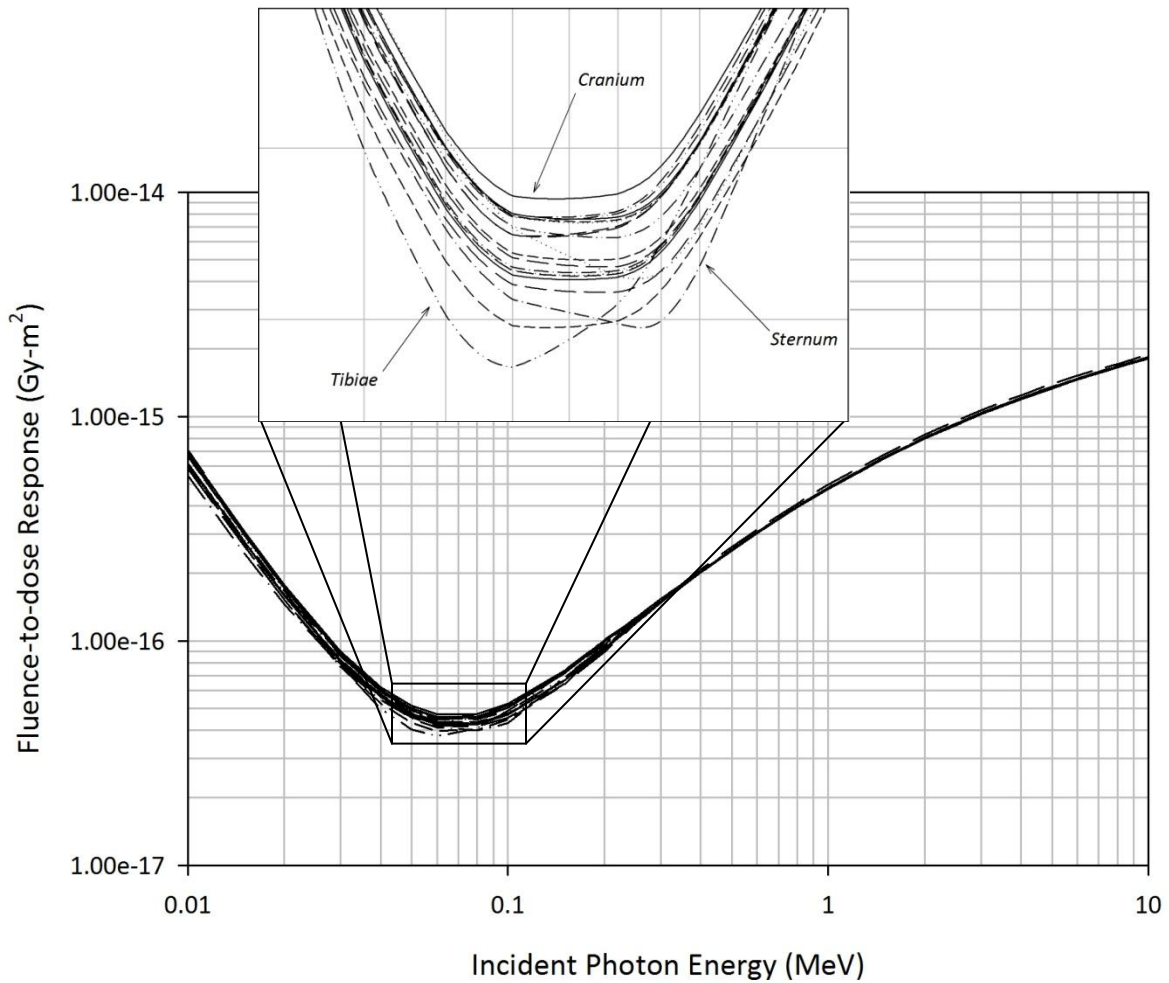


Figure 3-11. Skeletal fluence-to-dose response functions for all bone sites in the UFH00MF phantom for the TM₅₀ target. A legend was not given because the intent of the figure was to show general trends of the response functions.

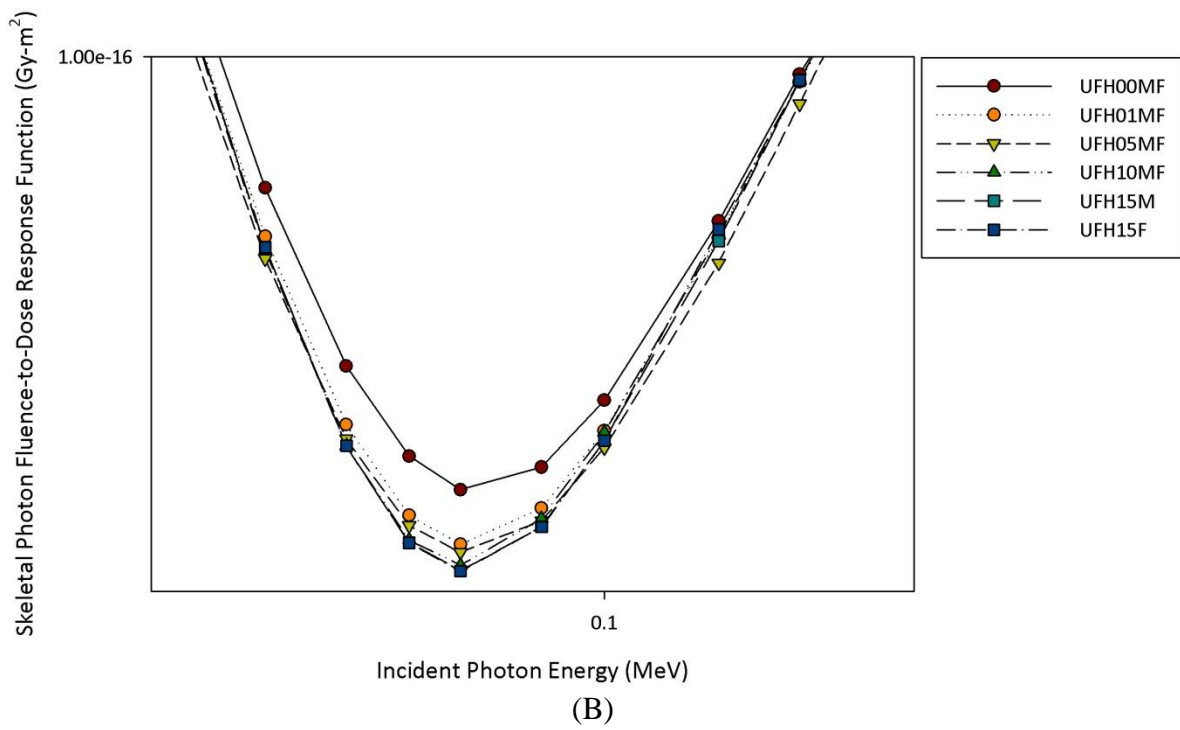
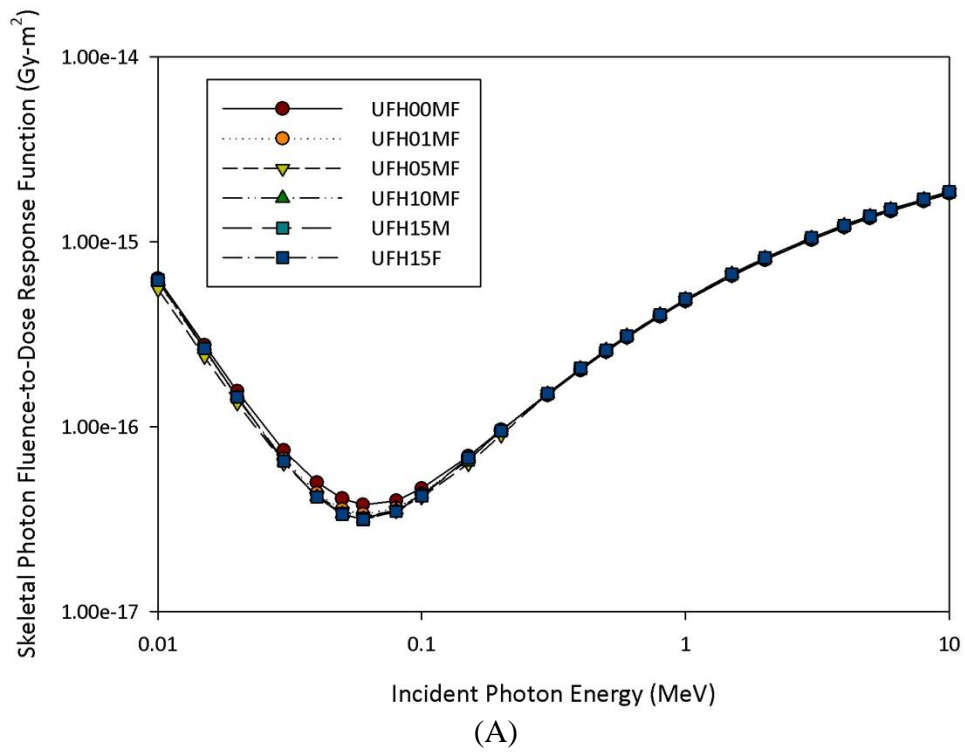
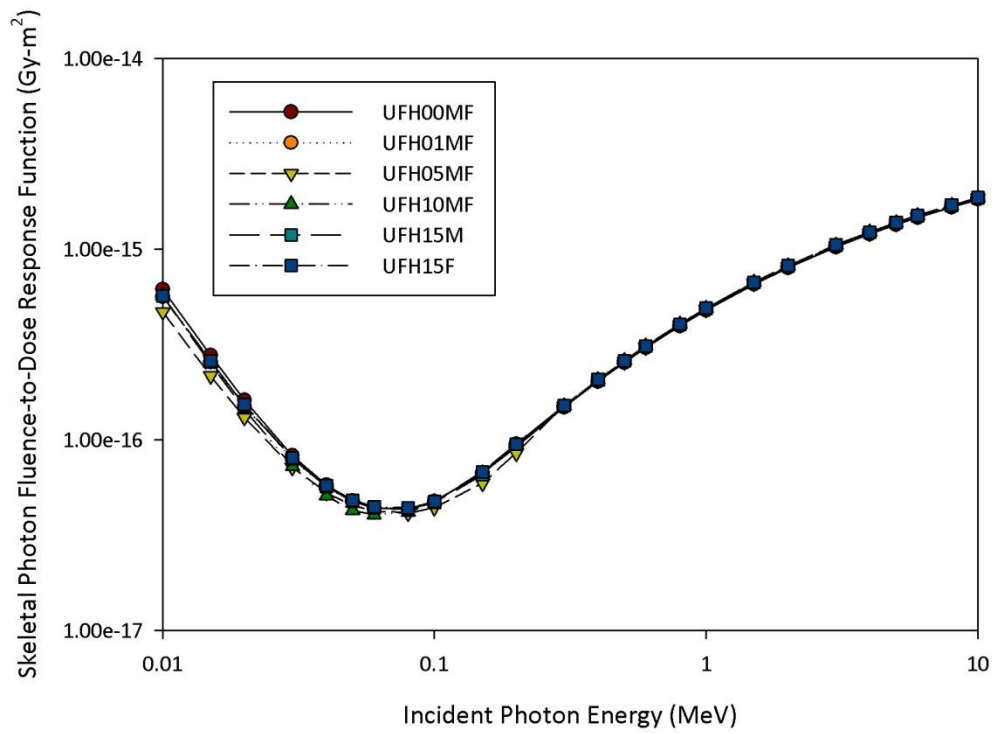
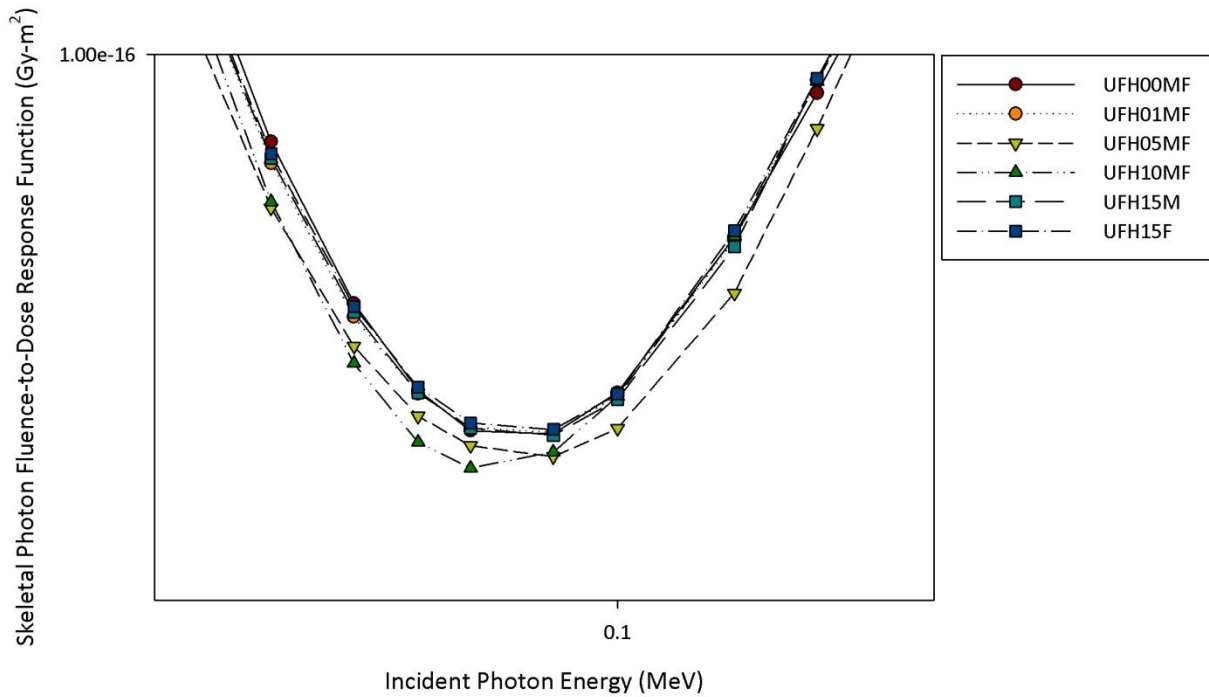


Figure 3-12. Skeletal fluence-to-dose response functions for the AM target in the cervical vertebra of all pediatric and adolescent phantoms.



(A)



(B)

Figure 3-13. Skeletal fluence-to-dose response functions for the TM₅₀ target in the cervical vertebra of all pediatric and adolescent phantoms.

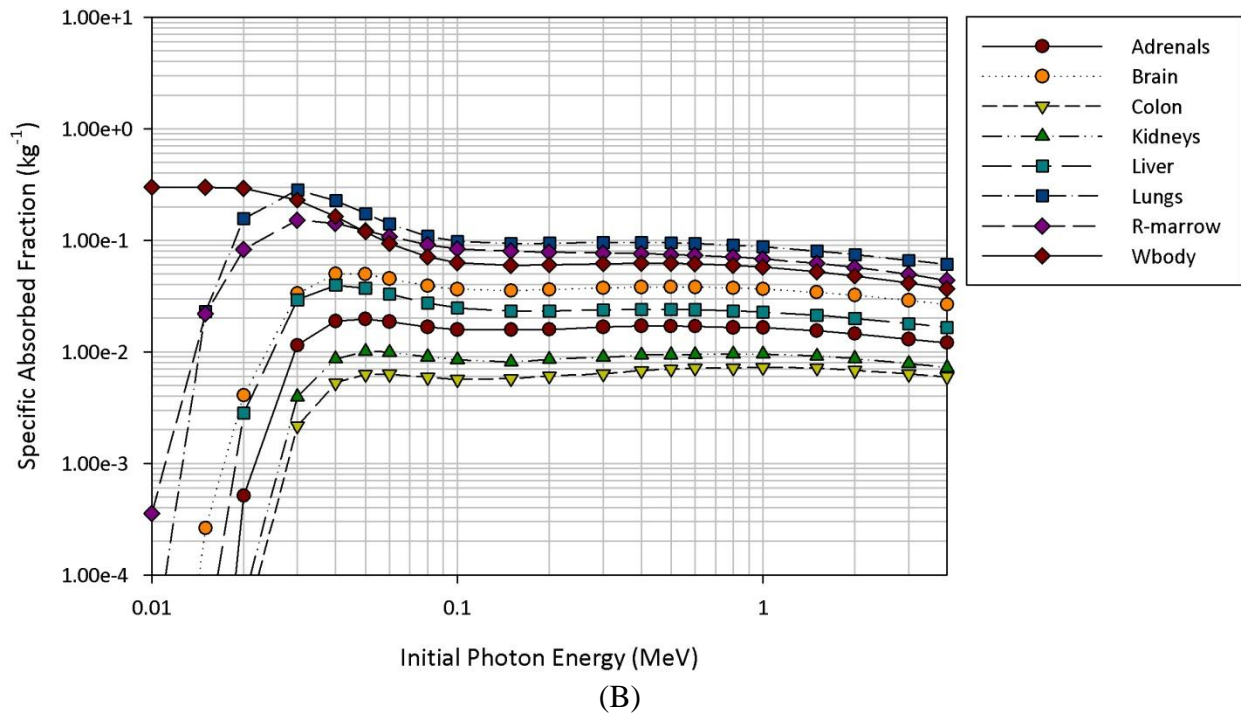
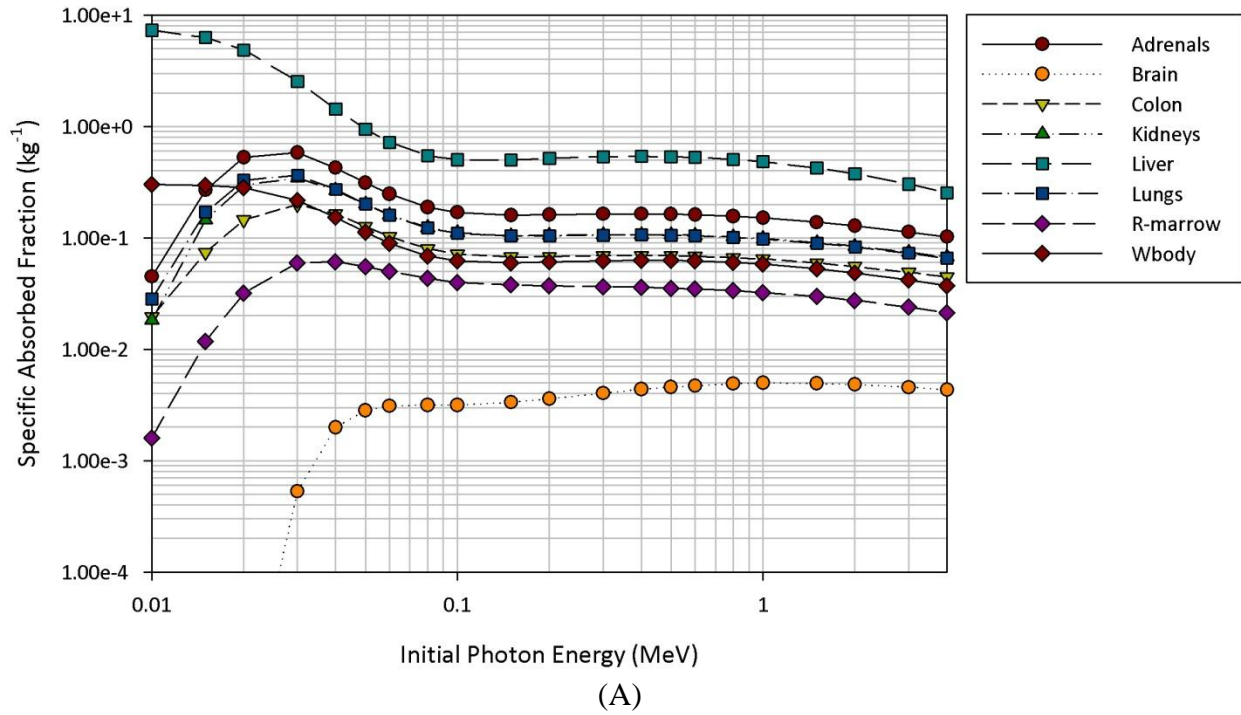


Figure 3-14. Excerpt of the photon SAF curves for a (A) large (liver) and (B) small (thyroid) source tissue in the UFH00MF phantoms.

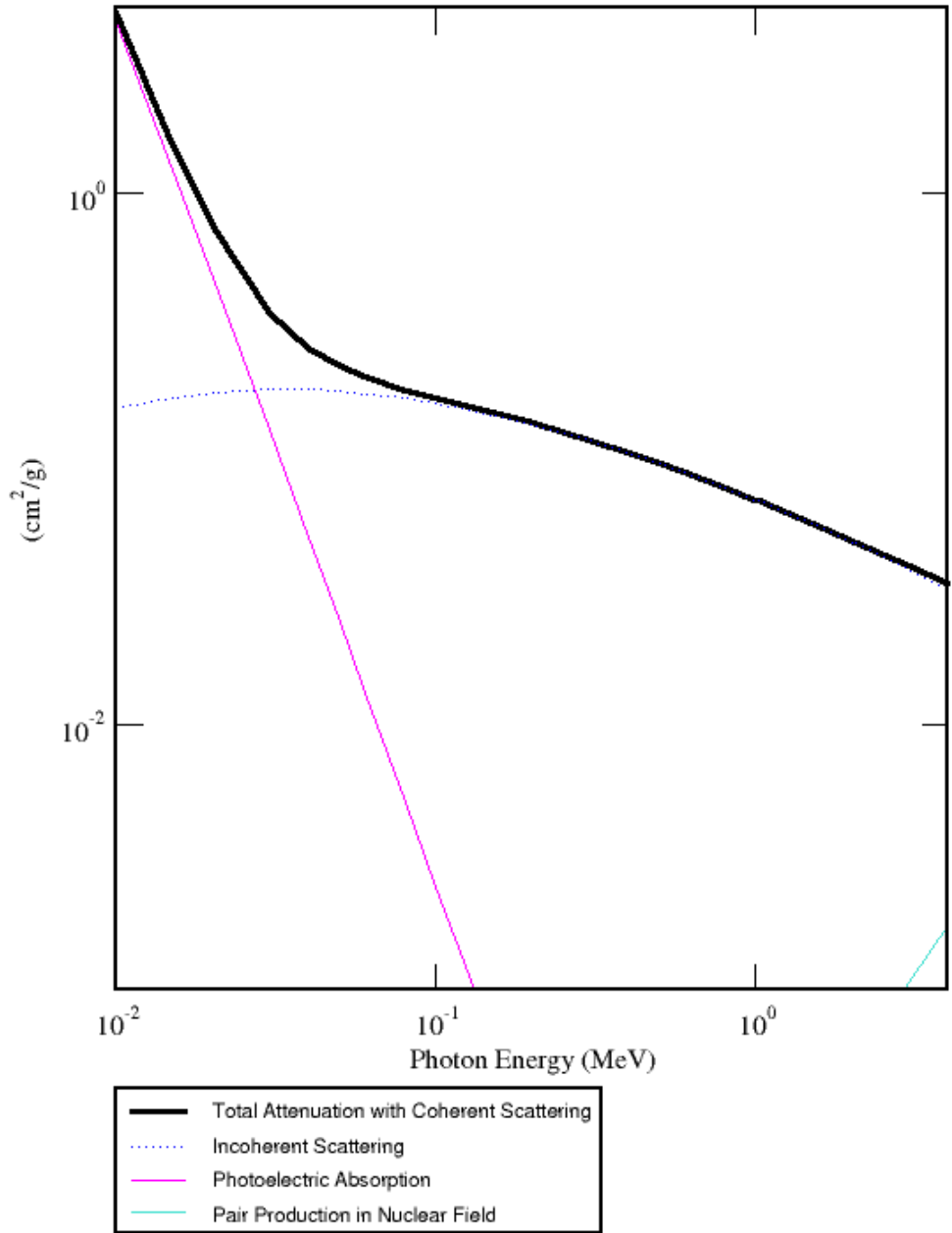


Figure 3-15. Photon mass attenuation coefficients in units of cm^2/g as a function of initial photon energy for photoelectric absorption, incoherent (Compton) scattering, pair production in a nuclear field, and total attenuation (NIST 2011).

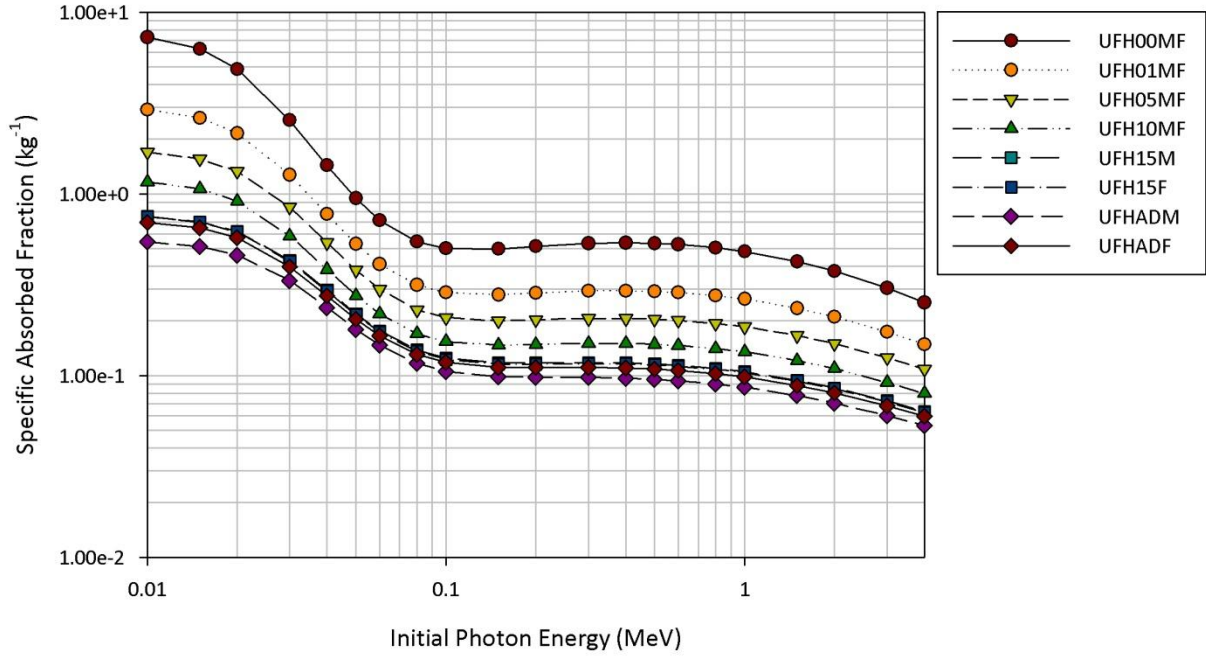


Figure 3-16. Photon SAFs showing $\Phi(\text{liver} \leftarrow \text{liver})$ for all phantoms in the UF phantom family.

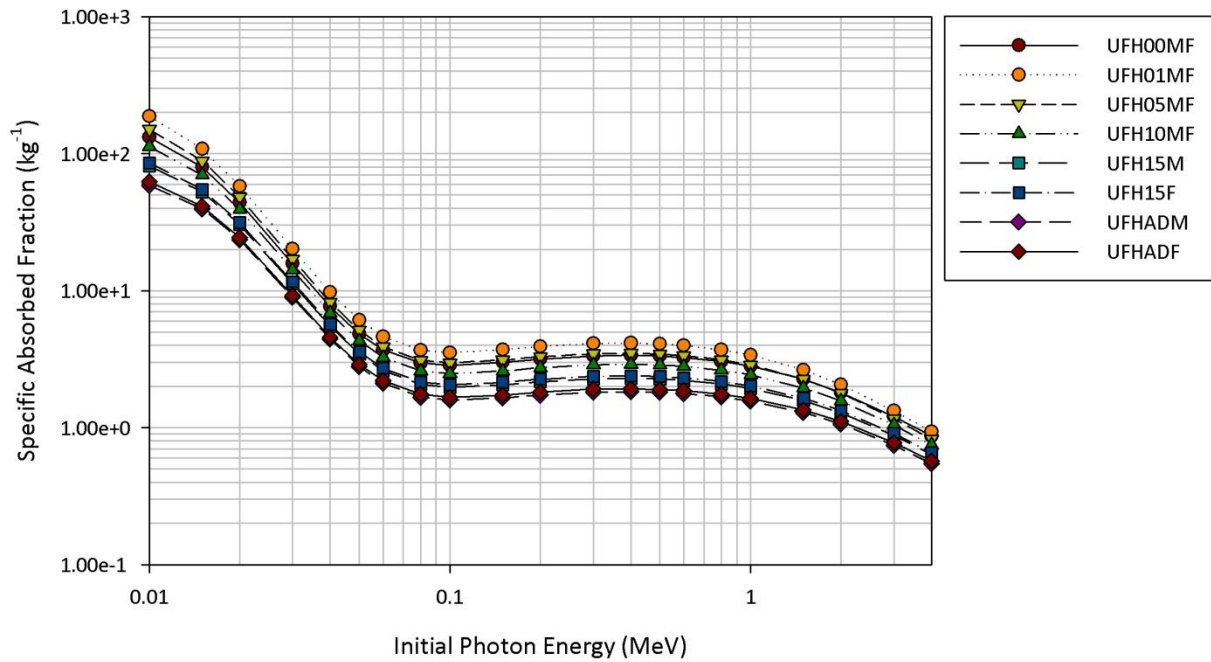


Figure 3-17. Photon SAFs showing $\Phi(\text{adrenals} \leftarrow \text{adrenals})$ for all phantoms in the UF phantom family.

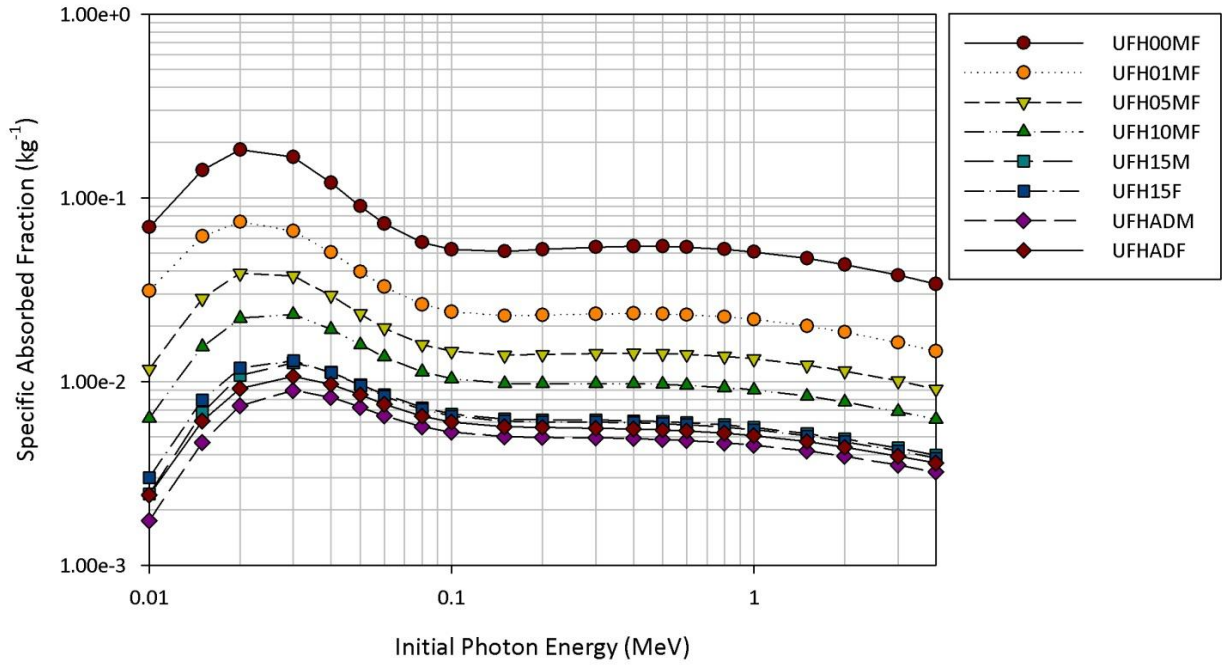


Figure 3-18. Photon SAFs showing $\Phi(\text{muscle} \leftarrow \text{lungs})$ for all phantoms in the UF phantom family.

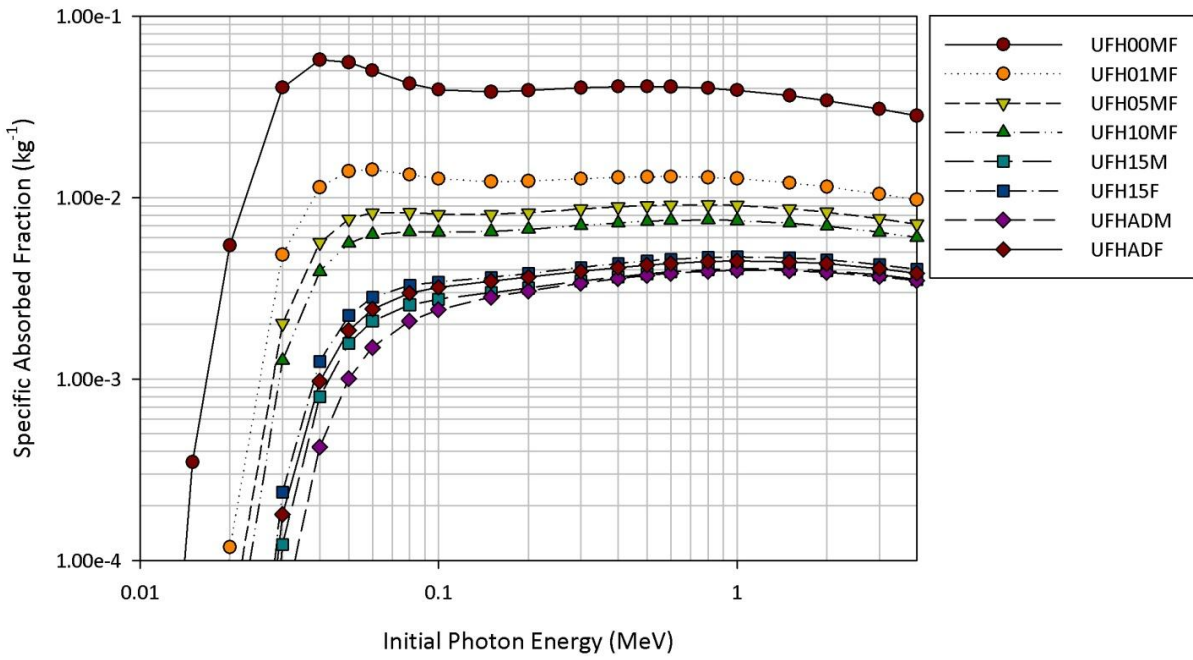


Figure 3-19. Photon SAFs showing $\Phi(\text{brain} \leftarrow \text{thyroid})$ for all phantoms in the UF phantom family.

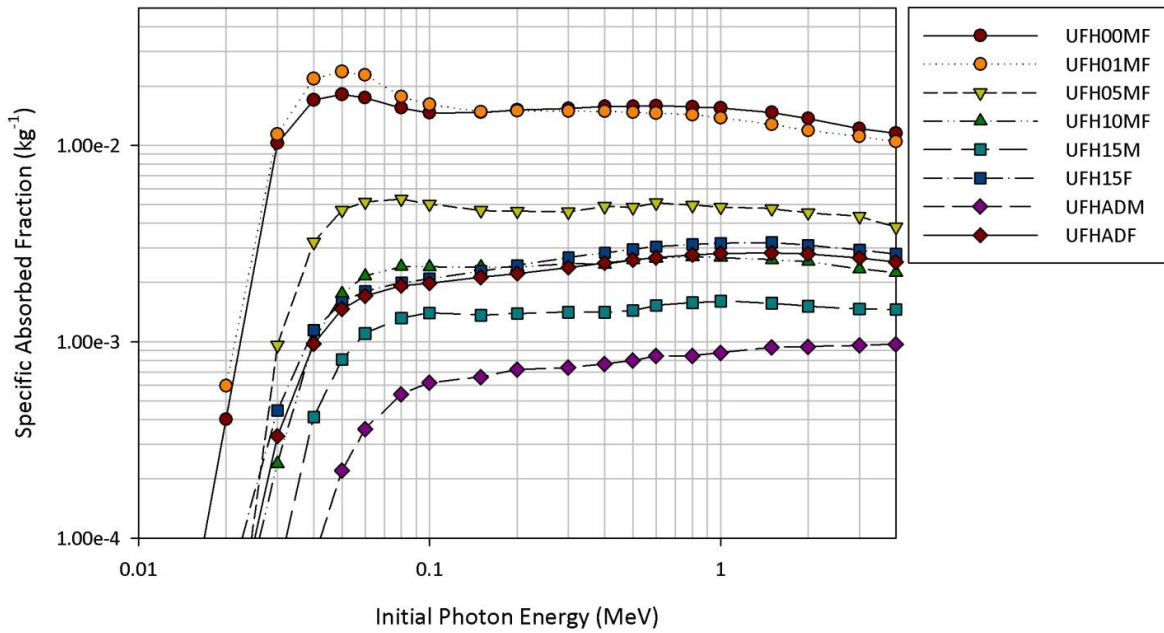


Figure 3-20. Photon SAFs showing $\Phi(adrenals \leftarrow thyroid)$ for all phantoms in the UF phantom family.

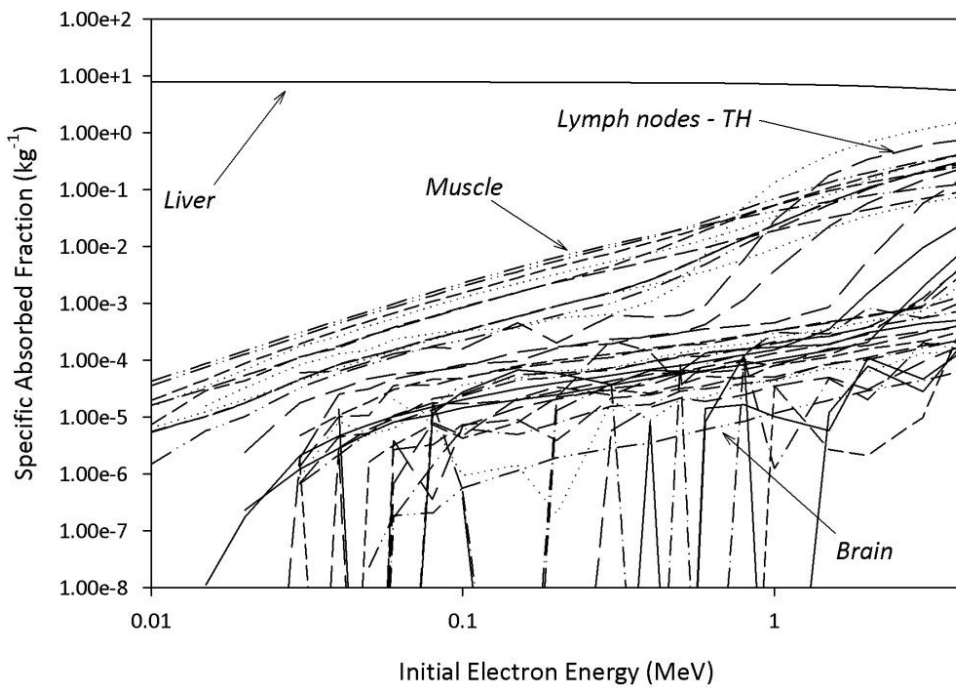


Figure 3-21. Electron SAFs for a uniform electron source in the liver of the UFH00M phantom using full transport techniques (i.e., no two-simulation improvement).

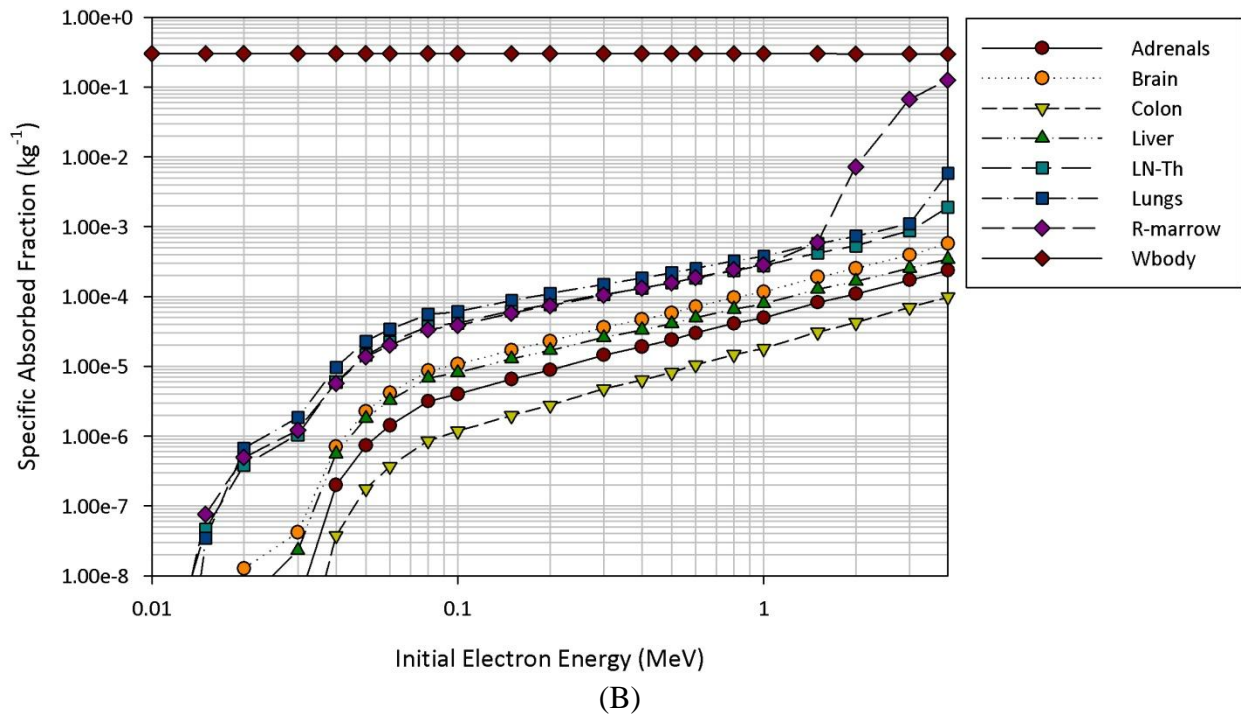
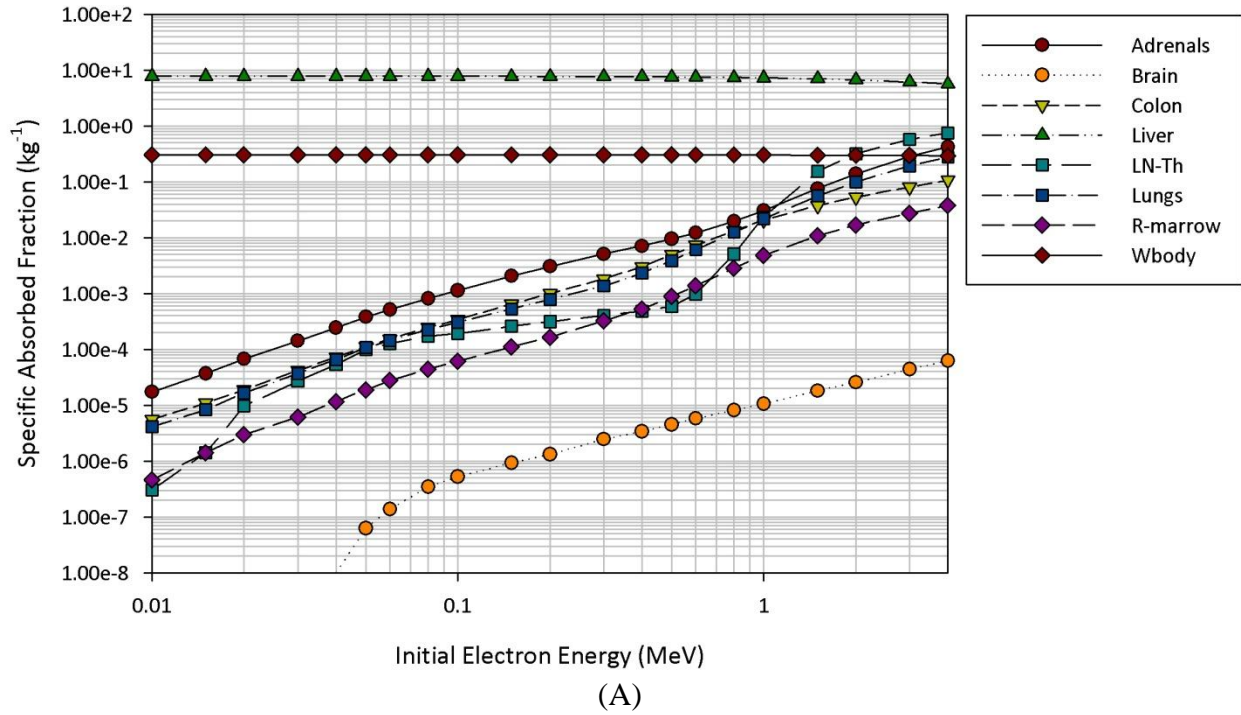


Figure 3-22. A subset of the electron SAF curves for a (A) large (liver) and (B) small (thyroid) source tissue in the UFH00MF phantoms.

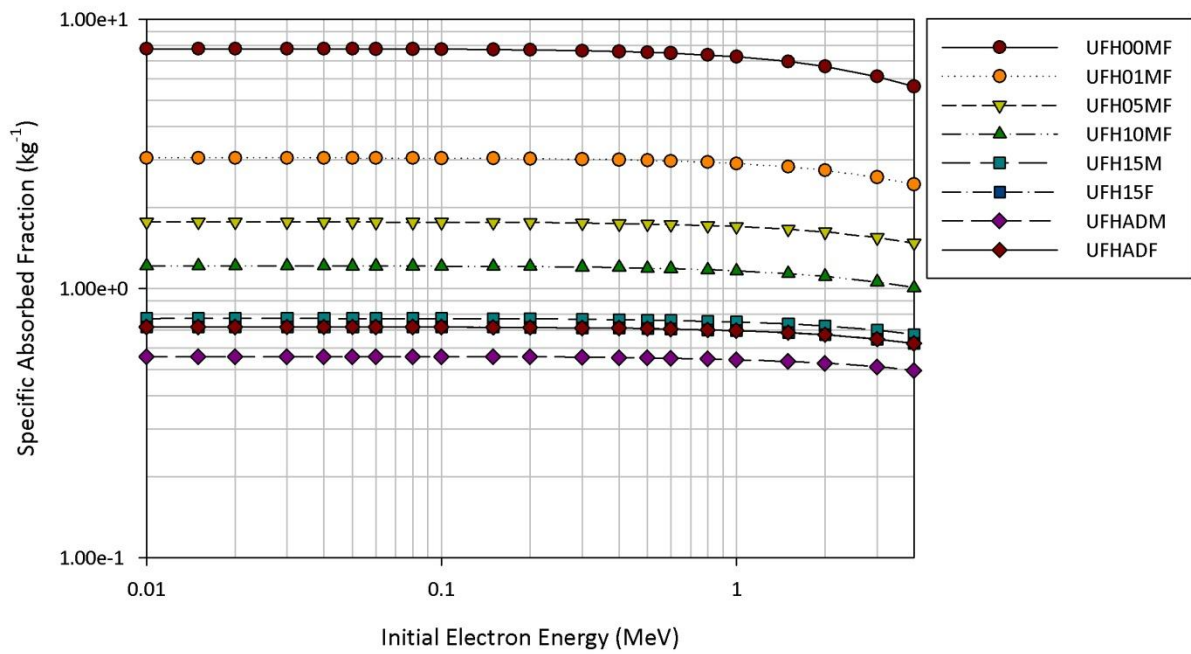


Figure 3-23. Electron SAFs showing $\Phi(\text{liver} \leftarrow \text{liver})$ for all phantoms in the UF phantom family.

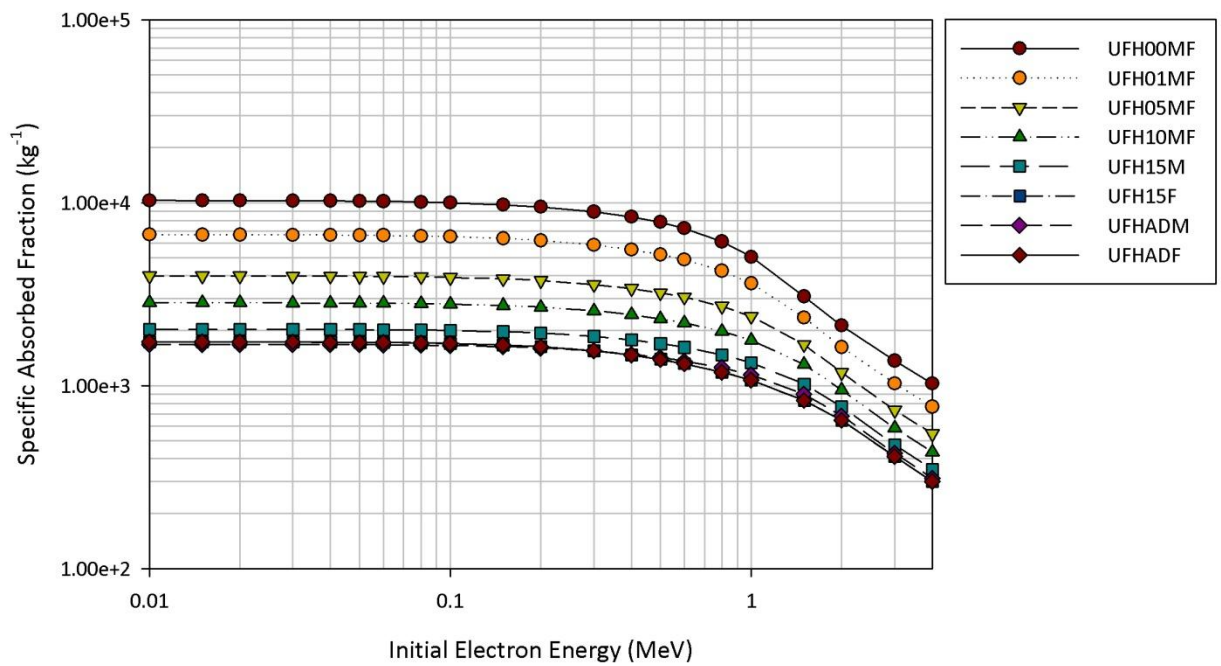


Figure 3-24. Electron SAFs showing $\Phi(\text{pituitary gland} \leftarrow \text{pituitary gland})$ for all phantoms in the UF phantom family.

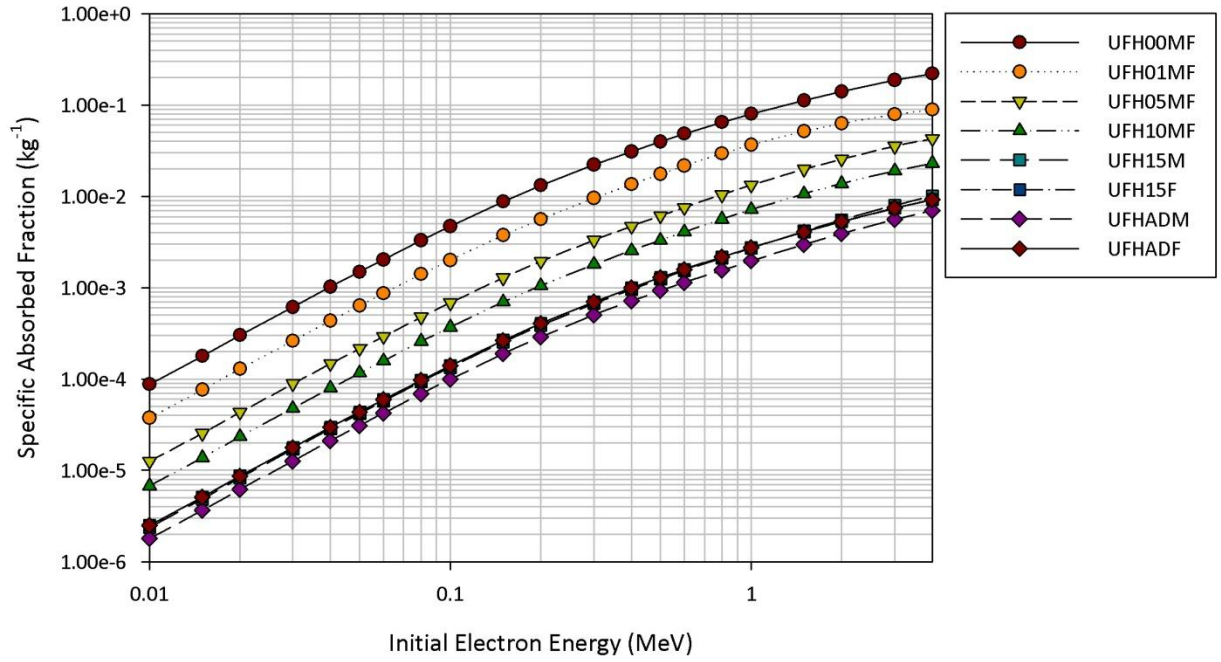


Figure 3-25. Electron SAFs showing $\Phi(\text{muscle} \leftarrow \text{lungs})$ for all phantoms in the UF phantom family.

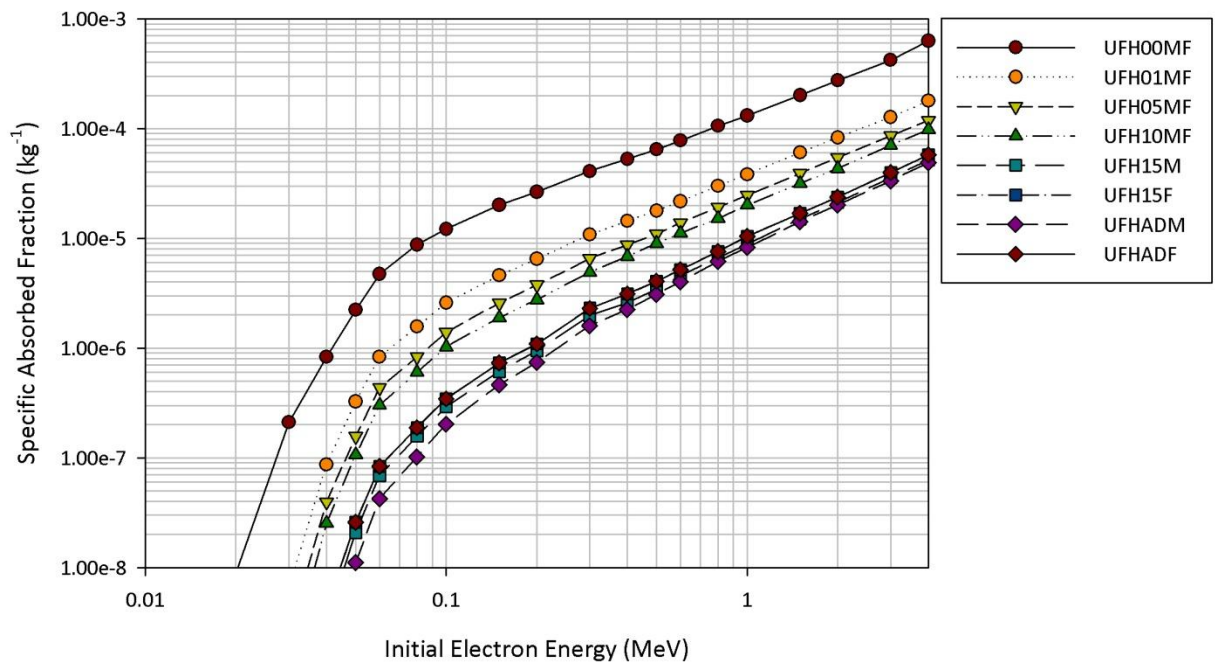


Figure 3-26. Electron SAFs showing $\Phi(\text{brain} \leftarrow \text{thyroid})$ for all phantoms in the UF phantom family.

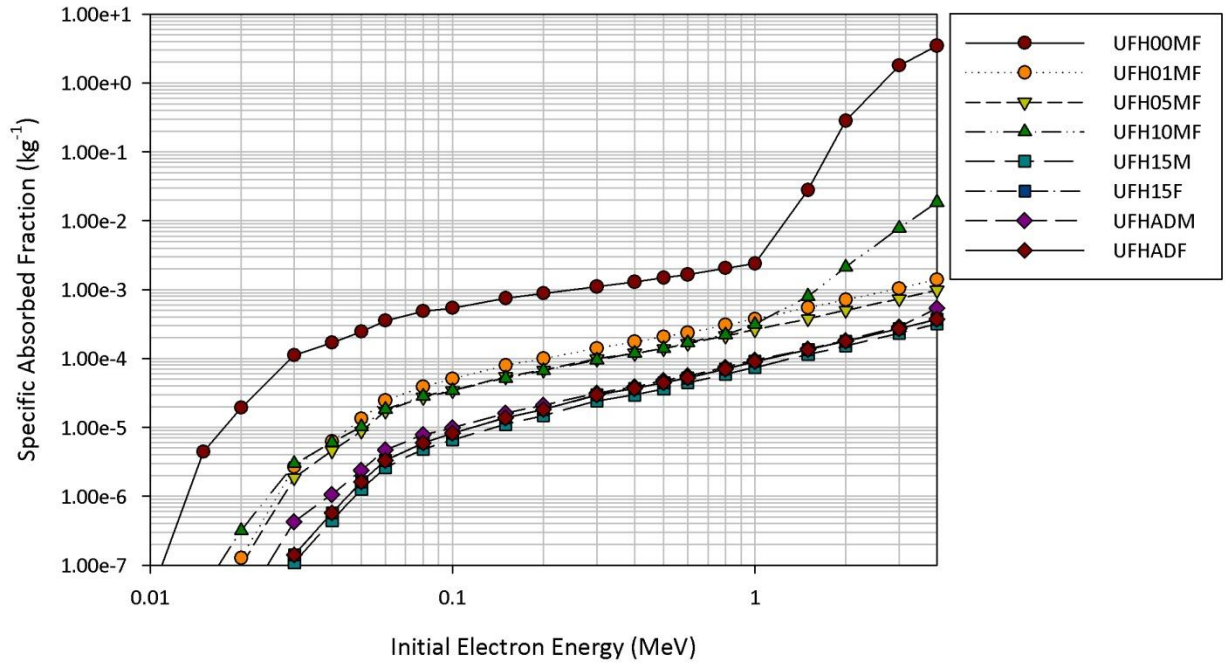


Figure 3-27. Electron SAFs showing $\Phi(\text{salivary glands} \leftarrow \text{thyroid})$ for all phantoms in the UF phantom family.

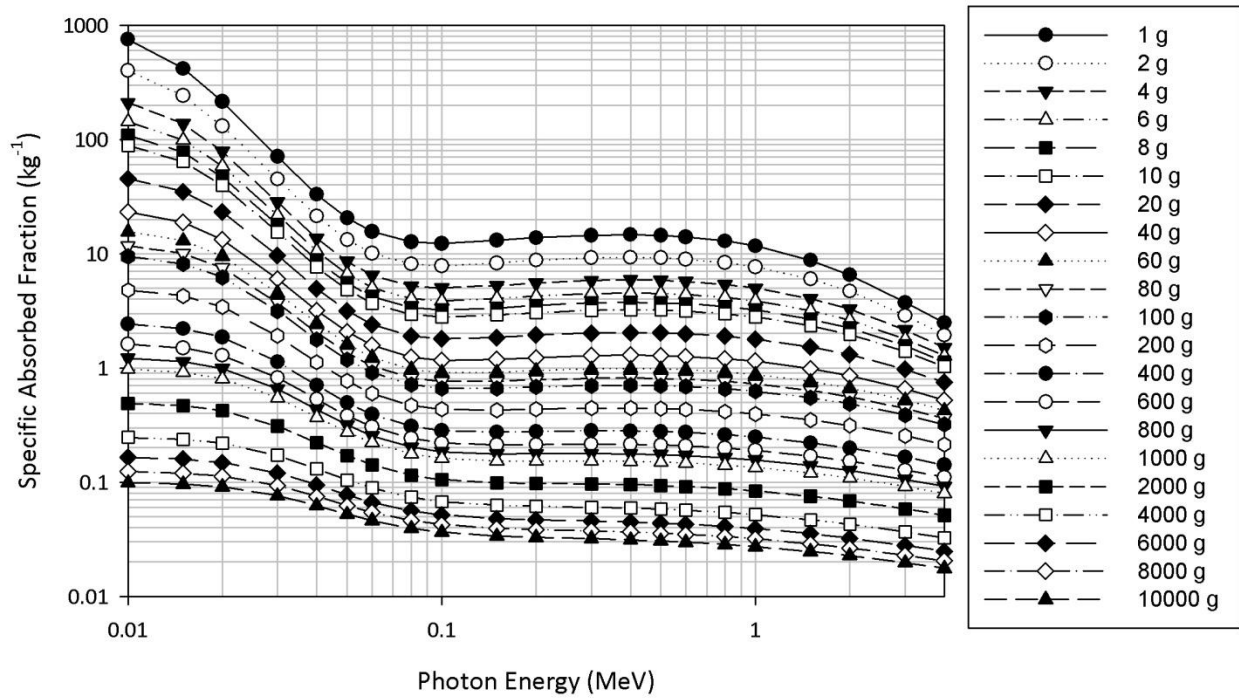


Figure 3-28. Sphere self-dose SAFs as a function of initial photon energy and sphere size for the photon self-dose scaling study.

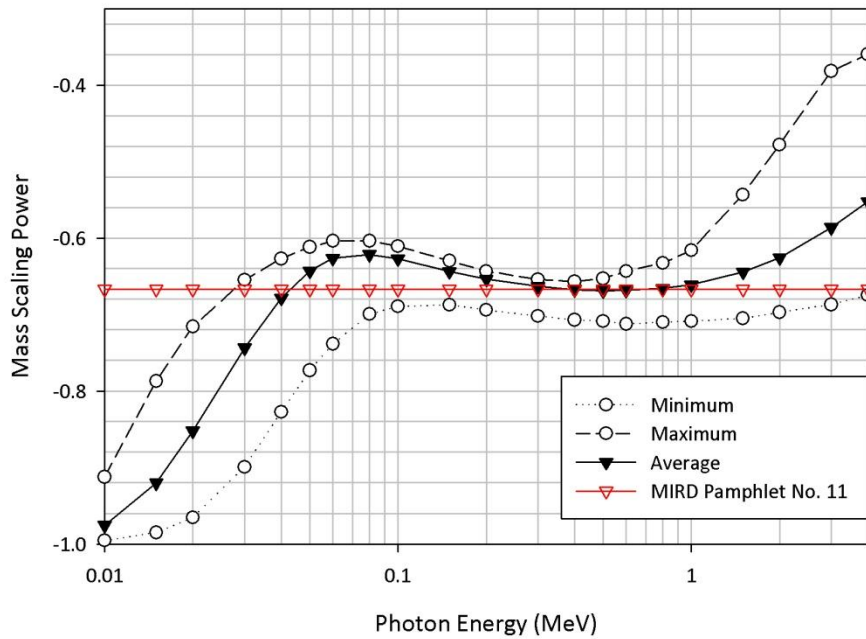


Figure 3-29. Mass scaling powers for photon self-dose showing the minimum, maximum, and average values at each photon energy and the corresponding recommendation from MIRD Pamphlet No. 11 (Snyder *et al.* 1975).

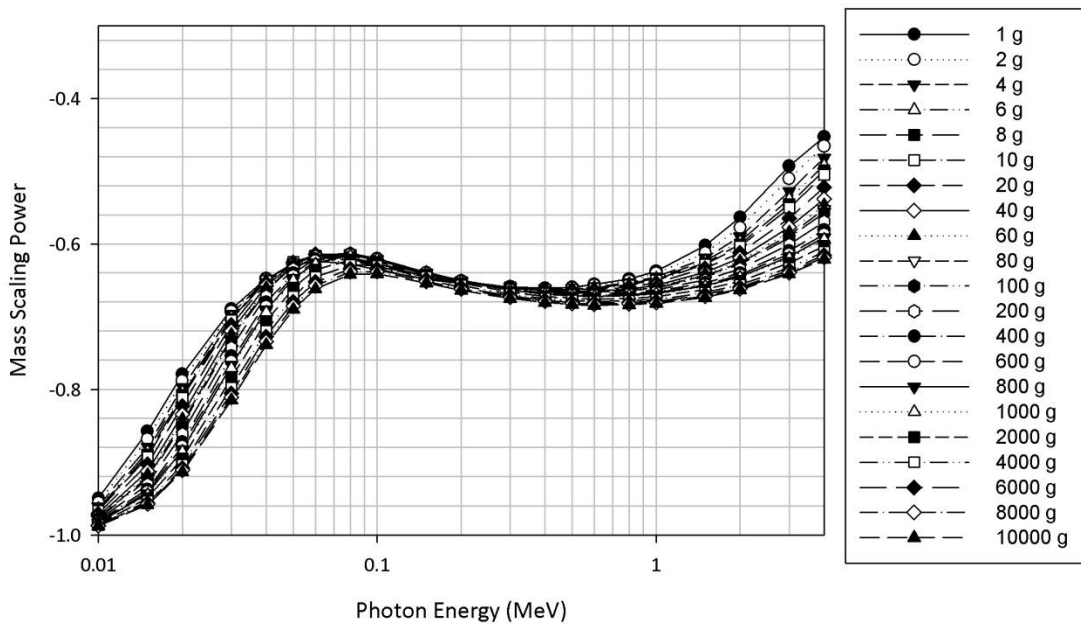


Figure 3-30. Mass scaling powers for photon self-dose as a function of both reference sphere mass and initial photon energy.

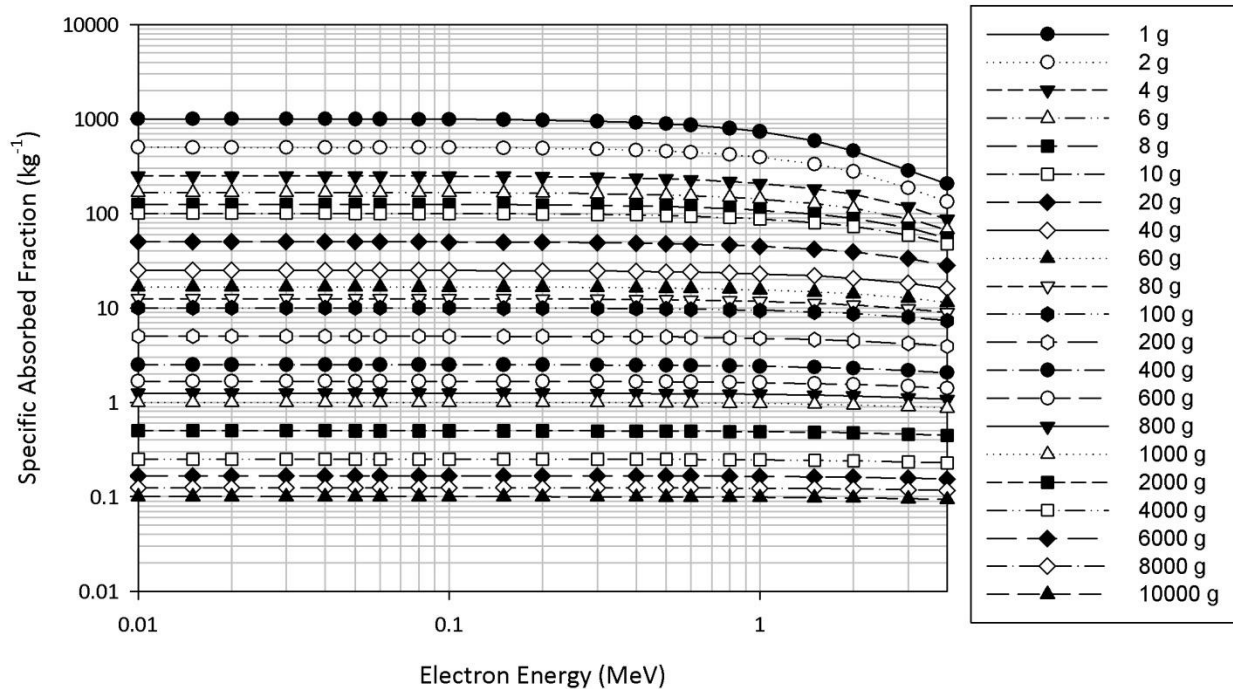


Figure 3-31. Sphere self-dose SAFs as a function of initial electron energy and sphere size for the electron self-dose scaling study.

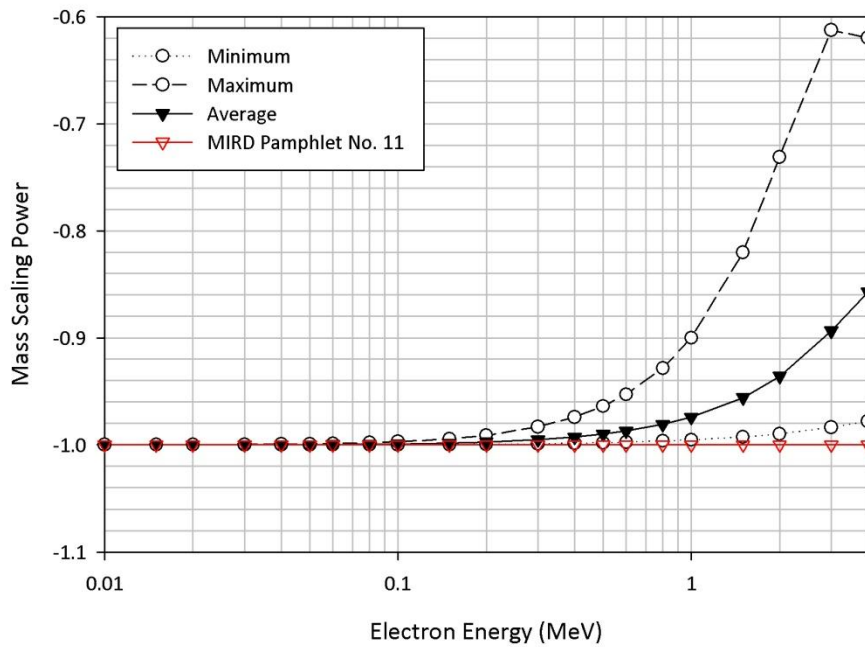


Figure 3-32. Mass scaling powers for electron self-dose showing the minimum, maximum, and average values at each electron energy and the corresponding recommendation from MIRDP Pamphlet No. 11 (Snyder *et al.* 1975).

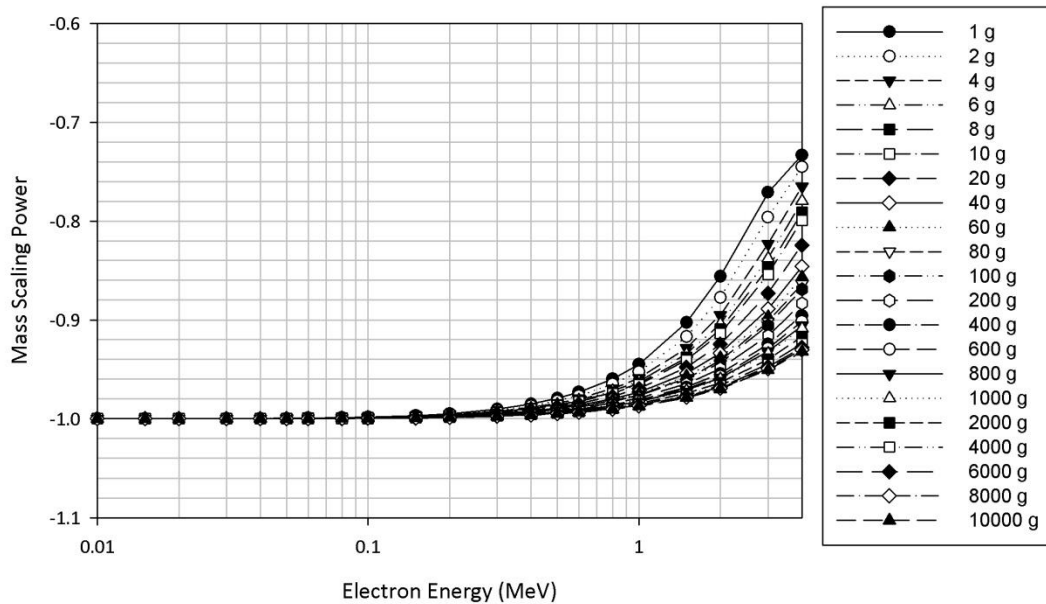


Figure 3-33. Mass scaling powers for electron self-dose as a function of both reference sphere mass and initial electron energy.

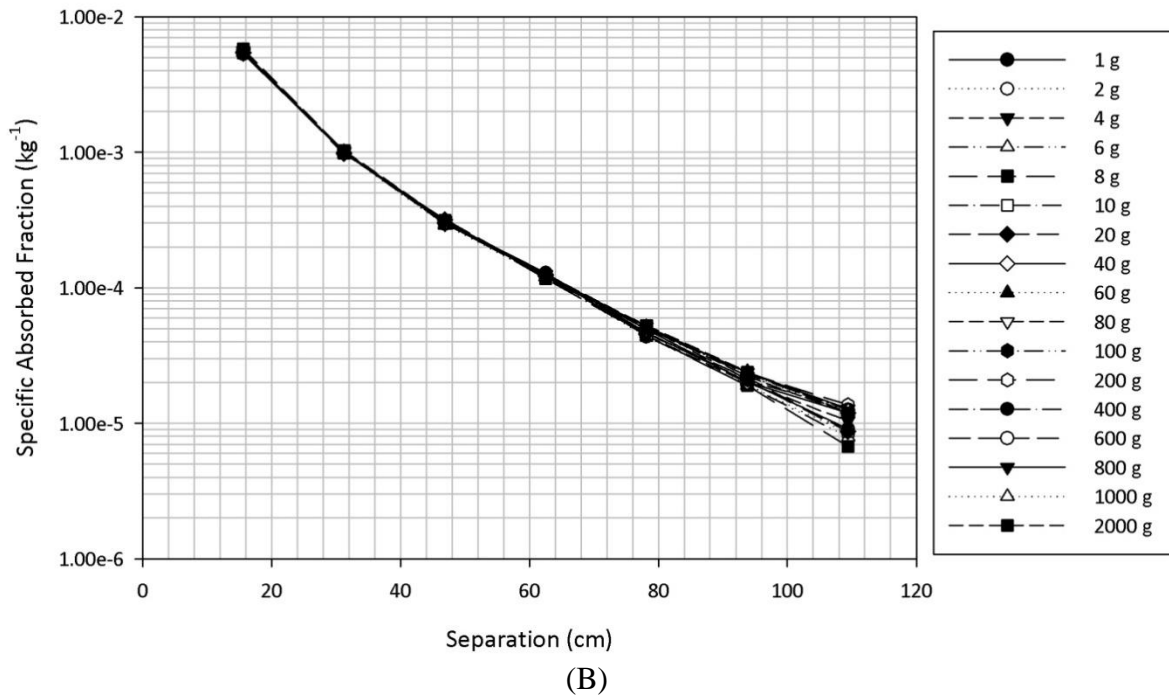
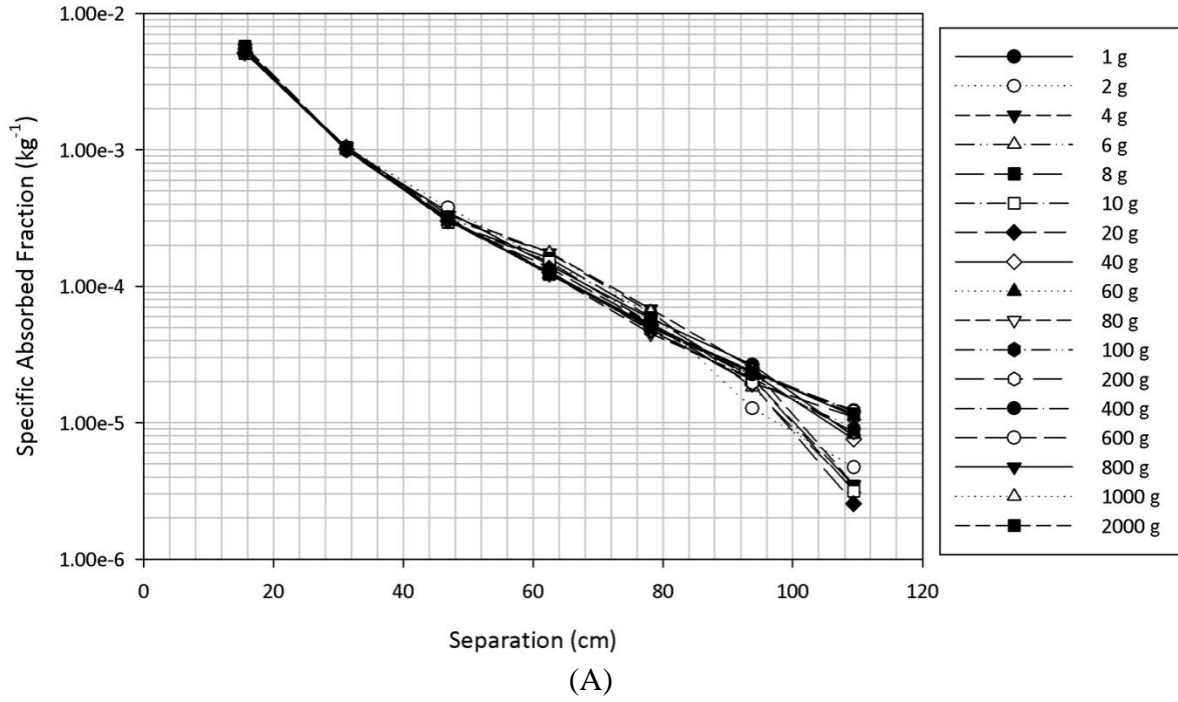


Figure 3-34. Photon specific absorbed fractions for the (A) 1 g, (B) 100 g, and (C) 2 kg (following page) source spheres and 4 MeV photons as a function of sphere separation and target sphere mass.

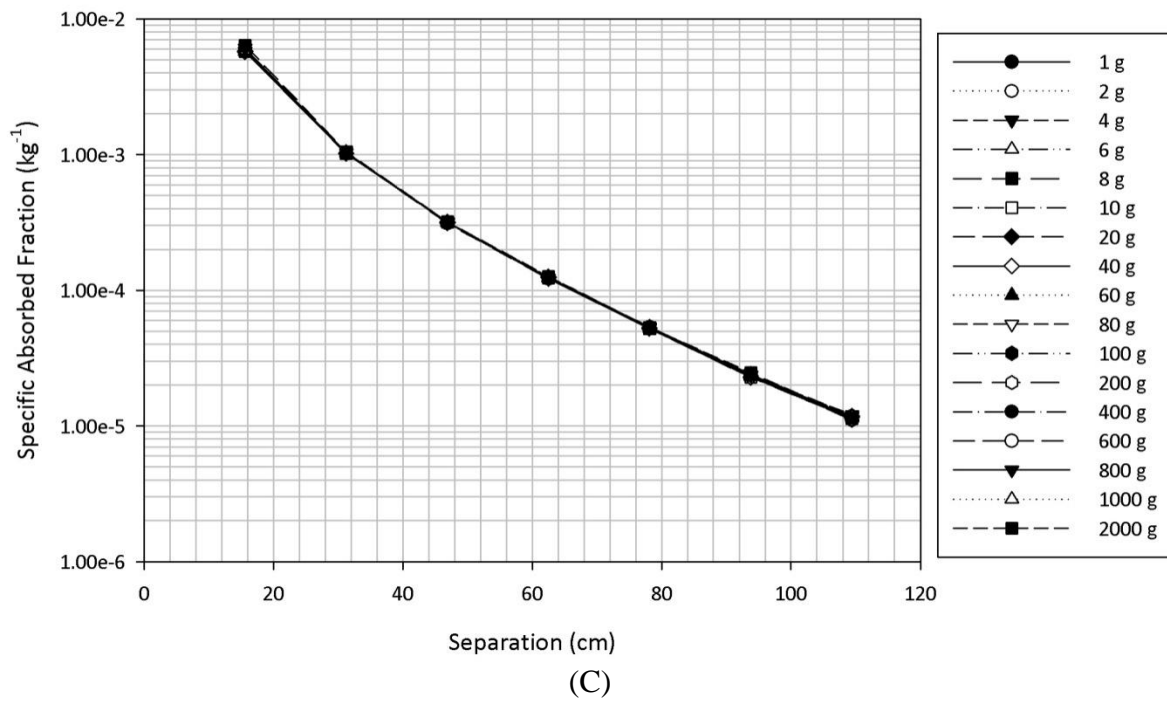


Figure 3-34. Continued.

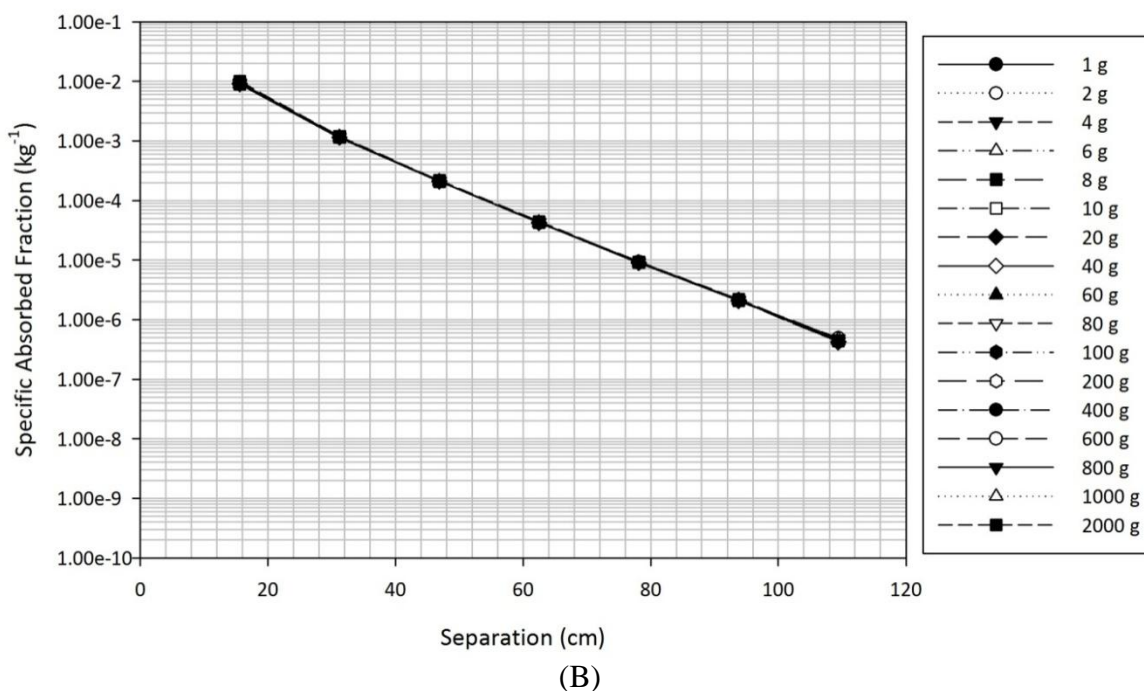
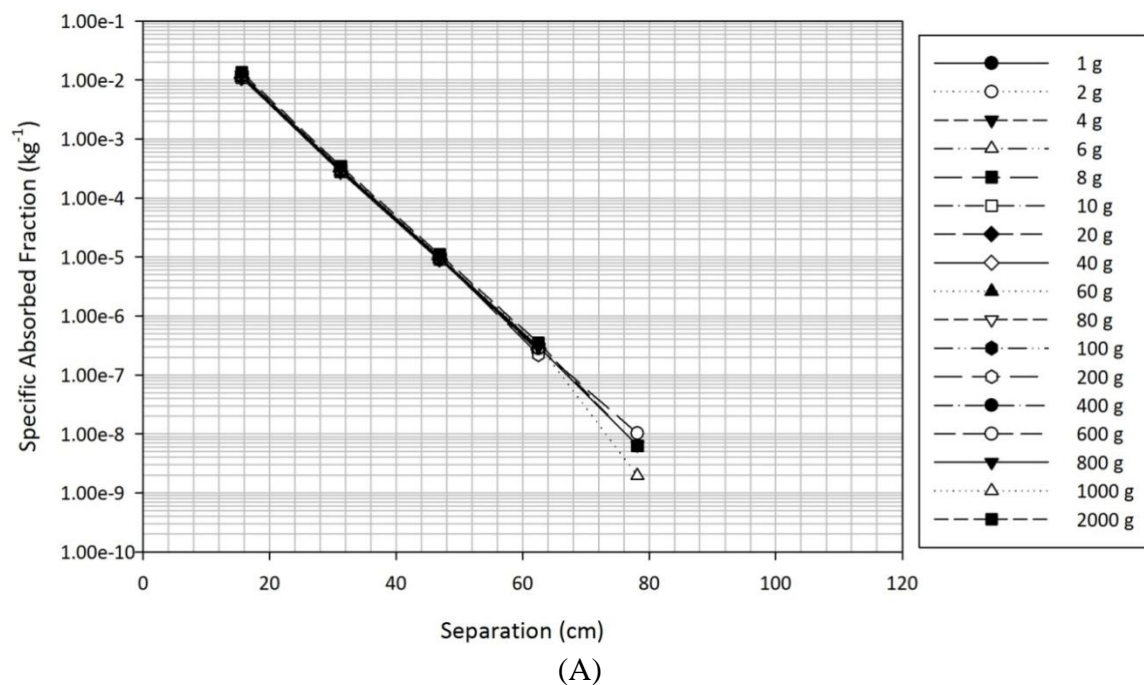


Figure 3-35. Photon specific absorbed fractions for the 2 kg source spheres and (A) 50 keV and (B) 500 keV photons as a function of sphere separation and target sphere mass (the 4 MeV – 2 kg irradiation geometry can be seen in Figure 3-34 for comparison).

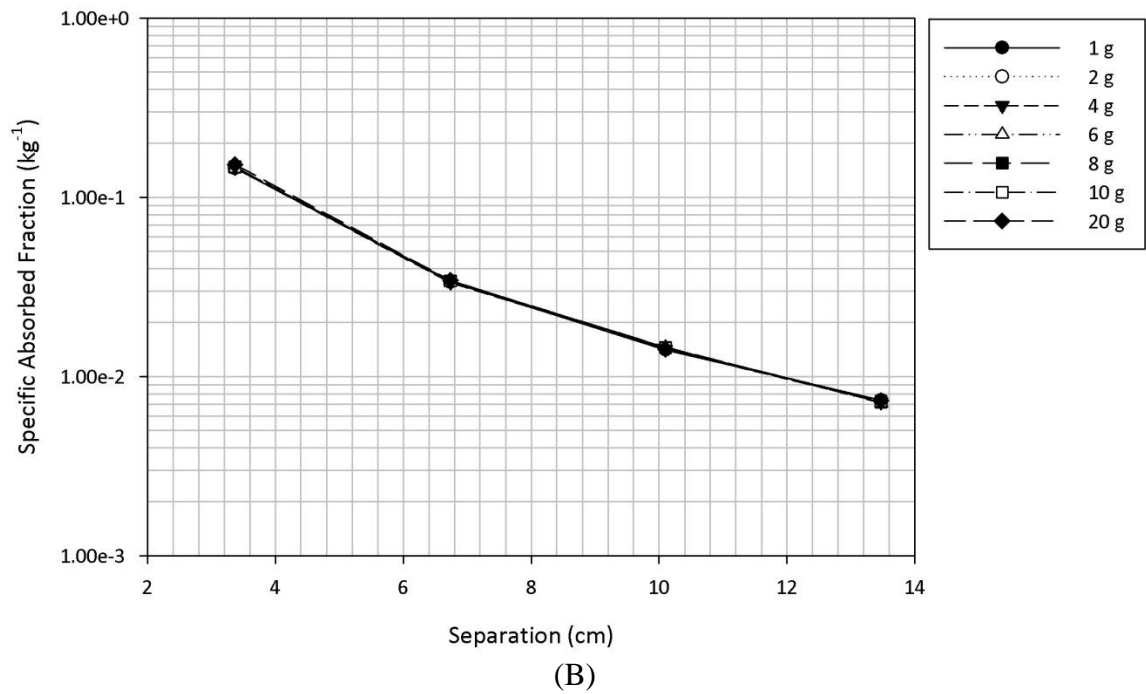
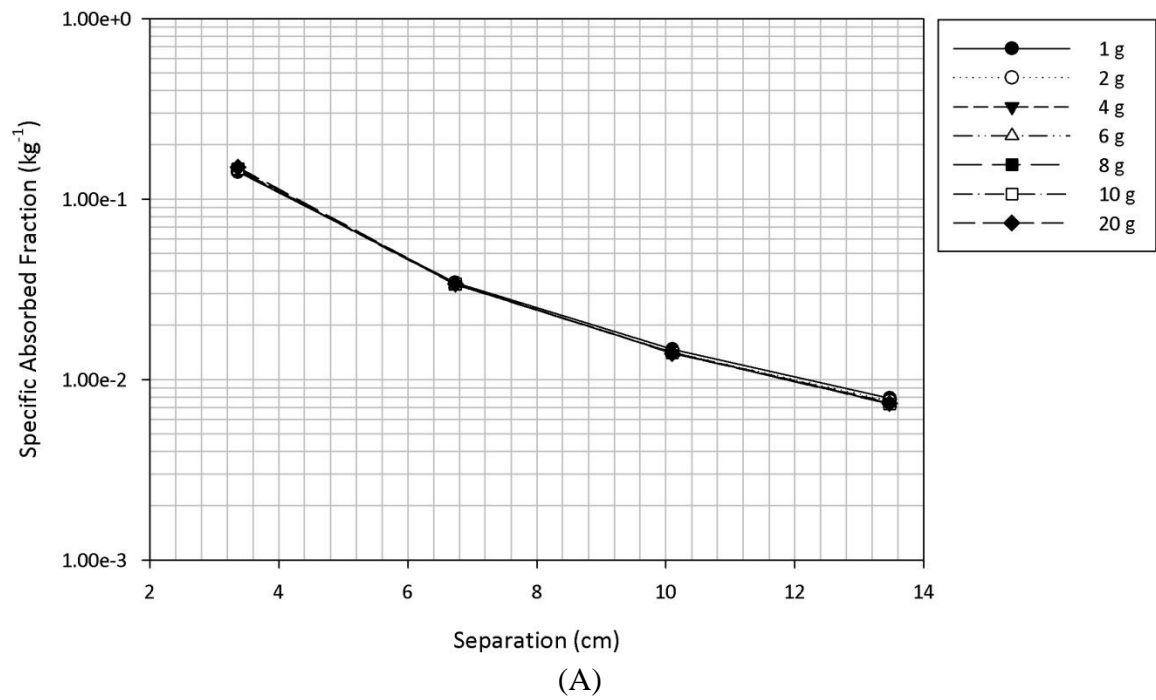


Figure 3-36. Photon specific absorbed fractions for the (A) 1 g, (B) 6 g, and (C) 20 g (following page) source spheres and 4 MeV photons as a function of sphere separation and target sphere mass.

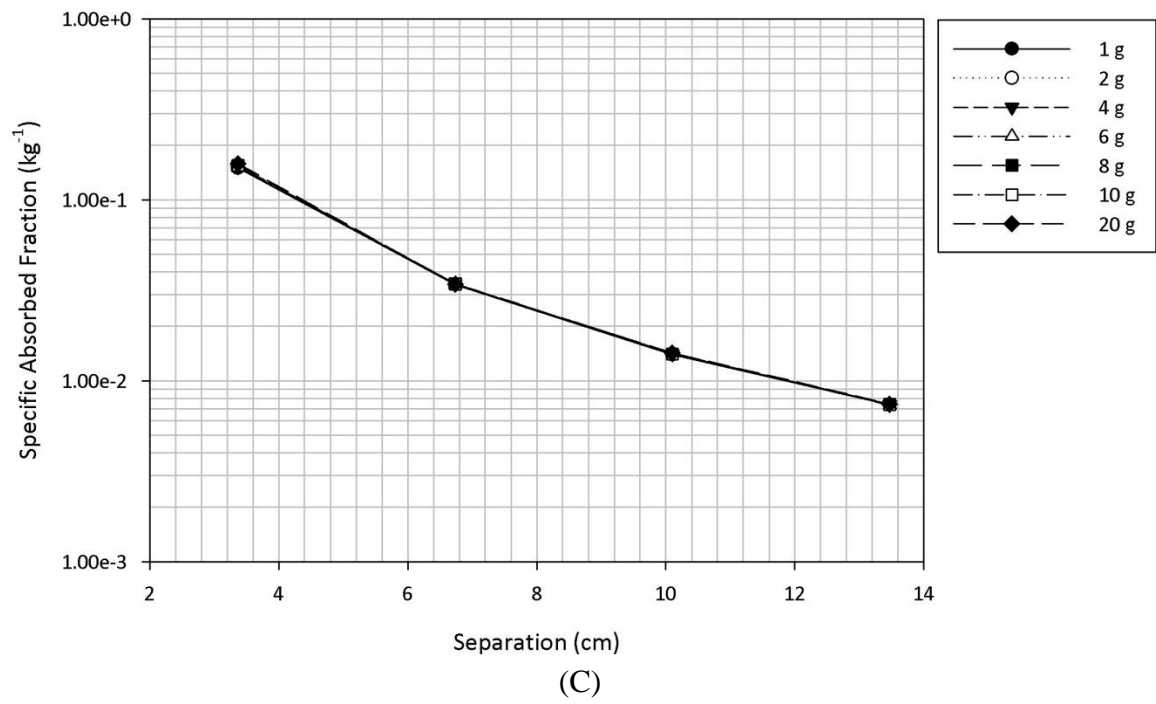


Figure 3-36. Continued.

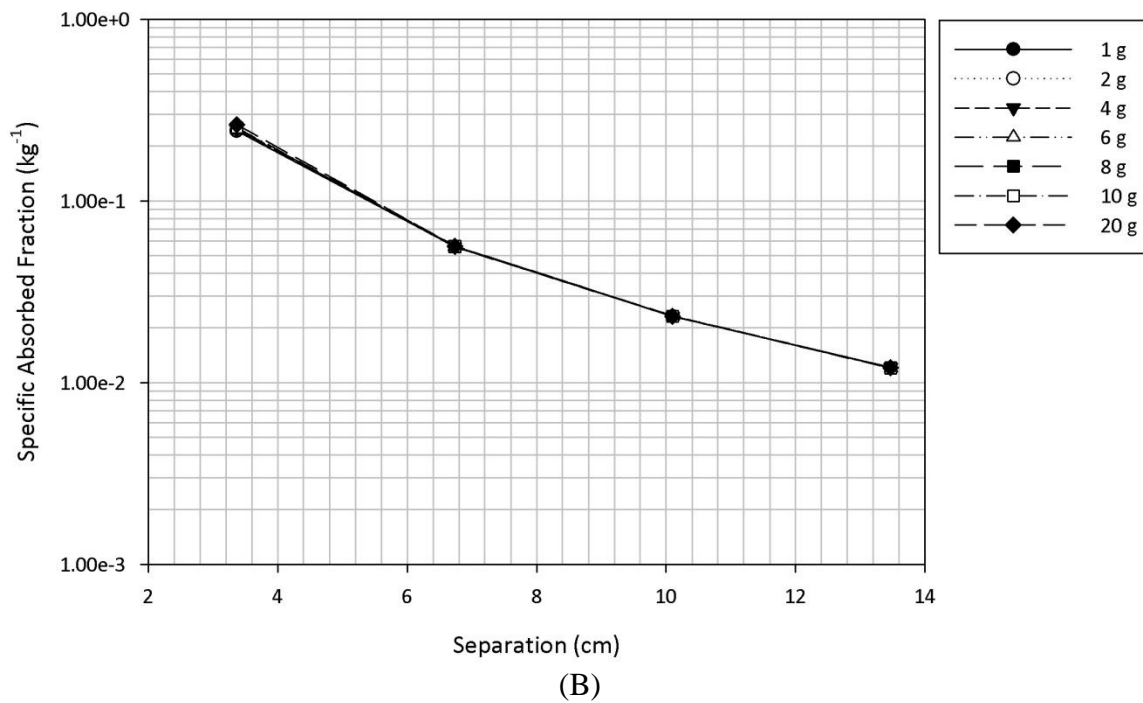
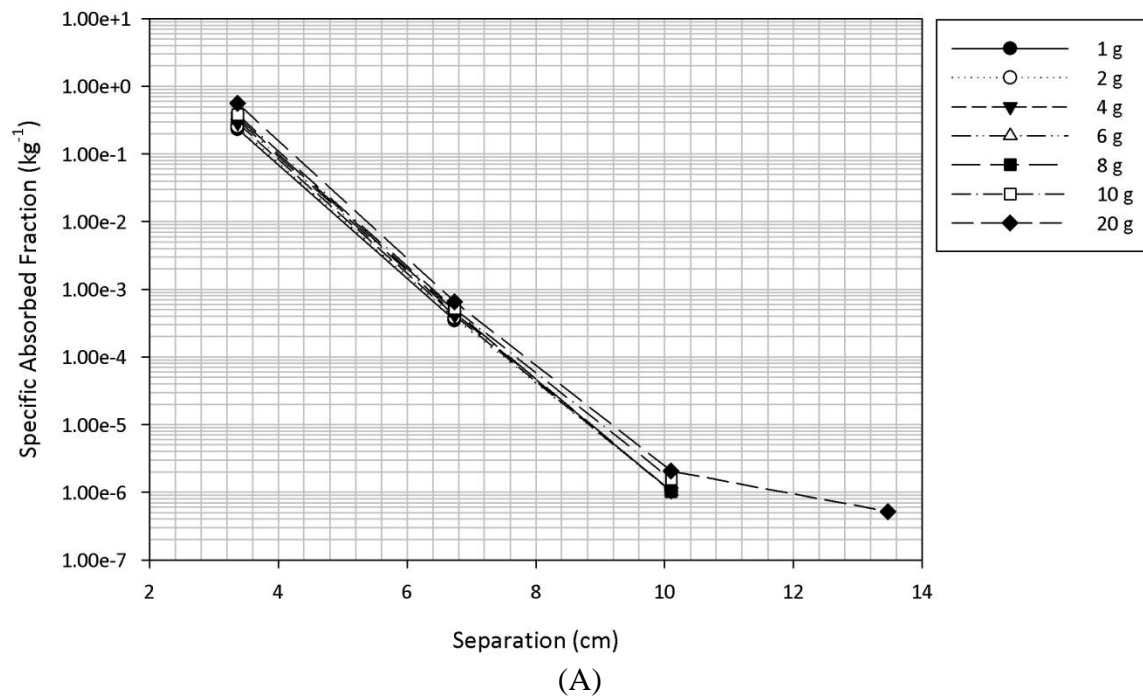


Figure 3-37. Photon specific absorbed fractions for the 20 g source spheres and (A) 15 keV and (B) 500 keV photons as a function of sphere separation and target sphere mass.

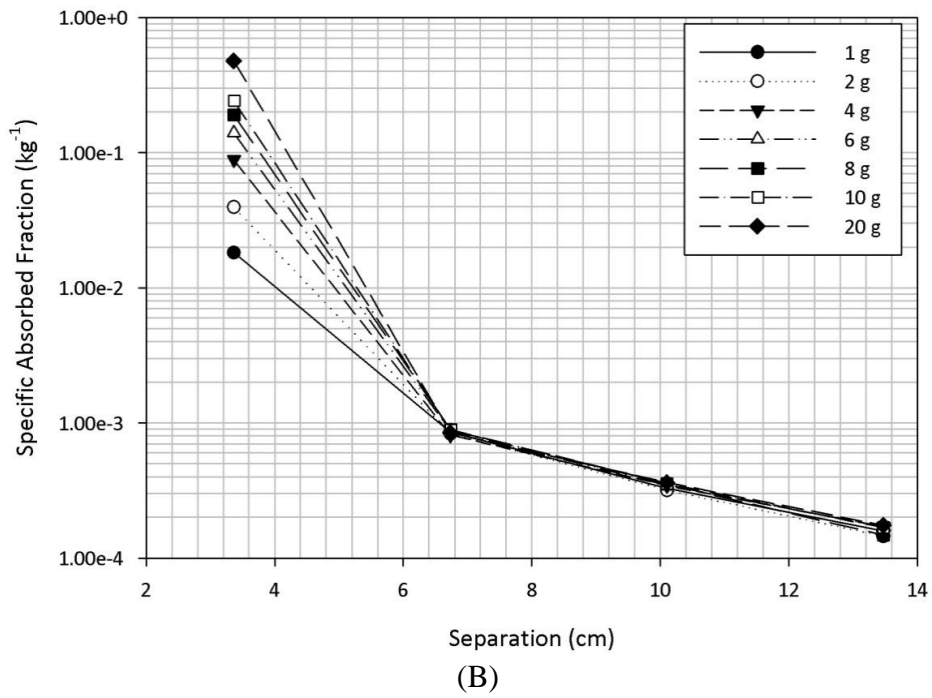
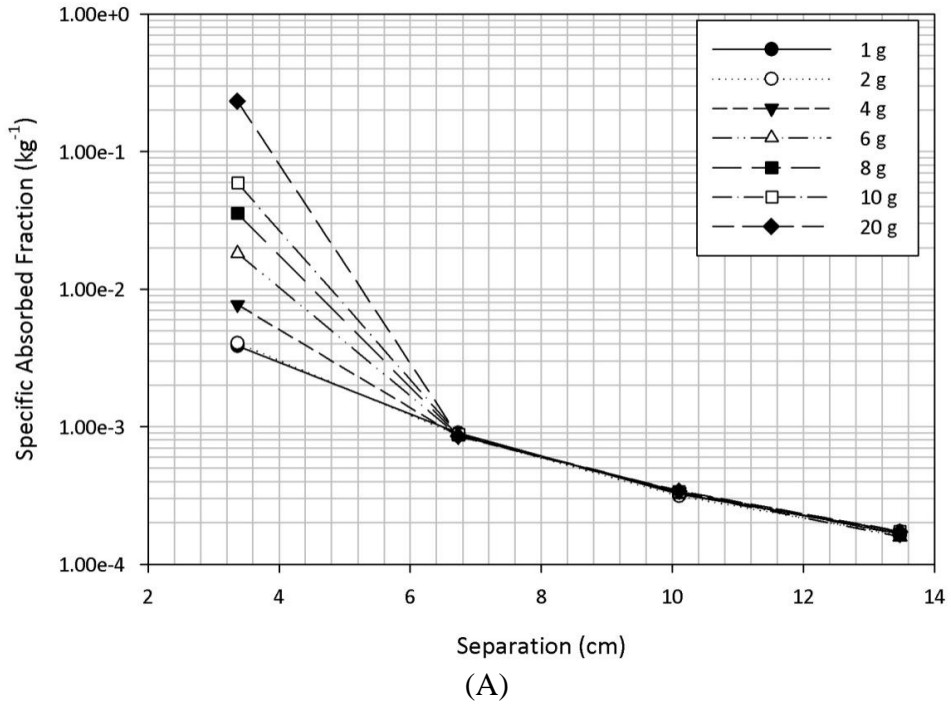


Figure 3-38. Electron specific absorbed fractions for the (A) 1 g, (B) 6 g, and (C) 20 g (following page) source spheres and 4 MeV electrons as a function of sphere separation and target sphere mass.

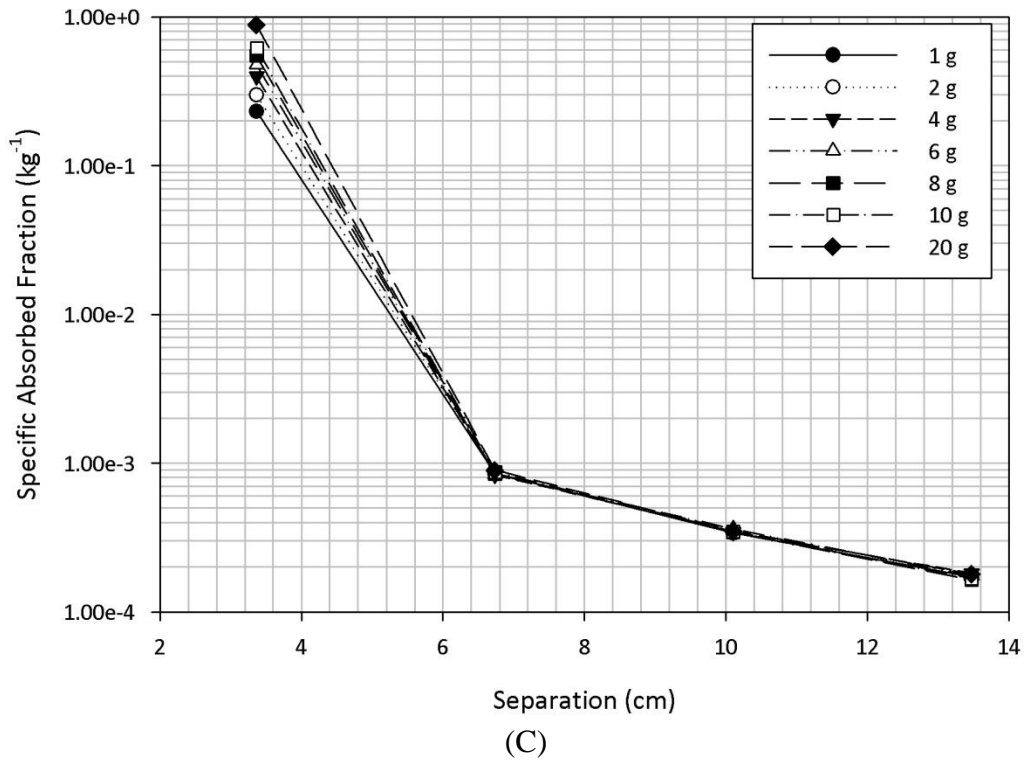


Figure 3-38. Continued.

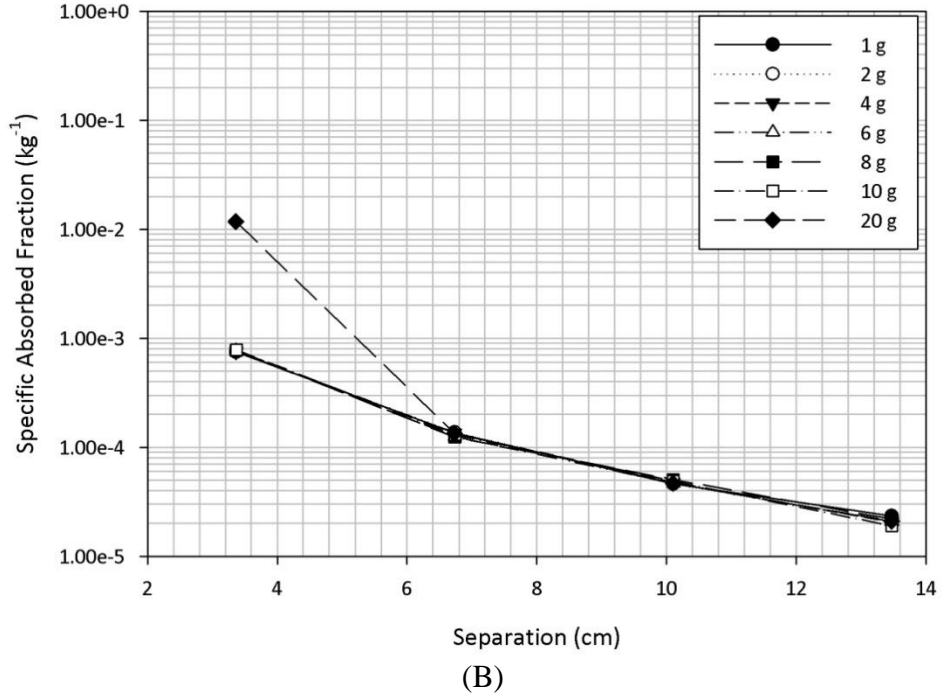
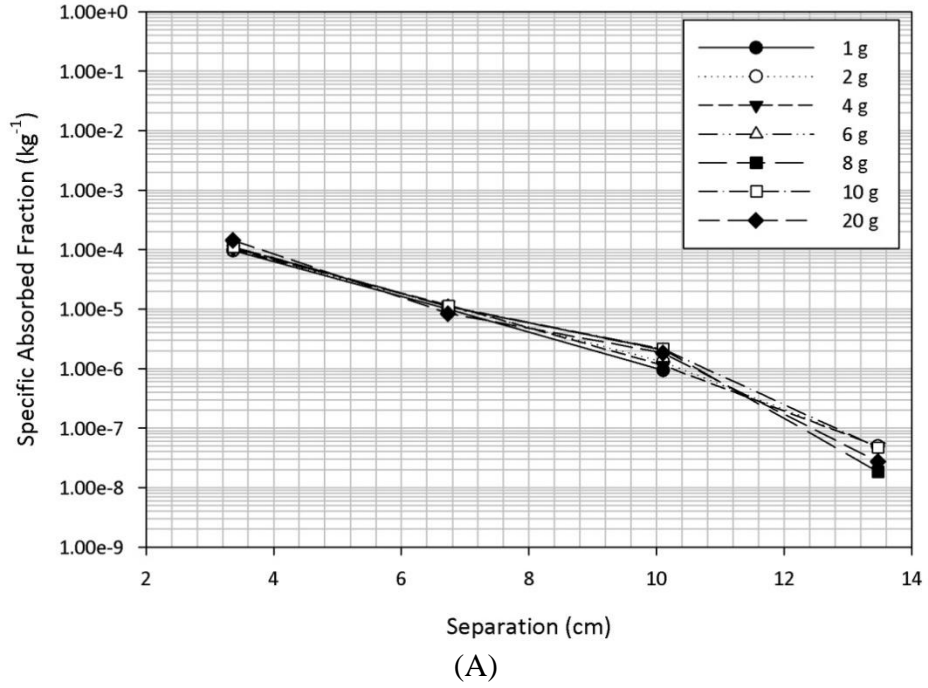


Figure 3-39. Electron specific absorbed fractions for the 20 g source spheres and (A) 50 keV and (B) 500 keV electrons as a function of sphere separation and target sphere mass.

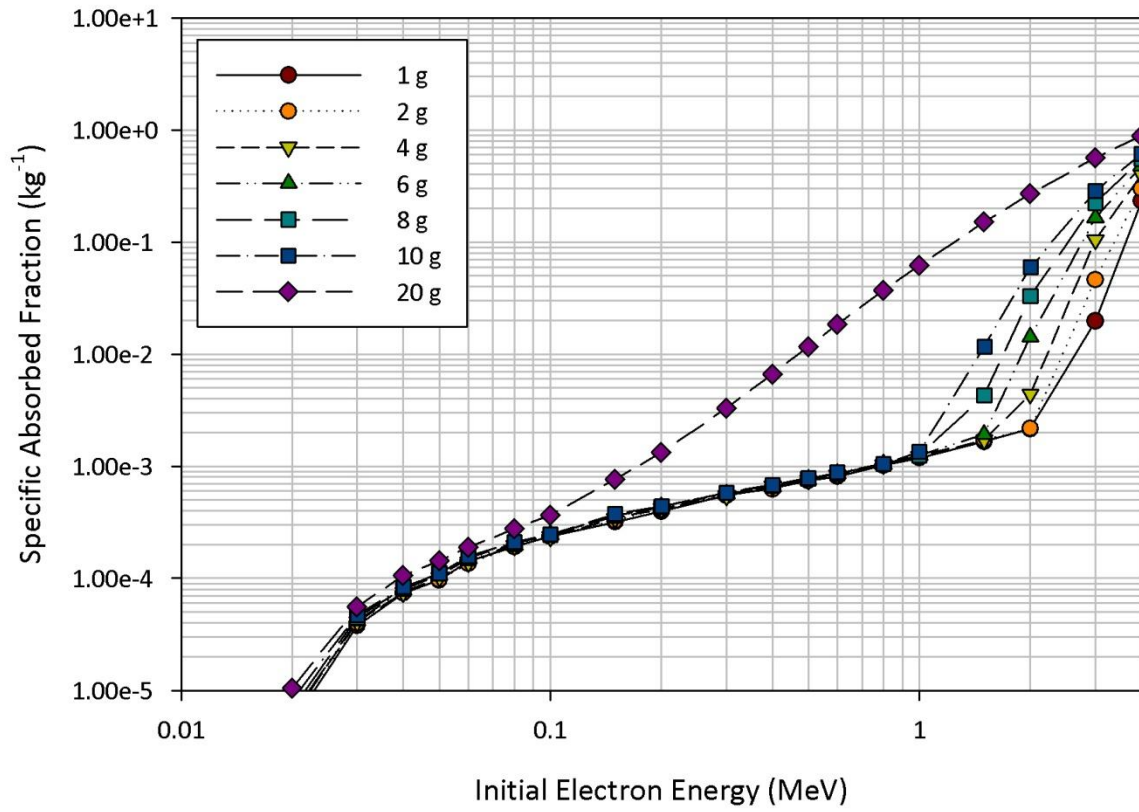


Figure 3-40. Electron cross-dose SAFs for differing target sphere sizes for the 3.368 cm center-to-center separation and 20 g source sphere.

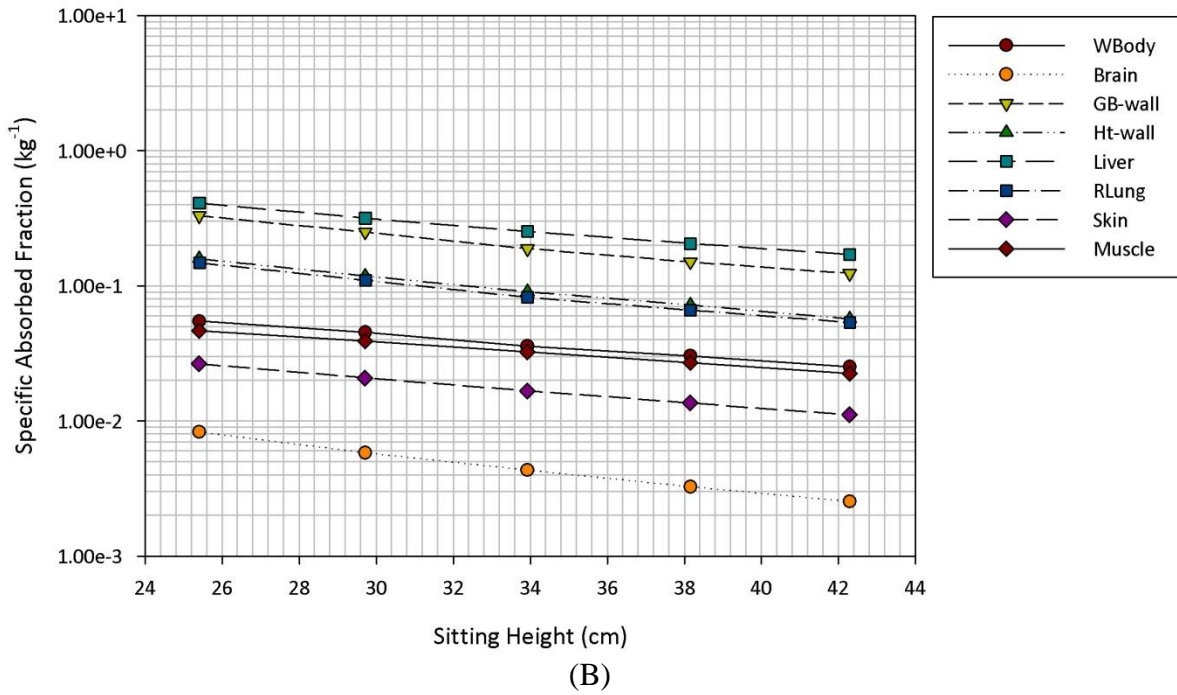
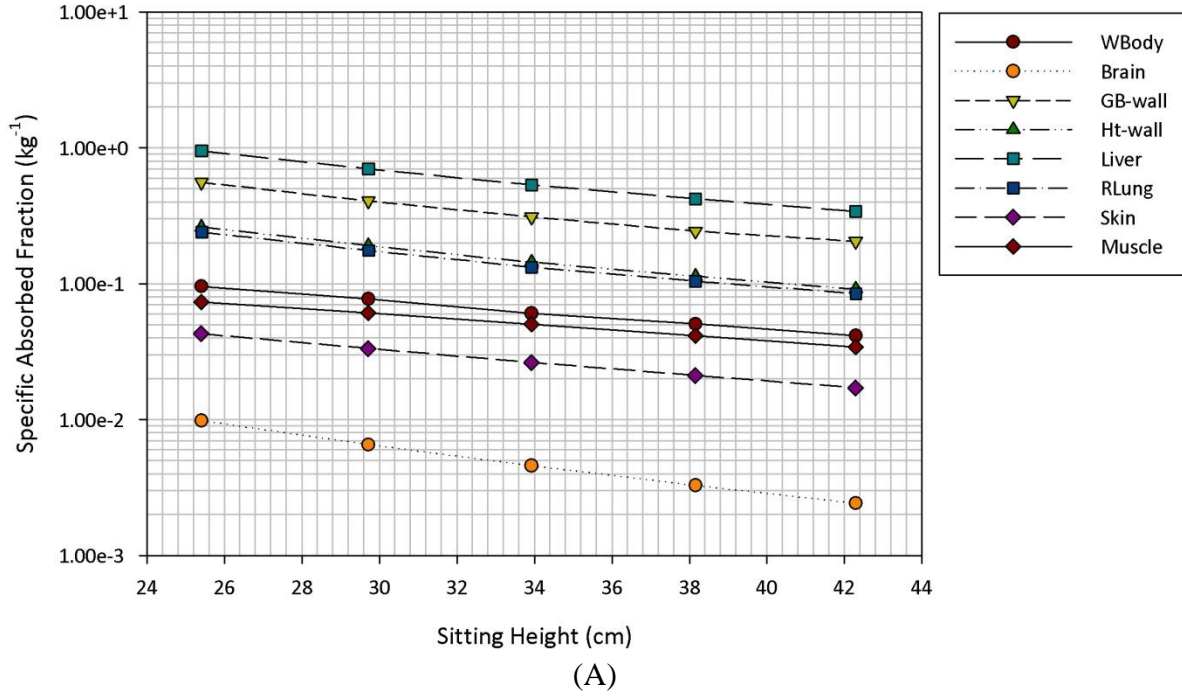


Figure 3-41. Variations in SAF with changes in sitting height for uniform (A) 500 keV and (B) 4 MeV photon sources in the liver of the UFH00M-based phantoms for a limited number of target tissues.

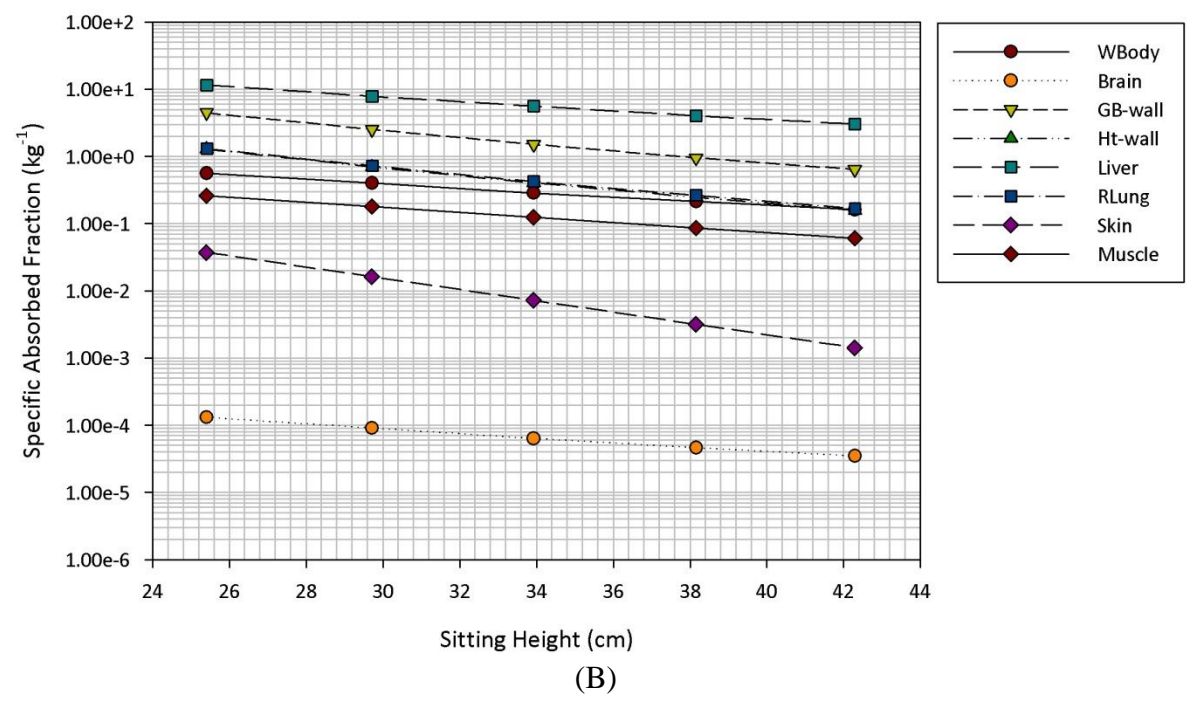
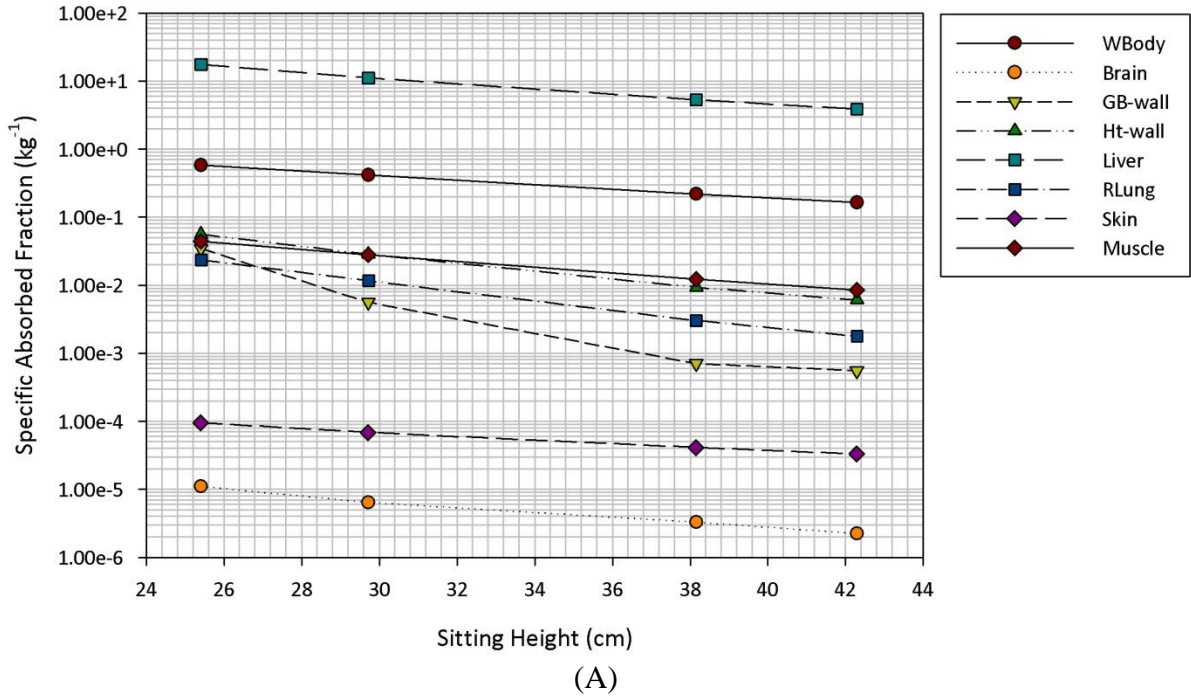


Figure 3-42. Variations in SAF with changes in sitting height for uniform (A) 500 keV and (B) 4 MeV electron sources in the liver of the UFH00M-based phantoms for a limited number of target tissues.

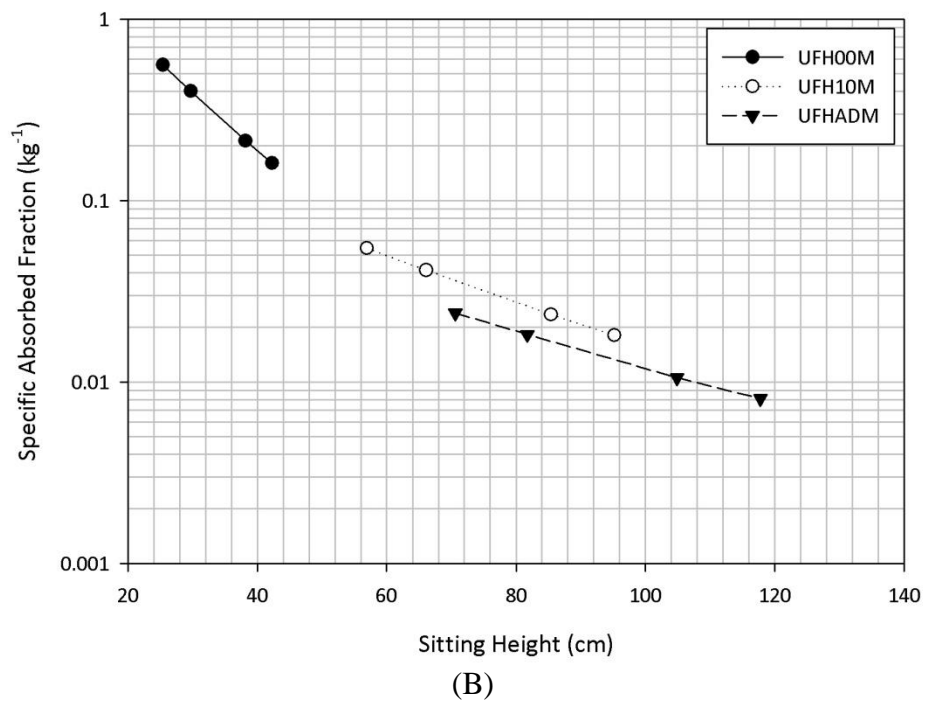
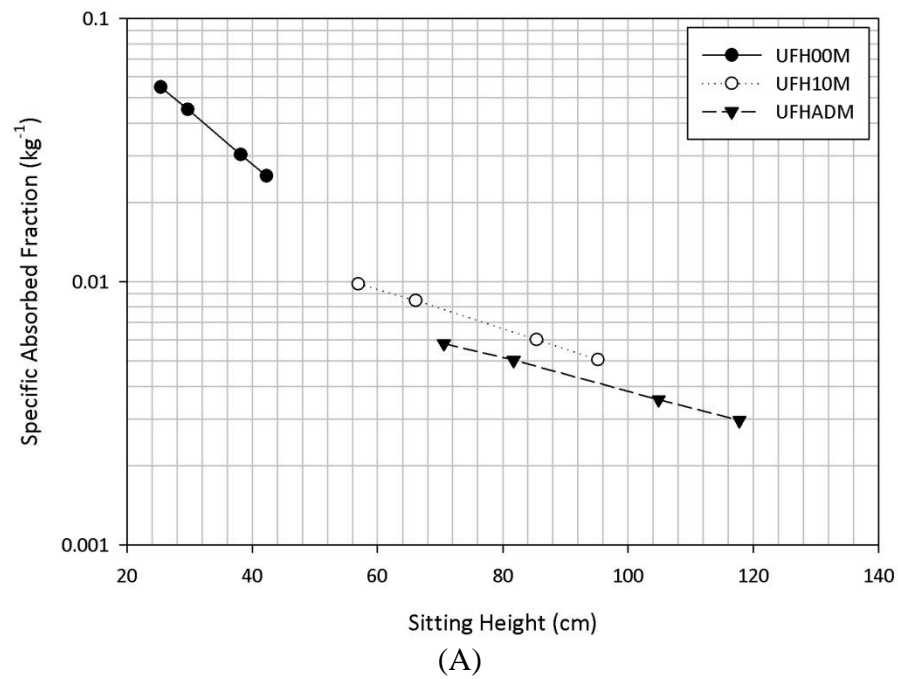


Figure 3-43. Variations in whole-body SAF with changes in sitting height for uniform 4 MeV (A) photon and (B) electron sources in the liver of the UFH00M-, UFH10M-, and UFHADM-based phantoms.

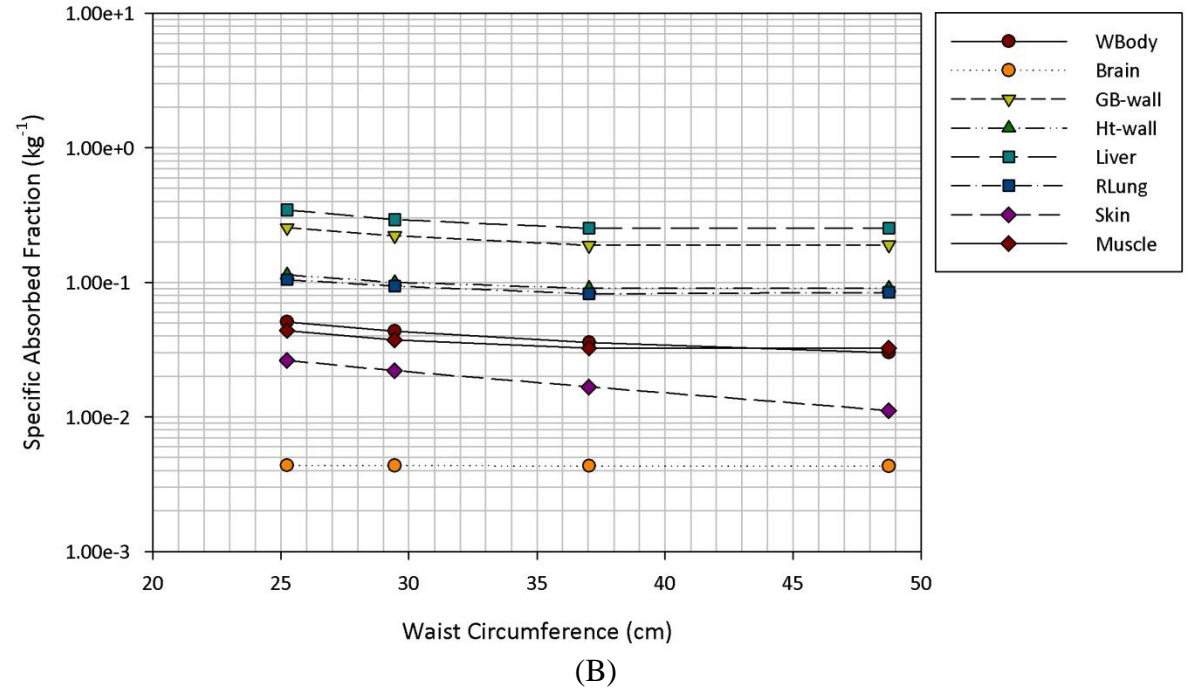
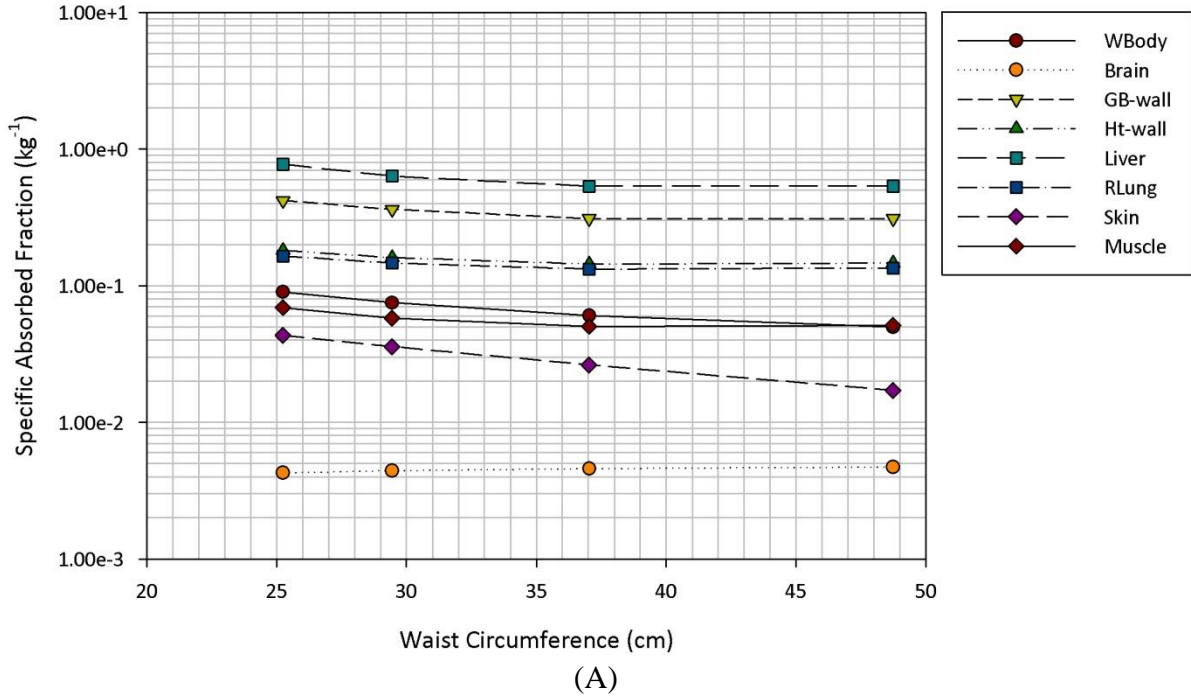


Figure 3-44. Variations in SAF with changes in weight (waist circumference is used as an analog) for uniform (A) 500 keV and (B) 4 MeV photon sources in the liver of the UFH00M-based phantoms for a limited number of target tissues.

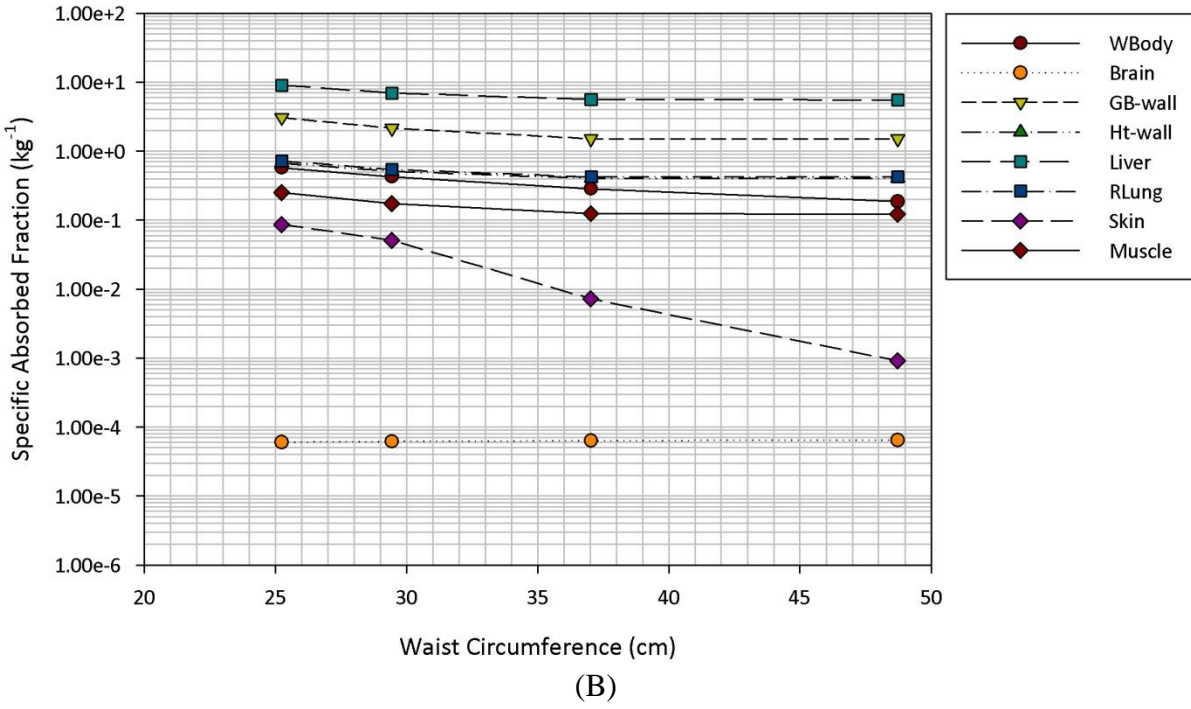
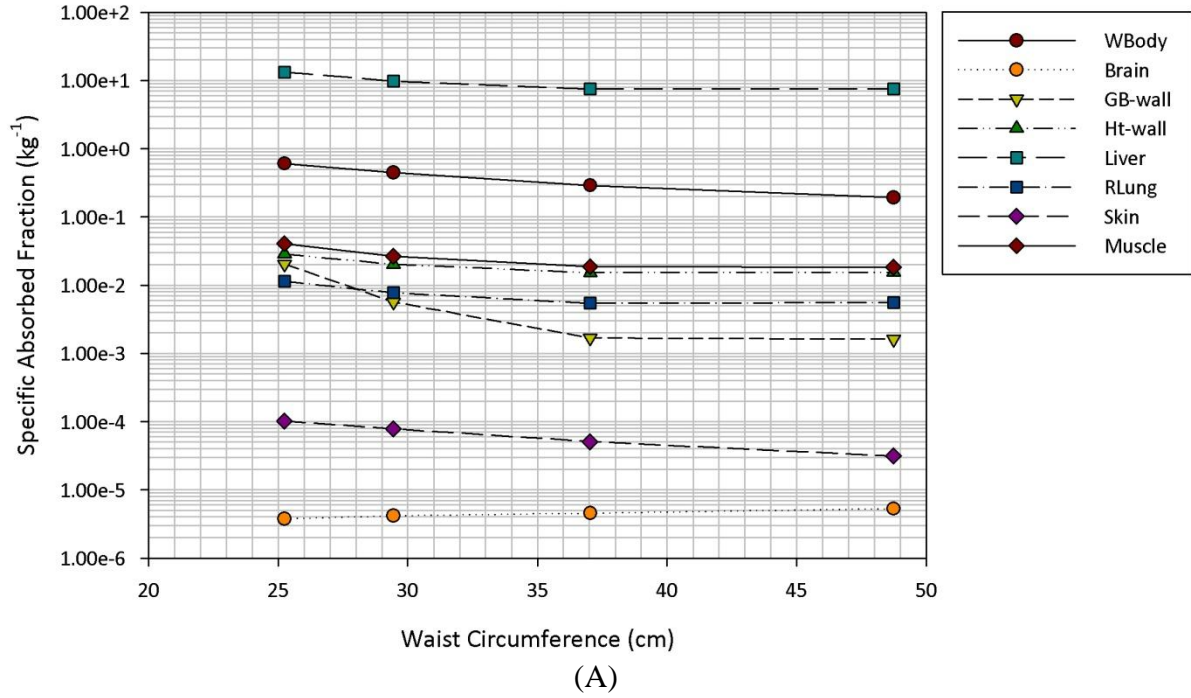


Figure 3-45. Variations in SAF with changes in weight (waist circumference is used as an analogue) for uniform (A) 500 keV and (B) 4 MeV electron sources in the liver of the UFH00M-based phantoms for a limited number of target tissues.

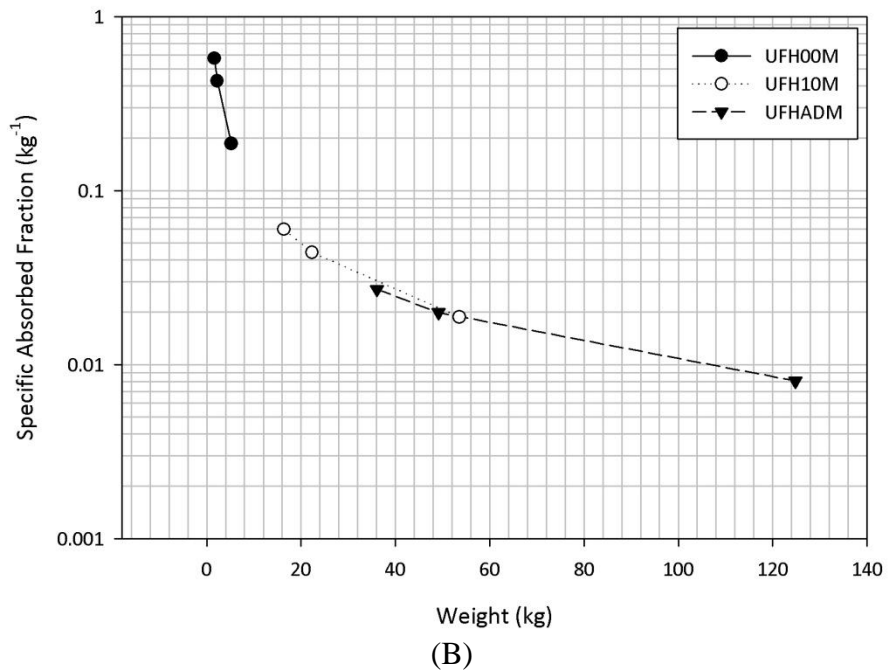
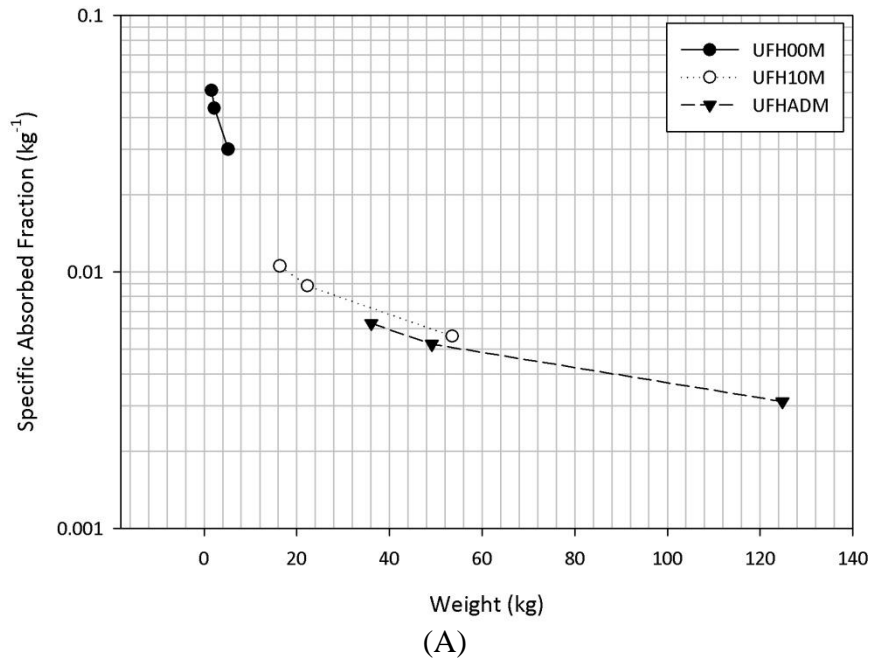


Figure 3-46. Variations in whole-body SAF with changes in weight (waist circumference is used as an analog) for uniform 4 MeV (A) photon and (B) electron sources in the liver of the UFH00M-, UFH10M-, and UFHADM-based phantoms.

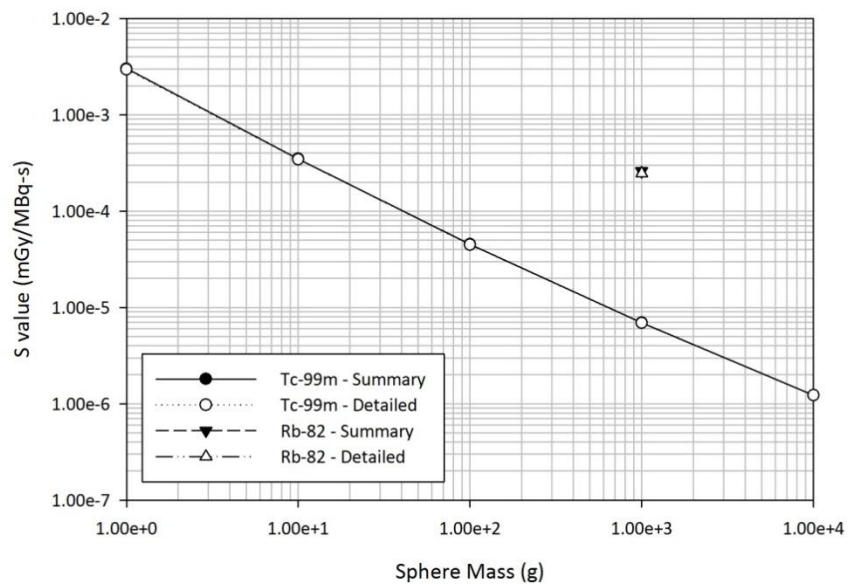


Figure 3-47. Radionuclide S values calculated using a summary of the radionuclide spectra compared to those calculated using the entire radionuclide spectra as given by ICRP Publication 107 (ICRP 2008) for ^{99m}Tc and ^{82}Rb for a point source located at the center of spheres of different masses.

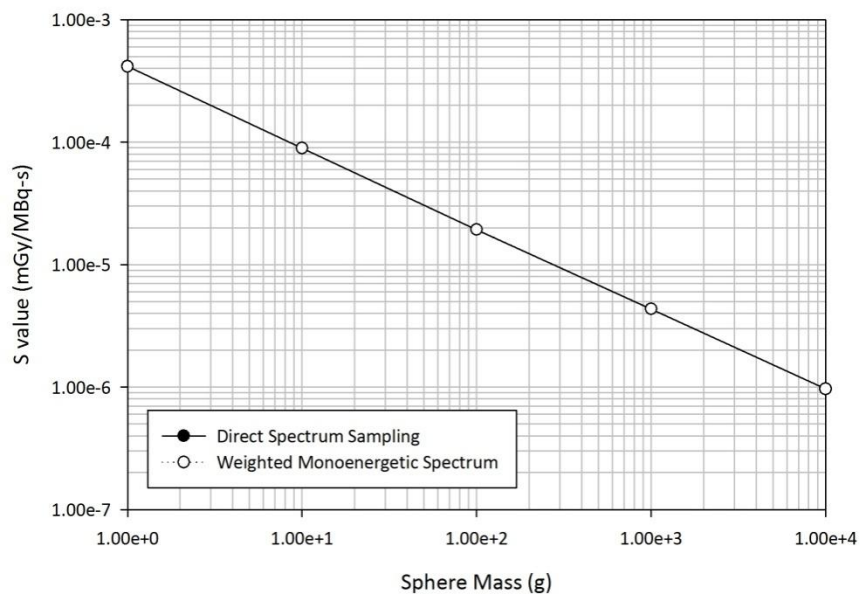


Figure 3-48. Radionuclide S values calculated using direct spectrum sampling as compared to those calculated using an assembling of monoenergetic SAFs. Spectra from ICRP Publication 107 (ICRP 2008) for ^{99m}Tc for a point source located at the center of spheres of different masses.

CHAPTER 4 DISCUSSION

UF Hybrid Phantom Blood Vessel System

Construction of the blood vessel system for all phantoms in the UF hybrid phantom family provided the update needed for the latest generation of the phantoms. With the introduction of separable adipose tissue and a voxel-based lymphatic node model, the phantoms resulting from the addition of the blood vessel systems represented the most up-to-date version of the phantoms. Despite the low percentage of total vessel volume that was modeled, the blood vessels improved the overall anatomic picture of the phantoms, making them visually more anatomically accurate as well as providing a vehicle to simulate short-lived radionuclide blood-borne sources.

Even if the total targeted large artery and large vein blood volume was modeled, there was a certain arbitrary component to the construction process. Construction was stylistic in nature, as was the case for several other tissues in the phantoms including the small intestine wall and contents (Lee *et al.* 2010). Miniscule, intricate cylindrical structures would have to be forced into every available space to approach the targeted vessel blood volume in addition to placing an inordinate number of vessels into the extremities of the phantoms. If total blood volume was valued over anatomic realism, this may have been a reasonable approach. However, matching total blood volume was not set as a high priority. When distributed blood sources were simulated, the missing blood volume was simply apportioned to the muscle of the phantom, where many of the major blood vessels reside. This still gave a good approximation of the true distribution of blood vessels throughout the body.

A distributed blood source was provided in the SAF and S value results from the current study, but any arbitrary blood distribution could be applied to the monoenergetic SAFs by calculating relative contributions of the SAF of each blood-containing tissue. The following

generalized equation (Equation 4-1) was used to calculate the SAF to each target tissue for a distributed blood source:

$$\Phi(r_T \leftarrow \text{blood}) = \sum_i f_i \Phi(r_T \leftarrow i) \quad (4-1)$$

where $\Phi(r_T \leftarrow \text{blood})$ is the SAF to target tissue r_T from blood distributed throughout the body, f_i is the fraction of total blood volume located in source tissue i , and $\Phi(r_T \leftarrow i)$ is the SAF to target tissue r_T from source tissue i .

Photon and electron SAFs for the whole-body blood source for the UFH00M phantom are shown in Figures 4-1 and 4-2, respectively. The photon SAF curves follow the general shape of SAF curves of most other sources because the shape of the curves is very similar for self- and cross-dose at energies exceeding 40 keV. Since blood is distributed throughout many organs, self-dose and cross-dose are competing processes, and this is manifested in many of the SAF curve shapes. This competitive process is most evident in Figure 4-2 for the electron SAFs. Some SAF curves decline at higher energies while others increase. If a curve decreases with energy at higher energies, electron escape is dominating the influx of electrons from surrounding tissue. If a curve increases with energy at higher energies, electron cross-fire is overriding the effect of electron escape. This particular circumstance is evident for the heart wall target due to a high concentration of blood in the heart chambers.

To show the effect the newly developed age-dependent regional blood distributions have on distributed blood dosimetry, monoenergetic photon SAFs were calculated with both the new distributions and adult distributions for each phantom; these are then plotted in Figure 4-3. The viewing window was purposefully narrowed to emphasize the higher energy SAFs (the effects at lower energies are at least as great as at higher energies). The overall average absolute percent difference between the blood SAFs calculated with the new distributions and those calculated

with the adult distributions was 9% (0.1% – 42%). The only phantom that did not demonstrate the benefit of age-dependent regional blood distributions was the UFH15F at an average absolute percent difference of 0.8%. However, all other phantoms (especially the UFH00M and UFH01M phantoms) showed marked difference when the adult blood distributions were applied, suggesting that age-dependent regional blood distributions are beneficial to performing internal dosimetry for distributed blood sources. The differences were due to changes in blood vessel concentration in the brain, kidneys, and mineral bone as well as varying rates of growth of organs as a function of age.

Vascular Dosimetry

A dose averaging methodology was developed to estimate absorbed dose to blood vessel walls from whole-body, distributed blood sources. The body is full of blood vessels that cross-irradiate when the blood is infused with a radioactive source, so the dose to blood vessel walls would be overestimated if the whole-body model was reduced to a single vessel model. In other words, one possible approach to estimating vessel wall dose would be to model the entire blood vessel system as a single blood vessel for the sake of simplicity. In doing so, the radioactivity would be completely confined to a single vessel, while in reality the amount of radioactivity confined to the single vessel would actually be distributed through all blood vessels in the body. It follows then that the absorbed dose from radiation to a blood vessel wall of interest would decrease according to the number of blood vessels in the model.

Bearing this in mind, a reasonable blood vessel wall dose estimate requires that the number of blood vessels in the body to be approximated in the dosimetry model. To illustrate the effect blood vessel distribution has on dose to the blood vessel wall, the blood vessel wall simulation results were modified to account for dose averaging effects when other blood vessels are

included in the model. Vessel wall “self”-dose¹, cross-dose to an adjacent blood vessel, and cross-dose to a distant blood vessel were all calculated during the simulations. The single-vessel model predicts that the absorbed dose to all vessel walls in the body is equal to the self-dose. If the cross-dose from the adjacent vessel were included in the estimate, the absorbed dose to all vessels in the body would be equal to the linear average of the vessel self-dose and the adjacent vessel cross-dose. If the distant vessel were included in the model, the absorbed dose estimate would be equal to the linear average of the vessel self-dose, the adjacent vessel cross-dose, and the distant vessel cross-dose. Cross-doses could then be extrapolated for any number of imaginary vessels distant from the vessel of interest and averaged to create a model with a higher concentration of blood vessels. That same set of blood vessels could then be superimposed on the other side of the blood vessel of interest and averaged, creating a two-direction vessel arrangement. This process could be repeated for as many directions as desired and is illustrated in Figure 4-4. Figure 4-4 shows that average dose to the blood vessel wall decreases with increasing number of adjacent vessels and increasing number of directions of inclusion, keeping in mind that all blood vessels are treated as straight and parallel to one another.

Absorbed dose to the blood vessel wall was observed to increase with decreasing vessel length, so it would be reasonable to assume that an age (stature)-dependent model is needed. Blood vessel wall dose for the newborn patient will be greater than blood vessel wall dose for an adult patient for the same AA. In addition, a conservative approach is favored due to the admittedly approximate nature of this vascular dosimetry study. With this in mind, rectangular prisms approximating the size of the torsos of the newborn, adult male, and adult female were

¹ The term “self” in this context will refer to the blood vessel contents irradiating the surrounding blood vessel wall. Normally, “self-dose” refers to the irradiation scenario where the source and target are the same tissue, but the term was changed in this instance to distinguish it from the irradiation scenario where the blood vessel contents of one vessel is irradiating the blood vessel wall of a different blood vessel, referred to as “cross-dose”.

defined to represent the volume to which all blood vessels would be restricted. Contributions from the extremities and head to total blood vessel wall dose would only lower the whole-body average vessel wall dose and so were neglected to maintain conservatism. Dimensions for the rectangular prisms in the antero-posterior, lateral, and axial directions were $10\text{ cm} \times 14\text{ cm} \times 14\text{ cm}$ for the UFH00MF phantom, $25\text{ cm} \times 38\text{ cm} \times 67\text{ cm}$ for the UFHADM phantom, and $20\text{ cm} \times 32\text{ cm} \times 60\text{ cm}$ for the UFHADF phantom.

Results for the 14.38 cm vessel length were assigned to the UFH00MF phantom, and results for the 41.61 cm vessel length were assigned to both the UFHADM and UFHADF phantoms. Since the number of vessels with a particular lumen diameter and wall thickness could not be confidently assumed, SAFs were averaged over all vessel sizes at the two vessel lengths. Additionally, results were averaged at each radiation energy – 10 keV , 500 keV , and 4 MeV . Two vessel directions were used, and SAFs were calculated as the average of the blood vessel wall self-dose and cross-doses at the antero-posterior and lateral extremes. An illustration of the final irradiation geometry can be seen in Figure 4-5. The SAF estimate for the central blood vessel was used as the whole-body estimate, again to maintain conservatism. Blood vessel wall SAFs for the UFH01MF, UFH05MF, UFH10MF, and UFH15F phantoms were interpolated between those for the UFH00MF and UFHADF phantoms (the UFHADF phantom was used instead of the UFHADM phantom because the SAFs were slightly higher, and conservatism was maintained) based on similarly developed rectangular prisms at all ages as shown in Table 4-1. SAFs for the UFH15M phantom were interpolated between those for the UFH00MF phantom and UFHADM phantom. Interpolation with respect to rectangular prism volume accounts for changes in both vessel radial distribution and vessel length. Final blood

vessel wall SAF estimates are shown in Table 4-2, and the photon and electron SAF curves are displayed in Figures 4-6 and 4-7, respectively.

Skeletal Photon Fluence-to-Dose Response Functions

During the development of the ORNL series of phantoms, skeletal photon fluence-to-dose response functions were developed based on Equation 2-2 (Cristy *et al.* 1987). There were two distinct differences between the UF and ORNL skeletal photon fluence-to-dose response function calculation methods. First, ORNL used chord-length distributions of trabeculae and marrow cavities to obtain electron AFs (Cristy *et al.* 1987) while UF performed detailed 3-D radiation transport using the microstructure and macrostructure of all bone sites using PIRT with EGSnrc for the UFH00MF, UFH15MF, and UFHADMF phantoms² (Hough *et al.* 2011, Pafundi *et al.* 2010). Second, the UF skeletal photon fluence-to-dose response functions were calculated based on image sets specific to each phantom of interest³ while the ORNL data was based on a 44-year-old male and applied to phantoms of all ages (Pafundi *et al.* 2010, Cristy *et al.* 1987). One immediately noticeable difference between newborn and adult skeletal microstructure is that the newborn has almost no IM while the adult has many bone sites with no AM. This difference leads to different radiation interaction probabilities and marrow volume fractions, so age-dependent skeletal photon fluence-to-dose response functions are potentially needed.

Three bone sites, the cervical vertebra, lumbar vertebra, and ribs, from the ORNL skeletal photon fluence-to-dose response function data were selected for comparison, and the skeletal target tissue was chosen to be AM. The UF newborn and ORNL adult skeletal photon fluence-

² Chord-length distributions were used for the CBIST simulations for the UFH01MF, UFH05MF, and UFH10MF phantoms.

³ The UFH01MF, UFH05MF, and UFH10MF skeletal photon fluence-to-dose response functions were developed based on macroscopic models specific to the phantom of interest, but weighted averages of electron AFs obtained from chord-length distributions of certain bone sites were used for the microscopic models.

to-dose response functions for those bone sites and the AM target along with the percent difference between them can be seen in Table 4-3. The average absolute percent difference across all photon energies was found to be approximately 11% (0.2% – 33%). At intermediate incident photon energies, the response functions were found to be in relatively good agreement, but they tended to diverge at higher energies and at those energies where the response function ceased to decline and began to increase. A graphical depiction of this comparison can be seen in Figure 4-8. The difference between the UF and ORNL response functions can be attributed to reasons previously discussed – superior physical modeling and anatomic specificity utilized in the development of the UF response functions.

Photon Specific Absorbed Fractions

The UFH00MF phantoms were selected to highlight the differences between the UF photon SAFs and other available models. The current standard for monoenergetic photon SAFs for the ICRP-reference newborn phantom is the ORNL/TM-8381/V6 report (Cristy *et al.* 1987). Therefore, results from the current study were compared to the ORNL/TM-8381/V6 report in addition to a more recent model, the GSF BABY phantom (Petoussi-Henss *et al.* 2002). Two source tissues, the liver and thyroid, were chosen for comparison to illuminate differences with organ size. The adrenals, brain, liver, and thyroid were chosen as target tissues for the liver source, and the adrenals, thymus, and thyroid were chosen as target tissues for the thyroid source. Results of the comparison for the liver and thyroid sources are shown in Figures 4-9 (A) and 4-9 (B), respectively.

Variations in SAFs were calculated as the ratio of the UF SAFs to the ORNL and GSF SAFs. Considering the chosen source-target combinations, differences between monoenergetic photon SAFs ranged from -77% for $\Phi(\text{thyroid} \leftarrow \text{thyroid}, 4 \text{ MeV})_{GSF}^{UF}$ to a factor of 90 times

greater for $\Phi(\text{thyroid} \leftarrow \text{liver}, 15 \text{ keV})_{\text{ORNL}}^{\text{UF}}$. Some SAF variations can be explained by examining differences between physical characteristics of the phantoms themselves, but some differences may be due to different simulation techniques. For example, liver masses in the UF, ORNL, and GSF phantoms are 129 g, 121 g, and 182 g, respectively (Cristy *et al.* 1987, Petoussi-Henss *et al.* 2002). Across all energies, the UF self-dose SAFs for a uniform photon source in the liver was, on average, 8% less than the ORNL SAFs and 21% greater than the GSF SAFs for the same irradiation geometry. It is well documented that increases in tissue mass result in decreases in self-dose SAFs and vice-versa (Petoussi-Henss *et al.* 2007), so the overall differences between SAFs for this irradiation scenario can be explained by the variations in liver size. However, there is a noticeable downturn in the UF SAF curve compared to the ORNL and GSF SAF curves at higher photon energies, which is also apparent when looking at thyroid self-dose. Physical characteristics of the phantom models alone do not seem sufficient to explain this difference in curve behavior. An energy balance was used for the UF SAFs wherein secondary electrons were tracked while the kerma approximation was used for the ORNL and GSF calculations (Cristy *et al.* 1987, Petoussi-Henss *et al.* 1998). An accentuated downward turn of the UF SAFs for photon self-dose was observed because secondary electrons created within the volume of interest escape into adjacent regions while the other models assume the secondary electrons to be locally deposited.

Despite the inability to completely account for differences between the UF, ORNL, and GSF monoenergetic photon SAFs, noticeable, but not unusually large, differences were seen. In looking at the liver source for all energies and 23 target tissues in the ORNL phantom, 33% of the UF SAFs differed from the ORNL SAFs by 50% or more while 42% of the UF SAFs differed from the ORNL SAFs by 50% or more for the thyroid source. The same analysis was

done for the GSF BABY phantom, and 25% and 43% of the UF SAFs differed from the GSF SAFs by 50% or more for the liver and thyroid sources, respectively.

Monoenergetic photon SAFs for the remainder of the UF hybrid phantom family were then compared to the ORNL stylized phantom family SAFs to illustrate differences present across the phantom size spectrum. Differences similar to those seen for the UFH00MF phantom were expected, so a cursory comparison was performed. SAFs for the following cross-irradiation scenarios were analyzed to cover different source-target size combinations: $\Phi(\textit{large} \leftarrow \textit{large})$, $\Phi(\textit{large} \leftarrow \textit{small})$ ⁴, and $\Phi(\textit{small} \leftarrow \textit{small})$. Self-irradiation was examined for $\Phi(\textit{large} \leftarrow \textit{large})$ and $\Phi(\textit{small} \leftarrow \textit{small})$. The SAFs selected for comparison were $\Phi(\textit{liver} \leftarrow \textit{liver})$, $\Phi(\textit{adrenals} \leftarrow \textit{adrenals})$, $\Phi(\textit{muscle} \leftarrow \textit{lungs})$, $\Phi(\textit{brain} \leftarrow \textit{thyroid})$, and $\Phi(\textit{adrenals} \leftarrow \textit{thyroid})$.

Overall and absolute percent differences between the photon SAFs of the UF and ORNL phantoms are shown in Tables 4-4 and 4-5, respectively. The overall percent differences take into account whether the UF values are less than or greater than the ORNL values while the absolute percent differences indicate the extent to which the UF values deviate from the ORNL values. For example, if two photon energies were considered, and the percent differences associated with these energies were -100% and 100% , the overall average percent difference would be 0% while the average absolute percent difference would be 100% . If the yield of these two photon energies were the same for a given radionuclide, then the 100% deviation of the UF SAFs from the ORNL SAFs would not show any difference in the final radionuclide S value. However, since non-uniform irradiation and varying spectra are characteristic of nuclear medicine dosimetry, the absolute percent difference is the measure of greatest interest.

⁴ $\Phi(\textit{small} \leftarrow \textit{large})$ was omitted from analysis because the reciprocity principle renders it approximately equal to $\Phi(\textit{large} \leftarrow \textit{small})$.

Immediately, an outlier irradiation scenario can be identified as $\Phi(adrenals \leftarrow thyroid)$ because of the absolute percent differences on the order of thousands of percent. These large percent differences are mostly due to those at low energies where statistical uncertainties are larger. For example, the SAFs for the UFH10MF and 10-year ORNL phantom at 20 keV are $2.03 \times 10^{-5} \text{ kg}^{-1}$ and $5.50 \times 10^{-9} \text{ kg}^{-1}$, respectively, leading to an absolute percent difference of 369821% (four orders of magnitude difference). The UF photon SAFs are mostly within the same order of magnitude as the ORNL photon SAFs and range from about 0% to 200% difference, excluding the $\Phi(adrenals \leftarrow thyroid)$ example.

These comparisons show that using the new UF hybrid phantoms and simulation techniques produce monoenergetic photon SAFs that vary significantly (but not unreasonably) from the widely used ORNL values. More detailed and physically accurate human anatomy in the UF hybrid phantoms should give reason to consider these dosimetric differences real and an indication that standard SAFs should be migrated to those generated in the present study, after rigorous beta testing and checking by external researchers.

Electron Specific Absorbed Fractions

It is of interest to explore the impact of using transport-generated electron SAFs as opposed to the ICRP Publication 30 method whereby $\phi_{electron}(target \leftarrow source) = 1$ when the source and target are the same and $\phi_{electron}(target \leftarrow source) = 0$ when the source and target are different, or the approach used in the OLINDA/EXM code whereby previously calculated electron self-dose AFs to spheres of various sizes are implemented for estimates of tumor and organ self-dose (ICRP 1979, Stabin 2005). Consequently, S values were generated for the monoenergetic electron (Auger and IC) and beta components of the ^{90}Y decay scheme for a uniform ^{90}Y source in the liver of the UFH00MF phantoms using each of these three methods.

The UF liver self-dose S value for the combined monoenergetic electron and beta contributions was 8% greater than that calculated using the ICRP Publication 30 method and about 1% greater than that calculated using the sphere AF approach. This seems to indicate that the ICRP Publication 30 method was improved upon with the introduction of the two-simulation electron dosimetry method. However, even though the OLINDA/EXM approach of using electron AFs to spheres of various sizes gave results similar to the two-simulation method, electron cross-dose is not accounted for with the OLINDA/EXM tissue-sphere approach. In this particular comparison study, cross-dose S values were as significant as about 5% of the self-dose S value. Cross-dose could be potentially significant in other circumstances. It is thus proposed in this study that patient dosimetry in nuclear medicine should employ the most current patient anatomic model and transport techniques as they become available for deployment in the clinic.

Beyond comparing the UF electron transport methods and those of the ICRP and OLINDA/EXM research groups, the novel two-simulation electron transport technique was validated. A validation study was performed to show the efficacy of the novel two-simulation method for computational internal electron dosimetry. A uniform electron source was simulated in the liver of the UFH00M phantom using the traditional full transport method (FTM), and the resulting SAFs were compared to those generated using the two-simulation method (TSM). Four target tissues were selected for comparison, and the results for those target tissues are in Figure 4-10. Poor statistical uncertainties for the FTM manifested in unreliable, and sometimes non-existent, curve shapes at low electron energies. The TSM showed considerable improvement over the FTM at these energies as seemingly reliable curve shapes gave reasonable values at all electron energies.

Despite this, validation could only be performed when the FTM showed good statistical uncertainties. In this example, all four target tissues displayed reliable statistical uncertainties at energies of 1 *MeV* and greater. Average uncertainties over this energy range for the gall bladder wall, esophagus, brain, and ET₂ region were 0.7%, 2.48%, 3.21%, and 11.36%, respectively. SAFs for the ET₂ region were still considered fairly reliable since the uncertainties were right around 10%. Figure 4-10 shows good agreement between the FTM and TSM for this energy range, indicating that the TSM is a good method to closely match what would be calculated using the FTM. Of particular interest are the brain and ET₂ target tissues since no primary electrons reach these target tissues, ensuring that all absorbed dose can be attributed to radiative losses. Comparing the TSM to the FTM for these target tissues over this energy range allows for a direct comparison of the spectrum weighting technique utilized in the TSM. Most importantly, the assumptions made in the development of the TSM model were tested – particularly the assumptions that any recorded photon is uniformly distributed throughout the source tissue and that all photons created outside of the source tissue originate from within the source tissue. The results seem to suggest that the spectrum weighting technique, along with its assumptions, is a valid approach to computational electron dosimetry.

The validation results show that the TSM gives good results at high energies where statistical uncertainties for the FTM may be acceptable but greatly improves the reliability of the electron SAFs at low- to mid-energy ranges. “Reliability” in this context was determined based on what curve was expected and how closely the TSM results displayed the expected results. The TSM curves in Figure 4-10 assume the shapes that were expected for the each target tissue. Both partial-collisional and full-radiative electron SAF curves were identified in this analysis, the curve types that most clearly communicate the importance of the TSM. Full-collisional

curves are dominated by the collisional contributions, so the radiative contributions (the contributions that utilize the benefit of the TSM) are not apparent.

An important fact that necessitates the work in the current study is that no standardized set of monoenergetic electron SAFs has yet been developed. OLINDA/EXM 1.0 assumes the electron AF to be unity when the source and target are equal and zero if the source and target are different (except in the case of tumor dosimetry) (Stabin 2005). It has been shown in the current study that these assumptions are only valid for a very small subset of circumstances. Electron escape becomes significant at higher energies and for smaller organs. Since the simulation techniques and phantoms used in this study are state-of-the-art, migration from simple assumptions to these full dosimetry simulations is recommended upon extensive beta testing and spot checking.

Dosimetric Sensitivity Studies

Variation in Source and Target Size and Separation

Photons

Since all dose scaling techniques will be applied within the internal dosimetry software in development, empirical scaling equations were not necessary. Improved accuracy could be gained by simply utilizing all SAFs generated over the course of these dose variation simulations. If an empirical equation was applied, further uncertainty could be introduced at the points for which actual data is available. It would be relatively straightforward to use the previously generated data within the internal dosimetry software to adjust reference doses to non-reference conditions. The benefit of using all generated data as opposed to averaged data is explored in this section.

Self-dose application – Mass ratios were used as the basis for dose scaling for photon self-dose. As previously discussed, a scaling power was calculated for each source-target-energy

combination based on the ratio of masses of the source and target and the ratio of the SAFs of both. A 3-D matrix of scaling power ratios was developed as a function of photon energy, source size, and target size. A sample of this 3-D matrix showing scaling power ratios for 4 MeV photons can be seen in Table 4-6. As an example, if the reference tissue mass was 60 g and the non-reference tissue mass was 80 g, the non-reference SAF would be calculated using Equation 4-2 (based on Equation 2-39).

$$\Phi(r_T \leftarrow r_S, 4 \text{ MeV}, 80 \text{ g}) = \Phi(r_T \leftarrow r_S, 4 \text{ MeV}, 60 \text{ g}) \cdot \left(\frac{80 \text{ g}}{60 \text{ g}} \right)^{-0.548} \quad (4-2)$$

In this example, the SAF for the non-reference, larger sphere is obtained by multiplying the reference SAF by a factor of 0.854. This is expected because previously studied dosimetric trends predict that the photon self-dose SAF decreases with increasing tissue mass (Petoussi-Hens *et al.* 2007). For practical application within the internal dosimetry software, 3-D interpolation is performed to obtain mass ratio scaling powers unique to the reference mass, non-reference mass, and photon energy of interest.

Self-dose validation – The first validation study for photon self-dose was the uniform scaling of the UFH00MF liver and thyroid and the patient-specific example of the liver and spleen. Uniform ^{99m}Tc photon sources were simulated in all of these tissues. At each emission energy, the monoenergetic photon SAFs for the UFH00MF and UFHADF phantoms were interpolated and scaled according to the reference organ masses for the UFH00MF and UFHADF phantoms and the non-reference organ masses of the scaled liver and thyroid and patient-specific liver and spleen. Mass ratio scaling powers in the form of a 3-D matrix were interpolated as detailed in the previous section, and a mass ratio scaling power of $-2/3$ was also applied to all mass ratios to simulate the method suggested in MIRD Pamphlet No. 11. To assess

the benefit of using the entire mass ratio scaling power dataset instead of averaged values, the mass ratio scaling powers were averaged over all source-target size combinations at each energy, resulting in a solely energy-dependent dataset. Reference values were scaled using this averaged dataset and compared to the MIRD method as well. Absolute percent differences were compared to determine how closely the scaling method predicted the actual S values, giving no regard to whether the predicted S values were less than or greater than the actual S values. Results of this validation study are in Table 4-7.

When the entire dataset was used, the UF method gave better results in three of the six irradiation scenarios. The MIRD method tended to do a better job predicting the non-reference S value when the non-reference organ mass was less than that of the reference organ mass, and the UF method tended to be more accurate when the non-reference mass was greater than the reference mass. When the averaged dataset was used, the only irradiation scenario for which the UF method transitioned from the less accurate method to the more accurate method was for the smaller UFH00MF liver self-irradiation. Despite this, the UF method using the entire dataset was generally more accurate than using the averaged dataset. When the entire dataset was used, the greatest deviation from the actual S value in this study was 6.25% for either the MIRD or UF method, and the greatest percentage gain in accuracy was 1.49%. The average percent gain in accuracy was less than a percent when the entire dataset was used. These results indicate that the UF method is more correctly applied when the whole dataset is utilized rather than an averaged dataset. However, no clear conclusions about the superiority of the UF method over the MIRD method could be drawn since each method was more accurate in different circumstances.

Another validation study was performed on the liver and thyroid self-dose models using monoenergetic 4 MeV photons. Energy-dependence was a point of interest in the dose scaling

studies, and the previous validation study may have not proven conclusively that the UF method should be adopted over the MIRD method because of the emission energies of ^{99m}Tc . The comparisons performed in the previous validation study were performed for the monoenergetic 4 MeV photons, and the results are in Table 4-8. The UF method proved to be more accurate by up to 24.74% than the MIRD method for every irradiation scenario, and the “averaged powers” UF method proved to be less accurate than when the entire dataset was utilized. The UF method was also compared to the MIRD method for the same irradiation geometries but for 10 keV photons and only mass- and energy-dependent scaling powers, and the results are in Table 4-9. The UF method was better at predicting the actual dose for all irradiation geometries by up to about 24%. It became clear that the UF method was not unequivocally more accurate than the MIRD method for the ^{99m}Tc photon application because the MIRD method does not appreciably deviate from the UF method over the important emission energies of ^{99m}Tc . Specifically, the principle photon emission energy for ^{99m}Tc is about 141 keV, and the MIRD and UF mass ratio scaling powers at that energy are -0.667 and about -0.644, respectively. The MIRD method may be effectively utilized from about 100 keV to 1 MeV. However, at high ($> 1 \text{ MeV}$) and low ($< 100 \text{ keV}$) energies, the UF method becomes the preferred method. One possible source of error and reason why the UF method does not predict changes in dose more accurately than the MIRD method in every circumstance is the assumption that using volumes with the same surface shape and taking ratios of SAFs eliminates surface dependence. This assumption may not be entirely true, and may explain why the MIRD method can predict dose changes marginally better in some cases.

Finally, the set of patient-specific phantoms were used to compare the UF and MIRD photon self-dose scaling methods. Uniform ^{131}I photon sources were simulated in the liver and

spleen of 14 male and 13 female patient-specific phantoms. All mass ratio scaling powers were used for the UF scaling method, and the results of this validation study are in Table 4-10. The MIRD and UF self-dose scaling methods are both very good at predicting dose changes for the given set of patient-specific phantoms. There does not seem to be a firm distinction between the two methods. However, for the ^{131}I photon spectrum, the average gain in accuracy between the two methods is well below 1%. The principle photon emission energy for ^{131}I is 364 keV, so the MIRD and UF method tend to converge for this application.

Even when the MIRD method gave more accurate dose scaling results than the UF method, it was never by a significant amount. In these validation studies, the maximum accuracy gain over the UF method by the MIRD method was 1.49% when all UF mass ratio scaling powers were used. Alternatively, for the high energy validation study, the UF scaling method gained up to 25% in accuracy over the MIRD method. In addition, up to 24% gains in accuracy were observed for the low energy applications. Since the UF method showed such noticeable improvements over the MIRD method for the high and low energy applications and closely approximated the MIRD method for the mid-range energy application, it is proposed in this study that the UF photon self-dose scaling methodology should be utilized in the UF internal dosimetry software code in lieu of the MIRD method. It is also proposed that the entire mass ratio scaling power dataset should be used instead of the averaged dataset because, on average, the UF self-dose scaling method gives better results when the entire dataset is used.

Cross-dose application – Instead of using mass ratio scaling powers for the cross-dose scaling methodology, simple SAF ratios were used to scale reference cross-dose SAFs based on inputs of reference and non-reference center-to-center separations, reference source and target masses, non-reference source and target masses, and radionuclide emission energies. An excerpt

of the photon cross-dose tables can be seen in Table 4-11. To illustrate how the photon cross-dose sphere SAFs were utilized, consider an arbitrary reference irradiation geometry where the source tissue is 1.00 *g*, the target tissue is 2.00 *g*, the center-to-center separation is 15.632 *cm*, and the photon energy is 4 *MeV*. The non-reference source tissue mass, target tissue mass, center-to-center separation, and photon energy are 2.00 *g*, 4.00 *g*, 31.264 *cm*, and 4 *MeV*, respectively. The equivalent reference sphere SAF is $5.22 \times 10^{-3} \text{ kg}^{-1}$, and the equivalent non-reference sphere SAF is $1.09 \times 10^{-3} \text{ kg}^{-1}$. To obtain the predicted non-reference SAF, the reference SAF would be multiplied by the ratio of the equivalent non-reference SAF to the equivalent reference SAF, which comes to 0.2088. The table only shows an excerpt of the photon cross-dose sphere SAFs. The full dataset contains 17 source sizes, 17 target sizes, 7 center-to-center separations, and 21 photon energies. The equivalent reference and non-reference sphere SAFs are interpolated between the available data points.

Cross-dose validation – First, validation was performed using two sets of spheres where one was defined to be the reference configuration, and the other was defined to be the non-reference configuration. Monoenergetic 3.5 *MeV* photons and the $^{99\text{m}}\text{Tc}$ photon spectrum were simulated, and the reference configuration S value was scaled using the photon cross-dose sphere SAF ratios. The scaled reference S value was compared to the actual S value to assess efficacy of the cross-dose scaling method. Results of these validation studies are given in Table 4-12. Currently, no cross-dose scaling is performed in OLINDA/EXM, so the conventional approach is to only scale self-dose and leave cross-dose unadjusted. This validation study shows that, for this irradiation scenario, the UF photon cross-dose scaling methodology would be 354% and 706% more accurate for 3.5 *MeV* photons and the $^{99\text{m}}\text{Tc}$ photon spectrum, respectively, than if one were to simply use the reference S values. The UF method predicted the true non-reference

S value to within 17% and 41% for 3.5 MeV photons and the ^{99m}Tc photon spectrum, respectively. Since the average ^{99m}Tc photon energy is considerably lower than 3.5 MeV, it was expected that the UF cross-dose scaling method would be more effective for the 3.5 MeV photons because of statistical uncertainty issues. However, even at the lower energies of the ^{99m}Tc photon spectrum, the UF scaling method proved to be reasonably accurate. Actual anatomic configurations would rarely exhibit instances in which source-target center-to-center separations changed from 16 cm to 30 cm. However, this validation study was done at distance extremes to test the photon cross-dose scaling method itself.

A similarly formatted validation study was performed using the UFHADM phantom by scaling and moving both the liver and pancreas and simulating uniformly distributed 3.5 MeV and ^{99m}Tc photons in the pancreas of the non-reference irradiation geometry (pancreas is the source and liver is the target). Previously calculated reference monoenergetic photon SAFs were scaled according to interpolated photon cross-dose SAF ratios, and the resulting scaled non-reference S values were compared to the actual non-reference S values obtained through direct simulation, and these results may also be seen in Table 4-12. Cross-dose scaling accounted for an 18% and 21% percentage point gain in accuracy for the monoenergetic 3.5 MeV and ^{99m}Tc photons, respectively. This is a real application example and one that shows the probable magnitude of gains in accuracy. A 20% gain in accuracy is significant, and this validation study makes an argument for the use of the newly calculated sphere cross-dose SAFs for cross-dose scaling.

Finally, reference UFHADM and UFHADDF monoenergetic SAFs were scaled with the UF photon cross-dose scaling technique to attempt to predict actual S values observed in the patient-specific phantoms. Uniformly distributed ^{131}I photons were simulated in the liver of each of the

phantoms, and SAFs were calculated to a pancreas target in each phantom. Results from this validation study are in Table 4-13. The percentage point gain in this situation is always relative to the UF scaling method. Scaling cross-dose photon SAFs for actual clinical application shows improvement for most of the patient-specific phantoms. A limiting factor for photon cross-dose scaling is the fact that most non-reference organs will not have the same shape as the reference models. Because of this, one can only hope to scale doses in as reasonable a way as possible to push the reference values closer to the actual values. Using the methods developed in this study will never guarantee complete accuracy, but the methods do seem to more accurately predict non-reference scenarios than the reference values. Again, it is recommended that the photon cross-dose scaling procedure detailed in this section be applied in the UF internal dosimetry software program since non-reference doses have been shown to be effectively predicted using the procedure.

Electrons

Self-dose application – Mass ratios were again used as the basis for dose scaling for electron self-dose. A scaling power was calculated for each source-target-energy combination based on the ratio of masses of the source and target and the ratio of the SAFs of both. A 3-D matrix of scaling power ratios was developed as a function of electron energy, source size, and target size. A sample of this 3-D matrix showing scaling power ratios for 4 MeV electrons can be seen in Table 4-14. As an example, if the reference tissue mass was 20 g and the non-reference tissue mass was 40 g, the non-reference SAF would be calculated using Equation 4-3 (based on Equation 2-39).

$$\Phi(r_T \leftarrow r_S, 4 \text{ MeV}, 40 \text{ g}) = \Phi(r_T \leftarrow r_S, 4 \text{ MeV}, 20 \text{ g}) \cdot \left(\frac{40 \text{ g}}{20 \text{ g}} \right)^{-0.809} \quad (4-3)$$

In this example, the SAF for the non-reference, larger sphere is obtained by multiplying the reference SAF by a factor of 0.571. This is expected because previously studied dosimetric trends predict that the electron self-dose SAF decreases with increasing tissue mass (ICRP 1979). Interestingly, for this reference/non-reference sphere combination, traditional electron self-dose scaling algorithms would assign a mass ratio scaling power of -1 when that is not the case according to present study. For practical application within the internal dosimetry software, 3-D interpolation is performed to obtain mass ratio scaling powers unique to the reference mass, non-reference mass, and electron energy of interest.

Self-dose validation – The same self-dose validation studies performed for photons were also performed for electrons with the exception that monoenergetic electrons were used instead of monoenergetic photons for the UFH00MF- and patient-specific-based studies, the ^{99m}Tc monoenergetic electron spectrum was used instead of the ^{99m}Tc photon spectrum for the UFH00MF- and UFHADF-based studies, and the ^{90}Y beta spectrum was used instead of the ^{99m}Tc photon spectrum for the 14 adult male and 13 adult female patient-specific phantoms study. Results for ^{99m}Tc electrons in the scaled liver and thyroid of the UFH00MF and the scaled liver and spleen of the patient-specific phantom are in Table 4-15. Results for the monoenergetic 4 MeV electrons for the same irradiation geometries are in Table 4-16. Results for the monoenergetic 10 keV electrons for the same irradiation geometries are in Table 4-17. Results for the uniform ^{90}Y beta sources in the liver and spleen of the 14 adult male and 13 adult female patient-specific phantoms are in Table 4-18.

Upon investigation, electron self-dose scaling results mirrored those of photons. Mid-range to low electron energies did not spotlight the benefit of using the UF mass ratio scaling powers because electron AFs are close to unity at the electron energies seen for ^{99m}Tc and ^{90}Y .

In some instances, the MIRD method (scaling power of -1) had a slightly better predictive quality than the UF method. However, the 4 MeV electrons in the UFH00MF scaled organs demonstrated the scenario in which the MIRD method begins to break down. At high enough electron energies and for smaller source sizes, the electron AF deviates significantly from unity due to increased electron range. This concept is evidenced by the average percentage point gain in accuracy of about 13% with the maximum gain in accuracy of 37% for the smaller UFH00MF thyroid.

It is recommended that the UF electron self-dose scaling approach should be utilized in the internal dosimetry software instead of the MIRD method. Electron self-dose does scale linearly⁵ with changes in source mass for large source masses and intermediate to low electron energies since the electrons in that irradiation scenario are typically absorbed within the emitting tissue. However, at higher electron energies and for smaller source tissues, the assumption that the electron AFs are unity breaks down as electrons attain enough energy to escape into surrounding regions. To capture this effect, the UF electron self-dose scaling method will be implemented in the internal dosimetry software package.

Cross-dose application – Surface shape and surface-to-surface distance heavily impact perturbations in electron cross-dose with changes in source and target size. A target tissue may be out of the range of primary electrons in the reference model, but in the range of primary electrons in the non-reference model. When this is the case, electron dose differences between the two models may be orders of magnitude. Segmenting individual organs in the clinic is impractical, so defining surface shape on a case-by-case basis was abandoned as a possible

⁵ The same scaling may be done by setting the mass ratio scaling power to unity.

concept to assist in electron cross-dose scaling. Instead, the radiative component of the electron dose was selected as the scalable part of electron dose.

The radiative component of electron dose can be attributed entirely to photons generated during the course of electron energy loss. Photon cross-dose scaling techniques could be applied in this case since the radiative component of electron simulations is effectively accomplished by photon transport. Collisional contributions to dose (primary dose) were not scaled and were subject to the uncertainties associated with changes in source-target shape and surface-to-surface distance. Principal gains in dosimetric accuracy were confined to the radiative component and therefore more distant organ pairs.

Cross-dose validation – The UFHADM brain and liver were scaled and slightly translated to create a non-reference irradiation geometry, and 3.5 *MeV* electrons were uniformly simulated in the liver. Absorbed dose was recorded in the brain and compared to scaled reference values. Collisional contributions to dose were excluded due to the large center-to-center distance between the brain and the liver. Photon cross-dose scaling techniques were applied to the radiative component of electron dose and compared to actual simulation estimates, and the results are in Table 4-19. There is a 2% gain in accuracy using the UF scaling method for monoenergetic 3.5 *MeV* electrons, but there is a 2% loss in accuracy for the ^{82}Rb beta spectrum. Poor statistical uncertainties (~20%) could be the reason for the loss in accuracy for the ^{82}Rb beta spectrum test.

Patient-specific phantoms were also utilized for validation purposes. A validation technique similar to that used for the patient-specific phantom study for photon cross-dose scaling was used to investigate the electron cross-dose scaling method. Instead of uniform ^{131}I photon sources in the liver of the phantoms, ^{90}Y beta sources were simulated, and dose was

recorded in the pancreas. Results from this study are given in Table 4-20. Most phantoms displayed the beneficial nature of the UF electron cross-dose scaling method. Gains in accuracy were observed in most cases with a maximum gain of about 9% and average gain of about 2%. This is admittedly not a drastic gain in accuracy, but the overwhelming number of cases indicates that photon cross-dose scaling can be applied to the radiative component of electron dose. It is therefore recommended that this scaling technique should be applied in the internal dosimetry code in development.

Variation in Anthropometric Characteristics

Sitting height dose scaling application

Patient measurement-based internal dose scaling techniques could not be finalized until several methods were applied to the validation studies. However, the general approach was the same for each method. Non-reference SAFs obtained by scaling reference SAFs was the final goal, so naturally a scaling factor or set of scaling factors could be envisioned as the general approach. Monoenergetic SAFs for all target tissues in reference and non-reference hybrid phantoms for five source tissues were available for analysis. Sitting height information was available for all phantoms systematically created for the sitting height dose scaling study. As a result, for a given photon or electron energy, monoenergetic SAFs could be interpolated for a given phantom and subsequently interpolated between the two nearest phantoms based on the initial energy of the radiation and sitting height of the patient, defined by user input. The non-reference SAF would then be obtained using Equations 4-4 and 4-5.

$$\Phi(r_T \leftarrow r_S, E_i, H_{non-ref}) = \Phi(r_T \leftarrow r_S, E_i, H_{ref}) \cdot f(r_T \leftarrow r_S, E_i, H_{non-ref}, H_{ref}) \quad (4-4)$$

$$f(r_T \leftarrow r_S, E_i, H_{non-ref}, H_{ref}) = \frac{\Phi(r_T \leftarrow r_S, E_i, H_{non-ref})}{\Phi(r_T \leftarrow r_S, E_i, H_{ref})} \quad (4-5)$$

where $\Phi(r_T \leftarrow r_S, E_i, H_{non-ref})$ is the SAF for source tissue r_S irradiating target tissue r_T at radiation energy E_i for a patient with sitting height $H_{non-ref}$, $\Phi(r_T \leftarrow r_S, E_i, H_{ref})$ is the same measure for the reference phantom with sitting height H_{ref} , and $f(r_T \leftarrow r_S, E_i, H_{non-ref}, H_{ref})$ is the dose scaling factor for source tissue r_S irradiating target tissue r_T at radiation energy E_i for a patient with sitting height $H_{non-ref}$ based on the reference phantom with sitting height H_{ref} .

The scaling factor may initially seem unnecessary since the two equations together imply that the non-reference SAF could be obtained by simply interpolating between the available SAFs. However, only the UFH00M, UFH10M, and UFHADM phantoms were simulated in this study, so it was clear that scaling factors for other phantoms would have to be interpolated between scaling factors calculated for these few reference phantoms. To accomplish this, sitting height ratios could be correlated with SAF ratios for the UFH00M, UFH10M, and UFHADM phantoms. Then, to obtain scaling factors for the UFH01MF, UFH05MF, UFH15MF, and UFHADF phantoms⁶, scaling factors would be interpolated for the UFH00M, UFH10M, and UFHADM phantoms based on the ratio of the patient sitting height to the reference phantom (one of the non-simulated phantoms) sitting height. It was shown in Figure 3-43 that scaling factors probably vary depending on which reference phantom was used as the base phantom for the sitting height application (e.g., dose seemed to vary more for phantoms based on the UFH00M phantom than the UFHADM phantom). As a result, final scaling factors for the non-simulated phantoms would be interpolated between the sitting height ratio-interpolated scaling factors of the UFH00M, UFH10M, and UFHADM phantoms based on the sitting height of the actual base reference phantom.

⁶ Scaling factors for the UFH00F and UFH10F phantoms would be equal to those of the UFH00M and UFH10M phantoms due to almost identical internal anatomy.

It was unclear prior to the validation studies how the scaling factors would be developed. Five source tissues were simulated to perform the sitting height dose scaling computational experiment. If the dose scaling factors for each target tissue were found to vary drastically by source tissue, then internal dose scaling could prove to be too complicated to effectively implement in an internal dosimetry software package. However, if the target tissue-dependent dose scaling factors were found to minimally vary with source tissue, then dose scaling would be feasible, and target tissue-average and overall average dose scaling factors could be developed. To investigate this, different levels of dose scaling factor averaging were compared in the validation studies.

Since variance reduction techniques were not used in the systematic sitting height dose scaling study, many SAFs were found to be zero or had large statistical uncertainties. SAFs from the systematic study with large uncertainties could lead to unacceptably large errors in predicted changes in dose, so all SAFs with uncertainties greater than 10% were set to zero. If either the non-reference SAF or the reference SAF in the SAF ratio were zero, both non-reference and reference SAFs were set to zero. After these actions were performed, if a target tissue had an SAF of zero, the dose scaling factor was set to the overall target-average scaling factor. Trends observed in Figure 3-41 indicated that dose scales fairly consistently for all target tissues with changes in sitting height.

Sitting height dose scaling validation

Uniform ^{131}I photon and ^{90}Y electron sources were simulated in the liver of a UFH00M-based phantom with decreased sitting height, a UFH10M-based phantom with decreased sitting height, and a UFHADM-based phantom with increased sitting height. Radionuclide S values were predicted for all target tissues by applying dose scaling factors to each target tissue according to the sitting height of the scaled phantom and the reference phantom upon which the

scaled phantom was based. The predicted S values were then compared to those obtained through direct simulation. S values determined using overall average and target-average dose scaling factors were compared to S values determined using dose scaling factors that were calculated from the AM, brain, liver, lungs, and spleen simulations. Complete results for the ^{131}I and ^{90}Y study for the UFH00M-based phantom are given in Tables 4-21 and 4-22, respectively. Overall results for the ^{131}I and ^{90}Y studies for all phantoms are given in Tables 4-23 and 4-24, respectively. Target tissues with greater than 10% uncertainty in the direct simulations were excluded from comparison because the predictive quality of the scaling factors cannot be assessed with a reasonable amount of certainty when the standard values themselves have larger uncertainties. While S value estimates with uncertainties greater than 10% uncertainty can still provide useful estimates, they were considered detrimental to this investigation.

It was found that fairly significant increases in accuracy could be attained when using dose scaling factors based on sitting height for both photons and electrons. The gains in accuracy for the UFH00M- and UFH10M-based phantoms were on the order of 15% while the gains in accuracy for the UFHADM-based phantom were on the order of 5% for both photons and electrons. It was foreseen that problems may arise for electron dose scaling since electrons do not penetrate as deeply as photons into tissue. As a result, surface-to-surface distances between organ pairs can cause dose scaling factors to vary widely between phantoms of differing sitting heights. For example, the thyroid and salivary glands of the reference phantom may be oriented such that primary electrons emitted from the thyroid reach the salivary glands but may not reach for a non-reference phantom, leading to an orders of magnitude difference in dose. Dose scaling factors cannot always accurately predict these anatomical changes in source/target tissues.

For all three irradiation scenarios, photon and electron dose scaling factors proved to increase the accuracy of dose estimates for non-reference internal photon and electron dosimetry. All scaling factor types showed increased accuracy, and no strong source dependence was observed. Because of this, it is proposed that target-average photon and electron dose scaling factors should be used to calculate non-reference doses based on sitting height alone. It would be beneficial to use average values so that no one source tissue must be selected as the source tissue upon which all dose scaling is based. Target-average dose scaling factors seemed to predict doses as accurately as overall average dose scaling factors, so target-average dose scaling factors were adopted as those that would be used in the internal dosimetry software package since not all target tissue doses scale by the same amount.

Weight dose scaling application

An approach similar to that used for the sitting height dose scaling study was used for the weight dose scaling study. Reference SAFs were scaled by factors calculated as the ratio of an interpolated non-reference SAF to the reference SAF. This process was adapted from Equations 4-4 and 4-5 and is given in Equations 4-6 and 4-7.

$$\Phi(r_T \leftarrow r_S, E_i, WC_{non-ref}) = \Phi(r_T \leftarrow r_S, E_i, WC_{ref}) \cdot f(r_T \leftarrow r_S, E_i, WC_{non-ref}, WC_{ref}) \quad (4-6)$$

$$f(r_T \leftarrow r_S, E_i, WC_{non-ref}, WC_{ref}) = \frac{\Phi(r_T \leftarrow r_S, E_i, WC_{non-ref})}{\Phi(r_T \leftarrow r_S, E_i, WC_{ref})} \quad (4-7)$$

where $\Phi(r_T \leftarrow r_S, E_i, WC_{non-ref})$ is the SAF for source tissue r_S irradiating target tissue r_T at radiation energy E_i for a patient with waist circumference $WC_{non-ref}$, $\Phi(r_T \leftarrow r_S, E_i, WC_{ref})$ is the same measure for the reference phantom with waist circumference WC_{ref} , and $f(r_T \leftarrow r_S, E_i, WC_{non-ref}, WC_{ref})$ is the dose scaling factor for source tissue r_S irradiating target tissue

r_T at radiation energy E_i for a patient with waist circumference $WC_{non-ref}$ based on the reference phantom with waist circumference WC_{ref} .

In a fashion similar to that utilized in the sitting height study, waist circumference ratios could be correlated with SAF ratios for the UFH00M, UFH10M, and UFHADM phantoms. Then, to obtain scaling factors for the UFH01MF, UFH05MF, UFH15MF, and UFHADF phantoms⁷, interpolation would be performed for the UFH00M, UFH10M, and UFHADM phantoms based on the ratio of the patient waist circumference to the reference phantom (one of the non-simulated phantoms) waist circumference. It was shown in Figure 3-46 that scaling factors probably vary depending on which reference phantom was used as the base phantom for the weight/waist circumference application (e.g., dose seemed to vary more for phantoms based on the UFH00M phantom than the UFHADM phantom). As a result, final scaling factors for the non-simulated phantoms would be interpolated between the waist circumference ratio-interpolated scaling factors of the UFH00M, UFH10M, and UFHADM phantoms based on the waist circumference of the actual base reference phantom.

Since variance reduction techniques were not used in the systematic weight dose scaling study, many SAFs were found to be zero or had large statistical uncertainties. SAFs from the systematic study with large uncertainties could lead to unacceptably large errors in predicted changes in dose, so all SAFs with uncertainties greater than 10% were set to zero. If either the non-reference SAF or the reference SAF in the SAF ratio were zero, both non-reference and reference SAFs were set to zero. After these actions were performed, if a target tissue had an SAF of zero, the dose scaling factor was set to the overall target-average scaling factor. Trends

⁷ Scaling factors for the UFH00F and UFH10F phantoms would be equal to those of the UFH00M and UFH10M phantoms due to almost identical internal anatomy.

observed in Figure 3-44 and 3-45 indicated that dose scales fairly consistently for all target tissues with changes in waist circumference.

Weight dose scaling validation

Uniform ^{131}I photon and ^{90}Y electron sources were simulated in the liver of a UFH00M-based phantom with decreased weight/waist circumference, a UFH10M-based phantom with increased weight/waist circumference, and a series of UFHADM-based phantoms with increased and decreased weight/waist circumference. Radionuclide S values were predicted for all target tissues by applying dose scaling factors to each target tissue according to the waist circumference of the scaled phantom and the reference phantom upon which the scaled phantom was based.

The predicted S values were then compared to those obtained through direct simulation. S values determined using overall average and target-average dose scaling factors were compared to S values determined using dose scaling factors that were calculated from the AM, brain, liver, lungs, and spleen simulations. Complete results for the ^{131}I and ^{90}Y studies for the UFH00M-based phantom are in Tables 4-25 and 4-26, respectively. Overall results for the ^{131}I and ^{90}Y studies for all phantoms are in Tables 4-27 and 4-28, respectively. Target tissues with greater than 10% uncertainty in the direct simulations were excluded from comparison because the predictive quality of the scaling factors cannot be assessed with a reasonable amount of certainty when the standard values themselves have larger uncertainties.

It was found that increases in accuracy (approximately 7%) could be attained when using dose scaling factors based on waist circumference when simulating photons for underweight phantoms, but no significant gains were seen for overweight phantoms. This was expected because overweight phantoms are constructed by simply adding adipose tissue around the body, but no significant changes in internal anatomy are made. However, considering electron

dosimetry, no appreciable gains in accuracy for overweight or underweight phantoms were found when scaling based on waist circumference was performed. An overall average gain in accuracy of only 2% was found.

It is recommended that the target-average dose scaling factors should be used for underweight patients in the internal dosimetry software package because waist circumference-based dose scaling factors were effective in adjusting reference doses to non-reference doses for photon dosimetry in underweight phantoms. No gain in accuracy was seen for overweight phantoms, so reference values should be used in those cases.

It is not recommended to use electron dose scaling factors to predict non-reference electron dose for either overweight or underweight phantoms as no benefit was observed in the waist circumference scaling study. Electron range considerations⁸ prevent any general methodology for electron dose scaling. However, some amount of patient-specificity may be obtained by using electron self-dose scaling methods previously discussed.

Combined dose scaling application

For the combined sitting height and weight dose scaling procedure, the methods described in the sitting height and weight dose scaling sections were simply mathematically combined, as given in Equations 4-8 and 4-9.

$$\Phi(r_T \leftarrow r_S, E_i, H_{non-ref}, WC_{non-ref}) = \Phi(r_T \leftarrow r_S, E_i, H_{ref}, WC_{ref}) \cdot f(r_T \leftarrow r_S, E_i, H_{non-ref}, H_{ref}, WC_{non-ref}, WC_{ref}) \quad (4-8)$$

⁸ Any given source-target combination may have very different levels of primary electron contribution, depending on the body habitus of the phantom. In one instance, primary electrons may deposit dose in the target tissue while in another, no primary dose may be present. These dose differences can be order of magnitude and are very difficult to predict.

$$f(r_T \leftarrow r_S, E_i, H_{non-ref}, H_{ref}, WC_{non-ref}, WC_{ref}) = \frac{\Phi(r_T \leftarrow r_S, E_i, H_{non-ref})}{\Phi(r_T \leftarrow r_S, E_i, H_{ref})} \times \frac{\Phi(r_T \leftarrow r_S, E_i, WC_{non-ref})}{\Phi(r_T \leftarrow r_S, E_i, WC_{ref})} \quad (4-9)$$

where $\Phi(r_T \leftarrow r_S, E_i, H_{non-ref}, WC_{non-ref})$ is the SAF for source tissue r_S irradiating target tissue r_T at radiation energy E_i for a patient with sitting height $H_{non-ref}$ and waist circumference $WC_{non-ref}$, $\Phi(r_T \leftarrow r_S, E_i, H_{ref}, WC_{ref})$ is the same measure for the reference phantom with sitting height H_{ref} and waist circumference WC_{ref} , and

$f(r_T \leftarrow r_S, E_i, H_{non-ref}, H_{ref}, WC_{non-ref}, WC_{ref})$ is the dose scaling factor for source tissue r_S irradiating target tissue r_T at radiation energy E_i for a patient with sitting height $H_{non-ref}$ and waist circumference $WC_{non-ref}$ based on the reference phantom with sitting height H_{ref} and waist circumference WC_{ref} .

Combined dose scaling validation

Uniform ^{131}I photon and ^{90}Y electron sources were simulated in the liver of a UFH00M-based phantom with increased sitting height and decreased weight/waist circumference, a UFH10M-based phantom with decreased sitting height and increased weight/waist circumference, and a series of UFHADM-based phantom with various combinations of increased and decreased sitting height and weight/waist circumference. Radionuclide S values were predicted for all target tissues by applying two dose scaling factors to each target tissue according to the sitting height and waist circumference of the scaled phantom and the reference phantom upon which the scaled phantom was based. The predicted S values were then compared to those obtained through direct simulation. S values determined using overall average and target-average dose scaling factors were compared to S values determined using dose scaling factors that were calculated from the AM, brain, liver, lungs, and spleen simulations. Complete

results for the ^{131}I and ^{90}Y study for the UFH00M-based phantom are in Tables 4-29 and 4-30, respectively. Overall results for the ^{131}I and ^{90}Y studies for all phantoms are in Tables 4-31 and 4-32, respectively. Target tissues with greater than 10% uncertainty in the direct simulations were excluded from comparison because the predictive quality of the scaling factors cannot be assessed with a reasonable amount of certainty when the standard values themselves have larger uncertainties.

It was found that increases in accuracy could be attained when using dose scaling factors based on the combination of sitting height and waist circumference for photons. The gains in accuracy for the UFH00M-based phantom were on the order of 5%, and gains for the UFH10M-based phantoms were on the order of 15%. Gains in accuracy for the UFHADM-based phantom set varied between almost no gains in accuracy to about 22%. The greatest gains in accuracy for the photon simulations were seen for the shorter, underweight phantoms. The three largest target-average scaling factor-based gains in accuracy were 11%, 15%, 22%, and these belonged to the m5010 phantom (50th percentile by height and 10th percentile by weight), the scaled UFH10M phantom (decreased height and increased waist circumference), and the m1010 patient-dependent phantom (10th percentile by height and 10th percentile by weight), respectively.

In contrast, dose scaling factors proved to be largely unhelpful for predicting non-reference dose across all phantoms for the electron simulations. Percentage point gains varied quite a bit across all target tissues, but most phantoms did not show appreciable increases in dose prediction accuracy. Again, this is probably due to the complexity of primary versus radiative electron dose. Orders of magnitude variations in electron dose depending on the patient's unique body morphometry render predictions of internal electron dose subject to very large uncertainties.

Upon examination of the percentage point gains in accuracy for both photon and electron dose scaling, it is recommended that only sitting height-based scaling factors should be utilized in the internal dosimetry software package for both photon and electron components of internal dose. Photon and electron internal dose scaling seems plausible based on the validation simulations that were performed for the sitting height-only scaling. Up to an overall average of about 17% gain in accuracy was observed with greater gains in accuracy seen at the organ level. Changes in dose seem to be dominated by changes in sitting height rather than changes in waist circumference.

Final morphometric dose scaling factors

LUT-type data was needed for the internal dosimetry software, so sitting height- and waist circumference-based internal dose scaling factors were calculated for the data generated for the UFH00M, UFH10M, and UFHADM. Target tissue-specific scaling factors were first calculated for each source-target-energy combination simulated in the morphometry-based dosimetric sensitivity study. Final scaling factors were averaged over all source tissues for each target tissue. Several pre-processing conditions were set before the scaling factors were calculated – (1) any SAF with uncertainty greater than 10% was set to zero, (2) both reference and non-reference SAFs were required to be greater than zero for a unique scaling factor to be calculated⁹, and (3) if either reference or non-reference SAF was zero, the scaling factor was set to the average of all other scaling factors¹⁰.

⁹ Scaling factors in this step (Condition 2) that did not meet the required conditions were temporarily set to zero, an action necessary to execute Condition 3.

¹⁰ Before this step (Condition 3) was performed, an overall average scaling factor was calculated at each initial radiation energy including all non-zero scaling factors. These energy-dependent overall average scaling factors were used for target tissues meeting the requirements of Condition 3.

An excerpt of the photon dosimetry sitting height-based results for the shortest and tallest UFH00M-based phantoms are in Tables 4-33 and 4-34, respectively, and were selected to show both ends of the scaling spectrum. Expected trends in dose scaling factors were observed in both examples. Absorbed doses were expected to increase in general for the shortest phantom, resulting in scaling factors greater than unity, and most scaling factors in Table 4-33 are greater than unity. Alternatively, the tallest phantom was expected to have scaling factors less than unity, and this is manifested in Table 4-34. In both cases, the scaling factors tended to flatten out at energies greater than or equal to 50 keV while they tended to shift away from unity at lower energies, increasing for the shortest phantom and decreasing for the tallest phantom. Absorbed dose scales more radically with changes in body morphometry at lower initial radiation energies due to the less penetrating nature of the radiation of interest. Similar tables were generated for both sitting height- and waist circumference-based photon dosimetry for the UFH00M-, UFH10M- and UFHADM-based phantom series.

Scaling factors for UFH00F- and UFH10F-based non-reference phantoms were inherently calculated because the internal structure of the UFH00F and UFH10F reference phantoms is almost identical to that of the UFH00M and UFH10M phantoms, respectively. Gender-specific organs were assigned the energy-dependent overall average scaling factors. However, no surrogate set of data could be assigned to the UFH01MF-, UFH05MF-, UFH15M-, UFH15F-, or UFHADDF-based non-reference phantoms. Scaling factors for these phantoms were interpolated between the existing datasets based on sitting height and waist-circumference ratios. As was observed in Figures 3-43 and 3-46, morphometric dependence changed according to the anchor phantom upon which the non-reference phantom was constructed.

To accommodate this conclusion, scaling factors for the phantoms for which surrogate data could not be assigned were calculated by interpolating between scaling factors of the UFH00M-, UFH10M-, and UFHADM-based phantoms according to the sitting height and waist circumference of the phantom of interest. Interpolated scaling factors could only be so calculated if a sitting height and waist circumference ratio was assigned to each virtual phantom in the non-reference series. Essentially, imaginary “shortest”, “short”, “tall”, “tallest”, “thinnest”, “thin”, and “fat” phantoms were created for the UFH01MF, UFH05MF, UFH15M, UFH15F, and UFHADF reference phantoms. The sitting height and waist circumference ratios of the UFH00M-based phantoms were assigned to the imaginary UFH01MF-based phantoms. The sitting height and waist circumference ratios of the UFH10M-based phantoms were assigned to the imaginary UFH05MF-based phantoms. The sitting height and waist circumference ratios of the UFHADM-based phantoms were assigned to the imaginary UFH15M-, UFH15F-, and UFHADF-based phantoms. New scaling factors were calculated for the UFH00M-, UFH10M-, and UFHADM-based phantom series so that the sitting height and waist circumference ratios (ratio of non-reference to reference) were constant and equal to the imaginary phantom series (e.g., UFH01MF-based phantoms of variable height and waist circumference) of interest. Finally, scaling factors specific to the imaginary phantom series of interest were interpolated between the appropriate scaling factor sets for which actual data was available according to reference sitting height.

The UFH01MF phantom was chosen as an example to explain the scaling factor interpolation method. Consider 4 MeV photons, the whole body as the target tissue, and the shortest non-reference phantom for which scaling factors were calculated. One would expect dose trends for the UFH01MF phantom to fall somewhere between the UFH00M and UFH10M

phantoms, and the original scaling factors for this scenario and the UFH00M- and UFH10M-based phantoms are 1.525 and 1.399, respectively. The ratios of the sitting height of the shortest UFH00M- and UFH10M-based phantoms to the reference UFH00M and UFH10M phantoms are 0.749 and 0.754, respectively. The shortest imaginary UFH01MF-based phantom was assigned a sitting height ratio of 0.749, so to interpolate between the UFH00M- and UFH10M-based scaling factors, the scaling factors for the shortest UFH10M-based phantom had to be extrapolated to represent a UFH10M-based phantom with a sitting height ratio of 0.749. The new scaling factors for the shortest UFH10M-based phantom with a sitting height ratio of 0.749 for 4 MeV photons and the whole-body target increased from 1.399 to 1.406. The final UFH01MF scaling factor was obtained by interpolating between the reference sitting heights of the UFH00M and UFH10M phantoms (33.92 cm and 75.50 cm, respectively) according to the reference UFH01MF sitting height of 48.22 cm. In this example, the final scaling factor was calculated to be 1.484.

Despite the large quantities of interpolation, this approach was considered reasonable given the trends observed in Figures 3-43 and 3-46. Absorbed dose scaled more dramatically with changes in sitting height for the UFH00M-based phantoms than for the UFHADM-based phantoms, and the UFH10M-based phantoms were somewhere in between in terms of dosimetric sensitivity. Therefore, it is not unreasonable to assume that dosimetric sensitivity for the UFH01MF and UFH05MF would fall between trends seen for the UFH00M- and UFH10M-based phantoms or that dosimetric sensitivity for the UFH15M, UFH15F, and UFHADF would fall between trends seen for the UFH10M- and UFHADM-based phantoms. To prove this, one phantom was constructed at heights less than the reference for the UFH01MF, UFH05MF,

UFH15M¹¹, and UFHADF phantoms, and the ^{99m}Tc photon spectrum was simulated in the liver of each phantom using MCNPX. Radionuclide S values were calculated for all target tissues, and S values for target tissues displaying statistical uncertainties less than 10% were compared to those scaled from reference values.

Percentage point gains in accuracy for individual target tissues and overall averages for this validation study are shown in Table 4-35. All four phantom validation studies showed the benefit of sitting height- and waist circumference-based internal dose scaling and the validity of the interpolation methods used to assign dose scaling factors to phantoms that were not explicitly simulated. An overall average gain in accuracy range of approximately 4% to 44% was observed with the UFH15M phantom showing the highest gains in accuracy at about 44%. The theoretical basis for the interpolation techniques used to assign scaling factors to the UFH01MF, UFH05MF, UFH15M, UFH15F, and UFHADF appeared sound based on the validation study and implications from earlier studies, and the evidence suggests that interpolation is a reasonable approach. These derived scaling factors are recommended for use in the internal dosimetry software package upon further beta testing.

Internal Dosimetry Software

Internal dosimetry software allows the user to quickly perform radiation dosimetry studies for patients undergoing a variety of nuclear medicine procedures including those that are diagnostic or therapeutic in nature. This is in stark contrast to the approach one would use to obtain patient-specific dose estimates. Segmented patient images and full radiation transport would be needed to perform accurate internal dosimetry on a case-by-case basis. Since this approach is time consuming, pre-simulated internal dosimetry for reference individuals scaled to

¹¹ The UFH15F phantom was not included in this validation because of its similarities to the UFH15M and UFHADF phantoms.

non-reference parameters (e.g., organ sizes, body morphometry, etc.) is the optimized method of choice for whole-body dosimetry. All of the time-consuming radiation transport simulations and even the relatively time-consuming S value construction algorithms are completed prior to software release, allowing for direct LUT-type actions. Current patient specific methods, such as 3D-RD (Kolbert 1997), are necessary for high-dose radionuclide therapy procedures, but whole-body models to assess absorbed dose to all tissues in the body cannot be readily constructed with those methods.

Currently, OLINDA/EXM 1.0 is one of the most widely used internal dosimetry software programs in the world. Combining many input screens with LUT-type algorithms, OLINDA/EXM 1.0 gives a somewhat user-friendly, albeit not optimized, software environment. In addition, older phantoms and simulation techniques are utilized. A more optimized software experience is being developed at UF and NCI of the NIH that will have less input screens and a more streamlined visual layout for the user. The blood vessel model, skeletal photon fluence-to-dose response functions, photon and electron SAFs, and dose scaling techniques based on user input of organ size and separation or patient morphometric characteristics will all be included in the software. In addition, the NCI-hosted software package will include a CT component that will allow for dual PET/CT or SPECT/CT dose estimates (Lee *et al.* 2011).

Although the GUIs were not developed at UF, the core concepts used in the nuclear medicine portion of the future software were developed in this work and in the dissertation studies of fellow UF student Laura Padilla. The collaboration between UF and NCI will benefit the worldwide exposure of the software upon release and will facilitate further dosimetry investigations between the two organizations.

Case Studies

In its entirety, the current body of works aimed to improve the methods and approaches used to determine radiation absorbed dose to radiosensitive tissues in the human body. Many validations and checks have been performed to ensure the validity of the data, but real examples will show the usefulness of the data in the clinic. Two radiopharmaceuticals were selected to perform dosimetric analysis – (1) ^{99m}Tc – *red blood cells* (RBC) and (2) ^{67}Ga – *citrate*. The first was selected to showcase the blood models developed in the current study while the second was chosen to force examination of a more complicated biokinetic model. Dosimetry was performed for all phantoms in the UF hybrid phantom family, and dosimetric results were compared to dose estimates from other sources.

Radiopharmaceuticals

Tc-99m labeled red blood cells

^{99m}Tc is produced using a ^{99}Mo – ^{99m}Tc radionuclide generator, and ^{99m}Tc has a physical half-life of 6 hours through isomeric transition decay (Cherry *et al.* 2003). The primary photon decay energy is 140.5 keV with an absolute yield of 0.89 (ICRP 2008). ^{99m}Tc also produces IC and Auger electrons at a relative delta value contribution of about 11% with gamma rays and x rays accounting for the remaining 89% (ICRP 2008). Beta particles are also emitted, but at an insignificant relative delta value contribution of only 0.003% (ICRP 2008). ^{99m}Tc is tagged to RBCs for the purpose of ^{99m}Tc – RBC scintigraphy to diagnose gastrointestinal bleeding (Treves 1995). Since the ^{99m}Tc is tagged to RBCs, it remains in the blood pool for a longer time than most other radiopharmaceuticals, necessitating a distributed blood source for internal dosimetry. Average absorbed dose to blood vessel walls was also determined in this example.

Ga-67-citrate

^{67}Ga is a cyclotron produced radionuclide with a physical half-life of 3.3 days and decays through electron capture (EC) (Treves 1995). Primary photon decay energies are 93 keV, 185 keV, and 300 keV with corresponding absolute yields of 0.39, 0.21, and 0.17 (ICRP 2008). ^{67}Ga also produces IC and Auger electrons with a relative delta value contribution of about 19% with gamma rays and x rays accounting for the remaining 81% (ICRP 2008). $^{67}\text{Ga} - \text{citrate}$ can be used for various clinical applications of SPECT for diagnosis of abnormalities, including infection and inflammation.

Biokinetics

Biokinetic data for $^{99\text{m}}\text{Tc} - \text{RBC}$ was taken from ICRP Publication 106 (ICRP 2007), and biokinetic data for $^{67}\text{Ga} - \text{citrate}$ was taken from ICRP Publication 53 (ICRP 1988). Values from important biokinetic equations for $^{99\text{m}}\text{Tc} - \text{RBC}$ and $^{67}\text{Ga} - \text{citrate}$ are given in Tables 4-36 and 4-37, respectively (ICRP 2007, ICRP 1988). The important parameter for these case studies is A_s/A_o , which is the time-integrated activity coefficient (or total number of decays per unit administered activity). Time-integrated activity coefficients are multiplied by the radionuclide S value for each relevant source tissue to determine the absorbed dose to all target tissues of interest per unit AA. Time-integrated activity coefficients take into account the distribution of the radiopharmaceutical throughout the body, considering physical/radioactive decay and the half-life of the radiopharmaceutical in each source tissue.

Dosimetry

Dosimetry for both radiopharmaceuticals was performed using Equation 4-10.

$$\frac{D(r_T)}{A_o} = \sum_{r_s} S(r_T \leftarrow r_s) \cdot \left[\frac{\tilde{A}_s}{A_o} \right]_{r_s} \quad (4-10)$$

where $D(r_T)/A_o$ is the absorbed dose to target tissue r_T per unit AA A_o , $S(r_T \leftarrow r_S)$ is the radionuclide S value to target tissue r_T from source tissue r_S , and $[\tilde{A}_s/A_o]_{r_s}$ is the time-integrated activity coefficient for source tissue r_s . Radionuclide S values were calculated by energy-interpolating the monoenergetic photon and electron SAFs developed in the current study for application in Equation 4-10. Effective doses for the UFH00MF, UFH01MF, UFH05MF, UFH10MF, UFH15MF, and UFHADMF phantoms were calculated using tissue weighting factors from ICRP Publication 103 (ICRP 2007) in addition to absorbed dose to all target tissues. Results for the UFH00MF phantom were provided even though dose estimates from the selected sources were unavailable for the newborn.

A secondary reason for selecting $^{99m}Tc - RBC$ as a radiopharmaceutical of interest was to provide blood vessel wall dose estimates. Twenty four percent of the total number of nuclear transformations in blood was apportioned to the large arteries and veins, as these were the vessels under consideration for blood vessel wall dose. The derived monoenergetic photon and electron SAFs for the blood vessel walls were separately interpolated and applied in the S value formulation.

Results

Equivalent dose per unit AA estimated for the UF phantom family for a variety of target tissues relevant to the ICRP Publication 103 (ICRP 2007) tissue weighting factors for $^{99m}Tc - RBC$ and $^{67}Ga - citrate$ as compared to estimates given in ICRP Publication 80 (ICRP 1998) as seen in Tables 4-38 and 4-39, respectively. Whole-body effective dose was also calculated for both radiopharmaceuticals using maximum typical AAs for adults and scaled AAs for pediatric and adolescents. Maximum typical AAs for adults for $^{99m}Tc - RBC$ and $^{67}Ga - citrate$ were found to be 740 MBq and 185 MBq, respectively (Lægemedelstyrelsen 2008, Medi-Physics,

Inc. 1994). Maximum AAs were considered over average AAs to estimate some of the highest doses expected in the clinic for these procedures. Four AA scaling rules (defined earlier), Clark's Rule, Young's Rule, Webster's Rule, and Fried's Rule, were used to scale the adult AA to the pediatric and adolescent ages, and the average of the four results at each age was taken as the AA for that age. Whole-body effective dose estimates for the UF phantom family for $^{99m}\text{Tc} - \text{RBC}$ and $^{67}\text{Ga} - \text{citrate}$ as compared to two other sources can be seen in Tables 4-40 and 4-41, respectively.

First looking at the whole-body effective dose estimates, the UF estimates are very close to the estimates of ICRP Publication 80 (ICRP 1998). An average absolute percent difference of 10% (2% – 27%) was observed across all age groups except the newborn (no estimate was provided for the newborn by the data sources) for $^{99m}\text{Tc} - \text{RBC}$. Slightly greater differences were seen for $^{67}\text{Ga} - \text{citrate}$ with an average absolute percent difference of 15% (8% – 32%). In every case, the UF effective dose estimates were greater than the ICRP 80 estimates, and this was expected due to the phantom differences used for dosimetry. ICRP Publication 80 used SAFs from Cristy and Eckerman (1987) that are based on the ORNL stylized phantom family (ICRP 1998). One key difference between the UF hybrid phantoms and ORNL stylized phantom is the relative orientation of the internal organs. Figure 4-11 shows that the separation between organs for the UFH10F phantom is less than that of the ORNL 10-year-old phantom. The UFH10F models more closely what is observed in reality – human organs are pressed up together, not spaced apart as mathematical shapes necessitate. Resultantly, it was expected that UF dose estimates would be slightly higher in general than the ICRP Publication 80 estimates due to increased cross-dose contributions. This was not always the case as position of the organs themselves could vary between the UF and ORNL phantoms. Tables 4-38 and 4-39 show that in

many (but not the majority of) instances, the ICRP Publication 80 dose estimates are greater than the UF estimates. Even though the whole-body effective dose estimates were fairly similar between the two estimation sources, UF estimates of equivalent doses to individual organs deviated from the ICRP estimates by an average absolute percent difference of 44% (0% – 606%). Differences in individual organ equivalent doses can be just as important as estimates of whole-body effective dose¹² because individual organ doses can influence procedural details based on known organ toxicity dose thresholds. In addition, accurate individual organ doses are still needed to estimate individual cancer risk. The range of effective doses ($4\text{ mSv} - 24\text{ mSv}$) compared well with current estimates of typical nuclear medicine imaging effective doses ($1.8\text{ mSv} - 41.0\text{ mSv}$) (Health Physics Society 2010).

Another area of focus in this section was the determination of a whole-body average blood vessel wall dose for the $^{99m}\text{Tc} - \text{RBC}$ procedure. Patient-specific AAs from the internal dosimetry analysis was used again for the blood vessel wall dose estimates. Blood vessel wall dose in mGy for $^{99m}\text{Tc} - \text{RBC}$ for the entire UF phantom family can be seen in Table 4-42. The maximum (average of four AA scaling methods) wall dose was found to be about 200 mGy , well below the threshold for blood vessel wall toxicity (23 Gy (Hull *et al.* 2003)). However, ^{99m}Tc is primarily a photon emitter, and wall doses are expected to be at a maximum for short-range particle emitters such as ^{18}F . To investigate wall dose for a short-range particle emitter, $^{18}\text{F} - \text{FDG}$ was simulated with the AAs as recommended by the 2010 North American Consensus Guidelines (Gelfand *et al.* 2010). $^{18}\text{F} - \text{FDG}$ clears the blood vessels quite quickly with a biological half-life of about 1 minute (ICRP 2008), so no complications were expected.

¹² The importance of whole-body effective dose as related to patients undergoing nuclear medicine procedures is currently under debate in the field. Optimization and procedure inter-comparison for a single patient are probably the two most useful applications of whole-body effective dose.

However, to illustrate the effect of short-range particles, $^{18}\text{F} - \text{FDG}$ was assumed to have the same number of nuclear transformations in the blood vessels as $^{99\text{m}}\text{Tc} - \text{RBC}$. This is conservative because both the physical and biological half-lives of $^{99\text{m}}\text{Tc}$ are greater than ^{18}F (ICRP 2008, ICRP 2008). Results for this analysis are in Table 4-43. A maximum wall dose of about 800 mSv was observed for $^{18}\text{F} - \text{FDG}$ across all phantoms, still well below the threshold for wall toxicity. In fact, most nuclear medicine imaging procedures would probably not garner enough radiation dose to the blood vessel walls to cause concern.

Clinical Application

The work from the current study can be immediately applied to optimize nuclear medicine procedures, as detailed in Sgouros *et al.* (2011). Methods utilized in the current study were used in Sgouros *et al.* (2011) to calculate absorbed dose to various tissues in the body. The study attempted to optimize the administered activity (AA) given to two patients undergoing a $^{99\text{m}}\text{Tc} - \text{DMSA}$ SPECT study for renal imaging (Sgouros *et al.* 2011). Two 10-year-old females of equal weight but different statures were addressed in the study, and the tradeoff between cancer risk and diagnostic quality was examined based on several factors (Sgouros *et al.* 2011). Currently, AA for these two girls would be calculated as a fraction of the adult AA based on the weight of each, so the same AA would be given for both girls, regardless of their difference in stature – one was tall and thin, and one was short and stout (Sgouros *et al.* 2011). However, the same AA should probably not be given to both patients because differences in body morphometry will lead to differences in image quality.

Biokinetic information for $^{99\text{m}}\text{Tc} - \text{DMSA}$ was taken from Evans *et al.* (1996) and Smith *et al.* (1996), and the whole-body clearance rate was calculated by fitting a monoexponential function to the complement of the urine data (Sgouros *et al.* 2011). Biokinetic data was

necessary to calculate internal doses as well as simulate SPECT images. Cancer risk was estimated as age- and gender-specific lifetime attributable risk (LAR) (cancer incidence risk), as given in the National Academy of Science's BEIR VII Report (National Research Council 2005). Internal dose estimates were obtained with consideration for the source tissues of interest for $^{99m}\text{Tc} - \text{DMSA}$ and the total number of nuclear transformations in each source tissue calculated from the biokinetic models using general radiation transport methodology very similar to that used in the current study with the primary difference being that the ^{99m}Tc spectra were directly sampled during simulation. Projection images were created using an analytic projection code modeling random variations in tissue uptake (Sgouros *et al.* 2011). A defect was placed in three different positions with varying levels of uptake reduction (Sgouros *et al.* 2011). The images were then scaled to represent 25%, 50%, 75%, 100%, 125%, and 150% of the count level that would be observed if a low-energy, high-resolution dual camera system were used with a 30 min acquisition time (Sgouros *et al.* 2011). These increases and decreases in count level corresponded to a proportional change in AA. Coronal images of pixel dimensions 64×64 were extracted and subjected to a channelized Hotelling observer (CHO) study whereby diagnostic quality was assessed through the production of receiver-operating-characteristic (ROC) curves (Sgouros *et al.* 2011). The CHO has been shown to accurately predict responses of real radiologists, and the ROC curves indicate diagnostic quality. The study showed that the same diagnostic quality could be obtained for the tall, thin patient if the AA was reduced by about 50%. If this new AA was administered rather than the original weight-based AA, less than half of the cancer incidence could be expected for the tall, thin patient than the short, stout patient (based on an exposed population) (Sgouros *et al.* 2011).

This is one example of how the methods used in the current study could be used to optimize nuclear medicine procedures, and in this case, a nuclear medicine imaging procedure. Accurate internal dose estimates are necessary for comparing cancer risks associated with the use of radionuclides in medicine to investigate the tradeoff between cancer risk and diagnostic quality. The results of the current study are important to this end and may be used in the future to optimize more protocols. In fact, a grant awarded to researchers at Johns Hopkins University and the University of Florida by the National Institute of Biomedical Imaging and Bioengineering (NIBIB) of the National Institutes of Health (NIH) will address optimization of $^{99m}\text{Tc} - \text{DMSA}$ and $^{99m}\text{Tc} - \text{MDP}$ protocols (extensions may be made to $^{18}\text{F} - \text{FDG}$ in the future).

Table 4-1. Anterio-posterior (AP), lateral (LAT), and axial dimensions and prism volumes for blood vessel wall scaling methodology.

Phantom	AP (cm)	LAT (cm)	Axial (cm)	Prism Volume (cm ³)
UFH00MF	10	14	14	1960
UFH01MF	15	15	29	6525
UFH05MF	15	21	39	12285
UFH10MF	18	26	51	23868
UFH15M	23	30	59	40710
UFH15F	20	28	55	30800
UFHADM	25	38	67	63650
UFHADDF	20	32	60	38400

Table 4-2. SAFs to the blood vessel walls for a uniformly distributed blood source for the UF phantom family.

Phantom	Photon Energy (MeV)			Electron Energy (MeV)		
	0.01	0.50	4.00	0.01	0.50	4.00
UFH00MF	3.67E+01	9.27E-01	2.60E-01	1.44E+01	4.89E+01	1.28E+01
UFH01MF	3.37E+01	8.52E-01	2.40E-01	1.32E+01	4.49E+01	1.18E+01
UFH05MF	2.99E+01	7.58E-01	2.14E-01	1.17E+01	3.98E+01	1.05E+01
UFH10MF	2.23E+01	5.68E-01	1.61E-01	8.73E+00	2.97E+01	7.81E+00
UFH15M	2.16E+01	5.51E-01	1.56E-01	8.48E+00	2.88E+01	7.59E+00
UFH15F	1.77E+01	4.54E-01	1.30E-01	6.94E+00	2.36E+01	6.23E+00
UFHADM	1.27E+01	3.28E-01	9.51E-02	4.97E+00	1.69E+01	4.50E+00
UFHADDF	1.27E+01	3.29E-01	9.57E-02	4.97E+00	1.69E+01	4.50E+00

Table 4-3. Percent difference between the UFH00MF phantom and the ORNL adult stylized phantom skeletal fluence-to-dose response functions for selected bone sites (Cristy *et al.* 1987).

Photon Energy (MeV)	Fluence-to-dose Response Function (Gy·m ²)								
	UFH00MF			ORNL Adult Male			Difference		
	Cervical vertebrae	Lumbar vertebrae	Ribs	Cervical vertebrae	Lumbar vertebrae	Ribs	Cervical vertebrae	Lumbar vertebrae	Ribs
0.010	6.32E-16	6.32E-16	6.33E-16	6.16E-16	6.14E-16	6.12E-16	3%	3%	3%
0.015	2.76E-16	2.75E-16	2.76E-16	2.62E-16	2.61E-16	2.59E-16	5%	6%	7%
0.020	1.55E-16	1.55E-16	1.55E-16	1.45E-16	1.43E-16	1.41E-16	7%	8%	10%
0.030	7.44E-17	7.42E-17	7.45E-17	6.60E-17	6.44E-17	6.29E-17	13%	15%	19%
0.040	4.98E-17	4.95E-17	4.99E-17	4.27E-17	4.11E-17	3.99E-17	17%	21%	25%
0.050	4.07E-17	4.05E-17	4.08E-17	3.45E-17	3.31E-17	3.20E-17	18%	22%	27%
0.060	3.77E-17	3.76E-17	3.79E-17	3.26E-17	3.11E-17	3.01E-17	16%	21%	26%
0.080	3.97E-17	3.96E-17	3.97E-17	3.58E-17	3.45E-17	3.36E-17	11%	15%	18%
0.100	4.61E-17	4.61E-17	4.61E-17	4.33E-17	4.22E-17	4.14E-17	6%	9%	11%
0.150	6.90E-17	6.91E-17	6.88E-17	6.83E-17	6.74E-17	6.68E-17	1%	3%	3%
0.200	9.61E-17	9.63E-17	9.56E-17	9.63E-17	9.57E-17	9.52E-17	0%	1%	0%
0.300	1.48E-16	1.48E-16	1.49E-16	1.54E-16	1.54E-16	1.53E-16	-4%	-4%	-3%
0.400	2.01E-16	2.02E-16	2.03E-16	2.12E-16	2.10E-16	2.10E-16	-5%	-4%	-3%
0.500	2.53E-16	2.54E-16	2.56E-16	2.67E-16	2.66E-16	2.65E-16	-5%	-5%	-4%
0.600	3.02E-16	3.03E-16	3.05E-16	3.20E-16	3.19E-16	3.17E-16	-6%	-5%	-4%
0.800	3.94E-16	3.95E-16	3.97E-16	4.17E-16	4.15E-16	4.14E-16	-6%	-5%	-4%
1.000	4.76E-16	4.78E-16	4.81E-16	5.06E-16	5.03E-16	5.01E-16	-6%	-5%	-4%
1.500	6.52E-16	6.54E-16	6.59E-16	6.95E-16	6.91E-16	6.89E-16	-6%	-5%	-4%
2.000	7.97E-16	7.99E-16	8.05E-16	8.56E-16	8.50E-16	8.47E-16	-7%	-6%	-5%
3.000	1.02E-15	1.03E-15	1.03E-15	1.13E-15	1.12E-15	1.11E-15	-9%	-8%	-7%
4.000	1.20E-15	1.20E-15	1.21E-15	1.37E-15	1.37E-15	1.35E-15	-13%	-12%	-10%
5.000	1.34E-15	1.34E-15	1.35E-15	1.60E-15	1.59E-15	1.57E-15	-16%	-15%	-14%
6.000	1.46E-15	1.47E-15	1.47E-15	1.82E-15	1.80E-15	1.78E-15	-20%	-19%	-17%
8.000	1.66E-15	1.66E-15	1.67E-15	2.27E-15	2.23E-15	2.20E-15	-27%	-26%	-24%
10.000	1.82E-15	1.82E-15	1.83E-15	2.71E-15	2.66E-15	2.62E-15	-33%	-31%	-30%

Table 4-4. Energy-averaged percent differences between the UF hybrid phantom and ORNL stylized phantom monoenergetic photon SAFs.

Phantom	$\Phi(\text{liv} \leftarrow \text{liv})$	$\Phi(\text{adr} \leftarrow \text{adr})$	$\Phi(\text{mus} \leftarrow \text{lun})$	$\Phi(\text{bra} \leftarrow \text{trd})$	$\Phi(\text{adr} \leftarrow \text{trd})$
Newborn	-10%	-15%	13%	56%	2152%
1-year	-9%	-20%	8%	-8%	603%
5-year	3%	-9%	18%	-20%	376%
10-year	-1%	-4%	21%	-21%	19569%
15-year male	7%	0%	4%	-59%	227%
15-year female	6%	4%	4%	-50%	954%
Adult male	9%	7%	7%	-59%	73%
Adult female	1%	2%	-7%	18%	575%

Table 4-5. Absolute energy-averaged percent differences between the UF hybrid phantom and ORNL stylized phantom monoenergetic photon SAFs.

Phantom	$\Phi(\text{liv} \leftarrow \text{liv})$	$\Phi(\text{adr} \leftarrow \text{adr})$	$\Phi(\text{mus} \leftarrow \text{lun})$	$\Phi(\text{bra} \leftarrow \text{trd})$	$\Phi(\text{adr} \leftarrow \text{trd})$
Newborn	10%	15%	19%	56%	2157%
1-year	10%	20%	8%	11%	603%
5-year	6%	15%	18%	20%	376%
10-year	6%	14%	21%	21%	19569%
15-year male	8%	16%	6%	59%	227%
15-year female	7%	17%	4%	50%	954%
Adult male	9%	17%	9%	59%	73%
Adult female	4%	15%	7%	19%	575%

Table 4-6. Excerpt of the 3-D mass ratio scaling power matrix used to scaled photon self-dose showing results for 4 MeV photons.

Sphere Mass (g)	Sphere Mass (g)									
	1	4	8	10	40	80	100	400	800	1000
1	--	-0.365	-0.379	-0.384	-0.421	-0.440	-0.446	-0.478	-0.493	-0.498
2	-0.360	-0.371	-0.389	-0.394	-0.435	-0.455	-0.461	-0.494	-0.509	-0.513
4	-0.365	--	-0.406	-0.411	-0.455	-0.474	-0.480	-0.513	-0.527	-0.531
6	-0.373	-0.398	-0.417	-0.422	-0.467	-0.486	-0.492	-0.524	-0.537	-0.541
8	-0.379	-0.406	--	-0.429	-0.476	-0.495	-0.500	-0.531	-0.545	-0.549
10	-0.384	-0.411	-0.429	--	-0.483	-0.502	-0.507	-0.538	-0.551	-0.555
20	-0.402	-0.433	-0.453	-0.461	-0.506	-0.522	-0.528	-0.555	-0.567	-0.571
40	-0.421	-0.455	-0.476	-0.483	--	-0.539	-0.544	-0.570	-0.582	-0.585
60	-0.432	-0.466	-0.487	-0.494	-0.532	-0.548	-0.553	-0.579	-0.589	-0.593
80	-0.440	-0.474	-0.495	-0.502	-0.539	--	-0.559	-0.584	-0.595	-0.598
100	-0.446	-0.480	-0.500	-0.507	-0.544	-0.559	--	-0.588	-0.598	-0.602
200	-0.463	-0.497	-0.517	-0.524	-0.559	-0.573	-0.578	-0.598	-0.609	-0.612
400	-0.478	-0.513	-0.531	-0.538	-0.570	-0.584	-0.588	--	-0.619	-0.623
600	-0.487	-0.521	-0.539	-0.545	-0.577	-0.590	-0.594	-0.613	-0.629	-0.631
800	-0.493	-0.527	-0.545	-0.551	-0.582	-0.595	-0.598	-0.619	--	-0.635
1000	-0.498	-0.531	-0.549	-0.555	-0.585	-0.598	-0.602	-0.623	-0.635	--
2000	-0.511	-0.543	-0.560	-0.566	-0.595	-0.607	-0.611	-0.630	-0.639	-0.640
4000	-0.523	-0.554	-0.571	-0.576	-0.604	-0.615	-0.619	-0.637	-0.645	-0.647
6000	-0.529	-0.560	-0.577	-0.582	-0.609	-0.620	-0.624	-0.642	-0.649	-0.651
8000	-0.534	-0.564	-0.580	-0.585	-0.612	-0.623	-0.627	-0.644	-0.652	-0.654
10000	-0.537	-0.568	-0.583	-0.588	-0.615	-0.626	-0.629	-0.646	-0.654	-0.656

Table 4-7. Photon self-dose scaling validation study analyzing the benefit of using all mass ratio scaling powers as compared to using mass-averaged mass ratio scaling powers for the photon spectrum of ^{99m}Tc . “f-175-136” is the shorthand designation for the patient-specific female at 175 cm in height and 136 kg in weight.

Method	Phantom	Target Tissue	Mass (g)	Actual S value (mGy/MBq-s)	MIRD deviation (%)	UF deviation (%)	Preferred Method	Percent Gain (%)
All powers	UFH00MF	Liver	54.44	2.04E-05	2.56%	3.19%	MIRD	0.63%
			252.12	7.45E-06	3.82%	3.21%	UF	0.61%
	f-175-136	Thyroid	0.55	3.73E-04	2.67%	4.16%	MIRD	1.49%
			2.51	1.35E-04	2.80%	1.95%	UF	0.86%
Average powers	UFH00MF	Liver	2176.34	1.74E-06	1.66%	2.11%	MIRD	0.45%
			256.75	7.40E-06	6.25%	5.63%	UF	0.62%
	f-175-136	Liver	54.44	2.04E-05	2.56%	2.39%	UF	0.17%
			252.12	7.45E-06	3.82%	3.69%	UF	0.14%
	UFH00MF	Thyroid	0.55	3.73E-04	2.67%	5.36%	MIRD	2.69%
			2.51	1.35E-04	2.80%	1.29%	UF	1.51%
	f-175-136	Liver	2176.34	1.74E-06	1.66%	2.25%	MIRD	0.59%
			256.75	7.40E-06	6.25%	6.11%	UF	0.15%

Table 4-8. Photon self-dose scaling validation study analyzing the benefit of using all mass ratio scaling powers as compared to using mass-averaged mass ratio scaling powers for 4 MeV photons. “f-175-136” is the shorthand designation for the patient-specific female at 175 cm in height and 136 kg in weight.

Method	Phantom	Target Tissue	Mass (g)	Actual S value (mGy/MBq-s)	MIRD deviation (%)	UF deviation (%)	Preferred Method	Percent Gain (%)	
All powers	UFH00MF	Liver	54.44	2.62E-04	9.80%	0.18%	UF	9.62%	
			252.12	1.09E-04	5.28%	0.05%	UF	5.23%	
		Thyroid	0.55	1.57E-03	27.24%	2.50%	UF	24.74%	
			2.51	8.65E-04	15.86%	2.94%	UF	12.92%	
Average powers	f-175-136	Liver	2176.34	2.80E-05	1.36%	2.39%	MIRD	1.03%	
		Spleen	256.75	1.12E-04	12.10%	7.04%	UF	5.05%	
		UFH00MF	Liver	54.44	2.62E-04	9.80%	0.48%	UF	9.32%
				252.12	1.09E-04	5.28%	2.25%	UF	3.04%
Thyroid	0.55	1.57E-03	27.24%	15.45%	UF	11.79%			
	2.51	8.65E-04	15.86%	9.23%	UF	6.64%			
f-175-136	Liver	2176.34	2.80E-05	1.36%	6.66%	MIRD	5.30%		
		Spleen	256.75	1.12E-04	12.10%	4.94%	UF	7.16%	

Table 4-9. Photon self-dose scaling validation study analyzing 10 keV photons. “f-175-136” is the shorthand designation for the patient-specific female at 175 cm in height and 136 kg in weight.

Method	Phantom	Target Tissue	Mass (g)	Actual S value (mGy/MBq-s)	MIRD deviation (%)	UF deviation (%)	Preferred Method	Percent Gain (%)
All powers	UFH00MF	Liver	54.44	2.71E-05	23.21%	0.51%	UF	22.69%
			252.12	6.04E-06	23.75%	0.05%	UF	23.70%
		Thyroid	0.55	1.78E-03	15.60%	3.34%	UF	12.26%
			2.51	4.68E-04	16.72%	1.33%	UF	15.39%
f-175-136	Liver	2176.34	7.14E-07	15.98%	0.27%	UF	15.70%	
		Spleen	256.75	5.92E-06	23.51%	0.65%	UF	22.86%

Table 4-10. Patient-specific photon self-dose scaling validation study using all UF mass ratio scaling powers for ^{131}I photons. The patient-specific naming convention is [gender][height in centimeters][weight in kilograms] (e.g., m-193-132 is a 193 *cm* tall, 132 *kg* male).

Phantom	Self-S value (mGy/MBq-s)		UF deviation (%)		MIRD deviation (%)		Preferred method		Percentage point gain (%)	
	Liver	Spleen	Liver	Spleen	Liver	Spleen	Liver	Spleen	Liver	Spleen
Male										
m-193-132	3.90E-06	1.38E-05	1.93%	0.63%	2.76%	0.88%	UF	UF	0.84%	0.25%
m-183-120	4.56E-06	1.07E-05	0.57%	0.71%	0.07%	0.56%	MIRD	MIRD	0.50%	0.15%
m-183-112	5.14E-06	1.85E-05	1.56%	1.89%	1.75%	1.67%	UF	MIRD	0.20%	0.22%
m-183-86	5.50E-06	8.58E-06	5.31%	1.32%	5.30%	1.34%	MIRD	UF	0.00%	0.03%
m-180-82	4.90E-06	2.66E-05	1.43%	0.05%	1.73%	0.12%	UF	UF	0.30%	0.07%
m-178-100	5.06E-06	8.03E-06	0.94%	0.06%	1.18%	0.17%	UF	UF	0.24%	0.11%
m-178-73	5.60E-06	1.50E-05	6.53%	0.19%	6.47%	0.46%	MIRD	UF	0.06%	0.27%
m-175-81	5.47E-06	2.34E-05	2.15%	5.67%	2.22%	5.82%	UF	UF	0.06%	0.15%
m-175-66	5.80E-06	1.74E-05	5.15%	1.66%	5.05%	1.91%	MIRD	UF	0.10%	0.25%
m-173-98	5.72E-06	2.13E-05	2.86%	2.12%	2.79%	1.95%	MIRD	MIRD	0.07%	0.17%
m-173-74	6.42E-06	4.37E-05	0.79%	0.71%	0.96%	0.46%	UF	MIRD	0.17%	0.26%
m-168-78	7.86E-06	2.46E-05	1.90%	4.85%	1.41%	4.76%	MIRD	MIRD	0.49%	0.09%
m-165-74	6.03E-06	2.27E-05	0.58%	0.53%	0.49%	0.67%	MIRD	UF	0.09%	0.14%
m-157-44	9.60E-06	1.02E-05	3.76%	4.67%	3.06%	4.52%	MIRD	MIRD	0.70%	0.15%
Female										
f-164-59	5.79E-06	4.49E-05	5.12%	13.30%	4.84%	13.16%	MIRD	MIRD	0.28%	0.14%
f-175-136	4.90E-06	2.16E-05	0.71%	8.57%	0.18%	8.78%	MIRD	UF	0.53%	0.21%
f-173-82	5.63E-06	2.60E-05	4.50%	11.37%	4.18%	11.51%	MIRD	UF	0.32%	0.14%
f-165-63	8.16E-06	5.35E-05	0.42%	10.13%	0.70%	9.84%	UF	MIRD	0.28%	0.29%
f-163-117	3.79E-06	1.32E-05	3.18%	7.34%	2.01%	7.61%	MIRD	UF	1.17%	0.27%
f-163-80	5.23E-06	2.64E-05	2.01%	6.86%	1.60%	6.98%	MIRD	UF	0.42%	0.12%
f-160-61	6.56E-06	4.52E-05	2.28%	10.92%	2.24%	10.74%	MIRD	MIRD	0.04%	0.17%
f-160-52	8.44E-06	4.06E-05	0.87%	5.19%	0.54%	5.04%	MIRD	MIRD	0.33%	0.14%
f-160-51	6.81E-06	2.44E-05	4.55%	5.60%	4.43%	5.75%	MIRD	UF	0.12%	0.15%
f-155-98	6.66E-06	3.71E-05	3.85%	7.40%	3.81%	7.34%	MIRD	MIRD	0.04%	0.06%
f-155-70	5.75E-06	1.96E-05	0.70%	0.42%	0.48%	0.65%	MIRD	UF	0.23%	0.23%
f-155-48	6.37E-06	3.08E-05	2.22%	6.18%	2.14%	6.22%	MIRD	UF	0.08%	0.04%
f-152-66	6.04E-06	2.21E-05	3.18%	6.44%	3.27%	6.63%	UF	UF	0.09%	0.19%

Table 4-11. Excerpt of the photon cross-dose sphere SAFs showing a subset of the source masses, target masses, photon energies, and center-to-center separations.

Source mass (g)	Target mass (g)	15.632 cm separation					31.264 cm separation				
		Photon energy (MeV)					Photon energy (MeV)				
		1.000	1.500	2.000	3.000	4.000	1.000	1.500	2.000	3.000	4.000
1.00	1.00	7.51E-03	7.13E-03	6.51E-03	5.30E-03	5.29E-03	1.19E-03	1.20E-03	9.97E-04	1.09E-03	1.01E-03
	2.00	7.44E-03	6.78E-03	6.17E-03	5.39E-03	5.22E-03	1.19E-03	1.29E-03	1.07E-03	1.14E-03	1.04E-03
	4.00	7.46E-03	6.61E-03	6.20E-03	5.48E-03	5.14E-03	1.10E-03	1.14E-03	1.07E-03	1.10E-03	1.05E-03
	6.00	7.32E-03	6.55E-03	6.25E-03	5.59E-03	5.15E-03	1.09E-03	1.10E-03	1.10E-03	1.04E-03	1.05E-03
	8.00	7.27E-03	6.57E-03	6.27E-03	5.65E-03	5.11E-03	1.09E-03	1.11E-03	1.10E-03	1.03E-03	1.04E-03
2.00	10.00	7.36E-03	6.66E-03	6.32E-03	5.69E-03	5.10E-03	1.11E-03	1.12E-03	1.12E-03	1.05E-03	1.02E-03
	1.00	7.44E-03	6.78E-03	6.17E-03	5.39E-03	5.22E-03	1.19E-03	1.29E-03	1.07E-03	1.14E-03	1.04E-03
	2.00	7.36E-03	6.69E-03	6.17E-03	5.74E-03	5.38E-03	1.16E-03	1.17E-03	1.05E-03	1.01E-03	1.04E-03
	4.00	7.28E-03	6.50E-03	6.15E-03	5.76E-03	5.19E-03	1.12E-03	1.14E-03	1.10E-03	1.10E-03	1.09E-03
	6.00	7.20E-03	6.43E-03	6.24E-03	5.79E-03	5.18E-03	1.12E-03	1.11E-03	1.13E-03	1.08E-03	1.08E-03
4.00	8.00	7.22E-03	6.49E-03	6.30E-03	5.78E-03	5.22E-03	1.10E-03	1.09E-03	1.10E-03	1.09E-03	1.04E-03
	10.00	7.26E-03	6.59E-03	6.30E-03	5.74E-03	5.22E-03	1.10E-03	1.10E-03	1.09E-03	1.10E-03	1.03E-03
	1.00	7.46E-03	6.61E-03	6.20E-03	5.48E-03	5.14E-03	1.10E-03	1.14E-03	1.07E-03	1.10E-03	1.05E-03
	2.00	7.28E-03	6.50E-03	6.15E-03	5.76E-03	5.19E-03	1.12E-03	1.14E-03	1.10E-03	1.10E-03	1.09E-03
	4.00	7.29E-03	6.69E-03	6.22E-03	5.61E-03	5.11E-03	1.14E-03	1.15E-03	1.15E-03	1.03E-03	1.02E-03
10.00	6.00	7.31E-03	6.69E-03	6.30E-03	5.78E-03	5.16E-03	1.13E-03	1.14E-03	1.13E-03	1.01E-03	1.03E-03
	8.00	7.27E-03	6.69E-03	6.39E-03	5.79E-03	5.15E-03	1.11E-03	1.11E-03	1.13E-03	1.02E-03	1.03E-03
	10.00	7.34E-03	6.74E-03	6.44E-03	5.80E-03	5.18E-03	1.14E-03	1.10E-03	1.11E-03	1.01E-03	1.03E-03

Table 4-12. Photon cross-dose validation study using an arbitrary reference and non-reference set of spheres and liver- and pancreas-adjusted reference UFHADM phantom.

Energy (MeV)	Reference S value (mGy/MBq-s)	Non-reference S value (mGy/MBq-s)	Predicted non-reference S value (mGy/MBq-s)	Percent difference (Predicted to non-reference) (%)	Percent difference (Reference to non-reference) (%)	Percentage point gain (%)
Spheres						
Monoenergetic 3.5 MeV	3.05E-06	6.46E-07	7.58E-07	17%	372%	354%
Tc-99m photon spectrum	2.04E-07	2.40E-08	3.40E-08	41%	748%	706%
Phantom						
Monoenergetic 3.5 MeV	4.35E-06	3.20E-06	3.78E-06	18%	36%	18%
Tc-99m photon spectrum	2.74E-07	1.90E-07	2.34E-07	23%	44%	21%

Table 4-13. Photon cross-dose scaling validation study showing predictive quality of UF scaling method as applied to patient-specific phantoms for ^{131}I photons. The patient-specific naming convention is [gender][height in centimeters][weight in kilograms] (e.g., m-193-132 is a 193 *cm* tall, 132 *kg* male).

Phantom	Reference cross-S value (mGy/MBq-s)	Actual cross-S value (mGy/MBq-s)	Predicted cross-S value (mGy/MBq-s)	Reference difference (%)	Predicted difference (%)	Percentage point gain (%)
Male						
m-193-132	6.91E-07	8.95E-07	7.18E-07	23%	20%	3.02%
m-183-120	6.91E-07	8.46E-07	7.27E-07	18%	14%	4.23%
m-183-112	6.91E-07	8.92E-07	7.19E-07	23%	19%	3.04%
m-183-86	6.91E-07	9.23E-07	7.31E-07	25%	21%	4.31%
m-180-82	6.91E-07	1.37E-06	8.14E-07	49%	40%	8.96%
m-178-100	6.91E-07	9.67E-07	7.15E-07	28%	26%	2.48%
m-178-73	6.91E-07	7.01E-07	6.81E-07	1%	3%	-1.42%
m-175-81	6.91E-07	1.19E-06	7.44E-07	42%	38%	4.38%
m-175-66	6.91E-07	1.22E-06	7.55E-07	43%	38%	5.22%
m-173-98	6.91E-07	7.39E-07	6.50E-07	6%	12%	-5.62%
m-173-74	6.91E-07	1.12E-06	7.54E-07	38%	33%	5.53%
m-168-78	6.91E-07	1.37E-06	7.42E-07	50%	46%	3.65%
m-165-74	6.91E-07	1.83E-06	8.26E-07	62%	55%	7.35%
m-157-44	6.91E-07	3.82E-06	9.66E-07	82%	75%	7.20%
Female						
f-164-59	1.12E-06	1.20E-06	1.09E-06	7%	10%	-2.75%
f-175-136	1.12E-06	1.48E-06	1.20E-06	24%	19%	5.54%
f-173-82	1.12E-06	1.39E-06	1.14E-06	19%	18%	1.34%
f-165-63	1.12E-06	1.37E-06	1.11E-06	18%	19%	-0.87%
f-163-117	1.12E-06	8.43E-07	1.06E-06	33%	25%	7.70%
f-163-80	1.12E-06	1.28E-06	1.15E-06	12%	10%	2.42%
f-160-61	1.12E-06	1.60E-06	1.13E-06	30%	29%	0.67%
f-160-52	1.12E-06	1.99E-06	1.14E-06	44%	43%	0.77%
f-160-51	1.12E-06	2.39E-06	1.22E-06	53%	49%	4.03%
f-155-98	1.12E-06	1.96E-06	1.17E-06	43%	40%	2.77%
f-155-70	1.12E-06	1.62E-06	1.16E-06	31%	29%	2.28%
f-155-48	1.12E-06	1.90E-06	1.21E-06	41%	36%	4.92%
f-152-66	1.12E-06	1.07E-06	1.15E-06	5%	7%	-2.60%

Table 4-14. Excerpt of the 3-D mass ratio scaling power matrix used to scaled electron self-dose showing results for 4 MeV electrons.

Sphere Mass (g)	Sphere Mass (g)									
	1	4	8	10	40	80	100	400	800	1000
1	--	-0.626	-0.633	-0.640	-0.691	-0.717	-0.725	-0.769	-0.787	-0.792
2	-0.632	-0.620	-0.634	-0.643	-0.705	-0.734	-0.742	-0.787	-0.805	-0.810
4	-0.626	--	-0.649	-0.660	-0.731	-0.760	-0.768	-0.812	-0.829	-0.834
6	-0.628	-0.636	-0.667	-0.680	-0.751	-0.779	-0.787	-0.829	-0.845	-0.849
8	-0.633	-0.649	--	-0.696	-0.766	-0.793	-0.801	-0.841	-0.856	-0.860
10	-0.640	-0.660	-0.696	--	-0.777	-0.804	-0.811	-0.849	-0.864	-0.868
20	-0.664	-0.697	-0.733	-0.745	-0.809	-0.833	-0.840	-0.874	-0.886	-0.890
40	-0.691	-0.731	-0.766	-0.777	--	-0.857	-0.863	-0.893	-0.904	-0.908
60	-0.707	-0.748	-0.782	-0.793	-0.848	-0.869	-0.874	-0.903	-0.913	-0.916
80	-0.717	-0.760	-0.793	-0.804	-0.857	--	-0.881	-0.909	-0.919	-0.922
100	-0.725	-0.768	-0.801	-0.811	-0.863	-0.881	--	-0.913	-0.923	-0.925
200	-0.748	-0.792	-0.823	-0.832	-0.879	-0.897	-0.902	-0.925	-0.933	-0.936
400	-0.769	-0.812	-0.841	-0.849	-0.893	-0.909	-0.913	--	-0.942	-0.944
600	-0.780	-0.822	-0.850	-0.858	-0.900	-0.915	-0.919	-0.939	-0.946	-0.948
800	-0.787	-0.829	-0.856	-0.864	-0.904	-0.919	-0.923	-0.942	--	-0.951
1000	-0.792	-0.834	-0.860	-0.868	-0.908	-0.922	-0.925	-0.944	-0.951	--
2000	-0.807	-0.848	-0.873	-0.880	-0.917	-0.930	-0.933	-0.950	-0.957	-0.959
4000	-0.821	-0.860	-0.883	-0.890	-0.924	-0.936	-0.940	-0.956	-0.961	-0.963
6000	-0.828	-0.866	-0.889	-0.895	-0.928	-0.940	-0.943	-0.958	-0.964	-0.965
8000	-0.832	-0.870	-0.892	-0.899	-0.931	-0.942	-0.945	-0.960	-0.965	-0.967
10000	-0.836	-0.873	-0.895	-0.901	-0.933	-0.944	-0.947	-0.961	-0.966	-0.968

Table 4-15. Electron self-dose scaling validation study analyzing the benefit of using all mass ratio scaling powers as compared to using mass-averaged mass ratio scaling powers for the electron spectrum of ^{99m}Tc . “f-175-136” is the shorthand designation for the patient-specific female at 175 cm in height and 136 kg in weight.

Method	Phantom	Target Tissue	Mass (g)	Actual S value (mGy/MBq-s)	MIRD deviation (%)	UF deviation (%)	Preferred Method	Percent Gain (%)	
All powers	UFH00MF	Liver	54.44	4.63E-05	2.79%	2.70%	UF	0.08%	
			252.12	1.00E-05	2.58%	2.63%	MIRD	0.05%	
		Thyroid	0.55	4.48E-03	3.54%	3.19%	UF	0.34%	
			2.51	9.90E-04	2.60%	2.83%	MIRD	0.22%	
Average powers	f-175-136	Liver	2176.34	1.16E-06	2.45%	2.46%	MIRD	0.02%	
			Spleen	256.75	9.84E-06	2.24%	2.30%	MIRD	0.05%
		UFH00MF	Liver	54.44	4.63E-05	2.79%	2.69%	UF	0.09%
				252.12	1.00E-05	2.58%	2.65%	MIRD	0.07%
Average powers	f-175-136	Thyroid	0.55	4.48E-03	3.54%	3.45%	UF	0.09%	
			2.51	9.90E-04	2.60%	2.68%	MIRD	0.07%	
		Liver	2176.34	1.16E-06	2.45%	2.49%	MIRD	0.05%	
			Spleen	256.75	9.84E-06	2.24%	2.32%	MIRD	0.07%

Table 4-16. Electron self-dose scaling validation study analyzing the benefit of using all mass ratio scaling powers as compared to using mass-averaged mass ratio scaling powers for 4 MeV electrons. “f-175-136” is the shorthand designation for the patient-specific female at 175 cm in height and 136 kg in weight.

Method	Phantom	Target Tissue	Mass (g)	Actual S value (mGy/MBq-s)	MIRD deviation (%)	UF deviation (%)	Preferred Method	Percent Gain (%)	
All powers	UFH00MF	Liver	54.44	7.44E-03	14.69%	3.19%	UF	11.51%	
			252.12	1.94E-03	4.96%	0.98%	UF	3.98%	
		Thyroid	0.55	1.57E-01	38.78%	1.88%	UF	36.90%	
			2.51	5.72E-02	16.43%	7.08%	UF	9.36%	
Average powers	f-175-136	Liver	2176.34	2.54E-04	0.65%	2.41%	MIRD	1.76%	
		Spleen	256.75	1.91E-03	7.69%	1.81%	UF	5.88%	
		UFH00MF	Liver	54.44	7.44E-03	14.69%	1.41%	UF	13.29%
			252.12	1.94E-03	4.96%	4.59%	UF	0.36%	
Thyroid	0.55	1.57E-01	38.78%	22.87%	UF	15.91%			
	2.51	5.72E-02	16.43%	8.10%	UF	8.33%			
f-175-136	Liver	2176.34	2.54E-04	0.65%	7.28%	MIRD	6.63%		
	Spleen	256.75	1.91E-03	7.69%	1.81%	UF	5.88%		

Table 4-17. Electron self-dose scaling validation study analyzing the benefit of using all mass ratio scaling powers as compared to using mass-averaged mass ratio scaling powers for 10 keV electrons. “f-175-136” is the shorthand designation for the patient-specific female at 175 cm in height and 136 kg in weight.

Method	Phantom	Target Tissue	Mass (g)	Actual S value (mGy/MBq-s)	MIRD deviation (%)	UF deviation (%)	Preferred Method	Percent Gain (%)
All powers	UFH00MF	Liver	54.44	2.94E-05	0.19%	0.19%	UF	0.00%
			252.12	6.35E-06	95.90%	95.90%	MIRD	0.00%
		Thyroid	0.55	2.92E-03	0.45%	0.44%	UF	0.00%
			2.51	6.38E-04	0.76%	0.76%	MIRD	0.00%
f-175-136	Liver	2176.34	7.36E-07	0.03%	0.03%	UF	0.00%	
	Spleen	256.75	6.24E-06	0.04%	0.05%	MIRD	0.00%	

Table 4-18. Patient-specific electron self-dose scaling validation study using all UF mass ratio scaling powers for ^{90}Y beta particles. The patient-specific naming convention is [gender][height in centimeters][weight in kilograms] (e.g., m-193-132 is a 193 cm tall, 132 kg male).

Phantom	Self-S value (mGy/MBq-s)		UF deviation (%)		MIRD deviation (%)		Preferred method		Percentage point gain (%)		
	Liver	Spleen	Liver	Spleen	Liver	Spleen	Liver	Spleen	Liver	Spleen	
Male											
m-193-132	4.66E-05	2.87E-04	0.79%	0.38%	0.28%	1.88%	MIRD	UF	0.51%	1.50%	
m-183-120	5.62E-05	2.02E-04	0.78%	0.48%	0.44%	2.29%	MIRD	UF	0.34%	1.81%	
m-183-112	6.90E-05	4.56E-04	0.93%	0.96%	0.78%	0.52%	MIRD	MIRD	0.15%	0.44%	
m-183-86	7.99E-05	1.47E-04	1.30%	0.23%	1.30%	2.95%	UF	UF	0.00%	2.72%	
m-180-82	6.42E-05	7.54E-04	0.93%	1.33%	0.72%	0.88%	MIRD	MIRD	0.22%	0.45%	
m-178-100	6.70E-05	1.31E-04	0.76%	0.15%	0.59%	3.17%	MIRD	UF	0.18%	3.02%	
m-178-73	8.36E-05	3.27E-04	1.29%	0.40%	1.34%	1.66%	UF	UF	0.05%	1.26%	
m-175-81	7.62E-05	5.82E-04	0.77%	0.14%	0.72%	0.88%	MIRD	UF	0.05%	0.74%	
m-175-66	8.63E-05	3.97E-04	1.35%	0.46%	1.44%	1.27%	UF	UF	0.08%	0.81%	
m-173-98	7.58E-05	5.63E-04	0.59%	1.05%	0.53%	0.03%	MIRD	MIRD	0.06%	1.01%	
m-173-74	9.25E-05	1.55E-03	0.78%	1.48%	0.93%	2.91%	UF	UF	0.15%	1.43%	
m-168-78	1.29E-04	7.20E-04	1.16%	1.85%	1.69%	1.30%	UF	MIRD	0.53%	0.54%	
m-165-74	8.59E-05	5.98E-04	0.87%	0.75%	0.94%	0.21%	UF	MIRD	0.07%	0.53%	
m-157-44	1.77E-04	1.97E-04	1.26%	1.63%	2.20%	1.20%	UF	MIRD	0.94%	0.44%	
Female											
f-164-59	7.90E-05	1.48E-03	0.52%	1.14%	0.24%	0.26%	MIRD	MIRD	0.28%	0.87%	
f-175-136	6.59E-05	5.40E-04	0.82%	0.55%	0.36%	2.03%	MIRD	UF	0.46%	1.48%	
f-173-82	7.65E-05	6.85E-04	0.45%	1.12%	0.14%	2.13%	MIRD	UF	0.31%	1.01%	
f-165-63	1.39E-04	2.00E-03	1.27%	0.30%	1.63%	1.53%	UF	UF	0.36%	1.23%	
f-163-117	4.40E-05	2.68E-04	0.54%	1.08%	0.28%	3.75%	MIRD	UF	0.26%	2.66%	
f-163-80	7.12E-05	7.46E-04	0.64%	0.32%	0.26%	1.13%	MIRD	UF	0.38%	0.81%	
f-160-61	9.87E-05	1.55E-03	0.72%	0.70%	0.68%	0.32%	MIRD	MIRD	0.04%	0.38%	
f-160-52	1.49E-04	1.44E-03	1.26%	0.60%	1.70%	1.44%	UF	UF	0.44%	0.84%	
f-160-51	1.15E-04	6.77E-04	1.12%	0.02%	1.24%	1.00%	UF	UF	0.13%	0.98%	
f-155-98	9.82E-05	1.22E-03	0.94%	0.23%	0.89%	0.61%	MIRD	UF	0.05%	0.38%	
f-155-70	8.33E-05	5.22E-04	0.75%	1.05%	0.53%	0.49%	MIRD	MIRD	0.22%	0.57%	
f-155-48	9.45E-05	9.47E-04	0.73%	0.01%	0.65%	0.27%	MIRD	UF	0.09%	0.26%	
f-152-66	9.40E-05	5.80E-04	1.39%	0.35%	1.31%	1.69%	MIRD	UF	0.09%	1.34%	

Table 4-19. Electron cross-dose validation study using the liver- and brain-adjusted reference UFHADM phantom.

Energy (MeV)	Reference S value (mGy/MBq-s)	Non-reference S value (mGy/MBq-s)	Predicted non-reference S value (mGy/MBq-s)	Percent difference (Predicted to non-reference) (%)	Percent difference (Reference to non-reference) (%)	Percentage point gain (%)
Phantom						
Monoenergetic 3.5 MeV	2.40E-06	2.34E-06	2.34E-06	0%	2%	2%
Rb-82 beta spectrum	8.64E-07	8.65E-07	8.50E-07	2%	0%	-2%

Table 4-20. Electron cross-dose scaling validation study showing predictive quality of UF scaling method as applied to patient-specific phantoms for ⁹⁰Y beta particles. The patient-specific naming convention is [gender][height in centimeters][weight in kilograms] (e.g., m-193-132 is a 193 *cm* tall, 132 *kg* male).

Phantom	Reference cross-S value (mGy/MBq-s)	Actual cross-S value (mGy/MBq-s)	Predicted cross-S value (mGy/MBq-s)	Reference difference (%)	Predicted difference (%)	Percentage point gain (%)
Male						
m-193-132	7.30E-09	1.07E-08	7.58E-09	32%	29%	2.65%
m-183-120	7.30E-09	9.30E-09	7.66E-09	22%	18%	3.92%
m-183-112	7.30E-09	9.79E-09	7.58E-09	25%	23%	2.86%
m-183-86	7.30E-09	1.05E-08	7.71E-09	31%	27%	3.86%
m-180-82	7.30E-09	1.53E-08	8.55E-09	52%	44%	8.17%
m-178-100	7.30E-09	1.03E-08	7.54E-09	29%	27%	2.38%
m-178-73	7.30E-09	6.91E-09	7.20E-09	6%	4%	1.45%
m-175-81	7.30E-09	1.69E-07	7.83E-09	96%	95%	0.32%
m-175-66	7.30E-09	1.48E-08	7.95E-09	51%	46%	4.41%
m-173-98	7.30E-09	7.17E-09	6.88E-09	2%	4%	-2.22%
m-173-74	7.30E-09	1.41E-08	7.94E-09	48%	44%	4.52%
m-168-78	7.30E-09	5.02E-08	7.82E-09	85%	84%	1.03%
m-165-74	7.30E-09	2.13E-07	8.68E-09	97%	96%	0.65%
m-157-44	7.30E-09	4.92E-08	1.01E-08	85%	79%	5.72%
Female						
f-164-59	1.23E-08	1.38E-08	1.18E-08	11%	15%	-3.60%
f-175-136	1.23E-08	3.05E-08	1.30E-08	60%	57%	2.31%
f-173-82	1.23E-08	1.57E-08	1.23E-08	22%	21%	0.34%
f-165-63	1.23E-08	1.67E-08	1.20E-08	26%	28%	-1.50%
f-163-117	1.23E-08	9.00E-09	1.14E-08	36%	27%	9.08%
f-163-80	1.23E-08	1.38E-08	1.24E-08	11%	10%	1.31%
f-160-61	1.23E-08	4.97E-08	1.22E-08	75%	75%	-0.04%
f-160-52	1.23E-08	4.28E-07	1.23E-08	97%	97%	0.01%
f-160-51	1.23E-08	5.55E-08	1.31E-08	78%	76%	1.55%
f-155-98	1.23E-08	3.94E-08	1.27E-08	69%	68%	1.11%
f-155-70	1.23E-08	2.60E-08	1.25E-08	53%	52%	0.97%
f-155-48	1.23E-08	2.20E-08	1.31E-08	44%	40%	3.87%
f-152-66	1.23E-08	1.06E-08	1.24E-08	16%	17%	-1.46%

Table 4-21. Percentage point gain in accuracy over reference values using different dose scaling factors based on sitting height for the UFH00M-based phantom for ^{131}I photons (e.g., “Brain” indicates that scaling factors based on the brain source from the sitting height dose sensitivity study were used).

Target tissue	Overall average (%)	Target-average (%)	Active marrow (%)	Brain (%)	Liver (%)	Lungs (%)	Spleen (%)
WBody	14%	15%	14%	15%	15%	15%	15%
Adipose	15%	14%	14%	14%	14%	14%	14%
LAdrenal	15%	15%	15%	13%	16%	16%	16%
RAdrenal	11%	8%	10%	2%	10%	10%	9%
Brain	14%	19%	17%	16%	16%	19%	16%
ROB	15%	12%	13%	12%	12%	13%	11%
Bronchi-bas	15%	18%	17%	16%	17%	15%	17%
RC-wall	13%	9%	11%	-1%	12%	11%	10%
Oesophagus	13%	10%	13%	5%	12%	12%	10%
Eye-balls	15%	9%	12%	13%	10%	8%	2%
GB-wall	11%	13%	10%	2%	11%	10%	9%
Ht-wall	15%	12%	12%	8%	13%	13%	13%
LKidney-C	15%	14%	13%	14%	14%	14%	14%
RKidney-C	14%	14%	13%	14%	14%	14%	14%
LKidney-M	15%	14%	13%	14%	14%	14%	14%
RKidney-M	12%	11%	10%	11%	12%	11%	11%
LKidney-P	14%	13%	12%	13%	14%	13%	13%
RKidney-P	15%	16%	16%	15%	15%	15%	15%
ET2-bas-OCL	12%	11%	10%	11%	11%	11%	11%
Liver	13%	10%	11%	4%	12%	12%	11%
LLung	15%	13%	13%	9%	13%	14%	14%
RLung	14%	11%	12%	8%	12%	13%	12%
O-mucosa	14%	11%	11%	13%	11%	11%	10%
Pancreas	14%	9%	11%	1%	11%	11%	13%
RSig-wall	15%	14%	14%	2%	16%	15%	15%
S-glands	15%	12%	12%	13%	10%	12%	11%
SI-wall	13%	8%	11%	-1%	12%	10%	11%
Skin	15%	13%	13%	12%	14%	14%	14%
Sp-cord	13%	10%	11%	8%	10%	11%	9%
Spleen	13%	10%	12%	3%	11%	12%	12%
St-wall	12%	9%	11%	2%	11%	10%	11%
Thymus	15%	13%	14%	10%	13%	14%	12%
Thyroid	11%	6%	7%	4%	5%	8%	7%
Tongue	6%	2%	3%	3%	2%	3%	1%
Trachea	14%	17%	17%	18%	15%	16%	17%
UB-wall	14%	14%	12%	5%	15%	15%	12%
LC-wall	15%	13%	15%	3%	16%	14%	16%
Muscle	15%	11%	12%	12%	11%	11%	11%
Cartilage	15%	14%	15%	13%	14%	14%	14%
C-bone-V	12%	11%	12%	9%	10%	10%	12%
Prostate	15%	13%	14%	-54%	11%	-34%	15%

Table 4-22. Percentage point gain in accuracy over reference values using different dose scaling factors based on sitting height for the UFH00M-based phantom for ⁹⁰Y beta particles (e.g., “Brain” indicates that scaling factors based on the brain source from the sitting height dose sensitivity study were used).

Target tissue	Overall average (%)	Target-average (%)	Active marrow (%)	Brain (%)	Liver (%)	Lungs (%)	Spleen (%)
WBody	12%	19%	19%	19%	19%	19%	19%
Adipose	26%	3%	30%	10%	0%	-2%	-21%
LAdrenal	-2%	-4%	-21%	1%	8%	8%	-18%
RAdrenal	25%	31%	5%	22%	24%	18%	15%
Brain	21%	22%	6%	23%	24%	21%	21%
ROB	25%	31%	26%	27%	27%	29%	18%
RC-wall	26%	10%	-90%	24%	23%	12%	17%
Oesophagus	24%	24%	29%	21%	27%	35%	-25%
GB-wall	25%	22%	14%	22%	29%	20%	19%
Ht-wall	26%	28%	11%	16%	21%	21%	16%
LKidney-C	9%	15%	16%	12%	12%	14%	15%
RKidney-C	26%	20%	14%	23%	23%	21%	20%
RKidney-M	25%	19%	13%	21%	21%	19%	18%
Liver	10%	0%	-6%	-17%	15%	-9%	18%
LLung	26%	29%	24%	20%	19%	19%	23%
RLung	26%	26%	29%	22%	20%	19%	17%
Pancreas	-22%	-25%	-46%	-18%	-7%	-14%	-40%
SI-wall	26%	22%	16%	24%	22%	17%	18%
Skin	0%	-11%	-9%	-43%	1%	-15%	8%
Sp-cord	-29%	-28%	-52%	-28%	-19%	-24%	-18%
Spleen	-12%	-16%	-37%	-8%	-3%	-27%	-3%
St-wall	26%	28%	23%	23%	23%	23%	21%
Thymus	9%	12%	2%	18%	15%	-2%	18%
LC-wall	1%	-1%	-22%	4%	11%	-8%	10%
Muscle	23%	23%	25%	22%	23%	23%	23%
Cartilage	25%	25%	19%	23%	30%	25%	24%
C-bone-V	20%	23%	15%	21%	24%	23%	16%

Table 4-23. Average percentage point gain in accuracy over reference values using different dose scaling factors based on sitting height for all the non-reference phantoms used for the sitting height dose scaling validation study for ^{131}I photons (e.g., “Brain” indicates that scaling factors based on the brain source from the sitting height dose sensitivity study were used).

Non-reference phantom	Overall average (%)	Target-average (%)	Active marrow (%)	Brain (%)	Liver (%)	Lungs (%)	Spleen (%)
Scaled UFH00M	14%	12%	12%	7%	12%	11%	12%
Scaled UFH10M	15%	16%	18%	7%	18%	17%	17%
Scaled UFHADM	5%	5%	4%	3%	5%	4%	5%
Average	11%	11%	11%	6%	12%	11%	11%

Table 4-24. Average percentage point gain in accuracy over reference values using different dose scaling factors based on sitting height for all the non-reference phantoms used for the sitting height dose scaling validation study for ^{90}Y beta particles (e.g., “Brain” indicates that scaling factors based on the brain source from the sitting height dose sensitivity study were used).

Non-reference phantom	Overall average (%)	Target-average (%)	Active marrow (%)	Brain (%)	Liver (%)	Lungs (%)	Spleen (%)
Scaled UFH00M	15%	13%	2%	11%	16%	11%	9%
Scaled UFH10M	16%	17%	7%	16%	22%	14%	15%
Scaled UFHADM	5%	7%	5%	6%	6%	-4%	4%
Average	12%	12%	5%	11%	15%	7%	9%

Table 4-25. Percentage point gain in accuracy over reference values using different dose scaling factors based on waist circumference for the UFH00M-based phantom for ^{131}I photons (e.g., “Brain” indicates that scaling factors based on the brain source from the weight dose sensitivity study were used).

Target tissue	Overall average (%)	Target-average (%)	Active marrow (%)	Brain (%)	Liver (%)	Lungs (%)	Spleen (%)
WBody	2%	7%	6%	4%	6%	6%	6%
Adipose	2%	5%	8%	-21%	-5%	-7%	-10%
LAdrenal	2%	2%	3%	-3%	6%	1%	5%
RAdrenal	2%	2%	3%	-2%	5%	0%	7%
Brain	-2%	-1%	-4%	-5%	0%	1%	0%
ROB	2%	3%	1%	2%	2%	1%	2%
Bronchi-bas	2%	2%	4%	-1%	1%	5%	0%
RC-wall	2%	2%	3%	-3%	3%	0%	5%
Oesophagus	2%	4%	4%	0%	5%	5%	4%
Eye-balls	-2%	-3%	-5%	-5%	-1%	-2%	-1%
GB-wall	2%	-2%	2%	-25%	4%	0%	6%
Ht-wall	2%	3%	4%	0%	3%	4%	2%
ET2-bas-OCL	-2%	-4%	-5%	-4%	-3%	-4%	-4%
Liver	2%	3%	3%	-1%	5%	3%	6%
LLung	2%	3%	4%	0%	4%	5%	1%
RLung	2%	3%	4%	-1%	3%	5%	4%
Pancreas	2%	2%	3%	-2%	4%	0%	2%
RSig-wall	2%	1%	4%	1%	0%	-1%	-1%
S-glands	-2%	-1%	-5%	-1%	1%	-1%	1%
SI-wall	2%	1%	4%	-2%	2%	0%	2%
Skin	2%	8%	7%	5%	7%	7%	7%
Sp-cord	2%	3%	4%	0%	5%	4%	5%
Spleen	2%	3%	3%	-1%	6%	2%	4%
St-wall	2%	3%	3%	-1%	4%	1%	5%
Thymus	2%	2%	-1%	-1%	0%	-1%	1%
Thyroid	2%	1%	2%	1%	-1%	0%	-1%
Tongue	-2%	-1%	-5%	-2%	0%	-2%	1%
Trachea	2%	1%	3%	-1%	-1%	4%	0%
UB-wall	-1%	-2%	-5%	-11%	-1%	-2%	-1%
LC-wall	2%	2%	4%	-2%	3%	0%	3%
Muscle	2%	4%	4%	3%	4%	4%	3%
Cartilage	2%	4%	4%	4%	4%	4%	4%
C-bone-V	2%	3%	4%	4%	3%	4%	3%

Table 4-26. Percentage point gain in accuracy over reference values using different dose scaling factors based on waist circumference for the UFH00M-based phantom for ⁹⁰Y beta particles (e.g., “Brain” indicates that scaling factors based on the brain source from the weight dose sensitivity study were used).

Target tissue	Overall average (%)	Target-average (%)	Active marrow (%)	Brain (%)	Liver (%)	Lungs (%)	Spleen (%)
WBody	9%	8%	8%	8%	8%	8%	8%
Adipose	14%	9%	-14%	-65%	-8%	-11%	-12%
LAdrenal	7%	9%	3%	8%	8%	0%	5%
RAdrenal	13%	9%	17%	7%	12%	0%	7%
Brain	-4%	4%	-4%	3%	-1%	-1%	-1%
ROB	10%	10%	10%	8%	12%	11%	2%
RC-wall	13%	11%	-50%	8%	11%	-10%	4%
Oesophagus	14%	10%	12%	8%	9%	14%	-7%
GB-wall	14%	7%	4%	8%	13%	4%	6%
Ht-wall	7%	7%	4%	-7%	7%	8%	3%
Liver	8%	7%	5%	-4%	7%	9%	7%
LLung	9%	7%	10%	-3%	10%	6%	7%
RLung	8%	6%	11%	-1%	9%	6%	4%
Pancreas	-7%	0%	-9%	-1%	2%	-1%	-1%
SI-wall	13%	5%	4%	6%	11%	-1%	3%
Skin	3%	-333%	-29%	-11%	-630%	-470%	-526%
Sp-cord	-6%	0%	-10%	2%	4%	2%	3%
Spleen	1%	5%	0%	6%	6%	7%	6%
St-wall	13%	7%	2%	8%	10%	1%	13%
Thymus	-15%	-4%	-13%	-5%	-2%	-16%	0%
LC-wall	13%	11%	-20%	8%	4%	-10%	3%
Muscle	13%	10%	11%	9%	10%	10%	10%
RBreast	2%	1%	1%	1%	1%	1%	1%
Cartilage	13%	10%	7%	8%	13%	9%	13%
C-bone-V	13%	9%	6%	8%	10%	10%	12%

Table 4-27. Average percentage point gain in accuracy over reference values using different dose scaling factors based on waist circumference for all the non-reference phantoms used for the weight dose scaling validation study for ^{131}I photons (e.g., “Brain” indicates that scaling factors based on the brain source from the sitting height dose sensitivity study were used). The patient-dependent naming convention is [gender][height percentile][weight percentile] (e.g., m5090 is a 50th percentile height, 90th percentile weight male).

Non-reference phantom	Overall average (%)	Target-average (%)	Active marrow (%)	Brain (%)	Liver (%)	Lungs (%)	Spleen (%)
Scaled UFH00M	1%	2%	2%	-2%	2%	1%	2%
Scaled UFH10M	0%	0%	0%	-4%	0%	0%	-1%
m5090	-1%	0%	-1%	-6%	0%	-3%	1%
m5075	0%	0%	0%	0%	0%	-1%	0%
m5010	6%	12%	12%	2%	13%	11%	12%
Overweight average	0%	0%	0%	-3%	0%	-1%	0%
Underweight average	4%	7%	7%	0%	8%	6%	7%
Overall average	1%	3%	3%	-2%	3%	2%	3%

Table 4-28. Average percentage point gain in accuracy over reference values using different dose scaling factors based on waist circumference for all the non-reference phantoms used for the sitting height dose scaling validation study for ^{90}Y beta particles (e.g., “Brain” indicates that scaling factors based on the brain source from the weight dose sensitivity study were used). The patient-dependent naming convention is [gender][height percentile][weight percentile] (e.g., m5090 is a 50th percentile height, 90th percentile weight male).

Non-reference phantom	Overall average (%)	Target-average (%)	Active marrow (%)	Brain (%)	Liver (%)	Lungs (%)	Spleen (%)
Scaled UFH00M	7%	-7%	-1%	1%	-19%	-17%	-17%
Scaled UFH10M	0%	0%	-1%	-1%	1%	-1%	-2%
m5090	-1%	4%	-3%	0%	0%	-13%	0%
m5075	0%	2%	-1%	0%	0%	6%	0%
m5010	1%	10%	-7%	-1%	-3%	-64%	-1%
Overweight average	-1%	2%	-2%	0%	0%	-3%	-1%
Underweight average	4%	1%	-4%	0%	-11%	-40%	-9%
Overall average	1%	2%	-3%	0%	-4%	-18%	-4%

Table 4-29. Percentage point gain in accuracy over reference values using different dose scaling factors based on sitting height and waist circumference for the UFH00M-based phantom for ^{131}I photons (e.g., “Brain” indicates that scaling factors based on the brain source from the combined dose sensitivity study were used).

Target tissue	Overall average (%)	Target-average (%)	Active marrow (%)	Brain (%)	Liver (%)	Lungs (%)	Spleen (%)
WBody	-6%	2%	2%	3%	2%	3%	2%
Adipose	-7%	-3%	-2%	4%	-5%	-5%	-6%
LAdrenal	-14%	-13%	-11%	-20%	-11%	-12%	-10%
RAdrenal	-7%	-7%	-5%	-14%	-4%	-6%	-4%
Brain	24%	24%	21%	19%	28%	25%	28%
ROB	9%	11%	12%	10%	11%	13%	11%
Bronchi-bas	22%	20%	19%	19%	20%	17%	17%
RC-wall	-4%	-4%	-2%	-11%	-2%	-4%	-3%
Oesophagus	-7%	-5%	-4%	-8%	-4%	-5%	-5%
Eye-balls	24%	23%	20%	21%	26%	26%	24%
GB-wall	-5%	-9%	-6%	-30%	-2%	-3%	-3%
Ht-wall	2%	4%	5%	0%	5%	6%	4%
ET2-bas-OCL	22%	19%	18%	19%	20%	19%	19%
Liver	-9%	-8%	-7%	-13%	-6%	-7%	-6%
LLung	-7%	-5%	-4%	-8%	-4%	-4%	-5%
RLung	1%	3%	4%	0%	4%	5%	3%
O-mucosa	23%	22%	19%	21%	26%	22%	21%
Pancreas	-7%	-7%	-6%	-14%	-5%	-6%	-5%
RSig-wall	21%	20%	18%	15%	21%	18%	21%
S-glands	23%	22%	19%	22%	24%	21%	25%
SI-wall	2%	3%	5%	-4%	5%	2%	4%
Skin	-7%	-2%	-1%	-4%	-1%	-1%	-1%
Sp-cord	-7%	-5%	-4%	-7%	-4%	-4%	-4%
Spleen	-16%	-15%	-15%	-19%	-13%	-14%	-13%
St-wall	-10%	-9%	-9%	-13%	-7%	-8%	-7%
Thymus	17%	19%	19%	16%	19%	17%	18%
Thyroid	10%	12%	15%	12%	9%	13%	12%
Tongue	23%	22%	20%	21%	25%	21%	24%
Trachea	14%	15%	15%	12%	15%	17%	14%
UB-wall	23%	24%	14%	23%	23%	26%	22%
LC-wall	-7%	-8%	-6%	-15%	-5%	-8%	-5%
Muscle	-4%	2%	2%	2%	2%	3%	2%
Cartilage	-6%	-1%	-2%	-1%	-1%	-1%	-1%
C-bone-V	1%	8%	8%	7%	7%	9%	9%

Table 4-30. Percentage point gain in accuracy over reference values using different dose scaling factors based on sitting height and waist circumference for the UFH00M-based phantom for ^{90}Y beta particles (e.g., “Brain” indicates that scaling factors based on the brain source from the combined dose sensitivity study were used).

Target tissue	Overall average (%)	Target-average (%)	Active marrow (%)	Brain (%)	Liver (%)	Lungs (%)	Spleen (%)
WBody	-7%	-2%	-2%	-2%	-2%	-2%	-2%
Adipose	11%	-1%	9%	9%	-10%	-12%	-3%
LAdrenal	-9%	-13%	-22%	-10%	-6%	-7%	-19%
RAdrenal	5%	1%	-12%	4%	-6%	8%	12%
Brain	29%	33%	44%	30%	33%	28%	31%
ROB	4%	-4%	-9%	-3%	-7%	-5%	6%
RC-wall	-8%	-5%	1%	-9%	-16%	-7%	-3%
Oesophagus	-11%	-22%	-28%	-13%	-24%	-23%	-22%
GB-wall	6%	5%	13%	5%	-5%	5%	7%
Ht-wall	23%	17%	11%	20%	12%	11%	20%
ET2-bas-OCL	0%	1%	7%	-1%	-1%	0%	1%
Liver	-8%	-10%	-17%	-8%	-8%	-19%	-1%
LLung	18%	13%	10%	21%	7%	19%	7%
RLung	22%	19%	14%	23%	10%	23%	20%
Pancreas	-19%	-22%	-31%	-20%	-15%	-16%	-31%
SI-wall	-9%	-8%	-4%	-11%	-15%	-7%	-5%
Skin	-13%	-43%	-15%	-15%	-119%	-77%	-99%
Sp-cord	-20%	-22%	-33%	-27%	-15%	-15%	-19%
Spleen	-20%	-22%	-30%	-21%	-13%	-28%	-19%
St-wall	4%	2%	10%	2%	-4%	7%	-6%
Thymus	26%	27%	19%	22%	26%	20%	24%
LC-wall	5%	8%	6%	4%	14%	8%	8%
Muscle	-4%	-6%	-7%	-5%	-6%	-6%	-6%
Cartilage	-9%	-12%	-9%	-13%	-14%	-13%	-13%
C-bone-V	-12%	-17%	-8%	-21%	-18%	-16%	-21%

Table 4-31. Average percentage point gain in accuracy over reference values using different dose scaling factors based on sitting height and waist circumference for all the non-reference phantoms used for the sitting height dose scaling validation study for ^{131}I photons (e.g., “Brain” indicates that scaling factors based on the brain source from the combined dose sensitivity study were used). The patient-dependent naming convention is [gender][height percentile][weight percentile] (e.g., m5090 is a 50th percentile height, 90th percentile weight male).

Non-reference phantom	Overall average (%)	Target-average (%)	Active marrow (%)	Brain (%)	Liver (%)	Lungs (%)	Spleen (%)
Scaled UFH00M	4%	5%	5%	2%	6%	6%	6%
Scaled UFH10M	13%	15%	15%	5%	17%	16%	15%
m9090	-2%	3%	1%	1%	2%	0%	4%
m9050	4%	5%	5%	3%	5%	4%	5%
m7590	-2%	0%	-1%	-4%	0%	-3%	2%
m7550	1%	1%	1%	1%	0%	-1%	0%
m7525	1%	4%	4%	-5%	3%	2%	4%
m7510	1%	8%	7%	-4%	10%	9%	8%
m5090	-2%	1%	-1%	-3%	0%	-1%	1%
m5075	0%	0%	0%	1%	0%	0%	0%
m5010	5%	11%	11%	0%	13%	12%	11%
m2575	4%	5%	4%	1%	5%	5%	5%
m2550	2%	-2%	0%	-8%	1%	-4%	1%
m1050	8%	6%	8%	1%	7%	4%	8%
m1010	22%	22%	21%	17%	20%	19%	18%
Overweight average	2%	4%	3%	0%	4%	3%	5%
Underweight average	7%	10%	10%	2%	10%	10%	9%
Tall average	1%	4%	3%	-1%	4%	2%	4%
Short average	10%	9%	10%	3%	10%	8%	10%
Overall average	4%	6%	5%	1%	6%	4%	6%

Table 4-32. Average percentage point gain in accuracy over reference values using different dose scaling factors based on sitting height and waist circumference for all the non-reference phantoms used for the sitting height dose scaling validation study for ⁹⁰Y beta particles (e.g., “Brain” indicates that scaling factors based on the brain source from the combined dose sensitivity study were used). The patient-dependent naming convention is [gender][height percentile][weight percentile] (e.g., m5090 is a 50th percentile height, 90th percentile weight male).

Non-reference phantom	Overall average (%)	Target-average (%)	Active marrow (%)	Brain (%)	Liver (%)	Lungs (%)	Spleen (%)
Scaled UFH00M	0%	-3%	-3%	-2%	-8%	-5%	-5%
Scaled UFH10M	16%	19%	5%	18%	24%	16%	16%
m9090	3%	-4%	-1%	3%	4%	-46%	4%
m9050	6%	5%	4%	7%	7%	-4%	7%
m7590	0%	-5%	-2%	0%	1%	-35%	0%
m7550	-1%	-3%	-3%	1%	0%	-17%	0%
m7525	0%	-4%	-8%	1%	4%	-43%	3%
m7510	6%	0%	-5%	3%	9%	-68%	8%
m5090	0%	-5%	-2%	-1%	1%	-28%	0%
m5075	0%	-2%	-1%	0%	0%	-8%	0%
m5010	9%	4%	-4%	5%	12%	-41%	11%
m2575	3%	-2%	-1%	-2%	5%	-23%	4%
m2550	-14%	-26%	-31%	-15%	-4%	-107%	-5%
m1050	-2%	-12%	-18%	-3%	6%	-83%	4%
m1010	1%	-13%	-46%	12%	19%	-215%	15%
Overweight average	4%	0%	0%	3%	6%	-21%	4%
Underweight average	3%	-3%	-13%	4%	7%	-74%	6%
Tall average	2%	-2%	-3%	2%	2%	-31%	2%
Short average	1%	-7%	-18%	2%	10%	-83%	7%
Overall average	2%	-3%	-8%	2%	5%	-47%	4%

Table 4-33. Photon internal dosimetry scaling factors (excerpt) for the shortest UFH00M-based phantom of the sitting height dosimetric sensitivity study.

Target Tissue	Photon Energy (MeV)														
	0.010	0.015	0.020	0.030	0.040	0.050	0.060	0.080	0.100	0.200	0.500	0.800	1.000	2.000	4.000
WBody	2.019	1.998	1.936	1.761	1.632	1.557	1.519	1.502	1.512	1.561	1.585	1.585	1.582	1.564	1.525
LAdrenal	4.504	4.165	3.181	2.904	2.196	1.915	1.837	1.822	1.846	1.873	1.899	1.909	1.892	1.846	1.750
Brain	4.624	4.085	8.351	3.950	2.744	2.330	2.147	2.016	1.993	2.008	1.986	1.958	1.944	1.893	1.837
ROB	4.249	4.053	3.095	2.305	1.965	1.818	1.754	1.730	1.750	1.818	1.852	1.856	1.846	1.837	1.800
RC-wall	4.614	4.351	5.113	3.451	2.506	2.211	2.071	1.946	1.906	1.979	1.943	1.936	1.910	1.885	1.864
Oesophagus	5.897	3.437	2.940	2.192	1.865	1.732	1.696	1.684	1.705	1.778	1.805	1.813	1.822	1.804	1.744
GB-wall	4.680	5.384	4.229	2.675	2.104	1.946	1.777	1.827	1.819	1.875	1.856	1.855	1.867	1.820	1.830
Ht-wall	4.438	4.436	5.024	2.632	2.108	1.906	1.811	1.769	1.775	1.839	1.875	1.867	1.875	1.838	1.821
Kidney-C	4.499	3.828	3.762	3.371	2.517	2.171	2.039	1.948	1.927	1.947	1.935	1.919	1.900	1.878	1.816
Kidney-P	7.503	4.769	4.157	2.786	2.606	2.221	1.979	1.972	1.929	2.013	1.932	1.931	1.889	1.868	1.834
Eye-lens	4.932	4.379	3.655	2.363	2.135	1.846	1.780	1.810	1.819	1.804	1.861	1.879	1.891	1.851	1.768
LLung	3.452	3.039	4.080	2.432	2.035	1.873	1.797	1.760	1.769	1.824	1.845	1.841	1.836	1.800	1.742
ET1-bas	4.932	4.290	3.781	2.429	1.958	1.853	1.820	1.786	1.745	1.862	1.892	1.927	1.899	1.788	1.730
Pancreas	4.548	4.601	3.892	3.228	2.393	2.085	1.936	1.863	1.850	1.916	1.921	1.888	1.904	1.845	1.803
RSig-wall	5.226	5.596	4.749	3.202	2.425	2.363	2.259	2.119	2.011	2.042	1.995	1.980	1.935	1.920	1.837
S-glands	5.126	5.802	5.182	2.617	2.046	1.855	1.770	1.754	1.763	1.839	1.859	1.863	1.866	1.832	1.811
Sp-cord	4.959	5.291	3.308	2.380	2.042	1.879	1.797	1.757	1.762	1.820	1.849	1.854	1.847	1.851	1.798
St-wall	6.549	4.022	3.283	2.919	2.252	1.992	1.907	1.808	1.823	1.874	1.916	1.891	1.880	1.837	1.807
Thymus	4.454	6.843	4.350	2.446	1.971	1.797	1.728	1.714	1.726	1.820	1.854	1.861	1.845	1.843	1.781
Tongue	6.121	6.585	6.018	2.786	2.168	1.941	1.831	1.779	1.790	1.855	1.868	1.864	1.863	1.867	1.789
Trachea	4.935	5.035	3.814	2.337	1.916	1.765	1.685	1.697	1.686	1.831	1.934	1.875	1.865	1.843	1.796
RBreast	4.932	4.704	3.867	2.697	2.038	1.890	1.745	1.860	1.831	1.855	1.947	1.902	1.970	1.838	1.747
C-bone-V	2.404	2.188	2.008	1.719	1.551	1.454	1.396	1.340	1.326	1.394	1.444	1.439	1.458	1.456	1.363
Testes	4.932	4.502	3.853	3.026	2.590	2.157	2.119	2.028	1.988	1.966	1.971	1.906	1.918	1.908	1.688

Table 4-34. Photon internal dosimetry scaling factors (excerpt) for the tallest UFH00M-based phantom of the sitting height dosimetric sensitivity study.

Target Tissue	Photon Energy (MeV)														
	0.010	0.015	0.020	0.030	0.040	0.050	0.060	0.080	0.100	0.200	0.500	0.800	1.000	2.000	4.000
WBody	0.568	0.571	0.581	0.620	0.660	0.689	0.706	0.718	0.717	0.698	0.688	0.688	0.688	0.695	0.707
LAdrenal	0.351	0.321	0.392	0.480	0.511	0.547	0.578	0.599	0.606	0.606	0.601	0.614	0.609	0.622	0.629
Brain	0.364	0.375	0.361	0.359	0.443	0.497	0.532	0.562	0.572	0.573	0.577	0.584	0.587	0.601	0.615
ROB	0.311	0.333	0.384	0.472	0.537	0.580	0.605	0.628	0.633	0.623	0.616	0.616	0.616	0.620	0.626
RC-wall	0.357	0.334	0.287	0.410	0.469	0.521	0.559	0.588	0.595	0.588	0.584	0.584	0.588	0.591	0.614
Oesophagus	0.291	0.346	0.408	0.475	0.540	0.582	0.605	0.631	0.633	0.626	0.613	0.610	0.614	0.620	0.622
GB-wall	0.341	0.350	0.311	0.426	0.501	0.549	0.580	0.612	0.604	0.615	0.624	0.618	0.617	0.600	0.615
Ht-wall	0.345	0.336	0.402	0.472	0.552	0.599	0.625	0.643	0.644	0.625	0.615	0.615	0.617	0.617	0.626
Kidney-C	0.341	0.362	0.382	0.477	0.510	0.558	0.586	0.617	0.617	0.599	0.595	0.598	0.599	0.613	0.613
Kidney-P	0.347	0.290	0.331	0.469	0.533	0.582	0.592	0.613	0.615	0.601	0.598	0.609	0.582	0.598	0.615
Eye-lens	0.347	0.310	0.361	0.460	0.510	0.532	0.534	0.575	0.567	0.596	0.617	0.610	0.631	0.625	0.648
LLung	0.383	0.429	0.467	0.505	0.567	0.605	0.625	0.641	0.642	0.629	0.621	0.623	0.624	0.630	0.647
ET1-bas	0.347	0.343	0.376	0.443	0.460	0.512	0.566	0.576	0.530	0.609	0.618	0.616	0.605	0.623	0.600
Pancreas	0.341	0.309	0.345	0.459	0.503	0.554	0.583	0.611	0.615	0.604	0.601	0.600	0.603	0.603	0.617
RSig-wall	0.318	0.341	0.306	0.382	0.467	0.527	0.562	0.553	0.579	0.585	0.565	0.587	0.581	0.598	0.610
S-glands	0.329	0.258	0.287	0.386	0.469	0.522	0.552	0.590	0.596	0.604	0.601	0.603	0.605	0.612	0.618
Sp-cord	0.296	0.271	0.371	0.475	0.537	0.580	0.605	0.628	0.631	0.621	0.617	0.618	0.619	0.620	0.630
St-wall	0.357	0.345	0.402	0.488	0.523	0.575	0.603	0.623	0.631	0.612	0.604	0.605	0.606	0.606	0.621
Thymus	0.340	0.320	0.300	0.434	0.516	0.565	0.593	0.621	0.624	0.620	0.612	0.610	0.610	0.620	0.620
Tongue	0.347	0.334	0.323	0.397	0.489	0.547	0.577	0.608	0.615	0.610	0.614	0.613	0.613	0.615	0.627
Trachea	0.316	0.332	0.327	0.423	0.500	0.547	0.589	0.609	0.613	0.623	0.621	0.613	0.621	0.617	0.605
RBreast	0.347	0.345	0.356	0.450	0.490	0.537	0.549	0.559	0.577	0.604	0.605	0.594	0.613	0.585	0.595
C-bone-V	0.422	0.472	0.512	0.580	0.633	0.672	0.699	0.732	0.743	0.719	0.679	0.669	0.678	0.686	0.669
Testes	0.347	0.345	0.458	0.464	0.464	0.459	0.496	0.539	0.560	0.582	0.588	0.604	0.619	0.651	0.636

Table 4-35. Percentage point gains in accuracy for interpolated sitting height- and waist circumference-based target-average dose scaling factors. Comparison between actual simulations and doses predicted using reference SAFs and the dose scaling factors. Uniform ^{99m}Tc photon source in the liver of each phantom.

Target tissue	T-average percentage point gain (%)			
	ufh01f	ufh05f	ufh15m	ufhadf
WBody	9.24%	16.45%	32.31%	15.51%
Adipose	10.39%	22.91%	39.52%	7.57%
LAdrenal	12.70%	1.68%	51.19%	-13.63%
RAdrenal	-1.49%	-3.59%	49.40%	-4.44%
Brain	27.69%	24.24%	33.71%	25.76%
ROB	16.09%	13.76%	45.26%	54.65%
Bronchi-bas	17.78%	24.31%	36.69%	8.81%
RC-wall	0.29%	3.42%	54.52%	-19.00%
Oesophagus	20.65%	8.79%	44.06%	-5.23%
Eye-balls	2.78%	2.69%	42.18%	-43.10%
GB-wall	-7.08%	-10.32%	55.47%	-29.18%
Ht-wall	4.96%	2.02%	52.15%	-28.52%
ET2-bas	13.10%	12.70%	35.52%	22.63%
LLung	19.80%	16.92%	42.45%	15.40%
RLung	11.75%	8.73%	44.39%	0.66%
O-mucosa	39.40%	28.53%	40.06%	17.35%
Pancreas	8.08%	8.63%	48.11%	-7.19%
RSig-wall	19.40%	14.28%	46.16%	3.11%
S-glands	39.20%	32.34%	34.62%	26.11%
SI-wall	4.22%	4.46%	50.26%	-13.58%
Skin	7.25%	16.59%	41.25%	7.16%
Sp-cord	11.77%	10.40%	43.01%	4.47%
Spleen	9.18%	6.33%	52.87%	-11.60%
St-wall	3.78%	0.86%	54.35%	-24.07%
Thymus	30.65%	18.22%	43.60%	8.71%
Thyroid	27.59%	10.89%	47.48%	-2.04%
Tongue	31.65%	32.47%	42.75%	10.31%
Trachea	23.44%	22.97%	40.06%	9.58%
UB-wall	15.14%	10.93%	50.92%	-2.84%
LC-wall	8.05%	7.77%	52.86%	-15.05%
Muscle	30.23%	31.62%	25.18%	29.68%
Cartilage	-4.83%	2.05%	52.49%	-20.56%
C-bone-V	33.99%	34.80%	24.61%	34.94%
Prostate	--	--	--	--
Testes	--	--	33.03%	--
LOvary	24.68%	37.15%	--	13.49%
ROvary	-20.47%	-18.69%	--	32.12%
Uterus	--	12.97%	--	21.87%
Average	14.32%	13.06%	43.60%	3.61%

Table 4-36. Biokinetic data for $^{99m}\text{Tc} - \text{RBC}$ (ICRP 2007). S indicates the source tissue, F_S indicates the fractional distribution of the radiopharmaceutical to source tissue S , T is the biological half life, a is the fraction of F_S with biological half-life T , and A_S/A_0 is the total number of nuclear transformations per unit AA.

Organ (S)	F_S	T (h)	a	A_S/A_0	
Blood	1.0	60	1.0	7.89	h
Kidneys	1.0			2.60	min
Bladder Contents	1.0			9.00	min

Table 4-37. Biokinetic data for $^{67}\text{Ga} - \text{citrate}$ (ICRP 1988). S indicates the source tissue, F_S indicates the fractional distribution of the radiopharmaceutical to source tissue S , T is the biological half life, a is the fraction of F_S with biological half-life T , and A_S/A_0 is the total number of nuclear transformations per unit AA.

Organ (S)	F_S	T (d)	a	A_S/A_0	
Total body	1.0	1.25	0.17	3.69	d
(excluding GIT and bladder contents)			0.83		
Adrenals	0.00053	1.25	0.17	2.8	min
		25.5	0.83		
Bone	0.13	1.25	0.17	11.5	h
		25.5	0.83		
GI-tract contents					
SI	0.09			20.9	min
ULI	0.09			1.01	h
LLI	0.09			1.54	h
Kidneys	0.0084	1.25	0.17	44.6	min
		25.5	0.83		
Liver	0.05	1.25	0.17	4.42	h
		25.5	0.83		
Red marrow	0.054	1.25	0.17	4.78	h
		25.5	0.83		
Spleen	0.0074	1.25	0.17	39.3	min
		25.5	0.83		
Bladder contents	0.91			20.8	min

Table 4-38. Comparison between UF and ICRP Publication 80 estimated values of equivalent dose per unit AA (mSv/MBq) for $^{99m}Tc - RBC$ for radiosensitive tissues of the human body (ICRP 1998).

Target tissue	Age group / Data source									
	1 year old		5 years old		10 years old		15 years old		Adult	
	ICRP 80	UF	ICRP 80	UF	ICRP 80	UF	ICRP 80	UF	ICRP 80	UF
Adrenals	0.056	0.050	0.030	0.027	0.020	0.017	0.012	0.012	0.010	0.011
Bladder	0.031	0.032	0.017	0.014	0.014	0.009	0.011	0.007	0.009	0.006
Bone surfaces	0.074	0.018	0.036	0.008	0.019	0.005	0.012	0.006	0.007	0.003
Brain	0.022	0.014	0.012	0.008	0.008	0.005	0.005	0.003	0.004	0.002
Breasts	0.019	0.016	0.011	0.011	0.007	0.008	0.004	0.005	0.004	0.005
Gall bladder	0.030	0.041	0.020	0.025	0.013	0.017	0.008	0.012	0.007	0.011
Gastrointestinal tract										
Stomach	0.025	0.056	0.014	0.028	0.010	0.019	0.006	0.012	0.005	0.011
Small intestine	0.021	0.054	0.012	0.029	0.008	0.017	0.005	0.012	0.004	0.010
Colon	0.020	0.049	0.012	0.025	0.008	0.016	0.005	0.010	0.004	0.009
Heart	0.110	0.063	0.066	0.036	0.043	0.026	0.029	0.017	0.023	0.016
Kidneys	0.110	0.057	0.057	0.038	0.036	0.023	0.022	0.016	0.018	0.014
Liver	0.072	0.070	0.040	0.037	0.026	0.024	0.017	0.016	0.013	0.015
Lungs	0.110	0.079	0.056	0.040	0.035	0.029	0.022	0.020	0.018	0.017
Muscles	0.017	0.018	0.009	0.011	0.006	0.006	0.004	0.004	0.003	0.004
Oesophagus	0.023	0.056	0.015	0.031	0.010	0.020	0.007	0.014	0.006	0.013
Gonads	0.016	0.017	0.009	0.011	0.006	0.006	0.004	0.005	0.003	0.004
Pancreas	0.033	0.049	0.019	0.027	0.013	0.018	0.008	0.012	0.006	0.011
Red marrow	0.037	0.017	0.020	0.007	0.012	0.005	0.008	0.007	0.002	0.004
Skin	0.012	0.013	0.006	0.006	0.004	0.003	0.002	0.003	0.014	0.002
Spleen	0.081	0.083	0.043	0.042	0.027	0.026	0.017	0.017	0.002	0.016
Thymus	0.023	0.037	0.015	0.023	0.010	0.017	0.007	0.010	0.006	0.010
Thyroid	0.036	0.034	0.019	0.016	0.012	0.010	0.007	0.007	0.006	0.006
Uterus	0.019	0.032	0.011	0.019	0.007	0.013	0.005	0.008	0.004	0.008

Table 4-39. Comparison between UF and ICRP Publication 80 estimated values of equivalent dose per unit AA (mSv/MBq) for $^{67}Ga - citrate$ for radiosensitive tissues of the human body (ICRP 1998).

Target tissue	Age group / Data source									
	1 year old		5 years old		10 years old		15 years old		Adult	
	ICRP 80	UF	ICRP 80	UF	ICRP 80	UF	ICRP 80	UF	ICRP 80	UF
Adrenals	0.570	0.727	0.360	0.499	0.260	0.335	0.180	0.235	0.130	0.195
Bladder	0.370	0.452	0.200	0.247	0.150	0.155	0.110	0.104	0.081	0.095
Bone surfaces	5.200	0.735	2.200	0.337	1.300	0.177	0.810	0.145	0.630	0.139
Brain	0.340	0.313	0.190	0.203	0.120	0.114	0.072	0.068	0.057	0.062
Breasts	0.290	0.373	0.150	0.224	0.093	0.131	0.061	0.083	0.047	0.078
Gall bladder	0.380	0.614	0.250	0.375	0.170	0.229	0.110	0.152	0.082	0.141
Gastrointestinal tract										
Stomach	0.390	0.441	0.210	0.248	0.140	0.160	0.090	0.099	0.069	0.092
Small intestine	0.280	0.434	0.160	0.258	0.110	0.160	0.074	0.106	0.059	0.098
Colon	1.000	0.472	0.540	0.269	0.330	0.172	0.200	0.111	0.160	0.104
Heart	0.380	0.404	0.210	0.241	0.140	0.152	0.089	0.091	0.069	0.088
Kidneys	0.510	0.700	0.290	0.436	0.200	0.263	0.140	0.181	0.120	0.160
Liver	0.610	0.811	0.330	0.491	0.230	0.323	0.150	0.213	0.120	0.189
Lungs	0.360	0.656	0.190	0.385	0.130	0.254	0.083	0.156	0.063	0.135
Muscles	0.350	0.353	0.180	0.206	0.120	0.123	0.076	0.075	0.060	0.068
Oesophagus	0.350	0.405	0.190	0.248	0.120	0.153	0.079	0.097	0.061	0.093
Gonads	0.390	0.357	0.210	0.222	0.135	0.135	0.091	0.089	0.069	0.079
Pancreas	0.430	0.428	0.240	0.261	0.160	0.169	0.100	0.108	0.081	0.101
Red marrow	1.500	1.302	0.710	0.341	0.380	0.194	0.230	0.178	0.210	0.151
Skin	0.290	0.251	0.150	0.144	0.092	0.084	0.057	0.050	0.045	0.045
Spleen	0.860	0.990	0.480	0.584	0.310	0.368	0.200	0.232	0.140	0.221
Thymus	0.350	0.550	0.190	0.316	0.120	0.192	0.079	0.115	0.061	0.108
Thyroid	0.380	0.372	0.200	0.203	0.130	0.115	0.080	0.073	0.062	0.066
Uterus	0.420	0.574	0.230	0.333	0.150	0.200	0.097	0.124	0.076	0.121

Table 4-40. Comparison between whole-body effective dose estimates (mSv) for the UF phantom family and two other sources for $^{99m}Tc - RBC$ (ICRP 1998).

Data source	Patient age					
	Newborn	1 year old	5 years old	10 years old	15 years old	Adult
ICRP Publication 80 (1998)	--	4.0	5.6	6.1	5.4	4.7
UF (2012)	4.2	4.1	5.7	6.3	6.1	6.0

Table 4-41. Comparison between whole-body effective dose estimates (mSv) for the UF phantom family and two other sources for $^{67}Ga - citrate$ (ICRP 1998).

Data source	Patient age					
	Newborn	1 year old	5 years old	10 years old	15 years old	Adult
ICRP Publication 80 (1998)	--	16.2	22.1	21.9	19.7	16.8
UF (2012)	21.6	17.7	23.9	24.1	22.4	22.3

Table 4-42. Estimated absorbed dose to the walls of the large blood vessels for $^{99m}Tc - RBC$ for the UF phantom family based on different AA scaling rules.

Phantom	Dose (mGy/MBq)	Dose (mGy)				Average
		Clark's Rule	Young's Rule	Webster's Rule	Fried's Rule	
UFH00MF	2.33	20	9	73	9	28
UFH01MF	2.14	54	29	95	30	52
UFH05MF	1.90	85	99	169	135	122
UFH10MF	1.42	117	115	164	202	150
UFH15M	1.38	201	136	179	295	203
UFH15F	1.14	153	112	147	242	163
UFHADM	0.82	146	146	146	146	146
UFHADF	0.82	120	120	120	120	120

Table 4-37. Estimated absorbed dose to the walls of the large blood vessels for $^{18}\text{F} - \text{FDG}$ for the UF phantom family.

Phantom	Dose (mGy/MBq)	Dose (mGy)
		2010 North American Consensus Guidelines
UFH00MF	4.39	162
UFH01MF	4.03	208
UFH05MF	3.58	329
UFH10MF	2.68	452
UFH15M	2.60	775
UFH15F	2.14	589
UFHADM	1.54	586
UFHADP	1.54	481

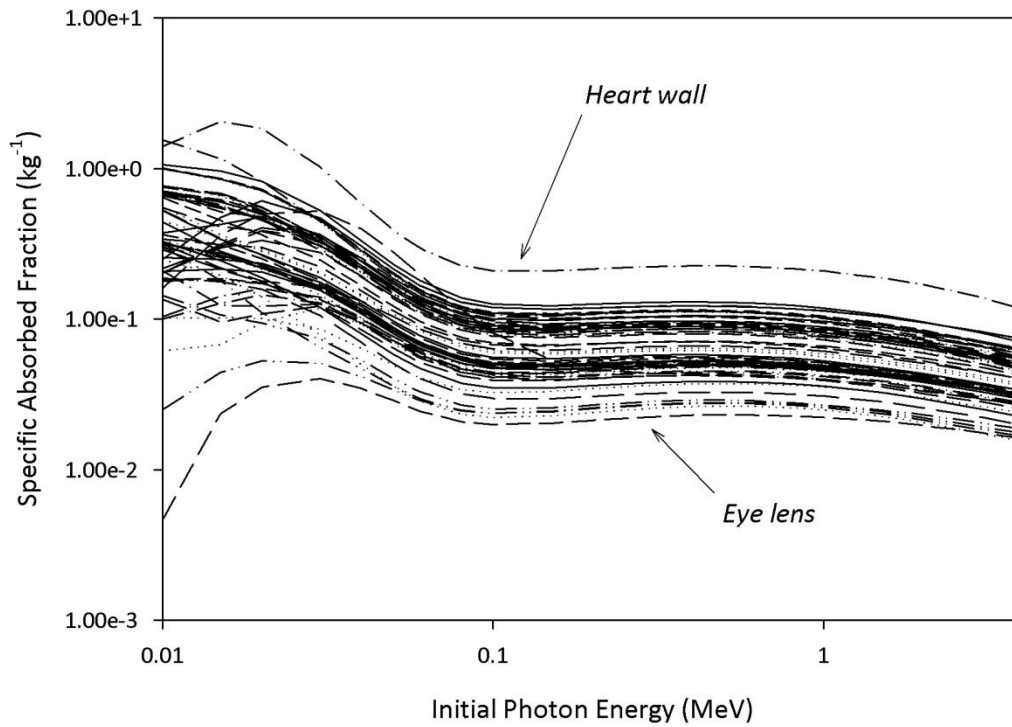


Figure 4-1. Monoenergetic photon SAFs for a uniform blood source in the UFH00M phantom.

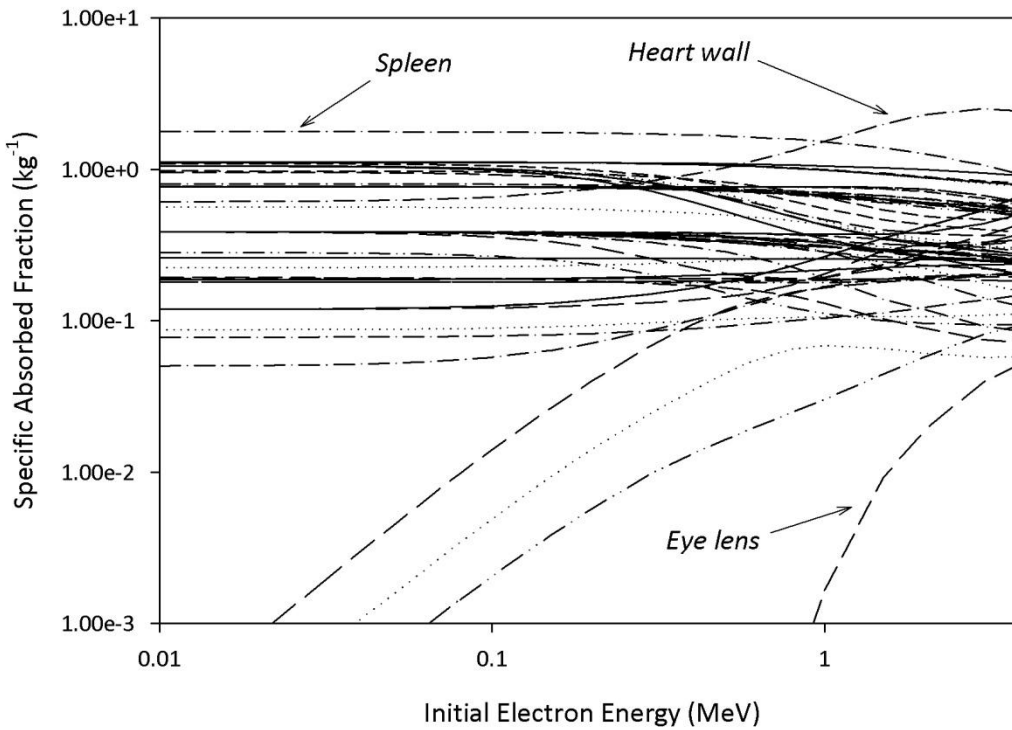


Figure 4-2. Monoenergetic electron SAFs for a uniform blood source in the UFH00M phantom.

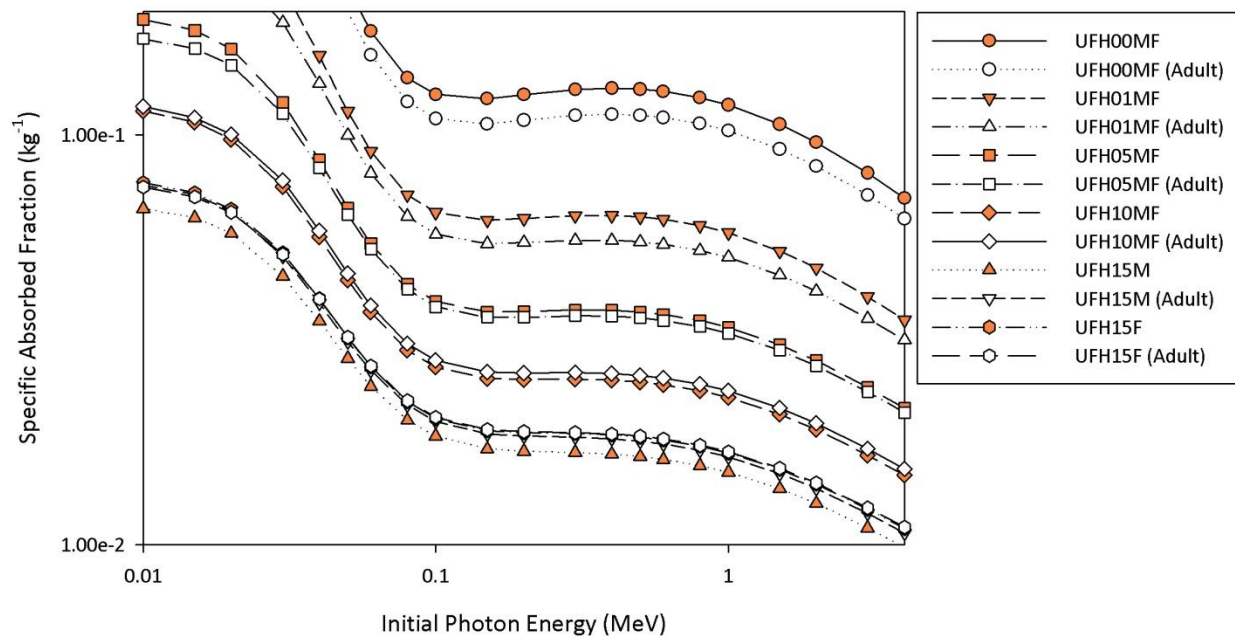


Figure 4-3. Monoenergetic photon SAFs for a uniformly distributed blood source in all pediatric and adolescent phantoms in the UF hybrid phantom family as calculated with the newly developed age-dependent regional blood distributions. The SAFs were also calculated using the gender-dependent adult regional blood distributions to demonstrate the effect (signified by “Adult” in parentheses).

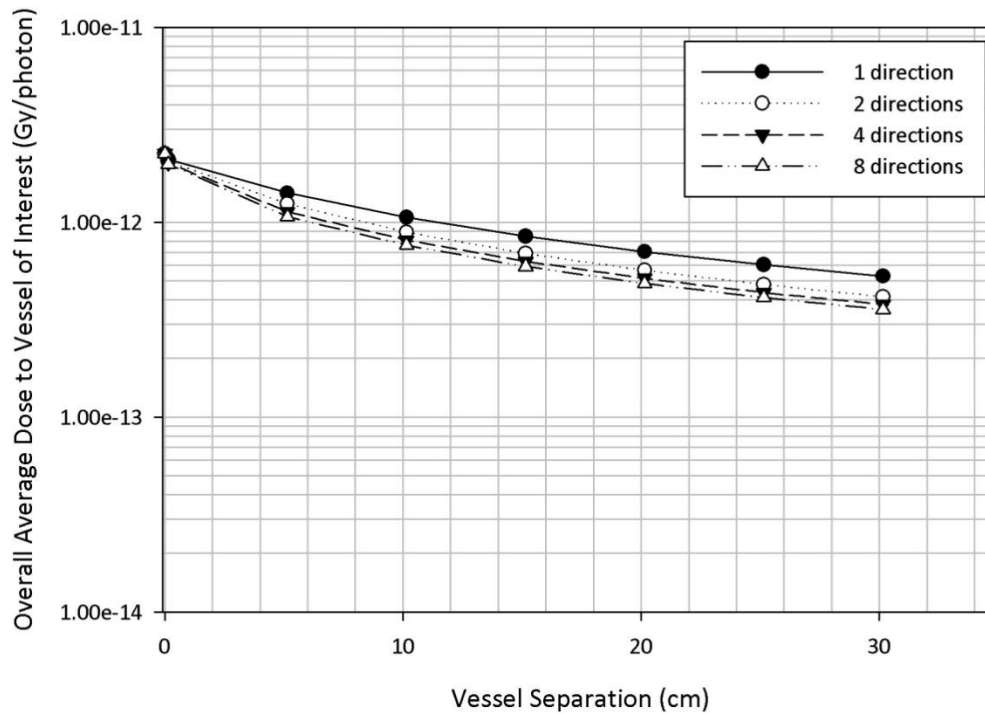


Figure 4-4. Absorbed dose to the blood vessel wall of interest averaged over adjacent vessels located at distances defined by the vessel separation axis and over the number of directions the additional blood vessels are added. For example, the third data point of the “2 directions” dataset represents the absorbed dose to the blood vessel wall at zero separation averaged over the self-dose to the blood vessel wall at zero separation, the cross-dose from two vessels on either side of the blood vessel wall at zero separation to the blood vessel wall at 5 *cm* separation, and the cross-dose from two vessels on either side of the blood vessel wall at zero separation to the blood vessel wall at 10 *cm* separation. This data is valid for a uniform 4 *MeV* photon source for blood vessels with a 0.15 *cm* lumen diameter, 1 μm wall thickness, and 3.21 *cm* vessel length.

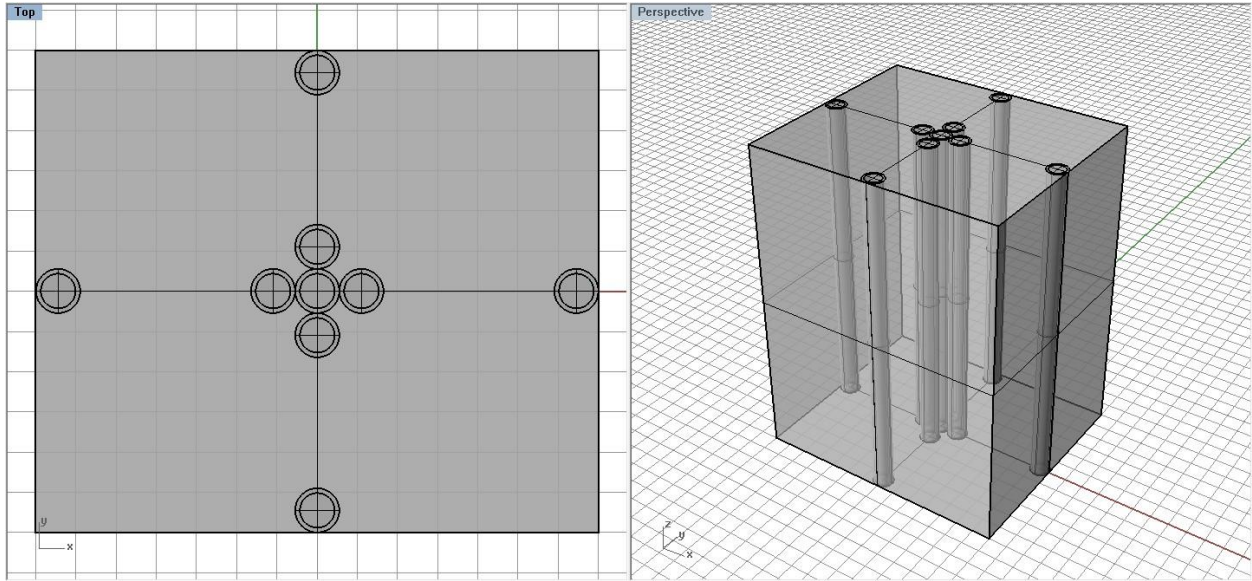


Figure 4-5. Top and perspective views of the final irradiation geometry designed to provide estimates of radiation absorbed dose to the walls of blood vessels in the human body (not to scale).

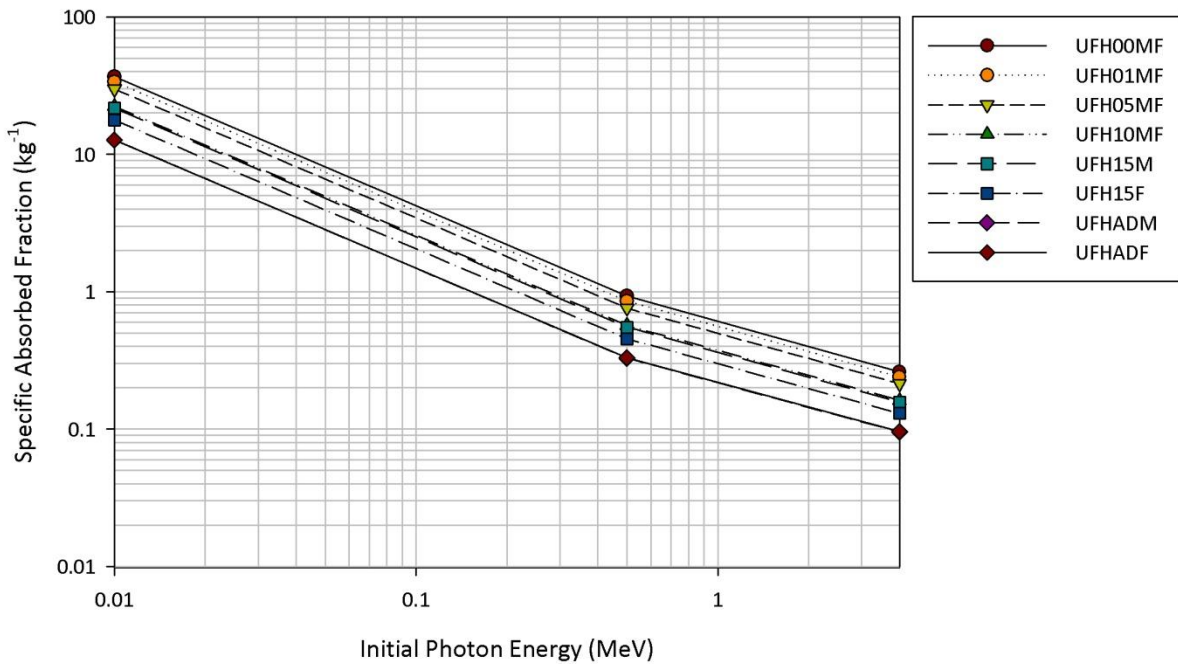


Figure 4-6. Monoenergetic photon SAFs to the blood vessel walls for a uniformly distributed blood source.

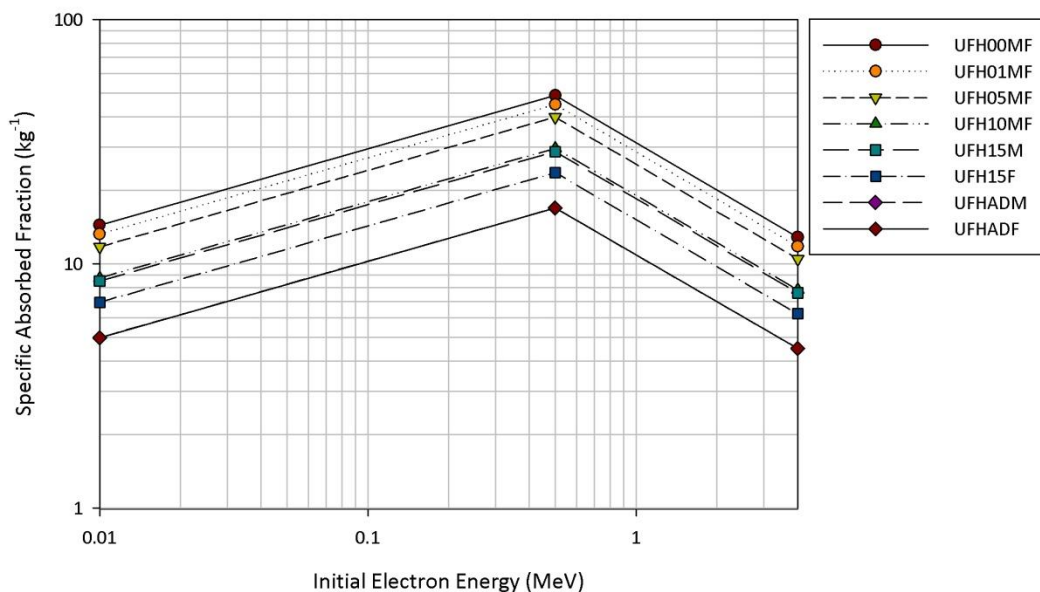


Figure 4-7. Monoenergetic electron SAFs to the blood vessel walls for a uniformly distributed blood source.

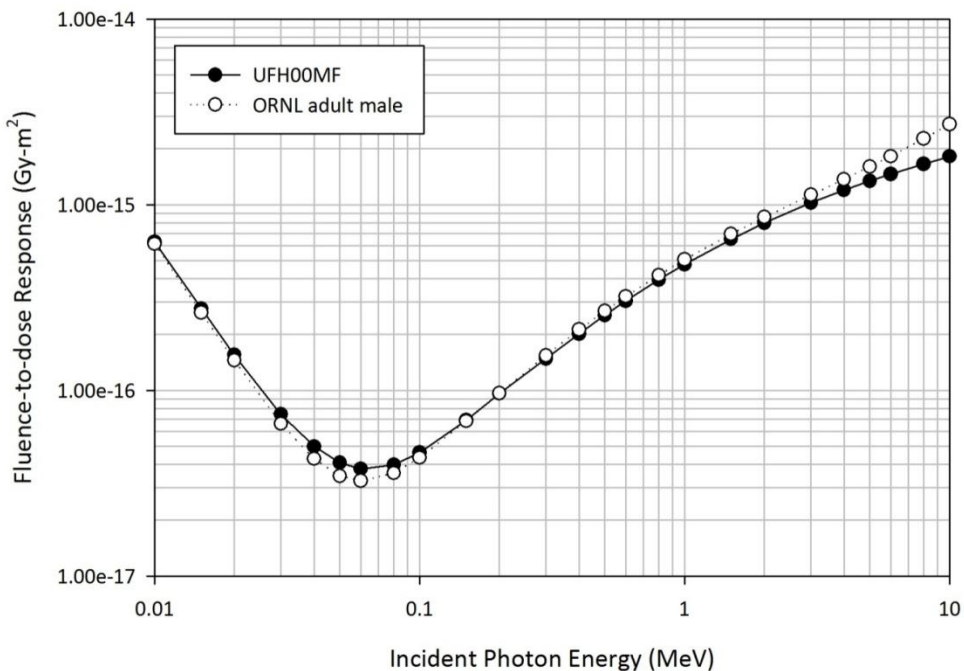


Figure 4-8. UF newborn hybrid phantom and ORNL adult male stylized phantom fluence-to-dose response functions for the cervical vertebra for the AM target (Cristy *et al.* 1987).

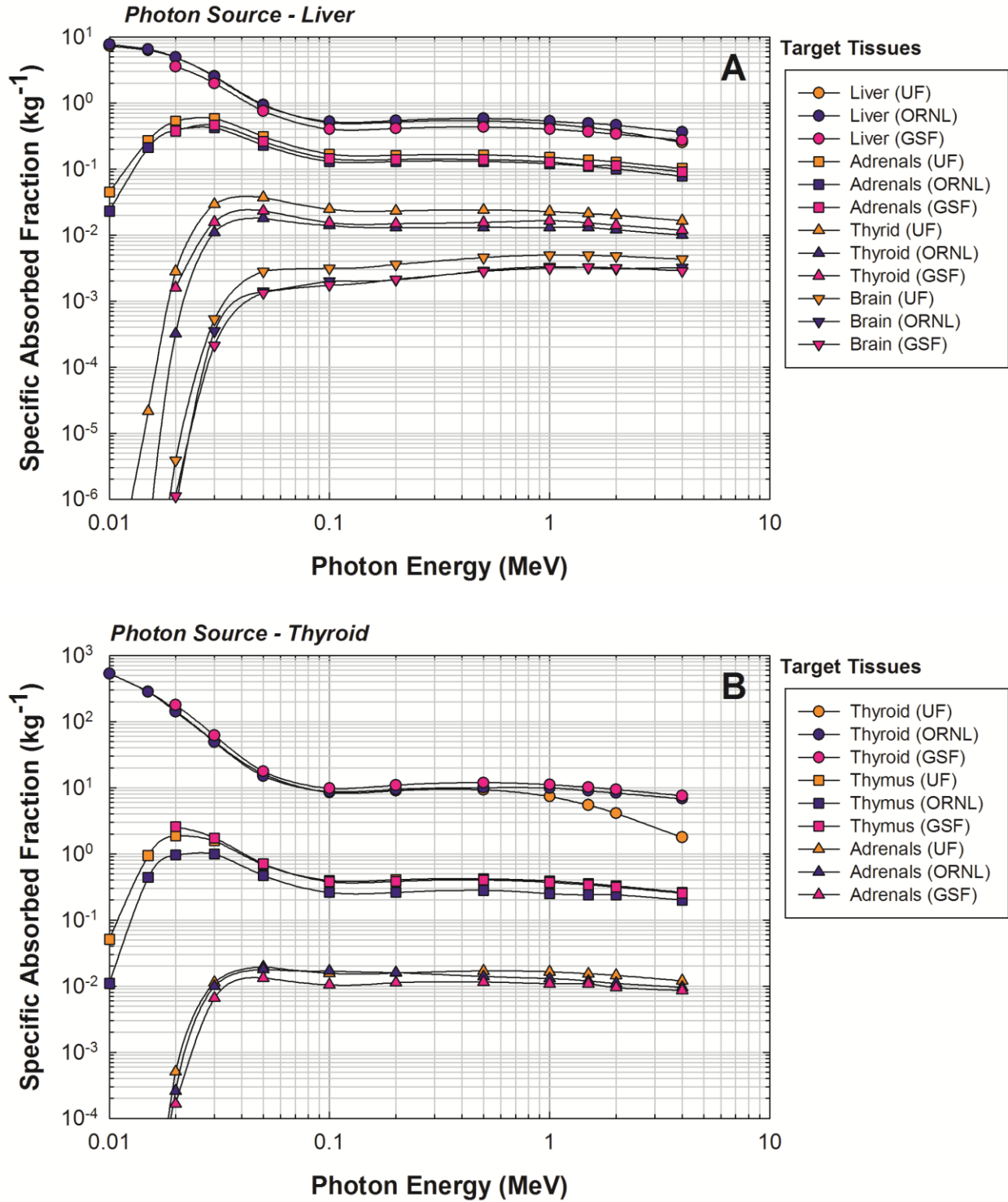


Figure 4-9. Comparison of specific absorbed fractions for photons sources in the (A) liver and (B) thyrid as given by the current hybrid phantom study (UF), those from the ORNL stylized newborn (Cristy *et al.* 1987), and those from the GSF 2-month BABY phantom (Petoussi-Henss *et al.* 2002).

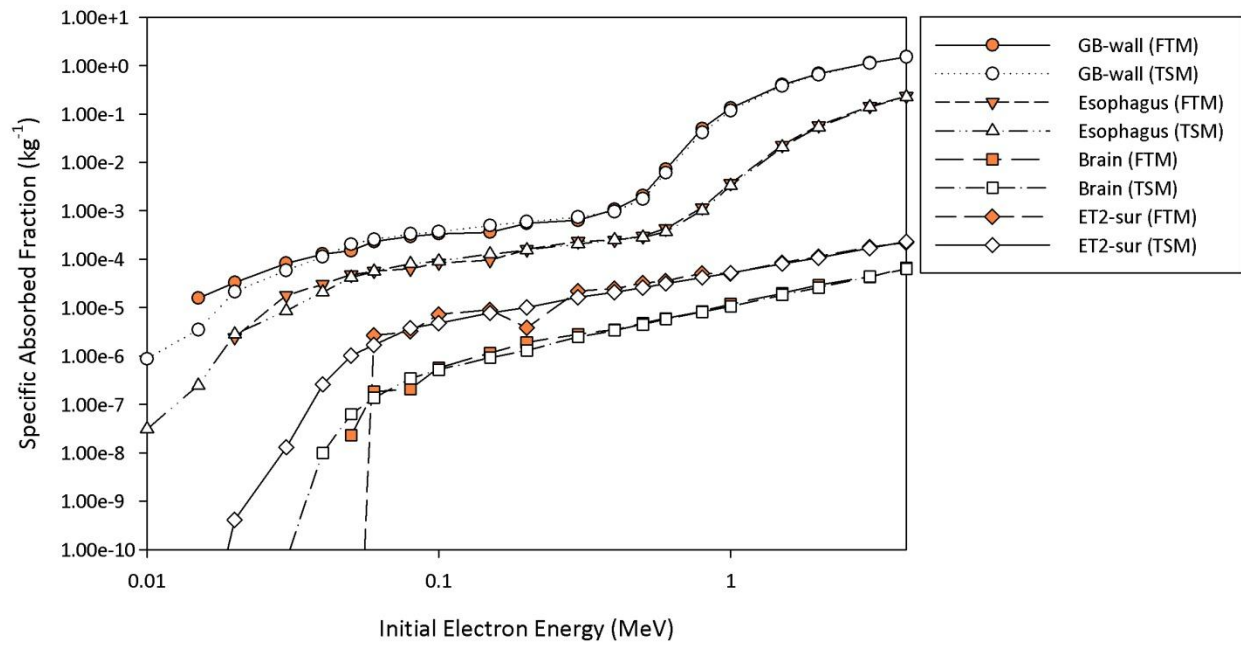


Figure 4-10. Validation study comparing electron SAFs for a uniform electron source in the liver of the UFH00M phantom generated using the full transport method (FTM) and the two-simulation method (TSM).

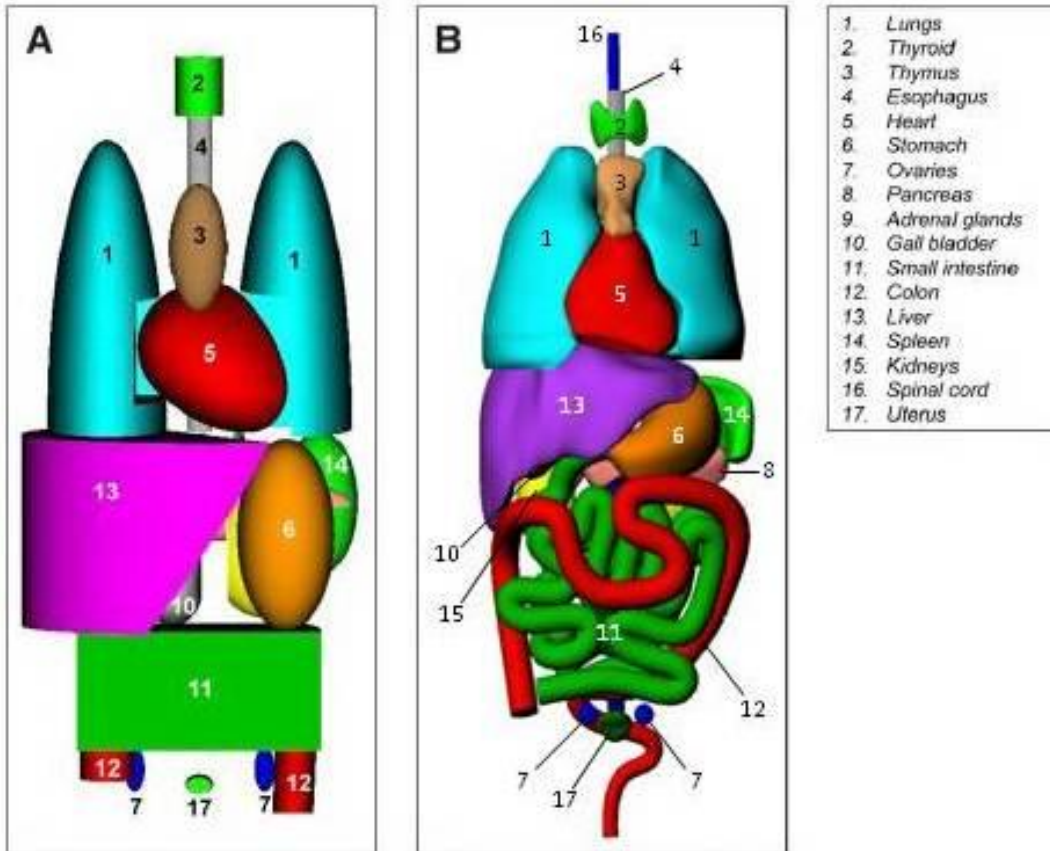


Figure 4-11. Internal anatomy comparison between the (A) ORNL stylized 10-year-old and (B) UFH10F phantom (Cristy *et al.* 1987).

CHAPTER 5 CONCLUSIONS

Organ-level dosimetry in nuclear medicine is important for the assessment of stochastic risks associated with nuclear medicine imaging as well as deterministic risks associated with nuclear medicine therapy. Values of administered activity (AA) for imaging procedures may be adjusted according to dose estimates for a particular exam type. For instance, if a dose estimate for a patient was generated using older dosimetric models, and an up-to-date estimate predicted a lower dose per unit AA than the older estimate, the standard AA for that patient could potentially be increased to provide better diagnostic quality. Alternatively, if the up-to-date estimate predicted a higher dose per unit AA, the standard AA for that patient might have to be lowered to balance risk versus diagnostic quality. With the current limitations of on-the-fly whole-body patient-specific dosimetry, pre-computed estimates to reference individuals may be used to compare different imaging procedures for a particular patient, and this was the main focus of the present study.

Blood Vessel Model

In consideration of possible future adoption by the scientific community, a blood vessel system was crafted using 3-D surfaces to complete the final updates to the UF hybrid phantom family, updates that included the addition of a separable adipose tissue layer, muscle, and lymphatic nodes. The blood vessels were designed to reflect major blood vessels in the head and neck, thoracic and abdominal region, arms, and legs. Total reference vessel volumes were not closely matched due to lack of space in the phantoms, but mathematical apportionment techniques were developed to effectively model a distributed blood source. Relating to the blood vessel model, approximate energy-dependent blood wall dose models were developed for both photons and electrons. If the blood vessel radiopharmaceutical number of nuclear

transformations is known, overall average blood vessel wall dose can be calculated. However, these dose estimates neglect any localized effects. The addition of the physical blood vessel model and blood vessel wall dose model adds another dimension to the detail that can be obtained by using the internal dosimetry given in the current study.

Specific Absorbed Fractions and Skeletal Dosimetry

The bulk of the final product from this work is the monoenergetic photon and electron SAFs. SAFs were calculated because these values are the quantities that contain the dosimetric information that cannot be obtained through any means other than full radiation transport simulations. SAFs contain information regarding the geometry of the phantom organ and body anatomy, and the energy of the radiation of interest. When they are combined with radionuclide decay and biokinetic information, absorbed doses to radiosensitive tissues in the human body may be estimated. Consequently, SAFs are the cornerstone of nuclear medicine dosimetry. Several major factors went in to producing these values – (1) new blood-inclusive tissue elemental compositions, (2) skeletal photon fluence-to-dose response functions, and (3) MCNPX v2.6 radiation transport simulations.

The original tissue elemental compositions of the UF phantom series were exclusive of their blood content; resultantly, these elemental compositions had to be recalculated to include the blood component of all blood-bearing organs. Photon and electron interactions with tissue depend on the elemental composition of the tissue through which they pass, so the original elemental compositions could not be used with confidence. Since the mass of blood in each blood-bearing organ was required to adjust the elemental composition, age-dependent regional blood distributions were needed. However, current literature only recognizes regional blood distributions for the adult male and female. Consequently, age-dependent regional blood distributions were calculated based on age-relative organ sizes and the general assumption that

blood volume per unit organ volume was constant for all ages (a fact assumed for all tissues with the exception of the brain, kidneys, and mineral bone). The results showed that blood distribution does vary with age, as would be expected. Variations in the fraction of blood located in each blood-bearing organ influence the relative dose contribution of that organ when a radionuclide is uniformly distributed throughout the blood in the human body. Correspondingly, both the elemental compositions and regional blood distributions were important advancements in dose modeling capabilities of this study.

Estimating absorbed dose to radiosensitive tissues in the skeleton (AM and TM_{50}) has proven to be a daunting task for dosimetry researchers across the years. Complicated skeletal microstructure and age-dependent skeletal tissue distributions make it difficult to develop empirical solutions to estimating absorbed dose to these tissues. In addition, the dimensions of the microstructure are such that traditional radiation transport techniques cannot handle the large file sizes needed to faithfully represent the true geometry of the skeletal microstructure at the level of a whole-body anatomic model. This study introduced a method by which absorbed dose to the radiosensitive skeletal tissues could be estimated per unit photon fluence incident upon the spongiosa of the skeleton. Detailed electron transport was performed at the microscopic level of the skeletal tissues, the results of which were combined with information regarding the expected secondary electron spectra, photon mass interaction coefficients, and relative tissue masses to yield a comprehensive set of bone and age dependent skeletal fluence-to-dose response functions. These response functions were used in conjunction with volume-average photon fluence tracking capabilities within MCNPX v2.6 to obtain final estimates of $\Phi(AM \leftarrow r_S, E_i)$ and $\Phi(TM_{50} \leftarrow r_S, E_i)$, where Φ is the SAF, r_S is any arbitrary source tissue, and E_i is any arbitrary initial radiation energy. The level of detail inherent to the assembly of the skeletal

photon fluence-to-dose response functions, both in physical modeling and age-specificity, suggest that the advancements made in the field of skeletal dosimetry through these methods are state-of-the-art.

Currently, OLINDA/EXM 1.0 is one of the most widely used internal dosimetry software programs in the world. At present, this program uses stylized/mathematical representations of humans and radiation transport that was performed over 20 years ago. Not only are the hybrid phantoms used in the current study far superior in terms of anatomic realism, but computing power has progressed to a point that allows high volume simulations not available to those who developed the monoenergetic photon SAFs used in OLINDA/EXM. Simulations in the past required very careful in-code variance reduction techniques to maximize utility of particle histories necessary for the Monte Carlo transport method that were on the order of tens of thousands. Particle histories ranging from ten million to one hundred million were used in the current study, and thus statistical reliability of the results in this study is unmatched in that regard.

Monoenergetic photon and electron SAFs were calculated in this study for a total of 12 phantoms including male and female phantoms of the newborn, 1-year-old, 5-year-old, 10-year-old, 15-year-old, and adult. SAFs were calculated at 21 radiation energies ranging from 10 *keV* to 4 *MeV* for between 92 and 95 source tissues per phantom and between 78 and 80 target tissues per phantom. In contrast, OLINDA/EXM provides only photon SAFs for 21 radiation energies ranging from 10 *keV* to 4 *MeV* for 26 source tissues per phantom and 27 target tissues per phantom.

In the current study, electron SAFs were calculated using a two-simulation method wherein collisional and radiative energy loss contributions to absorbed dose are separately

modeled to improve poor statistical uncertainties associated with the radiative energy loss contributions to tissue dose. Photon energy spectra were generated during the radiative energy loss simulations and were subsequently weighted by the previously calculated monoenergetic photon SAFs. The separate collisional and radiative SAFs were then combined to yield final monoenergetic electron SAFs. Electron SAFs were not generated by radiation transport for OLINDA/EXM. In fact, the assumption that electron self-dose AFs were unity and cross-dose AFs were zero was used in the code, and these assumptions were proven to be poor under certain conditions, specifically for higher energy radionuclide. Clearly, the simulation techniques and physical models utilized in the current study are a vast improvement over the current standard that is OLINDA/EXM 1.0.

These comparisons are not meant to slight the hard work that was put in to developing OLINDA/EXM 1.0. At the time of its inception, both the photon SAFs from the work of Cristy and Eckerman in the mid 1980s and the development of MIRDOSE, the precursor to OLINDA/EXM 1.0, in the early 1990s were state-of-the-art in their own right. In this field, innovation and advancement force updates of models and simulation techniques at a quickening pace. In fact, with the current research in quantum computing, full patient-specific dose estimates using radiation transport codes will probably become everyday practice in the future. The work of Cristy and Eckerman was outstanding at the time, and this work is simply trying to carry forward their efforts.

Results from most aims in the current study were used to perform dosimetry for two common nuclear medicine imaging procedures and the resulting dose estimates compared fairly well to current estimates based on stylized phantoms but were a little higher due to decreased inter-organ spacing in the UF hybrid phantom family. Individual organ dose estimates differed

from current estimates fairly significantly. As a result, the dosimetry models developed in this study could potentially lead to advances in nuclear medicine imaging (as well as therapy) protocols. The two clinical case studies demonstrated that the SAFs computed in the current study are easily applicable to real-life situations and provide reasonable dose estimates that compare well to current estimates but provide greater detail at the organ level.

Internal Dose Scaling

Another key contribution from this work was the development of updated photon and electron self- and cross-dose scaling factors. The updated self-dose scaling factors were of greater consequence than the cross-dose scaling factors because cross-dose is not as sensitive to changes in source and target size as self-dose. These scaling factors allow a user of the internal dosimetry software, currently in development, to enter the size of any organ in the body and the center-to-center separation of any organ pair in the body, and the reference self- and cross-doses will be changed according to these inputs. Validation studies were performed and showed that in certain applications, the scaling factors greatly improve the dose estimates. At the very worst, no appreciable increase in dose estimate accuracy was observed. OLINDA/EXM 1.0 assumes a self-dose mass ratio scaling power of -0.667 for photons and -1.000 for electrons when in reality, self-dose scaling powers were found to vary between -0.357 and -0.996 for photons and between -0.600 and -1.000 for electrons over the energy range considered in this study. Applications where the UF scaling powers give much better non-reference dose estimates were demonstrated and showed that personalized dosimetry could be improved by using the UF scaling factors. OLINDA/EXM 1.0 does not scale cross-dose, and thus most non-reference irradiation conditions are better predicted using the UF cross-dose scaling factors.

When patient-specific information on organ volumes is not available, reference SAF (and subsequently, S value) scaling may still be applied given anthropometric measurements of the

patient. To this end, dosimetric sensitivity for internal emitters was investigated for dependence on in-clinic measurable morphometric characteristics such as sitting height and waist circumference. The idea was that if a patient came in for a nuclear medicine procedure, a hospital professional could measure the sitting height and waist circumference of the patient and enter this information into the software program. Reference dose estimates are intended for the average person, but dosimetry for a non-average person can be quite different, and this study attempted to predict this difference so that the sitting height and waist circumference that was entered into the software would adjust the reference dose estimates to attempt to better predict the actual absorbed doses of the patient of interest. It was shown that patient-specific photon absorbed doses could be better estimated by up to 20% using morphometric dose scaling techniques. However, electron dose could not be reliably scaled from patient-specific measurements due to the differences in physical interactions in tissue. Nevertheless, final absorbed dose estimates for patients will be more accurately calculated using the scaling techniques developed in this study, and this is one step in the direction of more patient-specific dose estimates in nuclear medicine.

Deliverables

All together, the deliverables of the seven specific aims in this study – (1) blood vessel model, (2) skeletal photon fluence-to-dose response functions, (3) monoenergetic photon SAFs, (4) monoenergetic electron SAFs, (5) radionuclide S values for commonly used radionuclides, (6) internal dosimetry scaling factors for photon and electron self- and cross-dose and scaling factors based on anthropometric characteristics, and (7) implementation techniques for a future internal dosimetry software code – create the core of the nuclear medicine component of a future software package being developed at UF and NCI that will feature combined CT and nuclear medicine dosimetry. Through extensive beta testing and peer review, the results of this work are

intended for eventual worldwide use in the nuclear medicine community. It is the hope of this investigator that the information given in this work will be used to optimize the way nuclear medicine procedures are performed and possibly reduce the risk of secondary cancers for diagnostic studies or the occurrence of normal organ toxicities for therapeutic procedures.

Future Work

Various checks and validation studies have been performed in this study to show the efficacy of the methods developed, and all recommendations made were based on positive outcomes of these checks and validation studies. However, due to the vast quantity of data, even though no bugs or inconsistencies were observed in the current research, it is possible that small errors may be present. Therefore, before distribution to the scientific community, alpha testing must be performed. Specifically, for a determined period of time, any internal dosimetry studies within the ALRADS research could be performed both with MCNPX v2.6 and with the photon and electron SAFs generated in the current study and the results compared. Care must be taken to ensure that only low uncertainty direct simulation results should be compared to the current SAF results. It was shown through one of the current validation studies that differences up to a factor of 40 could be observed between direct spectrum sampled simulations and assembly of pre-computed monoenergetic SAFs. In fact, multiple orders of magnitude difference could be seen if the statistical uncertainty of the direct simulation is large. That said, once extensive in-house testing has been performed, migration to the NCI CT dose software could be achieved and beta testing could begin. Any bugs or inconsistent data would then be reported back to the ALRADS research group, and troubleshooting would commence.

Most of the aims in the current study were completed in their entirety, so no completion by subsequent researchers will be necessary. One possible area for improvement would be age-specific skeletal models for the UFH01MF, UFH05MF, and UFH10MF phantoms, but this

would be an extremely time-consuming process that would probably not yield results all too different from the SIRT-CBIST model. It is the opinion of this investigator that the limit of computationally-based patient-specific internal dose scaling is being approached as advances in patient-specific modeling may begin to take over. One of the most predictable dose scaling scenarios is self-dose, and mass- and energy-dependent dose scaling factors were introduced in this study that account for high and low energy situations much better than current approaches. At this point, individual variability in internal anatomy precludes further significant gains in this area, short of patient-specific phantom modeling.

Patient-based modeling of obese patients was treated in the current study by adding layers of subcutaneous fat, but other internal fat deposits such as visceral fat deposits and para- and perirenal fat are usually found in obese patients. This possibility was not addressed in the current study but is an issue that can be separately investigated in the future. Fat in between the folds of the intestines could decrease absorbed dose to those structures for sources external to the intestines and could decrease absorbed dose to other structures when the intestines are the source. In addition, fat deposits behind the kidneys could push them further into the body cavity, leading to increases in absorbed dose to the kidneys and other structures. Further investigation is needed into these issues.

Another extension of the work in this study is the evaluation of the benefit of phantom specificity in predicting actual patient doses. An analysis would attempt to answer the question, how much more accurately can absorbed doses be predicted for an actual patient by using either patient-dependent phantoms or scaled reference doses than by using the reference phantom itself. If significant accuracy could be gained by using either of these methods, then generation of more sets of phantoms or scaling methodologies would be warranted. However, if no further

significant gains in accuracy were observed, then reference phantoms could potentially be used to great effect, and the extra effort required to perform dosimetry on patient-dependent phantoms could be bypassed.

Finally, the deliverables of this work will be incorporated into a tumor dose algorithm currently in development by Laura Padilla. This algorithm allows for user placement of ellipsoidal tumors and the calculation of tumor self- and cross-dose based on the integration of point source kernels. By adding this module to the internal dosimetry code, a number of dose estimates may be obtained for radiosensitive organs in the human body as well as for stylistically modeled tumors, a truly significant advancement in the study of internal dosimetry.

APPENDIX A LARGE TABLES

Some tables spanned several pages each, so instead of placing them between chapters within the main text, they were grouped in Appendix A for easy lookup and to assist the flow of the main text. The contents of Appendix A are as follows:

- Tissue density information for the UF phantom family
- Tissue mass information for the UF phantom family
- Blood-inclusive tissue elemental compositions for the UF phantom family
- Non-uniform sampling probabilities for the UF phantom family

Table A-1. All tissue names, tag identification numbers, and densities in g/cm^3 for all phantoms in the UF hybrid phantom family.

Tissue	ID Number	UFH00MF		UFH01MF		UFH05MF		UFH10MF		UFH15MF		UFHADMF	
		Male	Female										
Adipose Tissue	1	0.99	0.99	0.96	0.96	0.96	0.96	0.96	0.96	0.96	0.96	0.96	0.96
Left adrenal	2	1.03	1.03	1.03	1.03	1.03	1.03	1.03	1.03	1.03	1.02	1.03	1.02
Right adrenal	3	1.03	1.03	1.03	1.03	1.03	1.03	1.03	1.03	1.03	1.02	1.03	1.02
Brain	4	1.03	1.03	1.03	1.03	1.04	1.04	1.04	1.04	1.04	1.04	1.04	1.04
Left breast	5	0.99	0.99	0.96	0.96	0.96	0.96	0.96	0.96	0.94	0.94	0.94	0.94
Bronchi	6	1.07	1.07	1.07	1.07	1.07	1.07	1.07	1.07	1.07	1.07	1.07	1.07
Right colon wall	7	1.03	1.03	1.03	1.03	1.03	1.03	1.03	1.03	1.03	1.03	1.03	1.03
Right colon contents	8	1.03	1.03	1.03	1.03	1.03	1.03	1.03	1.03	1.03	1.02	1.03	1.02
Ears	9	1.10	1.10	1.10	1.10	1.10	1.10	1.10	1.10	1.10	1.10	1.10	1.10
Esophagus	10	1.03	1.03	1.03	1.03	1.03	1.03	1.03	1.03	1.03	1.03	1.03	1.03
External nose	11	1.05	1.05	1.05	1.05	1.05	1.05	1.05	1.05	1.05	1.05	1.05	1.05
Eye balls	12	1.03	1.03	1.03	1.03	1.03	1.03	1.03	1.03	1.03	1.02	1.03	1.02
Gall bladder wall	13	1.03	1.03	1.03	1.03	1.03	1.03	1.03	1.03	1.03	1.02	1.03	1.02
Gall bladder contents	14	1.03	1.03	1.03	1.03	1.03	1.03	1.03	1.03	1.03	1.02	1.03	1.02
Heart wall	15	1.04	1.04	1.04	1.04	1.04	1.04	1.04	1.04	1.04	1.04	1.05	1.05
Heart contents	16	1.07	1.07	1.06	1.06	1.06	1.06	1.06	1.06	1.06	1.06	1.06	1.06
Kidneys													
Left cortex	17	1.03	1.03	1.04	1.04	1.04	1.04	1.04	1.04	1.04	1.04	1.05	1.05
Right cortex	18	1.03	1.03	1.04	1.04	1.04	1.04	1.04	1.04	1.04	1.04	1.05	1.05
Left medulla	19	1.03	1.03	1.04	1.04	1.04	1.04	1.04	1.04	1.04	1.04	1.05	1.05
Right medulla	20	1.03	1.03	1.04	1.04	1.04	1.04	1.04	1.04	1.04	1.04	1.05	1.05
Left pelvis	21	1.03	1.03	1.04	1.04	1.04	1.04	1.04	1.04	1.04	1.04	1.05	1.05
Right pelvis	22	1.03	1.03	1.04	1.04	1.04	1.04	1.04	1.04	1.04	1.04	1.05	1.05
Larynx	23	1.07	1.07	1.07	1.07	1.07	1.07	1.07	1.07	1.07	1.07	1.07	1.07
Lens	24	1.07	1.07	1.07	1.07	1.07	1.07	1.07	1.07	1.07	1.07	1.07	1.07
Liver	25	1.04	1.04	1.05	1.05	1.05	1.05	1.05	1.05	1.05	1.05	1.06	1.06
Left lung	26	0.61	0.61	0.40	0.40	0.39	0.39	0.33	0.33	0.32	0.31	0.36	0.34
Right lung	27	0.61	0.61	0.40	0.40	0.39	0.39	0.33	0.33	0.32	0.31	0.36	0.34
Anterior nasal layer	28	1.03	1.03	1.03	1.03	1.03	1.03	1.03	1.03	1.03	1.02	1.03	1.02
Posterior nasal layer	29	1.03	1.03	1.03	1.03	1.03	1.03	1.03	1.03	1.03	1.02	1.03	1.02
Oral cavity layer	30	1.03	1.03	1.03	1.03	1.03	1.03	1.03	1.03	1.03	1.02	1.03	1.02
Left ovary	31	1.05	1.05	1.05	1.05	1.05	1.05	1.05	1.05	1.05	1.05	1.05	1.05

Table A-1. Continued.

Tissue	ID Number	UFH00MF		UFH01MF		UFH05MF		UFH10MF		UFH15MF		UFHADMF	
		Male	Female										
Pancreas	32	1.03	1.03	1.03	1.03	1.03	1.03	1.03	1.03	1.03	1.02	1.03	1.02
Penis	33	1.05	1.05	1.05	1.05	1.05	1.05	1.05	1.05	1.05	1.05	1.05	1.05
Pharynx	34	1.03	1.03	1.03	1.03	1.03	1.03	1.03	1.03	1.03	1.02	1.03	1.03
Pituitary gland	35	1.03	1.03	1.03	1.03	1.03	1.03	1.03	1.03	1.03	1.02	1.03	1.02
Prostate	36	1.03	1.03	1.03	1.03	1.03	1.03	1.03	1.03	1.03	1.03	1.03	1.03
Rectosigmoid wall	37	1.03	1.03	1.03	1.03	1.03	1.03	1.03	1.03	1.03	1.03	1.03	1.03
Rectosigmoid contents	38	1.03	1.03	1.03	1.03	0.86	0.86	1.03	1.03	0.49	1.02	0.97	1.02
Parotid salivary glands	39	1.03	1.03	1.03	1.03	1.03	1.03	1.03	1.03	1.03	1.02	1.03	1.02
Scrotum	40	1.03	1.03	1.03	1.03	1.03	1.03	1.03	1.03	1.03	1.03	1.03	1.03
Small intestine wall	41	1.03	1.03	1.03	1.03	1.03	1.03	1.03	1.03	1.03	1.03	1.03	1.03
Small intestine contents	42	1.03	1.03	1.03	1.03	1.03	1.03	0.54	0.54	0.41	0.45	0.44	0.52
Skin	43	1.10	1.10	1.10	1.10	1.10	1.10	1.10	1.10	1.10	1.10	1.10	1.10
Spinal cord	44	1.03	1.03	1.04	1.04	1.04	1.04	1.04	1.04	1.04	1.04	1.04	1.04
Spleen	45	1.04	1.04	1.06	1.06	1.06	1.06	1.06	1.06	1.06	1.06	1.06	1.06
Stomach wall	46	1.03	1.03	1.03	1.03	1.03	1.03	1.03	1.03	1.03	1.03	1.03	1.03
Stomach contents	47	1.03	1.03	1.03	1.03	1.03	1.03	1.03	1.03	1.03	1.02	1.03	1.02
Testes	48	1.04	1.04	1.04	1.04	1.04	1.04	1.04	1.04	1.04	1.04	1.04	1.04
Thymus	49	1.07	1.07	1.03	1.03	1.03	1.03	1.03	1.03	1.03	1.03	1.03	1.03
Thyroid	50	1.05	1.05	1.05	1.05	1.05	1.05	1.05	1.05	1.05	1.05	1.05	1.05
Tongue	51	1.05	1.05	1.05	1.05	1.05	1.05	1.05	1.05	1.05	1.05	1.05	1.05
Tonsil	52	1.03	1.03	1.03	1.03	1.03	1.03	1.03	1.03	1.03	1.02	1.03	1.02
Trachea	53	1.07	1.07	1.07	1.07	1.07	1.07	1.07	1.07	1.07	1.07	1.07	1.07
Urinary bladder wall	54	1.04	1.04	1.04	1.04	1.04	1.04	1.04	1.04	1.04	1.04	1.04	1.04
Urinary bladder contents	55	1.01	1.01	1.01	1.01	1.01	1.01	1.01	1.01	1.01	1.01	1.01	1.01
Uterus	56	1.05	1.05	1.05	1.05	1.05	1.05	1.05	1.05	1.05	1.05	1.05	1.05
Air (in body)	57	0.00	0.00	0.00	0.00	0.00	0.00	0.00	0.00	0.00	0.00	0.00	0.00
Left colon wall	58	1.03	1.03	1.03	1.03	1.03	1.03	1.03	1.03	1.03	1.03	1.03	1.03
Left colon contents	59	0.65	0.65	0.95	0.95	0.76	0.76	0.49	0.49	0.34	0.98	0.66	1.02
Submaxillary salivary glands	60	1.03	1.03	1.03	1.03	1.03	1.03	1.03	1.03	1.03	1.02	1.03	1.02
Sublingual salivary glands	61	1.03	1.03	1.03	1.03	1.03	1.03	1.03	1.03	1.03	1.02	1.03	1.02
Right breast	62	0.99	0.99	0.96	0.96	0.96	0.96	0.96	0.96	0.94	0.94	0.94	0.94
Right ovary	63	1.05	1.05	1.05	1.05	1.05	1.05	1.05	1.05	1.05	1.05	1.05	1.05

Table A-1. Continued.

Tissue	ID Number	UFH00MF		UFH01MF		UFH05MF		UFH10MF		UFH15MF		UFHADMF	
		Male	Female										
Muscle	64	1.05	1.05	1.05	1.05	1.05	1.05	1.05	1.05	1.05	1.05	1.05	1.05
Blood Vessels													
Head	65	1.06	1.06	1.06	1.06	1.06	1.06	1.06	1.06	1.06	1.06	1.06	1.06
Thoracic	66	1.06	1.06	1.06	1.06	1.06	1.06	1.06	1.06	1.06	1.06	1.06	1.06
Arms	67	1.06	1.06	1.06	1.06	1.06	1.06	1.06	1.06	1.06	1.06	1.06	1.06
Legs	68	1.06	1.06	1.06	1.06	1.06	1.06	1.06	1.06	1.06	1.06	1.06	1.06
Lymphatic Nodes													
Extrathoracic	71	1.03	1.03	1.03	1.03	1.03	1.03	1.03	1.03	1.03	1.02	1.03	1.02
Cervical	72	1.03	1.03	1.03	1.03	1.03	1.03	1.03	1.03	1.03	1.02	1.03	1.02
Upper thoracic	73	1.03	1.03	1.03	1.03	1.03	1.03	1.03	1.03	1.03	1.02	1.03	1.02
Lower thoracic	74	1.03	1.03	1.03	1.03	1.03	1.03	1.03	1.03	1.03	1.02	1.03	1.02
Right breast	75	1.03	1.03	1.03	1.03	1.03	1.03	1.03	1.03	1.03	1.02	1.03	1.02
Left breast	76	1.03	1.03	1.03	1.03	1.03	1.03	1.03	1.03	1.03	1.02	1.03	1.02
Right mesentary	77	1.03	1.03	1.03	1.03	1.03	1.03	1.03	1.03	1.03	1.02	1.03	1.02
Left mesentary	78	1.03	1.03	1.03	1.03	1.03	1.03	1.03	1.03	1.03	1.02	1.03	1.02
Right axillary	79	1.03	1.03	1.03	1.03	1.03	1.03	1.03	1.03	1.03	1.02	1.03	1.02
Left axillary	80	1.03	1.03	1.03	1.03	1.03	1.03	1.03	1.03	1.03	1.02	1.03	1.02
Right cubital	81	1.03	1.03	1.03	1.03	1.03	1.03	1.03	1.03	1.03	1.02	1.03	1.02
Left cubital	82	1.03	1.03	1.03	1.03	1.03	1.03	1.03	1.03	1.03	1.02	1.03	1.02
Right inguinal	83	1.03	1.03	1.03	1.03	1.03	1.03	1.03	1.03	1.03	1.02	1.03	1.02
Left inguinal	84	1.03	1.03	1.03	1.03	1.03	1.03	1.03	1.03	1.03	1.02	1.03	1.02
Right popliteal	85	1.03	1.03	1.03	1.03	1.03	1.03	1.03	1.03	1.03	1.02	1.03	1.02
Left popliteal	86	1.03	1.03	1.03	1.03	1.03	1.03	1.03	1.03	1.03	1.02	1.03	1.02
Bone-associated Cartilage													
Cranium	101	1.10	1.10	1.10	1.10	1.10	1.10	1.10	1.10	1.10	1.10	1.10	1.10
Mandible	102	1.10	1.10	1.10	1.10	1.10	1.10	1.10	1.10	1.10	1.10	1.10	1.10
Scapulae	103	1.10	1.10	1.10	1.10	1.10	1.10	1.10	1.10	1.10	1.10	1.10	1.10
Clavicles	104	1.10	1.10	1.10	1.10	1.10	1.10	1.10	1.10	1.10	1.10	1.10	1.10
Sternum	105	1.10	1.10	1.10	1.10	1.10	1.10	1.10	1.10	1.10	1.10	1.10	1.10
Ribs	106	1.10	1.10	1.10	1.10	1.10	1.10	1.10	1.10	1.10	1.10	1.10	1.10
Cervical vertebrae	107	1.10	1.10	1.10	1.10	1.10	1.10	1.10	1.10	1.10	1.10	1.10	1.10
Thoracic vertebrae	108	1.10	1.10	1.10	1.10	1.10	1.10	1.10	1.10	1.10	1.10	1.10	1.10

Table A-1. Continued.

Tissue	ID Number	UFH00MF		UFH01MF		UFH05MF		UFH10MF		UFH15MF		UFHADMF	
		Male	Female										
Lumbar vertebrae	109	1.10	1.10	1.10	1.10	1.10	1.10	1.10	1.10	1.10	1.10	1.10	1.10
Sacrum	110	1.10	1.10	1.10	1.10	1.10	1.10	1.10	1.10	1.10	1.10	1.10	1.10
Os coxae	111	1.10	1.10	1.10	1.10	1.10	1.10	1.10	1.10	1.10	1.10	1.10	1.10
Proximal femora	112	1.10	1.10	1.10	1.10	1.10	1.10	1.10	1.10	1.10	1.10	1.10	1.10
Distal femora	113	1.10	1.10	1.10	1.10	1.10	1.10	1.10	1.10	1.10	1.10	1.10	1.10
Proximal tibiae	114	1.10	1.10	1.10	1.10	1.10	1.10	1.10	1.10	1.10	1.10	1.10	1.10
Distal tibiae	115	1.10	1.10	1.10	1.10	1.10	1.10	1.10	1.10	1.10	1.10	1.10	1.10
Proximal fibulae	116	1.10	1.10	1.10	1.10	1.10	1.10	1.10	1.10	1.10	1.10	1.10	1.10
Distal fibulae	117	1.10	1.10	1.10	1.10	1.10	1.10	1.10	1.10	1.10	1.10	1.10	1.10
Patellae	118	1.10	1.10	1.10	1.10	1.10	1.10	1.10	1.10	1.10	1.10	1.10	1.10
Ankles and feet	119	1.10	1.10	1.10	1.10	1.10	1.10	1.10	1.10	1.10	1.10	1.10	1.10
Proximal humera	120	1.10	1.10	1.10	1.10	1.10	1.10	1.10	1.10	1.10	1.10	1.10	1.10
Distal humera	121	1.10	1.10	1.10	1.10	1.10	1.10	1.10	1.10	1.10	1.10	1.10	1.10
Proximal radii	122	1.10	1.10	1.10	1.10	1.10	1.10	1.10	1.10	1.10	1.10	1.10	1.10
Distal radii	123	1.10	1.10	1.10	1.10	1.10	1.10	1.10	1.10	1.10	1.10	1.10	1.10
Proximal ulnae	124	1.10	1.10	1.10	1.10	1.10	1.10	1.10	1.10	1.10	1.10	1.10	1.10
Distal ulnae	125	1.10	1.10	1.10	1.10	1.10	1.10	1.10	1.10	1.10	1.10	1.10	1.10
Wrists and hands	126	1.10	1.10	1.10	1.10	1.10	1.10	1.10	1.10	1.10	1.10	1.10	1.10
Other Cartilage													
Cranial cap	127	1.10	1.10	1.10	1.10	1.10	1.10	1.10	1.10	1.10	1.10	1.10	1.10
Costal cartilage of the ribs	128	1.10	1.10	1.10	1.10	1.10	1.10	1.10	1.10	1.10	1.10	1.10	1.10
Cervical discs	129	1.10	1.10	1.10	1.10	1.10	1.10	1.10	1.10	1.10	1.10	1.10	1.10
Thoracic discs	130	1.10	1.10	1.10	1.10	1.10	1.10	1.10	1.10	1.10	1.10	1.10	1.10
Lumbar discs	131	1.10	1.10	1.10	1.10	1.10	1.10	1.10	1.10	1.10	1.10	1.10	1.10
Cortical Bone													
Cranium	151	1.65	1.65	1.66	1.66	1.70	1.70	1.75	1.75	1.80	1.80	1.90	1.90
Mandible	152	1.65	1.65	1.66	1.66	1.70	1.70	1.75	1.75	1.80	1.80	1.90	1.90
Scapulae	153	1.65	1.65	1.66	1.66	1.70	1.70	1.75	1.75	1.80	1.80	1.90	1.90
Clavicles	154	1.65	1.65	1.66	1.66	1.70	1.70	1.75	1.75	1.80	1.80	1.90	1.90
Sternum	155	1.65	1.65	1.66	1.66	1.70	1.70	1.75	1.75	1.80	1.80	1.90	1.90
Ribs	156	1.65	1.65	1.66	1.66	1.70	1.70	1.75	1.75	1.80	1.80	1.90	1.90
Cervical vertebrae	157	1.65	1.65	1.66	1.66	1.70	1.70	1.75	1.75	1.80	1.80	1.90	1.90

Table A-1. Continued.

Tissue	ID Number	UFH00MF		UFH01MF		UFH05MF		UFH10MF		UFH15MF		UFHADMF	
		Male	Female										
Thoracic vertebrae	158	1.65	1.65	1.66	1.66	1.70	1.70	1.75	1.75	1.80	1.80	1.90	1.90
Lumbar vertebrae	159	1.65	1.65	1.66	1.66	1.70	1.70	1.75	1.75	1.80	1.80	1.90	1.90
Sacrum	160	1.65	1.65	1.66	1.66	1.70	1.70	1.75	1.75	1.80	1.80	1.90	1.90
Os coxae	161	1.65	1.65	1.66	1.66	1.70	1.70	1.75	1.75	1.80	1.80	1.90	1.90
Proximal femora	162	1.65	1.65	1.66	1.66	1.70	1.70	1.75	1.75	1.80	1.80	1.90	1.90
Upper shaft of the femora	163	1.65	1.65	1.66	1.66	1.70	1.70	1.75	1.75	1.80	1.80	1.90	1.90
Lower shaft of the femora	164	1.65	1.65	1.66	1.66	1.70	1.70	1.75	1.75	1.80	1.80	1.90	1.90
Distal femora	165	1.65	1.65	1.66	1.66	1.70	1.70	1.75	1.75	1.80	1.80	1.90	1.90
Proximal tibiae	166	1.65	1.65	1.66	1.66	1.70	1.70	1.75	1.75	1.80	1.80	1.90	1.90
Shaft of the tibiae	167	1.65	1.65	1.66	1.66	1.70	1.70	1.75	1.75	1.80	1.80	1.90	1.90
Distal tibiae	168	1.65	1.65	1.66	1.66	1.70	1.70	1.75	1.75	1.80	1.80	1.90	1.90
Proximal fibulae	169	1.65	1.65	1.66	1.66	1.70	1.70	1.75	1.75	1.80	1.80	1.90	1.90
Shaft of the fibulae	170	1.65	1.65	1.66	1.66	1.70	1.70	1.75	1.75	1.80	1.80	1.90	1.90
Distal fibulae	171	1.65	1.65	1.66	1.66	1.70	1.70	1.75	1.75	1.80	1.80	1.90	1.90
Patellae	172	1.65	1.65	1.66	1.66	1.70	1.70	1.75	1.75	1.80	1.80	1.90	1.90
Ankles and feet	173	1.65	1.65	1.66	1.66	1.70	1.70	1.75	1.75	1.80	1.80	1.90	1.90
Proximal humera	174	1.65	1.65	1.66	1.66	1.70	1.70	1.75	1.75	1.80	1.80	1.90	1.90
Upper shaft of the humera	175	1.65	1.65	1.66	1.66	1.70	1.70	1.75	1.75	1.80	1.80	1.90	1.90
Lower shaft of the humera	176	1.65	1.65	1.66	1.66	1.70	1.70	1.75	1.75	1.80	1.80	1.90	1.90
Distal humera	177	1.65	1.65	1.66	1.66	1.70	1.70	1.75	1.75	1.80	1.80	1.90	1.90
Proximal radii	178	1.65	1.65	1.66	1.66	1.70	1.70	1.75	1.75	1.80	1.80	1.90	1.90
Shaft of the radii	179	1.65	1.65	1.66	1.66	1.70	1.70	1.75	1.75	1.80	1.80	1.90	1.90
Distal radii	180	1.65	1.65	1.66	1.66	1.70	1.70	1.75	1.75	1.80	1.80	1.90	1.90
Proximal ulnae	181	1.65	1.65	1.66	1.66	1.70	1.70	1.75	1.75	1.80	1.80	1.90	1.90
Shaft of the ulnae	182	1.65	1.65	1.66	1.66	1.70	1.70	1.75	1.75	1.80	1.80	1.90	1.90
Distal ulnae	183	1.65	1.65	1.66	1.66	1.70	1.70	1.75	1.75	1.80	1.80	1.90	1.90
Wrists and hands	184	1.65	1.65	1.66	1.66	1.70	1.70	1.75	1.75	1.80	1.80	1.90	1.90
Teeth	185	1.65	1.65	1.65	1.65	1.65	1.65	2.33	2.33	3.00	3.00	3.00	3.00

Table A-1. Continued.

Tissue	ID Number	UFH00MF		UFH01MF		UFH05MF		UFH10MF		UFH15MF		UFHADMF	
		Male	Female										
Spongiosa and Medullary Cavities													
Cranium	201	1.433	1.433	1.435	1.435	1.374	1.374	1.294	1.294	1.250	1.253	1.491	1.600
Mandible	202	1.244	1.244	1.415	1.415	1.338	1.338	1.258	1.258	1.225	1.225	1.077	1.131
Scapulae	203	1.257	1.257	1.287	1.287	1.258	1.258	1.177	1.177	1.244	1.243	1.134	1.047
Clavicles	204	1.257	1.257	1.295	1.295	1.233	1.233	1.135	1.135	1.142	1.142	1.099	1.067
Sternum	205	1.245	1.245	1.249	1.249	1.163	1.163	1.085	1.085	1.089	1.088	1.086	1.086
Ribs	206	1.244	1.244	1.251	1.251	1.236	1.236	1.135	1.135	1.110	1.109	1.114	1.093
Cervical vertebrae	207	1.338	1.338	1.210	1.210	1.234	1.234	1.150	1.150	1.139	1.139	1.169	1.170
Thoracic vertebrae	208	1.351	1.351	1.169	1.169	1.175	1.175	1.114	1.114	1.115	1.115	1.096	1.114
Lumbar vertebrae	209	1.307	1.307	1.274	1.274	1.233	1.233	1.160	1.160	1.098	1.098	1.105	1.126
Sacrum	210	1.307	1.307	1.276	1.276	1.160	1.160	1.075	1.075	1.056	1.055	1.117	1.138
Os coxae	211	1.257	1.257	1.214	1.214	1.190	1.190	1.124	1.124	1.093	1.092	1.091	1.046
Proximal femora	212	1.307	1.307	1.344	1.344	1.294	1.294	1.236	1.236	1.167	1.166	1.125	1.199
Upper shaft of the femora	213	1.030	1.030	1.026	1.026	1.018	1.018	1.005	1.005	0.998	0.997	0.994	0.989
Lower shaft of the femora	214	1.030	1.030	1.025	1.025	1.016	1.016	1.004	1.004	0.990	0.990	0.981	0.981
Distal femora	215	1.307	1.307	1.306	1.306	1.256	1.256	1.210	1.210	1.202	1.202	1.112	1.164
Proximal tibiae	216	1.307	1.307	1.354	1.354	1.270	1.270	1.187	1.187	1.057	1.057	1.084	1.123
Shaft of the tibiae	217	1.030	1.030	1.025	1.025	1.009	1.009	0.991	0.991	0.980	0.980	0.981	0.981
Distal tibiae	218	1.307	1.307	1.324	1.324	1.161	1.161	1.127	1.127	1.129	1.129	1.093	1.135
Proximal fibulae	219	1.307	1.307	1.369	1.369	1.185	1.185	1.141	1.141	1.102	1.102	1.051	1.091
Shaft of the fibulae	220	1.030	1.030	1.024	1.024	1.009	1.009	0.991	0.991	0.980	0.980	0.981	0.981
Distal fibulae	221	1.307	1.307	1.364	1.364	1.182	1.182	1.140	1.140	1.192	1.192	1.113	1.144
Patellae	222	1.244	1.244	1.215	1.215	1.099	1.099	1.034	1.034	1.078	1.077	1.112	1.149
Ankles and feet	223	1.244	1.244	1.273	1.273	1.243	1.243	1.153	1.153	1.078	1.077	1.112	1.063
Proximal humera	224	1.307	1.307	1.364	1.364	1.295	1.295	1.226	1.226	1.127	1.127	1.078	1.080
Upper shaft of the humera	225	1.030	1.030	1.027	1.027	1.018	1.018	1.005	1.005	0.997	0.997	0.994	0.989
Lower shaft of the humera	226	1.030	1.030	1.026	1.026	1.017	1.017	1.004	1.004	0.990	0.990	0.981	0.981
Distal humera	227	1.307	1.307	1.364	1.364	1.281	1.281	1.196	1.196	1.153	1.152	1.117	1.135

Table A-1. Continued.

Tissue	ID Number	UFH00MF		UFH01MF		UFH05MF		UFH10MF		UFH15MF		UFHADMF	
		Male	Female										
Proximal radii	228	1.307	1.307	1.374	1.374	1.186	1.186	1.151	1.151	1.145	1.145	1.061	1.089
Shaft of the radii	229	1.030	1.030	1.025	1.025	1.008	1.008	0.992	0.992	0.980	0.980	0.981	0.981
Distal radii	230	1.307	1.307	1.391	1.391	1.255	1.255	1.199	1.199	1.138	1.137	1.085	1.101
Proximal ulnae	231	1.307	1.307	1.437	1.437	1.296	1.296	1.239	1.239	1.183	1.183	1.125	1.223
Shaft of the ulnae	232	1.030	1.030	1.025	1.025	1.008	1.008	0.992	0.992	0.980	0.980	0.981	0.981
Distal ulnae	233	1.307	1.307	1.297	1.297	1.112	1.112	1.095	1.095	1.129	1.129	1.106	1.016
Wrists and hands	234	1.244	1.244	1.281	1.281	1.229	1.229	1.135	1.135	1.078	1.077	1.117	1.062

Table A-2. Tissue masses in grams for all phantoms in the UF hybrid phantom family after voxelization.

Tissue	UFH00MF		UFH01MF		UFH05MF		UFH10MF		UFH15MF		UFHADMF	
	Male	Female	Male	Female	Male	Female	Male	Female	Male	Female	Male	Female
Adipose Tissue	661.81	661.12	3486.82	3488.16	4577.66	4574.50	6733.25	6730.27	7322.78	12237.12	11642.88	13723.20
Left adrenal	2.98	2.98	1.98	1.98	2.48	2.48	3.41	3.41	5.04	4.58	6.96	6.46
Right adrenal	2.95	2.95	1.97	1.97	2.51	2.51	3.44	3.44	4.67	4.55	6.82	6.47
Brain	315.34	315.34	946.10	946.10	1241.14	1241.14	1306.24	1306.24	1416.58	1293.14	1441.65	1298.96
Left breast	0.04	0.04	0.22	0.22	0.47	0.47	3.59	3.77	7.40	149.21	11.04	239.92
Bronchi	0.38	0.38	2.00	2.00	3.02	3.02	3.50	3.50	7.96	7.47	16.06	8.98
Right colon wall	6.89	6.89	19.95	19.95	48.78	48.78	84.11	84.11	121.80	121.60	150.28	144.46
Right colon contents	15.51	15.51	15.06	15.06	26.48	26.48	27.52	27.52	70.92	42.85	98.35	50.45
Ears	1.19	1.19	3.22	3.22	5.36	5.36	4.04	4.04	6.76	7.11	11.08	6.70
Esophagus	1.93	1.93	4.84	4.84	9.72	9.72	17.58	17.58	28.90	29.29	38.96	34.38
External nose	0.32	0.32	2.17	2.17	3.95	3.95	6.72	6.72	4.27	3.75	7.64	14.90
Eye balls	5.89	5.89	6.93	6.93	10.95	10.95	11.96	11.96	12.99	12.79	15.01	14.86
Gall bladder wall	0.49	0.49	1.38	1.38	2.61	2.61	4.32	4.32	7.73	7.10	10.31	7.94
Gall bladder contents	2.79	2.79	7.95	7.95	14.90	14.90	25.91	25.91	44.86	41.83	57.51	47.81
Heart wall	19.82	19.82	49.83	49.83	84.51	84.51	139.11	139.11	229.60	220.00	328.45	249.38
Heart contents	6.00	6.00	47.70	47.70	134.28	134.28	229.09	229.09	426.77	317.66	507.36	367.05
Kidneys												
Left cortex	9.13	9.13	25.61	25.61	40.18	40.18	65.80	65.80	91.53	87.72	113.56	100.41
Right cortex	9.14	9.14	25.56	25.56	40.22	40.22	65.88	65.88	91.40	87.76	113.14	100.73
Left medulla	3.26	3.26	9.11	9.11	14.38	14.38	23.56	23.56	32.74	31.40	40.62	36.04
Right medulla	3.26	3.26	9.11	9.11	14.40	14.40	23.52	23.52	32.77	31.49	40.64	35.93
Left pelvis	0.65	0.65	1.82	1.82	2.86	2.86	4.70	4.70	6.54	6.30	8.04	7.21
Right pelvis	0.65	0.65	1.82	1.82	2.85	2.85	4.71	4.71	6.55	6.19	8.06	7.23
Larynx	1.30	1.30	4.00	4.00	7.05	7.05	12.01	12.01	21.99	14.74	27.70	19.09
Lens	0.13	0.13	0.22	0.22	0.33	0.33	0.35	0.35	0.49	0.40	0.41	0.46
Liver	128.94	128.94	327.96	327.96	566.94	566.94	826.13	826.13	1294.23	1295.91	1791.61	1392.31
Left lung	28.19	28.19	68.55	68.55	146.29	146.29	232.41	232.41	392.06	378.11	522.11	415.31
Right lung	30.77	30.77	80.84	80.84	151.12	151.12	257.50	257.50	498.05	379.32	675.32	511.46
Anterior nasal layer	0.09	0.09	0.14	0.14	0.41	0.41	0.46	0.46	2.03	0.44	1.81	0.49
Posterior nasal layer	0.72	0.72	1.99	1.99	8.22	8.22	9.96	9.96	9.55	8.56	5.43	8.81
Oral cavity layer	0.73	0.73	0.53	0.53	1.29	1.29	1.00	1.00	5.02	7.68	2.24	1.81
Left ovary	0.00	0.15	0.00	0.39	0.00	0.99	0.00	1.74	0.00	3.02	0.00	5.50

Table A-2. Continued.

Tissue	UFH00MF		UFH01MF		UFH05MF		UFH10MF		UFH15MF		UFHADMF	
	Male	Female	Male	Female								
Pancreas	5.94	5.94	19.78	19.78	34.73	34.73	59.40	59.40	109.26	99.44	138.82	119.45
Penis	0.58	0.00	3.53	0.00	6.74	0.00	6.62	0.00	30.67	0.00	22.50	0.00
Pharynx	0.29	0.29	0.83	0.83	1.88	1.88	2.01	2.01	2.58	2.82	2.25	1.47
Pituitary gland	0.10	0.10	0.15	0.15	0.25	0.25	0.35	0.35	0.49	0.47	0.60	0.58
Prostate	0.79	0.00	1.00	0.00	1.04	0.00	1.64	0.00	4.27	0.00	16.90	0.00
Rectosigmoid wall	2.98	2.98	9.85	9.85	21.75	21.75	39.82	39.82	55.03	56.04	70.25	70.34
Rectosigmoid contents	9.45	9.45	14.37	14.37	24.48	24.48	31.21	31.21	38.66	50.66	73.06	54.93
Parotid salivary glands	3.47	3.47	13.86	13.86	19.93	19.93	25.78	25.78	39.07	35.98	49.82	40.71
Scrotum	1.17	0.00	2.17	0.00	2.30	0.00	2.19	0.00	20.13	0.00	39.29	0.00
Small intestine wall	28.89	28.99	81.54	81.52	210.50	210.55	355.50	355.50	499.85	494.61	627.58	578.13
Small intestine contents	31.09	31.09	48.02	48.02	37.95	37.95	160.04	160.04	264.72	274.45	344.03	273.46
Skin	116.15	115.43	250.75	249.71	535.33	533.26	988.45	986.71	1855.59	1680.36	2664.64	1849.43
Spinal cord	6.27	6.27	22.53	22.53	29.83	29.83	49.08	49.08	46.30	56.74	71.44	45.82
Spleen	9.43	9.43	28.86	28.86	49.67	49.67	79.51	79.51	128.61	128.80	149.20	129.25
Stomach wall	6.93	6.93	19.75	19.75	49.56	49.56	84.21	84.21	118.98	119.16	149.27	139.34
Stomach contents	25.18	25.18	66.85	66.85	82.49	82.49	116.83	116.83	197.76	199.76	252.31	230.53
Testes	0.84	0.00	1.50	0.00	1.68	0.00	1.99	0.00	15.80	0.00	34.79	0.00
Thymus	12.91	12.91	15.99	15.99	29.92	29.92	37.41	37.41	35.07	29.78	24.90	20.07
Thyroid	1.29	1.29	1.78	1.78	3.38	3.38	7.81	7.81	11.94	11.94	19.93	16.92
Tongue	3.50	3.50	9.96	9.96	18.81	18.81	31.93	31.93	55.43	52.83	72.40	59.68
Tonsil	0.10	0.10	0.51	0.51	1.96	1.96	2.96	2.96	3.04	2.95	2.98	2.98
Trachea	0.51	0.51	1.49	1.49	2.51	2.51	4.52	4.52	7.45	5.97	10.02	8.06
Urinary bladder wall	3.96	3.97	8.96	8.94	15.90	15.93	24.97	24.84	39.87	34.78	49.55	39.78
Urinary bladder contents	9.99	9.99	10.97	10.05	61.58	61.52	98.36	98.38	152.84	133.88	201.58	161.57
Uterus	0.00	3.95	0.00	1.48	0.00	2.99	0.00	3.98	0.00	29.86	0.00	79.67
Air (in body)	0.00	0.00	0.01	0.01	0.03	0.03	0.07	0.07	0.46	0.15	0.10	0.06
Left colon wall	6.96	6.96	19.79	19.79	48.64	48.64	84.78	84.78	121.66	122.03	149.56	144.99
Left colon contents	11.91	11.91	19.68	19.68	24.65	24.65	16.24	16.24	30.10	58.30	34.44	73.81
Submaxillary salivary glands	1.79	1.79	6.96	6.96	9.97	9.97	12.95	12.95	19.89	18.94	24.94	20.36
Sublingual salivary glands	0.69	0.69	3.01	3.01	3.98	3.98	4.98	4.98	7.88	7.89	10.03	7.95
Right breast	0.04	0.04	0.21	0.21	0.47	0.47	3.53	3.76	7.40	149.63	10.81	239.60
Right ovary	0.00	0.15	0.00	0.40	0.00	0.99	0.00	1.74	0.00	3.02	0.00	5.50

Table A-2. Continued.

Tissue	UFH00MF		UFH01MF		UFH05MF		UFH10MF		UFH15MF		UFHADMF	
	Male	Female	Male	Female	Male	Female	Male	Female	Male	Female	Male	Female
Muscle	1500.77	1497.83	3189.06	3190.53	7173.08	7173.71	15951.60	15951.60	33800.55	25579.05	40062.75	29303.40
Blood Vessels												
Head	1.31	1.31	2.43	2.43	5.24	5.24	9.69	9.69	19.63	18.51	22.51	19.69
Thoracic	0.49	0.49	0.78	0.78	2.09	2.09	4.68	4.68	8.53	5.43	11.89	5.68
Arms	4.38	4.38	8.67	8.67	22.15	22.15	47.99	47.99	88.76	79.15	119.14	103.99
Legs	5.18	5.18	11.58	11.58	32.61	32.61	69.33	69.33	128.59	120.91	175.63	145.02
Lymphatic Nodes												
Extrathoracic	0.45	0.60	2.75	3.30	2.16	4.21	1.23	2.46	4.48	3.50	2.85	2.19
Cervical	1.36	0.90	6.03	6.48	5.04	4.32	6.14	6.14	13.73	2.09	27.54	14.66
Upper thoracic	0.04	0.02	0.23	0.03	0.74	1.07	0.00	0.00	4.64	3.25	3.77	5.86
Lower thoracic	0.09	0.03	0.08	0.12	1.85	1.28	0.46	0.46	6.97	6.13	5.46	7.28
Right breast	0.60	0.60	0.16	0.16	2.52	3.24	3.69	4.92	2.29	9.38	7.11	14.27
Left breast	0.60	0.60	0.16	0.16	2.52	3.24	3.69	4.92	2.29	9.38	7.11	14.27
Right mesentary	0.26	0.23	0.92	0.67	1.70	1.82	9.79	9.56	7.88	4.60	12.70	14.17
Left mesentary	0.26	0.23	0.92	0.67	1.70	1.78	9.79	9.56	7.88	4.60	12.70	14.05
Right axillary	0.75	0.98	2.70	2.55	6.12	6.12	7.37	5.53	19.45	17.72	18.49	2.19
Left axillary	0.75	0.98	2.70	2.55	6.12	6.12	7.37	5.53	19.45	17.72	18.49	2.19
Right cubital	0.45	0.38	1.27	1.43	1.08	1.08	2.46	2.46	11.44	14.60	9.96	21.95
Left cubital	0.45	0.38	1.27	1.43	1.08	1.08	2.46	2.46	11.44	14.60	9.96	21.95
Right inguinal	0.90	1.21	4.61	3.98	6.48	6.48	8.60	8.60	19.45	18.77	27.03	3.29
Left inguinal	0.90	1.21	4.61	3.98	6.48	6.48	8.60	8.60	19.45	18.77	27.03	3.29
Right popliteal	1.05	0.90	0.32	0.48	4.68	3.24	10.45	10.45	4.58	2.09	9.96	14.27
Left popliteal	1.05	0.90	0.32	0.48	4.68	3.24	10.45	10.45	4.58	2.09	9.96	14.27
Bone-associated Cartilage												
Cranium	38.52	38.52	0.00	0.00	0.00	0.00	0.00	0.00	0.00	0.00	0.00	0.00
Mandible	2.67	2.67	0.00	0.00	0.00	0.00	0.00	0.00	0.00	0.00	0.00	0.00
Scapulae	2.75	2.75	0.00	0.00	0.00	0.00	0.00	0.00	0.00	0.00	0.00	0.00
Clavicles	1.34	1.34	0.00	0.00	0.00	0.00	0.00	0.00	0.00	0.00	0.00	0.00
Sternum	1.57	1.57	0.00	0.00	0.00	0.00	0.00	0.00	0.00	0.00	0.00	0.00
Ribs	4.34	4.34	0.00	0.00	0.00	0.00	0.00	0.00	0.00	0.00	0.00	0.00
Cervical vertebrae	4.15	4.15	0.00	0.00	0.00	0.00	0.00	0.00	0.00	0.00	0.00	0.00
Thoracic vertebrae	7.92	7.92	0.00	0.00	0.00	0.00	0.00	0.00	0.00	0.00	0.00	0.00

Table A-2. Continued.

Tissue	UFH00MF		UFH01MF		UFH05MF		UFH10MF		UFH15MF		UFHADMF	
	Male	Female										
Lumbar vertebrae	4.19	4.19	0.00	0.00	0.00	0.00	0.00	0.00	0.00	0.00	0.00	0.00
Sacrum	1.94	1.94	0.00	0.00	0.00	0.00	0.00	0.00	0.00	0.00	0.00	0.00
Os coxae	5.85	5.85	0.00	0.00	0.00	0.00	0.00	0.00	0.00	0.00	0.00	0.00
Proximal femora	2.67	2.67	0.00	0.00	0.00	0.00	0.00	0.00	0.00	0.00	0.00	0.00
Distal femora	2.36	2.36	0.00	0.00	0.00	0.00	0.00	0.00	0.00	0.00	0.00	0.00
Proximal tibiae	1.77	1.77	0.00	0.00	0.00	0.00	0.00	0.00	0.00	0.00	0.00	0.00
Distal tibiae	1.66	1.66	0.00	0.00	0.00	0.00	0.00	0.00	0.00	0.00	0.00	0.00
Proximal fibulae	0.70	0.70	0.00	0.00	0.00	0.00	0.00	0.00	0.00	0.00	0.00	0.00
Distal fibulae	0.92	0.92	0.00	0.00	0.00	0.00	0.00	0.00	0.00	0.00	0.00	0.00
Patellae	0.14	0.14	0.00	0.00	0.00	0.00	0.00	0.00	0.00	0.00	0.00	0.00
Ankles and feet	4.14	4.14	0.00	0.00	0.00	0.00	0.00	0.00	0.00	0.00	0.00	0.00
Proximal humera	1.66	1.66	0.00	0.00	0.00	0.00	0.00	0.00	0.00	0.00	0.00	0.00
Distal humera	1.96	1.96	0.00	0.00	0.00	0.00	0.00	0.00	0.00	0.00	0.00	0.00
Proximal radii	0.65	0.65	0.00	0.00	0.00	0.00	0.00	0.00	0.00	0.00	0.00	0.00
Distal radii	0.93	0.93	0.00	0.00	0.00	0.00	0.00	0.00	0.00	0.00	0.00	0.00
Proximal ulnae	0.96	0.96	0.00	0.00	0.00	0.00	0.00	0.00	0.00	0.00	0.00	0.00
Distal ulnae	0.99	0.99	0.00	0.00	0.00	0.00	0.00	0.00	0.00	0.00	0.00	0.00
Wrists and hands	4.27	4.27	0.00	0.00	0.00	0.00	0.00	0.00	0.00	0.00	0.00	0.00
Other Cartilage												
Cranial cap	11.14	11.14	4.55	4.55	0.00	0.00	0.00	0.00	0.00	0.00	0.00	0.00
Costal cartilage of the ribs	11.54	11.54	23.07	23.07	22.81	22.81	42.33	42.33	72.87	86.40	52.53	38.01
Cervical discs	0.23	0.23	1.49	1.49	1.03	1.03	2.67	2.67	2.39	2.70	1.93	2.73
Thoracic discs	0.77	0.77	5.57	5.57	16.88	16.88	36.14	36.14	36.66	34.86	33.92	34.70
Lumbar discs	0.53	0.53	3.57	3.57	14.04	14.04	34.60	34.60	23.53	22.34	31.56	15.30
Cortical Bone												
Cranium	21.24	21.24	91.06	91.06	214.85	214.85	308.12	308.12	528.48	409.73	1222.18	582.35
Mandible	1.72	1.72	7.05	7.05	17.30	17.30	21.38	21.38	51.70	42.08	32.22	39.12
Scapulae	2.39	2.39	9.67	9.67	28.54	28.54	57.90	57.90	116.10	170.63	318.93	221.27
Clavicles	0.93	0.93	1.44	1.44	6.01	6.01	14.22	14.22	41.23	54.51	50.77	42.20
Sternum	0.18	0.18	0.62	0.62	2.39	2.39	5.32	5.32	22.53	16.04	37.25	18.47
Ribs	6.22	6.22	18.77	18.77	39.31	39.31	61.73	61.73	165.31	171.02	235.45	248.67
Cervical vertebrae	3.68	3.68	3.11	3.11	6.67	6.67	13.73	13.73	32.65	41.74	61.75	43.17

Table A-2. Continued.

Tissue	UFH00MF		UFH01MF		UFH05MF		UFH10MF		UFH15MF		UFHADMF	
	Male	Female										
Thoracic vertebrae	8.32	8.32	11.55	11.55	31.54	31.54	69.43	69.43	87.36	72.53	143.72	84.55
Lumbar vertebrae	2.72	2.72	6.98	6.98	15.30	15.30	37.60	37.60	35.95	46.74	119.08	79.02
Sacrum	1.11	1.11	6.57	6.57	11.16	11.16	15.69	15.69	68.97	86.31	90.95	96.06
Os coxae	6.11	6.11	21.14	21.14	55.05	55.05	125.56	125.56	194.00	213.44	418.25	278.12
Proximal femora	0.66	0.66	6.93	6.93	21.71	21.71	77.71	77.71	82.76	66.53	39.65	33.97
Upper shaft of the femora	3.14	3.14	7.21	7.21	26.65	26.65	83.88	83.88	226.85	166.63	126.09	112.91
Lower shaft of the femora	4.94	4.94	10.28	10.28	20.49	20.49	70.13	70.13	175.28	189.61	98.19	130.31
Distal femora	0.53	0.53	10.22	10.22	26.38	26.38	81.06	81.06	67.15	62.67	57.50	61.93
Proximal tibiae	0.53	0.53	8.69	8.69	26.24	26.24	90.80	90.80	100.63	89.27	45.31	41.57
Shaft of the tibiae	3.64	3.64	12.69	12.69	32.43	32.43	102.39	102.39	253.91	211.61	150.63	168.05
Distal tibiae	0.28	0.28	4.83	4.83	12.47	12.47	44.03	44.03	22.84	20.67	24.05	18.89
Proximal fibulae	0.05	0.05	0.81	0.81	2.59	2.59	8.88	8.88	12.97	9.95	8.61	5.13
Shaft of the fibulae	1.03	1.03	1.50	1.50	4.85	4.85	14.64	14.64	46.22	33.71	52.86	33.26
Distal fibulae	0.10	0.10	0.73	0.73	2.64	2.64	8.90	8.90	12.25	9.94	12.04	7.59
Patellae	0.05	0.05	0.16	0.16	1.24	1.24	2.86	2.86	20.77	17.37	6.48	6.99
Ankles and feet	1.19	1.19	7.17	7.17	32.34	32.34	89.81	89.81	213.07	171.85	286.01	218.29
Proximal humera	0.44	0.44	6.04	6.04	14.83	14.83	46.62	46.62	45.91	34.17	49.66	27.58
Upper shaft of the humera	1.58	1.58	6.60	6.60	13.53	13.53	40.06	40.06	108.16	88.64	109.50	83.40
Lower shaft of the humera	1.50	1.50	5.13	5.13	11.78	11.78	33.51	33.51	96.28	76.94	97.88	72.55
Distal humera	0.24	0.24	4.21	4.21	10.09	10.09	33.33	33.33	73.99	56.27	61.91	35.13
Proximal radii	0.07	0.07	1.27	1.27	2.46	2.46	7.99	7.99	10.16	7.24	9.51	5.77
Shaft of the radii	1.01	1.01	2.78	2.78	8.08	8.08	22.34	22.34	72.59	65.85	78.03	58.90
Distal radii	0.08	0.08	1.58	1.58	4.03	4.03	12.69	12.69	13.06	9.98	17.92	7.77
Proximal ulnae	0.20	0.20	2.38	2.38	6.49	6.49	21.27	21.27	26.63	21.76	33.56	14.46
Shaft of the ulnae	1.27	1.27	4.49	4.49	10.39	10.39	28.99	28.99	88.95	77.16	93.80	69.49
Distal ulnae	0.09	0.09	0.57	0.57	1.74	1.74	5.22	5.22	5.69	4.12	4.85	2.59
Wrists and hands	0.79	0.79	9.87	9.87	9.16	9.16	31.55	31.55	126.64	105.72	170.56	141.61
Teeth	0.00	0.00	0.00	0.00	5.91	5.91	12.32	12.32	29.44	14.14	32.70	16.81

Table A-2. Continued.

Tissue	UFH00MF		UFH01MF		UFH05MF		UFH10MF		UFH15MF		UFHADMF	
	Male	Female										
Spongiosa and Medullary Cavities												
Cranium	69.28	69.28	265.98	265.98	464.79	464.79	448.50	448.50	422.09	367.99	502.90	444.06
Mandible	4.77	4.77	12.02	12.02	25.76	25.76	24.29	24.29	32.40	25.67	31.12	28.14
Scapulae	3.75	3.75	13.35	13.35	37.19	37.19	80.01	80.01	99.91	128.73	359.98	194.10
Clavicles	1.40	1.40	1.72	1.72	6.91	6.91	14.95	14.95	18.73	23.28	45.21	30.84
Sternum	0.56	0.56	1.88	1.88	7.27	7.27	18.24	18.24	35.66	24.51	49.48	31.49
Ribs	17.87	17.87	51.87	51.87	71.84	71.84	121.60	121.60	167.79	180.20	207.64	191.79
Cervical vertebrae	6.14	6.14	8.15	8.15	11.92	11.92	26.76	26.76	47.91	59.12	73.11	48.09
Thoracic vertebrae	9.14	9.14	24.93	24.93	64.24	64.24	184.46	184.46	221.66	202.41	255.75	205.79
Lumbar vertebrae	6.71	6.71	19.68	19.68	51.13	51.13	140.90	140.90	215.72	233.61	256.31	258.79
Sacrum	2.67	2.67	13.52	13.52	29.86	29.86	49.28	49.28	102.07	123.94	164.37	162.78
Os coxae	7.27	7.27	30.56	30.56	87.64	87.64	251.60	251.60	438.05	486.57	754.09	510.00
Proximal femora	4.92	4.92	7.96	7.96	22.70	22.70	66.11	66.11	215.29	163.80	268.11	195.86
Upper shaft of the femora	0.57	0.57	0.84	0.84	6.91	6.91	22.78	22.78	44.96	32.25	126.05	64.14
Lower shaft of the femora	0.92	0.92	1.38	1.38	4.83	4.83	15.51	15.51	34.04	36.18	94.70	72.95
Distal femora	4.09	4.09	7.93	7.93	25.36	25.36	81.16	81.16	277.93	246.77	302.43	236.83
Proximal tibiae	3.49	3.49	5.57	5.57	16.48	16.48	46.71	46.71	172.91	149.32	238.57	186.69
Shaft of the tibiae	0.52	0.52	1.93	1.93	7.15	7.15	24.82	24.82	57.73	47.38	145.30	76.69
Distal tibiae	2.15	2.15	1.01	1.01	3.75	3.75	9.92	9.92	75.72	65.74	84.11	67.96
Proximal fibulae	0.47	0.47	0.28	0.28	1.25	1.25	3.48	3.48	14.28	11.22	19.02	14.31
Shaft of the fibulae	0.09	0.09	0.19	0.19	1.66	1.66	5.21	5.21	7.97	5.68	11.91	7.80
Distal fibulae	0.72	0.72	0.22	0.22	1.18	1.18	3.28	3.28	14.79	11.44	17.19	13.13
Patellae	0.14	0.14	0.51	0.51	4.83	4.83	11.77	11.77	21.15	16.72	35.48	25.13
Ankles and feet	3.98	3.98	18.78	18.78	64.65	64.65	150.51	150.51	364.99	291.54	396.24	269.87
Proximal humera	3.00	3.00	7.90	7.90	17.43	17.43	46.31	46.31	147.15	117.83	165.03	120.52
Upper shaft of the humera	0.25	0.25	0.74	0.74	3.16	3.16	8.80	8.80	17.67	13.99	32.82	23.34
Lower shaft of the humera	0.26	0.26	0.70	0.70	3.03	3.03	8.91	8.91	15.39	11.76	28.83	20.53
Distal humera	2.37	2.37	4.11	4.11	9.66	9.66	23.69	23.69	64.05	50.84	86.54	70.25

Table A-2. Continued.

Tissue	UFH00MF		UFH01MF		UFH05MF		UFH10MF		UFH15MF		UFHADMF	
	Male	Female										
Proximal radii	0.51	0.51	0.34	0.34	0.81	0.81	1.85	1.85	11.25	8.56	13.41	10.01
Shaft of the radii	0.10	0.10	0.32	0.32	1.98	1.98	5.93	5.93	6.41	5.52	14.54	15.77
Distal radii	0.92	0.92	0.67	0.67	2.07	2.07	4.67	4.67	23.68	17.61	24.92	20.34
Proximal ulnae	1.23	1.23	1.60	1.60	4.49	4.49	10.67	10.67	42.04	32.85	46.81	42.54
Shaft of the ulnae	0.11	0.11	0.51	0.51	2.21	2.21	6.55	6.55	8.17	6.78	18.50	18.58
Distal ulnae	0.63	0.63	0.05	0.05	0.38	0.38	0.86	0.86	7.44	5.38	9.50	6.86
Wrists and hands	2.70	2.70	2.18	2.18	15.11	15.11	35.33	35.33	57.97	46.93	57.44	43.17

Table A-3. Blood inclusive elemental compositions in mass percent for all tissues in the UFH00MF phantoms (ICRP 2002).

Tissue	Element													
	H	C	N	O	Na	Mg	P	S	Cl	Ar	K	Ca	Fe	I
Adrenals	10.47	15.59	2.44	71.22	0.02	0.00	0.02	0.12	0.04	0.00	0.04	0.00	0.02	0.00
Tongue	10.36	10.60	2.57	75.75	0.10	0.00	0.10	0.11	0.20	0.00	0.20	0.00	0.01	0.00
Esophagus	10.44	15.42	2.55	71.27	0.03	0.00	0.03	0.13	0.05	0.00	0.05	0.00	0.03	0.00
Stomach	10.44	11.94	2.69	74.25	0.10	0.00	0.10	0.13	0.20	0.00	0.13	0.00	0.03	0.00
Small intestine	10.42	11.99	2.75	74.16	0.10	0.00	0.10	0.13	0.20	0.00	0.13	0.00	0.03	0.00
Large intestine	10.42	11.98	2.74	74.16	0.10	0.00	0.10	0.13	0.20	0.00	0.13	0.00	0.03	0.00
Liver	10.20	12.76	3.12	72.88	0.10	0.00	0.24	0.20	0.20	0.00	0.27	0.00	0.03	0.00
Gall bladder wall	10.54	15.96	2.21	71.11	0.01	0.00	0.01	0.11	0.02	0.00	0.02	0.00	0.01	0.00
Pancreas	10.46	16.03	2.61	70.00	0.18	0.00	0.18	0.12	0.20	0.00	0.20	0.00	0.02	0.00
Blood	10.00	13.10	4.00	72.00	0.10	0.00	0.10	0.20	0.20	0.00	0.20	0.00	0.10	0.00
Brain	10.76	5.91	1.26	81.08	0.19	0.00	0.29	0.11	0.20	0.00	0.20	0.00	0.01	0.00
Heart	10.50	8.48	2.18	78.02	0.18	0.00	0.10	0.12	0.20	0.00	0.20	0.00	0.02	0.00
Eye	9.60	19.50	5.70	64.60	0.10	0.00	0.10	0.30	0.10	0.00	0.00	0.00	0.00	0.00
Fat	11.08	29.39	0.96	58.26	0.10	0.00	0.10	0.10	0.00	0.00	0.00	0.00	0.00	0.00
Skin	10.38	10.56	2.87	75.29	0.19	0.00	0.10	0.20	0.29	0.00	0.11	0.00	0.01	0.00
Muscle	10.39	10.35	2.43	76.13	0.10	0.00	0.10	0.10	0.20	0.00	0.20	0.00	0.00	0.00
Pituitary gland	10.54	15.96	2.21	71.11	0.01	0.00	0.01	0.11	0.02	0.00	0.02	0.00	0.01	0.00
Trachea	10.59	16.23	2.04	71.02	0.00	0.00	0.00	0.10	0.00	0.00	0.00	0.00	0.00	0.00
Larynx	9.64	10.24	2.39	74.15	0.46	0.00	1.98	0.83	0.29	0.00	0.02	0.00	0.01	0.00
Lung	10.41	9.35	2.50	76.90	0.17	0.00	0.17	0.13	0.20	0.00	0.13	0.00	0.03	0.00
Spleen	10.25	10.89	3.21	74.75	0.15	0.00	0.15	0.15	0.20	0.00	0.20	0.00	0.05	0.00
Thymus	10.54	15.96	2.21	71.11	0.01	0.00	0.01	0.11	0.02	0.00	0.02	0.00	0.01	0.00
Thyroid	10.34	12.09	2.66	74.09	0.18	0.00	0.10	0.12	0.20	0.00	0.12	0.00	0.02	0.08
Tonsils	10.54	15.96	2.21	71.11	0.01	0.00	0.01	0.11	0.02	0.00	0.02	0.00	0.01	0.00
Kidney	10.54	7.96	2.16	78.45	0.18	0.00	0.18	0.12	0.20	0.00	0.20	0.08	0.02	0.00
Ureters	10.60	16.30	2.00	71.00	0.00	0.00	0.00	0.10	0.00	0.00	0.00	0.00	0.00	0.00
Urinary	10.49	9.68	2.63	76.01	0.20	0.00	0.20	0.20	0.30	0.00	0.30	0.00	0.00	0.00
Urethra	10.60	16.30	2.00	71.00	0.00	0.00	0.00	0.10	0.00	0.00	0.00	0.00	0.00	0.00
Epididymes	10.60	16.30	2.00	71.00	0.00	0.00	0.00	0.10	0.00	0.00	0.00	0.00	0.00	0.00
Breast - Male	10.97	27.77	1.26	59.62	0.10	0.00	0.10	0.11	0.02	0.00	0.02	0.00	0.01	0.00
Testes	10.56	16.09	2.13	71.06	0.01	0.00	0.01	0.11	0.01	0.00	0.01	0.00	0.01	0.00

Table A-3. Continued.

Tissue	Element													
	H	C	N	O	Na	Mg	P	S	Cl	Ar	K	Ca	Fe	I
Prostate	10.53	15.93	2.23	71.12	0.01	0.00	0.01	0.11	0.02	0.00	0.02	0.00	0.01	0.00
Breast - Female	10.99	28.10	1.20	59.35	0.10	0.00	0.10	0.11	0.02	0.00	0.02	0.00	0.01	0.00
Ovaries	10.55	16.04	2.16	71.08	0.01	0.00	0.01	0.11	0.02	0.00	0.02	0.00	0.01	0.00
Fallopian tubes	10.60	16.30	2.00	71.00	0.00	0.00	0.00	0.10	0.00	0.00	0.00	0.00	0.00	0.00
Uterus	10.54	15.99	2.19	71.10	0.01	0.00	0.01	0.11	0.02	0.00	0.02	0.00	0.01	0.00
Cartilage	9.61	9.94	2.22	74.37	0.49	0.00	2.17	0.89	0.30	0.00	0.00	0.00	0.00	0.00
Teeth	2.20	9.50	2.90	42.10	0.00	0.70	13.70	0.00	0.00	0.00	28.90	0.00	0.00	0.00
Bulk soft tissue	10.60	16.30	2.00	71.00	0.00	0.00	0.00	0.10	0.00	0.00	0.00	0.00	0.00	0.00
Soft tissue - Female	10.60	31.50	2.40	54.70	0.10	0.00	0.20	0.20	0.10	0.00	0.20	0.00	0.00	0.00
Water	11.20	0.00	0.00	88.80	0.00	0.00	0.00	0.00	0.00	0.00	0.00	0.00	0.00	0.00
Air	0.00	0.01	75.53	23.18	0.00	0.00	0.00	0.00	0.00	1.28	0.00	0.00	0.00	0.00
Lens	9.60	19.50	5.70	64.60	0.10	0.00	0.10	0.30	0.10	0.00	0.00	0.00	0.00	0.00
Cortical bone	4.53	15.83	4.47	51.44	0.01	0.28	7.55	0.29	0.01	0.00	0.01	15.56	0.01	0.00
Spongiosa/MC														
Cranium	6.29	19.39	4.19	53.36	0.04	0.23	5.31	0.27	0.04	0.00	0.04	10.82	0.03	0.00
Mandible	7.93	25.30	3.91	52.47	0.07	0.20	3.25	0.24	0.05	0.00	0.05	6.47	0.06	0.00
Vertebrae - C	7.06	22.16	4.06	52.94	0.06	0.21	4.34	0.26	0.04	0.00	0.05	8.77	0.04	0.00
Vertebrae - T	6.95	21.76	4.09	53.00	0.06	0.22	4.48	0.26	0.04	0.00	0.05	9.07	0.04	0.00
Vertebrae - L	7.34	23.15	4.02	52.79	0.06	0.21	4.00	0.26	0.04	0.00	0.05	8.05	0.04	0.00
Sternum	7.92	25.24	3.92	52.48	0.07	0.20	3.27	0.25	0.05	0.00	0.05	6.51	0.05	0.00
Ribs	7.93	25.30	3.91	52.47	0.07	0.20	3.25	0.24	0.05	0.00	0.05	6.47	0.06	0.00
Scapulae	7.81	24.84	3.94	52.54	0.07	0.20	3.42	0.25	0.05	0.00	0.05	6.81	0.05	0.00
Clavicles	7.81	24.84	3.94	52.54	0.07	0.20	3.42	0.25	0.05	0.00	0.05	6.81	0.05	0.00
Os Coxae	7.81	24.84	3.94	52.54	0.07	0.20	3.42	0.25	0.05	0.00	0.05	6.81	0.05	0.00
Sacrum	7.34	23.15	4.02	52.79	0.06	0.21	4.00	0.26	0.04	0.00	0.05	8.05	0.04	0.00
Humera-proximal	7.34	23.15	4.02	52.79	0.06	0.21	4.00	0.26	0.04	0.00	0.05	8.05	0.04	0.00
Humera-distal	7.34	23.15	4.02	52.79	0.06	0.21	4.00	0.26	0.04	0.00	0.05	8.05	0.04	0.00
Radii-proximal	7.34	23.15	4.02	52.79	0.06	0.21	4.00	0.26	0.04	0.00	0.05	8.05	0.04	0.00
Radii-distal	7.34	23.15	4.02	52.79	0.06	0.21	4.00	0.26	0.04	0.00	0.05	8.05	0.04	0.00
Ulnae-proximal	7.34	23.15	4.02	52.79	0.06	0.21	4.00	0.26	0.04	0.00	0.05	8.05	0.04	0.00

Table A-3. Continued.

Tissue	Element													
	H	C	N	O	Na	Mg	P	S	Cl	Ar	K	Ca	Fe	I
Ulnae-distal	7.34	23.15	4.02	52.79	0.06	0.21	4.00	0.26	0.04	0.00	0.05	8.05	0.04	0.00
Wrists and hands	7.93	25.30	3.91	52.47	0.07	0.20	3.25	0.24	0.05	0.00	0.05	6.47	0.06	0.00
Femora-proximal	7.34	23.15	4.02	52.79	0.06	0.21	4.00	0.26	0.04	0.00	0.05	8.05	0.04	0.00
Femora-distal	7.34	23.15	4.02	52.79	0.06	0.21	4.00	0.26	0.04	0.00	0.05	8.05	0.04	0.00
Patellae	7.93	25.30	3.91	52.47	0.07	0.20	3.25	0.24	0.05	0.00	0.05	6.47	0.06	0.00
Tibiae-proximal	7.34	23.15	4.02	52.79	0.06	0.21	4.00	0.26	0.04	0.00	0.05	8.05	0.04	0.00
Tibiae-distal	7.34	23.15	4.02	52.79	0.06	0.21	4.00	0.26	0.04	0.00	0.05	8.05	0.04	0.00
Fibulae-proximal	7.34	23.15	4.02	52.79	0.06	0.21	4.00	0.26	0.04	0.00	0.05	8.05	0.04	0.00
Fibulae-distal	7.34	23.15	4.02	52.79	0.06	0.21	4.00	0.26	0.04	0.00	0.05	8.05	0.04	0.00
Ankles and feet	7.93	25.30	3.91	52.47	0.07	0.20	3.25	0.24	0.05	0.00	0.05	6.47	0.06	0.00
Humera-upper shaft	10.39	34.05	3.50	51.19	0.11	0.15	0.19	0.21	0.05	0.00	0.06	0.00	0.09	0.00
Humera-lower shaft	10.39	34.05	3.50	51.19	0.11	0.15	0.19	0.21	0.05	0.00	0.06	0.00	0.09	0.00
Radii-shaft	10.39	34.05	3.50	51.19	0.11	0.15	0.19	0.21	0.05	0.00	0.06	0.00	0.09	0.00
Ulnae-shaft	10.39	34.05	3.50	51.19	0.11	0.15	0.19	0.21	0.05	0.00	0.06	0.00	0.09	0.00
Femora-upper shaft	10.39	34.05	3.50	51.19	0.11	0.15	0.19	0.21	0.05	0.00	0.06	0.00	0.09	0.00
Femora-lower shaft	10.39	34.05	3.50	51.19	0.11	0.15	0.19	0.21	0.05	0.00	0.06	0.00	0.09	0.00
Tibiae-shaft	10.39	34.05	3.50	51.19	0.11	0.15	0.19	0.21	0.05	0.00	0.06	0.00	0.09	0.00
Fibulae-shaft	10.39	34.05	3.50	51.19	0.11	0.15	0.19	0.21	0.05	0.00	0.06	0.00	0.09	0.00
Lymph nodes	10.57	16.13	2.10	71.05	0.01	0.00	0.01	0.11	0.01	0.00	0.01	0.00	0.01	0.00
Ears	9.64	10.24	2.39	74.15	0.46	0.00	1.98	0.83	0.29	0.00	0.02	0.00	0.01	0.00
External nose	9.64	10.24	2.39	74.15	0.46	0.00	1.98	0.83	0.29	0.00	0.02	0.00	0.01	0.00
Nasal layers	10.54	15.96	2.21	71.11	0.01	0.00	0.01	0.11	0.02	0.00	0.02	0.00	0.01	0.00
Oral cavity layer	10.54	15.96	2.21	71.11	0.01	0.00	0.01	0.11	0.02	0.00	0.02	0.00	0.01	0.00
Pharynx	10.54	15.96	2.21	71.11	0.01	0.00	0.01	0.11	0.02	0.00	0.02	0.00	0.01	0.00
Sal glands	10.54	15.96	2.21	71.11	0.01	0.00	0.01	0.11	0.02	0.00	0.02	0.00	0.01	0.00
Spinal cord	10.72	6.31	1.41	80.58	0.19	0.00	0.28	0.11	0.20	0.00	0.20	0.00	0.01	0.00
Penis	10.35	10.62	2.59	75.71	0.10	0.00	0.10	0.11	0.20	0.00	0.20	0.00	0.01	0.00
Scrotum	10.53	15.93	2.23	71.12	0.01	0.00	0.01	0.11	0.02	0.00	0.02	0.00	0.01	0.00

Table A-4. Blood inclusive elemental compositions in mass percent for all tissues in the UFH01MF phantoms (ICRP 2002).

Tissue	Element													
	H	C	N	O	Na	Mg	P	S	Cl	Ar	K	Ca	Fe	I
Adrenals	10.45	23.30	2.79	62.45	0.10	0.00	0.18	0.28	0.22	0.00	0.20	0.00	0.02	0.00
Tongue	10.20	14.07	3.39	71.25	0.10	0.00	0.19	0.29	0.11	0.00	0.39	0.00	0.01	0.00
Esophagus	10.44	22.74	2.82	63.00	0.10	0.00	0.18	0.28	0.22	0.00	0.20	0.00	0.02	0.00
Stomach	10.52	11.40	2.42	74.98	0.10	0.00	0.10	0.12	0.22	0.00	0.12	0.00	0.02	0.00
Small intestine	10.52	11.39	2.43	74.97	0.10	0.00	0.10	0.12	0.22	0.00	0.12	0.00	0.02	0.00
Large intestine	10.51	11.39	2.44	74.97	0.10	0.00	0.10	0.12	0.22	0.00	0.12	0.00	0.02	0.00
Liver	10.28	16.88	2.91	68.77	0.18	0.00	0.18	0.28	0.22	0.00	0.28	0.00	0.02	0.00
Gall bladder wall	10.48	24.57	2.74	61.21	0.10	0.00	0.19	0.29	0.21	0.00	0.20	0.00	0.01	0.00
Pancreas	10.53	15.93	2.38	70.24	0.18	0.00	0.18	0.12	0.22	0.00	0.20	0.00	0.02	0.00
Blood	10.20	11.00	3.30	74.50	0.10	0.00	0.10	0.20	0.30	0.00	0.20	0.00	0.10	0.00
Brain	10.68	14.37	2.24	71.32	0.20	0.00	0.39	0.20	0.30	0.00	0.30	0.00	0.00	0.00
Heart	10.38	13.54	2.95	72.14	0.10	0.00	0.19	0.20	0.21	0.00	0.29	0.00	0.01	0.00
Eye	9.60	19.50	5.70	64.60	0.10	0.00	0.10	0.30	0.10	0.00	0.00	0.00	0.00	0.00
Fat	11.38	59.13	0.74	28.45	0.10	0.00	0.10	0.10	0.00	0.00	0.00	0.00	0.00	0.00
Skin	10.01	20.03	4.16	64.90	0.20	0.00	0.10	0.20	0.30	0.00	0.10	0.00	0.00	0.00
Muscle	10.20	14.26	3.40	71.04	0.10	0.00	0.20	0.30	0.10	0.00	0.40	0.00	0.00	0.00
Pituitary gland	10.48	24.57	2.74	61.21	0.10	0.00	0.19	0.29	0.21	0.00	0.20	0.00	0.01	0.00
Trachea	10.50	25.42	2.71	60.38	0.10	0.00	0.20	0.30	0.20	0.00	0.20	0.00	0.00	0.00
Larynx	9.64	9.98	2.28	74.41	0.47	0.00	2.05	0.85	0.30	0.00	0.01	0.00	0.01	0.00
Lung	10.27	10.67	3.17	74.76	0.17	0.00	0.17	0.27	0.30	0.00	0.20	0.00	0.03	0.00
Spleen	10.26	11.19	3.24	74.24	0.10	0.00	0.23	0.20	0.24	0.00	0.26	0.00	0.04	0.00
Thymus	10.48	24.57	2.74	61.21	0.10	0.00	0.19	0.29	0.21	0.00	0.20	0.00	0.01	0.00
Thyroid	10.38	11.80	2.50	74.50	0.19	0.00	0.10	0.11	0.21	0.00	0.11	0.00	0.01	0.09
Tonsils	10.48	24.57	2.74	61.21	0.10	0.00	0.19	0.29	0.21	0.00	0.20	0.00	0.01	0.00
Kidney	10.28	12.84	3.05	72.75	0.18	0.00	0.18	0.20	0.22	0.00	0.20	0.08	0.02	0.00
Ureters	10.50	25.60	2.70	60.20	0.10	0.00	0.20	0.30	0.20	0.00	0.20	0.00	0.00	0.00
Urinary	10.50	9.62	2.61	76.07	0.20	0.00	0.20	0.20	0.30	0.00	0.30	0.00	0.00	0.00
Urethra	10.50	25.60	2.70	60.20	0.10	0.00	0.20	0.30	0.20	0.00	0.20	0.00	0.00	0.00
Epididymes	10.50	25.60	2.70	60.20	0.10	0.00	0.20	0.30	0.20	0.00	0.20	0.00	0.00	0.00
Breast - Male	11.31	56.19	0.89	31.25	0.10	0.00	0.01	0.11	0.11	0.00	0.01	0.00	0.01	0.00
Testes	10.58	9.95	2.06	76.50	0.20	0.00	0.10	0.20	0.20	0.00	0.20	0.00	0.00	0.00

Table A-4. Continued.

Tissue	Element													
	H	C	N	O	Na	Mg	P	S	Cl	Ar	K	Ca	Fe	I
Prostate	10.48	24.52	2.74	61.26	0.10	0.00	0.19	0.29	0.21	0.00	0.20	0.00	0.01	0.00
Breast - Female	11.51	49.16	0.22	39.05	0.01	0.00	0.01	0.01	0.02	0.00	0.01	0.00	0.01	0.00
Ovaries	10.48	24.76	2.73	61.02	0.10	0.00	0.19	0.29	0.21	0.00	0.20	0.00	0.01	0.00
Fallopian tubes	10.60	31.50	2.40	54.70	0.10	0.00	0.20	0.20	0.10	0.00	0.20	0.00	0.00	0.00
Uterus	10.57	30.13	2.46	56.03	0.10	0.00	0.19	0.20	0.11	0.00	0.20	0.00	0.01	0.00
Cartilage	9.64	9.98	2.28	74.41	0.47	0.00	2.05	0.85	0.30	0.00	0.01	0.00	0.01	0.00
Teeth	2.20	9.50	2.90	42.10	0.00	0.70	13.70	0.00	0.00	0.00	28.90	0.00	0.00	0.00
Bulk soft tissue	10.50	25.60	2.70	60.20	0.10	0.00	0.20	0.30	0.20	0.00	0.20	0.00	0.00	0.00
Soft tissue - Female	10.60	31.50	2.40	54.70	0.10	0.00	0.20	0.20	0.10	0.00	0.20	0.00	0.00	0.00
Water	11.20	0.00	0.00	88.80	0.00	0.00	0.00	0.00	0.00	0.00	0.00	0.00	0.00	0.00
Air	0.00	0.01	75.53	23.18	0.00	0.00	0.00	0.00	0.00	1.28	0.00	0.00	0.00	0.00
Lens	9.60	19.50	5.70	64.60	0.10	0.00	0.10	0.30	0.10	0.00	0.00	0.00	0.00	0.00
Cortical bone	4.33	15.81	4.45	50.25	0.00	0.29	8.18	0.30	0.01	0.00	0.01	16.36	0.00	0.00
Spongiosa/MC														
Cranium	6.14	20.22	4.11	51.61	0.04	0.24	5.80	0.27	0.04	0.00	0.04	11.47	0.03	0.00
Mandible	6.31	20.84	4.08	51.50	0.04	0.24	5.59	0.27	0.04	0.00	0.04	11.04	0.03	0.00
Vertebrae - C	8.22	28.12	3.71	50.19	0.07	0.20	3.12	0.24	0.04	0.00	0.04	5.99	0.06	0.00
Vertebrae - T	8.67	29.83	3.63	49.89	0.08	0.19	2.54	0.24	0.04	0.00	0.04	4.80	0.06	0.00
Vertebrae - L	7.56	25.61	3.84	50.65	0.06	0.21	3.97	0.24	0.04	0.00	0.04	7.73	0.05	0.00
Sternum	7.80	26.53	3.79	50.48	0.06	0.21	3.65	0.24	0.04	0.00	0.04	7.09	0.05	0.00
Ribs	7.79	26.48	3.79	50.49	0.06	0.21	3.67	0.24	0.04	0.00	0.04	7.13	0.05	0.00
Scapulae	7.44	25.14	3.87	50.73	0.06	0.22	4.13	0.25	0.04	0.00	0.04	8.06	0.05	0.00
Clavicles	7.36	24.85	3.87	50.78	0.06	0.22	4.23	0.25	0.04	0.00	0.04	8.26	0.05	0.00
Os Coxae	8.17	27.95	3.72	50.23	0.07	0.20	3.17	0.24	0.04	0.00	0.04	6.11	0.06	0.00
Sacrum	7.54	25.53	3.85	50.66	0.06	0.21	3.99	0.25	0.04	0.00	0.04	7.79	0.05	0.00
Humera-proximal	6.73	22.35	4.01	51.32	0.05	0.23	5.03	0.26	0.04	0.00	0.04	9.91	0.04	0.00
Humera-distal	6.73	22.86	3.95	50.77	0.05	0.23	5.07	0.26	0.04	0.00	0.04	9.99	0.04	0.00
Radii-proximal	6.64	22.41	3.98	50.95	0.05	0.23	5.17	0.26	0.04	0.00	0.04	10.20	0.03	0.00
Radii-distal	6.50	21.85	4.01	51.08	0.05	0.23	5.35	0.26	0.04	0.00	0.04	10.56	0.03	0.00
Ulnae-proximal	6.13	20.38	4.09	51.40	0.04	0.24	5.83	0.27	0.04	0.00	0.04	11.54	0.03	0.00
Ulnae-distal	7.34	25.18	3.83	50.35	0.06	0.21	4.28	0.25	0.04	0.00	0.04	8.38	0.04	0.00

Table A-4. Continued.

Tissue	Element													
	H	C	N	O	Na	Mg	P	S	Cl	Ar	K	Ca	Fe	I
Wrists and hands	7.47	28.53	3.46	47.28	0.05	0.18	4.29	0.24	0.04	0.00	0.04	8.40	0.03	0.00
Femora-proximal	6.90	23.00	3.98	51.21	0.05	0.23	4.81	0.26	0.04	0.00	0.04	9.45	0.04	0.00
Femora-distal	7.25	24.96	3.83	50.29	0.05	0.21	4.40	0.25	0.04	0.00	0.04	8.63	0.04	0.00
Patellae	8.15	28.43	3.66	49.65	0.07	0.20	3.23	0.24	0.04	0.00	0.04	6.24	0.06	0.00
Tibiae-proximal	6.82	23.11	3.94	50.80	0.05	0.23	4.95	0.26	0.04	0.00	0.04	9.74	0.04	0.00
Tibiae-distal	7.08	24.16	3.89	50.58	0.05	0.22	4.61	0.25	0.04	0.00	0.04	9.05	0.04	0.00
Fibulae-proximal	6.69	22.58	3.97	50.92	0.05	0.23	5.11	0.26	0.04	0.00	0.04	10.09	0.04	0.00
Fibulae-distal	6.73	22.77	3.96	50.88	0.05	0.23	5.06	0.26	0.04	0.00	0.04	9.96	0.04	0.00
Ankles and feet	7.55	28.95	3.44	47.11	0.05	0.18	4.19	0.24	0.04	0.00	0.04	8.20	0.03	0.00
Humera-upper shaft	10.50	37.12	3.24	48.31	0.11	0.15	0.19	0.20	0.05	0.00	0.04	0.00	0.09	0.00
Humera-lower shaft	10.52	37.50	3.20	47.96	0.11	0.15	0.19	0.20	0.05	0.00	0.04	0.00	0.08	0.00
Radii-shaft	10.53	37.89	3.16	47.61	0.11	0.15	0.19	0.20	0.05	0.00	0.04	0.00	0.08	0.00
Ulnae-shaft	10.53	37.89	3.16	47.61	0.11	0.15	0.19	0.20	0.05	0.00	0.04	0.00	0.08	0.00
Femora-upper shaft	10.50	37.12	3.24	48.31	0.11	0.15	0.19	0.20	0.05	0.00	0.04	0.00	0.09	0.00
Femora-lower shaft	10.52	37.50	3.20	47.96	0.11	0.15	0.19	0.20	0.05	0.00	0.04	0.00	0.08	0.00
Tibiae-shaft	10.53	37.89	3.16	47.61	0.11	0.15	0.19	0.20	0.05	0.00	0.04	0.00	0.08	0.00
Fibulae-shaft	10.53	37.89	3.16	47.61	0.11	0.15	0.19	0.20	0.05	0.00	0.04	0.00	0.08	0.00
Lymph nodes	10.49	25.06	2.72	60.73	0.10	0.00	0.20	0.30	0.20	0.00	0.20	0.00	0.00	0.00
Ears	9.64	9.98	2.28	74.41	0.47	0.00	2.05	0.85	0.30	0.00	0.01	0.00	0.01	0.00
External nose	9.64	9.98	2.28	74.41	0.47	0.00	2.05	0.85	0.30	0.00	0.01	0.00	0.01	0.00
Nasal layers	10.48	24.57	2.74	61.21	0.10	0.00	0.19	0.29	0.21	0.00	0.20	0.00	0.01	0.00
Oral cavity layer	10.48	24.57	2.74	61.21	0.10	0.00	0.19	0.29	0.21	0.00	0.20	0.00	0.01	0.00
Pharynx	10.48	24.57	2.74	61.21	0.10	0.00	0.19	0.29	0.21	0.00	0.20	0.00	0.01	0.00
Sal glands	10.48	24.57	2.74	61.21	0.10	0.00	0.19	0.29	0.21	0.00	0.20	0.00	0.01	0.00
Spinal cord	10.66	14.25	2.28	71.43	0.19	0.00	0.38	0.20	0.30	0.00	0.29	0.00	0.01	0.00
Penis	10.20	14.06	3.39	71.26	0.10	0.00	0.19	0.29	0.11	0.00	0.39	0.00	0.01	0.00
Scrotum	10.48	24.52	2.74	61.26	0.10	0.00	0.19	0.29	0.21	0.00	0.20	0.00	0.01	0.00

Table A-5. Blood inclusive elemental compositions in mass percent for all tissues in the UFH05MF phantoms (ICRP 2002).

Tissue	Element													
	H	C	N	O	Na	Mg	P	S	Cl	Ar	K	Ca	Fe	I
Adrenals	10.44	22.63	2.82	63.11	0.10	0.00	0.18	0.28	0.22	0.00	0.20	0.00	0.02	0.00
Tongue	10.20	13.85	3.39	71.48	0.10	0.00	0.19	0.29	0.13	0.00	0.37	0.00	0.01	0.00
Esophagus	10.42	21.89	2.85	63.84	0.10	0.00	0.17	0.27	0.23	0.00	0.20	0.00	0.03	0.00
Stomach	10.50	11.37	2.48	74.95	0.10	0.00	0.10	0.13	0.23	0.00	0.13	0.00	0.03	0.00
Small intestine	10.49	11.36	2.51	74.93	0.10	0.00	0.10	0.13	0.23	0.00	0.13	0.00	0.03	0.00
Large intestine	10.49	11.36	2.51	74.93	0.10	0.00	0.10	0.13	0.23	0.00	0.13	0.00	0.03	0.00
Liver	10.27	16.37	2.95	69.28	0.17	0.00	0.17	0.27	0.23	0.00	0.27	0.00	0.03	0.00
Gall bladder wall	10.46	23.61	2.78	62.15	0.10	0.00	0.19	0.29	0.21	0.00	0.20	0.00	0.01	0.00
Pancreas	10.51	15.64	2.43	70.49	0.18	0.00	0.18	0.12	0.22	0.00	0.20	0.00	0.02	0.00
Blood	10.20	11.00	3.30	74.50	0.10	0.00	0.10	0.20	0.30	0.00	0.20	0.00	0.10	0.00
Brain	10.67	14.30	2.26	71.39	0.19	0.00	0.38	0.20	0.30	0.00	0.29	0.00	0.01	0.00
Heart	10.37	13.43	2.97	72.24	0.10	0.00	0.18	0.20	0.22	0.00	0.28	0.00	0.02	0.00
Eye	9.60	19.50	5.70	64.60	0.10	0.00	0.10	0.30	0.10	0.00	0.00	0.00	0.00	0.00
Fat	11.38	58.92	0.75	28.64	0.10	0.00	0.10	0.10	0.01	0.00	0.00	0.00	0.00	0.00
Skin	10.01	19.96	4.16	64.97	0.20	0.00	0.10	0.20	0.30	0.00	0.10	0.00	0.00	0.00
Muscle	10.20	14.24	3.40	71.07	0.10	0.00	0.20	0.30	0.10	0.00	0.40	0.00	0.00	0.00
Pituitary gland	10.46	23.61	2.78	62.15	0.10	0.00	0.19	0.29	0.21	0.00	0.20	0.00	0.01	0.00
Trachea	10.50	25.37	2.71	60.43	0.10	0.00	0.20	0.30	0.20	0.00	0.20	0.00	0.00	0.00
Larynx	9.68	10.05	2.35	74.41	0.45	0.00	1.91	0.80	0.30	0.00	0.03	0.00	0.01	0.00
Lung	10.25	10.73	3.19	74.71	0.15	0.00	0.15	0.25	0.30	0.00	0.20	0.00	0.05	0.00
Spleen	10.25	11.16	3.25	74.29	0.10	0.00	0.21	0.20	0.25	0.00	0.25	0.00	0.05	0.00
Thymus	10.46	23.61	2.78	62.15	0.10	0.00	0.19	0.29	0.21	0.00	0.20	0.00	0.01	0.00
Thyroid	10.37	11.76	2.54	74.50	0.18	0.00	0.10	0.12	0.22	0.00	0.12	0.00	0.02	0.08
Tonsils	10.46	23.61	2.78	62.15	0.10	0.00	0.19	0.29	0.21	0.00	0.20	0.00	0.01	0.00
Kidney	10.27	12.50	3.10	73.07	0.17	0.00	0.17	0.20	0.23	0.00	0.20	0.07	0.03	0.00
Ureters	10.50	25.60	2.70	60.20	0.10	0.00	0.20	0.30	0.20	0.00	0.20	0.00	0.00	0.00
Urinary	10.49	9.63	2.61	76.07	0.20	0.00	0.20	0.20	0.30	0.00	0.30	0.00	0.00	0.00
Urethra	10.50	25.60	2.70	60.20	0.10	0.00	0.20	0.30	0.20	0.00	0.20	0.00	0.00	0.00
Epididymes	10.50	25.60	2.70	60.20	0.10	0.00	0.20	0.30	0.20	0.00	0.20	0.00	0.00	0.00
Breast - Male	11.24	53.18	1.05	34.14	0.10	0.00	0.01	0.11	0.13	0.00	0.03	0.00	0.01	0.00
Testes	10.58	9.97	2.08	76.47	0.19	0.00	0.10	0.20	0.21	0.00	0.20	0.00	0.01	0.00

Table A-5. Continued.

Tissue	Element													
	H	C	N	O	Na	Mg	P	S	Cl	Ar	K	Ca	Fe	I
Prostate	10.46	23.62	2.78	62.14	0.10	0.00	0.19	0.29	0.21	0.00	0.20	0.00	0.01	0.00
Breast - Female	11.41	46.28	0.45	41.72	0.01	0.00	0.01	0.03	0.04	0.00	0.03	0.00	0.01	0.00
Ovaries	10.48	24.51	2.74	61.26	0.10	0.00	0.19	0.29	0.21	0.00	0.20	0.00	0.01	0.00
Fallopian tubes	10.60	31.50	2.40	54.70	0.10	0.00	0.20	0.20	0.10	0.00	0.20	0.00	0.00	0.00
Uterus	10.55	28.68	2.52	57.42	0.10	0.00	0.19	0.20	0.13	0.00	0.20	0.00	0.01	0.00
Cartilage	9.63	9.96	2.26	74.41	0.48	0.00	2.09	0.86	0.30	0.00	0.01	0.00	0.01	0.00
Teeth	2.20	9.50	2.90	42.10	0.00	0.70	13.70	0.00	0.00	0.00	28.90	0.00	0.00	0.00
Bulk soft tissue	10.50	25.60	2.70	60.20	0.10	0.00	0.20	0.30	0.20	0.00	0.20	0.00	0.00	0.00
Soft tissue - Female	10.60	31.50	2.40	54.70	0.10	0.00	0.20	0.20	0.10	0.00	0.20	0.00	0.00	0.00
Water	11.20	0.00	0.00	88.80	0.00	0.00	0.00	0.00	0.00	0.00	0.00	0.00	0.00	0.00
Air	0.00	0.01	75.53	23.18	0.00	0.00	0.00	0.00	0.00	1.28	0.00	0.00	0.00	0.00
Lens	9.60	19.50	5.70	64.60	0.10	0.00	0.10	0.30	0.10	0.00	0.00	0.00	0.00	0.00
Cortical bone	4.22	15.82	4.46	47.90	0.10	0.19	8.68	0.30	0.01	0.00	0.01	18.31	0.00	0.00
Spongiosa/MC														
Cranium	6.88	23.67	3.85	49.26	0.10	0.16	5.10	0.25	0.05	0.00	0.04	10.60	0.04	0.00
Mandible	7.18	24.97	3.78	48.98	0.10	0.16	4.71	0.25	0.05	0.00	0.04	9.76	0.04	0.00
Vertebrae - C	8.11	28.46	3.62	48.70	0.10	0.16	3.44	0.23	0.05	0.00	0.04	7.04	0.06	0.00
Vertebrae - T	8.70	30.93	3.48	48.28	0.10	0.15	2.65	0.23	0.05	0.00	0.04	5.33	0.06	0.00
Vertebrae - L	8.12	28.50	3.61	48.70	0.10	0.16	3.43	0.23	0.05	0.00	0.04	7.02	0.06	0.00
Sternum	8.84	31.52	3.45	48.17	0.10	0.15	2.46	0.22	0.05	0.00	0.04	4.94	0.07	0.00
Ribs	8.09	28.37	3.62	48.72	0.10	0.16	3.47	0.23	0.05	0.00	0.04	7.10	0.06	0.00
Scapulae	7.87	27.99	3.61	48.36	0.10	0.15	3.78	0.23	0.05	0.00	0.04	7.76	0.05	0.00
Clavicles	8.11	29.09	3.55	48.05	0.10	0.15	3.47	0.23	0.05	0.00	0.04	7.11	0.05	0.00
Os Coxae	8.55	30.99	3.44	47.66	0.10	0.15	2.89	0.23	0.05	0.00	0.04	5.86	0.06	0.00
Sacrum	8.87	32.38	3.36	47.35	0.10	0.15	2.48	0.22	0.05	0.00	0.04	4.96	0.06	0.00
Humera-proximal	7.53	26.62	3.69	48.56	0.10	0.16	4.23	0.24	0.05	0.00	0.04	8.74	0.04	0.00
Humera-distal	7.66	28.02	3.56	47.51	0.10	0.15	4.12	0.23	0.05	0.00	0.03	8.52	0.04	0.00
Radii-proximal	8.57	33.94	3.14	44.62	0.10	0.12	3.02	0.21	0.05	0.00	0.03	6.14	0.05	0.00
Radii-distal	7.88	30.31	3.37	45.92	0.10	0.13	3.90	0.23	0.05	0.00	0.03	8.04	0.04	0.00
Ulnae-proximal	7.51	28.37	3.49	46.60	0.10	0.14	4.38	0.24	0.05	0.00	0.03	9.07	0.03	0.00

Table A-5. Continued.

Tissue	Element													
	H	C	N	O	Na	Mg	P	S	Cl	Ar	K	Ca	Fe	I
Ulnae-distal	9.42	38.41	2.87	43.01	0.10	0.11	1.93	0.19	0.04	0.00	0.03	3.82	0.05	0.00
Wrists and hands	8.11	35.02	2.89	41.74	0.10	0.10	3.83	0.21	0.04	0.00	0.03	7.92	0.02	0.00
Femora-proximal	7.55	26.70	3.68	48.53	0.10	0.16	4.21	0.24	0.05	0.00	0.04	8.70	0.05	0.00
Femora-distal	7.88	29.07	3.50	47.24	0.10	0.14	3.84	0.23	0.05	0.00	0.03	7.89	0.04	0.00
Patellae	9.57	38.74	2.83	43.21	0.10	0.11	1.73	0.19	0.04	0.00	0.03	3.38	0.05	0.00
Tibiae-proximal	7.75	29.60	3.41	46.18	0.10	0.14	4.07	0.23	0.05	0.00	0.03	8.41	0.04	0.00
Tibiae-distal	8.85	35.41	3.05	44.10	0.10	0.12	2.65	0.21	0.04	0.00	0.03	5.37	0.05	0.00
Fibulae-proximal	8.59	33.92	3.14	44.71	0.10	0.12	2.99	0.21	0.05	0.00	0.03	6.09	0.05	0.00
Fibulae-distal	8.62	34.07	3.13	44.66	0.10	0.12	2.96	0.21	0.05	0.00	0.03	6.01	0.05	0.00
Ankles and feet	7.97	34.15	2.95	42.15	0.10	0.11	4.00	0.21	0.04	0.00	0.03	8.29	0.02	0.00
Humera-upper shaft	10.65	41.18	2.84	44.58	0.10	0.13	0.17	0.18	0.05	0.00	0.04	0.00	0.07	0.00
Humera-lower shaft	10.67	41.57	2.80	44.23	0.10	0.12	0.17	0.18	0.05	0.00	0.04	0.00	0.07	0.00
Radii-shaft	10.81	45.24	2.42	40.86	0.10	0.10	0.15	0.16	0.04	0.00	0.03	0.00	0.06	0.00
Ulnae-shaft	10.81	45.32	2.42	40.80	0.10	0.10	0.15	0.16	0.04	0.00	0.03	0.00	0.06	0.00
Femora-upper shaft	10.65	41.12	2.84	44.65	0.10	0.13	0.17	0.18	0.05	0.00	0.04	0.00	0.07	0.00
Femora-lower shaft	10.67	41.63	2.80	44.17	0.10	0.12	0.17	0.18	0.05	0.00	0.04	0.00	0.07	0.00
Tibiae-shaft	10.81	45.34	2.42	40.77	0.10	0.10	0.15	0.16	0.04	0.00	0.03	0.00	0.06	0.00
Fibulae-shaft	10.81	45.14	2.43	40.96	0.10	0.10	0.15	0.16	0.04	0.00	0.03	0.00	0.06	0.00
Lymph nodes	10.49	24.89	2.73	60.89	0.10	0.00	0.20	0.30	0.20	0.00	0.20	0.00	0.00	0.00
Ears	9.68	10.05	2.35	74.41	0.45	0.00	1.91	0.80	0.30	0.00	0.03	0.00	0.01	0.00
External nose	9.68	10.05	2.35	74.41	0.45	0.00	1.91	0.80	0.30	0.00	0.03	0.00	0.01	0.00
Nasal layers	10.46	23.61	2.78	62.15	0.10	0.00	0.19	0.29	0.21	0.00	0.20	0.00	0.01	0.00
Oral cavity layer	10.46	23.61	2.78	62.15	0.10	0.00	0.19	0.29	0.21	0.00	0.20	0.00	0.01	0.00
Pharynx	10.46	23.61	2.78	62.15	0.10	0.00	0.19	0.29	0.21	0.00	0.20	0.00	0.01	0.00
Sal glands	10.46	23.61	2.78	62.15	0.10	0.00	0.19	0.29	0.21	0.00	0.20	0.00	0.01	0.00
Spinal cord	10.63	14.02	2.35	71.65	0.19	0.00	0.36	0.20	0.30	0.00	0.29	0.00	0.01	0.00
Penis	10.20	13.85	3.39	71.48	0.10	0.00	0.19	0.29	0.13	0.00	0.37	0.00	0.01	0.00
Scrotum	10.46	23.62	2.78	62.14	0.10	0.00	0.19	0.29	0.21	0.00	0.20	0.00	0.01	0.00

Table A-6. Blood inclusive elemental compositions in mass percent for all tissues in the UFH10MF phantoms (ICRP 2002).

Tissue	Element													
	H	C	N	O	Na	Mg	P	S	Cl	Ar	K	Ca	Fe	I
Adrenals	10.44	22.63	2.82	63.11	0.10	0.00	0.18	0.28	0.22	0.00	0.20	0.00	0.02	0.00
Tongue	10.20	13.78	3.38	71.55	0.10	0.00	0.18	0.28	0.13	0.00	0.37	0.00	0.02	0.00
Esophagus	10.42	21.89	2.85	63.84	0.10	0.00	0.17	0.27	0.23	0.00	0.20	0.00	0.03	0.00
Stomach	10.50	11.37	2.48	74.95	0.10	0.00	0.10	0.13	0.23	0.00	0.13	0.00	0.03	0.00
Small intestine	10.49	11.36	2.51	74.93	0.10	0.00	0.10	0.13	0.23	0.00	0.13	0.00	0.03	0.00
Large intestine	10.49	11.36	2.51	74.93	0.10	0.00	0.10	0.13	0.23	0.00	0.13	0.00	0.03	0.00
Liver	10.27	16.37	2.95	69.28	0.17	0.00	0.17	0.27	0.23	0.00	0.27	0.00	0.03	0.00
Gall bladder wall	10.45	23.29	2.80	62.47	0.10	0.00	0.18	0.28	0.22	0.00	0.20	0.00	0.02	0.00
Pancreas	10.51	15.64	2.43	70.49	0.18	0.00	0.18	0.12	0.22	0.00	0.20	0.00	0.02	0.00
Blood	10.20	11.00	3.30	74.50	0.10	0.00	0.10	0.20	0.30	0.00	0.20	0.00	0.10	0.00
Brain	10.67	14.31	2.26	71.38	0.19	0.00	0.38	0.20	0.30	0.00	0.29	0.00	0.01	0.00
Heart	10.37	13.43	2.97	72.24	0.10	0.00	0.18	0.20	0.22	0.00	0.28	0.00	0.02	0.00
Eye	9.60	19.50	5.70	64.60	0.10	0.00	0.10	0.30	0.10	0.00	0.00	0.00	0.00	0.00
Fat	11.38	58.92	0.75	28.64	0.10	0.00	0.10	0.10	0.01	0.00	0.00	0.00	0.00	0.00
Skin	10.01	20.06	4.17	64.86	0.20	0.00	0.10	0.20	0.30	0.00	0.10	0.00	0.00	0.00
Muscle	10.20	14.24	3.40	71.06	0.10	0.00	0.20	0.30	0.10	0.00	0.40	0.00	0.00	0.00
Pituitary gland	10.45	23.29	2.80	62.47	0.10	0.00	0.18	0.28	0.22	0.00	0.20	0.00	0.02	0.00
Trachea	10.49	25.30	2.71	60.49	0.10	0.00	0.20	0.30	0.20	0.00	0.20	0.00	0.00	0.00
Larynx	9.70	10.07	2.37	74.42	0.44	0.00	1.87	0.79	0.30	0.00	0.03	0.00	0.02	0.00
Lung	10.25	10.77	3.21	74.68	0.15	0.00	0.15	0.25	0.30	0.00	0.20	0.00	0.05	0.00
Spleen	10.25	11.16	3.25	74.29	0.10	0.00	0.21	0.20	0.25	0.00	0.25	0.00	0.05	0.00
Thymus	10.45	23.29	2.80	62.47	0.10	0.00	0.18	0.28	0.22	0.00	0.20	0.00	0.02	0.00
Thyroid	10.37	11.76	2.54	74.50	0.18	0.00	0.10	0.12	0.22	0.00	0.12	0.00	0.02	0.08
Tonsils	10.45	23.29	2.80	62.47	0.10	0.00	0.18	0.28	0.22	0.00	0.20	0.00	0.02	0.00
Kidney	10.27	12.50	3.10	73.07	0.17	0.00	0.17	0.20	0.23	0.00	0.20	0.07	0.03	0.00
Ureters	10.50	25.60	2.70	60.20	0.10	0.00	0.20	0.30	0.20	0.00	0.20	0.00	0.00	0.00
Urinary	10.49	9.63	2.61	76.07	0.20	0.00	0.20	0.20	0.30	0.00	0.30	0.00	0.00	0.00
Urethra	10.50	25.60	2.70	60.20	0.10	0.00	0.20	0.30	0.20	0.00	0.20	0.00	0.00	0.00
Epididymes	10.50	25.60	2.70	60.20	0.10	0.00	0.20	0.30	0.20	0.00	0.20	0.00	0.00	0.00
Breast - Male	11.21	51.89	1.12	35.37	0.10	0.00	0.02	0.12	0.13	0.00	0.03	0.00	0.02	0.00
Testes	10.58	9.97	2.08	76.47	0.19	0.00	0.10	0.20	0.21	0.00	0.20	0.00	0.01	0.00

Table A-6. Continued.

Tissue	Element													
	H	C	N	O	Na	Mg	P	S	Cl	Ar	K	Ca	Fe	I
Prostate	10.45	23.23	2.80	62.52	0.10	0.00	0.18	0.28	0.22	0.00	0.20	0.00	0.02	0.00
Breast - Female	11.38	45.56	0.51	42.39	0.02	0.00	0.02	0.03	0.05	0.00	0.03	0.00	0.02	0.00
Ovaries	10.48	24.51	2.74	61.26	0.10	0.00	0.19	0.29	0.21	0.00	0.20	0.00	0.01	0.00
Fallopian tubes	10.60	31.50	2.40	54.70	0.10	0.00	0.20	0.20	0.10	0.00	0.20	0.00	0.00	0.00
Uterus	10.54	28.32	2.54	57.77	0.10	0.00	0.18	0.20	0.13	0.00	0.20	0.00	0.02	0.00
Cartilage	9.62	9.93	2.23	74.40	0.49	0.00	2.14	0.88	0.30	0.00	0.01	0.00	0.00	0.00
Teeth	2.20	9.50	2.90	42.10	0.00	0.70	13.70	0.00	0.00	0.00	28.90	0.00	0.00	0.00
Bulk soft tissue	10.50	25.60	2.70	60.20	0.10	0.00	0.20	0.30	0.20	0.00	0.20	0.00	0.00	0.00
Soft tissue - Female	10.60	31.50	2.40	54.70	0.10	0.00	0.20	0.20	0.10	0.00	0.20	0.00	0.00	0.00
Water	11.20	0.00	0.00	88.80	0.00	0.00	0.00	0.00	0.00	0.00	0.00	0.00	0.00	0.00
Air	0.00	0.01	75.53	23.18	0.00	0.00	0.00	0.00	0.00	1.28	0.00	0.00	0.00	0.00
Lens	9.60	19.50	5.70	64.60	0.10	0.00	0.10	0.30	0.10	0.00	0.00	0.00	0.00	0.00
Cortical bone	4.06	15.87	4.37	46.34	0.10	0.19	9.26	0.30	0.01	0.00	0.01	19.49	0.00	0.00
Spongiosa/MC														
Cranium	7.68	28.19	3.47	47.01	0.10	0.14	4.26	0.23	0.05	0.00	0.04	8.79	0.04	0.00
Mandible	7.98	29.76	3.39	46.50	0.10	0.14	3.86	0.23	0.05	0.00	0.04	7.93	0.04	0.00
Vertebrae - C	9.03	33.18	3.31	46.87	0.10	0.15	2.34	0.22	0.05	0.00	0.04	4.66	0.07	0.00
Vertebrae - T	9.42	35.02	3.22	46.43	0.10	0.14	1.81	0.21	0.05	0.00	0.04	3.51	0.07	0.00
Vertebrae - L	8.93	32.72	3.33	46.98	0.10	0.15	2.48	0.22	0.05	0.00	0.04	4.95	0.07	0.00
Sternum	9.77	36.65	3.14	46.04	0.10	0.14	1.33	0.20	0.05	0.00	0.04	2.48	0.07	0.00
Ribs	9.19	33.94	3.27	46.69	0.10	0.15	2.12	0.21	0.05	0.00	0.04	4.19	0.07	0.00
Scapulae	8.74	33.69	3.17	45.23	0.10	0.13	2.85	0.21	0.05	0.00	0.04	5.76	0.05	0.00
Clavicles	9.19	36.27	3.01	44.19	0.10	0.12	2.27	0.20	0.05	0.00	0.03	4.51	0.06	0.00
Os Coxae	9.30	35.63	3.12	45.34	0.10	0.13	2.03	0.21	0.05	0.00	0.03	4.00	0.06	0.00
Sacrum	9.90	38.55	2.97	44.50	0.10	0.13	1.23	0.19	0.05	0.00	0.03	2.28	0.06	0.00
Humera-proximal	8.27	30.71	3.36	46.59	0.10	0.14	3.44	0.23	0.05	0.00	0.04	7.03	0.05	0.00
Humera-distal	8.54	36.85	2.76	41.08	0.10	0.10	3.37	0.20	0.04	0.00	0.03	6.91	0.03	0.00
Radii-proximal	9.01	40.64	2.47	38.84	0.10	0.08	2.82	0.19	0.04	0.00	0.03	5.75	0.03	0.00
Radii-distal	8.51	37.31	2.69	40.45	0.10	0.10	3.46	0.20	0.04	0.00	0.03	7.10	0.02	0.00
Ulnae-proximal	8.12	34.76	2.87	41.67	0.10	0.11	3.94	0.21	0.04	0.00	0.03	8.13	0.02	0.00

Table A-6. Continued.

Tissue	Element													
	H	C	N	O	Na	Mg	P	S	Cl	Ar	K	Ca	Fe	I
Ulnae-distal	9.68	44.98	2.18	36.77	0.10	0.07	1.99	0.17	0.03	0.00	0.03	3.98	0.03	0.00
Wrists and hands	9.20	45.01	2.04	34.89	0.10	0.06	2.78	0.17	0.03	0.00	0.03	5.70	0.01	0.00
Femora-proximal	8.18	30.27	3.39	46.72	0.10	0.14	3.56	0.23	0.05	0.00	0.04	7.28	0.05	0.00
Femora-distal	8.40	35.95	2.81	41.49	0.10	0.11	3.54	0.20	0.04	0.00	0.03	7.28	0.03	0.00
Patellae	10.52	50.44	1.81	34.16	0.10	0.06	0.95	0.15	0.03	0.00	0.02	1.74	0.03	0.00
Tibiae-proximal	8.64	38.15	2.64	40.05	0.10	0.09	3.30	0.20	0.04	0.00	0.03	6.76	0.02	0.00
Tibiae-distal	9.28	42.41	2.35	38.00	0.10	0.08	2.48	0.18	0.04	0.00	0.03	5.03	0.03	0.00
Fibulae-proximal	9.12	41.35	2.42	38.51	0.10	0.08	2.68	0.18	0.04	0.00	0.03	5.46	0.03	0.00
Fibulae-distal	9.14	41.47	2.41	38.45	0.10	0.08	2.67	0.18	0.04	0.00	0.03	5.41	0.03	0.00
Ankles and feet	8.99	43.51	2.15	35.70	0.10	0.06	3.03	0.17	0.03	0.00	0.03	6.22	0.01	0.00
Humera-upper shaft	10.89	47.70	2.24	38.56	0.10	0.09	0.15	0.16	0.04	0.00	0.03	0.00	0.05	0.00
Humera-lower shaft	10.90	47.95	2.21	38.33	0.10	0.09	0.15	0.16	0.04	0.00	0.03	0.00	0.05	0.00
Radii-shaft	11.16	54.68	1.53	32.15	0.10	0.05	0.13	0.13	0.03	0.00	0.02	0.00	0.02	0.00
Ulnae-shaft	11.16	54.68	1.53	32.15	0.10	0.05	0.13	0.13	0.03	0.00	0.02	0.00	0.02	0.00
Femora-upper shaft	10.89	47.70	2.24	38.56	0.10	0.09	0.15	0.16	0.04	0.00	0.03	0.00	0.05	0.00
Femora-lower shaft	10.90	47.95	2.21	38.33	0.10	0.09	0.15	0.16	0.04	0.00	0.03	0.00	0.05	0.00
Tibiae-shaft	11.16	54.68	1.53	32.15	0.10	0.05	0.13	0.13	0.03	0.00	0.02	0.00	0.02	0.00
Fibulae-shaft	11.16	54.68	1.53	32.15	0.10	0.05	0.13	0.13	0.03	0.00	0.02	0.00	0.02	0.00
Lymph nodes	10.49	24.89	2.73	60.89	0.10	0.00	0.20	0.30	0.20	0.00	0.20	0.00	0.00	0.00
Ears	9.70	10.07	2.37	74.42	0.44	0.00	1.87	0.79	0.30	0.00	0.03	0.00	0.02	0.00
External nose	9.70	10.07	2.37	74.42	0.44	0.00	1.87	0.79	0.30	0.00	0.03	0.00	0.02	0.00
Nasal layers	10.45	23.29	2.80	62.47	0.10	0.00	0.18	0.28	0.22	0.00	0.20	0.00	0.02	0.00
Oral cavity layer	10.45	23.29	2.80	62.47	0.10	0.00	0.18	0.28	0.22	0.00	0.20	0.00	0.02	0.00
Pharynx	10.45	23.29	2.80	62.47	0.10	0.00	0.18	0.28	0.22	0.00	0.20	0.00	0.02	0.00
Sal glands	10.45	23.29	2.80	62.47	0.10	0.00	0.18	0.28	0.22	0.00	0.20	0.00	0.02	0.00
Spinal cord	10.62	13.95	2.37	71.72	0.18	0.00	0.35	0.20	0.30	0.00	0.28	0.00	0.02	0.00
Penis	10.20	13.77	3.38	71.57	0.10	0.00	0.18	0.28	0.13	0.00	0.37	0.00	0.02	0.00
Scrotum	10.45	23.23	2.80	62.52	0.10	0.00	0.18	0.28	0.22	0.00	0.20	0.00	0.02	0.00

Table A-7. Blood inclusive elemental compositions in mass percent for all tissues in the UFH15M phantom (ICRP 2002).

Tissue	Element													
	H	C	N	O	Na	Mg	P	S	Cl	Ar	K	Ca	Fe	I
Adrenals	10.43	21.99	2.85	63.74	0.10	0.00	0.18	0.28	0.22	0.00	0.20	0.00	0.02	0.00
Tongue	10.20	13.66	3.38	71.67	0.10	0.00	0.18	0.28	0.14	0.00	0.36	0.00	0.02	0.00
Esophagus	10.41	21.16	2.88	64.55	0.10	0.00	0.17	0.27	0.23	0.00	0.20	0.00	0.03	0.00
Stomach	10.48	11.35	2.53	74.92	0.10	0.00	0.10	0.13	0.23	0.00	0.13	0.00	0.03	0.00
Small intestine	10.47	11.33	2.57	74.90	0.10	0.00	0.10	0.13	0.23	0.00	0.13	0.00	0.03	0.00
Large intestine	10.46	11.33	2.58	74.89	0.10	0.00	0.10	0.13	0.23	0.00	0.13	0.00	0.03	0.00
Liver	10.27	16.14	2.96	69.49	0.17	0.00	0.17	0.27	0.23	0.00	0.27	0.00	0.03	0.00
Gall bladder wall	10.44	22.79	2.82	62.95	0.10	0.00	0.18	0.28	0.22	0.00	0.20	0.00	0.02	0.00
Pancreas	10.50	15.44	2.47	70.66	0.18	0.00	0.18	0.12	0.22	0.00	0.20	0.00	0.02	0.00
Blood	10.20	11.00	3.30	74.50	0.10	0.00	0.10	0.20	0.30	0.00	0.20	0.00	0.10	0.00
Brain	10.67	14.31	2.26	71.38	0.19	0.00	0.38	0.20	0.30	0.00	0.29	0.00	0.01	0.00
Heart	10.36	13.39	2.97	72.28	0.10	0.00	0.18	0.20	0.22	0.00	0.28	0.00	0.02	0.00
Eye	9.60	19.50	5.70	64.60	0.10	0.00	0.10	0.30	0.10	0.00	0.00	0.00	0.00	0.00
Fat	11.38	58.84	0.75	28.72	0.10	0.00	0.10	0.10	0.01	0.00	0.00	0.00	0.00	0.00
Skin	10.01	19.97	4.16	64.96	0.20	0.00	0.10	0.20	0.30	0.00	0.10	0.00	0.00	0.00
Muscle	10.20	14.23	3.40	71.08	0.10	0.00	0.20	0.30	0.10	0.00	0.40	0.00	0.00	0.00
Pituitary gland	10.44	22.79	2.82	62.95	0.10	0.00	0.18	0.28	0.22	0.00	0.20	0.00	0.02	0.00
Trachea	10.48	24.76	2.73	61.02	0.10	0.00	0.19	0.29	0.21	0.00	0.20	0.00	0.01	0.00
Larynx	9.72	10.11	2.41	74.42	0.42	0.00	1.80	0.77	0.30	0.00	0.04	0.00	0.02	0.00
Lung	10.24	10.81	3.22	74.65	0.14	0.00	0.14	0.24	0.30	0.00	0.20	0.00	0.06	0.00
Spleen	10.25	11.14	3.25	74.32	0.10	0.00	0.19	0.20	0.25	0.00	0.25	0.00	0.05	0.00
Thymus	10.44	22.79	2.82	62.95	0.10	0.00	0.18	0.28	0.22	0.00	0.20	0.00	0.02	0.00
Thyroid	10.37	11.74	2.56	74.50	0.18	0.00	0.10	0.12	0.22	0.00	0.12	0.00	0.02	0.08
Tonsils	10.44	22.79	2.82	62.95	0.10	0.00	0.18	0.28	0.22	0.00	0.20	0.00	0.02	0.00
Kidney	10.26	12.37	3.11	73.19	0.16	0.00	0.16	0.20	0.24	0.00	0.20	0.06	0.04	0.00
Ureters	10.50	25.60	2.70	60.20	0.10	0.00	0.20	0.30	0.20	0.00	0.20	0.00	0.00	0.00
Urinary	10.49	9.63	2.62	76.06	0.20	0.00	0.20	0.20	0.30	0.00	0.30	0.00	0.00	0.00
Urethra	10.50	25.60	2.70	60.20	0.10	0.00	0.20	0.30	0.20	0.00	0.20	0.00	0.00	0.00
Epididymes	10.50	25.60	2.70	60.20	0.10	0.00	0.20	0.30	0.20	0.00	0.20	0.00	0.00	0.00
Breast - Male	11.17	50.41	1.20	36.79	0.10	0.00	0.02	0.12	0.14	0.00	0.04	0.00	0.02	0.00
Testes	10.57	9.97	2.09	76.46	0.19	0.00	0.10	0.20	0.21	0.00	0.20	0.00	0.01	0.00

Table A-7. Continued.

Tissue	Element													
	H	C	N	O	Na	Mg	P	S	Cl	Ar	K	Ca	Fe	I
Prostate	10.44	22.79	2.82	62.95	0.10	0.00	0.18	0.28	0.22	0.00	0.20	0.00	0.02	0.00
Breast - Female	11.49	48.79	0.25	39.39	0.01	0.00	0.01	0.02	0.02	0.00	0.02	0.00	0.01	0.00
Ovaries	10.48	24.59	2.74	61.19	0.10	0.00	0.19	0.29	0.21	0.00	0.20	0.00	0.01	0.00
Fallopian tubes	10.60	31.50	2.40	54.70	0.10	0.00	0.20	0.20	0.10	0.00	0.20	0.00	0.00	0.00
Uterus	10.57	29.94	2.47	56.20	0.10	0.00	0.19	0.20	0.12	0.00	0.20	0.00	0.01	0.00
Cartilage	9.61	9.93	2.23	74.40	0.49	0.00	2.15	0.88	0.30	0.00	0.00	0.00	0.00	0.00
Teeth	2.20	9.50	2.90	42.10	0.00	0.70	13.70	0.00	0.00	0.00	28.90	0.00	0.00	0.00
Bulk soft tissue	10.50	25.60	2.70	60.20	0.10	0.00	0.20	0.30	0.20	0.00	0.20	0.00	0.00	0.00
Soft tissue - Female	10.60	31.50	2.40	54.70	0.10	0.00	0.20	0.20	0.10	0.00	0.20	0.00	0.00	0.00
Water	11.20	0.00	0.00	88.80	0.00	0.00	0.00	0.00	0.00	0.00	0.00	0.00	0.00	0.00
Air	0.00	0.01	75.53	23.18	0.00	0.00	0.00	0.00	0.00	1.28	0.00	0.00	0.00	0.00
Lens	9.60	19.50	5.70	64.60	0.10	0.00	0.10	0.30	0.10	0.00	0.00	0.00	0.00	0.00
Cortical bone	3.93	15.89	4.28	45.82	0.20	0.20	9.30	0.30	0.01	0.00	0.00	20.07	0.00	0.00
Spongiosa/MC														
Cranium	8.16	31.01	3.18	45.85	0.14	0.12	3.60	0.22	0.05	0.00	0.04	7.58	0.04	0.00
Mandible	8.40	32.34	3.11	45.35	0.13	0.12	3.29	0.22	0.05	0.00	0.04	6.90	0.04	0.00
Vertebrae - C	9.23	33.97	3.16	46.81	0.12	0.13	2.05	0.21	0.06	0.00	0.04	4.16	0.06	0.00
Vertebrae - T	9.49	35.20	3.10	46.48	0.12	0.13	1.71	0.20	0.06	0.00	0.04	3.41	0.07	0.00
Vertebrae - L	9.67	36.07	3.06	46.25	0.11	0.13	1.47	0.20	0.06	0.00	0.04	2.88	0.07	0.00
Sternum	9.78	36.59	3.03	46.11	0.11	0.13	1.33	0.20	0.05	0.00	0.04	2.56	0.07	0.00
Ribs	9.55	35.48	3.09	46.40	0.12	0.13	1.64	0.20	0.06	0.00	0.04	3.24	0.07	0.00
Scapulae	8.25	31.47	3.16	45.68	0.14	0.12	3.50	0.22	0.05	0.00	0.04	7.35	0.04	0.00
Clavicles	9.20	37.24	2.82	43.19	0.12	0.11	2.29	0.20	0.05	0.00	0.03	4.70	0.05	0.00
Os Coxae	9.74	38.25	2.85	44.19	0.11	0.12	1.49	0.19	0.05	0.00	0.04	2.92	0.06	0.00
Sacrum	10.18	40.58	2.73	43.42	0.11	0.11	0.90	0.18	0.05	0.00	0.03	1.63	0.06	0.00
Humera-proximal	9.36	37.65	2.82	43.36	0.12	0.11	2.06	0.20	0.05	0.00	0.03	4.20	0.05	0.00
Humera-distal	9.08	44.26	2.05	35.22	0.13	0.06	2.89	0.17	0.03	0.00	0.02	6.08	0.01	0.00
Radii-proximal	9.16	44.87	2.01	34.88	0.13	0.06	2.79	0.17	0.03	0.00	0.02	5.87	0.01	0.00
Radii-distal	9.24	45.51	1.96	34.52	0.13	0.05	2.69	0.17	0.03	0.00	0.02	5.65	0.01	0.00
Ulnae-proximal	8.75	41.81	2.22	36.59	0.13	0.07	3.27	0.18	0.03	0.00	0.02	6.90	0.01	0.00

Table A-7. Continued.

Tissue	Element													
	H	C	N	O	Na	Mg	P	S	Cl	Ar	K	Ca	Fe	I
Ulnae-distal	9.34	46.24	1.91	34.12	0.13	0.05	2.58	0.17	0.03	0.00	0.02	5.40	0.01	0.00
Wrists and hands	9.98	51.07	1.58	31.44	0.12	0.04	1.82	0.15	0.02	0.00	0.02	3.75	0.01	0.00
Femora-proximal	8.95	35.39	2.94	44.20	0.13	0.12	2.59	0.20	0.05	0.00	0.04	5.35	0.05	0.00
Femora-distal	8.56	40.37	2.32	37.40	0.14	0.07	3.49	0.19	0.04	0.00	0.03	7.39	0.01	0.00
Patellae	9.98	51.07	1.58	31.44	0.12	0.04	1.82	0.15	0.02	0.00	0.02	3.75	0.01	0.00
Tibiae-proximal	10.26	53.16	1.43	30.29	0.12	0.03	1.49	0.14	0.02	0.00	0.02	3.04	0.01	0.00
Tibiae-distal	9.34	46.28	1.91	34.10	0.13	0.05	2.57	0.17	0.03	0.00	0.02	5.39	0.01	0.00
Fibulae-proximal	9.67	48.72	1.74	32.74	0.12	0.04	2.19	0.16	0.03	0.00	0.02	4.56	0.01	0.00
Fibulae-distal	8.66	41.13	2.27	36.97	0.13	0.07	3.37	0.18	0.04	0.00	0.03	7.13	0.01	0.00
Ankles and feet	9.98	51.07	1.58	31.44	0.12	0.04	1.82	0.15	0.02	0.00	0.02	3.75	0.01	0.00
Humera-upper shaft	11.04	51.31	1.85	35.26	0.10	0.06	0.13	0.15	0.03	0.00	0.02	0.00	0.04	0.00
Humera-lower shaft	11.20	55.69	1.43	31.22	0.10	0.04	0.12	0.13	0.02	0.00	0.02	0.00	0.02	0.00
Radii-shaft	11.44	61.92	0.82	25.48	0.10	0.00	0.10	0.11	0.01	0.00	0.01	0.00	0.00	0.00
Ulnae-shaft	11.44	61.92	0.82	25.48	0.10	0.00	0.10	0.11	0.01	0.00	0.01	0.00	0.00	0.00
Femora-upper shaft	11.04	51.31	1.85	35.26	0.10	0.06	0.13	0.15	0.03	0.00	0.02	0.00	0.04	0.00
Femora-lower shaft	11.20	55.69	1.43	31.22	0.10	0.04	0.12	0.13	0.02	0.00	0.02	0.00	0.02	0.00
Tibiae-shaft	11.44	61.92	0.82	25.48	0.10	0.00	0.10	0.11	0.01	0.00	0.01	0.00	0.00	0.00
Fibulae-shaft	11.44	61.92	0.82	25.48	0.10	0.00	0.10	0.11	0.01	0.00	0.01	0.00	0.00	0.00
Lymph nodes	10.48	24.80	2.73	60.99	0.10	0.00	0.19	0.29	0.21	0.00	0.20	0.00	0.01	0.00
Ears	9.72	10.11	2.41	74.42	0.42	0.00	1.80	0.77	0.30	0.00	0.04	0.00	0.02	0.00
External nose	9.72	10.11	2.41	74.42	0.42	0.00	1.80	0.77	0.30	0.00	0.04	0.00	0.02	0.00
Nasal layers	10.44	22.79	2.82	62.95	0.10	0.00	0.18	0.28	0.22	0.00	0.20	0.00	0.02	0.00
Oral cavity layer	10.44	22.79	2.82	62.95	0.10	0.00	0.18	0.28	0.22	0.00	0.20	0.00	0.02	0.00
Pharynx	10.44	22.79	2.82	62.95	0.10	0.00	0.18	0.28	0.22	0.00	0.20	0.00	0.02	0.00
Sal glands	10.44	22.79	2.82	62.95	0.10	0.00	0.18	0.28	0.22	0.00	0.20	0.00	0.02	0.00
Spinal cord	10.60	13.83	2.41	71.84	0.18	0.00	0.34	0.20	0.30	0.00	0.28	0.00	0.02	0.00
Penis	10.20	13.66	3.38	71.67	0.10	0.00	0.18	0.28	0.14	0.00	0.36	0.00	0.02	0.00
Scrotum	10.44	22.79	2.82	62.95	0.10	0.00	0.18	0.28	0.22	0.00	0.20	0.00	0.02	0.00

Table A-8. Blood inclusive elemental compositions in mass percent for all tissues in the UFH15F phantom (ICRP 2002).

Tissue	Element													
	H	C	N	O	Na	Mg	P	S	Cl	Ar	K	Ca	Fe	I
Adrenals	10.45	23.05	2.80	62.70	0.10	0.00	0.18	0.28	0.22	0.00	0.20	0.00	0.02	0.00
Tongue	10.20	14.05	3.39	71.27	0.10	0.00	0.19	0.29	0.12	0.00	0.38	0.00	0.01	0.00
Esophagus	10.44	22.44	2.83	63.30	0.10	0.00	0.18	0.28	0.22	0.00	0.20	0.00	0.02	0.00
Stomach	10.51	11.39	2.44	74.97	0.10	0.00	0.10	0.12	0.22	0.00	0.12	0.00	0.02	0.00
Small intestine	10.50	11.38	2.46	74.96	0.10	0.00	0.10	0.12	0.22	0.00	0.12	0.00	0.02	0.00
Large intestine	10.51	11.38	2.46	74.96	0.10	0.00	0.10	0.12	0.22	0.00	0.12	0.00	0.02	0.00
Liver	10.27	16.52	2.94	69.12	0.17	0.00	0.17	0.27	0.23	0.00	0.27	0.00	0.03	0.00
Gall bladder wall	10.48	24.49	2.75	61.29	0.10	0.00	0.19	0.29	0.21	0.00	0.20	0.00	0.01	0.00
Pancreas	10.52	15.78	2.41	70.37	0.18	0.00	0.18	0.12	0.22	0.00	0.20	0.00	0.02	0.00
Blood	10.20	11.00	3.30	74.50	0.10	0.00	0.10	0.20	0.30	0.00	0.20	0.00	0.10	0.00
Brain	10.68	14.36	2.24	71.33	0.20	0.00	0.39	0.20	0.30	0.00	0.30	0.00	0.00	0.00
Heart	10.37	13.46	2.96	72.21	0.10	0.00	0.18	0.20	0.22	0.00	0.28	0.00	0.02	0.00
Eye	9.60	19.50	5.70	64.60	0.10	0.00	0.10	0.30	0.10	0.00	0.00	0.00	0.00	0.00
Fat	11.38	58.98	0.74	28.58	0.10	0.00	0.10	0.10	0.01	0.00	0.00	0.00	0.00	0.00
Skin	10.01	19.99	4.16	64.94	0.20	0.00	0.10	0.20	0.30	0.00	0.10	0.00	0.00	0.00
Muscle	10.20	14.24	3.40	71.06	0.10	0.00	0.20	0.30	0.10	0.00	0.40	0.00	0.00	0.00
Pituitary gland	10.48	24.49	2.75	61.29	0.10	0.00	0.19	0.29	0.21	0.00	0.20	0.00	0.01	0.00
Trachea	10.49	24.88	2.73	60.90	0.10	0.00	0.20	0.30	0.20	0.00	0.20	0.00	0.00	0.00
Larynx	9.65	9.98	2.28	74.41	0.47	0.00	2.04	0.85	0.30	0.00	0.02	0.00	0.01	0.00
Lung	10.25	10.77	3.21	74.68	0.15	0.00	0.15	0.25	0.30	0.00	0.20	0.00	0.05	0.00
Spleen	10.26	11.18	3.24	74.26	0.10	0.00	0.22	0.20	0.24	0.00	0.26	0.00	0.04	0.00
Thymus	10.48	24.49	2.75	61.29	0.10	0.00	0.19	0.29	0.21	0.00	0.20	0.00	0.01	0.00
Thyroid	10.37	11.78	2.52	74.50	0.19	0.00	0.10	0.11	0.21	0.00	0.11	0.00	0.01	0.09
Tonsils	10.48	24.49	2.75	61.29	0.10	0.00	0.19	0.29	0.21	0.00	0.20	0.00	0.01	0.00
Kidney	10.27	12.59	3.08	72.99	0.17	0.00	0.17	0.20	0.23	0.00	0.20	0.07	0.03	0.00
Ureters	10.50	25.60	2.70	60.20	0.10	0.00	0.20	0.30	0.20	0.00	0.20	0.00	0.00	0.00
Urinary	10.49	9.63	2.61	76.07	0.20	0.00	0.20	0.20	0.30	0.00	0.30	0.00	0.00	0.00
Urethra	10.50	25.60	2.70	60.20	0.10	0.00	0.20	0.30	0.20	0.00	0.20	0.00	0.00	0.00
Epididymes	10.50	25.60	2.70	60.20	0.10	0.00	0.20	0.30	0.20	0.00	0.20	0.00	0.00	0.00
Breast - Male	11.17	50.41	1.20	36.79	0.10	0.00	0.02	0.12	0.14	0.00	0.04	0.00	0.02	0.00
Testes	10.57	9.97	2.09	76.46	0.19	0.00	0.10	0.20	0.21	0.00	0.20	0.00	0.01	0.00

Table A-8. Continued.

Tissue	Element													
	H	C	N	O	Na	Mg	P	S	Cl	Ar	K	Ca	Fe	I
Prostate	10.44	22.79	2.82	62.95	0.10	0.00	0.18	0.28	0.22	0.00	0.20	0.00	0.02	0.00
Breast - Female	11.49	48.79	0.25	39.39	0.01	0.00	0.01	0.02	0.02	0.00	0.02	0.00	0.01	0.00
Ovaries	10.48	24.59	2.74	61.19	0.10	0.00	0.19	0.29	0.21	0.00	0.20	0.00	0.01	0.00
Fallopian tubes	10.60	31.50	2.40	54.70	0.10	0.00	0.20	0.20	0.10	0.00	0.20	0.00	0.00	0.00
Uterus	10.57	29.94	2.47	56.20	0.10	0.00	0.19	0.20	0.12	0.00	0.20	0.00	0.01	0.00
Cartilage	9.61	9.92	2.22	74.40	0.49	0.00	2.16	0.89	0.30	0.00	0.00	0.00	0.00	0.00
Teeth	2.20	9.50	2.90	42.10	0.00	0.70	13.70	0.00	0.00	0.00	28.90	0.00	0.00	0.00
Bulk soft tissue	10.50	25.60	2.70	60.20	0.10	0.00	0.20	0.30	0.20	0.00	0.20	0.00	0.00	0.00
Soft tissue - Female	10.60	31.50	2.40	54.70	0.10	0.00	0.20	0.20	0.10	0.00	0.20	0.00	0.00	0.00
Water	11.20	0.00	0.00	88.80	0.00	0.00	0.00	0.00	0.00	0.00	0.00	0.00	0.00	0.00
Air	0.00	0.01	75.53	23.18	0.00	0.00	0.00	0.00	0.00	1.28	0.00	0.00	0.00	0.00
Lens	9.60	19.50	5.70	64.60	0.10	0.00	0.10	0.30	0.10	0.00	0.00	0.00	0.00	0.00
Cortical bone	3.92	15.91	4.28	45.76	0.20	0.20	9.32	0.30	0.01	0.00	0.00	20.11	0.00	0.00
Spongiosa/MC														
Cranium	8.12	31.65	3.17	45.00	0.14	0.13	3.69	0.22	0.05	0.00	0.03	7.77	0.04	0.00
Mandible	8.36	33.02	3.09	44.48	0.13	0.12	3.38	0.21	0.05	0.00	0.03	7.08	0.04	0.00
Vertebrae - C	9.20	34.87	3.15	45.76	0.12	0.14	2.12	0.21	0.05	0.00	0.03	4.29	0.06	0.00
Vertebrae - T	9.47	36.16	3.09	45.40	0.12	0.13	1.77	0.20	0.04	0.00	0.03	3.52	0.06	0.00
Vertebrae - L	9.66	37.08	3.04	45.14	0.11	0.13	1.52	0.20	0.04	0.00	0.03	2.97	0.07	0.00
Sternum	9.77	37.62	3.02	44.99	0.11	0.13	1.37	0.20	0.04	0.00	0.03	2.65	0.07	0.00
Ribs	9.53	36.46	3.07	45.31	0.12	0.13	1.69	0.20	0.04	0.00	0.03	3.35	0.06	0.00
Scapulae	8.20	32.12	3.14	44.82	0.14	0.13	3.58	0.22	0.05	0.00	0.03	7.53	0.04	0.00
Clavicles	9.18	38.04	2.80	42.28	0.12	0.11	2.34	0.19	0.04	0.00	0.03	4.82	0.04	0.00
Os Coxae	9.73	39.21	2.83	43.15	0.11	0.12	1.53	0.19	0.04	0.00	0.03	3.00	0.06	0.00
Sacrum	10.19	41.62	2.71	42.34	0.11	0.12	0.92	0.18	0.04	0.00	0.03	1.68	0.06	0.00
Humera-proximal	9.34	38.49	2.79	42.41	0.12	0.11	2.12	0.19	0.04	0.00	0.03	4.31	0.05	0.00
Humera-distal	9.07	44.69	2.03	34.74	0.13	0.06	2.91	0.17	0.03	0.00	0.02	6.13	0.01	0.00
Radii-proximal	9.15	45.30	1.99	34.41	0.13	0.06	2.82	0.17	0.03	0.00	0.02	5.92	0.01	0.00
Radii-distal	9.24	45.95	1.95	34.05	0.13	0.06	2.71	0.17	0.03	0.00	0.02	5.70	0.01	0.00
Ulnae-proximal	8.74	42.26	2.20	36.09	0.13	0.07	3.30	0.18	0.03	0.00	0.02	6.97	0.01	0.00

Table A-8. Continued.

Tissue	Element													
	H	C	N	O	Na	Mg	P	S	Cl	Ar	K	Ca	Fe	I
Ulnae-distal	9.33	46.67	1.90	33.66	0.13	0.05	2.60	0.16	0.03	0.00	0.02	5.45	0.01	0.00
Wrists and hands	9.98	51.48	1.56	31.03	0.12	0.04	1.83	0.15	0.02	0.00	0.02	3.78	0.01	0.00
Femora-proximal	8.92	36.16	2.92	43.29	0.13	0.12	2.65	0.20	0.04	0.00	0.03	5.49	0.05	0.00
Femora-distal	8.55	40.81	2.30	36.89	0.14	0.07	3.52	0.18	0.03	0.00	0.02	7.46	0.01	0.00
Patellae	9.98	51.48	1.56	31.03	0.12	0.04	1.83	0.15	0.02	0.00	0.02	3.78	0.01	0.00
Tibiae-proximal	10.26	53.55	1.42	29.90	0.12	0.03	1.50	0.14	0.02	0.00	0.02	3.05	0.01	0.00
Tibiae-distal	9.34	46.71	1.89	33.64	0.13	0.05	2.59	0.16	0.03	0.00	0.02	5.43	0.01	0.00
Fibulae-proximal	9.66	49.14	1.72	32.31	0.12	0.04	2.21	0.15	0.02	0.00	0.02	4.59	0.01	0.00
Fibulae-distal	8.65	41.57	2.25	36.47	0.14	0.07	3.40	0.18	0.03	0.00	0.02	7.20	0.01	0.00
Ankles and feet	9.98	51.48	1.56	31.03	0.12	0.04	1.83	0.15	0.02	0.00	0.02	3.78	0.01	0.00
Humera-upper shaft	11.06	52.18	1.81	34.42	0.10	0.07	0.14	0.14	0.02	0.00	0.02	0.00	0.04	0.00
Humera-lower shaft	11.22	56.35	1.40	30.59	0.10	0.04	0.12	0.13	0.02	0.00	0.02	0.00	0.02	0.00
Radii-shaft	11.44	62.23	0.81	25.19	0.10	0.00	0.10	0.11	0.01	0.00	0.01	0.00	0.00	0.00
Ulnae-shaft	11.44	62.23	0.81	25.19	0.10	0.00	0.10	0.11	0.01	0.00	0.01	0.00	0.00	0.00
Femora-upper shaft	11.06	52.18	1.81	34.42	0.10	0.07	0.14	0.14	0.02	0.00	0.02	0.00	0.04	0.00
Femora-lower shaft	11.22	56.35	1.40	30.59	0.10	0.04	0.12	0.13	0.02	0.00	0.02	0.00	0.02	0.00
Tibiae-shaft	11.44	62.23	0.81	25.19	0.10	0.00	0.10	0.11	0.01	0.00	0.01	0.00	0.00	0.00
Fibulae-shaft	11.44	62.23	0.81	25.19	0.10	0.00	0.10	0.11	0.01	0.00	0.01	0.00	0.00	0.00
Lymph nodes	10.49	24.97	2.73	60.82	0.10	0.00	0.20	0.30	0.20	0.00	0.20	0.00	0.00	0.00
Ears	9.65	9.98	2.28	74.41	0.47	0.00	2.04	0.85	0.30	0.00	0.02	0.00	0.01	0.00
External nose	9.65	9.98	2.28	74.41	0.47	0.00	2.04	0.85	0.30	0.00	0.02	0.00	0.01	0.00
Nasal layers	10.48	24.49	2.75	61.29	0.10	0.00	0.19	0.29	0.21	0.00	0.20	0.00	0.01	0.00
Oral cavity layer	10.48	24.49	2.75	61.29	0.10	0.00	0.19	0.29	0.21	0.00	0.20	0.00	0.01	0.00
Pharynx	10.48	24.49	2.75	61.29	0.10	0.00	0.19	0.29	0.21	0.00	0.20	0.00	0.01	0.00
Sal glands	10.48	24.49	2.75	61.29	0.10	0.00	0.19	0.29	0.21	0.00	0.20	0.00	0.01	0.00
Spinal cord	10.66	14.23	2.28	71.45	0.19	0.00	0.38	0.20	0.30	0.00	0.29	0.00	0.01	0.00
Penis	10.20	13.66	3.38	71.67	0.10	0.00	0.18	0.28	0.14	0.00	0.36	0.00	0.02	0.00
Scrotum	10.44	22.79	2.82	62.95	0.10	0.00	0.18	0.28	0.22	0.00	0.20	0.00	0.02	0.00

Table A-9. Blood inclusive elemental compositions in mass percent for all tissues in the UFHADM phantom (ICRP 2002).

Tissue	Element													
	H	C	N	O	Na	Mg	P	S	Cl	Ar	K	Ca	Fe	I
Adrenals	10.43	22.09	2.84	63.63	0.10	0.00	0.18	0.28	0.22	0.00	0.20	0.00	0.02	0.00
Tongue	10.20	13.57	3.38	71.77	0.10	0.00	0.18	0.28	0.14	0.00	0.36	0.00	0.02	0.00
Esophagus	10.41	21.30	2.88	64.41	0.10	0.00	0.17	0.27	0.23	0.00	0.20	0.00	0.03	0.00
Stomach	10.48	11.35	2.52	74.92	0.10	0.00	0.10	0.13	0.23	0.00	0.13	0.00	0.03	0.00
Small intestine	10.47	11.34	2.56	74.90	0.10	0.00	0.10	0.13	0.23	0.00	0.13	0.00	0.03	0.00
Large intestine	10.47	11.33	2.57	74.90	0.10	0.00	0.10	0.13	0.23	0.00	0.13	0.00	0.03	0.00
Liver	10.27	16.24	2.96	69.40	0.17	0.00	0.17	0.27	0.23	0.00	0.27	0.00	0.03	0.00
Gall bladder wall	10.43	22.37	2.83	63.36	0.10	0.00	0.18	0.28	0.22	0.00	0.20	0.00	0.02	0.00
Pancreas	10.50	15.49	2.46	70.62	0.18	0.00	0.18	0.12	0.22	0.00	0.20	0.00	0.02	0.00
Blood	10.20	11.00	3.30	74.50	0.10	0.00	0.10	0.20	0.30	0.00	0.20	0.00	0.10	0.00
Brain	10.68	14.34	2.25	71.35	0.20	0.00	0.39	0.20	0.30	0.00	0.30	0.00	0.00	0.00
Heart	10.37	13.41	2.97	72.26	0.10	0.00	0.18	0.20	0.22	0.00	0.28	0.00	0.02	0.00
Eye	9.60	19.50	5.70	64.60	0.10	0.00	0.10	0.30	0.10	0.00	0.00	0.00	0.00	0.00
Fat	11.38	58.86	0.75	28.70	0.10	0.00	0.10	0.10	0.01	0.00	0.00	0.00	0.00	0.00
Skin	10.01	19.97	4.16	64.96	0.20	0.00	0.10	0.20	0.30	0.00	0.10	0.00	0.00	0.00
Muscle	10.20	14.23	3.40	71.07	0.10	0.00	0.20	0.30	0.10	0.00	0.40	0.00	0.00	0.00
Pituitary gland	10.43	22.37	2.83	63.36	0.10	0.00	0.18	0.28	0.22	0.00	0.20	0.00	0.02	0.00
Trachea	10.49	24.96	2.73	60.83	0.10	0.00	0.20	0.30	0.20	0.00	0.20	0.00	0.00	0.00
Larynx	9.73	10.14	2.44	74.42	0.41	0.00	1.74	0.75	0.30	0.00	0.04	0.00	0.02	0.00
Lung	10.24	10.79	3.22	74.67	0.14	0.00	0.14	0.24	0.30	0.00	0.20	0.00	0.06	0.00
Spleen	10.25	11.14	3.25	74.31	0.10	0.00	0.20	0.20	0.25	0.00	0.25	0.00	0.05	0.00
Thymus	10.43	22.37	2.83	63.36	0.10	0.00	0.18	0.28	0.22	0.00	0.20	0.00	0.02	0.00
Thyroid	10.37	11.75	2.55	74.50	0.18	0.00	0.10	0.12	0.22	0.00	0.12	0.00	0.02	0.08
Tonsils	10.43	22.37	2.83	63.36	0.10	0.00	0.18	0.28	0.22	0.00	0.20	0.00	0.02	0.00
Kidney	10.26	12.40	3.11	73.16	0.16	0.00	0.16	0.20	0.24	0.00	0.20	0.06	0.04	0.00
Ureters	10.50	25.60	2.70	60.20	0.10	0.00	0.20	0.30	0.20	0.00	0.20	0.00	0.00	0.00
Urinary	10.49	9.63	2.62	76.06	0.20	0.00	0.20	0.20	0.30	0.00	0.30	0.00	0.00	0.00
Urethra	10.50	25.60	2.70	60.20	0.10	0.00	0.20	0.30	0.20	0.00	0.20	0.00	0.00	0.00
Epididymes	10.50	25.60	2.70	60.20	0.10	0.00	0.20	0.30	0.20	0.00	0.20	0.00	0.00	0.00
Breast - Male	11.13	49.01	1.27	38.13	0.10	0.00	0.02	0.12	0.14	0.00	0.04	0.00	0.02	0.00
Testes	10.57	9.97	2.08	76.47	0.19	0.00	0.10	0.20	0.21	0.00	0.20	0.00	0.01	0.00

Table A-9. Continued.

Tissue	Element													
	H	C	N	O	Na	Mg	P	S	Cl	Ar	K	Ca	Fe	I
Prostate	10.43	22.37	2.83	63.36	0.10	0.00	0.18	0.28	0.22	0.00	0.20	0.00	0.02	0.00
Breast - Female	11.47	48.05	0.31	40.07	0.01	0.00	0.01	0.02	0.03	0.00	0.02	0.00	0.01	0.00
Ovaries	10.48	24.51	2.74	61.27	0.10	0.00	0.19	0.29	0.21	0.00	0.20	0.00	0.01	0.00
Fallopian tubes	10.60	31.50	2.40	54.70	0.10	0.00	0.20	0.20	0.10	0.00	0.20	0.00	0.00	0.00
Uterus	10.56	29.57	2.48	56.56	0.10	0.00	0.19	0.20	0.12	0.00	0.20	0.00	0.01	0.00
Cartilage	9.61	9.92	2.22	74.40	0.49	0.00	2.16	0.89	0.30	0.00	0.00	0.00	0.00	0.00
Teeth	2.20	9.50	2.90	42.10	0.00	0.70	13.70	0.00	0.00	0.00	28.90	0.00	0.00	0.00
Bulk soft tissue	10.50	25.60	2.70	60.20	0.10	0.00	0.20	0.30	0.20	0.00	0.20	0.00	0.00	0.00
Soft tissue - Female	10.60	31.50	2.40	54.70	0.10	0.00	0.20	0.20	0.10	0.00	0.20	0.00	0.00	0.00
Water	11.20	0.00	0.00	88.80	0.00	0.00	0.00	0.00	0.00	0.00	0.00	0.00	0.00	0.00
Air	0.00	0.01	75.53	23.18	0.00	0.00	0.00	0.00	0.00	1.28	0.00	0.00	0.00	0.00
Lens	9.60	19.50	5.70	64.60	0.10	0.00	0.10	0.30	0.10	0.00	0.00	0.00	0.00	0.00
Cortical bone	3.57	15.95	4.19	44.81	0.30	0.20	9.40	0.30	0.00	0.00	0.00	21.28	0.00	0.00
Spongiosa/MC														
Cranium	5.94	26.80	3.47	42.18	0.23	0.16	6.44	0.25	0.01	0.00	0.01	14.48	0.02	0.00
Mandible	9.96	46.05	2.23	36.81	0.13	0.09	1.46	0.17	0.03	0.00	0.02	3.03	0.04	0.00
Vertebrae - C	8.86	35.99	3.09	43.38	0.15	0.14	2.56	0.21	0.03	0.00	0.02	5.52	0.06	0.00
Vertebrae - T	9.68	39.13	2.92	43.14	0.13	0.13	1.49	0.19	0.04	0.00	0.02	3.06	0.06	0.00
Vertebrae - L	9.60	38.23	2.95	43.77	0.13	0.13	1.59	0.19	0.04	0.00	0.03	3.29	0.06	0.00
Sternum	9.82	39.40	2.90	43.35	0.12	0.13	1.31	0.19	0.04	0.00	0.03	2.65	0.07	0.00
Ribs	9.48	37.90	2.97	43.69	0.13	0.13	1.74	0.20	0.04	0.00	0.03	3.63	0.06	0.00
Scapulae	9.27	42.53	2.45	37.96	0.15	0.10	2.30	0.18	0.03	0.00	0.02	4.98	0.04	0.00
Clavicles	9.69	46.05	2.21	35.79	0.14	0.09	1.85	0.17	0.02	0.00	0.01	3.95	0.03	0.00
Os Coxae	9.77	43.29	2.49	39.04	0.13	0.10	1.59	0.18	0.03	0.00	0.02	3.32	0.05	0.00
Sacrum	9.46	37.61	2.98	43.91	0.13	0.13	1.76	0.20	0.04	0.00	0.03	3.68	0.06	0.00
Humera-proximal	9.97	48.79	1.96	33.91	0.13	0.07	1.59	0.16	0.02	0.00	0.01	3.36	0.03	0.00
Humera-distal	9.49	50.82	1.64	29.98	0.15	0.05	2.41	0.15	0.01	0.00	0.01	5.29	0.00	0.00
Radii-proximal	10.25	55.57	1.30	27.76	0.13	0.03	1.53	0.13	0.01	0.00	0.01	3.27	0.00	0.00
Radii-distal	9.91	53.44	1.46	28.76	0.14	0.04	1.93	0.14	0.01	0.00	0.01	4.18	0.00	0.00
Ulnae-proximal	9.38	50.11	1.69	30.32	0.15	0.05	2.54	0.16	0.01	0.00	0.01	5.58	0.00	0.00
Ulnae-distal	9.63	51.73	1.58	29.54	0.15	0.05	2.25	0.15	0.01	0.00	0.01	4.91	0.00	0.00

Table A-9. Continued.

Tissue	Element													
	H	C	N	O	Na	Mg	P	S	Cl	Ar	K	Ca	Fe	I
Wrists and hands	9.49	50.86	1.64	29.93	0.15	0.05	2.41	0.15	0.01	0.00	0.01	5.29	0.00	0.00
Femora-proximal	9.37	45.52	2.17	35.15	0.15	0.08	2.31	0.17	0.02	0.00	0.01	5.02	0.02	0.00
Femora-distal	9.55	51.18	1.62	29.82	0.15	0.05	2.34	0.15	0.01	0.00	0.01	5.13	0.00	0.00
Patellae	9.55	51.18	1.62	29.81	0.15	0.05	2.34	0.15	0.01	0.00	0.01	5.13	0.00	0.00
Tibiae-proximal	9.91	53.46	1.45	28.75	0.14	0.04	1.92	0.14	0.01	0.00	0.01	4.16	0.00	0.00
Tibiae-distal	9.80	52.75	1.51	29.08	0.14	0.04	2.05	0.14	0.01	0.00	0.01	4.47	0.00	0.00
Fibulae-proximal	10.38	56.41	1.24	27.38	0.13	0.03	1.37	0.13	0.01	0.00	0.01	2.91	0.00	0.00
Fibulae-distal	9.54	51.12	1.62	29.84	0.15	0.05	2.36	0.15	0.01	0.00	0.01	5.16	0.00	0.00
Ankles and feet	9.55	51.18	1.62	29.81	0.15	0.05	2.34	0.15	0.01	0.00	0.01	5.13	0.00	0.00
Humera-upper shaft	11.18	55.52	1.52	31.32	0.10	0.05	0.12	0.13	0.02	0.00	0.01	0.00	0.03	0.00
Humera-lower shaft	11.47	63.32	0.75	24.14	0.10	0.00	0.10	0.10	0.01	0.00	0.00	0.00	0.00	0.00
Radii-shaft	11.47	63.34	0.75	24.12	0.10	0.00	0.10	0.10	0.01	0.00	0.00	0.00	0.00	0.00
Ulnae-shaft	11.48	63.38	0.75	24.08	0.10	0.00	0.10	0.10	0.01	0.00	0.00	0.00	0.00	0.00
Femora-upper shaft	11.17	55.43	1.52	31.41	0.10	0.05	0.12	0.13	0.02	0.00	0.01	0.00	0.03	0.00
Femora-lower shaft	11.47	63.28	0.75	24.17	0.10	0.00	0.10	0.10	0.01	0.00	0.00	0.00	0.00	0.00
Tibiae-shaft	11.47	63.28	0.75	24.18	0.10	0.00	0.10	0.10	0.01	0.00	0.00	0.00	0.00	0.00
Fibulae-shaft	11.47	63.31	0.75	24.15	0.10	0.00	0.10	0.10	0.01	0.00	0.00	0.00	0.00	0.00
Lymph nodes	10.48	24.82	2.73	60.96	0.10	0.00	0.19	0.29	0.21	0.00	0.20	0.00	0.01	0.00
Ears	9.73	10.14	2.44	74.42	0.41	0.00	1.74	0.75	0.30	0.00	0.04	0.00	0.02	0.00
External nose	9.73	10.14	2.44	74.42	0.41	0.00	1.74	0.75	0.30	0.00	0.04	0.00	0.02	0.00
Nasal layers	10.43	22.37	2.83	63.36	0.10	0.00	0.18	0.28	0.22	0.00	0.20	0.00	0.02	0.00
Oral cavity layer	10.43	22.37	2.83	63.36	0.10	0.00	0.18	0.28	0.22	0.00	0.20	0.00	0.02	0.00
Pharynx	10.43	22.37	2.83	63.36	0.10	0.00	0.18	0.28	0.22	0.00	0.20	0.00	0.02	0.00
Sal glands	10.43	22.37	2.83	63.36	0.10	0.00	0.18	0.28	0.22	0.00	0.20	0.00	0.02	0.00
Spinal cord	10.59	13.73	2.44	71.93	0.18	0.00	0.33	0.20	0.30	0.00	0.28	0.00	0.02	0.00
Penis	10.20	13.57	3.38	71.77	0.10	0.00	0.18	0.28	0.14	0.00	0.36	0.00	0.02	0.00
Scrotum	10.43	22.37	2.83	63.36	0.10	0.00	0.18	0.28	0.22	0.00	0.20	0.00	0.02	0.00

Table A-10. Blood inclusive elemental compositions in mass percent for all tissues in the UFHADF phantom (ICRP 2002).

Tissue	Element													
	H	C	N	O	Na	Mg	P	S	Cl	Ar	K	Ca	Fe	I
Adrenals	10.44	22.84	2.81	62.90	0.10	0.00	0.18	0.28	0.22	0.00	0.20	0.00	0.02	0.00
Tongue	10.20	13.99	3.39	71.33	0.10	0.00	0.19	0.29	0.12	0.00	0.38	0.00	0.01	0.00
Esophagus	10.43	22.18	2.84	63.55	0.10	0.00	0.18	0.28	0.22	0.00	0.20	0.00	0.02	0.00
Stomach	10.51	11.38	2.46	74.96	0.10	0.00	0.10	0.12	0.22	0.00	0.12	0.00	0.02	0.00
Small intestine	10.50	11.37	2.49	74.94	0.10	0.00	0.10	0.13	0.23	0.00	0.13	0.00	0.03	0.00
Large intestine	10.50	11.37	2.48	74.95	0.10	0.00	0.10	0.13	0.23	0.00	0.13	0.00	0.03	0.00
Liver	10.27	16.37	2.95	69.27	0.17	0.00	0.17	0.27	0.23	0.00	0.27	0.00	0.03	0.00
Gall bladder wall	10.47	24.23	2.76	61.55	0.10	0.00	0.19	0.29	0.21	0.00	0.20	0.00	0.01	0.00
Pancreas	10.52	15.69	2.43	70.45	0.18	0.00	0.18	0.12	0.22	0.00	0.20	0.00	0.02	0.00
Blood	10.20	11.00	3.30	74.50	0.10	0.00	0.10	0.20	0.30	0.00	0.20	0.00	0.10	0.00
Brain	10.68	14.37	2.24	71.32	0.20	0.00	0.39	0.20	0.30	0.00	0.30	0.00	0.00	0.00
Heart	10.37	13.42	2.97	72.24	0.10	0.00	0.18	0.20	0.22	0.00	0.28	0.00	0.02	0.00
Eye	9.60	19.50	5.70	64.60	0.10	0.00	0.10	0.30	0.10	0.00	0.00	0.00	0.00	0.00
Fat	11.38	58.90	0.75	28.66	0.10	0.00	0.10	0.10	0.01	0.00	0.00	0.00	0.00	0.00
Skin	10.01	19.95	4.16	64.98	0.20	0.00	0.10	0.20	0.30	0.00	0.10	0.00	0.00	0.00
Muscle	10.20	14.24	3.40	71.06	0.10	0.00	0.20	0.30	0.10	0.00	0.40	0.00	0.00	0.00
Pituitary gland	10.47	24.23	2.76	61.55	0.10	0.00	0.19	0.29	0.21	0.00	0.20	0.00	0.01	0.00
Trachea	10.49	24.93	2.73	60.85	0.10	0.00	0.20	0.30	0.20	0.00	0.20	0.00	0.00	0.00
Larynx	9.66	10.00	2.30	74.41	0.46	0.00	2.00	0.83	0.30	0.00	0.02	0.00	0.01	0.00
Lung	10.25	10.77	3.21	74.68	0.15	0.00	0.15	0.25	0.30	0.00	0.20	0.00	0.05	0.00
Spleen	10.26	11.17	3.24	74.28	0.10	0.00	0.21	0.20	0.24	0.00	0.26	0.00	0.04	0.00
Thymus	10.47	24.23	2.76	61.55	0.10	0.00	0.19	0.29	0.21	0.00	0.20	0.00	0.01	0.00
Thyroid	10.37	11.77	2.53	74.50	0.19	0.00	0.10	0.11	0.21	0.00	0.11	0.00	0.01	0.09
Tonsils	10.47	24.23	2.76	61.55	0.10	0.00	0.19	0.29	0.21	0.00	0.20	0.00	0.01	0.00
Kidney	10.27	12.54	3.09	73.03	0.17	0.00	0.17	0.20	0.23	0.00	0.20	0.07	0.03	0.00
Ureters	10.50	25.60	2.70	60.20	0.10	0.00	0.20	0.30	0.20	0.00	0.20	0.00	0.00	0.00
Urinary	10.49	9.63	2.61	76.07	0.20	0.00	0.20	0.20	0.30	0.00	0.30	0.00	0.00	0.00
Urethra	10.50	25.60	2.70	60.20	0.10	0.00	0.20	0.30	0.20	0.00	0.20	0.00	0.00	0.00
Epididymes	10.50	25.60	2.70	60.20	0.10	0.00	0.20	0.30	0.20	0.00	0.20	0.00	0.00	0.00
Breast - Male	11.13	49.01	1.27	38.13	0.10	0.00	0.02	0.12	0.14	0.00	0.04	0.00	0.02	0.00
Testes	10.57	9.97	2.08	76.47	0.19	0.00	0.10	0.20	0.21	0.00	0.20	0.00	0.01	0.00

Table A-10. Continued.

Tissue	Element													
	H	C	N	O	Na	Mg	P	S	Cl	Ar	K	Ca	Fe	I
Prostate	10.43	22.37	2.83	63.36	0.10	0.00	0.18	0.28	0.22	0.00	0.20	0.00	0.02	0.00
Breast - Female	11.47	48.05	0.31	40.07	0.01	0.00	0.01	0.02	0.03	0.00	0.02	0.00	0.01	0.00
Ovaries	10.48	24.51	2.74	61.27	0.10	0.00	0.19	0.29	0.21	0.00	0.20	0.00	0.01	0.00
Fallopian tubes	10.60	31.50	2.40	54.70	0.10	0.00	0.20	0.20	0.10	0.00	0.20	0.00	0.00	0.00
Uterus	10.56	29.57	2.48	56.56	0.10	0.00	0.19	0.20	0.12	0.00	0.20	0.00	0.01	0.00
Cartilage	9.82	10.31	2.61	74.44	0.35	0.00	1.42	0.64	0.30	0.00	0.07	0.00	0.04	0.00
Teeth	2.20	9.50	2.90	42.10	0.00	0.70	13.70	0.00	0.00	0.00	28.90	0.00	0.00	0.00
Bulk soft tissue	10.50	25.60	2.70	60.20	0.10	0.00	0.20	0.30	0.20	0.00	0.20	0.00	0.00	0.00
Soft tissue - Female	10.60	31.50	2.40	54.70	0.10	0.00	0.20	0.20	0.10	0.00	0.20	0.00	0.00	0.00
Water	11.20	0.00	0.00	88.80	0.00	0.00	0.00	0.00	0.00	0.00	0.00	0.00	0.00	0.00
Air	0.00	0.01	75.53	23.18	0.00	0.00	0.00	0.00	0.00	1.28	0.00	0.00	0.00	0.00
Lens	9.60	19.50	5.70	64.60	0.10	0.00	0.10	0.30	0.10	0.00	0.00	0.00	0.00	0.00
Cortical bone	3.57	15.95	4.19	44.82	0.30	0.20	9.40	0.30	0.00	0.00	0.00	21.27	0.00	0.00
Spongiosa/MC														
Cranium	5.96	26.73	3.47	42.34	0.23	0.16	6.41	0.25	0.02	0.00	0.01	14.41	0.02	0.00
Mandible	9.96	46.55	2.22	36.27	0.13	0.09	1.47	0.17	0.02	0.00	0.01	3.07	0.04	0.00
Vertebrae - C	8.91	35.08	3.10	44.51	0.15	0.14	2.47	0.21	0.04	0.00	0.03	5.32	0.06	0.00
Vertebrae - T	9.68	39.25	2.92	43.00	0.13	0.13	1.50	0.19	0.03	0.00	0.02	3.07	0.06	0.00
Vertebrae - L	9.58	38.80	2.94	43.12	0.13	0.13	1.62	0.19	0.03	0.00	0.02	3.35	0.06	0.00
Sternum	9.81	39.66	2.90	43.06	0.12	0.13	1.32	0.19	0.04	0.00	0.02	2.68	0.07	0.00
Ribs	9.48	38.15	2.97	43.40	0.13	0.13	1.75	0.20	0.04	0.00	0.02	3.67	0.06	0.00
Scapulae	9.27	42.70	2.45	37.77	0.15	0.10	2.31	0.18	0.02	0.00	0.02	5.00	0.03	0.00
Clavicles	9.69	45.89	2.21	35.96	0.14	0.09	1.85	0.17	0.02	0.00	0.01	3.94	0.03	0.00
Os Coxae	9.77	43.36	2.48	38.96	0.13	0.10	1.59	0.18	0.03	0.00	0.02	3.33	0.05	0.00
Sacrum	9.42	39.04	2.96	42.26	0.14	0.14	1.85	0.20	0.03	0.00	0.02	3.88	0.06	0.00
Humera-proximal	9.97	48.39	1.97	34.35	0.13	0.07	1.57	0.16	0.02	0.00	0.01	3.32	0.03	0.00
Humera-distal	9.49	50.86	1.64	29.93	0.15	0.05	2.41	0.15	0.01	0.00	0.01	5.29	0.00	0.00
Radii-proximal	10.25	55.52	1.31	27.81	0.13	0.03	1.53	0.13	0.01	0.00	0.01	3.27	0.00	0.00
Radii-distal	9.91	53.44	1.46	28.75	0.14	0.04	1.93	0.14	0.01	0.00	0.01	4.18	0.00	0.00
Ulnae-proximal	9.38	50.02	1.70	30.42	0.15	0.05	2.53	0.16	0.01	0.00	0.01	5.57	0.00	0.00
Ulnae-distal	9.63	52.05	1.56	29.19	0.15	0.05	2.26	0.15	0.01	0.00	0.00	4.95	0.00	0.00

Table A-10. Continued.

Tissue	Element													
	H	C	N	O	Na	Mg	P	S	Cl	Ar	K	Ca	Fe	I
Wrists and hands	9.49	51.04	1.63	29.73	0.15	0.05	2.43	0.15	0.01	0.00	0.01	5.32	0.00	0.00
Femora-proximal	9.37	45.31	2.18	35.38	0.15	0.08	2.30	0.17	0.02	0.00	0.01	4.99	0.03	0.00
Femora-distal	9.55	51.16	1.62	29.84	0.15	0.05	2.34	0.15	0.01	0.00	0.01	5.13	0.00	0.00
Patellae	9.55	51.18	1.62	29.81	0.15	0.05	2.34	0.15	0.01	0.00	0.01	5.13	0.00	0.00
Tibiae-proximal	9.91	53.45	1.45	28.77	0.14	0.04	1.92	0.14	0.01	0.00	0.01	4.16	0.00	0.00
Tibiae-distal	9.80	52.74	1.51	29.08	0.14	0.04	2.05	0.14	0.01	0.00	0.01	4.47	0.00	0.00
Fibulae-proximal	10.38	56.36	1.25	27.44	0.13	0.03	1.37	0.13	0.01	0.00	0.01	2.91	0.00	0.00
Fibulae-distal	9.54	51.13	1.62	29.83	0.15	0.05	2.36	0.15	0.01	0.00	0.01	5.16	0.00	0.00
Ankles and feet	9.55	51.39	1.61	29.57	0.15	0.05	2.36	0.15	0.01	0.00	0.01	5.16	0.00	0.00
Humera-upper shaft	11.19	56.31	1.48	30.55	0.10	0.05	0.12	0.13	0.01	0.00	0.01	0.00	0.03	0.00
Humera-lower shaft	11.47	63.29	0.75	24.16	0.10	0.00	0.10	0.10	0.01	0.00	0.00	0.00	0.00	0.00
Radii-shaft	11.47	63.30	0.75	24.16	0.10	0.00	0.10	0.10	0.01	0.00	0.00	0.00	0.00	0.00
Ulnae-shaft	11.47	63.30	0.75	24.16	0.10	0.00	0.10	0.10	0.01	0.00	0.00	0.00	0.00	0.00
Femora-upper shaft	11.19	56.27	1.49	30.59	0.10	0.05	0.12	0.13	0.01	0.00	0.01	0.00	0.03	0.00
Femora-lower shaft	11.47	63.27	0.76	24.19	0.10	0.00	0.10	0.10	0.01	0.00	0.00	0.00	0.00	0.00
Tibiae-shaft	11.47	63.27	0.76	24.19	0.10	0.00	0.10	0.10	0.01	0.00	0.00	0.00	0.00	0.00
Fibulae-shaft	11.47	63.30	0.75	24.16	0.10	0.00	0.10	0.10	0.01	0.00	0.00	0.00	0.00	0.00
Lymph nodes	10.49	24.91	2.73	60.88	0.10	0.00	0.20	0.30	0.20	0.00	0.20	0.00	0.00	0.00
Ears	9.66	10.00	2.30	74.41	0.46	0.00	2.00	0.83	0.30	0.00	0.02	0.00	0.01	0.00
External nose	9.66	10.00	2.30	74.41	0.46	0.00	2.00	0.83	0.30	0.00	0.02	0.00	0.01	0.00
Nasal layers	10.47	24.23	2.76	61.55	0.10	0.00	0.19	0.29	0.21	0.00	0.20	0.00	0.01	0.00
Oral cavity layer	10.47	24.23	2.76	61.55	0.10	0.00	0.19	0.29	0.21	0.00	0.20	0.00	0.01	0.00
Pharynx	10.47	24.23	2.76	61.55	0.10	0.00	0.19	0.29	0.21	0.00	0.20	0.00	0.01	0.00
Sal glands	10.47	24.23	2.76	61.55	0.10	0.00	0.19	0.29	0.21	0.00	0.20	0.00	0.01	0.00
Spinal cord	10.65	14.17	2.30	71.51	0.19	0.00	0.37	0.20	0.30	0.00	0.29	0.00	0.01	0.00
Penis	10.20	13.57	3.38	71.77	0.10	0.00	0.18	0.28	0.14	0.00	0.36	0.00	0.02	0.00
Scrotum	10.43	22.37	2.83	63.36	0.10	0.00	0.18	0.28	0.22	0.00	0.20	0.00	0.02	0.00

Table A-11. Non-uniform source sampling probabilities for the UFH00MF phantoms (Pafundi 2009).

Skeletal Site	Source					
	A-marrow	C-marrow	T-marrow	T-bone-S	T-bone-V	C-bone-V
Cranium	0.2412	--	0.2540	0.1648	0.5170	0.2716
Mandible	0.0433	--	0.0456	0.0541	0.0217	0.0215
Scapulae	0.0373	--	0.0393	0.0450	0.0375	0.0477
Clavicles	0.0516	--	0.0543	0.0661	0.0572	0.1082
Sternum	0.0470	--	0.0495	0.0565	0.0377	0.0345
Ribs	0.0051	--	0.0053	0.0067	0.0026	0.0022
Cervical vertebrae	0.1628	--	0.1714	0.2031	0.0817	0.0809
Thoracic vertebrae	0.0323	--	0.0341	0.0382	0.0180	0.0309
Lumbar vertebrae	0.0122	--	0.0128	0.0144	0.0068	0.0116
Sacrum	0.0631	--	0.0664	0.0745	0.0351	0.0778
Os coxae	0.0188	--	0.0198	0.0226	0.0151	0.0138
Proximal femora	0.0212	--	0.0223	0.0254	0.0170	0.0048
Upper shaft of the femora	0.0045	0.0898	--	--	--	0.0197
Lower shaft of the femora	0.0045	0.0893	--	--	--	0.0196
Distal femora	0.0166	--	0.0175	0.0200	0.0133	0.0038
Proximal tibiae	0.0036	--	0.0038	0.0043	0.0029	0.0008
Shaft of the tibiae	0.0017	0.0344	--	--	--	0.0132
Distal tibiae	0.0065	--	0.0068	0.0078	0.0052	0.0015
Proximal fibulae	0.0086	--	0.0091	0.0104	0.0069	0.0020
Shaft of the fibulae	0.0020	0.0393	--	--	--	0.0169
Distal fibulae	0.0044	--	0.0046	0.0053	0.0035	0.0010
Patellae	0.0242	--	0.0255	0.0182	0.0122	0.0106
Ankles and feet	0.0346	--	0.0364	0.0416	0.0277	0.0079
Proximal humera	0.0103	0.2049	--	--	--	0.0397
Upper shaft of the humera	0.0164	0.3255	--	--	--	0.0631
Lower shaft of the humera	0.0286	--	0.0301	0.0344	0.0229	0.0065
Distal humera	0.0013	--	0.0014	0.0010	0.0007	0.0006
Proximal radii	0.0246	--	0.0259	0.0295	0.0197	0.0056
Shaft of the radii	0.0094	0.1861	--	--	--	0.0477
Distal radii	0.0151	--	0.0159	0.0181	0.0121	0.0034
Proximal ulnae	0.0033	--	0.0034	0.0039	0.0026	0.0007
Shaft of the ulnae	0.0015	0.0306	--	--	--	0.0128
Distal ulnae	0.0050	--	0.0053	0.0061	0.0040	0.0011
Wrists and hands	0.0375	--	0.0394	0.0282	0.0188	0.0163

Table A-12. Non-uniform source sampling probabilities for the UFH01MF phantoms (Pafundi 2009).

Skeletal Site	Source					
	A-marrow	C-marrow	T-marrow	T-bone-S	T-bone-V	C-bone-V
Cranium	0.3274	--	0.3257	0.2186	0.6169	0.3146
Mandible	0.0167	--	0.0166	0.0095	0.0268	0.0246
Scapulae	0.0270	--	0.0269	0.0218	0.0099	0.0113
Clavicles	0.0944	--	0.0940	0.0538	0.0245	0.0396
Sternum	0.0524	--	0.0522	0.0682	0.0311	0.0243
Ribs	0.0055	--	0.0054	0.0060	0.0027	0.0022
Cervical vertebrae	0.1506	--	0.1498	0.1675	0.0758	0.0702
Thoracic vertebrae	0.0339	--	0.0337	0.0544	0.0220	0.0332
Lumbar vertebrae	0.0044	--	0.0043	0.0074	0.0030	0.0047
Sacrum	0.1007	--	0.1002	0.1059	0.0383	0.0729
Os coxae	0.0359	--	0.0357	0.0595	0.0216	0.0188
Proximal femora	0.0148	--	0.0144	0.0268	0.0160	0.0208
Upper shaft of the femora	0.0041	0.1122	--	--	--	0.0228
Lower shaft of the femora	0.0038	0.1065	--	--	--	0.0177
Distal femora	0.0068	--	0.0074	0.0140	0.0084	0.0133
Proximal tibiae	0.0006	--	0.0006	0.0012	0.0007	0.0043
Shaft of the tibiae	0.0017	0.0484	--	--	--	0.0096
Distal tibiae	0.0010	--	0.0011	0.0025	0.0015	0.0055
Proximal fibulae	0.0018	--	0.0019	0.0063	0.0037	0.0081
Shaft of the fibulae	0.0027	0.0776	--	--	--	0.0155
Distal fibulae	0.0001	--	0.0001	0.0002	0.0001	0.0019
Patellae	0.0170	--	0.0322	0.0370	0.0220	0.0186
Ankles and feet	0.0164	--	0.0160	0.0330	0.0154	0.0237
Proximal humera	0.0048	0.1303	--	--	--	0.0249
Upper shaft of the humera	0.0074	0.2069	--	--	--	0.0354
Lower shaft of the humera	0.0170	--	0.0184	0.0299	0.0140	0.0352
Distal humera	0.0016	--	0.0017	0.0011	0.0007	0.0005
Proximal radii	0.0099	--	0.0106	0.0185	0.0110	0.0301
Shaft of the radii	0.0102	0.2905	--	--	--	0.0439
Distal radii	0.0021	--	0.0022	0.0032	0.0019	0.0166
Proximal ulnae	0.0005	--	0.0005	0.0010	0.0006	0.0028
Shaft of the ulnae	0.0010	0.0275	--	--	--	0.0051
Distal ulnae	0.0004	--	0.0004	0.0008	0.0005	0.0025
Wrists and hands	0.0254	--	0.0480	0.0521	0.0310	0.0249

Table A-13. Non-uniform source sampling probabilities for the UFH05MF phantoms (Pafundi 2009).

Skeletal Site	Source					
	A-marrow	C-marrow	T-marrow	T-bone-S	T-bone-V	C-bone-V
Cranium	0.3254	--	0.3209	0.2231	0.5437	0.3014
Mandible	0.0212	--	0.0209	0.0116	0.0283	0.0254
Scapulae	0.0152	--	0.0141	0.0191	0.0096	0.0092
Clavicles	0.0955	--	0.0886	0.0763	0.0385	0.0432
Sternum	0.0640	--	0.0594	0.0797	0.0402	0.0219
Ribs	0.0113	--	0.0105	0.0071	0.0040	0.0032
Cervical vertebrae	0.0850	--	0.0789	0.0956	0.0546	0.0504
Thoracic vertebrae	0.0404	--	0.0398	0.0662	0.0324	0.0384
Lumbar vertebrae	0.0080	--	0.0080	0.0113	0.0055	0.0081
Sacrum	0.1138	--	0.1137	0.1193	0.0566	0.0762
Os coxae	0.0429	--	0.0429	0.0348	0.0165	0.0153
Proximal femora	0.0166	--	0.0166	0.0250	0.0173	0.0197
Upper shaft of the femora	0.0063	0.1018	--	--	--	0.0183
Lower shaft of the femora	0.0058	0.0966	--	--	--	0.0158
Distal femora	0.0083	--	0.0095	0.0134	0.0092	0.0135
Proximal tibiae	0.0008	--	0.0011	0.0008	0.0006	0.0034
Shaft of the tibiae	0.0030	0.0646	--	--	--	0.0109
Distal tibiae	0.0016	--	0.0022	0.0027	0.0018	0.0053
Proximal fibulae	0.0030	--	0.0041	0.0065	0.0045	0.0088
Shaft of the fibulae	0.0035	0.0737	--	--	--	0.0137
Distal fibulae	0.0005	--	0.0006	0.0002	0.0002	0.0023
Patellae	0.0043	--	0.0169	0.0187	0.0129	0.0122
Ankles and feet	0.0216	--	0.0216	0.0370	0.0222	0.0292
Proximal humera	0.0138	0.2224	--	--	--	0.0359
Upper shaft of the humera	0.0095	0.1571	--	--	--	0.0282
Lower shaft of the humera	0.0235	--	0.0268	0.0370	0.0222	0.0351
Distal humera	0.0059	--	0.0082	0.0026	0.0018	0.0015
Proximal radii	0.0121	--	0.0168	0.0225	0.0155	0.0357
Shaft of the radii	0.0109	0.2310	--	--	--	0.0439
Distal radii	0.0038	--	0.0052	0.0032	0.0022	0.0167
Proximal ulnae	0.0012	--	0.0017	0.0012	0.0009	0.0035
Shaft of the ulnae	0.0025	0.0528	--	--	--	0.0065
Distal ulnae	0.0011	--	0.0016	0.0012	0.0008	0.0035
Wrists and hands	0.0176	--	0.0694	0.0839	0.0579	0.0436

Table A-14. Non-uniform source sampling probabilities for the UFH10MF phantoms (Pafundi 2009).

Skeletal Site	Source					
	A-marrow	C-marrow	T-marrow	T-bone-S	T-bone-V	C-bone-V
Cranium	0.1753	--	0.1714	0.1455	0.3557	0.1882
Mandible	0.0108	--	0.0106	0.0072	0.0177	0.0143
Scapulae	0.0202	--	0.0160	0.0191	0.0116	0.0081
Clavicles	0.1525	--	0.1212	0.0983	0.0596	0.0392
Sternum	0.1035	--	0.0823	0.1065	0.0646	0.0211
Ribs	0.0162	--	0.0129	0.0052	0.0041	0.0030
Cervical vertebrae	0.0948	--	0.0753	0.0592	0.0468	0.0404
Thoracic vertebrae	0.0448	--	0.0438	0.0652	0.0420	0.0340
Lumbar vertebrae	0.0092	--	0.0093	0.0096	0.0062	0.0083
Sacrum	0.1812	--	0.1599	0.1339	0.0919	0.0740
Os coxae	0.0399	--	0.0352	0.0147	0.0101	0.0096
Proximal femora	0.0245	--	0.0222	0.0345	0.0300	0.0273
Upper shaft of the femora	0.0059	0.0899	--	--	--	0.0234
Lower shaft of the femora	0.0058	0.0897	--	--	--	0.0197
Distal femora	0.0055	--	0.0121	0.0169	0.0147	0.0190
Proximal tibiae	0.0004	--	0.0011	0.0011	0.0009	0.0046
Shaft of the tibiae	0.0018	0.0606	--	--	--	0.0132
Distal tibiae	0.0009	--	0.0024	0.0035	0.0030	0.0075
Proximal fibulae	0.0017	--	0.0048	0.0089	0.0077	0.0125
Shaft of the fibulae	0.0020	0.0667	--	--	--	0.0169
Distal fibulae	0.0002	--	0.0006	0.0003	0.0003	0.0031
Patellae	--	--	0.0204	0.0196	0.0171	0.0187
Ankles and feet	0.0342	--	0.0310	0.0524	0.0446	0.0447
Proximal humera	0.0152	0.2310	--	--	--	0.0498
Upper shaft of the humera	0.0100	0.1552	--	--	--	0.0402
Lower shaft of the humera	0.0183	--	0.0401	0.0627	0.0534	0.0471
Distal humera	0.0033	--	0.0091	0.0020	0.0018	0.0015
Proximal radii	0.0089	--	0.0246	0.0326	0.0284	0.0535
Shaft of the radii	0.0077	0.2532	--	--	--	0.0595
Distal radii	0.0022	--	0.0060	0.0050	0.0043	0.0253
Proximal ulnae	0.0007	--	0.0021	0.0019	0.0017	0.0052
Shaft of the ulnae	0.0016	0.0538	--	--	--	0.0084
Distal ulnae	0.0007	--	0.0019	0.0018	0.0016	0.0051
Wrists and hands	--	--	0.0837	0.0925	0.0804	0.0538

Table A-15. Non-uniform source sampling probabilities for the UFH15M phantom (Pafundi 2009).

Skeletal Site	Source					
	A-marrow	C-marrow	T-marrow	T-bone-S	T-bone-V	C-bone-V
Cranium	0.1198	--	0.0941	0.1315	0.2150	0.1646
Mandible	0.0099	--	0.0078	0.0102	0.0149	0.0179
Scapulae	0.0252	--	0.0145	0.0170	0.0134	0.0102
Clavicles	0.1252	--	0.0720	0.0703	0.0515	0.0275
Sternum	0.1261	--	0.0726	0.0638	0.0419	0.0107
Ribs	0.0214	--	0.0123	0.0103	0.0062	0.0067
Cervical vertebrae	0.0951	--	0.0548	0.0431	0.0366	0.0512
Thoracic vertebrae	0.0277	--	0.0217	0.0230	0.0468	0.0377
Lumbar vertebrae	0.0066	--	0.0054	0.0042	0.0056	0.0131
Sacrum	0.2205	--	0.1487	0.1291	0.0851	0.0571
Os coxae	0.0559	--	0.0377	0.0168	0.0110	0.0211
Proximal femora	0.0589	--	0.0462	0.0478	0.0414	0.0129
Upper shaft of the femora	0.0059	0.0906	--	--	--	0.0334
Lower shaft of the femora	0.0030	0.0805	--	--	--	0.0297
Distal femora	--	--	0.0183	0.0246	0.0244	0.0210
Proximal tibiae	--	--	0.0032	0.0038	0.0040	0.0031
Shaft of the tibiae	--	0.0337	--	--	--	0.0226
Distal tibiae	--	--	0.0070	0.0077	0.0083	0.0038
Proximal fibulae	--	--	0.0110	0.0149	0.0182	0.0086
Shaft of the fibulae	--	0.0428	--	--	--	0.0274
Distal fibulae	--	--	0.0022	0.0026	0.0024	0.0017
Patellae	--	--	0.0190	0.0150	0.0127	0.0395
Ankles and feet	0.0772	--	0.0606	0.0808	0.0768	0.0254
Proximal humera	0.0151	0.2312	--	--	--	0.0699
Upper shaft of the humera	0.0066	0.1760	--	--	--	0.0532
Lower shaft of the humera	--	--	0.0692	0.1002	0.1298	0.0205
Distal humera	--	--	0.0071	0.0056	0.0047	0.0065
Proximal radii	--	--	0.0611	0.0450	0.0312	0.0305
Shaft of the radii	--	0.3034	--	--	--	0.0779
Distal radii	--	--	0.0227	0.0260	0.0251	0.0070
Proximal ulnae	--	--	0.0046	0.0045	0.0040	0.0038
Shaft of the ulnae	--	0.0418	--	--	--	0.0143
Distal ulnae	--	--	0.0037	0.0053	0.0066	0.0038
Wrists and hands	--	--	0.1227	0.0967	0.0821	0.0658

Table A-16. Non-uniform source sampling probabilities for the UFH15F phantom (Pafundi 2009).

Skeletal Site	Source					
	A-marrow	C-marrow	T-marrow	T-bone-S	T-bone-V	C-bone-V
Cranium	0.0983	--	0.0820	0.1169	0.1933	0.1491
Mandible	0.0078	--	0.0065	0.0087	0.0129	0.0156
Scapulae	0.0316	--	0.0193	0.0231	0.0185	0.0142
Clavicles	0.1132	--	0.0693	0.0690	0.0511	0.0278
Sternum	0.1385	--	0.0848	0.0760	0.0505	0.0137
Ribs	0.0149	--	0.0091	0.0078	0.0047	0.0052
Cervical vertebrae	0.1036	--	0.0634	0.0509	0.0438	0.0617
Thoracic vertebrae	0.0380	--	0.0318	0.0343	0.0705	0.0571
Lumbar vertebrae	0.0085	--	0.0075	0.0060	0.0081	0.0188
Sacrum	0.2460	--	0.1765	0.1563	0.1041	0.0712
Os coxae	0.0684	--	0.0491	0.0223	0.0147	0.0286
Proximal femora	0.0469	--	0.0392	0.0414	0.0362	0.0116
Upper shaft of the femora	0.0047	0.0862	--	--	--	0.0297
Lower shaft of the femora	0.0023	0.0752	--	--	--	0.0259
Distal femora	--	--	0.0154	0.0211	0.0212	0.0184
Proximal tibiae	--	--	0.0026	0.0032	0.0033	0.0026
Shaft of the tibiae	--	0.0346	--	--	--	0.0220
Distal tibiae	--	--	0.0056	0.0063	0.0069	0.0033
Proximal fibulae	--	--	0.0091	0.0126	0.0155	0.0074
Shaft of the fibulae	--	0.0429	--	--	--	0.0260
Distal fibulae	--	--	0.0018	0.0022	0.0020	0.0014
Patellae	--	--	0.0166	0.0133	0.0114	0.0358
Ankles and feet	0.0593	--	0.0495	0.0672	0.0647	0.0218
Proximal humera	0.0109	0.2000	--	--	--	0.0563
Upper shaft of the humera	0.0071	0.2260	--	--	--	0.0637
Lower shaft of the humera	--	--	0.0659	0.0973	0.1274	0.0207
Distal humera	--	--	0.0061	0.0049	0.0042	0.0058
Proximal radii	--	--	0.0565	0.0425	0.0298	0.0295
Shaft of the radii	--	0.2993	--	--	--	0.0714
Distal radii	--	--	0.0208	0.0244	0.0238	0.0068
Proximal ulnae	--	--	0.0038	0.0039	0.0034	0.0033
Shaft of the ulnae	--	0.0357	--	--	--	0.0114
Distal ulnae	--	--	0.0031	0.0045	0.0057	0.0033
Wrists and hands	--	--	0.1045	0.0839	0.0721	0.0586

Table A-17. Non-uniform source sampling probabilities for the UFHADM phantom (Hough *et al.* 2011).

Skeletal Site	Source					
	A-marrow	C-marrow	T-marrow	T-bone-S	T-bone-V	C-bone-V
Cranium	0.0323	--	0.0303	0.1160	0.2223	0.2150
Mandible	0.0089	--	0.0084	0.0053	0.0047	0.0130
Scapulae	0.0925	--	0.0870	0.0817	0.0897	0.0831
Clavicles	0.0093	--	0.0100	0.0065	0.0075	0.0114
Sternum	0.0250	--	0.0128	0.0094	0.0065	0.0089
Ribs	0.1029	--	0.0525	0.0413	0.0391	0.0594
Cervical vertebrae	0.0274	--	0.0140	0.0173	0.0174	0.0138
Thoracic vertebrae	0.1186	--	0.0605	0.0432	0.0360	0.0335
Lumbar vertebrae	0.1330	--	0.0679	0.0550	0.0450	0.0284
Sacrum	0.0845	--	0.0432	0.0362	0.0329	0.0245
Os coxae	0.2589	--	0.1928	0.1645	0.1217	0.1071
Proximal femora	0.0433	--	0.0619	0.0631	0.0623	0.0098
Upper shaft of the femora	0.0270	0.2670	--	--	--	0.0312
Lower shaft of the femora	--	0.2029	--	--	--	0.0237
Distal femora	--	--	0.0710	0.0796	0.0694	0.0139
Proximal tibiae	--	--	0.0597	0.0553	0.0445	0.0113
Shaft of the tibiae	--	0.3118	--	--	--	0.0364
Distal tibiae	--	--	0.0204	0.0194	0.0167	0.0063
Proximal fibulae	--	--	0.0051	0.0033	0.0025	0.0021
Shaft of the fibulae	--	0.0250	--	--	--	0.0127
Distal fibulae	--	--	0.0040	0.0044	0.0040	0.0030
Patellae	--	--	0.0083	0.0093	0.0081	0.0016
Ankles and feet	--	--	0.0925	0.1038	0.0905	0.0697
Proximal humera	0.0296	--	0.0422	0.0279	0.0256	0.0124
Upper shaft of the humera	0.0068	0.0675	--	--	--	0.0272
Lower shaft of the humera	--	0.0600	--	--	--	0.0242
Distal humera	--	--	0.0200	0.0223	0.0203	0.0151
Proximal radii	--	--	0.0035	0.0016	0.0019	0.0025
Shaft of the radii	--	0.0296	--	--	--	0.0193
Distal radii	--	--	0.0062	0.0057	0.0046	0.0045
Proximal ulnae	--	--	0.0107	0.0110	0.0117	0.0082
Shaft of the ulnae	--	0.0361	--	--	--	0.0235
Distal ulnae	--	--	0.0022	0.0026	0.0020	0.0013
Wrists and hands	--	--	0.0128	0.0143	0.0130	0.0421

Table A-18. Non-uniform source sampling probabilities for the UFHADDF phantom (Sinclair *et al.* 2009).

Skeletal Site	Source					
	A-marrow	C-marrow	T-marrow	T-bone-S	T-bone-V	C-bone-V
Cranium	0.0318	--	0.0305	0.1805	0.3366	0.2014
Mandible	0.0086	--	0.0083	0.0040	0.0074	0.0144
Scapulae	0.0742	--	0.0713	0.0263	0.0207	0.0710
Clavicles	0.0097	--	0.0108	0.0060	0.0047	0.0132
Sternum	0.0204	--	0.0107	0.0062	0.0049	0.0060
Ribs	0.1244	--	0.0650	0.0418	0.0329	0.0786
Cervical vertebrae	0.0327	--	0.0171	0.0235	0.0190	0.0170
Thoracic vertebrae	0.1245	--	0.0650	0.0529	0.0428	0.0287
Lumbar vertebrae	0.1559	--	0.0814	0.0818	0.0604	0.0243
Sacrum	0.0651	--	0.0495	0.0614	0.0453	0.0297
Os coxae	0.2495	--	0.1899	0.0565	0.0478	0.0872
Proximal femora	0.0491	--	0.0512	0.0912	0.0767	0.0107
Upper shaft of the femora	0.0109	0.2146	--	--	--	0.0354
Lower shaft of the femora	--	0.2450	--	--	--	0.0404
Distal femora	--	--	0.0654	0.1011	0.0851	0.0203
Proximal tibiae	--	--	0.0566	0.0670	0.0542	0.0130
Shaft of the tibiae	--	0.2585	--	--	--	0.0525
Distal tibiae	--	--	0.0197	0.0257	0.0208	0.0061
Proximal fibulae	--	--	0.0047	0.0041	0.0033	0.0015
Shaft of the fibulae	--	0.0255	--	--	--	0.0105
Distal fibulae	--	--	0.0038	0.0053	0.0043	0.0024
Patellae	--	--	0.0072	0.0104	0.0084	0.0021
Ankles and feet	--	--	0.0925	0.0579	0.0468	0.0696
Proximal humera	0.0394	--	0.0411	0.0265	0.0214	0.0089
Upper shaft of the humera	0.0039	0.0766	--	--	--	0.0261
Lower shaft of the humera	--	0.0675	--	--	--	0.0230
Distal humera	--	--	0.0208	0.0270	0.0218	0.0113
Proximal radii	--	--	0.0033	0.0029	0.0023	0.0019
Shaft of the radii	--	0.0515	--	--	--	0.0184
Distal radii	--	--	0.0066	0.0064	0.0051	0.0024
Proximal ulnae	--	--	0.0103	0.0238	0.0193	0.0048
Shaft of the ulnae	--	0.0608	--	--	--	0.0219
Distal ulnae	--	--	0.0025	0.0006	0.0005	0.0009
Wrists and hands	--	--	0.0148	0.0092	0.0075	0.0445

APPENDIX B SAMPLE FILES

To provide a clearer picture of the computational methods used in this work, excerpts from important files along with technical descriptions used during radiation transport are presented.

Contents of Appendix B are as follows:

- Lattice file for voxel phantom definition
- Source file for uniformly distributed radiation sources
- Source file for non-uniformly distributed radiation sources
- MCNPX v2.6 input file for radiation transport simulations

Lattice File

Filename = ufhadm_pe.lat – This is an excerpt of the lattice file generated for the UFHADM phantom for use in the MCNPX input files. The pneumonics “imp:p” and “imp:e” indicate the importance of photons and electrons in the problem, and the value of unity for these pneumonics indicates that both photons and electrons were being considered in the simulation. The “fill” mnemonic defines the number of voxels in the x-, y-, and z-directions. For this application, the zeroth voxel index was filled with a voxel tag identification number, so the size of this phantom was 362 voxels in the x-direction, 195 voxels in the y-direction, and 796 voxels in the z-direction. The body of the file lists the tag identification numbers associated with each voxel. The “r” operator indicates repetition, so the file is read in this way: the tissue tag identification number 57 applies to voxel number 1 and to the 160839 voxels after voxel number 1. After MCNPX reaches voxel number 362, it begins to fill the next y-level with tissue tag numbers. In this case, the tissue tag number 57 fills up 2 z-levels and 54 y-levels and fills 112 x-levels before reaching a voxel with the tissue tag number 43. In this fashion, the three-dimensional phantom matrix was defined.

START FILE

1000 0 -200 lat=1 u=999 imp:p=1 imp:e=1 fill=0:361 0:194 0:795
57 160839r 43 1r 57 134r 43 1r 57 221r 43 2r 57 134r 43 2r
57 65003r 43 2r 57 164r 43 2r 57 188r 43 1r 1 2r 43 57 162r
43 1 2r 43 1r 57 186r 43 1 3r 43 57 162r 43 1 3r 43
57 187r 43 3r 57 164r 43 3r 57 572r 43 3r 57 120r 43 3r
57 230r 43 1r 64 3r 43 1r 57 116r 43 1r 64 3r 43 1r
57 226r 43 1r 64 7r 43 57 114r 43 64 7r 43 1r 57 223r 43
64 9r 43 57 114r 43 64 9r 43 57 221r 43 64 10r 43 57 114r
(continued...)

END FILE

Uniform Source File

Filename = liver.src – This is an excerpt of a source file generated for the liver of the UFHADM phantom with a uniform source distribution. The pneumonics “si” and “sp” refer to distribution definitions, and the value “5” attached to them indicates that the current distribution applies to distribution 5 in the input file. The flag “1” indicates a discrete variable. That is, each voxel location is a discrete point, and MCNPX should not sample between voxel locations in the fashion of a bin distribution. The generalized format for each voxel location is represented by Equation X.

$$(A < B [C \ D \ E] < F) \quad (X-X)$$

where A is the tissue tag identification number of the source tissue, B is the cell number of the lattice definition where the tissue tag numbers are assigned to all voxel coordinates in the phantom, C is the location of the voxel in the x-direction, D is the location of the voxel in the y-direction, E is the location of the voxel in the z-direction, and F is the cell number of the rectangular prism defining the boundaries of the entire voxel phantom. The line “sp5 1 307169r” indicates that there is a probability of voxel selection for source sampling of unity assigned to all 307170 voxels in the file. This technique guarantees that the source tissue will be uniformly sampled to the best approximation.

START FILE

si5 1 (25<1000[113 97 509]<1001) (25<1000[113 98 509]<1001)
(25<1000[114 98 509]<1001) (25<1000[113 99 509]<1001)
(25<1000[114 99 509]<1001) (25<1000[112 100 509]<1001)
(25<1000[113 100 509]<1001) (25<1000[114 100 509]<1001)
(25<1000[112 101 509]<1001) (25<1000[113 101 509]<1001)
(25<1000[114 101 509]<1001) (25<1000[115 101 509]<1001)
(25<1000[116 101 509]<1001) (25<1000[112 102 509]<1001)
(*continued...*)
(25<1000[133 131 579]<1001) (25<1000[134 131 579]<1001)
(25<1000[135 131 579]<1001) (25<1000[136 131 579]<1001)

sp5 1 307169r

END FILE

Non-Uniform Source File

Filename = am.src – This is an excerpt of a source file generated for the whole-body active bone marrow of the UFHADM phantom with a non-uniform source distribution. The voxel location definition format is the same as for a uniform source distribution, but the source sampling specification is different to account for non-uniformity. The “s” flag in the “si5” mnemonic indicates that the source distribution consists of a series of sub-distributions. The mnemonic “d201” defines a sub-distribution with identification number 201. The “sp5” mnemonic assigns a probability of selection of each sub-distribution for source sampling. In this case, sub-distribution 201 (spongiosa of the cranium) has a 3.23% chance of being selected for source sampling (with 1,000,000 particle histories simulated, this is actually a substantial number of particles). Then, for each sub-distribution, separate “si” and “sp” pneumonics are defined in the same way as for the uniform source distribution. Conceptually, MCNPX randomly selects a sub-distribution to sample based on the assigned probabilities of selection, but once a sub-distribution is selected, the source component for which the sub-distribution applies is uniformly sampled.

START FILE

si5 s d201 d207 d208 d209 d206 d204 d202 d211 d210 d203
d205 d224 d225 d212 d213
sp5 0.0323 0.0274 0.1186 0.1330 0.1029 0.0093 0.0089 0.2589
0.0845 0.0925 0.0250 0.0296 0.0068 0.0433 0.0270
si201 l (201<1000[182 45 715]<1001) (201<1000[178 46 716]<1001)
(201<1000[179 46 716]<1001) (201<1000[180 46 716]<1001)
(201<1000[182 46 716]<1001) (201<1000[183 46 716]<1001)
(*continued...*)
sp201 l 61291r
si207 l (207<1000[176 112 678]<1001) (207<1000[177 112 678]<1001)
(207<1000[178 112 678]<1001) (207<1000[179 112 678]<1001)
(207<1000[180 112 678]<1001) (207<1000[181 112 678]<1001)
(207<1000[182 112 678]<1001) (207<1000[183 112 678]<1001)
(*continued...*)
(207<1000[168 115 720]<1001) (207<1000[169 115 720]<1001)
(207<1000[167 116 720]<1001) (207<1000[168 116 720]<1001)
sp207 l 11367r

END FILE

Input File

Filename = liv21mp – This is an excerpt of an input file generated to model monoenergetic photons of energy 4 MeV for the UFHADM phantom. The line “read file=ufhadm_pe.lat noecho” calls the lattice file that contains the location of all tissue tag identification numbers in the phantom. The following lines under the “Body compositions, densities, and volumes” header assume the form of Equation X.

$$A \ B \ C \ D \ u = E \ imp : p, e = F \ vol = G \ \$ \ H \tag{X-X}$$

where A is the cell number of tissue H of interest, B is the material number associated with tissue H , C is the density associated with tissue H in g/cm^3 , D is the surface number within which tissue H is located, E is the tissue tag identification (or universe) number of tissue H , F is the importance of photons and electrons in the simulation, G is the volume of tissue H , and $\$$ indicates that everything following should be ignored by MCNPX and is used to clarify information for the user.

The line “100 rpp” defines the dimensions of the rectangular prism that describes the total x-, y-, and z-boundaries of the whole phantom while the line “200 rpp” defines the dimensions of the voxels. “Mode p e” indicates to MCNPX that both photons and electrons should be tracked during the simulation. For the material cards, a mnemonic consisting of the letter “M” followed by the material identification number is used. This identification number is used in the definition of the tissues (the variable B in Equation X). Below the material number, a list of element identification numbers (defined in the MCNP manual) is given along with their corresponding mass fractions (or percents). Next, the tallies are listed, and as an example, the mnemonic

“*f18:p,e” indicates that the *F8 tally (energy deposition accounting for all photons and electrons in the problem) is being invoked and given an identification number of unity. The numbers that follow this mnemonic tell MCNPX which cells (tissues) should be tallied. F4 tallies are used for application of the skeletal photon fluence-to-dose response functions. These tallies are used in the example “F2014:p 201”. This line indicates that an F4 tally is being used and given an identification number of 201 and should be applied to cell 201. The following lines define the energy bins for tallying.

Finally, the source definition line “sdef par=p erg=4.000 cel=d5 x=d1 y=d2 z=d3” indicates that the particle type (par) is photon, the energy (erg) is 4 MeV, the cells (voxels) that should be sampled (cel) is defined in distribution 5, and the x-, y-, and z-dimensions that should be sampled once a voxel is selected are defined in distributions 1, 2, and 3, respectively. “Si1”, “si2”, and “si3” define the x-, y-, and z-dimensions of the voxels, respectively, and “sp1”, “sp2”, and “sp3” define the sampling probability of the x-, y-, and z-dimensions, respectively. “NPS 10000000” creates ten million particle histories, and “dbcn 17j 1” turns on the ITS-style nearest-bin electron energy-indexing algorithm.

START FILE

```
c -----  
c -----  
c  
c Complete Internal Dosimetry Characterization  
c Mike Wayson  
c The University of Florida  
c Department of Biomedical Engineering  
c ALRADS Research Group  
c  
c Phantom = UFHADMF  
c Gender = Male  
c Radiation = Photon  
c  
c -----  
c -----  
c  
c read file=ufhadm_pe.lat noecho  
c 1001 0 -100 fill=999 imp:p,e=1 $ Surrounding Box  
c  
c -----  
c -----  
c  
c Body compositions, densities, and volumes  
c  
c -----  
c -----  
c  
c 1 14 -0.960 -70 u=1 imp:p,e=1 vol=12128.0000 $ Adipose Tissue  
c 2 1 -1.030 -70 u=2 imp:p,e=1 vol=6.7572 $ Adrenal (L)  
c 3 1 -1.030 -70 u=3 imp:p,e=1 vol=6.6196 $ Adrenal (R)  
c 4 11 -1.040 -70 u=4 imp:p,e=1 vol=1386.2000 $ Brain  
c 5 30 -0.940 -70 u=5 imp:p,e=1 vol=11.7480 $ Breast (L)  
c 6 18 -1.070 -70 u=6 imp:p,e=1 vol=15.0060 $ Bronchi  
c (continued...)  
  
c  
c -----  
c -----  
c  
c Surface Card  
c  
c -----  
c -----  
c
```

```
c -----  
c Phantom/Voxel/Outer Sphere Dimensions  
c Phantom Array Size = ( 0:361 0:194 0:795 )  
c -----
```

```
c  
100 rpp 0 57.002 0 30.633 0 175.457  
200 rpp 0 0.1579 0 0.1579 0 0.2207  
1000 so 500  
70 so 500
```

```
c  
c -----  
c MODE Definition  
c -----
```

```
c  
mode p e  
c  
c -----  
c -----
```

```
c  
c Material Cards  
c  
c -----  
c -----
```

```
c  
c -- Adrenals --  
c
```

```
M1  
1000 -10.428 $ Hydrogen  
6000 -22.082 $ Carbon  
7000 -2.845 $ Nitrogen  
8000 -63.645 $ Oxygen  
11000 -0.100 $ Sodium  
15000 -0.176 $ Phosphorus  
16000 -0.276 $ Sulfur  
17000 -0.224 $ Chlorine  
19000 -0.200 $ Potassium  
26000 -0.024 $ Iron
```

```
c  
c -- Tongue --  
c
```

```
M2  
1000 -10.200 $ Hydrogen  
6000 -14.300 $ Carbon  
7000 -3.400 $ Nitrogen  
8000 -71.000 $ Oxygen
```

11000 -0.100 \$ Sodium
15000 -0.200 \$ Phosphorus
16000 -0.300 \$ Sulfur
17000 -0.100 \$ Chlorine
19000 -0.400 \$ Potassium

(continued...)

c
c -----
c -----
c
c Tally Specification
c
c -----
c -----
c
c -----
c General Organ Tally
c -----

c
FC18 WBody
*f18:p,e (1 2 3 4 5 6 7 9 10 11 12 13 15 17 18 19 20 21 22
23 24 25 26 27 28 29 30 32 33 34 35 36 37 39 40 41
43 44 45 46 48 49 50 51 52 53 54 58 60 61 62 64 65
66 67 68 71 72 73 74 75 76 77 78 79 80 81 82 83
84 85 86 128 129 130 131 151 152 153 154 155 156 157
158 159 160 161 162 163 164 165 166 167 168 169
170 171 172 173 174 175 176 177 178 179 180 181 182
183 184 185 201 202 203 204 205 206 207 208 209
210 211 212 213 214 215 216 217 218 219 220 221 222
223 224 225 226 227 228 229 230 231 232 233 234)

FC28 Adipose
*f28:p,e 1
FC38 LAdrenal
*f38:p,e 2
(continued...)

c
c -----
c Spongiosa Tally
c -----
c
f2014:p 201
E2014 0.001
0.003
0.005
0.010
0.015

0.020
0.030
0.040
0.050
0.060
0.080
0.10
0.15
0.20
0.30
0.40
0.50
0.60
0.80
1.0
1.5
2.0
3.0
4.0
5.0
6.0
8.0
10.0
f2024:p 202
E2024 0.001
0.003
0.005
0.010
0.015
0.020
0.030
0.040
0.050
0.060
0.080
0.10
0.15
0.20
0.30
0.40
0.50
0.60
0.80
1.0
1.5
2.0

3.0
4.0
5.0
6.0
8.0
10.0

(continued...)

```
c
c -----
c -----
c
c           Source Definition
c
c -----
c -----
c
sdef par=p erg=4.000 cel=d5 x=d1 y=d2 z=d3
read file=liv.src noecho
# si1  sp1  si2  sp2  si3  sp3
  0   0   0   0   0   0
  0.1579 1  0.1579 1  0.2207 1
nps 10000000
dbcn 17j 1
prdmp j -10000

END FILE
```

LIST OF REFERENCES

- The Alliance for Radiation Safety in Pediatric Imaging 2009 *Image Gently...Step Lightly*
Retrieved September 2009 from
<http://spr.affiniscape.com/associations/5364/ig/index.cfm?page=584>
- American College of Radiology 2009 *Image Gently Campaign Named to Assocations Advance America Honor Roll* Retrieved September 2009 from
<http://www.acr.org/SecondaryMainMenuCategories/NewsPublications/FeaturedCategories/CcurrentACRNews/archive/ImageGentlyCampaignHonorRoll.aspx>
- Arnold R, Subramanian G, McAfee J, Blair R and Thomas F 1975 Comparison of tc-99m complexes for renal imaging *J. Nucl. Med.* **16** 357-67
- Attix F 2004 *Introduction to Radiological Physics and Radiation Dosimetry* (KGaA, Weinheim: WILEY-VCH Verlag GmbH & Co)
- Beddoe A H 1976 The microstructure of mammalian bone in relation to the dosimetry of bone-seeking radionuclides *Master's Thesis*
- Bolch W E, Shah A P, Watchman C J, Jokisch D W, Patton P W, Rajon D A, Zankl M, Petoussi-Henss N and Eckerman K F 2007 Skeletal absorbed fractions for electrons in the adult male: considerations of a revised 50-um definition of the bone endosteum *Radiat. Prot. Dosim.* **127** 169-73
- Bolch W E, Eckerman K F, Sgouros G and Thomas S R 2009 MIRD Pamphlet No. 21: a generalized schema for radiopharmaceutical dosimetry - standardization of nomenclature *J. Nucl. Med.* **50** 477-84
- Bouchet L, Bolch W, Howell R and Rao D 2000 S-values for radionuclides localized within the skeleton *J. Nucl. Med.* **41** 189-212
- Brosius F C, Waller B and Roberts W 1981 Radiation heart disease. Analysis of 16 young (aged 15 to 33 years) necropsy patients who received over 3,500 rads to the heart *Am. J. Med.* **70** 519-30
- Brownell G, Ellett W and Reddy A 1968 MIRD Pamphlet No. 3: absorbed fractions for photon dosimetry **9** 27-39
- Celsis P, Goldman T, Henriksen L and Lassen N 1981 A method for calculating regional cerebral blood flow from emission computed tomography of inert gas concentrations *J. Comput. Assist. Tomogr.* **5** 641-45
- Cherry S R, Sorenson J A and Phelps M E 2003 *Physics in Nuclear Medicine* (Philadelphia, PA: Saunders)

- Chiron C, Raynaud C, Maziere B, Zilbovicius M, Laflamme L, Masure M, Dulac O, Bourguignon M and Syrota A 1992 Changes in regional cerebral blood flow during brain maturation in children and adolescents *J. Nucl. Med.* **33** 696-703
- Christ A, Kainz W, Hahn E G, Honegger K, Zefferer M, Neufeld E, Rascher W, Janka R, Bautz W, Chen J, Kiefer B, Schmitt P, Hollenbach H P, Shen J, Oberle M, Szczerba D, Kam A, Guag J W and Kuster N 2010 The Virtual Family - development of surface-based anatomical models of two adults and two children for dosimetric simulations *Phys. Med. Biol.* **55** N23-N38
- Clark L D, Stabin M G, Fernald M J and Brill A B 2010 Changes in radiation dose with variations in human anatomy: moderately and severely obese adults *J. Nucl. Med.* **51** 929-32
- Cristy M 1980 Mathematical phantoms representing children of various ages for use in estimates of internal dose *ORNL/NUREG/TM-367* 1-110
- Cristy M and Eckerman K F 1987 Specific absorbed fractions of energy at various ages from internal photon sources. I. Methods *ORNL/TM-8381/V1* 1-100
- Cristy M and Eckerman K F 1987 Specific absorbed fractions of energy at various ages from internal photon sources. VI. Newborn *ORNL/TM-8381/V6* 1-72
- Dekaban A S 1978 Changes in brain weights during the span of human life: relation of brain weights to body weights and body heights *Ann. Neurol.* **4** 345-56
- Evans E, Lythgoe M, Anderson P, Smith T and Gordon I 1996 Biokinetic behavior of technetium-99m-DMSA in children *J. Nucl. Med.* **37** 1331-5
- Faw R E and Shultis J K 1999 *Radiological Assessment: Sources and Doses* (La Grange Park, IL: American Nuclear Society, Inc.)
- Gelfand M, Parisi M and Treves S 2011 Pediatric radiopharmaceutical administered doses: 2010 North American consensus guidelines *J. Nucl. Med.* **52** 318-22
- GlaxoSmithKline 2005 October *BEXXAR Package Insert* Retrieved December 6, 2011 from http://us.gsk.com/products/assets/us_bexxar.pdf
- Grandmaison G L, Clairand I and Durigon M 2001 Organ weight in 684 adult autopsies: new tables for a caucasoid population *Forensic Sci. Int.* **119** 149-54
- Hall E J and Giaccia A J 2006 *Radiobiology for the Radiologist, 6th Ed* (Philadelphia, PA: Lippincott Williams & Wilkins)
- Harrison J D and Streffer C 2007 The ICRP protection quantities, equivalent and effective dose: their basis and application *Radiat. Prot. Dosim.* **127** 12-8

Health Physics Society 2010 Radiation exposures from medical exams and procedures *Health Physics Society Fact Sheet*

Hobbs R F, Wahl R L, Lodge M A, Javadi M S, Cho S Y, Chien D T, Ewertz M E, Esaias C E, Ladenson P W and Sgouros G 2009 ^{124}I PET-based 3D-RD dosimetry for a pediatric thyroid cancer patient: real-time treatment planning and methodologic comparison *J. Nucl. Med.* **50** 1844-7

Hobbs R, Baechler S, Wahl R, He B, Song H, Esaias C, Frey E C, Jacene H and Sgouros G 2010 Arterial wall dosimetry for non-hodgkin lymphoma patients treated with radioimmunotherapy *J. Nucl. Med.* **51** 368-75

Hong X. and Sharma A 2010 December 15 *Expected Biodistribution of BEXXAR* (Washington University, Division of Nuclear Medicine) Retrieved December 6, 2011 from http://gamma.wustl.edu/newtfh/general/combined/small_118421.html

Hough M, Johnson P, Rajon D, Jokisch D, Lee C and Bolch W 2011 An image-based skeletal dosimetry model for the ICRP reference adult male - internal electron sources *Phys. Med. Biol.* **56** 2309-46

Hughes H 2005 Improved logic for sampling Landau straggling in MCNP5 *ANS Mathematics and Computation Topical Meeting* LA-UR-05-4404

Hull M, Morris C, Pepine C and Mendenhall N 2003 Valvular dysfunction and carotid, subclavian, and coronary artery disease in survivors of hodgkin lymphoma treated with radiation therapy *JAMA* **290** 2831-7

ICRP 1975 ICRP Publication 23: Report of the task group on reference man *Ann. ICRP* 1-476

ICRP 1979 ICRP Publication 30: Limits for intakes of radionuclides by workers *Ann. ICRP* **8**

ICRP 1988 ICRP Publication 53: Radiation dose to patients from radiopharmaceuticals *Ann. ICRP* **18**

ICRU 1992 Photon, electron, proton and neutron interaction data for body tissues *ICRU Report 46* (Bethesda, MD: ICRU)

ICRP 1998 ICRP Publication 80: Radiation dose to patients from radiopharmaceuticals *Ann. ICRP* **28**

ICRP 2002 ICRP Publication 89: Basic anatomical and physiological data for use in radiological protection: reference values *Ann. ICRP* **32** 1-277

ICRP 2007 ICRP Publication 103: 2007 recommendations of the international commission on radiological protection *Ann. ICRP* **37** 1-332

- ICRP 2008 ICRP Publication 106: Radiation dose to patients from radiopharmaceuticals – addendum 3 to ICRP Publication 53 *Ann. ICRP* **38**
- ICRP 2008 ICRP Publication 107: Nuclear decay data for dosimetric calculations *Ann. ICRP.* **38**
- ICRP 2009 ICRP Publication 110: Adult reference computational phantoms *Ann. ICRP* **39**
- Jeong J H, Kim C H, Yeom Y S, Cho S, Chung M S and Cho K W 2011 Direct Monte Carlo dose calculation using polygon-surface computational human model *Progress in Nuclear Science and Technology* **1** 130-3
- Joensuu H and Ahonen A 1987 Imaging of metastases of thyroid carcinoma with fluorine-18 fluorodeoxyglucose *J. Nucl. Med.* **28** 910-4
- Johnson P B, Whalen S R, Wayson M, Juneja B, Lee C and Bolch W E 2009 Hybrid patient-dependent phantoms covering statistical distributions of body morphometry in the U.S. adult and pediatric population *Proc. IEEE* **97** 2060-75
- Johnson P, Geyer A, Borrego D and Ficarrotta K 2011 The impact of anthropometric patient-phantom matching on organ dose: a hybrid phantom study for fluoroscopy guided interventions *Med. Phys.* **38** 1008-17
- Johnson P, Bahadori A, Eckerman K, Lee C and Bolch W 2011 Response functions for computing absorbed dose to skeletal tissues from photon irradiation - an update *Phys. Med. Biol.* **56** 2347-65
- Jokisch D W, Patton P W, Rajon D A, Inglis B A and Bolch W E 2001 Chord distributions across 3D digital images of a human thoracic vertebra *Med. Phys.* **28** 1493-504
- Jones A K, Bolch W E, Holman M M and Hintenlang D E 2006 Tomographic physical phantom of the newborn child with real-time dosimetry I. Methods and techniques for construction *Med. Phys.* **33** 3274-82
- Kolbert K S, Sgouros G, Scott A M, Bronstein J E, Malane R A, Zhang J, Kalaigian H, McNamara S, Schwartz L and Larson S M 1997 *J. Nucl. Med.* **38** 301-8
- Lægemiddelstyrelsen 2008 Summary of product characteristics for UltraTag – kit for radiopharmaceutical preparation *Product Pamphlet*
- LANL 2005 MCNX(TM) user's manual, version 2.5.0 *LA-CP-05-0369*
- Lee C, Lodwick D, Hasenauer D, Williams J, Lee C and Bolch W 2007 Hybrid computational phantoms of the male and female newborn patient: NURBS-based whole-body models *Phys. Med. Biol.* **52** 3309-33

- Lee C, Lodwick D, Hurtado J, Pafundi D, Williams J and Bolch W 2010 The UF family of reference hybrid phantoms for computational radiation dosimetry *Phys. Med. Biol.* **55** 339-63
- Lee C, Kim K P, Long D, Fisher R, Tien C, Simon S L, Bouville A and Bolch W E 2011 Organ doses for reference adult male and female undergoing computed tomography estimated by Monte Carlo simulations *Med. Phys.* **38** 1196-206
- Leggett R W 2001 Reliability of the ICRP's dose coefficients for members of the public. I. sources of uncertainty in the biokinetic models *Radiat. Prot. Dosim.* **95** 199-213
- Loevinger R 1969 Distributed radionuclide sources, In Attix F and Tochilin E *Radiation Dosimetry, 2nd Ed, Vol III, pp. 51-90* (New York: Academic Press)
- Marine P M, Stabin M G, Fernald M J and Brill A B 2010 Changes in radiation dose with variations in human anatomy: larger and smaller normal-stature adults *J. Nucl. Med.* **51** 806-11
- Medi-Physics, Inc. 1994 Neoscan gallium citrate Ga-67 diagnostic for intravenous use *Product Pamphlet*
- National Research Council 2005 *Health Risks from Exposure to Low Levels of Ionizing Radiation: BEIR VII – Phase 2* Washington, DC: National Research Council
- NCRP 1971 Report No. 38: Protection against neutron irradiation
- Nipper J C, Williams J L and Bolch W E 2002 Creation of two tomographic voxel models of paediatric patients in the first year of life *Phys. Med. Biol.* **47** 3143-64
- NIST 2011 December 9 *XCOM: Photon Cross Sections Database, 3.1* Retrieved January 11, 2012 from National Institute of Standards and Technology:
<http://www.nist.gov/pml/data/xcom/index.cfm>
- Pafundi D H 2009 Image-based skeletal tissue and electron dosimetry models for the ICRP reference pediatric age series *Doctoral Dissertation* 1-474
- Pafundi D, Lee C, Watchman C, Bourke V, Aris J, Shagina N, Harrison J, Fell T and Bolch W E 2009 An image-based skeletal tissue model for the ICRP reference newborn *Phys. Med. Biol.* **54** 4497-531
- Pafundi D, Rajon D, Jokisch D, Lee C and Bolch W E 2010 An image-based skeletal dosimetry model for the ICRP reference newborn - internal electron sources *Phys. Med. Biol.* **55** 1785-814
- Petoussi-Hens N and Zankl M 1998 Voxel anthropomorphic models as a tool for internal dosimetry *Radiat. Prot. Dosim.* **79** 415-8

- Petoussi-Henss N, Bolch W E, Zankl M, Sgouros G and Wessels B 2007 Patient-specific scaling of reference S-values for cross-organ radionuclide S-values: what is appropriate? *Radiat. Prot. Dosim.* **127** 192-6
- Petoussi-Henss N, Zankl M, Fill U and Regulla D 2002 The GSF family of voxel phantoms *Phys. Med. Biol.* **47** 89-106
- Prideaux A R, Song H, Hobbs R F, He B, Frey E C, Ladenson P W, Wahl R L and Sgouros G 2007 Three-dimensional radiobiologic dosimetry: application of radiobiologic modeling to patient-specific 3-dimensional imaging-based internal dosimetry *J. Nucl. Med.* **48** 1008-16
- Radiopharmacy, Inc. 2004 July *Monthly Scan, Volume 9, Issue 7* Retrieved December 6, 2011 from <http://www.radiopharmacy.com/NRC%20Newsletters/7.04.pdf>
- Rajon D A, Pichardo J C, Brindle J M, Kielar K M, Jokisch D W, Patton P W and Bolch W E 2006 Image segmentation of trabecular spongiosa by visual inspection of the gradient magnitude *Phys. Med. Biol.* **51** 4447-67
- Rubin M, Bruck E, Rapoport M, Snively M, McKay H and Baumler A 1949 Maturation of renal function in childhood: clearance studies *J. Clin. Invest.* **28** 1144-62
- Schlattl H, Zankl M and Petoussi-Henss N 2007 Organ dose conversion coefficients for voxel models of the reference male and female from idealized photon exposures *Phys. Med. Biol.* **52** 2123-45
- Schneider P J 1996 NURB curves: a guide for the uninitiated *MACtech: develop* **25**
- Segars W P 2001 Development and application of the new dynamic NURBS-based cardiac-torso (NCAT) phantom *Doctoral Dissertation* 1-221
- Segars W P and Tsui B M 2009 MCAT to XCAT: the evolution of 4-D computerized phantoms for imaging research *Pro. IEEE* **97** 1954-68
- Sgouros G, Frey E, Bolch W, Wayson M, Abadia A and Treves S 2011 An approach for balancing diagnostic image quality with cancer risk: application to pediatric diagnostic imaging of tc-99m-dimercaptosuccinic acid *J. Nucl. Med.* **52** 1923-9
- Shah A P, Bolch W E, Rajon D A, Patton P W and Jokisch D W 2005 A paired-image radiation transport model for skeletal dosimetry *J. Nucl. Med.* **46** 344-53
- Simonet W, Bronk J, Pinto M, Williams E, Meadows T and Kelly P 1988 Cortical and cancellous bone: age-related changes in morphologic features, fluid spaces, and calcium homeostasis in dogs *Mayo Clin. Proc.* **63** 154-60
- Sinclair L, Pafundi D and Bolch W E 2009 An image-based skeletal tissue model for the ICRP reference adult female *Master's Project*

- Smith T, Evans K, Lythgoe M, Anderson P and Gordon I 1996 Radiation dosimetry of technetium-99m-DMSA in children *J. Nucl. Med.* **37** 1336-42
- SNM 2011 February *Go with the Guidelines!* Retrieved June 4, 2012 from http://www.pedrad.org/associations/5364/files/ImGen11_Nu_Med_Poster.pdf
- Snyder W S, Ford M R, Warner G G and Watson S B 1975 MIRD Pamphlet No. 11: "S," Absorbed Dose Per Unit Cumulated Activity for Selected Radionuclides and Organs. 5-10
- Snyder W, Fisher H, Ford M and Warner G 1969 *Estimates of Absorbed Fractions for Monoenergetic Photon Sources Uniformly Distributed in Various Organs of a Heterogeneous Phantom* (MIRD Pamphlet No. 5. New York, NY: Society of Nuclear Medicine)
- Snyder W S, Ford M R and Warner G G 1978 *Estimates of Absorbed Fractions for Monoenergetic Photon Sources Uniformly Distributed in Various Organs of a Heterogeneous Phantom* (MIRD Pamphlet No. 5., revised New York, NY: Society of Nuclear Medicine)
- Spectrum Pharmaceuticals, Inc. 2011 November *Zevalin Package Insert* Retrieved December 6, 2011 from http://zevalin.com/v3/pdf/Zevalin_Package_Insert.pdf
- Spiers F W 1969 Determination of absorbed dose to bone and red marrow *Paper Presentation: Medical Radionuclides: Radiation Dose and Effects* Oak Ridge, TN
- Stabin M G 2005 *OLINDA 1.0 Documentation Package* User Manual
- Stabin M G, Eckerman K F, Bolch W E, Bouchet L. G and Patton P W 2002 Evolution and status of bone and marrow dose models *Cancer Biother. Radiopharm.* **17** 427-33
- Stabin M G, Sparks R B and Crowe E 2005 OLINDA/EXM: the second-generation personal computer software for internal dose assessment in nuclear medicine *J.Nucl. Med.* **46** 1023-7
- Stabin M, Brill A, Segars W, Emmons M, Gesner J and Milam R 2006 Realistic phantoms series for OLINDA/EXM 2.0 *J. Nucl. Med.* **47** (suppl. 1) 156P
- Stabin M, Farmer A, Sparks R and Pureskiy A 2010 OLINDA/EXM 2.0: a generational change *J. Nucl. Med.* **51** (suppl. 2) 308
- Treves S T 1995 *Pediatric Nuclear Medicine, 2nd Ed* (New York, NY: Springer-Verlag New York, Inc)
- Whitwell J R 1973 Theoretical investigations of energy loss by ionizing particles in bone *Master's Thesis*

X-5 Monte Carlo Team 2003 MCNP - a general Monte Carlo n-particle transport code, version 5
LA-UR-03-1987

Xu X, Chao T and Bozkurt A 2000 VIP-Man: an image-based whole-body adult male model constructed from color photographs of the Visible Human Project for multi-particle Monte Carlo calculations *Health Phys.* **78** 476-86

Zankl M, Fill U, Petoussi-Henss N and Regulla D 2002 Organ dose conversion coefficients for external photon irradiation of male and female voxel models *Phys. Med. Biol.* **47** 2367-85

BIOGRAPHICAL SKETCH

Michael Brice Wayson was born in Orlando, FL. The oldest of three boys to Mark and Niki Wayson, he was raised mostly in Brandon, Florida (a suburb of Tampa), graduating from Bloomingdale Senior High School in 2004. He graduated *cum laude* with a B.S. in nuclear engineering in December 2007 and an M.S. in nuclear engineering sciences in December 2009, both degrees earned from the University of Florida. Michael married his best friend and soul mate, Leslie Wayson, in January 2011.

Upon completion of his Ph.D. program, Michael will begin a two-year residency in diagnostic medical physics at Shands Hospital at the University of Florida in Gainesville, FL. Michael's interest in the medical field began at an early age when he started learning about cancer diagnosis and treatment from his father who works in the oncology division of a pharmaceutical company. His passion for physics ignited while taking advanced placement physics during his senior year of high school. During his undergraduate studies, he discovered the medical physics program which has provided him with a career opportunity combining both interests. Michael's long-term career goal is to become the chief clinical diagnostic medical physicist at a hospital located in the southeast region of the United States.

In his personal time, Michael enjoys traveling with his wife. He has visited 21 of the 50 United States in addition to Jamaica, the Cayman Islands, Canada, Italy, and Austria. He plans on making another trip to Italy in the coming year. He also enjoys playing competitive sports including basketball, golf, snow skiing and football. Michael has studied classical piano performance since age six and also enjoys composing music in a variety of genres.